DESIGN AND CHARACTERIZATION OF ACTIVELY-MOVING POLYMERS OBTAINED VIA DUAL-CURING PROCESSING

Alberto Francisco Belmonte Parra

Alberto Francisco Belmonte Parra

DESIGN AND CHARACTERIZATION OF ACTIVELY-MOVING POLYMERS OBTAINED VIA DUAL-CURING PROCESSING

DOCTORAL THESIS

Supervised by:
Prof. Silvia De la Flor and Prof. Xavier Fernández-Francos

Department of Mechanical Engineering

UNIVERSITAT ROVIRA I VIRGILI

Tarragona, Spain (2017)

UNIVERSITAT ROVIRA I VIRGILI
DESIGN AND CHARACTERIZATION OF ACTIVELY-MOVING POLYMERS OBTAINED VIA DUAL-CURING PROCESSING
Alberto Francisco Belmonte Parra

UNIVERSITAT ROVIRA I VIRGILI

Departament d'Enginyeria Mecànica
Campus Sescelades, Edifici E4
Avinguda dels Països Catalans, 26
43007 Tarragona, Spain

Professor Silvia De la Flor of the Department of Mechanical Engineering at the Universitat Rovira i Virgili and Professor Xavier Fernández-Francos of the Department of Heat Engines at ETSEIB, Universitat Politècnica de Catalunya,

Certify:

that the Doctoral Thesis, entitled "Design and characterization of actively-moving polymers obtained via dual-curing processing" presented by Alberto Francisco Belmonte Parra for the award of the degree of Doctor, has been carried out under our supervision and meets the requirements to qualify for the International Mention.

Tarragona, November 20th, 2017

Doctoral Thesis Supervisors

Prof. Silvia De la Flor

Prof. Xavier Fernández-Francos

UNIVERSITAT ROVIRA I VIRGILI
DESIGN AND CHARACTERIZATION OF ACTIVELY-MOVING POLYMERS OBTAINED VIA DUAL-CURING PROCESSING
Alberto Francisco Belmonte Parra

Agraïments

Podria dir que en aquest precís instant em sento feliç alhora que trist. Cada paraula que escric apropa més el final d'aquesta etapa de la meva vida… Han sigut tres anys intensos, tres anys plens de reptes i objectius que han resultat en hores i hores de laboratori, d'ordinador i de mals de cap. Però sobre tot d'alegries per sobre d'aquells moments de frustració, de motivació personal per sobre d'aquells reptes que semblaven inassolibles i de valentia per sobre d'aquells moments en que et planten davant de tothom a defensar el teu treball. I en això hi han molts que tenen a veure, molts que voldria agrair en aquest racó de la tesis.

Les meves primeres paraules són pels meus directors de tesis, Silvia De la Flor i Xavier Fernández-Francos. Gràcies, això no hagués estat possible sense el vostre vot de confiança, i tampoc sense els ànims i suport constant que heu dipositat en mi en tot moment.

Vull agrair a altres membres del grup que d'una manera o altre m'han ajudat tan personal com professionalment. A Xavier Ramis que, en certa manera, ha sigut el nexe de unió que ha fet possible endinsar-me en aquest camí. A Àngels Serra que, com sempre he dit, ha sigut la meva "jefa" de laboratori. Gràcies per acollir-me i presentar-me al grup de laboratori que ara considero la meva família de Tarragona.

Com he dit, han sigut tres anys d'alts i baixos, però certa persona sempre ha estat al meu costat, recolzant-me en totes les decisions que he pres, essent la primera el trasllat a Tarragona. El seu suport constant i sobre tot la seva companyia m'han ajudat a seguir endavant en tot moment. M'has ensenyat a dir que sí, m'has ensenyat a no dubtar, a prendre decisions i a equivocar-me Perquè en aquesta vida un s'ha d'equivocar per aprendre, però per equivocar-se un s'ha d'arriscar. Moltes gracies.

Vull agrair el suport rebut per part de la meva família. Gràcies per deixar-me escollir el meu camí des de que vaig començar a tenir consciència de la vida. Per aconsellarem i fer possible les meves decisions. Gràcies per confiar en mi quan la majoria ja s'endinsaven en el món laboral i a mi em va donar per refusar una oferta de treball per continuar en la universitat.

Companys… amics, família de Tarragona, sense vosaltres aquest camí hagués estat massa tortuós. Gràcies per les alegries, rialles i sobre

tot, els ànims i el suport incondicional en els mals moments. Espero haver sigut un bon amic i company per vosaltres. David, tu vas ser el primer en "aguantar-me", ho sento… Gràcies, sobre tot per aquells primers moments que són els més difícils. Cristina, malgrat el teu gust musical que per desgracia sempre s'ha imposat al laboratori… Gràcies per entendrem, per les dobles converses que manteníem. Xavier… les noticies matinals ja no són lo mateix sense tu. Dailyn, el meu icona de paciència, tranquil·litat i ànims al laboratori. I als altres que he anat coneixent durant aquests tres anys. Isaac, quan anem a la piscina…? avui toca cervesa no? Rubén s'apunta. Pues ja anem demà doncs! Als *italians del laboratori* (ho sento, hi ha massa diversitat cultural al laboratori jejeje, de fet ja ens supereu en número…). Als d'altres laboratoris… Lorena, espero haver-te ajudat, sobre tot en els moments finals de la tesis. Carmen i Pere, gràcies per aquests últims mesos de tesis, un cafè i una conversa quan estàs endinsat en l'escriptura ajuda molt. Krzys, el meu icona de responsabilitat, Dresden no hagués estat igual sense tu! Alguns que han passat només uns mesos … Yvonne, thank you for being so happy all the time, you inspired me. We miss you a lot. També vull agrair els primers companys que vaig tenir al laboratori de mecànica en el primer any de tesis. Finally, to all the guys I met in Naples during my stay abroad. I never felt alone there, thank you so much. I also want to acknowledge Veronica and Piero, they accepted and supported me all the time.

Sé que em deixo a uns quants, per això vull agrair a tots aquells que no hagi mencionat a dalt. Considero que tothom a contribuït en certa manera en aquesta etapa de la meva vida.

Mai me penediré d'haver escollit aquest camí.

ALBERTO

"*The scariest moment is always just before you start*"

Stephen King

UNIVERSITAT ROVIRA I VIRGILI
DESIGN AND CHARACTERIZATION OF ACTIVELY-MOVING POLYMERS OBTAINED VIA DUAL-CURING PROCESSING
Alberto Francisco Belmonte Parra

Abstract

In this investigation we delve into the field of stimuli-responsive polymers, specifically those responding with dimensional changes. They are called **Actively-moving polymers** (AMPs) because of the ability to adapt and transform their original shape upon appropriate stimulation, thus, in response to environmental changes. AMPs break down in two classes: **shape-memory polymers** (SMPs) and **shape-changing polymers** (SCPs). The main difference lies in their mechanism of shape-transformation. The former can achieve and retain a temporal shape through and external programming, to further recover the original shape upon stimulation, whereas the latter can adopt a temporal shape as long as the stimulus is applied and shift to the original shape when it is removed. Essentially, SMPs can maintain the temporal shape but a programming is required, while SCPs can reversibly shift from the original shape to the temporal shape but cannot retain the latter.

AMPs are **"intelligent" materials** capable to adapt their shape on-demand. This makes them interesting in many fields, such as biomedical applications, aerospace, microelectronics and robotics. Among the different application fields, in this doctoral thesis we focus on more mechanically demanding applications, such as smart actuators and biomimetics (i.e. soft robotics). The use of **thermoset-based AMPs** makes possible to attain the mechanical requirements in terms of strength, deformability and resistance. Moreover, the use of **epoxy-based thermoset** makes them attractive in aggressive environments, such as out-of-space, remote places on earth (i.e. mountain peaks) or industrial applications because of the excellent properties of the epoxy resin (electrical isolation, chemical resistance and low toxicity).

To this end, **we have used thiols and epoxy compounds of different functionality and chemical structure to develop and characterize SMPs with different structural and thermomechanical properties**. The "thiol-epoxy" reaction is a click reaction under the presence of tertiary amines. Click reactions are interesting due to the versatility, selectivity and efficiency, enhancing the control of the reaction kinetics and yielding to homogeneous network structures. This is of utmost importance when developing SMPs to achieve controlled shape-memory response. The effect of the thermomechanical and structural properties of the SMPs with the obtention of the temporary shape in terms of stress/strain limits, the fixation performance and the efficiency recovering the original shape, have been studied. Moreover, the relation

between the structural properties and structural relaxation with the recovery of the original shape has been investigated in order to define useful tools for the operational design of the SMPs. Finally, the effect of the programming conditions with the recovery time, temperature and speed have been thoroughly analysed.

On the other hand, **epoxy and dicarboxylic acids have been proposed for the development of SCPs**, more specifically, **liquid-crystalline networks** (LCNs, a class of SCPs that response upon thermomechanical or photomechanical stimulus). Dicarboxylic acids of different aliphatic chain length have been used to obtain LCNs with different liquid-crystalline transition temperatures, properties and thermomechanical response. The effect of their properties with the elongation-contraction response upon different stimulation conditions have been studied. Moreover, to analyse their potential capabilities as mechanical actuators, the LCNs have been investigated under constrained conditions to observe the stress generated.

Nevertheless, many applications demand materials with **complex shape designs** which is a difficult task when working with thermosetting polymers. The curing or fabrication of thermosets is a complex process involving drastic physical changes, from a liquid-like mixture to the solid material, taking place in tight times. This makes difficult to control the processing of complex shapes. In addition, the final shape cannot be processed anymore due to the presence of crosslinks within the network.

Considering the above, we have proposed **the use of dual-curing processing techniques for the development of AMPs**. Dual-curing processing makes possible to develop a solid-like, deformable and stable intermediate material after the 1st curing stage, which can be processed into complex shaped designs and fixed through the 2nd curing stage. This technique requires the combination of two compatible polymerization processes taking place sequentially. Usually, this is achieved by combining reactions triggered by different stimulus (i.e. UV-light and heat), but it is also possible by different reaction kinetics or the presence of latent catalysts.

Having in mind the potential capabilities as SMPs of the studied “thiol-epoxy” systems, **we took advantage of a dual-curing system based on off-stoichiometric “thiol-epoxy” mixtures developed by our group of research**. This system lies on the combination of the “thiol-epoxy” click reaction, which takes place at low temperature under the presence of tertiary amines, and the further homopolymerzation of the epoxy excess that is triggered at higher temperature. Therefore, it combines the

enhanced control of the structural properties due to the click chemistry and permit the development of complex shaped designs. Firstly, we have analysed different "thiol-epoxy" systems in terms of structural, physical and thermomechanical properties of the different intermediate and final materials obtained varying the "thiol-epoxy" ratio. Then, **we have developed and investigated the shape-memory response of SMPs with complex shaped designs** (i.e. spring, plaited and bent shapes). The bent-shaped designs have been investigated under unconstrained, partially-constrained and fully constrained conditions as potential mechanical actuators.

Finally, in view of the increasing demand of autonomous mechanisms, **we have combined the "thiol-epoxy" dual-curing processing with the studied LCNs to achieve thermally-triggered free-standing actuators**. Free-standing actuators are capable to shift from one shape to another in complex three-dimensional designs only upon thermal stimulation, thus, neither programming (SMPs), nor external force (LCNs) are required to attain the actuation. This is possible thanks to the mismatch between the LCN with the "thiol-epoxy" matrix that is elastically deformed when the LCN contracts, promoting the further elongation of the LCN. Free-standing actuators with different flexural designs have been assembled and analysed in view of controlling the level and rate of actuation. With this, a complex 3D motion design that actuates autonomously under heating-cooling processes has been designed, assembled and tested. Moreover, an analytical model has been developed to predict the actuation level of the different actuators depending on the design and structural properties.

UNIVERSITAT ROVIRA I VIRGILI
DESIGN AND CHARACTERIZATION OF ACTIVELY-MOVING POLYMERS OBTAINED VIA DUAL-CURING PROCESSING
Alberto Francisco Belmonte Parra

Table of Contents

UNIVERSITAT ROVIRA I VIRGILI
DESIGN AND CHARACTERIZATION OF ACTIVELY-MOVING POLYMERS OBTAINED VIA DUAL-CURING PROCESSING
Alberto Francisco Belmonte Parra

List of abbreviations

AMP	Actively-Moving Polymer
SMP	Shape-Memory Polymer
SCP	Shape-Changing Polymer
SCE	Shape-Changing Effect
SME	Shape-Memory Effect
SMR	Shape-Memory Response
SMC	Shape-Memory Cycle
LCN	Liquid-Crystalline Networks
LC	Liquid-Crystalline
$\mathbf{T_{trans}}$	Transition Temperature
$\mathbf{T_g}$	Glass Transition Temperature
$\mathbf{T_m}$	Melting Temperature
$\mathbf{T_{prog}}$	Programming Temperature
$\mathbf{T_g^{E'}}$	Onset Temperature
$\mathbf{T_s}$	Setting Temperature
$\boldsymbol{\varepsilon_D}$	Strain after Deformation
$\boldsymbol{\varepsilon_u}$	Programmed Strain
$\boldsymbol{\varepsilon_P}$	Permanent Strain
$\mathbf{T_r}$	Recovery Temperature
$\mathbf{F_{rec}}$	Recovery Force
$\boldsymbol{\sigma_{rec}}$	Recovery Stress
$\boldsymbol{\sigma_D}$	Programmed Stress
LCE	Liquid-Crystalline Elastomer
S	Ordering Parameter (LC networks)
P-M	Polydomain-to-Monodomain
$\mathbf{T_{iso}}$	Isotropization Temperature
$\mathbf{T_{aniso}}$	Anisotropization Temperature

DMA	Dynamic-Mechanical Analysis
DSC	Differential Scanning Calorimetry
TMA	Thermomechanical Analysis
SEM	Scanning Electron Microscopy
G	Shear Modulus
E	Elastic Modulus
G' / E'	Storage Moduli
G'' / E''	Loss Moduli
FWHM	Width at Half-Height
$\mathbf{T_c}$	Curing Temperature
$\mathbf{x_{gel}}$	Conversion at Gelation
$\boldsymbol{\sigma_b}$	Stress at Break
$\boldsymbol{\varepsilon_b}$	Strain at Break
$\mathbf{R_r}$	Shape-Recovery Ratio
$\mathbf{R_f}$	Shape-Fixation Ratio
W/V	Elastic Energy
$\mathbf{F_{prog}}$	Programming Force
$\mathbf{V_r}$	Shape-Recovery Rate
$\mathbf{T_{end}}$	End Temperature
$\mathbf{T_{half}}$	Half Temperature
$\mathbf{T_{peak}}$	Peak Temperature
W	Work Output
$\mathbf{F_{SR}}$	Recovery Force
$\mathbf{T_\infty}$	Isothermal Temperature
$\mathbf{t_{SR}}$	Isothermal Recovery-Time
$\mathbf{T_B}$	Bending Temperature
$\mathbf{T_U}$	Unbending Temperature
$\mathbf{t_B}$	Bending Time
$\mathbf{t_U}$	Unbending Time

B_{rate}	Bending Rate
U_{rate}	Unbending Rate
GT	Glassy Thermoset

UNIVERSITAT ROVIRA I VIRGILI
DESIGN AND CHARACTERIZATION OF ACTIVELY-MOVING POLYMERS OBTAINED VIA DUAL-CURING PROCESSING
Alberto Francisco Belmonte Parra

Chapter I

Introduction and Objectives

I

UNIVERSITAT ROVIRA I VIRGILI
DESIGN AND CHARACTERIZATION OF ACTIVELY-MOVING POLYMERS OBTAINED VIA DUAL-CURING PROCESSING
Alberto Francisco Belmonte Parra

I.1 Actively-moving polymers

Actively-moving polymers (AMPs) are stimuli-responsive materials that undergo large physical changes in response to an external stimulus[1]. The concept "stimuli-responsive" is inspired from the nature accounting for "smart" mechanisms of some living beings for survive and longevity by adaptation to environmental changes. The key element in these mechanisms is the transmission and amplification of small-scale strains into large-scale motion in response to external stimuli.

An example of natural mechanism is the resurrection plant *Selaginella lepidophyla* which exploits the principle of the cellulose orientation in response to moisture. It responses to dried and wet environments to limit photoinhibitory and thermal damages caused by arid environments: when dehydrated, the plant compactly curls to form a rough sphere, thus, reducing the solar radiation in the inner part[2]. Another example of natural adaptive motion is the bacteria flagella that is motile under the presence of glucose because of the formation of an electrical potential or pH gradient across the membrane that promotes the movement of the bacteria to favoured environments[3].

Adaptive movements in living beings has inspired many scientists in the development of smart devices that show complex shape transformations in response to external stimuli. AMPs are the straight synthetic competitors of natural mechanisms as a means of energy storing and release mechanisms. Their low-density and large-scale motion in response to external stimuli make them attractive for a wide range of applications in the field of soft actuators.

According to Behl and Lendlein[1], AMPs can be classified depending on their motion behaviour as **shape-memory polymers** (SMPs) and **shape-changing polymers** (SCPs). In both classes, the physical change or motion is caused by stimulation of molecular switching domains (small-scale changes) and the elastic response of their crosslinked networks (large-scale motion). In **SCPs**, the stimulation causes a global change in their shape that persists as long as they are exposed to the stimulus. Once the stimulus is removed, the original shape is recovered. This is called **shape-changing effect** (SCE). An example of SCP is presented in Figure I-1. The acrylate-based liquid-crystalline polymer elongates and contracts in response to the temperature change and to the weight of the hanging fasten. The temperature change stimulates the switching domains (in this

case, triggers the **liquid-crystalline** (LC) transition) and the weight promotes and aligns the dimensional change[4].

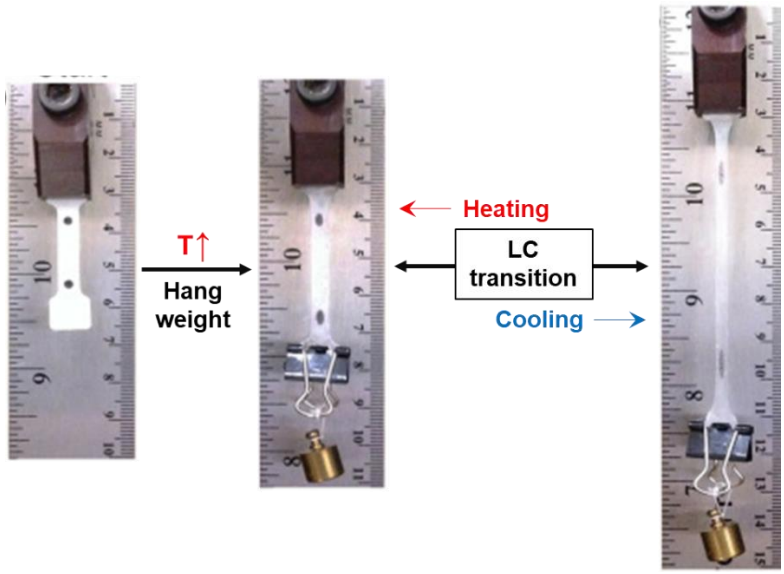

Figure I-1. SCE in acrylate-based liquid-crystalline elastomers by Yakacki et al.[4].

In contrast, **SMPs** can adopt and retain a new temporal shape after a mechanical procedure to further recover the original shape in response to an external stimulus through the so-called **shape-memory effect** (SME). An example of SMP is presented in Figure I-2. The polyurethane-based polymer is programmed from a round-shape into a star-shape through a thermomechanical procedure. Afterwards, the original shape is recovered upon stimulation of the network (in this case, triggering the glass transition)[5].

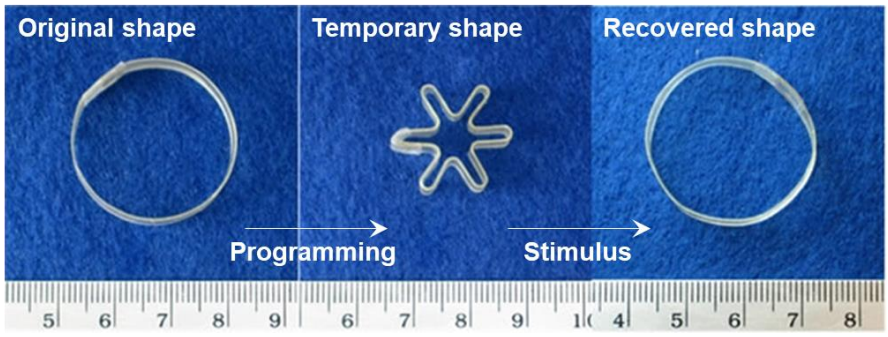

Figure I-2. SME in polyurethane-based SMPs by Huang et al.[5].

AMPs are characterized by network crosslinks that are responsible of memorizing the original shape. The nature of the crosslinks breaks

down the AMPs in two different subclasses: **physically** and **covalently crosslinked AMPs**. Physical crosslinking is caused by ordered phases (crystals) in semi-crystalline networks and chain entanglements in amorphous networks, whereas covalent crosslinks arise from chemical-bonding among monomers, some of them with three or higher functionality. The phase transitions, including melting, crystallization and LC transitions, as well as network relaxation processes, including glass transition and vitrification, and other phenomena such as swelling/deswelling effects are the responsible of the SME and SCE.

The **SCE** is mainly found in **liquid-crystalline networks** (LCN), caused by the induced stress-alignment of the LC domains, producing a macroscopic elongation that is further recovered through the disordering of the LC domains and the elastic response of the crosslinked network[6]. It can be also found in other polymers such as crosslinked hydrophilic polymers (hydrogels) through the swelling/deswelling effect or ability to swell in an aqueous environment because of their high water affinity, thus, increasing their volume[7–9]. The **SME** is mainly found in crosslinked glassy and semi-crystalline networks and it is caused by the drastic change in the internal volume suffered by the polymer during thermal transition processes (i.e. glass transition and melting transition) that makes possible large and controlled deformation protocols towards new and temporary shapes. The temporary shape is further stabilized by freezing the network mobility. Finally, the original shape is recovered through the softening of the network upon stimulation (typically heating above the structural transition).

Essentially, **SCPs** present a single and reversible shape-transformation in response to a stimulus (i.e. thermomechanical and photomechanical stimuli) which is limited to their network structural architecture, whereas **SMPs** can adopt different shape-transformation protocols in response to a stimulus (i.e. heat or UV-light), but a shape-programming procedure is required each time.

I.1.1 Shape-memory polymers

Shape-memory polymers are a class of stimuli-responsive materials with programmable shape-transformation in response to an external stimulus. As stated in section I.1 this ability is called SME and consists of an initial programming of the temporary shape, usually a thermomechanical procedure, and the further recovery of the original shape upon stimulation (typically heating)[10].

The **SME** was first proposed by Vernon in 1941 in a US patent of new materials for dental restoration naming the effect "elastic memory"[11]. It was not until 1960 when the shape-memory terminology was used for the well-known heat-shrinkable tubes and films made of polyethylene to protect connections, joints and conductors[12–14]. From the 1980's the interest in the "shape-memory" polymers substantially increased[15]. Most of the early examples in the shape-memory field are polyurethanes due to the discovery of segmented polyurethane SMPs by Mitsubishi Heavy Industries Ltd. Other relevant examples include polynorbornene, poly(trans-isoprene) and styrene–butadiene copolymers based SMPs[16].

SMPs enclose a wide-range of applications that have been exploited step by step along their history. The early stage was mainly focused in industrial applications due to the emerging material of that age, the polyethylene. Nevertheless, during the last decades, the progress and design of new polymeric networks and the appearance of new research fields such as aviation, electronics and more recently, nanotechnology, biotechnology and robotics, have branched out their scope. From surgical implants[17], sutures[18], cardiovascular stents[19] and catheters[20] in biomedical applications, through self-morphing and self-deploying structures[21] in aviation, to smart open-closing mechanisms[22,23] in industrial applications, the SMPs have become an interesting and full of possibilities field of research to cover the increasing demand of materials for smart applications.

I.1.1.1 Shape-memory effect

The **SME** is the ability of a SMP to store and release large energy inputs as a means of shape-transformation, hence, generating motion. The SME is not an intrinsic property of the polymer, but an external programming is necessary to reconfigure and adapt the network structure.

As introduced in section I.1.1 the **original shape** is given by the curing process or conventional fabrication of the polymer and it is **"memorized"** through the **permanent physical** or **chemical crosslinks**. From an energetic point of view, the programming of the temporary shape consists of an energy input imposed to overcome an energy barrier between the original and the temporary shapes (the SME is illustrated in Figure I-3 by Huang et al.[5]).

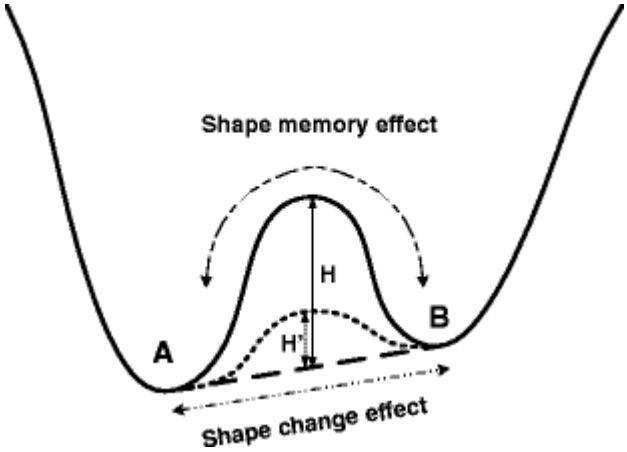

Figure I-3. Illustration of the energetical barrier for the SME and SCE by Huang et al.[5].

Usually, the programming is a thermomechanical process in which the switching domains of the network (i.e. reversible bonds or transition phases) are activated by increasing the temperature close to or above the **transition temperature** (T_{trans}) (i.e. the **glass transition temperature** (T_g) in covalently-crosslinked networks and the **melting temperature** (T_m) in physically-crosslinked networks). When the switching domains are activated, the network structure is more flexible and permits a deformation protocol (energy input) towards the new and temporary shape. If the applied deformation is maintained, the temporary shape can be stabilized below T_{trans}, thus, deactivating the switching domains. The hindrance of the chains at low temperature caused by the drastic decrease of the internal volume and/or the formation of physical interactions such as chain entanglements or physical bonding, impedes the recovery of the original state of the network. Upon appropriate stimulation of the switching domains, that is, triggering the structural transition, the original shape can be recovered thanks to the stored energy in the permanent crosslinks during the programming[24,25].

Considering the above, the **SME** can be interpreted as an entropic change associated to the conformation of the chains. After programming the temporary shape, the distortion the chains cause a transition from an equilibrium high entropic state to a non-equilibrium low entropic state stabilized by the network hindrance. Upon stimulation, the force driven by the entropic change causes the shape-recovery.

Other **non-thermally-induced SMEs** are found depending on the nature of the polymer. As an example, polymers containing photo-responsive molecules, such as, azobenzene molecules, are programmed

through **photomechanical** processes due to the molecular orientation of the azobenzene molecules that enhances or limits the network mobility, and the shape-recovery is triggered upon exposure to light[26–29].

Essentially, the SME consists of a programming and recovery cycle, commonly called **shape-memory cycle** (SMC), that can be repeated several times. In the next sections, the programming of the temporary shape (step 1) and the recovery of the original shape (step 2) are explained in detail considering thermomechanical programming and heat-induced recovery because the SMPs studied in this investigation are based on thermal structural transitions.

Step 1: Programming of the temporary shape

As stated above, the first step of the SME is the programming of the temporary shape. The programming involves a deformation step carried out at a temperature close to T_{trans}, the **programming temperature** (T_{prog}). According to the temperature region of the transition, Li et al.[30] classified the programming in cold (glassy region), warm (transition region) and hot programming (above the transition region). The straight difference between cold and hot programming lies on the mechanical stress/strain response of the SMP during the deformation step, which leads to completely different recovery processes. **Cold programming** mainly involves energetic forces, whereas **hot programming** are mostly entropic forces. This directly affects the performances fixing the temporary shape and recovering the original shape: cold programming leads to stress relaxation and chains friction resulting, in some cases, in irrecoverable structural damages, thus, worsening both, the fixation and recovery processes. In contrast, hot programming leads to more efficient and homogeneous recovery processes but considerably narrows the stress/strain limits during the deformation step.

Indeed, **warm programming** combines both, energetic and entropic forces due to the viscoelastic response of the network at the vicinity of T_{trans}. This can lead, at certain conditions, to enhanced stress/strain limits. Yakacki et al.[31] and Rousseau et al.[32] found that at a certain temperature below T_g related to the onset point of the modulus drop in thermo dynamic-mechanical analysis (the **onset temperature** ($T_g^{E'}$)), the **stress/strain limits** are three-to-five times enhanced in many polymeric materials. Nevertheless, warm programming also promotes stress relaxation and viscous friction between the chains that may worsen the recovery performance.

Generally speaking, cold programming leads to tougher and elastic stress/strain response, whereas warm programming is influenced by the

viscoelastic response of the network and hot programming leads to weak and elastic responses. In chapter III the effect of T_{prog} with both, the programming and recovery processes, is further discussed and analysed for "thiol-epoxy"-based SMPs.

After the deformation step, the temporary shape is stabilized by freezing the network below T_{trans} at a temperature called **setting temperature** (T_s,) thus, a cooling step is imposed. The cooling rate has a direct effect on the **aging behaviour** of the polymer. As it is well-known, polymeric networks in the glassy state are under a non-equilibrium state that is balanced by the low mobility of the chains. However, long periods of time lead to a progressive, although slow, transition towards the equilibrium state. This transition affects the thermal and physical relaxation of the network when it is heated up above T_{trans} (i.e. T_g or T_m), hence, directly affects the retention of the temporary shape and recovery of the original shape in SMPs. Many studies demonstrated that programmed SMPs progressively lose their temporary shape with the time and the further recovery of the original shape becomes more drastic[33,34]. In this investigation rapid cooling has been imposed to remove the effect of aging, that must be studied separately, on the characterization of the SMPs.

Step 2: Recovery of the original shape

The recovery of the original shape is divided in three different categories: **unconstrained** (stress-free), **partially-constrained** and **fully constrained** recovery processes.

Unconstrained recovery represents the definition of a SMP, a material capable to change its shape and recover the original or "memorized" shape. However, SMPs are mostly utilized under intermediate conditions between fully and unconstrained conditions. In medical applications, shape-memory stents must expand inside a blood vessel, hence, experiencing some resistance; in industrial applications, opening-closing mechanisms suffer the forces of the medium (i.e. in water pipelines) and fastening mechanisms, such as, joints, generate a stress rather than recover the original shape.

In Figure I-4(a), the unconstrained recovery process is shown in a typical strain-temperature plot, where the strain represents the dimensional change and its quantification depends on the type of loading (i.e. tensile, bending or compression). In Figure I-4(b), the unconstrained SME is schematized. As can be seen in Figure I-4(b), during the programming process a strain is fixed in form of a temporary shape, the **programmed strain** (ε_U), that is further recovered through the recovery

process, however, the recovered shape may suffer a **permanent strain** (ε_P) related to plastic or irrecoverable deformation. The unconstrained recovery is characterized by the efficiency achieving the original shape, hence, reducing ε_P. Commonly, this efficiency is related to the drastic response of the polymer network during the transition process and the roughness of the programming process.

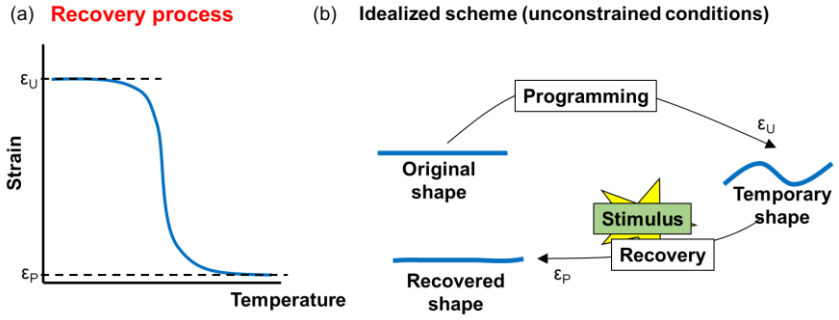

Figure I-4. Unconstrained recovery process: (a) strain-temperature plot and (b) idealized scheme of the process.

Many researches have demonstrated that the dynamics of the transition process is the key factor controlling the recovery process. As stated above, the shape-transformation is caused by the entropic change of the chains conformation. From a structural point of view, the relaxation mechanism of the network is therefore the responsible of this entropic change. Network structures with broad relaxation processes show slower recovery processes, whereas, drastic relaxations promote higher recovery rates and recovery ratios. Yakacki et al.[35] demonstrated the ability to control the unconstrained recovery time and temperature by tailoring the glass transition in acrylate-based glassy SMPs. On the other hand, Nair et al.[36] showed an approach to increase the recovery rate by forming homogeneous network structures, thus, narrow relaxation processes, through unique thiol-ene step-growth mechanism under photopolymerization.

Epoxy-based SMPs present excellent recovery performance mostly due to the abrupt decrease of the modulus (2 or 3 orders of magnitude) suffered during the glass transition that permits the recovery of large deformation processes. Several reports on epoxy-based systems can be found in the literature (i.e. epoxy-amines, epoxy-oxazolidone, epoxy-phenol and epoxy-anhydride systems)[37–49]. In this investigation, the potential shape-memory capabilities in “thiol-epoxy” based SMPs are studied and discussed in chapter III. The interest of using “thiol-epoxy” systems as SMPs is discussed in section I.2.

In **partially-constrained conditions**, the SMP is subject to an external force or stress, the **recovery force** or **stress** (F_{rec}) or (σ_{rec}), during the recovery process, thus, the original shape is partially-recovered, and a work output is generated. In Figure I-5(a) the partially-constrained recovery process is shown in a typical strain-temperature plot and the SME is schematized in Figure I-5(c). In addition, the typical equilibrium elastic stress/strain response of a SMP at a temperature above T_{trans} has been represented in Figure I-5(b) to further relate it with the **shape-memory response** (SMR).

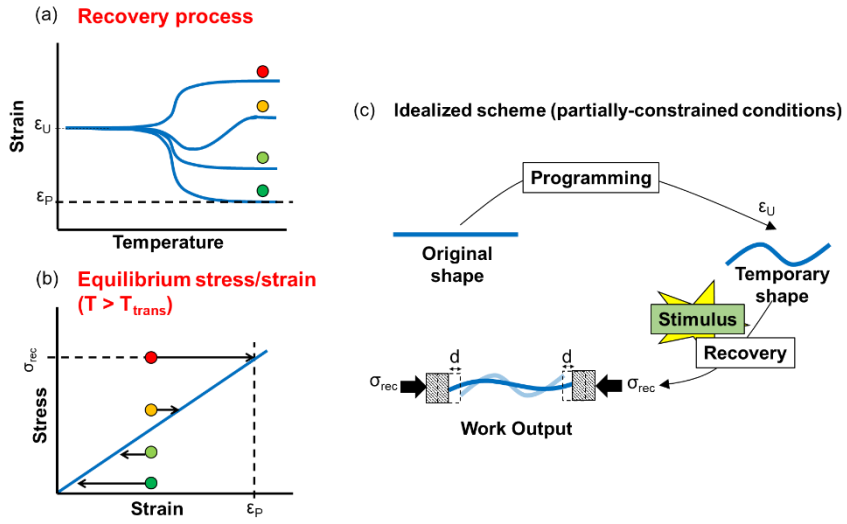

Figure I-5. Partially-constrained recovery process: (a) strain-temperature plot; (b) stress-strain equilibrium elastic response at $T > T_{trans}$ and (c) idealized scheme of the process.

As it can be seen in Figure I-5(a,) the process strongly depends on σ_{rec} and the material properties. The arrows in the equilibrium elastic stress/strain plot (Figure I-5(b)) represent the theoretical path of the SMP during the recovery process towards the stress/strain equilibrium. In unconstrained conditions, the equilibrium point corresponds to zero-stress and zero-strain, however, the presence of an external stress displace this equilibrium towards a higher strain. If σ_{rec} is higher than the corresponding stress in the equilibrium state, the SMP partially-recovers the original shape towards this new equilibrium (in Figure I-5(b) see the green points and arrows indicating the path followed by the SMP during the heating procedure and in Figure I-5(a) the resulting path in terms of shape-recovery). Otherwise, if σ_{rec} is lower than the equilibrium stress, the SMP elongates towards the new equilibrium, thus, a negative work output is generated (see the red dot in both graphics). A combined response is observed when the equilibrium stress and the σ_{rec} are similar (see the

curve corresponding to the yellow dot). In that case, an initial recovery is appreciated followed by a further elongation of the SMP. This is caused by the evolution of the equilibrium curve during the transition process. During this process, at certain temperatures, σ_{rec} is lower than the equilibrium stress, hence, the initial recovery[50–52].

Few studies focused on the effect of σ_{rec} and the SMP structural properties with the recovery process have been carried out in comparison with under unconstrained conditions. Lakhera et al.[53] investigated the partially-constrained recovery in cylindrical samples of a thermoplastic programmed under compression by using a bias-stress at different stress magnitudes (from 0 to 1.5 MPa) to constrain the recovery. The results suggested that the amount of recoverable strain scales with an exponentially decreasing relationship to bias force. Our research group with the work of Santiago et al.[50] studied the influence of the network mobility with the recoverable strain in partially-constrained conditions using hyperbranched-modified epoxy-based SMPs. While the observed trend for the recoverable strain was similar to Lakhera et al.[53], the decreasing trend was found more accused in formulations with lower network mobility (higher content of hyperbranched polymer). Regarding the programming conditions, it was found that cold programming leads to a strain overshoot during the recovery which has been related to a viscoelastic phenomenon. As stated above, cold programming leads to energetic forces that contributes to a drastic recovery, hence, the appearance of a strain overshoot.

In this investigation, the response of “thiol-epoxy” based SMPs under partially-constrained conditions are studied in flexural mode using bent-shaped sample designs (the development of bent-shaped samples is explained in detail in section II.7). The results and discussion are presented in chapter IV.

Fully constrained conditions are, in practice, a limiting scenario to investigate the maximum capabilities of the SMP as a mechanical actuator. In Figure I-6(a), the fully constrained recovery process is shown in a typical stress-temperature plot, where the stress refers to the stress released during the recovery, and the SME is schematized in Figure I-6(b).

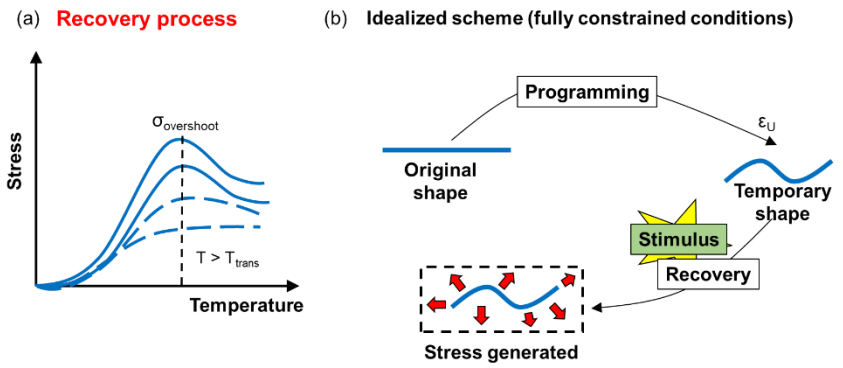

Figure I-6. Fully constrained recovery process: (a) stress-temperature plot and (b) idealized scheme of the process.

The **fully constrained recovery** process strongly depends on the programming conditions since the stress generated is consequence of the energy input. In unconstrained recovery, the energy input is released as a means of shape-transformation, thus, mainly depends on the network relaxation. In contrast, in constrained recoveries, the energy input is transformed in stress, thus, the structural and mechanical properties of the SMP have a crucial role. Our research group with the work of Santiago et al.[50] investigated the stress generation in hyperbranched-modified epoxy-based SMPs and found that, both, the crosslinking density and the homogeneity of the network, rather than the relaxation process, are the crucial parameters in the efficiency releasing the stored energy.

As can be observed in Figure I-6(a), the stress increases up to a certain value and stabilizes at a temperature above T_{trans}. When the SMP is programmed at a temperature lower than T_{trans}, a **stress overshoot** appears. Similar to the strain overshoot observed in partially-constrained conditions, this stress overshoot is attributed to incomplete network relaxation during the programming process that is released in form of stress. In practice, this overshoot can serve to maximize the stress generated, however, because of the severe programming conditions, the useful life of the SMP worsens. Arrieta et al.[51,52] investigated the impact of different programming conditions with the constrained recovery of acrylate-based glassy SMPs and found that the ideal conditions to enhance the stress generation with the less damage for the network structure are low settling temperatures (T_s << T_{trans}) with rapid cooling processes, increasing the pre-strain without being too close to the strain at break limit and reducing the stress relaxation in all the programming steps.

In this investigation, the response of “thiol-epoxy” based SMPs under fully constrained conditions are studied in flexural mode using bent-

shaped sample designs. The results and discussion are presented in chapter IV.

Cyclic life

The **cyclic life** of a SMP consists of a series of consecutive SMCs to evaluate the stability fixing the temporary shape and recovering the original shape, as well as the resistance at failure. Up to date, there is no concern about the methodology to test the cyclic life of a SMP. Neither the number of cycles, nor the programming protocol have been stipulated. Nevertheless, there is an initial and required cyclic process, called **"training process"**, to ensure repeatability of the SME. The number of cycles for this process depends on the nature of the SMP network. Thermoset-based SMPs usually demand 3 to 5 cycles to achieve stable response, whereas thermoplastic-based SMPs requires a higher number due to possible slippage of the chains and network reconfiguration. Our research group with the work of Santiago et al.[54] studied the influence of T_{prog} and the **programmed stress** (σ_D) with the stability of a commercial thermoplastic amorphous polyurethane-based SMP (Tecoflex©) subject to 25 consecutive SMCs under unconstrained conditions in tensile mode. The results showed a progressive decrease of the SMR with increasing the cycles regarding T_{prog} and σ_D. In addition, the variation of σ_D showed a high influence in the shape-fixation, whereas T_{prog} demonstrated a stronger effect on the mechanical properties (note that imposing a σ_D is another criterion of programming the temporary shape instead of ε_u as it has been explained in section I.1.1.1).

Overall, the performance recovering the original shape is affected by the **fatigue of the network** subject to consecutive thermomechanical procedures. Permanent and irrecoverable deformations may take place after each cycle eventually worsening the capability of the SMP to recover the original shape. From a structural point of view, the effect of cyclic processes is stronger in thermoplastic-based SMPs than in thermoset-based SMPs because of possible network reconfiguration after each cycle. Factors affecting the fatigue of the network are drastic programming processes, that means, low T_{prog} or high stress/strain rates, leading to rapid fatigue of the network, hence, early failure of the SMP. On the other hand, subjecting the SMP to fully or partially- constrained recovery conditions generates internal stresses resulting in an early fatigue of the network[55–57].

In conclusion, a balance between long "cyclic life" and recovery performance must be accomplished when designing the SMP workability for a specific application.

I.1.1.2 Classification of shape-memory polymers

SMPs can be classified through different categories: depending on their **network structural properties**, depending on the **triggering stimulus** for the SME and considering the **mechanism of the SME**. All of them are related and dependent of each other as it will be discussed in the following sections.

Classification of SMPs by network structure

The network structural properties depend on the nature of the crosslinks and the structural primary and secondary transitions of the network. As explained in section I.1 two different groups break down from the nature of the crosslinks: **covalently-** and **physically-crosslinked** SMPs. These groups break down in two other subclasses depending on the structural transitions: **glassy** and **semi-crystalline SMPs**.

Covalently-crosslinked glassy thermosets (I)

Covalently-crosslinked glassy thermosets are SMPs that memorize their permanent shape thanks to the formation of covalent crosslinks during the curing process, thus, the original shape is processed during the fabrication of the material (in Figure I-7 a scheme of the SME for this class of SMPs is presented). These crosslinks remain under an energy equilibrium state after the curing process, when the temperature increases above T_g, the network structure undergoes a transition from local or residual segmental mobility of the chains (rotation of lateral groups or oscillation of rings) to cooperative mobility, thus, a large deformation process towards a new macroscopic shape is enabled. During this deformation process, the crosslinks moves away from the equilibrium state and are further stabilized through vitrification of the network ($T_s << T_g$). The reduction of the chains mobility fixes the temporary shape under a non-equilibrium state of the crosslinks. Once the temperature rises to T_g again, the crosslinks can move towards the equilibrium state producing the shape-recovery phenomenon[58].

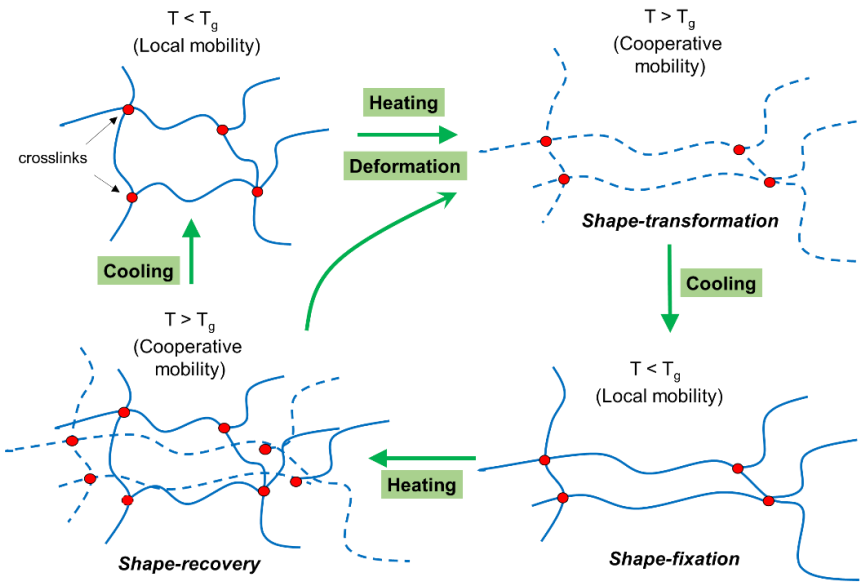

Figure I-7. Scheme of the shape-memory effect in covalently-crosslinked glassy polymers.

As introduced in section I.1.1.1 **epoxy-based thermosets** are common examples of covalently-crosslinked SMPs because of their excellent mechanical properties, electrical insulation, chemical resistance and thermal stability that make them attractive in many fields of application, such as aerospace[59] and industrial applications[60,61]. Nevertheless, their inherent rigidity is a common drawback for many applications[62]. To overcome this limitation, many researchers use curing agents with flexible and long aliphatic chains such as propylene oxide-based and ethylene oxide-based curing agents[42], to enhance the deformation limits at the expense of reducing the ultimate strength. Another well-known approach to interfere the less on the network structure consists of adjusting T_{prog} to $T_g^{E'}$[31,40]. As stated in section I.1.1.1 the ultimate strain and stress values are improved three-to-five times trough this methodology. However, programming at a temperature below T_g causes viscoelastic response that eventually affects the shape-recovery process and may damage the network structure.

An interesting solution that balances a considerably increase of the ultimate strain and maintains the mechanical strength of the materials is the use of specific **thiol-based curing agents**. In chapter III the investigation of "thiol-epoxy" systems as potential SMPs is presented and discussed.

Covalently-crosslinked semi-crystalline polymers (II)

Covalently-crosslinked semi-crystalline polymers are SMPs that like the first group of glassy materials, memorize the permanent shape thanks to the crosslinks formed during the curing process, meaning that the original shape cannot be reshaped after fabrication. Nevertheless, the responsible of fixing the temporary shape is the crystallization instead of the vitrification. These networks usually have moderate T_g and high T_m promoted by the formation of these ordered domains within the network. The ordered domains act as the switching domains by impeding the recovery of the original shape and promoting the recovery of the original shape when they are melted.

In comparison to the first class, the shape-recovery is usually sharper due to the triggering mechanism is a first order transition instead of a secondary transition (the glass transition). This class includes bulk polymers, such as semi-crystalline rubbers, LCNs and hydrogels with phase separated crystalline domains. Examples include the chemically-crosslinked trans-polyisopropene, polycycloctene-based polymers and poly-(ε-caprolactone)-based polymers[63,64].

Physically-crosslinked glassy copolymers (III)

Physically-crosslinked glassy copolymers are SMPs that memorize the permanent shape thanks to crystalline or rigid amorphous domains that behaves as physical crosslinks in the main phase of the copolymer. At least, another continuous glassy phase (secondary phase) must coexists within the network and it is the responsible of the SME. The T_g^2 (super-index ^{2} refers to the secondary phase) is adjusted to be lower than T_m of the main phase, thus, allowing the programming of a temporary shape through the softening of the network to a rubbery state at ($T_g^2 < T_m$) to further recover the original shape through the force driven by the physical crosslinks of the main phase that are under non-equilibrium. This class of SMPs is interesting to overcome one of the main issues in the development of thermoset-based SMPs from an industrial point of view: the processing. When the temperature overpasses the T_m of the main phase the material flow and therefore the original shape can be reprocessed.

This class includes miscible blends, semi-crystalline homopolymers and melt-miscible polymer blends with at least one semi-crystalline component. Examples include a miscible blend of a thermoplastic polyurethane with phenoxy resin in which the soft segment is a PCL and a melt-miscible blend of poly(vinyl acetate) and poly(lactic acid)[65,66].

Physically-crosslinked semi-crystalline block copolymers (IV)

Physically-crosslinked semi crystalline block copolymers are SMPs that memorizes the permanent shape in the same way that class three. The main difference lies on the secondary phase that, instead of a glassy network, consists of a semi-crystalline network, thus, the switching mechanism is a melting point. This class includes multiblock polyurethanes with PCO as soft segment, styrene-trans-butadiene-styrene (STBS) triblock copolymers and segmented polyurethanes with semi-crystalline flexible segments. STBS is a strongly segregated ABA-type triblock with a minor content of polystyrene (PS) and a major content of semi-crystalline poly(trans-butadiene) TPB. They are immiscible and therefore, PS forms amorphous blocks with a T_g of 93°C serving as physical crosslinks of the main phase (responsible of memorizing the permanent shape), whereas TPB forms a semi-crystalline matrix with a T_m of 68 °C and a T_g of -90 °C serving as switching domains of the secondary phase[67,68].

Classification of SMPs by the triggering stimulus

Besides the **SME** relies, in most cases, on thermal transitions the stimulus responsible of triggering the shape-recovery is not necessarily heating by temperature exchange. Here, two branches appear: on the one side, the use of other stimuli, such as, light, electrical current or magnetic fields to increase the temperature of the SMP and trigger the thermal transition, on the other side, the use of switching mechanisms, such as, photo-responsive molecules that are activated with other stimuli as introduced in section I.1.1.1.

The first branch usually refers to **filled SMPs**. The incorporation of metallic fillers in the polymeric matrix, not only modifies the mechanical properties, but also allows other stimuli, such as, electrical current (using conductive fillers) or magnetic fields (using magnetic fillers) to indirectly heat up the material through the Joule's effect and trigger the shape-recovery process. They are called **electrically-** and **magnetically-** activated SMPs respectively. Díaz-Lantada[69] presented a "surgical pincer" SMP activated using electrical current. The heating process was focalised in the lower part of the device leading to a controlled closing mechanism, whereas the upper part remained in the glassy state, thus, the modulus was high enough to catch and hold an object.

Regarding the second branch, the most investigated type are the so-called **photo-activated SMPs**. They possess certain molecular structures that upon irradiation to specific wavelengths changes their structural configuration. One approach is the use of compounds that undergo cycloadditions. For example, the reversible dimerization of

cinnamic acid derivates. This acid dimerizes at wavelengths λ > 260, thus forming new bonds between the chains that serves for the retention of the temporary shape. On decreasing the irradiation wavelength λ < 260, the bond is opened, and the shape-recovery takes place. Another approach is to take advantage of compounds that photoisomerizes. The most common example are azobenzene's. The azobenzene molecule can undergo cis-trans isomerization upon irradiation, resulting in a macroscopic volume change of the polymer. Despite this effect is mostly used for SCE (i.e. photomechanical response), it can be used for SME as demonstrated by White et al.[70,71] who synthesized an azobenzene-containing diacrylate which can act as a crosslinker, thus, maintaining the temporary shape. Upon irradiation, the crosslinks disband leading to the recovery of the original shape.

The **plasticizing effect** of polymeric materials[26], which effectively reduces the T_g, is another approach to trigger the shape-recovery process without heating up above T_{trans}. They are called **chemo-responsive SMPs** and are of particular interest in applications where the material is immersed in an aqueous medium or exposed to humid climate. Depending on the SME mechanism, three different categories are defined: softening SMP, swelling SMP and dissolving SMP. The **softening SME** is caused by the chemical incorporation of water or other solvents such as ethanol to the network structure of an already programmed SMP, effectively reducing the T_g and causing shape-recovery. These materials do not change in volume at macroscopic level and the solvent molecules can be eliminated by heating up to a certain temperature. The most common example are polyurethanes that response to water, ethanol or other chemical solvents[72] (see Figure I-8(a)). In contrast, **swelling SMPs** are capable to recover the original shape upon immersion to specific solvents at expenses of increasing their volume. One interesting application of the swelling-induced volume increase is the pre-processing of new shapes. Finally, **dissolving SMPs** are the extreme case in which theoretically the maximum volume increase is reached, that is removing the transition component by dissolving it. In this case, the original shape is recovered as long as the transition component disappears. An example is a silicone filled with sodium acetate trihydrate. The temporary shape is programmed through the T_m of the sodium compound and upon immersion in water,

the sodium progressively dissolves letting the SMP to recover the original shape[73] (see Figure I-8(b)).

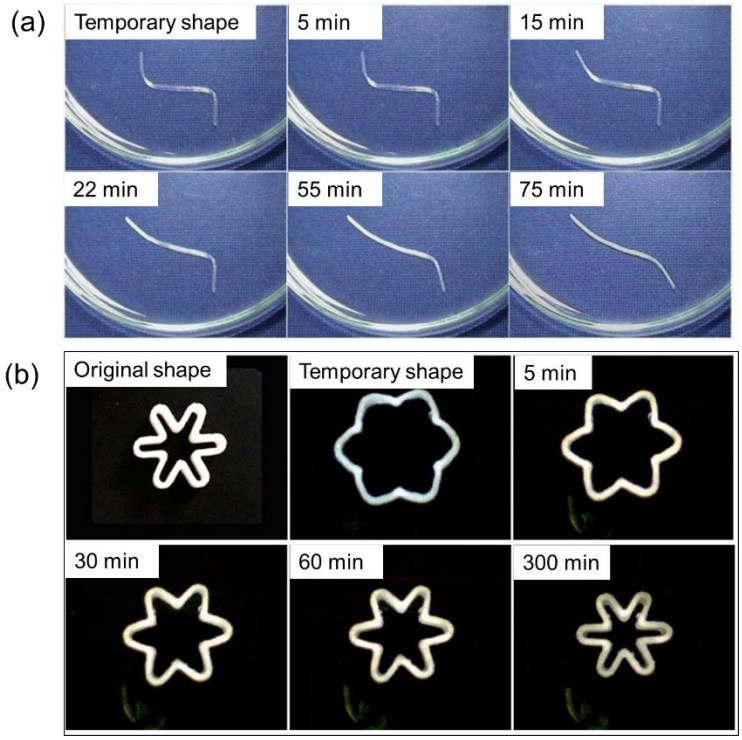

Figure I-8. (a) Water-driven softening shape-memory polyurethane by Huang et al.[72] and (b) water-driven dissolving shape-memory silicone-based hybrid rings by Huang et al.[73].

Classification of SMPs by the shape-memory effect mechanism

Traditionally, the SME has been limited to a **single transition** from a temporary shape to the original shape upon stimulation of the network. Recent advances have led to more complex mechanisms in which the transition follows various steps and multiple temporary shapes before the SMP completely recovers the original shape[74,75].

The **multiple SME** can be achieved by means of network structures with various transitions. The most common approach consists of **programming** each temporary shape **step by step**: parting from the ultimate transition and thanks to the softening of the network a new temporary shape can be processed and further stabilized by partially hindering the network through the corresponding transition. This process can be repeated in each transition until the lowest transition is attained. The further heating along the different transitions will trigger the different shape-recovery processes towards each temporary shape to finally

recover the original shape. An example is found by Lendlein et al.[76] who prepared two polymer networks: the first consisting of PCL and poly(cyclo hexyl methacrylate) (PCHMA) segments which form a crosslinked network and the second consisting of polyethylene glycol as side chain segments and PCL segments forming another crosslinked network. The first network showed two transition temperatures associated to the melting of PLC (T_m ≈ 50 °C) and to the glass transition of the PCHMA (T_g ≈ 140 °C), whereas the second network showed two transition processes related to the melting of the PEG (T_m ≈ 17-39 °C) and the melting of the PCL (T_m ≈ 50 °C). The system allows to program two temporary shapes: the material is deformed above T_m^{PLC} (T ≈ 70 °C) and the shape is fixed at a temperature below T_m^{PLC} and above T_m^{PEG} (T = 40 °C) by crystallization of the PLC segments. Afterwards, another deformation process is applied, and the new shape is fixed at a temperature below T_m^{PEG} (T = 0 °C) by crystallization of the PEG segments. Another example is found by Bowman et al.[77] who took advantage of dual-curing processing of thiol-acrylates to form two networks with different T_g (one at 10 ºC and the other at 55 ºC). As it is shown in Figure I-9, they coiled a strip in both ends into different directions to reveal the triple SME with a high performance.

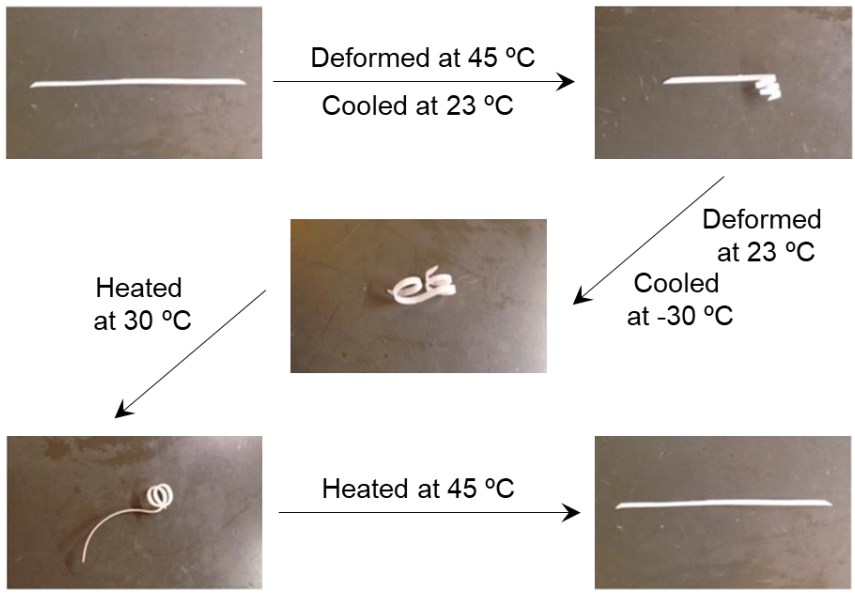

Figure I-9. Triple shape-memory effect of a strip coiled in both ends into different directions by Bowman et al.[77].

Another approach to attain multiple SME through various transition processes consists of **programming in one-single** step at a temperature below all transitions. After programming the temporary

shape, it is partially-recovered by heating above the first transition and completely recovered after heating above the ultimate transition. However, this methodology limits the motion to simple designs such as unidimensional elongation. An example are the copolymer networks obtained from crosslinking of star-shaped PCL and poly(u-pentadecalactone) (PPDL) precursors[78].

The last reported approach to attain multiple SME was proposed by Xie et al.[79], who demonstrated that a polymer with a **sufficiently broad transition** can fix various temporary shapes. This methodology extends to most of the common polymers since theoretically one can program infinite temporary shapes by heating/cooling procedures in narrow temperature ranges within the transition region. However, to consider the multiple SME effective, not only a transition between multiple shapes is required, but also stability of each temporary shape. Some examples are found in the literature, Li et al.[80] demonstrated that Nafion, with a broad glass transition (T_g from 55 °C to 130 °C), permit the programming of two temporary shapes (triple SME) using two separated programming temperatures (T_{prog}^1 = 100 °C and T_{prog}^2 = 60 °C). Moreover, they revealed a high impact of the thermomechanical properties, such as the programming conditions, with the triple-SME performance recovering the original shape in comparison with traditional single-SME polymers.

Despite in this investigation multiple-SME has not been studied, the possibility to tailor the glass transition from the molecular design in "thiol-epoxy" SMPs is discussed and presented in chapter III and can be applied for the development of SMPs with multiple-SMEs through the broad transition approach.

I.1.1.3 Modelling of shape-memory polymers

Mathematical modelling of the **SME** including both, the programming and recovery processes, has been a secondary task during many years after the appearance of the SMPs. SMP modelling is a tedious task involving not only materials properties, but also complicated thermomechanical conditions. Moreover, material properties are affected by the thermomechanical conditions, leading to numerous variables and dependencies. To this end, in this investigation modelling of the studied SMPs is out of scope but a brief description of the modelling approaches reviewing the most relevant reports and up-to-date work is presented in this section.

Basically, SMP modelling can be approached through constitutive models, thermoviscoelastic models or directly prediction of the response. **Constitutive models** link state functions, such as, entropy or internal

energy, with state variables, such as temperature change or deformation gradient. Liu and co-workers[81] in 2006 reported a constitutive model that, from a thermodynamic point of view and based on a phenomenological approach, was capable to predict the strain and stress recoveries of pre-deformed SMPs. The fundamental of the model was that all the entropic energy is progressively stored during the freezing of the network (frozen fraction) and it is further released upon reheating. The frozen fraction captures the micromechanics and physics of the glass transition and shape-memory response. Many later researchers used this model as basis to further incorporate a new parameter called "storage strain" to better capture the SME[82–84].

Thermoviscoelastic models are interesting because other time-dependent phenomenon affecting the network relaxation spectra, hence, the SMR, such as, physical aging or solvent driven SME (plasticizers), can be incorporated and effectively evaluated. The great challenge of thermoviscoelastic models is to reduce material parameters, especially when non-linear Maxwell and Voigt elements are used. Springs and dashpots elements are used to emulate the viscoelastic response of polymeric materials, however, simple solutions, such as, three-element system, does not capture real response of polymers, rather, multiple branches are necessary, hence, multiple parameters appear in the equations[85–88].

Since accurate modelling cost much time, precise knowledge of the material it is sometimes rather complicated, some researchers focused on the prediction of the shape-memory performance instead. In practice, an initial evaluation of a material as potential SMP lies on its performance. Simple methods to predict its response have been proposed. Moreover, excellent agreement predicting parameters related to the efficiency and velocity recovering the original shape and the performance fixing the temporary shape have been achieved. Diani et al.[89] used linear viscoelastic models and an Abaqus finite element code to predict large recovery strains with excellent agreement only at expense of carrying out a standardized dynamo mechanical analyses to determine viscoelastic parameters.

I.1.2 Shape-changing polymers

Shape-changing polymers are a class of stimuli-responsive materials capable to transform from one shape to another upon stimulation. As stated in section I.1 this effect is called SCE and is based in the macroscopic transformation caused by reversible structural changes

induced when the material is exposed to the appropriate stimulus (i.e. thermomechanical, photomechanical or humidity).

The **SCE** was first predicted by P. G. de Gennes in 1968[90], who stated that phase transitions in LC networks could lead to mechanical stress and strain. The first LCN was prepared by Liebert and Strzelecki in 1973 who crosslinked diacrylate Schiff base monomers within the liquid-crystalline state[91], however the phenomenon was not observed until Finkelman et al.[92] prepared the first **liquid-crystalline elastomer** (LCE). From the 1980's, the mechanical forces emerging from the monomorphic character of the LCNs were extensively investigated[93–96].

The **SCE** in LCN can be used in a wide range of applications. The mechanical force serves for artificial mussels or micro-grippers in robotics[97], smart actuators[98] and propulsion systems in microfluidics using microvalves[99]. The induced changes of the optical properties caused by the LC transition branches out the application scope towards sensors[100] or smart surfaces that change their properties in response to environmental variation[101]. Other SCPs, such as hydrogels, can be used as sensors, processors, actuators, or more interestingly, compound releasers (i.e. drug-release) due to their swelling/deswelling volume-change induced effect[102].

I.1.2.1 Liquid-crystalline networks

Among the different SCPs, **LCNs** are the most common class. Similar to LC polymers, that are polymers with liquid-crystallinity but absence of network structure, LCNs present segregated ordered phases called LC domains that are formed by the self-organization tendency of certain molecules, the mesogens, that are present in the backbone of the chains (main-chain LCNs) or as pendant groups anchored to the backbone (side-chain LCNs). The spatial configuration (orientation and position) of the mesogenic units in the polymer backbone or pendant groups determine the LC mesophase: from smectic mesophases (only orientationally order or one-dimensional order) to nematic mesophases (positional and orientationally order or two-dimensional order). More complex mesophases, such as blue or bent-core phases are unusual in LCNs due to the network mobility limitation[93,103].

LCNs are characterized by rather flexible backbones constituted by the mesogenic units and flexible segments called spacers. The mesogenic units are typically rod-like molecules, similar to those found in LC polymers[6] (note that in LC polymers, not only rod-like molecules can self-organize, but also disk-shaped molecules can organize in 3D columnar designs). From a macroscopic point of view, the LC domains are commonly

organized in polydomain structures with a percentage of orientationally ordering determined through the **ordering parameter**, *S*, that considers an orthogonal axis to quantify the degree of orientation of the domains in respect to this axis within the network. Upon stretching the LCN along the axis director, the LC domains are oriented and aligned increasing *S* and promoting large deformation processes with minimal force. This process is called soft elasticity and refers to the ability of the polymer to be stretched at near zero-stress[104,105]. During this process, there is a transition from a polydomain to an oriented monodomain structure, P-M transition, that begins at a critical strain level which depends on the structural properties of the LCN (crosslinking density, chains mobility, the structure of the mesogenic units and the configuration of the mesophase) and is enhanced at high strain levels[106].

The **LC domains** are stable under certain conditions of temperature, light or humidity depending on the nature of the polymer. The disordering of the LC domains is called **isotropization** and determines the point at which *S* tend to zero and the LCN becomes a rubber (lightly-crosslinked amorphous network). Usually, this is triggered at a certain temperature called **isotropization temperature** (T_{iso}) which is higher than the T_g of the LCN and depends on the stability of the LC domains within the flexible network.

Among the different LCNs, **epoxy-based LCNs** are of high interest due their excellent properties making them primary candidates from high performance materials in advanced composites to optical applications[95,107–109]. In this investigation, “epoxy-carboxylic” LCNs are synthesized and characterized as potentials SCPs for actuation purposes. The results and discussion are presented in chapter V.

I.1.2.2 Shape-changing effect

As stated in section I.1.2.1 **LCNs** suffer macroscopic volume changes upon disordering of the LC domains. Moreover, the soft elasticity phenomenon permits large strain processes with minimal forces. Both properties can be exploited to attain large recoverable strain when the appropriate stimulus is applied.

Commonly, **the isotropization** or disordering of the LC domains is caused by the increase of the temperature. However, the incorporation of photo-responsive mesogenic units, such as azobenzene molecules, permit re-orientation upon light exposure, hence, mesomorphic transitions. In this investigation, the thermomechanical SCE is studied in “epoxy-carboxylic” LCNs, thus, in the next section the thermomechanical

mechanism is analysed in detail to explain the fundamentals of the SCE, whereas other mechanisms are mentioned in a separate section.

Thermomechanical shape-changing effect

Thermomechanical SCE in LCNs is attained by combination of a mechanical stress and the stimulation of the network through heating. The process has been illustrated in Figure I-10 from a structural point of view of the network. The isotropization (typically nematic-to-isotropic in LCNs) takes place at T_{iso}, whereas the isotropic-to-anisotropic transition or **anisotropization** does not necessarily take place at the same temperature, but a temperature called **anisotropization temperature** (T_{aniso}). The isotropization causes the disordering of the LC domains, while the anisotropization promotes the formation of the LC domains. If an external force is applied during the anisotropization, thus on cooling, the LC domains are formed and stress-aligned, leading to a highly oriented monodomain promoted by the **soft elasticity** phenomenon. This causes a large macroscopic deformation along the stress director. Further heating above the isotropization will cause disorder of the LC domains, thus, elastic shrinkage towards the pre-deformed shape[110]. Note that, while the formation of the monodomain is caused by orientation and alignment of the LC domains during the P-M transition (see previous section I.1.2.1) in the SCE the LC domains are formed and aligned in the stretching direction, thus, no P-M transition exists, but isotropic-to-monodomain transition. This is important from a thermodynamic and structural point of view of the process.

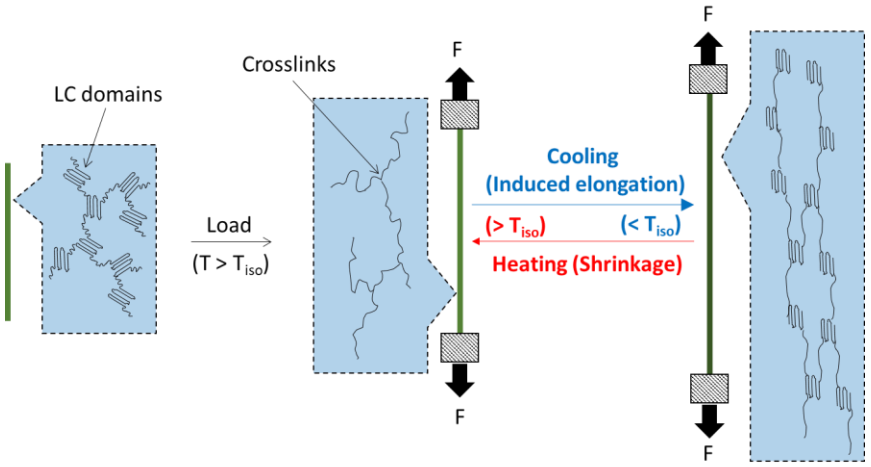

Figure I-10. Scheme of the SCE in LCNs (network structural point of view).

The **induced-elongation** strongly depends on the topographical configuration of the network and the stress director. Typically, large uniaxial deformation is attained in the direction of major order within the network. However, heterogeneous mechanical responses in LCN films can be generated through the electro-optical response of this materials and electrode patterning to produce topographical effects upon stimulation[111]. On the other hand, the crosslinking density, liquid-crystallinity and network rigidity are determinant parameters, not only to achieve large deformation, but also to generate large mechanical stress upon stimulation[112–114].

On the other hand, the crosslinks are the responsible of the **elastic shrinkage** during the isotropization. An increase of the temperature will cause disorder of the LC domains promoting the elastic response (entropic change) of the crosslinks, hence, the contraction towards the initial non-stretched random-coil conformation. Rousseau et al.[112] studied the effect of varying crosslinking density in main-chain smectic-C LCEs obtained through hydrosylilation and found an increasing trend of the induced-elongation and the threshold stress required to achieve actuation, with the increase of crosslinking density. Kessler et al.[114] studied the effect of the crosslinking density, network rigidity and LC order with the thermomechanical response of smectic main-chain epoxy-carboxylic LCNs obtained through variation of the epoxy-carboxylic ratio. Large dimensional change was achieved with increased liquid-crystallinity and reduced rigidity. However, the higher deformation led to lower stability with the presence of a higher amount of residual strain.

Other approaches to modulate the thermomechanical properties of the SCE are the incorporation of functional conjugated compounds or more recently, **metallic nanoparticles**[115,116], such as gold nanoparticles[117] or carbon nanotubes, to enhance the mechanical properties and thermal conductivity of the LCNs. Lama et al.[118] dispersed carbon nanotubes in epoxy-based LCNs demonstrating that T_{iso} and the threshold stress required for the actuation can be tailored by selecting the amount of carbon nanotubes.

Other mechanisms of shape-changing effect

Photomechanical SCE is the most common alternative to thermomechanical SCE. Light-responsive molecules, such as azobenzene, change their spatial configuration upon exposure to light. Coupling small-scale deformations can lead to macroscopic changes as introduced in section I.1. The control of the light intensity, polarization and wavelength, as well as the focus, makes possible the control of the resulting

deformation. Bending, twisting, turns and oscillatory responses have been reported[119] after the appearance of the first macroscopic deformation observed by Finkelman et al in 2001 with an azo-modified LCE[120].

In general, notable efforts are found in **photomechanical response of fibbers**. Yoshino et al[121] reported a precise directionally controlled motion with LCN fibbers containing azobenzene moieties in response to a photomechanical stimulus. The reconfiguration of the azobenzene molecules exposed to light with 366 nm wavelength, produce three-dimensional alignment of the bulk material controlled by focalising the light irradiation to specific fibber spots. Other investigations are found in bidirectional actuation or deflection mechanisms (both static and oscillatory). White et al.[122] presented a high-frequency photo-driven oscillator consisting of a cantilever made of an azo-LCN prepared by thermal curing of two azobenzene LC monomers. As it can be seen in Figure I-11, upon exposure to a 0.8 $W \cdot cm^{-2}$ Ar^+ laser beam, oscillatory deflection is attained because of the alternate exposure on the upper and down faces of the cantilever by cycling the laser from an orthogonal to a parallel position in respect to the nematic director of the LCN.

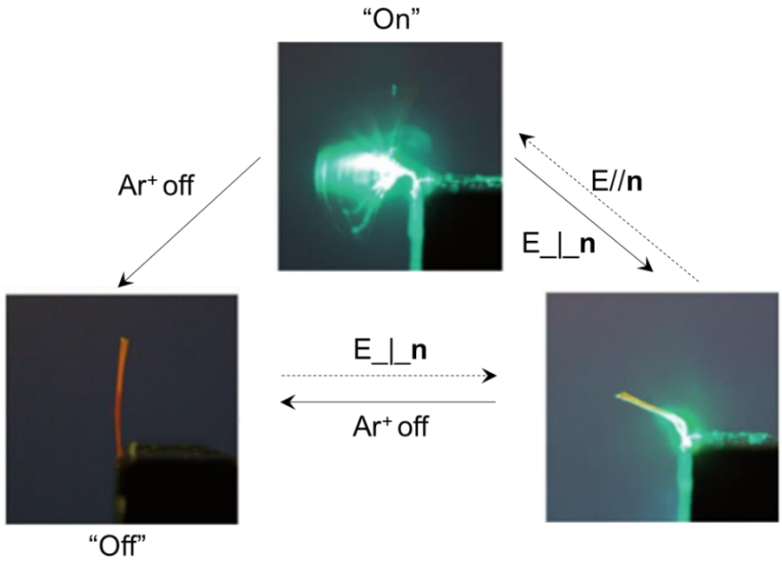

Figure I-11. Optical mechanism to turn "on" and "off" the oscillation mode in a photo-driven oscillator made of an azo-LCN cantilever by White et al.[122].

Indirect-heating is another common approach to trigger the SCE. As stated in section I.1.2.2 guest agents, such as metallic nanoparticles, can be incorporated in LCNs to enhance mechanical and thermal properties. Equally to the fillers utilized for SMPs in section I.1.1.1,

magnetic or electrically sensitive particles can be used to indirectly heat up the LCN under the Joule's effect upon magnetic or electrical fields to trigger the SCE.

I.1.2.3 Free-standing shape-changing effect

As stated in section I.1.2.2 the **SCE** leads to bidirectional actuation when the LC domains are stress-aligned, hence, an external mechanical load is required. Moreover, the SCE is limited by the original three-dimensional configuration of the network structure and the direction of the applied stress, in most cases leading to simple unidirectional motion mechanisms.

To attempt this drawback, the most common approach is the incorporation of an elastic component into an already stretched LCN, thus, impeding the LCN shrinkage during the isotropization, but adopting a metastable state-of-ease shape, that is further recovered due to the stress generated in the elastic component[123,124].

Generally speaking, the combination of a shape-shifting element, that is the LCN, and a stress-applying element, that is the elastic component, can lead to **free-standing bidirectional actuation** through the LC transition of the LCN. This "stress-applying" component can be internally incorporated through the crosslinking of a new network structure or externally incorporated by embedding an elastic matrix onto the stretched LCN.

Internal incorporation of the stress-applying component

In Figure I-12, a generic scheme of the **internal incorporation** and the actuation mechanism is presented. Dual-networks are typically achieved through **dual-curing processing**, that is, the combination of two compatible reaction mechanisms to form two networks simultaneously or sequentially (in section I.2 the dual-curing processing is explained in detail)[125]. Essentially, through dual-curing processing it is possible to control the formation of each network through different stimuli (i.e. heat and UV-light), reaction kinetics or formation of functional groups. Typically, photo- and thermally-triggered polymerization processes are combined and controlled through latent activation methods, such as, photo-activated or thermo-activated catalysts (latent catalysts)[126]. The concept of latent catalyst is detailed in section I.2.

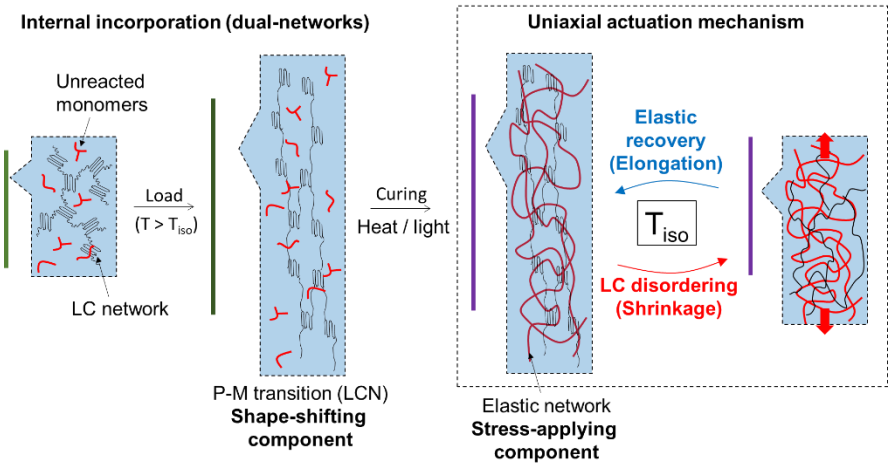

Figure I-12. Scheme of the free-standing SCE obtained via internal incorporation of a stress-applying component: molecular view and macroscopic mechanism.

Considering the above, the internal incorporation is achieved by curing an initial LCN network that is further stretched inducing the P-M transition towards high strain levels. If the imposed deformation is maintained during the formation of the 2nd elastic network, the already stretched LC network is physically and, in some cases, covalently interlaced with the new elastic network. Triggering the LC transition of the LCN in the resulting polymer will cause disorder of the LC domains, leading to a contraction of the elastic network (energy storage), to further promote the formation and stress-alignment of the LC domains through the elastic recovery of the contracted elastic network (energy release). Anthamatten et al.[127] achieved 15% of uniaxial free-standing actuation via internal incorporation: a semi-crystalline poly(ε-caprolactone) network was partially cured (1st curing stage), stretched up to 650% of strain and stabilized by UV-crosslinking (2nd curing stage). The photo-crosslinked network was the responsible of generating the stress due to the elastic response during the LC transition. Yakacki et al.[4,128] enhanced the actuation up to 110% by using dual-cured "thiol-acrylate" networks with crosslinks of different functionality.

External incorporation of the stress-applying component

In Figure I-13, a generic scheme of the **external incorporation** and the actuation mechanism is presented. The elastic matrix is usually a lightly-crosslinked polymer (rubber), however any material with an elastic response during the LC transition of the LCN can be used as stress-applying component. Crosslinked polymers with a T_g below the LC transition of the LCN or even metallic plates have been proposed as stress-applying

components[129]. The elastic matrix is embedded to an already stretched LCN to produce the mismatch between both, the LCN and the matrix itself, causing the free-standing bidirectional actuation.

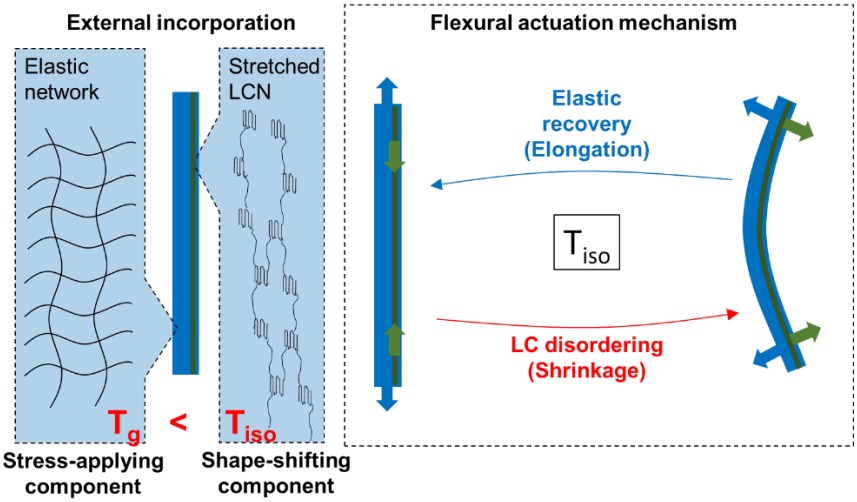

Figure I-13. Scheme of the free-standing SCE obtained via external incorporation of a stress-applying component: molecular view and macroscopic mechanism.

The first external incorporation was reported by Westbrook et al.[130,131] who achieved a transversal free-standing bidirectional actuation of about 10% of the initial length of the actuator (see the actuation of the resulting material in Figure I-14). The external incorporation of an elastomeric matrix onto a stretched poly(cyclooctene)-based LCN was carried out through direct thermal curing of the matrix over the LCN, thus, strong physical-bonding of the new network onto the LCN surface was achieved.

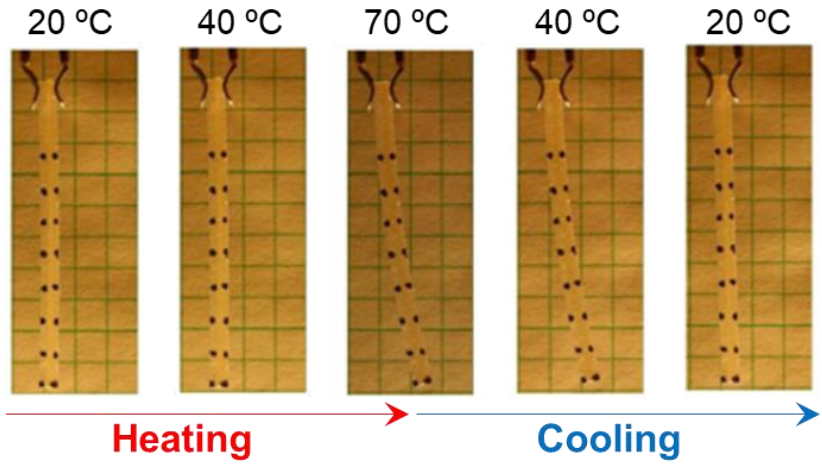

Figure I-14. Transversal free-standing actuation upon a heating-cooling process in free-standing shape-memory actuators by Westbrook et al.[130,131].

Overall, the **internal incorporation** depends on the compatibility and interaction between the networks, thus, structural properties at molecular level such as crosslinking density and network mobility influence the actuation performance. Moreover, the actuation process is defined through the molecular design of the network: mechanically asymmetric network architectures are used to produce two- or three-dimensional changes. In contrast, the **external incorporation** is highly affected by the adhesion and interaction between the faces of the LCN and the elastic component, hence, macroscopic changes such as thermal expansion strongly affects the actuation performance. In this case, two- and three- dimensional volume changes are attained by the configuration of the device.

In chapter V different **flexural bidirectional motion** designs are developed and characterized by using dual-curing processing of off-stoichiometric "thiol-epoxy" systems for the external incorporation of the stress-applying component in elongated "epoxy-carboxylic" LCNs.

Another approach to achieve free-standing bidirectional motion consists of **semi-crystalline networks with two crystalline domains** or **confined crystalline domains** interacting each other to produce reversible shape-changes. Zharinova et al.[132] reported free-standing bidirectional actuation in water-blown polyurethane foams. The broad crystallization process in these systems permit the separation of the crystalline segments in actuation segments and skeleton segments by fixing the temperature within the transition range (see Figure I-15). The actuation segments

contract upon heating, whereas skeleton segments remain unchanged, thus, interact with the actuation segments and generate the required stress to promote the induced-elongation upon cooling.

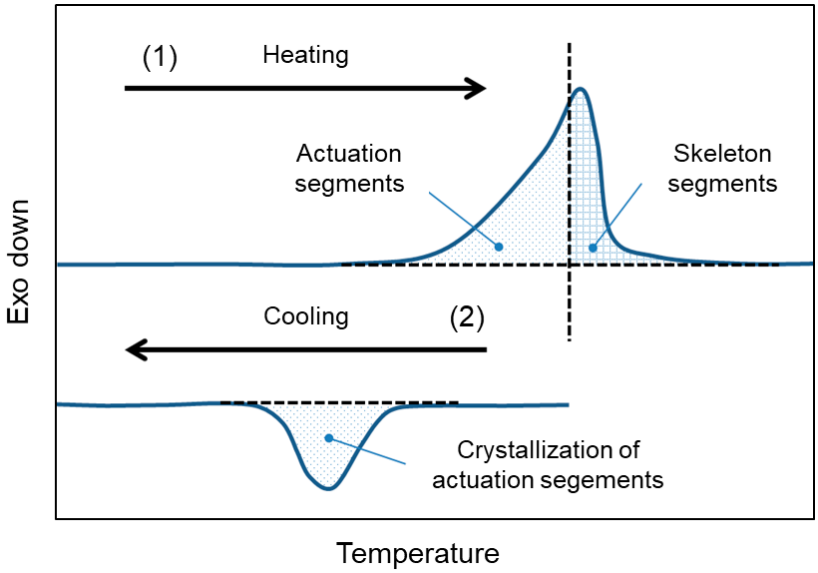

Figure I-15. Calorimetric scheme of "the actuation" and "skeleton" segments in water-blown polyurethane foams showing reversible bidirectional shape-shifting by Zharinova et al.[132].

I.1.3 Applications of actively-moving-polymers

Actively-moving polymers possess three crucial characteristics: they response to external stimuli by dimensionally-changing, they are low-weight materials and their properties can be tailored from the structural design of their networks. The coupling of these characteristics makes AMPs interesting in a vast range of applications.

The biocompatibility and biodegradability of the constitutive polymers make them attractive in biomedical applications[10]. The enhanced mechanical properties (high deformability coupled with strength and resistance at break) is crucial in industrial applications and aerospace[133]. The precise control from micro to macrostructural designs is exploited in micro robotics and nanocomposites[134,135]. Inherent properties such as the low density and soft motion are widely demanded in one of the emerging fields of investigation, soft robotics[136]. Other properties such as, chemical resistance, hydrophobic or hygroscopic character, thermal resistance and electrical insulation extend the application range to environmentally-aggressive applications, such as,

aerospace. Moreover, the possibility to incorporate guest agents, such as, metallic or magnetic fillers, make them comparable with the straight competitor, the shape-memory alloys in terms of mechanical properties.

In this section we review the most relevant applications: biomedical applications, aerospace applications and one of the novel fields: soft robotics.

I.1.3.1 Biomedical applications

In the **biomedical field** the basis of the structural design of the AMPs lies on the **biocompatibility** and **biodegradability** of the constitutive polymers. In addition, the AMPs must response within the temperature range of the body (usually called body-triggered AMPs) to avoid burning and damaging the human during the actuation. The applications are mostly focused on **self-expandable or self-closing mechanisms** for cardiovascular diseases, such as, stents, clot removal or aneurysms occlusion devices, thus, **minimally invasive surgical procedures**[35,134,137–139]. In Figure I-16, Yakacki et al.[139] presented a cardiovascular stent made of an acrylate-based SMP with a T_g of 52 °C. To illustrate the performance, the SMP was compacted to fit into a 6-mm catheter (programming of the temporary shape) and then released in a 22-mm glass-tube filled with water at body temperature (37 °C). During the deployment, the stent first unrolled (1-10 seconds) and then unfurled (10 – 100 seconds). The effective expansion takes place during the unfurling process in which the recovery force must be able to expand the vessel.

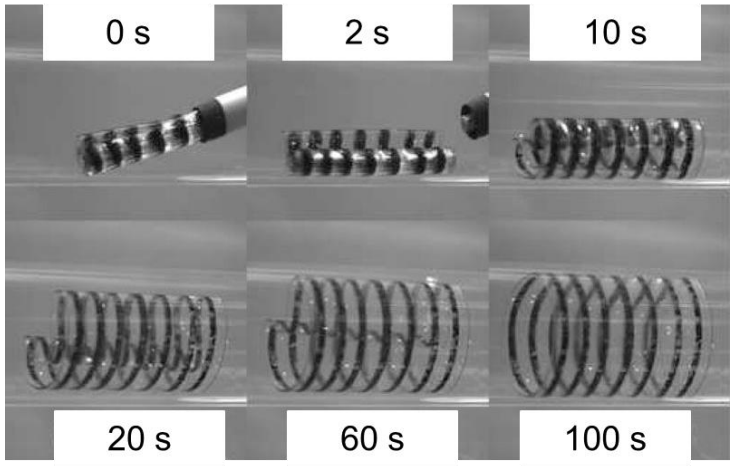

Figure I-16. Cardiovascular self-expandable stent made of an acrylate-based shape-memory polymer by Yakacki et al.[139].

Other applications are focused on **tissue engineering**[140] (reconstruction and repair of tissues and organs), wound closing or cardiac valve repair (self-closing rings to help cardiac valves with closing deficit). In Figure I-17, Lendlein et al.[141] presented a wound closure made of a biodegradable thermoplastic shape-memory fibber. The fibber was programmed up to 200% of strain and then used to suture an open incision in an animal specimen. The suture is tightened by increasing the temperature up to 40 °C (≈ body temperature) in only 20 seconds as illustrated in the frames (from the left to the right frame). The fibber slowly biodegrades (reported a 40% of the mass lost in the first 150 days), thus, it remains stable during the tissue regeneration and no further surgery is necessary to remove the fibber. This methodology is intended to help endoscopic surgery tying of a knot without using instruments through the self-controlled-tightening by programming the fibber.

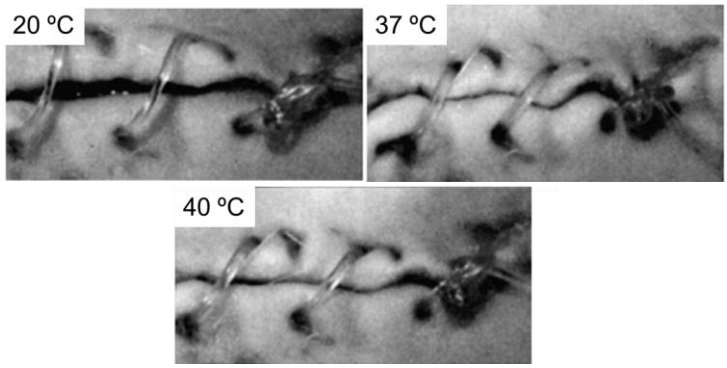

Figure I-17. Wound closure biodegradable shape-memory polymer by Lendlein et al.[141].

Finally, applications are found in more specialized fields, such as, **orthopaedics** (high strength SMPs can serve to heal the anterior cruciate ligament), **orthodontics** (treatment of dental malocclusion) or **prothesis** (biodegradable and self-deployable SMPs are used for minimal invasion when inserting the prothesis)[138].

I.1.3.2 Aerospace applications

In the **aerospace field** AMPs have awakened a great interest. The low-weight, the capability to adapt their shape upon environmental changes (i.e. pressure or temperature change), the strength and recovery force, and more importantly, the possibility to reduce their volume through folding and unfolding methodologies considerably reduce the cost and fit the operational requirements. A wide-range of applications and patents are found in this field. Overall, they can be divided in **components and structures**. Within the components, **smart hinges** and

booms are the most exploited types[21,142,143]. Hinges are driving mechanisms for the deployment of large structures. The great advantage of the AMPs as hinges is the reduction of the shock effect (the inertia of rigid mechanisms can damage the structure). Booms are used for the deployment of solar array or antenna once the structure have reached the target. They can be divided in foldable truss booms, coil able truss booms and storable tubular extendible members. In the structures field, **self-deployable reflector antennas** or panels, solar array and **morphing wings** are common examples[133,144].

In Figure I-18, Santo et al.[133] showed a self-deploying sheet based on the integration of a thermoset-based SMP layer in between two flexible layers made of thermosetting carbon fibber (sandwich-like configuration). The device was covered with an aluminium thin sheet (thickness of 100 µm) representing a solar sail. On heating up to 150 °C (above the T_g of the SMP), the size of the sheet can be reduced by folding it as illustrated in the top row of frames and further fixed on cooling down T_g. Afterwards, the unfolding process is triggered by heating up again. This methodology is especially interesting to reduce transport cost.

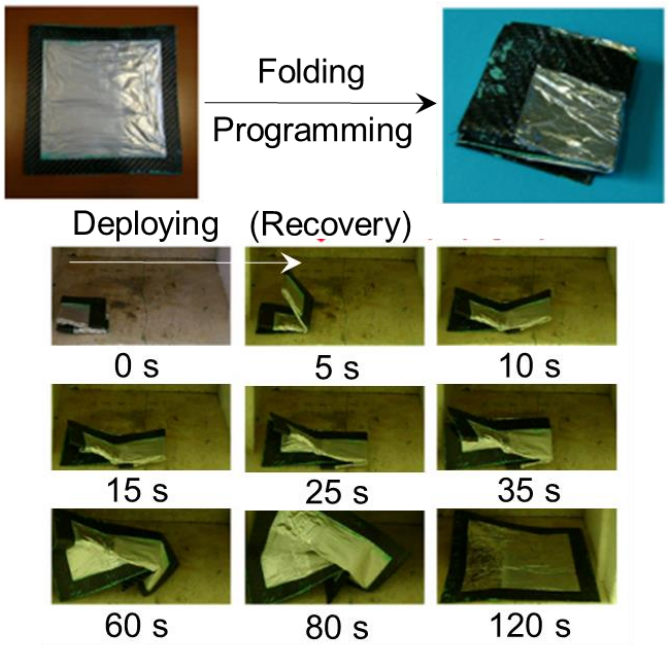

Figure I-18. Self-deploying mechanisms triggered through a thermosetting shape-memory layer for structural sheets or solar sails by Santo et al.[133].

In Figure I-19, Yu et al.[145] showed a morphing wing based on the adhesion of a programmed styrene-based SMP in a flexible plate. Upon heating, the curled wing is smoothly deployed providing stable flight.

Figure I-19. Morphing wing made of a styrene-based shape-memory thermoset by Yu et al.[145].

More recently, Yakacki et al.[143] demonstrated the possibility to reverse the deployment of aircraft pieces with a small airplane origami made of free-standing bidirectional SCPs (stress-induced LCEs), 3D printing and printed electronics (see Figure I-20). The LCE was obtained through dual-cure of thiol-acrylate systems and the stress-induced was achieved by pre-stretching the LCE in the intermediate stage as explained in section I.1.2.3. 3D printing was used to build up a soft substrate and pattern the silver wire on it. Afterwards, the stretched LCN was anchored to the soft substrate and the airplane device mounted piece-by-piece following the scheme in Figure I-20(a). Upon heating, the airplane morphs due to the bending of the soft actuators and upon cooling it goes back to the original flat shape.

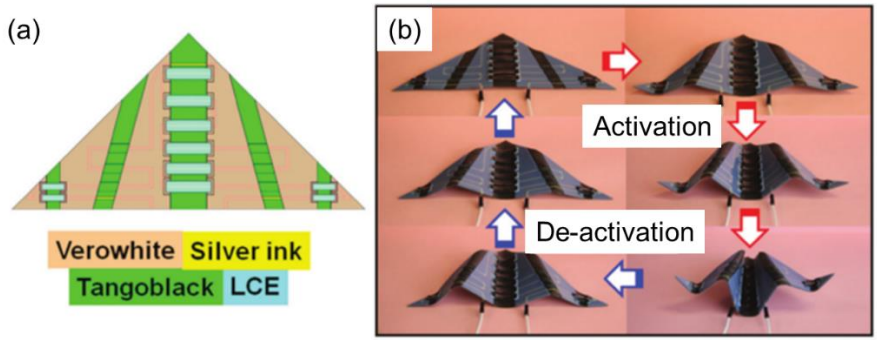

Figure I-20. (a) Airplane origami materials configuration and (b) airplane morphing upon heating (activation) and cooling (de-activation) by Yakacki et al.[143].

I.1.3.3 Soft robotics

Soft robotics is a subfield of robotics dealing with high compliance materials commonly targeting to emulate nature motion and adaptation to the environment. In contrast to traditional rigid robots, they are capable

to perform **soft non-linear motion** through low-weight soft materials (typically polymers), thus, minimizing damages during holding and carrying steps. AMPs are used in soft robotics due to their low-weight and the reduction of complex controlling mechanisms. The motion protocol is pre-designed in the AMP before assembling the robot and further triggered through the appropriate stimulus, thus, the number of required joints, links and rotatory mechanisms are considerably reduced or non-existent, and the controlling mechanism is mostly reduced to the stimulus variation[118,146–148].

Yang et al.[149] developed an electro-driven "carrier" robot using a hydrogel-based SCP. The hydrogel can bend towards the cathode in electrolyte solutions, thus, the "carrier" was investigated immersed in between two horizontally-placed carbon electrodes in a NaCl solution. Facing one leg to the cathode and the other to the anode, the "carrier" was able to walk upon alternate voltage of 10 or higher Volts. The bending level and time to walk could be controlled through the voltage amount. Additionally, the "carrier" could walk with different weights as it can be seen in frames (a)-(e) in Figure I-21.

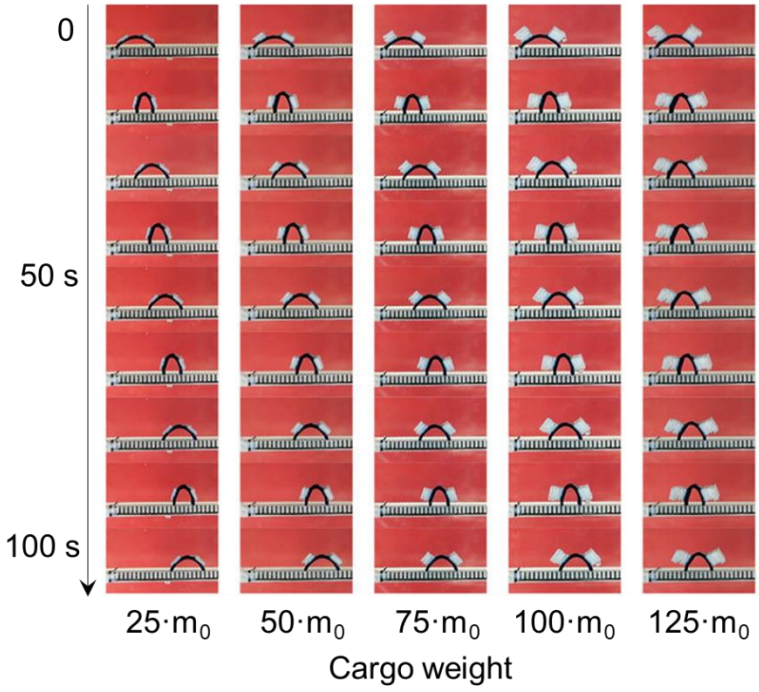

Figure I-21. Walking robot made of a hydrogel-based shape-changing polymer capable to walk carrying a weight by Yang et al.[149].

Huang et al.[150] designed a phot-driven micro swimming robot by using a photo-responsive azobenzene-based SCP film (see Figure I-22). The film responses to the UV-light due to the stimulation of the azobenzene moieties, leading to a configurational change, hence, a macroscopic bending process. Alternate exposure to light from both faces of the film leads to coupled bending processes in opposite directions, thus, the film swings behaving as a flipper. In an aqueous medium, the flipper can push the body of the robot from behind emulating the swimming mechanism of a fish.

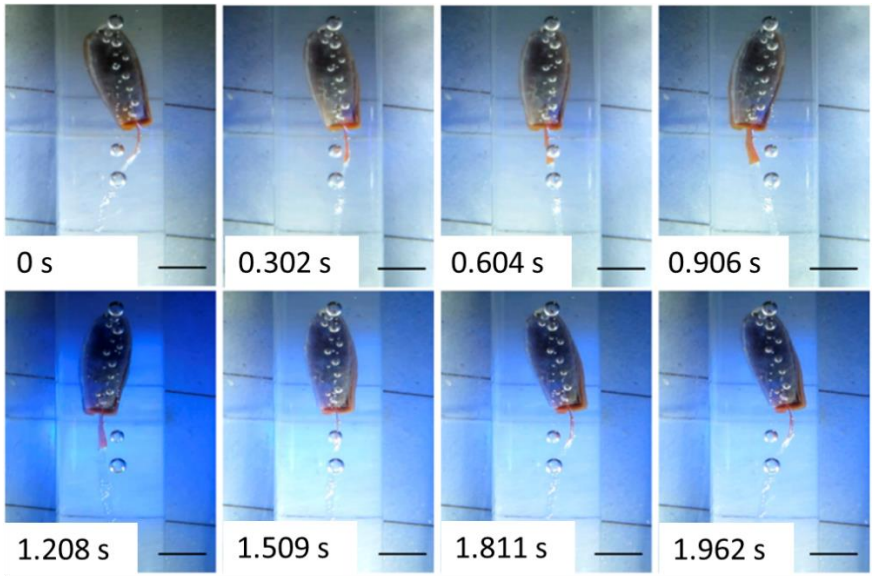

Figure I-22. Swimming robot made of photo-responsive azobenzene-based shape-changing polymer capable to swim upon exposure to alternate UV-light by Huang et al.[150].

Other examples are found in **soft mechanisms** to **catch**, **hold** and **transport** pieces in **remote or inaccessible places**, such as, Marts and mountains, or in service and rescue missions. The low-weight and reduced shock effect of AMPs are the main characteristics to step back in the traditional controlling systems that, although complex designs have been achieved, the remote control is still tedious and sometimes problematic. AMPs offer the possibility to reduce transport cost and make simpler and sometimes self-assisted the remote control. Ge et al.[151] took advantage of light-assisted 3D printing to shape complex SMP structures. As an example, in Figure I-23, a small, rubbery, claw-like gripper was 3D-printed, and the hinges opened through shape-memory programming. When the temperature of the air reaches 40 °C, the shape-recovery is triggered and

the minigripper is able to catch small pieces, such as, screws as depicted in the figure.

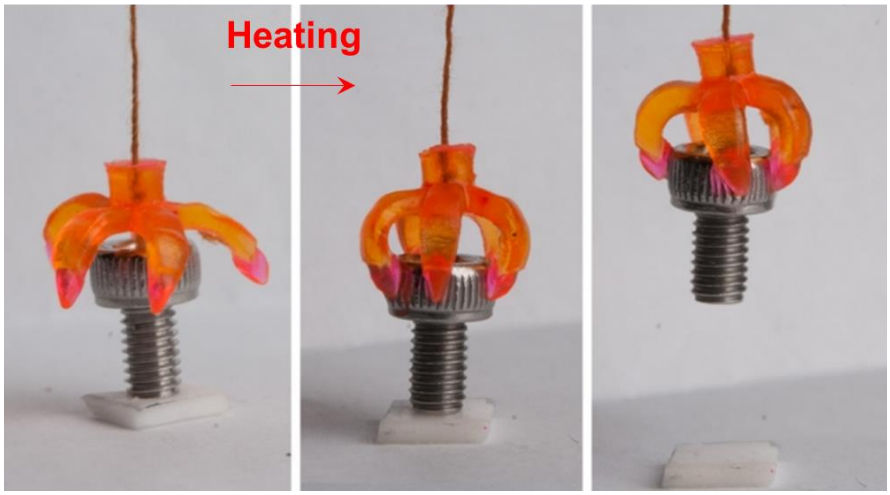

Figure I-23. 3D-printed shape-memory minigripper made of shape-memory hinges by Ge et al. [151].

I.2 Dual-curing processing

Dual-curing processing is a novel methodology to develop dual-network thermosets via two independent but compatible reaction processes. These reactions can be simultaneously activated or sequentially triggered by combination of different stimuli, such as, UV-light and heat, or different reaction kinetics. **Sequential dual-curing processing** is more attractive due to the possibility to achieve a large set of material properties in two stages that allows multi-stage processing scenarios. For example, in microelectronics or coatings, application and patterning of the resin in a persistent shape previously to fully cure and therefore attach the thermoset is highly demanded and can be accomplished through the **processing in the intermediate stage**. Besides, the cost in transport or storage steps during the processing of a piece of thermoset can be considerably reduced. Intermediate materials with high deformability and malleability can be cured and then folded into a reduced shape for the transport/storage stage and further unfolded on-situ trough the elastic recovery of the network. Moreover, the low T_g in the intermediate stage considerably improves the impact resistance (energy absorption), thus avoiding irrecoverable damages that may take place during these intermediate stages.

The precise **control of the material properties** in the intermediate stage (i.e. low T_g, low crosslinking density and high deformability) can be exploited as a pre-processing methodology for the development of complex three-dimensional structures without the requirement of complex moulds, a common drawback in thermosets that cannot be processed after crosslinking and therefore must be patterned from a liquid-like mixture. The absence of mould reduces and makes easier the control of the bubble formation during the curing process, another important issue in the cure of thermosets. In Figure I-24 the application of sequential dual-curing processing in the development of complex shaped designs is schematized (a spring-shaped final design is shown).

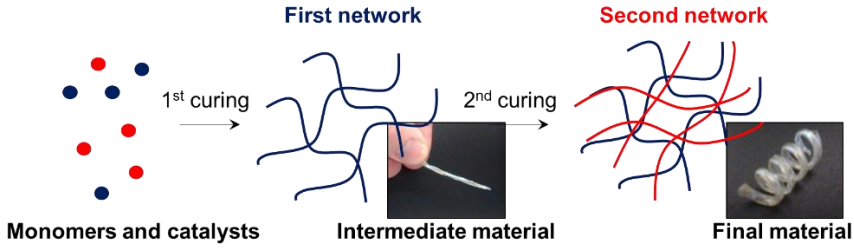

Figure I-24. Scheme of the dual-curing processing towards complex shaped designs with illustrations of the intermediate and final materials for a spring-shaped design.

The possibility to **attain complex shaped designs** have attracted many researchers in the field of AMPs[152]. Modern techniques, such as 3D printing, are being used for the development of complex shaped SMPs[151], however, the control of the material properties is still limited by the requirements of the 3D printer. In contrast, dual-curing processing emerges as a promising mechanism in which the progress controlling the polymerization dynamics and network built up of crosslinked polymers, enables the development of a wide range of AMPs with tuneable properties.

Examples of dual-curing processing include photo-curing/ thermal-curing click thiol-ene/thiol-epoxy systems, aza-Michael addition/free-radical polymerization of amine-acrylate systems and both photo-curing thiol/ene/cationic systems[126,153–155]. Nair et al.[125] designed a series of non-stoichiometric thiol-acrylate systems leading to intermediate materials with a broad range of rubbery moduli and T_g (from 0.5 MPa and T_g of -10 °C to 22 MPa and T_g of 22 °C). The intermediate materials were obtained via base-catalysed Michael addition of the thiol-acrylate "click" reaction and the final materials through further crosslinking of the excess of acrylic functional groups (2nd curing stage), leading to materials with moduli up to 200 MPa and T_g ranging from 5 °C up to 190 °C. Peng et al.[156] took advantage of the base-catalysed thiol-acrylate Michael addition to yield writeable substrates (intermediate materials) with an excess of thiol-allyl reacting species. Holograms were further recorded through coherent exposure to laser beams by triggering the thiol-allyl radical polymerization (2nd curing stage).

As it can be deduced from the examples above, "click" reactions are commonly used for dual-curing processing. The **click chemistry** concept was introduced in 2001 by K. B. Sharpless and co-workers[157] to describe reactions characterized by their selectivity, versatility and efficiency, that are environmentally friendly and take place in a simple way from an experimental point of view.

Cycloadditions and diel-alder reactions, ring-opening of strained rings through nucleophilic substitution (i.e. epoxides and aziridines), non-aldol carbonyl chemistry, addition reactions and Michael addition are examples of click reactions. The orthogonality of these set of reactions allows easy and compatible combination to attain dual-networks and the high-yielding and tolerance to various functional groups make possible the development of controlled network architectures.

Among the different click reactions, **"thiol-click" reactions** are interesting because they take place rapidly in comparison with other click

reactions and under mild conditions, producing radical or anionic species when the appropriate catalyst is selected[158]. Thiol reactions are divided in base-catalysed nucleophilic reactions (thiol-epoxy, thiol-isocyanate and thiol Michael[159]) and radical-mediated reactions (thiol-ene and thiol-yne). The **thiol-epoxy reaction** is a step-wise ring-opening mechanism catalysed by tertiary amines that basically consist of a nucleophilic attack to the oxirane ring by the thiolate anion. During the reaction, hydroxyl and thioether groups are formed which can be further transformed in other polymeric structures. This leads to soft functional materials with enhanced mechanical properties (high deformability and resistance at break), high impact resistance, adhesion and interestingly, high degree of transparency even in thin films[160]. All these properties make them attractive in coatings, adhesives and optical applications. Moreover, the enhanced mechanical properties are valuable features for the processing in the intermediate stage and the development of promising AMPs.

Our research group has recently published a book's chapter of dual-curing systems based on "click" reactions[161]. For further information we invite the reader to check the chapter of the book.

As stated above, dual-curing processing requires precise control of the polymerization processes. However, tertiary amines are usually too reactive in the catalysis of the thiol-epoxy reaction, limiting the pot-life of the initial mixture and making difficult the control of the reaction in a dual-stage scenario[162,163]. **Latent catalysts**, that means, passive catalysts that are activated through external stimulation (i.e. heat, UV-light, pH-change or moisture), are an interesting approach to increase the pot-life, control the reaction kinetics and produce well-defined and homogeneous networks[164,165]. Among the different latent systems, encapsulated mechanisms are used to control the release of the catalyst. Stimuli-responsive polymeric structures, such as, degradable or expandable capsules can be used to confine tertiary amines, thus, as a barrier to maintain the mixture under safe conditions until the amines are released usually by the effect of heat or UV-light, activating the "thiol-epoxy" reaction.

In this investigation, **thermally-activated encapsulated amines** are used as latent catalyst for the development of **"click" "thiol-epoxy" based SMPs** in chapter III and the application to the dual-curing processing of complex shaped designs and enhanced AMPs through off-stoichiometric click "thiol-epoxy" systems (presented in chapter IV). Finally, the dual-curing processing is utilised as a mechanism to prepare

free-standing bidirectional actuators via external incorporation of an elastomeric matrix. The results and discussion are presented in chapter V.

I.3 Objectives

The main objective of this investigation is to design, obtain and characterise enhanced AMPs via sequential dual-curing processing.

The investigation has been divided in different research lines: (1) the development and characterization of "thiol-epoxy" based SMPs through click chemistry and latent catalysts; (2) the development and characterization of complex-shaped "thiol-epoxy" based SMPs implementing the click chemistry to the sequential dual-curing processing; (3) the development and characterization of free-standing actuators obtained by combination of LCNs and dual-curing processing.

The specific objectives of the research line (1) are the following:

- To develop and characterize "thiol-epoxy" click based SMPs by using thiol and epoxy compounds with different functionality, chemical structure and proportion.
- To study the effect of the structural and thermomechanical properties of the SMPs with the shape-memory response in terms of programming and recovery performances.
- To investigate the relation between the polymer structural design and the shape-memory response to find useful tools for the operational design of the SMP.

The specific objectives of the research line (2) are the following:

- To characterise the structural, physical and thermomechanical properties of the intermediate and final materials obtained through the "thiol-epoxy" dual-curing systems.
- To design and develop complex-shaped SMPs for various applications in both, the intermediate and final stages.
- To study the shape-memory response of bent-shaped SMPs as potential mechanical actuators.

The specific objectives of the research line (3) are the following:

- Synthesis of epoxy-carboxylic LCNs and characterization of the thermal, structural, LC properties and SCE in view of the requirements for the development of the free-standing actuators.
- Application of the dual-curing processing for the external incorporation of an elastomeric matrix onto the LCNs (design of the free-standing actuator).
- Characterization of the obtained free-standing bidirectional actuators.

The three main research lines are presented and discussed in chapters III, IV and V respectively. The conclusions of each study are provided in each chapter and global conclusions are written in chapter VI.

I.4 References

[1] M. Behl, A. Lendlein, *Actively moving polymers*, Soft Matter. **2007**, 3, 58–67.

[2] A. Rafsanjani, V. Brulé, T.L. Western, D. Pasini, *Hydro-Responsive Curling of the Resurrection Plant Selaginella lepidophylla*, Sci. Rep. **2015,** 1–7.

[3] H. Terashima, S. Kojima, M. Homma, *Flagellar motility in bacteria structure and function of flagellar motor*, Int. Rev. Cell Mol. Biol. **2008**, 270, 39–85.

[4] M.O. Saed, A.H. Torbati, D.P. Nair, C.M. Yakacki, *Synthesis of Programmable Main-chain Liquid-crystalline Elastomers Using a Two-stage Thiol-acrylate Reaction*, J. Vis. Exp. **2016**, 107, 1–10.

[5] W.M. Huang, Y. Zhao, C.C. Wang, Z. Ding, H. Purnawali, C. Tang, J.L. Zhang, *Thermo/chemo-responsive shape memory effect in polymers: A sketch of working mechanisms, fundamentals and optimization*, J. Polym. Res. **2012**, 19.

[6] G.G. Barclay, C.K. Ober, *Liquid crystalline and rigid-rod networks*, Prog. Polym. Sci. **1993**, 18, 899–945.

[7] A. Matsuda, J. Sato, H. Yasunaga, Y. Osada, *Order-Disorder Transition of a Hydrogel Containing an n-Alkyl Acrylate*, Macromolecules. **1994**, 27, 7695–7698.

[8] Y. Tanaka, Y. Kagami, A. Matsuda, Y. Osada, *Thermoreversible Transition of Tensile Modulus of Hydrogel with Ordered Aggregates*, Macromolecules. **1995**, 28, 2574–2576.

[9] Y. Osada, A. Matsuda, *Shape memory in hydrogels,* Nature. **1995**, 376, 219.

[10] A. Lendlein, C. Wischke, K. Kratz, M. Heuchel, J. Zotzmann, B. Hiebl, A.T. Neffe, M. Behl, *B. Development, Shape-Memory Polymers*, Elsevier Ltd., **2011**.

[11] L.B. Vernon, H.M. Vernon, *Process of manufacturing articles of thermoplastic synthetic resins,* US Pat. 2234993A, **1941**.

[12] W.C. Rainer, E.M. Redding, J.J. Hitov, A.W. Sloan, W.D. Stewad, *Polyethylene product and process*, US Pat. 3144398A, **1964**.

[13] R.J. Perrone, *Heat-shrinkable articles made from silicone rubber– polyethylene compositions*, US Pat. 3326869A, 1967.

[14] P.E. Wray, *Elastic memory articles*, US Pat. GB1075704, **1967**.

[15] C. Liu, H. Qin, P.T. Mather, *Review of progress in shape-memory polymers*, J. Mater. Chem. **2007**, 17, 1543.

[16] M.D. Hager, S. Bode, C. Weber, U.S. Schubert, *Shape memory polymers: Past, present and future developments*, Prog. Polym. Sci. **2015**, 49–50, 3–33.

[17] M. Balk, M. Behl, C. Wischke, J. Zotzmann, A. Lendlein, *Recent advances in degradable lactide-based shape-memory polymers*, Adv. Drug Deliv. Rev. **2016**, 107, 136–152.

[18] R. Langer, A. Lendlein, *Biodegradable Shape Memory Polymeric Sutures*, US Pat. 8303625B2, **2003**.

[19] C.M. Yakacki, R. Shandas, C. Lanning, B. Rech, K. Gall, *Polymer Networks for Cardiovascular Applications*, **2009**, 28, 2255–2263.

[20] D.J. Maitland, M.F. Metzeger, D. Schumann, A. Lee, T.S. Wilson, *Photothermal properties of shape memory polymer micro actuators for treating stroke*, Lasers Surg. Med. **2004**, 30, 1–11.

[21] J. Sun, Q. Guan, Y. Liu, J. Leng, *Morphing aircraft based on smart materials and structures: A state-of-the-art review*, J. Intell. Mater. Syst. Struct. **2016**, 27, 2289–2312.

[22] E. Havens, E.A. Snyder, T.H. Tong, *Light-activated shape memory polymers and associated applications,* Proc. SPIE (Smart Struct. Mater. 2005: Industrial and Commercial Applications of Smart Structures Technologies). **2005**, 5762, 48-55.

[23] H. Tobushi, S. Hayashi, K. Hoshio, Y. Ejiri, *Shape recovery and irrecoverable strain control in polyurethane shape-memory polymer*, Sci. Technol. Adv. Mater. **2008**, 9, 7.

[24] A. Lendlein, T. Sauter, *Shape-memory effect in polymers*, Macromol. Chem. Phys. **2013**, 214, 1175–1177.

[25] M. Heuchel, T. Sauter, K. Kratz, A. Lendlein, *Thermally induced shape-memory effects in polymers: Quantification and related modeling approaches*, J. Polym. Sci. Part B Polym. Phys. **2013**, 51, 621–637.

[26] X. Wu, W.M. Huang, Y. Zhao, Z. Ding, C. Tang, J. Zhang, *Mechanisms of the shape memory effect in polymeric materials*, Polymers. **2013**, 5, 1169–1202.

[27] K. Wei, G. Zhu, Y. Tang, L. Niu, *Shape-memory effects of a hydro-epoxy resin system*, J. Polym. Res. **2013**, 20, 123.

[28] D. Habault, H. Zhang, Y. Zhao, *Light-triggered self-healing and shape-memory polymers*, Chem. Soc. Rev. **2013**, 42, 7244–56.

[29] H. Du, X. Lei, Y. Xu, Z. Liang, Y. Wang, *Multi-stimuli induced shape memory effect of polymers based on poly(vinyl alcohol)*, Prog. Chem. **2016**, 28, 1648–1657.

[30] G. Li, A. Wang, *Cold, warm, and hot programming of shape memory polymers*, J. Polym. Sci. Part B Polym. Phys. **2016**, 54, 1319–1339.

[31] C.M. Yakacki, S. Willis, C. Luders, K. Gall, *Deformation limits in shape-memory polymers*, Adv. Eng. Mater. **2008**, 10, 112–119.

[32] I.A. Rousseau, *Challenges of shape memory polymers: A review of the progress toward overcoming SMP's limitations*, Polym. Eng. Sci. **2008**, 48, 2075–2089.

[33] V. Lorenzo, A. Díaz-Lantada, P. Lafont, H. Lorenzo-Yustos, C. Fonseca, J. Acosta, *Physical aging of a PU-based shape memory polymer: Influence on their applicability to the development of medical devices*, Mater. Des. **2009**, 30, 2431–2434.

[34] J. Choi, A.M. Ortega, R. Xiao, C.M. Yakacki, T.D. Nguyen, *Effect of physical aging on the shape-memory behavior of amorphous networks*, Polymer. **2012**, 53, 2453–2464.

[35] C.M. Yakacki, R. Shandas, D. Safranski, A.M. Ortega, K. Sassaman, K. Gall, *Strong, tailored, biocompatible shape-memory polymer networks*, Adv. Funct. Mater. **2008**, 18, 2428–2435.

[36] D.P. Nair, N.B. Cramer, T.F. Scott, C.N. Bowman, R. Shandas, *Photopolymerized thiol-ene systems as shape memory polymers*, Polymer. **2010**, 51, 4383–4389.

[37] I. a. Rousseau, T. Xie, *Relationship between materials properties and shape memory behavior in epoxy-amine polymers*, Mater. Res. Soc. Symp. Proc. **2009**, 1190, 31–36.

[38] I. a. Rousseau, T. Xie, *Shape memory epoxy: Composition, structure, properties and shape memory performances*, J. Mater. Chem. **2010**, 20, 3431.

[39] Y. Liu, C. Han, H. Tan, X. Du, *Thermal, mechanical and shape memory properties of shape memory epoxy resin*, Mater. Sci. Eng. A. **2010**, 527, 2510–2514.

[40] D.M. Feldkamp, I. a. Rousseau, *Effect of the deformation temperature on the shape-memory behavior of epoxy networks*, Macromol. Mater. Eng. **2010**, 295, 726–734.

[41] W.B. Song, L.Y. Wang, Z.D. Wang, Synthesis and thermomechanical research of

shape memory epoxy systems, Mater. Sci. Eng. A. **2011**, 529, 29–34.

[42] D.M. Feldkamp, I. a. Rousseau, *Effect of Chemical Composition on the Deformability of Shape-Memory Epoxies*, Macromol. Mater. Eng. **2011**, 296, 1128–1141.

[43] A.B. Leonardi, L. a. Fasce, I. a. Zucchi, C.E. Hoppe, E.R. Soulé, C.J. Pérez, R.J.J. Williams, *Shape memory epoxies based on networks with chemical and physical crosslinks*, Eur. Polym. J. **2011**, 47, 362–369.

[44] Y. Gu, S.X. Li, *Thermo-Mechanical Behavior of Epoxy Shape Memory Polymer*, Adv. Mater. Res. **2013**, 721, 169–172.

[45] R. Biju, C.P.R. Nair, *Synthesis and characterization of shape memory epoxy-anhydride system*, J. Polym. Res. **2013**, 20, 82.

[46] S. Pandini, F. Bignotti, F. Baldi, S. Passera, *Network architecture and shape memory behavior of cold-worked epoxies*, J. Intell. Mater. Syst. Struct. **2013**, 24, 1583–1597.

[47] M. Fan, H. Yu, X. Li, J. Cheng, J. Zhang, *Thermomechanical and shape-memory properties of epoxy-based shape-memory polymer using diglycidyl ether of ethoxylated bisphenol-A*, Smart Mater. Struct. **2013**, 22, 55034.

[48] K.S. Santhosh Kumar, R. Biju, C.P. Reghunadhan Nair, *Progress in shape memory epoxy resins*, React. Funct. Polym. **2013**, 73, 421–430.

[49] N. Zheng, G. Fang, Z. Cao, Q. Zhao, T. Xie, *High strain epoxy shape memory polymer*, Polym. Chem. **2015**, 6, 3046–3053.

[50] D. Santiago, A. Fabregat-Sanjuan, F. Ferrando, S. De la Flor, *Recovery stress and work output in hyperbranched poly(ethyleneimine)-modified shape-memory epoxy polymers*, J. Polym. Sci. Part B Polym. Phys. **2016**, 54, 1002–1013.

[51] J.S. Arrieta, J. Diani, P. Gilormini, *Cyclic and monotonic testing of free and constrained recovery properties of a chemically crosslinked acrylate*, J. Appl. Polym. Sci. **2014**, 131, 1-8.

[52] S. Arrieta, J. Diani, P. Gilormini, *Experimental characterization and thermoviscoelastic modeling of strain and stress recoveries of an amorphous polymer network*, Mech. Mater. **2014**, 68, 95–103.

[53] C.M. Yakacki, A.M. Ortega, C.P. Frick, N. Lakhera, R. Xiao, T.D. Nguyen, *Unique Recovery Behavior in Amorphous Shape-Memory Polymer Networks*, Macromol. Mater. Eng. **2012**, 297, 1160–1166.

[54] D. Santiago, F. Ferrando, S. De La Flor, *Effect of different shape-memory processing methods on the thermomechanical cyclic properties of a shape-memory polyurethane*, J. Mater. Eng. Perform. **2014**, 23, 2561–2566.

[55] C. Schmidt, K. Neuking, G. Eggeler, *Functional fatigue of shape-memory polymers*, Adv. Eng. Mater. **2008**, 10, 922–927.

[56] C. Schmidt, A.M.S. Chodwdhury, K. Neuking, G. Eggeler, *Studies on the cycling, processing and programming of an industrially applicable shape memory polymer Tecoflex® (or TFX EG 72D)*, High Perform. Polym. **2011**, 23, 300–307.

[57] S. Mogharebi, R. Kazakeviciute-Makovska, H. Steeb, G. Eggeler, K. Neuking, *On the cyclic material stability of shape memory polymer*, Mater. Werkst. **2013**, 44, 521–526.

[58] F. Xie, L. Huang, J. Leng, Y. Liu, *Thermoset shape memory polymers and their composites*, J. Intell. Mater. Syst. Struct. **2016**, 27, 2433–2455.

[59] G.P. Tandon, A.J. McClung, J.W. Baur, *Shape-Memory Polymers for Aerospace Applications*, DEStech Publications, Inc., USA, **2015**.

[60] D. Santiago, X. Fernández-Francos, F. Ferrando, S. De la Flor, *Shape-memory effect in hyperbranched poly(ethyleneimine)-modified epoxy thermosets*, J. Polym. Sci. Part B Polym. Phys. **2015**, 53, 924-933.

[61] A. Arnebold, A. Hartwig, *Fast switchable, epoxy based shape-memory polymers with high strength and toughness*, Polymer. **2016**, 83, 40–49.

[62] M.A. Boyle, C.J. Martin, J.D. Neuner, *Epoxy Resins*, ASM International, USA, **2001**.

[63] B. Yan, S. Gu, Y. Zhang, *Polylactide-based thermoplastic shape memory polymer nanocomposites*, Eur. Polym. J. **2013**, 49, 366–378.

[64] A. Saralegi, E.J. Foster, C. Weder, A. Eceiza, M.A. Corcuera, *Thermoplastic shape-memory polyurethanes based on natural oils*, Smart Mater. Struct. **2014**, 23, 025033.

[65] H.M. Jeong, B.K. Ahn, B.K. Kim, *Miscibility and shape memory effect of thermoplastic polyurethane blends with phenoxy resin*, Eur. Polym. J. **2001**, 37, 2245–2252.

[66] H.M. Jeong, J.H. Song, S.Y. Lee, B.K. Kim, *Miscibility and shape memory property of poly (vinyl chloride)/ thermoplastic polyurethane blends*, J. Mater. Sci. **2001**, 6, 5457–5463

[67] T. Ikematsu, Y. Kishimoto, M. Karaushi, *Block Copolymer Bumpers With Good Shape Memory,* Japan Pat. 2022355, **1990**.

[68] K. Komiya, A. Shimizu, Y. Kishimoto, *Heat-sensitive Shape- memory Polyurethanes*, Japan Pat. 1282209, **1989**.

[69] A. Díaz-Lantada, *Systematic Development Strategy for Smart Devices Based on Shape-Memory Polymers*, Polymers. **2017**, 9, 496.

[70] K. Lee, H. Koerner, R. Vaia, T. Bunning, T. White, *Relationship between the photomechanical response and the thermomechanical properties of azobenzene liquid crystalline polymer networks*, Macromolecules. **2010**, 43, 8185–90.

[71] K. Lee, H. Koerner, R. Vaia, T. Bunning, T. White, *Light-activated shape memory of glassy, azobenzene liquid crystalline polymer networks*, Soft Matter. **2011**, 7, 4318–24.

[72] W.M. Huang, B. Yang, L. An, C. Li, Y.S. Chan, *Water-driven programmable polyurethane shape memory polymer: Demonstration and mechanism*, Appl. Phys. Lett. **2005**, 86, 1–3.

[73] W.M. Huang, C.L. Song, Y.Q. Fu, C.C. Wang, Y. Zhao, H. Purnawali, H.B. Lu, C. Tang, Z. Ding, J.L. Zhang, *Shaping tissue with shape memory materials*, Adv. Drug Deliv. Rev. **2013**, 65, 515–35.

[74] M. Behl, A. Lendlein, *Triple-shape polymers*, J. Mater. Chem. **2010**, 20, 3335.

[75] Q. Zhao, M. Behl, A. Lendlein, *Shape-memory polymers with multiple transitions: complex actively moving polymers*, Soft Matter. **2013**, 9, 1744–1755.

[76] I. Bellin, S. Kelch, R. Langer, A. Lendlein, *Polymeric triple-shape materials*, Proc. Natl. Acad. Sci. **2006**, 103, 18043–18047.

[77] C.N. Bowman, *Triple Shape Memory Materials Incorporating Two Distinct Polymer Networks Formed by Selective Thiol – Michael Addition Reactions*, Macromolecules. **2014**, 47, 4949–4954.

[78] J. Zotzmann, M. Behl, Y. Feng, A. Lendlein, *Copolymer networks based on poly(ω-pentadecalactone) and poly(ε-caprolactone)segments as a versatile triple-shape polymer system*, Adv. Funct. Mater. **2010**, 20, 3583–3594.

[79] T. Xie, *Tunable polymer multi-shape memory effect*, Nature. **2010**, 464, 267–270.

[80] J. Li, T. Xie, *Significant impact of thermo-mechanical conditions on polymer triple-shape memory effect*, Macromolecules. **2011**, 44, 175–180.

[81] Y. Liu, K. Gall, M.L. Dunn, A.R. Greenberg, J. Diani, *Thermomechanics of shape memory polymers: Uniaxial experiments and constitutive modeling*, Int. J. Plast. **2006**, 22, 279–313.

[82] M. Baghani, R. Naghdabadi, J. Arghavani, S. Sohrabpour, *A thermodynamically-consistent 3D constitutive model for shape memory polymers*, Int. J. Plast. **2012**, 35, 13–30.

[83] M. Baghani, R. Naghdabadi, J. Arghavani, *A large deformation framework for shape memory polymers: Constitutive modeling and finite element implementation*, J. Intell. Mater. Syst. Struct. **2012**, 24, 21-32.

[84] M. Baghani, R. Naghdabadi, J. Arghavani, S. Sohrabpour, *A constitutive model for shape memory polymers with application to torsion of prismatic bars*, J. Intell. Mater. Syst. Struct. **2012**, 23, 107–116.

[85] J. Morshedian, H. a. Khonakdar, S. Rasouli, *Modeling of shape memory induction and recovery in heat-shrinkable polymers*, Macromol. Theory Simulations. **2005**, 14, 428–434.

[86] H.A. Khonakdar, S.H. Jafari, S. Rasouli, J. Morshedian, H. Abedini, *Investigation and modeling of temperature dependence recovery behavior of shape-memory crosslinked polyethylene*, Macromol. Theory Simulations. **2007**, 16, 43–52.

[87] O.A. Balogun, C. Mo, *Three-dimensional thermo-mechanical viscoelastic model for shape memory polymers with binding factor*, J. Intell. Mater. Syst. Struct. **2016**, 27, 1908–1916.

[88] F. Cui, S. Moon, I. Rao, *Modeling the Viscoelastic Behavior of Amorphous Shape Memory Polymers at an Elevated Temperature*, Fluids. **2016**, 1, 15.

[89] J. Diani, P. Gilormini, C. Frédy, I. Rousseau, *Predicting thermal shape memory of crosslinked polymer networks from linear viscoelasticity*, Int. J. Solids Struct. 2012, 49, 793–799.

[90] P.G. de Gennes, *Possibilites of liquid-crystalline network polymers*, Phys. Lett. A. **1969**, 28, 725.

[91] L. Strzelecki, L. Liebert, Polymerisation neuer mesomorpher monomer, Bullet Soc. Chem. **1973**, 597.

[92] H. Finkelmann, J.H. Koch, G. Rehage, *Investigations on liquid crystalline polysiloxanes part: 3. Liquid crystalline elastomers — a new type of liquid crystalline material* , Makromolecular Chem. Rapid Commun. **1981**, 2, 317–322.

[93] H. Finkelmann, *Liquid Crystalline Polymers*, Angew. Chemie Int. Ed. English. **1987**, 26, 816–824.

[94] M. Giamberini, E. Amendola, C. Carfagna, *Liquid Crystalline Epoxy Thermosets*, Mol. Cryst. Liq. Cryst. Sci. Technol. Sect. A. Mol. Cryst. Liq. Cryst. **1995**, 266, 9–22.

[95] C. Carfagna, E. Amendola, M. Giamberini, *Liquid Crystalline Epoxy Based Polymers*, Prog. Polym. Sci. **1997**, 22, 1607–1647.

[96] Thomsen III, P. Keller, J. Naciri, R. Pink, H. Jeon, D. Shenoy, B.R. Ratna, *Liquid Crystal Elastomers with Mechanical Properties of a Muscle, Macromolecules*. **2001**, 34, 5868–5875.

[97] T. Mirfakhrai, J.D.W. Madden, R.H. Baughman, *Polymer artificial muscles*, Mater. Today. **2007**, 10, 30–38.

[98] C. Ohm, M. Brehmer, R. Zentel, *Liquid crystalline elastomers as actuators and sensors*, Adv. Mater. **2010**, 22, 3366–3387.

[99] A. Sánchez-Ferrer, T. Fischl, M. Stubenrauch, A. Albrecht, H. Wurmus, M. Hoffmann, H. Finkelmann, *Liquid-crystalline elastomer microvalve for microfluidics*, Adv. Mater. **2011**, 23, 4526–4530.

[100] E. Sungur, L. Mager, A. Boeglin, M.H. Li, P. Keller, K.D. Dorkenoo, *Temperature tunable optical gratings in nematic elastomer*, Appl. Phys. A Mater. Sci. Process. **2010**, 98, 119–122.

[101] Y. Hong, A. Buguin, J.M. Taulemesse, K. Kaneko, S. Méry, A. Bergeret, P. Keller, *Micron-sized main-chain liquid crystalline elastomer actuators with ultralarge amplitude contractions*, J. Am. Chem. Soc. **2009**, 131, 15000–15004.

[102] R. Yoshida, T. Okano, *Biomedical Applications of Hydrogels Handbook*, Springer, USA, **2010**.

[103] R. Zentel, *Liquid Crystalline Elastomers*, Angew. Chemie - Int. Ed. **1989**, 28, 1407–1415.

[104] M. Warner, E. Terentjev, P. Bladon, *"Soft elasticity" - deformation without resistance in liquid crystal elastomers*, J. Phys. II. **1994**, 4, 93–102.

[105] S. Dey, D. Agra-Kooijman, W. Ren, P. McMullan, A. Griffin, S. Kumar, *Soft Elasticity in Main Chain Liquid Crystal Elastomers*, Crystals. 2013, 3, 363–390.

[106] J.K. Whitmer, T.F. Roberts, R. Shekhar, N.L. Abbott, J.J. De Pablo, *Modeling the polydomain-monodomain transition of liquid crystal elastomers*, Phys. Rev. E - Stat. Nonlinear, Soft Matter Phys. **2013**, 87, 1–5.

[107] M. Giamberini, P. Cerruti, V. Ambrogi, C. Vestito, F. Covino, C. Carfagna, *Liquid crystalline elastomers based on diglycidyl terminated rigid monomers and aliphatic acids. Part 2. Mechanical characterization*, Polymer. **2005**, 46, 9113–9125.

[108] M. Giamberini, P. Cerruti, V. Ambrogi, C. Vestito, F. Covino, C. Carfagna, *Liquid crystalline elastomers based on diglycidyl terminated rigid monomers and aliphatic acids. Part 1. Synthesis and characterization*., Polymer. **2005**, 46, 9113–9125.

[109] J.F. Ban, S.R. Lu, D. Guo, K. Liu, C.X. Luo, *Thermomechanical Properties and Morphology of Liquid Crystalline Polyurethane/Epoxy Resin Composites*, Adv. Mater. Res. **2011**, 194–196, 1421–1425.

[110] R. Ishige, K. Osada, H. Tagawa, H. Niwano, M. Tokita, J. Watanabe, *Elongation behavior of a main-chain smectic liquid crystalline elastomer*, Macromolecules. **2008**, 41, 7566–7570.

[111] G.N. Mol, K.D. Harris, C.W.M. Bastiaansen, D.J. Broer, *Thermo-mechanical responses of liquid-crystal networks with a splayed molecular organization*, Adv. Funct. Mater. **2005**, 15, 1155–1159.

[112] K.A. Burke, I.A. Rousseau, P.T. Mather, *Reversible actuation in main-chain liquid crystalline elastomers with varying crosslink densities*, Polymer. **2014**, 55, 5897–5907.

[113] H. Guo, Y. Li, J. Zheng, J. Gan, L. Liang, K. Wu, M. Lu, *Reinforcement in the mechanical properties of shape memory liquid crystalline epoxy composites*, J. Appl. Polym. Sci. **2015**, 42616, 1–11.

[114] Y. Li, C. Pruitt, O. Rios, L. Wei, M. Rock, J.K. Keum, A.G. Mcdonald, M.R. Kessler, *Controlled shape memory behavior of a smectic main-chain liquid crystalline elastomer*, Macromolecules. **2015**, 48, 2864–2874.

[115] M. Chambers, H. Finkelmann, M. Remškar, A. Sánchez-Ferrer, B. Zalar, S. Žumer, *Liquid crystal elastomer–nanoparticle systems for actuation*, J. Mater. Chem.

2009, 19, 1524–1531.

[116] Y. Ji, J.E. Marshall, E.M. Terentjev, *Nanoparticle-liquid crystalline elastomer composites*, Polymers. **2012**, 4, 316–340.

[117] M.M. Wójcik, J. Wróbel, Z.Z. Jańczuk, J. Mieczkowski, E. Górecka, J. Choi, M. Cho, D. Pociecha, *Liquid-Crystalline Elastomers with Gold Nanoparticle Cross-Linkers*, Chem. - A Eur. J. **2017**, 23, 8912–8920.

[118] G.C. Lama, P. Cerruti, M. Lavorgna, C. Carfagna, V. Ambrogi, G. Gentile, *Controlled Actuation of a Carbon Nanotube/Epoxy Shape-Memory Liquid Crystalline Elastomer*, J. Phys. Chem. C. **2016**, 120, 24417–24426.

[119] M. Lippenberger, P. Dengler, A. Wandinger, M. Schmidt, *Photoresponsive liquid crystal elastomers as feedback controlled light-driven actuators - Theory, real-time behaviour, limitations*, Phys. Procedia. **2016**, 83, 1299–1307.

[120] H. Wermter, H. Finkelmann, *Liquid crystalline elastomers as artificial muscles*, E-Polymers. **2001**, 1, 1–13.

[121] T. Yoshino, M. Kondo, J.I. Mamiya, M. Kinoshita, Y. Yu, T. Ikeda, *Three-dimensional photomobility of crosslinked azobenzene liquid-crystalline polymer fibers*, Adv. Mater. **2010**, 22, 1361–1363.

[122] T.J. White, N. V. Tabiryan, S. V. Serak, U.A. Hrozhyk, V.P. Tondiglia, H. Koerner, R.A. Vaia, T.J. Bunning, *A high frequency photodriven polymer oscillator*, Soft Matter. **2008**, 4, 1796.

[123] J. Zhou, S.S. Sheiko, *Reversible shape-shifting in polymeric materials*, J. Polym. Sci. Part B Polym. Phys. **2016**, 1, 1–16.

[124] C.L. Lewis, E.M. Dell, *A Review of Shape Memory Polymers Bearing Reversible Binding Groups*, J. Polym. Sci. Part B Polym. Phys. **2016**, 54, 1340–1364.

[125] D.P. Nair, N.B. Cramer, J.C. Gaipa, M.K. McBride, E.M. Matherly, R.R. McLeod, R. Shandas, C.N. Bowman, *Two-Stage Reactive Polymer Network Forming Systems*, Adv. Funct. Mater. **2012**, 22, 1502–1510.

[126] D. Guzmán, X. Ramis, X. Fernández-Francos, A. Serra, *Preparation of click thiol-ene/thiol-epoxy thermosets by controlled photo/thermal dual curing sequence*, RSC Adv. **2015**, 5, 101623–101633.

[127] Y. Meng, J. Jiang, M. Anthamattern, *Shape actuation via internal stress-induced crystallization of dual-cure networks*, ACS Macro Lett. **2015**, 4, 115–118.

[128] M.O. Saed, A.H. Torbati, C.A. Starr, R. Visvanathan, N.A. Clark, C.M. Yakacki, *Thiol-Acrylate Main-Chain Liquid-Crystalline Elastomers with Tunable Thermomechanical Properties and Actuation Strain*, J. Polym. Sci. Part B Polym. Phys. 2016, 0, 1–12.

[129] B. Kumar, J. Hu, N. Pan, H. Narayana, *A smart orthopedic compression device based on a polymeric stress memory actuator*, Mater. Des. **2016**, 97, 222–229.

[130] K.K. Westbrook, P.T. Mather, V. Parakh, M.L. Dunn, Q. Ge, B.M. Lee, H.J. Qi, *Two-way reversible shape memory effects in a free-standing polymer composite*, Smart Mater. Struct. **2011**, 20, 65010.

[131] Q. Ge, K.K. Westbrook, P.T. Mather, M.L. Dunn, H. Jerry Qi, *Thermomechanical behavior of a two-way shape memory composite actuator*, Smart Mater. Struct. **2013**, 22, 55009.

[132] E. Zharinova, M. Heuchel, T. Weigel, D. Gerber, K. Kratz, A. Lendlein, *Water-blown polyurethane foams showing a reversible shape-memory effect*, Polymers. **2016**, 8, 412.

[133] L. Santo, F. Quadrini, A. Accettura, W. Villadei, *Shape Memory Composites for Self-*

deployable Structures in Aerospace Applications, Procedia Eng. **2014**, 88, 42–47.

[134] A.R. Studart, R.M. Erb, *Bioinspired materials that self-shape through programmed microstructures*, Soft Matter. **2014**, 10, 1284–94.

[135] W. Wang, Y. Liu, J. Leng, *Recent developments in shape memory polymer nanocomposites : Actuation methods and mechanisms*, Coord. Chem. Rev. **2016**, 320–321, 38–52.

[136] A. Miriyev, K. Stack, H. Lipson, *Soft material for soft actuators*, Nat. Commun. **2017**, 8, 596.

[137] J.J. Song, H.H. Chang, H.E. Naguib, *Biocompatible shape memory polymer actuators with high force capabilities*, Eur. Polym. J. **2015**, 67, 186–198.

[138] A. Lendlein, M. Behl, B. Hiebl, C. Wischke, S*hape-memory polymers as a technology platform for biomedical applications*, Expert Rev. Med. Devices. **2010**, 7, 357–79.

[139] C.M. Yakacki, R. Shandas, C. Lanning, B. Rech, A. Eckstein, K. Gall, *Unconstrained recovery characterization of shape-memory polymer networks for cardiovascular applications*, Biomaterials. **2007**, 28, 2255–2263.

[140] M. Ebara, *Shape-memory surfaces for cell mechanobiology*, Sci. Technol. Adv. Mater. **2015**, 16, 14804.

[141] A. Lendlein, R. Langer, *Biodegradable, Elastic Shape-Memory Polymers for Potential Biomedical Applications*, Science. **2002**, 296, 1673–1676.

[142] B.A. Kowalski, T.C. Guin, A.D. Auguste, N.P. Godman, T.J. White, *Pixelated Polymers: Directed Self Assembly of Liquid Crystalline Polymer Networks*, ACS Macro Lett. **2017**, 6, 436–441.

[143] C. Yuan, D.J. Roach, C.K. Dunn, Q. Mu, X. Kuang, C.M. Yakacki, T.J. Wang, K. Yu, H.J. Qi, *3D printed reversible shape changing soft actuators assisted by liquid crystal elastomers*, Soft Matter. **2017**, 13, 5558–5568.

[144] J. Leng, K. Yu, J. Sun, Y. Liu, *Deployable morphing structure based on shape memory polymer*, Aircr. Eng. Aerosp. Technol. **2015**, 87, 218–223.

[145] K. Yu, W. Yin, S. Sun, Y. Liu, J. Leng, *Design and analysis of morphing wing based on SMP composite*, Ind. Commer. Appl. Smart Struct., **2009**.

[146] H. Ko, A. Javey, *Smart Actuators and Adhesives for Reconfigurable Matter*, Acc. Chem. Res. **2017**, 50, 691–702.

[147] A. Firouzeh, S. Member, M. Salerno, J. Paik, *Stiffness Control With Shape Memory Polymer in Underactuated Robotic Origamis*, IEE transactions on Robotics. **2017**, 33, 767-777.

[148] Y.S. Sato, H. Kokawa, H.C. Park, S. Hirano, Y.S. Sato, H. Kokawa, S. Hirano, *An under-actuated origami gripper with adjustable stiffness joints for multiple grasp modes*, Mater. Sci. Eng. A. **2017**, 26, 0055035.

[149] C. Yang, W. Wang, C. Yao, R. Xie, X.-J. Ju, Z. Liu, L.-Y. Chu, *Hydrogel Walkers with Electro-Driven Motility for Cargo Transport*, Sci. Rep. **2015**, 5, 13622.

[150] C. Huang, J. Lv, X. Tian, Y. Wang, Y. Yu, J. Liu, *Miniaturized Swimming Soft Robot with Complex Movement Actuated and Controlled by Remote Light Signals*, Sci. Rep. **2015**, 5, 17414.

[151] Q. Ge, A.H. Sakhaei, H. Lee, C.K. Dunn, N.X. Fang, M.L. Dunn, *Multimaterial 4D Printing with Tailorable Shape Memory Polymers*, Sci. Rep. **2016**, 6, 31110.

[152] H. Sun, Y.Y. Liu, H.F. Tan, C.G. Wang, *The Two-Stage Curing Method for Shape-Memory Materials*, Adv. Mater. Res. **2012**, 476–478, 2227–2230.

[153] C.F. Carlborg, A. Vastesson, Y. Liu, W. Van Der Wijngaart, M. Johansson, T. Haraldsson, *Functional off-stoichiometry thiol-ene-epoxy thermosets featuring temporally controlled curing stages via an UV/UV dual cure process*, J. Polym. Sci. Part A Polym. Chem. **2014**, 52, 2604–2615.

[154] G. González, X. Fernández-Francos, À. Serra, M. Sangermano, X. Ramis, *Environmentally-friendly processing of thermosets by two-stage sequential aza-Michael addition and free-radical polymerization of amine–acrylate mixtures*, Polym. Chem. **2015**, 6, 6987-6997.

[155] C. Acebo, X. Fernández-Francos, X. Ramis, À. Serra, *Multifunctional allyl-terminated hyperbranched poly(ethyleneimine) as component of new thiol–ene/thiol–epoxy materials*, React. Funct. Polym. **2016**, 99, 17–25.

[156] K.M. Lee, H. Koerner, R.A. Vaia, T.J. Bunning, T.J. White, *Light-activated shape memory of glassy, azobenzene liquid crystalline polymer networks*, Soft Matter. **2011**, 7, 4318.

[157] H.C. Kolb, M.G. Finn, K.B. Sharpless, *Click Chemistry: diverse Chemical Function from a Few Good Reactions*, Angew. Chem. Int. Ed. Engl. **2001**, 40, 2004-2021.

[158] C.E. Hoyle, A.B. Lowe, C.N. Bowman, *Thiol-click chemistry: a multifaceted toolbox for small molecule and polymer synthesis*, Chem. Soc. Rev. 2010, 39, 1355–1387.

[159] D.P. Nair, M. Podgórski, S. Chatani, T. Gong, W. Xi, C.R. Fenoli, C.N. Bowman, *The Thiol-Michael addition click reaction: A powerful and widely used tool in materials* chemistry, Chem. Mater. **2014**, 26, 724–744.

[160] A. Brändle, A. Khan, *Thiol–epoxy "click" polymerization: efficient construction of reactive and functional polymers*, Polym. Chem. 2012, 3, 3224.

[161] X. Ramis, X. Fernández-Francos, S. De la Flor, F. Ferrando, A. Serra, *Thermosets: structure, properties and applicatons. Chapter 9: Click-based dual-curing thermosets*, 2nd Edition, Elsevier, **2017**.

[162] R.M. Loureiro, T.C. Amarelo, S.P. Abuin, E.R. Soulé, R.J.J. Williams, *Kinetics of the epoxy–thiol click reaction initiated by a tertiary amine: Calorimetric study using monofunctional components*, Thermochim. Acta. **2015**, 616, 79–86.

[163] K. Jin, W.H. Heath, J.M. Torkelson, *Kinetics of multifunctional thiol-epoxy click reactions studied by differential scanning calorimetry: Effects of catalysis and functionality*, Polymer. **2015**, 81, 70–78.

[164] D. Guzmán, X. Ramis, X. Fernández-Francos, A. Serra, *New Catalysts For Diglycidyl Ether Of Bisphenol A Curing Based On Thiol-Epoxy Click Reaction*, Eur. Polym. J. **2014**, 59, 377-386.

[165] D. Guzmán, X. Ramis, X. Fernández-Francos, A. Serra, *Enhancement in the Glass Transition Temperature in Latent Thiol-Epoxy Click Cured Thermosets*, Polymers. **2015**, 7, 680–694.

UNIVERSITAT ROVIRA I VIRGILI
DESIGN AND CHARACTERIZATION OF ACTIVELY-MOVING POLYMERS OBTAINED VIA DUAL-CURING PROCESSING
Alberto Francisco Belmonte Parra

Chapter II

Experimental methods and Materials

II

UNIVERSITAT ROVIRA I VIRGILI
DESIGN AND CHARACTERIZATION OF ACTIVELY-MOVING POLYMERS OBTAINED VIA DUAL-CURING PROCESSING
Alberto Francisco Belmonte Parra

II.1 Thermal and mechanical characterization

II.1.1 Dynamic-mechanical analysis (DMA)

Polymers from the liquid to the solid state are **viscoelastic materials**, meaning that their response to a deformation process depends on the deformation time. The viscous or elastic response depends on the relation between the deformation time and the polymer time. If the polymer time is lower than the deformation time, the polymer response is mainly viscous, meaning that a delay between the application and the polymer response is generated. Otherwise, if the polymer time is higher, the response is mainly elastic or instantaneous. In other words, the polymer behaves in between a liquid (completely viscous) and a solid (completely elastic) material[1].

Dynamic-mechanical analysis (DMA) stablish relationships between the viscous and elastic response of a polymer depending on the deformation time. Generally, in DMA analysis a sinusoidal pulse is applied to the sample and its response is measured (see Figure II-1).

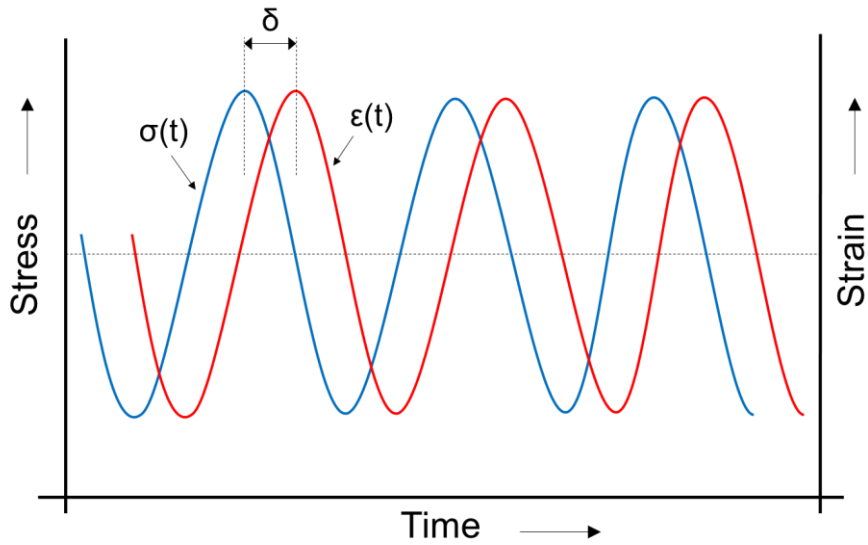

Figure II-1. Applied strain and related stress as a function of the time in DMA.

The strain applied to the sample, ε(t), follows the expression:

$$\varepsilon(t) = \varepsilon_0 \cdot \sin(\omega \cdot t) \quad \text{(II-1)}$$

Where ε_0 is the amplitude of oscillation, ω is the oscillation frequency, and t is the time. The stress associated, σ(t), has the same frequency but a phase delay δ:

$$\sigma(t) = \sigma_0 \cdot \cos(\omega \cdot t + \delta) \quad \text{(II-2)}$$

Since DMA is applied within the linear viscoelastic regime, the modulus can be defined as the quotient between the stress and the strain:

$$G(t) = \frac{\sigma(t)}{\varepsilon(t)} \quad \text{(II-3)}$$

Applying equations (II-1) and (II-2) in (II-3) leads to:

$$G(t) = \frac{\sigma_0}{\varepsilon_0} \cdot \cos\delta + \frac{\sigma_0}{\varepsilon_0} \cdot \sin\delta = G' + G'' \quad \text{(II-4)}$$

Where the **storage modulus** (G') refers to the elastic response or ability of the material to store energy and the **loss modulus** (G'') refers to the viscous response or ability of the material to lose energy. The relation between both moduli determines the damping capabilities of the polymer:

$$\tan\delta = \frac{G''}{G'} \quad \text{(II-5)}$$

Physics of the network structure formation during the curing of thermosets (Rheology)

The curing of thermosets is a complex process of network growing, weight distribution and branching in which two well-known phenomena take place, the **gelation** and the **vitrification** of the network. The gelation is defined as the time in which the chains form a unique path, hence, the molar mass becomes infinite. From an applicative point of view, it is defined as the time in which the material cannot be processed anymore. The gelation leads to a drastic change in the physical response: the viscosity tends to infinite and the material response becomes more elastic than viscous. The vitrification takes place when the material behaves as a glassy network and the glass transition temperature is close or higher to the **curing temperature** (T_c). This phenomenon happens when the T_g of the thermoset is too high, thus, two polymerization steps are usually performed: an initial pre-cure at $T_c < T_g$ and a final post-cure at $T_c > T_g$. During the pre-cure, the T_g approaches T_c resulting in the vitrification phenomenon that is overcome after the post-cure, enabling the completion of the polymerization[2].

The point at which gelation takes place can be determined through DMA at different frequencies. The first reported approach was

the crossover of *G*' and *G*'', point at which the material response is more elastic than viscous. However, if the experimental frequency changes, the crossover time too. Since the gel point is a material property, it must not change with experimental conditions. At the early stage of the curing process (pre-gel region, see in Figure II-2(a)), *G*'' increases due to the increase of the molecular weight of the chains and *G*' remains almost unchanged, thus, tanδ increases according to equation (II-5). At the vicinity of the gelation (critical region, see in Figure II-2(a)), G' drastically increases shifting the tanδ behaviour which decreases. It was found that the tanδ decrease depends on the angular frequency, thus, the crossing of the tanδ curves at three or more angular frequencies was stablished as the gel point determination criteria (see in Figure II-2(b)). Afterwards (post-gel, see in Figure II-2(a)), both *G*' and *G*'' are stabilized, being *G*' much higher than *G*'' due to the elastic response of the fully cured material.

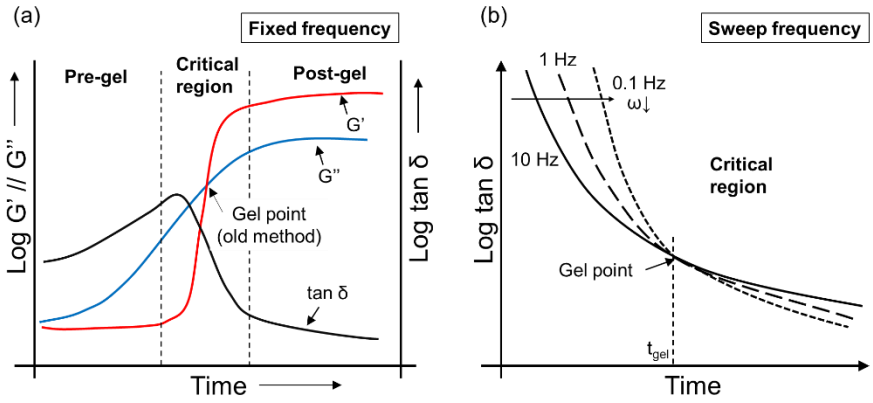

Figure II-2. Gel point determination of a typical thermoset: (a) crossover of the storage and loss moduli, G' and G'', and (b) crossover of the tanδ.

Vitrification is revealed as a peak of the tanδ curve and it is a time-dependent phenomenon, thus, the vitrification point depends on the angular frequency and cannot be considered a materials property.

In this investigation, the rheological experiments were carried out at *Departament de Química Orgànica i Química Analítica* of *Universitat Rovira i Virgili* using a Rheometer AR-G2 (Figure II-3(a)) (TA Instruments, New Castle, DE) equipped with an electrical heated plate (EHP) and parallel plate geometry (Figure II-3(b)). Oscillatory experiments at different frequencies and heating procedures were performed. The network formation and gel point determination of the "thiol-epoxy" dual-curing systems are presented and studied in chapter IV.

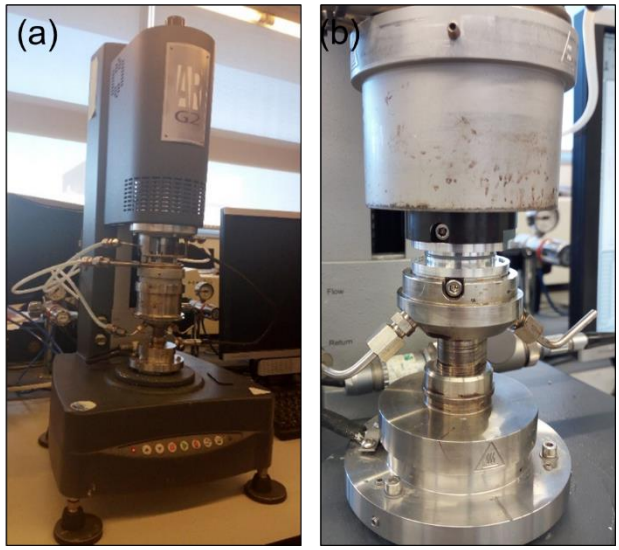

Figure II-3. Images of the rheometer AR-G2: (a) device and (b) parallel plate geometry.

Dynamic-mechanical analysis in cured glassy and semi-crystalline polymers

Glassy and **semi-crystalline**, including **liquid-crystalline**, polymers undergo different **structural transitions** that depends on the deformation time and temperature. DMA captures the structural transitions through the evolution of *E*', *E*'', and the tanδ curve. Commonly, oscillatory experiments at a fixed frequency of 1 Hz and dynamic heating (2 - 5 °C/min) are performed to follow the evolution of the different transitions and determine the thermomechanical parameters of the polymer. In Figure II-4 a typical DMA of a glassy thermoset (a) and a LCN (b) are shown. The transition processes are recognized by the appearance of a peak in the tanδ curve. The shape of the peak is a measure of the heterogeneity of the process: the broader and the smaller, the more heterogeneous. To quantify the heterogeneity, the **width at half-height** (FWHM) and the value of the peak are used. The nominal value of the transition is commonly determined as the peak of the tanδ curve (named T_g^{DMA}). However, other approaches are used since the tanδ curve depends on the frequency. Many researchers use the onset point of the storage modulus, *E*', drop as the glass transition temperature (named $T_g^{E'}$) as it appears to be closer to the T_g determined through pure thermal methods. Therefore, the determination criteria for the T_g is selected depending on the study, one must consider that thermal and mechanical relaxation do not necessarily take place at the same time, and the frequency and temperature conditions will affect the transitions[3].

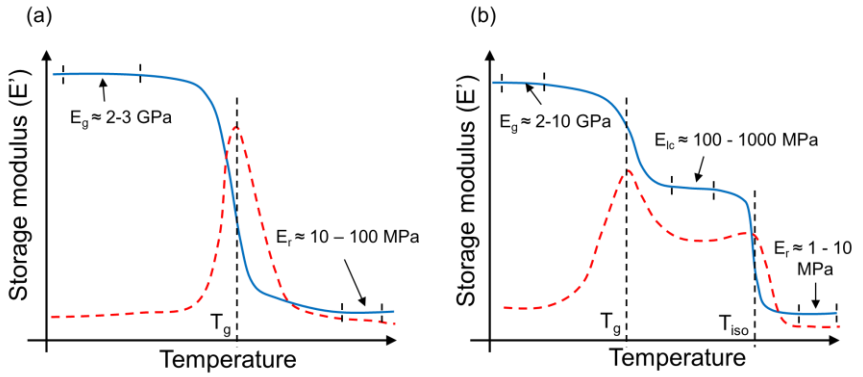

Figure II-4. Evolution of the storage modulus and tanδ as a function of the temperature in fixed frequency DMA experiments: (a) glassy thermosets and (b) liquid-crystalline networks.

The evolution of *E'* is related to the evolution of the polymer **elastic modulus** (E). Although in DMA the determination is through oscillatory analyses, since the experiment proceeds under linear elasticity conditions, that means, the stress/strain relation is always linear, the value is comparable to that obtained from static three-point-bending methods. Typically, *E'* decreases in different steps from the glassy state to the rubbery state in crosslinked materials. Each transition leads to a drop of the modulus and this amount strongly depends on the nature of the transition. The lower the order of the transition (i.e. melting or LC transitions), the larger the drop. It is worth noting that, high order transitions, such as, gamma and beta relaxations, can be captured through DMA analyses by properly adjusting the frequency and temperature range. After each transition there is a stable period or region with a plateau of *E'*. Glassy thermosets have a plateau before and after the glass transition (the glassy and rubbery plateaus, see in Figure II-4(a)), whereas LCNs have three different regions (before T_g, after T_g and after T_{iso}, see in Figure II-4(b)).

The value of the modulus within the different plateaus is used to analyse the structural properties of the polymer. E_g, E_{lc} and E_r are the **glassy**, **LC** and **rubbery moduli** respectively. According to the theory of elasticity, the rubbery modulus is related to the **crosslinking density** of a lightly-crosslinked polymer, however, this extends to glassy polymers and it is used for thermosets as an accepted approach[1]. The relation follows the next expression:

$$E_r = 3 \cdot R \cdot T \cdot v_f \qquad \text{(II-6)}$$

Where R is the universal constant for gases, T is the temperature at which the E_r is determined and v_f is the density of crosslinks.

DMA is also interesting to analyse the **shape-memory response** in SMPs. The heterogeneity of the tanδ is related to the velocity recovering the original shape and the stability of the temporary shape. Moreover, the relation between the modulus before and after the transition (i.e. E_g/E_r) is used as a measure of the performance[4]. The relation should be higher than two orders of magnitude to expect high performance during the programming and recovery processes.

In this investigation, DMA experiments were carried out at *Departament de Química Orgànica i Química Analítica* of *Universitat Rovira i Virgili* using a DMA Q800 (Figure II-5(a)) (TA Instruments, New Castle, DE) equipped with 3-point-bending or Tension film clamp geometries depending on the sample geometry (Figure II-5(b)), at oscillatory mode. The oscillation frequency was fixed to 1 Hz and the oscillation strain to 0.1%. A heating rate of 3 °C/min was imposed. The structural and thermomechanical properties of all the SMPs and LCNs are presented and studied in chapters III - V.

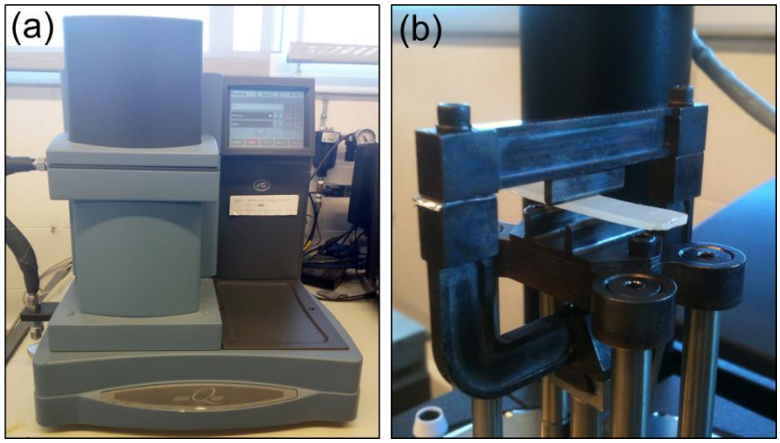

Figure II-5. Images of the TA Instruments DMA Q800 equipment: (a) device and (b) 3-point-bending clamp geometry.

II.1.2 Differential scanning calorimetry (DSC)

Network formation and structural transitions in polymeric materials involve heat release or absorption to happen. **Differential scanning calorimetry** (DSC) permits the detection and measurement of the heat exchange during the structural transitions of a sample subject to

dynamic or isothermal heating procedures. The technique is based on the temperature variation from the testing sample and a reference sample. The reference sample must be inert to the heating procedure, otherwise must possess a well-known thermal response. When the testing sample suffers a transition process, the temperature variation in respect to the reference sample is recorded. The knowledge of the oven thermodynamics permits to transform the temperature variation into a heat flow per units of time[5].

DSC can be used to follow and optimize the **evolution of the curing in thermosets** and other polymeric materials. During polymerization processes, the formation of new chemical and physical bonds lead to a progressive heat release (the typical curve obtained in a curing process is shown in Figure II-6(a)).

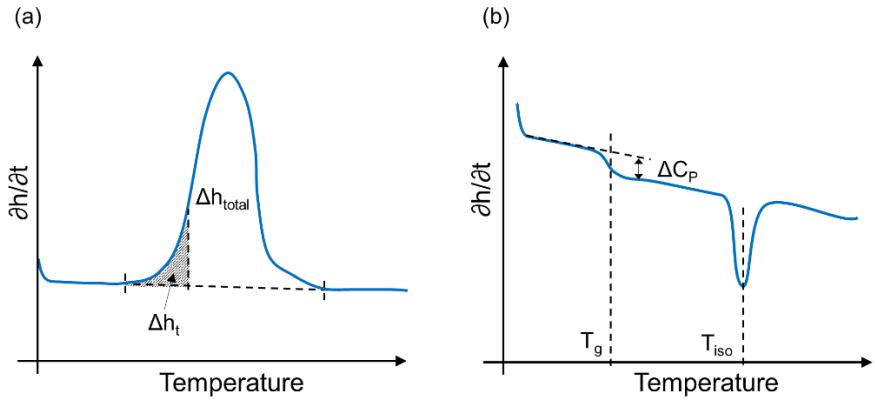

Figure II-6. DSC analysis of polymeric materials: (a) heat released as a function of the temperature during the curing process and (b) variation of the heat capacity as a function of the temperature in cured semi-crystalline networks.

The heat released can be directly related to the **reaction rate** and **conversion** as follows:

$$\frac{\partial x}{\partial t} = \frac{\partial h/\partial t}{\Delta h_t} \qquad \text{(II-7)}$$

$$x = \frac{\Delta h_t}{\Delta h_{total}} \qquad \text{(II-8)}$$

Where $\partial x/\partial t$ is the reaction rate, x is the conversion, $\partial h/\partial t$ is the heat flow, Δh_t is the heat released from the beginning to the time t and Δh_{total} is the total heat released during the curing process.

First order transitions, such as melting and LC transitions, can be measured through the **endothermic peak in the heat capacity**, ΔC_p, associated to the change in internal volume (see the typical endothermic peak of a LC transition in Figure II-6(b)). On the other hand, second order transitions, such as the glass transition, are measured through step **variation of the heat capacity** associated to the structural reorganization of the network (see the heat capacity jump and the determination method during the glass transition in Figure II-6(b)).

In this investigation, DSC experiments were carried out at *Departament de Química Orgànica i Química Analítica* of *Universitat Rovira i Virgili* using a Mettler DSC821e equipped with a robotic arm TSO801RO (Figure II-7(a)) and at *Institute for Polymers, Composites and Biomaterials, National Council of Research of Italy* using a TA Instruments DSC Q2000 (Figure II-7(b)) under N_2 atmosphere. The curing process of the LCNs and the glass and LC transitions of both, the SMPs obtained via dual-curing and the LCNs, are presented and studied in chapters III - V.

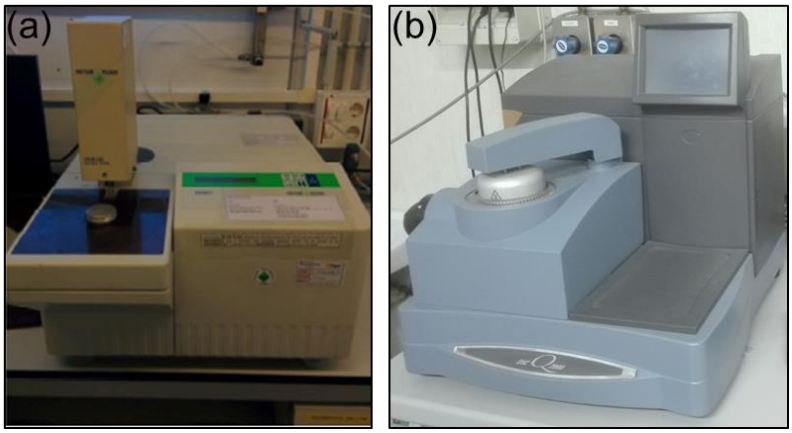

Figure II-7. Images of the calorimeters: (a) Mettler DSC821e and (b) TA Instruments DSC Q2000.

II.1.3 Thermomechanical analysis (TMA)

Polymeric materials suffer dimensional changes, contraction or expansion, during the formation of the network or when are subject to heating/cooling processes. **Thermomechanical analyses** (TMA) measure the unidirectional contraction or expansion through the displacement of a sounding line in touch with the sample (a minimal force is applied to ensure the contact with the sample). If the experiments are performed varying the force applied, the changes in the deformability of the sample are measured[6].

In static force mode, TMA can be used to determine the **coefficients of thermal expansion** (CTE) in polymeric materials and to analyse the different thermal transitions. In Figure II-8(a), an illustration of the volume-temperature evolution for a polymer with first and second order transitions (specifically, LC and glass transitions) is shown. As it can be seen, first order transitions show a discontinuity in the length-temperature curve, whereas second order transitions present a change in the slope according to the thermodynamics. The slope of the curve in each region determines the CTE. Note that in TMA analysis, "length" is the dimensional change of the sample in the direction of the force applied, not the length of the sample[7].

In oscillatory force mode, TMA can be used to determine the **gelation point** during the curing process of thermosets. The gelation of the network leads to a drastic reduction of the sample deformability that undergoes from a liquid-like to a solid-like response. In Figure II-8(b), the dynamic curing of a thermoset is illustrated. The amplitude of oscillation remains high and almost constant during the pre-gel region (liquid-like), whereas it drastically decreases during the gelation process and remains constant and low in the post-gel region (solid-like). The temperature at which the gelation takes place, T_{gel}, is usually determined as the beginning of the amplitude change[7].

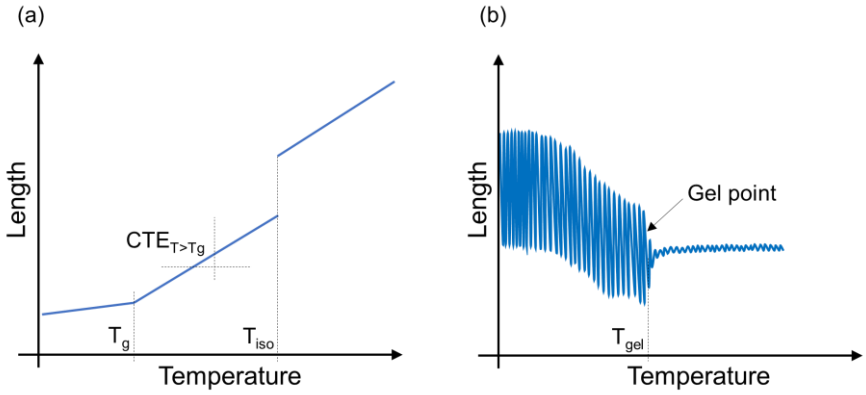

Figure II-8 – TMA analysis of polymeric materials: (a) determination of CTEs, glass transition and LC transition, and (b) determination of the gel point.

In this investigation, the TMA experiments were carried out at *Laboratori de Termodinàmica* of *Universitat Politècnica de Catalunya* using a Mettler TMA/SDTA840 (Figure II-9). The gel point of the materials obtained with the "thiol-epoxy" dual-curing systems is presented and studied in chapter IV.

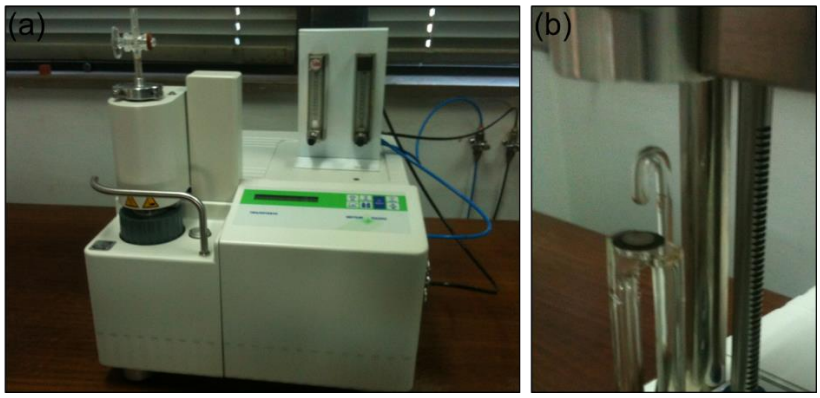

Figure II-9. Images of the Mettler TMA/SDTA840 equipment: (a) device and (b) measurement clamp.

II.1.4 Determination of the conversion at gelation

In sections II.1.1 and II.1.3 the **gelation point** was determined in terms of time or temperature. However, both magnitudes depend on the curing conditions of the thermoset. It is known that gelation occurs at a certain extent of the reaction regardless the curing conditions, therefore it is interesting to determine the **conversion at which gelation takes plac**e (x_{gel}).

DSC is not able to detect the process by itself because gelation does not involve changes in the heat capacity, equally the TMA or Rheological experiments are not able to quantify the extent of the reaction. A common approach to determine x_{gel} is to combine both, **TMA with DSC analyses**[8]. Ensuring comparable experimental setups, under isothermal or dynamic curing processes, the T_{gel} or t_{gel} obtained in the TMA can be applied in the x-t or x-T curves obtained from DSC to determine x_{gel}. In Figure II-10 this process is illustrated under dynamic heating conditions.

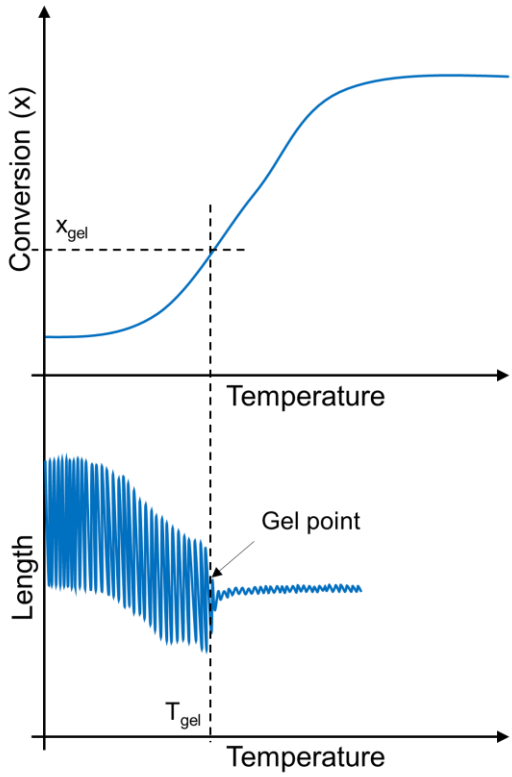

Figure II-10. Determination of the conversion at gelation through TMA and DSC analyses.

Another approach is to combine **DSC with rheological experiments**. The difference lies on the determination technique and the deviation between experimental setups. Both the TMA and rheological instruments have different oven geometries and sample dimensions in comparison with the DSC oven. Carrying out the curing process at low heating rates or curing temperature can help to minimize the error by extending the process.

In this investigation, the gel point in terms of time, temperature and conversion have been determined for the "thiol-epoxy" polymers obtained via dual-curing processing in chapter IV.

II.1.5 Mechanical properties in tension

The **mechanical characterization in tension** of a polymer refers to the **stress/strain response**, and depends on the experimental conditions, such as temperature, humidity and testing time[9]. In this investigation, tensile stress/strain experiments were performed at different temperatures.

Stress/strain experiments at room temperature

In Figure II-11(a) the typical stress-strain response of a glassy polymer at room temperature is presented. The **elastic modulus** (E), which quantifies the resistance of the material to be deformed in the elastic region, is determined from the slope of the curve within the initial part of the curve. The failure limits, **stress at break** (σ_b) and **strain at break** (ε_b), are determined from the failure point[9].

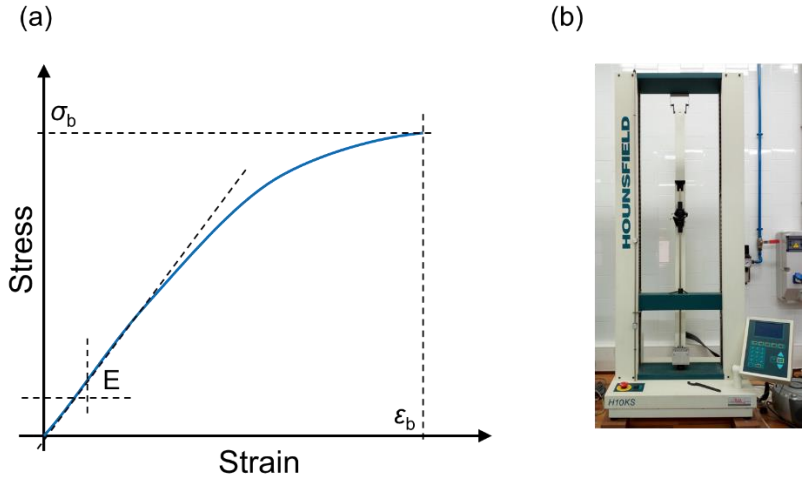

Figure II-11. (a) Stress/strain response of a glassy polymer at room temperature and (b) Tensile Machine (Hounsfield H 10 k-S).

In this investigation, uniaxial tensile experiments at room temperature were carried out at *Departament d'Enginyeria Mecànica* of *Universitat Rovira i Virgili* using an electromechanical Universal Tensile Machine (Hounsfield H 10 k-S) with special grips with a high-frictional surface in contact with the sample (Figure II-11(b)). Specimens with the size adapted from ASTMD638 requirements, adopting a Type IV dog-bone shape were used (Figure II-12). All the experiments were performed at a crosshead speed of 1 mm/min. The stress-strain response of the "thiol-epoxy" based SMPs is studied in chapter III.

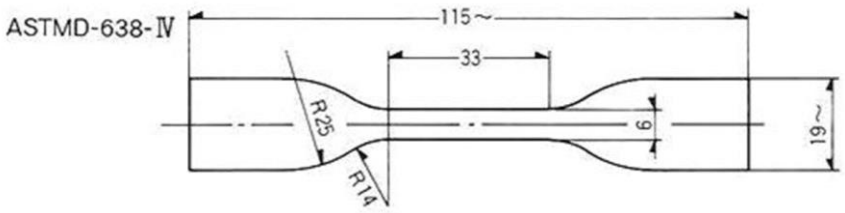

Figure II-12. ASTMD638 – IV specimen dimensions.

Stress/strain experiments at high temperature

In this investigation, uniaxial tensile experiments at high temperature were carried out at *Departament de Química Orgànica i Química Analítica* of *Universitat Rovira i Virgili* using a dynamic-mechanical analyser (DMA Q800, TA Instruments), equipped with a tension film clamp geometry at force-controlled mode (see equipment in section II.1.1). Bone-shaped samples with dimensions 15 x 0.4 x 1.4 mm^3 (length x width x thickness) were used. In Figure II-13 the DMA experimental setup (a) and the bone-shaped samples (b) are presented. The experiments were carried out at a force ramp of 3 N/min at different isothermal temperatures. The σ_b and ε_b were determined as explained in the previous section.

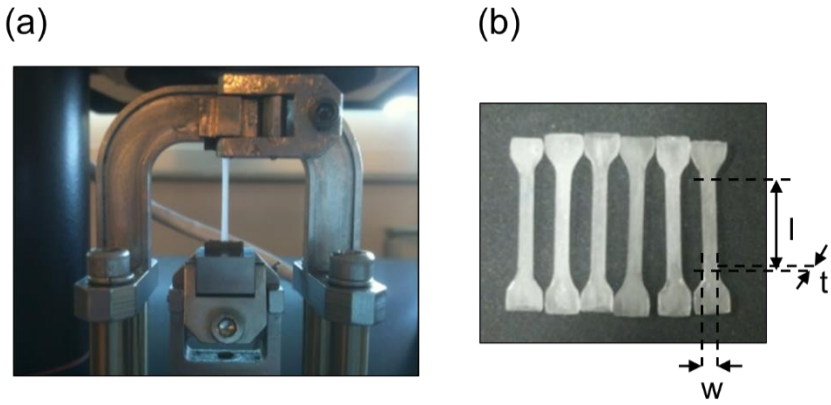

Figure II-13. Uniaxial stress-controlled programming: (a) Tension-film DMA clam geometry and (b) samples design.

II.1.6 Scanning electron microscope (SEM)

The surface topography, composition and other properties such as electrical conductivity, can be investigated at a resolution down to the nanometre scale through **scanning electron microscopy** (SEM). The SEM consists of an electron beam generated by an electron cathode and electromagnetic lenses of the column which swept across the surface of a sample. The main signals which are generated by the interaction of the primary electrons of the electron beam and the specimen´s bulk are secondary electrons and backscattered electrons and furthermore X-rays. The secondary electrons come from a small layer on the surface and yield the best resolution, which can be realized with a scanning electron microscope. The electrons interact with the atoms that make up the sample producing signals that contain information about the sample's surface[10].

In this investigation, the SEM analyses were carried out at *Institute for Polymers, Composites and Biomaterials, National Council of Research of Italy* using a FEI Quanta 200 FEG (Figure II-14) (Hillsboro "OR", Eindhoven, The Netherlands) in high vacuum mode, using a secondary electron detector and an accelerating voltage ranging between 15 and 20 kV. The surface topography of the free-standing actuators is presented and studied in chapter V.

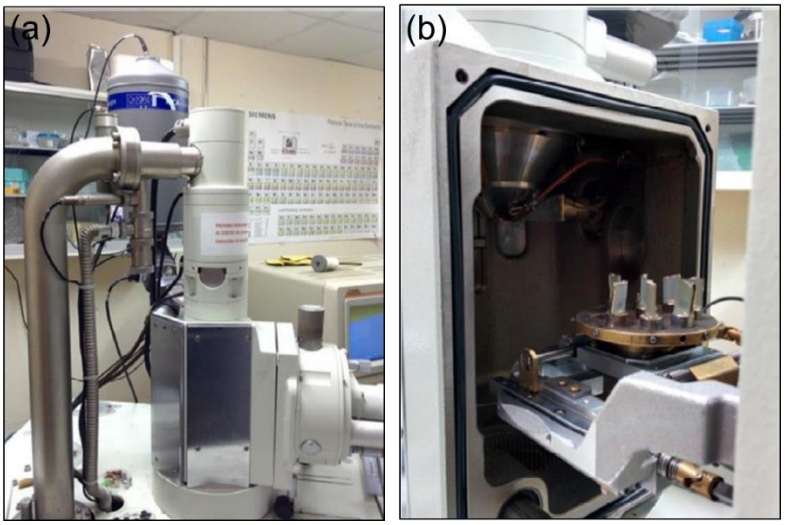

Figure II-14. Images of FEI Quanta 200 FEG (SEM): (a) device and (b) sample mounting.

II.2 Liquid-crystalline properties

II.2.1 X-ray diffraction (DXR)

X-ray diffraction is used to analyse the atomic arrangement of the materials. An X-ray beam with a wavelength (λ) comparable to the atomic dimensions hits the sample and the scattered intensity is detected. The principle is behind the **Bragg's law** (Figure II-15). According to this law, X-rays are reflected in-phase from the crystalline planes making possible to determine the distance between planes (d) and the angle between the incident beam and the scattering plane (Θ)[11].

$$2 \cdot d \cdot \sin\theta = n \cdot \lambda \qquad \text{(II-9)}$$

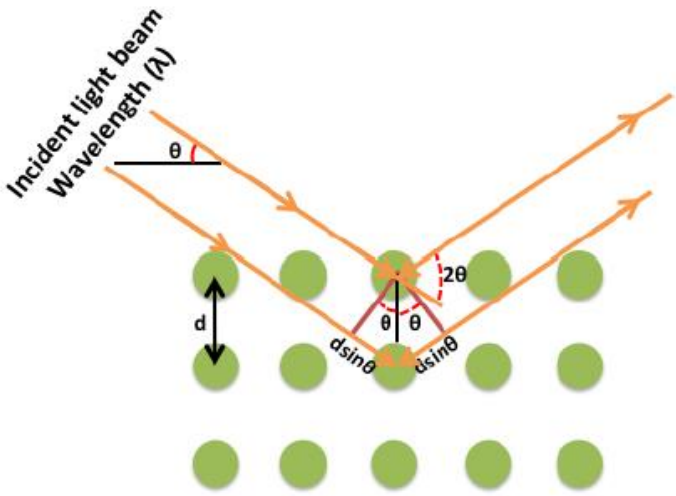

Figure II-15. Illustration of the Bragg's law.

In **LCNs**, amorphous and LC phases coexist, that is, ordered phases are present within the network. Amorphous structures lead to diffusive rings in the scattering plane due to the lack of order but certain amount of characteristic distances. In contrast, crystalline phases show defined spots due to the presence of well-defined ordered phases in one or various dimensions. In LCNs, the scattering planes can undergo from diffusive to well-defined rings, arcs and even spots. Usually an **order parameter**, S, is defined to quantify the level of ordering of a specific ordered phase in the network in respect to a normal director. This can be approached from the numerical analysis of the scattering profile (I) according to the **Herman's method** (equations (II-10)-(II-13)[11].

$$\cos\alpha = \cos\gamma \cdot \cos\theta \tag{II-10}$$

$$\langle\cos^2\alpha\rangle = \frac{\int_0^{\frac{\pi}{2}} I(\alpha)\cdot\sin\alpha\cdot\cos^2\alpha\cdot\partial\alpha}{\int_0^{\frac{\pi}{2}} I(\alpha)\cdot\sin\alpha\cdot\partial\alpha} \tag{II-11}$$

$$\langle\cos^2\varphi\rangle = 1 - 2\cdot\langle\cos^2\alpha\rangle \tag{II-12}$$

$$S = \frac{1}{2}\cdot(3\cdot\langle\cos^2\varphi\rangle - 1) \tag{II-13}$$

Where Θ is the scattering angle, γ is the azimuthal angle, α is the angle between the normal and the scattering planes, φ is the inclination

angle (angle of the ordered phase normal to the director) and $I(\alpha)$ is the distribution function.

In this investigation, the DXR were carried out at *Departament de Química Orgànica i Química Analítica* of *Universitat Rovira i Virgili* using a Bruker-AXS D8-Discover diffractometer (see Figure II-16) equipped with parallel incident beam (Göbel mirror), vertical θ-θ goniometer, XYZ motorized stage and with a GADDS (General Area Diffraction System). The X-ray diffractometer was operated at 40 kV and 40 mA to generate $Cu_{k\alpha}$ radiation. LCNs were studied at different stretching levels in chapter V.

Figure II-16. DXR equipment: Bruker-AXS D8-Discover.

II.3 Characterization of shape-memory polymers

SMPs undergo structural and dimensional changes during both, the **programming of the temporary** shape and **recovery of the original shape**. The characterization of a SMP starts from a global analysis of the efficiency programming the temporary shape and recovering the original shape, to the specific response in each process. In Figure II-17, an illustration of the typical **SMC** for a glassy or semi-crystalline SMP under unconstrained recovery conditions (in tensile mode) is presented in a 3D plot.

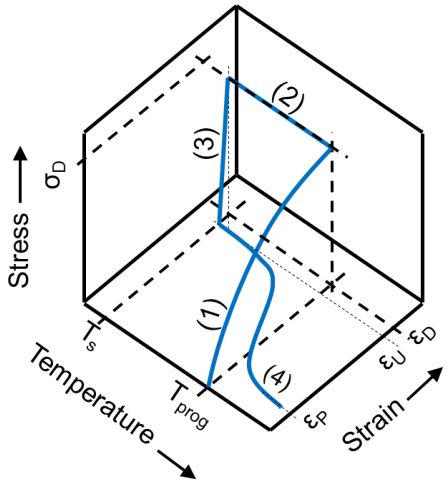

Figure II-17. 3D (stress-strain-temperature) SMC under unconstrained recovery conditions in tensile mode.

The 3D plot gives an overview of the cycle shape and makes possible to break it down in different steps: an initial and omitted step that consists of heating up the sample to T_{prog}, to further load the sample (**step 1**) by applying a stress or strain rate up to the **imposed strain** (ε_D) or stress (the σ_D). Straightaway (**step 2**), the network is frozen by cooling down to T_s, while maintaining the applied stress or strain (this step may lead to **creep phenomenon** when the process is stress-controlled or **stress relaxation** if the process is strain-controlled). Afterwards (**step 3**), the temporary shape is fixed by unloading the applied stress, usually at the same loading rate. During the unloading step, shape-losing usually takes place due to the elastic response of the network at low temperature, hence, the **programmed strain** ε_U is lower than ε_D. Once the temporary shape is fixed, the original shape can be recovered through a heating procedure (**step 4**). During the recovery, the original shape is not fully recovered, but a residual or **permanent strain** remains ($\varepsilon_P > 0$). As explained in section I.1.1.1, step 4 depends on the recovery conditions (unconstrained, partially-constrained and fully constrained conditions), leading to different responses.

Tensile programming processes are the most usual and are characterized using the DMA equipment and the Universal Tensile machine. However, non-standard SMEs, such as, bending, torsion or combined tri-dimensional processes are usually programmed through custom-made devices, and analysed under visual methodologies due to the complexity of finding devices capable to record their motion.

In this investigation, **uniaxial programming** is performed with the DMA equipment, whereas **flexural programming** is carried out using custom-made bending devices. The **recovery process** is recorded with the DMA equipped with appropriate clamp geometry for uniaxial or flexural recoveries at different heating and constraining conditions. Flexural motion is also analysed through isothermal procedures in an external oven and recorded with a high-resolution camera. All the experiments were carried out at *Departament de Química Orgànica i Química Analítica* and *Departament d'Enginyeria Mecànica* of *Universitat Rovira i Virgili*. The experiments were performed for the different "thiol-epoxy" based SMPs and the results and discussion are presented in chapters III and IV.

II.3.1 Stress-controlled uniaxial programming

As stated above, the **programming of the temporary shape** can be performed under stress-controlled or strain-controlled conditions. In stress-controlled procedures, a force ramp is imposed, and the resulting strain is recorded. In contrast, under strain-controlled conditions, the force ramp continuously changes to fit an imposed strain rate.

In this investigation, the uniaxial programming was carried out using a DMA apparatus equipped with a Tension Film clamp geometry at stress-controlled mode. Bone-shaped samples with dimensions 15 x 0.4 x 1.4 mm^3 (length x width x thickness) equal to those for the mechanical characterization, were used (see Figure II-13). The programming process is presented in a "2D" stress-strain plot in Figure II-18 (note that the steps nomenclature correspond to those indicated in the 3D plot in Figure II-17).

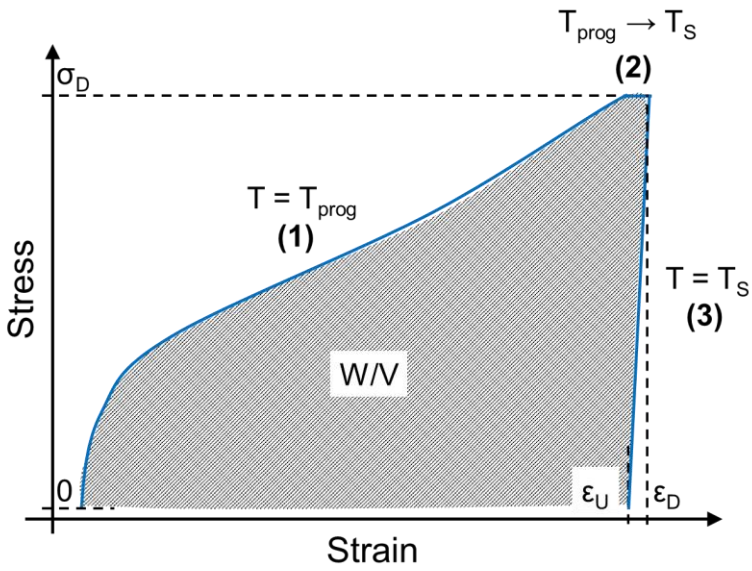

Figure II-18. "2D" stress-strain plot of the programming process in a SMP.

The experiments were performed as follows:

Step 1: Rapid heating up to T_{prog}.

Isothermal step for 10 minutes to ensure thermal stabilization of the sample.

Force ramp at 1 N/min up to a x (%) of ε_b or σ_b ($\varepsilon_D = x \cdot \varepsilon_b$ or $\sigma_D = x \cdot \sigma_b$).

Step 2: Rapid cooling down to T_s while maintaining the force applied.

Isothermal step for 15 minutes to ensure thermal stabilization of the sample.

Step 3: Unload the applied stress at 1 N/min down to zero-stress (ε_U) or to σ_{rec} in partially-constrained conditions.

Note that **step 3** varies depending on the recovery conditions: the sample is unloaded down to zero-stress in unconstrained and fully constrained conditions, or it is unloaded to σ_{rec} in partially-constrained conditions. As it will be discussed in section II.3.5 fully constrained recovery requires a change in the DMA working method, thus, the sample must be unloaded first.

The **programming process** is analysed through the "2D" stress/strain plot since it gives information about the structural changes

and **viscoelastic response** of the network, and it is related to the elastic energy input necessary to attain the temporary shape. As shown in Figure II-18 the process is divided in three steps, (1) loading process, (2) cooling process and (3) unloading process. The performance fixing the temporary shape is quantified through the **shape-fixation ratio** (R_f) which is determined considering the variation of ε_D with ε_U (see equation (II-14)).

$$R_f = \frac{\varepsilon_U}{\varepsilon_D} \cdot 100\ (\%) \qquad \text{(II-14)}$$

The **elastic energy input** (W/V), or energy necessary to program the temporary shape is measured as a means of work energy density through the integration of the stress/strain curve according to expression (II-15):

$$\frac{W}{V} = \int_0^{\varepsilon_D} \sigma \cdot d\varepsilon\ \ (MJ/m^3) \qquad \text{(II-15)}$$

As it can be seen, it is a metric measure that considers the fluctuations of the stress/strain curve, hence, the mechanical response of the polymers during the loading process[12].

II.3.2 Unconventional-programming methods

Flat-to-bent programming

Prismatic flat samples with (40 x 7.5 x 1.5) mm^3 of length x width x thickness (see scheme in Figure II-19) were programmed into a bent temporary shape using a custom-made bending device. The steps of the process are illustrated in Figure II-19 with a set of images: first, the sample is inserted and held among two slots onto the device. Then, the device is placed inside a preheated oven at T_{prog}. After 20 minutes to ensure thermal stabilization, the sample is pushed into the curved space of the device (step 1 loading) at a constant force, the **programming force** (F_{prog}). Afterwards, the device is placed inside a cold-water bath (T_s = 15 °C) for 3 minutes (step 2 cooling) to fix the bent temporary shape. Finally, the sample is removed from the device (step 3 unloading).

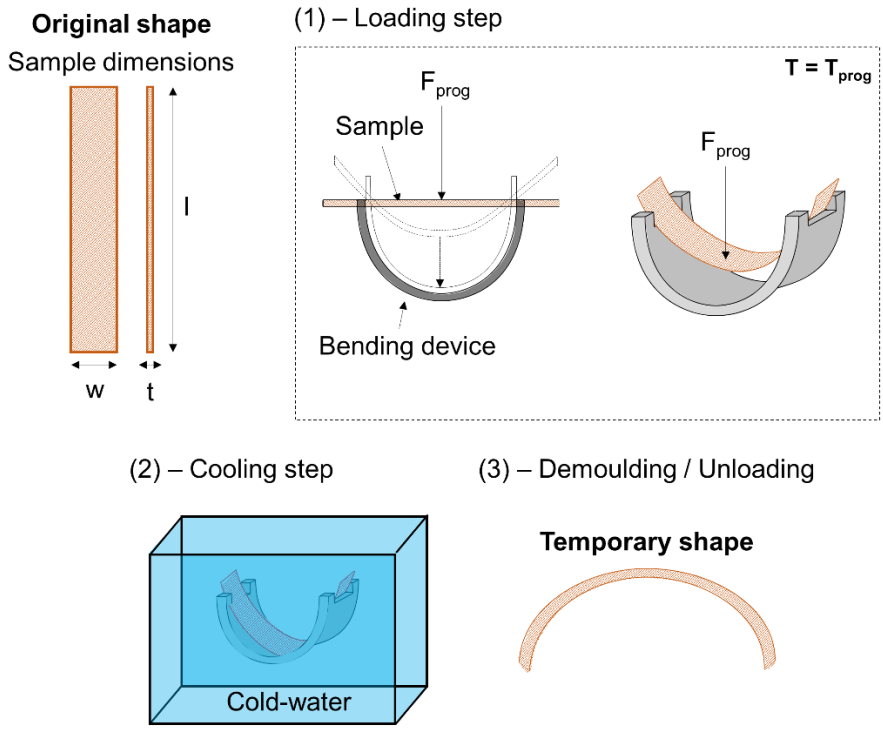

Figure II-19. Flat-to-bent programming process (the steps have been highlighted).

Bent-to-flat programming

Bent-shaped samples with dimensions (36 x 7.5 x 2) mm^3 of length x width x thickness and 10.5 mm of deflection (see scheme in Figure II-20) were programmed into a flat temporary shape using an "unbending" custom-made device (the processing of the bent-shaped sample design is carried out via dual-curing and it is detailed in chapter IV). In Figure II-20 the steps of the programming process are illustrated: first, the sample is placed onto the male part of the device. Then, the device is placed inside a preheated oven at T_{prog}. After 20 minutes of thermal stabilization, the female part of the device is inserted to the male part with no external forces, but its own weight (the mass of the female part is 0.5 kg) (step 1 loading). Afterwards, the device is placed inside a cold-water bath at T_s = 15 °C for 10 minutes (step 2 cooling) to fix the temporary shape. Finally, the device is disassembled, and the sample removed (step 3 unloading).

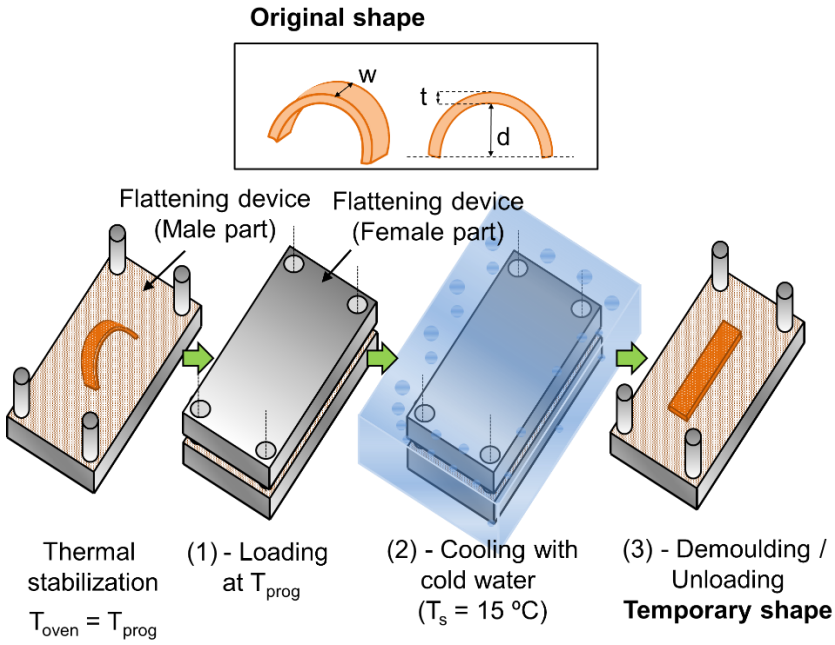

Figure II-20. Bent-to-flat programming process (the steps have been highlighted).

In step 1 (loading), F_{prog} can be approached through the beam formula for small deformations as follows:

$$F_{prog} = \frac{4 \cdot \left(d + \frac{t}{2}\right) \cdot E\left(T_{prog}\right) \cdot w \cdot t^3}{L^3} \qquad \text{(II-16)}$$

Where d is the deflection of the sample, t is the thickness, w is the width, L is the length and E is the modulus at T_{prog}.

II.3.3 Non-isothermal unconstrained recovery experiments

Non-isothermal unconstrained recovery experiments were performed in both, uniaxial and bent-to-flat programmed samples, using the DMA apparatus with the appropriate clamp geometry at stress-controlled mode.

The **uniaxial unconstrained recovery process** was performed with the Tension Film clamp geometry at a constant heating rate of 3 °C/min from room temperature up to T_g + 50 °C to ensure completion of process. The recovery process was followed through the variation of the strain during the heating procedure. The strain is calculated as the variation of the length in respect to the initial length of the sample:

$$\varepsilon(t) = \frac{L(t) - L_0}{L_0} \quad \text{(II-17)}$$

Where L(t) is the length at a time t during the SMC and L_0 is the initial length of the sample after the thermal stabilization step at T_{prog}. To analyse and compare the recovery process, ε(t) is usually normalized to ($\varepsilon_U - \varepsilon_P$), hence, the shape-recovery (SR) is obtained in % units.

$$SR(t) = (1 - \frac{\varepsilon(t) - \varepsilon_P}{\varepsilon_U - \varepsilon_P}) \cdot 100 \quad \text{(II-18)}$$

The **flexural unconstrained recovery process** was performed with the Compression clamp geometry using plates of 40 mm of diameter at a constant heating rate of 3 °C/min from room temperature up to T_g + 50 °C. A minimal force of 0.01 N was applied to ensure the contact between the clamp and the sample. In Figure II-21(a) the experimental setup and (b) the analysis methodology are presented.

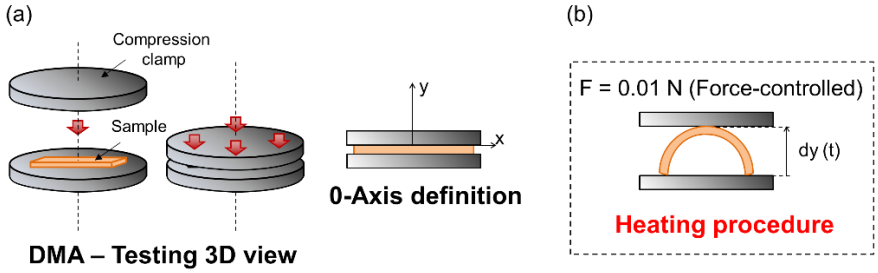

Figure II-21. Flexural unconstrained recovery process: (a) DMA experimental setup and (b) analysis methodology.

The recovery was followed through the displacement of the moveable clamp in the "y" axis, d_y(t), in respect to the deflection, d, of the original shape (see definition of d in Figure II-20) according to expression (II-19) (see scheme in Figure II-21(b)):

$$SR(t) = \frac{d_y(t)}{d} \cdot 100 \quad \text{(II-19)}$$

The main quantifier of the recovery process is the **shape-recovery ratio** (R_r) which is determined as the variation of ε_U with ε_P according to equation (II-20):

$$R_r = \frac{\varepsilon_U - \varepsilon_P}{\varepsilon_U} \cdot 100 \quad \text{(II-20)}$$

In **flexural experiments**, R_r was determined as the relation between the maximum displacement reached by the moveable clamp and the deflection of the original shape.

$$R_r = \frac{d_y^{max}}{d} \cdot 100 \quad \text{(II-21)}$$

Another important quantifier is the **shape-recovery rate** (V_r), which is related to the velocity recovering the original shape, and it is determined through the variation of SR in respect to the temperature (equation (II-22)) or to the time (equation (II-23)) within the range (15% - 85%) of SR:

$$V_r = \frac{SR(\%)_{15\%-85\%}}{\Delta T_{15\%-85\%}} \ (\%/°C) \quad \text{(II-22)}$$

$$V_r = \frac{SR(\%)_{15\%-85\%}}{\Delta t_{15\%-85\%}} \ (\%/min) \quad \text{(II-23)}$$

As illustrated in Figure II-22, the recovery process is analysed through the "2D" strain-temperature (a) or SR-temperature (b) plots.

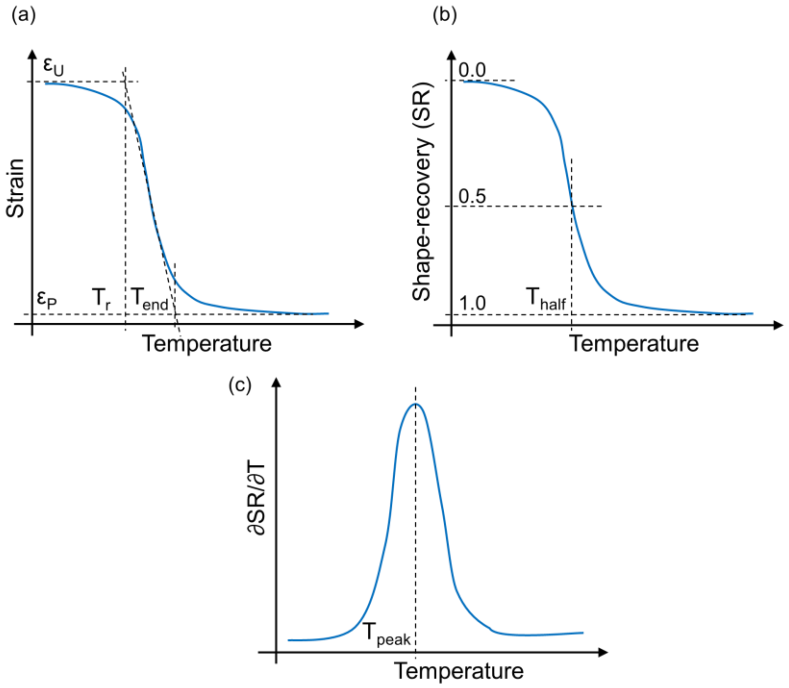

Figure II-22. Unconstrained recovery experiment: (a) strain-temperature plot; (b) shape-recovery-temperature plot and (c) derivative of the shape-recovery in respect to the temperature as a function of the temperature.

The **recovery temperature** (T_r) is the most important parameter. It is usually determined through the onset of the ε-T (a) or SR-T (b) curves, and it is related to the nominal temperature of the related transition process (i.e. glass or melting transitions). Other interesting parameters are the **end temperature** (T_{end}) which is determined from the offset of the ε-T (a) or SR-T (b) curves, the temperature corresponding to the middle of the process, **half temperature** (T_{half}) which is determined from the SR-T curve (b) and the temperature corresponding to the maximum speed, **peak temperature** (T_{peak}) which is determined from the (∂SR/∂T)-T (c) curve[12].

II.3.4 Non-isothermal partially-constrained recovery experiments

Non-isothermal partially-constrained recovery experiments were performed in **bent-to-flat programmed samples** using the DMA apparatus with the Compression clamp geometry (plates Φ = 40 mm) at force-controlled mode as illustrated in Figure II-23(a). In all the experiments a F_{rec} of 0.5 N was applied to produce a partially-constrained recovery (the decision on the magnitude of this force lies on the maximum force released in fully constrained experiments, and it is thoroughly explained in section IV.3). The experiments were carried out at a heating rate of 3 °C/min, and the recovery was followed through the displacement of the moveable clamp, d_y(t), as explained in section II.3.3.

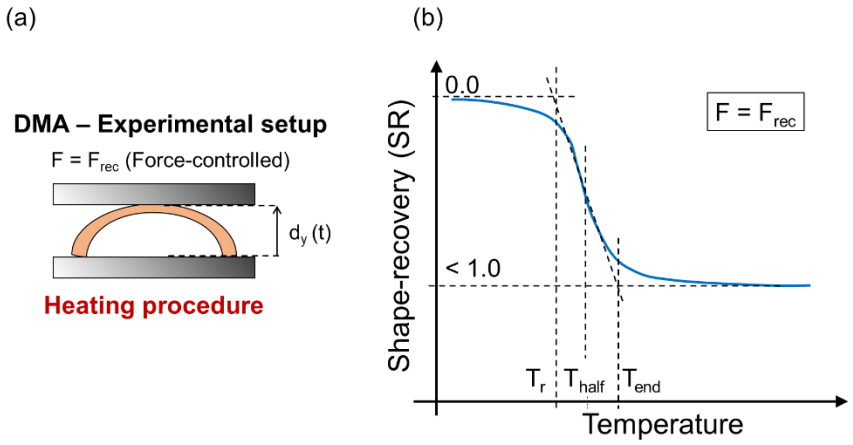

Figure II-23. Partially-constrained recovery experiment: (a) DMA experimental setup and (b) shape-recovery-temperature plot.

The main quantifier in partially-constrained experiments is the **work output** (W) which determines the potential capabilities of the SMP as a mechanical actuator. W is, by definition, the distance multiplied by

the **applied force**, thus the F_{rec} in N·m, or by the **applied stress**, σ_{rec} in N/m. In the present case, σ_{rec} cannot be directly applied due to the flexural recovery mode, thus, W must be expressed as a function of F_{rec}:

$$W = F_{rec} \cdot {d_y}^{max} \quad \text{(II-24)}$$

However, the **SMPs** are limited to a maximum dimensional change, thus, to allow comparison among different SMPs, W is determined relative to the maximum distance as follows:

$$W_{rel} = \frac{W}{d} = F_{rec} \cdot R_r = F_{rec} \cdot \frac{{d_y}^{max}}{d} \quad \text{(II-25)}$$

As illustrated in Figure II-23(b), the recovery process is analysed through the SR-temperature plot in the same way that in unconstrained conditions. The main quantifier of the recovery process, R_r, is calculated following equation (II-21) and all the parameters of analysis (T_r, T_{end}, T_{half} and T_{peak}) are determined as explained in the previous section.

II.3.5 Non-isothermal fully constrained recovery experiments

Non-isothermal fully constrained recovery experiments were performed in **bent-to-flat programmed samples** using the DMA apparatus with the Compression clamp geometry at iso-strain mode as illustrated in Figure II-24(a). A constraining strain of 0.05% was applied to prevent the shape-recovery. The experiments were carried out at a heating rate of 3 °C/min and the process was followed through the evolution of the force applied by the DMA clamp to maintain the imposed strain.

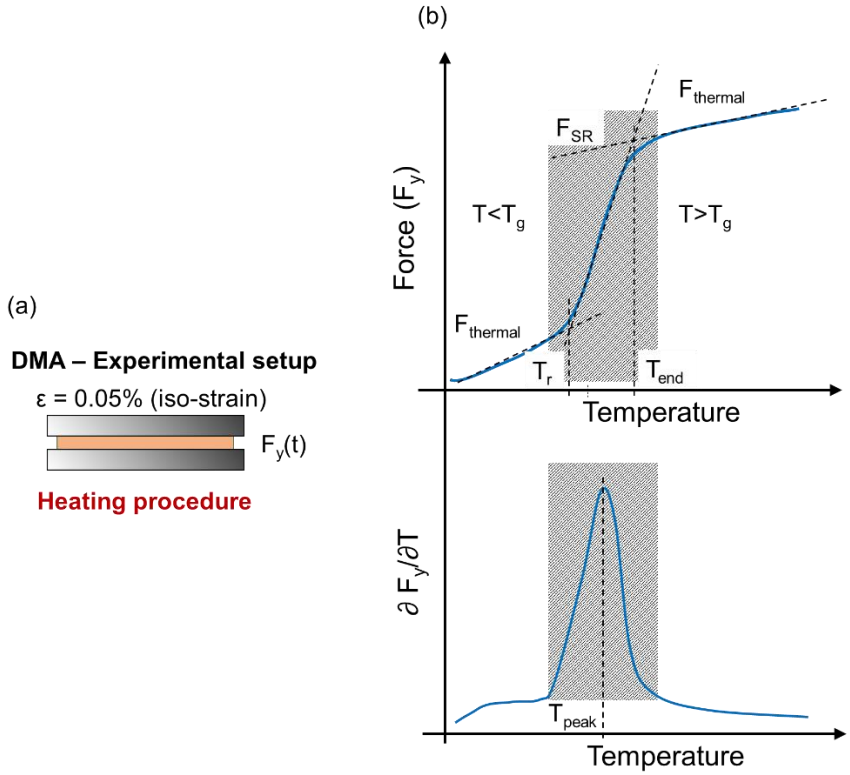

Figure II-24. Fully constrained recovery experiment: (a) DMA experimental setup and (b) force-temperature and derivative of the force in respect to the temperature, as a function of the temperature plots.

The process is analysed through the "2D" force-temperature plot (see Figure II-24(b)). As it was proposed by Li and Wang[13], in **fully constrained conditions**, the force generated by the DMA clamp, F_y, can be divided in different forces as follows:

$$F_y = F_{SR} + F_{residual} + F_{thermal} \quad \text{(II-26)}$$

Where F_{SR} is the force generated due to the SME (**recovery force**), $F_{residual}$ is the force caused by incomplete relaxation during the programming process, and $F_{thermal}$ is the force generated by the **thermal expansion** phenomenon. In uniaxial experiments, $F_{thermal}$ behaves in opposite direction to the recovery process, however, in the proposed configuration, the expansion takes place in the same direction than the recovery process, thus, $F_{thermal}$ has a crucial effect in both, glassy and rubbery states (see the increasing trend of F_y in Figure II-24(b)), and can be approached as follows:

$$F_{thermal} = E(T) \cdot CTE(T) \cdot (T - T_0) \cdot S_{eff} \quad \text{(II-27)}$$

Where E(T) is the modulus at a temperature T, CTE is the coefficient of thermal expansion at a temperature T, T_0 is the reference temperature (30 °C) and S_{eff} is the effective surface in contact with the clamp of the DMA. As it will be discussed in section IV.3, S_{eff} is not strictly the planar surface (width x length) of the flat programmed shape and can be approached through the initial force applied by the DMA to maintain the 0.05% of constraining strain as follows:

$$S_{eff} = \frac{f_{DMA}}{E_g \cdot \varepsilon} \quad \text{(II-28)}$$

Where f_{DMA} is the force applied by the DMA to maintain the 0.05% of strain, E_g is the modulus of the sample in the glassy state and ε is 0.05 (constraining strain).

In **fully constrained conditions**, F_{SR} can be determined from the force step of the F_y-T curve (b). Note that this force determines the maximum force released by the SMP during the recovery process, thus, in partially-constrained conditions, F_{rec} must not overpass this value to achieve a positive work output. For this reason and considering the results of the tested SMPs, F_{rec} was stipulated as 0.5 N as indicated in section II.3.4. The onset and offset of the F_y-T curve (b) can be used to determine T_r and T_{end}. In addition, F_y can be derived in respect to the temperature ($\partial F_y/\partial T$) to analyse the different stages during the process, and to determine the temperature corresponding to the maximum force generated during the recovery, T_{peak}.

II.3.6 Isothermal unconstrained recovery experiments

Isothermal unconstrained recovery experiments were performed in flat-to-bent programmed samples using a conventional oven preheated at an **isothermal temperature** (T_∞). Assuming the sample is sufficiently thin and the heat resistance inside the sample sufficiently low, the temperature profile of the sample at any T_∞ was determined applying the energy balance shown in equation (II-29), and experimentally fitting the coefficient of thermal convection using a thermocouple placed close to the sample.

$$m \cdot C_p \cdot \frac{dT}{dt} = -h \cdot A \cdot (T - T_\infty) \quad \text{(II-29)}$$

where M is the mass of the sample, C_p is the heat capacity, $\partial T/\partial t$ is the heat flow, h is the coefficient of thermal convection, A is the surface receiving the heat flow and T is the sample surface temperature assumed

equal along the thickness (this assumption is verified using the Biot number as detailed in chapter III).

The experimental setup for the recovery process is illustrated in Figure II-25: the sample was held on-air and placed in front of a high-resolution camera. The recovery process was recorded through a transparent wall of the oven and the evolution of the **opening angle**, Φ, was determined frame-by-frame using a computational software.

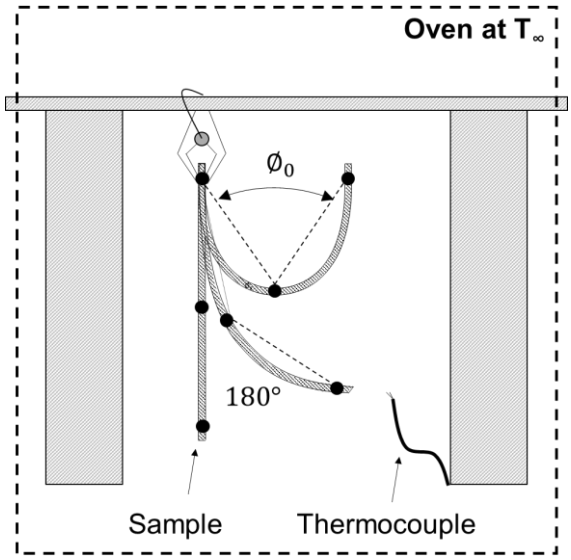

Figure II-25. Isothermal unconstrained flexural recovery experimental setup.

The shape-recovery was calculated considering the starting angle, $\Phi_0 \approx 90°$, and the fully recovered angle, $\Phi = 180°$ according to expression (II-30):

$$SR(t) = \frac{\Delta \emptyset_t}{180 - \emptyset_0} \cdot 100 \qquad \text{(II-30)}$$

Where $\Delta\Phi_t$ is the variation of the opening angle at a time t of the recovery process. In addition, the **isothermal recovery-time** (t_{SR}) was determined as follows:

$$t_{SR} = t_{offset} - t_{onset} \qquad \text{(II-31)}$$

Where t_{offset} and t_{onset} correspond to the offset and onset points of the SR-time curve, respectively.

II.4 Characterization of shape-changing polymers

SCPs undergo large reversible dimensional changes upon external stimulation through the SCE. The characterization of SCPs lies on the magnitude and efficiency of the mechanical actuation under **thermomechanical cycling processes**.

In this investigation, the SCE is studied in "epoxy-carboxylic" based LCNs using a DMA apparatus. Uniaxial thermomechanical processes at a constant load level and at different constrained conditions are performed to study the SCE in terms of dimensional change and force generated. The experiments were carried out at *Institute for Polymers, Composites and Biomaterials, National Council of Research of Italy* using a PerkinElmer Pyris Diamond DMA apparatus (see in Figure II-26).

Figure II-26. Image of the PerkinElmer Pyris Diamond DMA apparatus.

II.4.1 Non-isothermal thermomechanical cycling under a constant load

Uniaxial experiments at a constant load level were carried out using the DMA apparatus equipped with a Tension Film clamp geometry at force-controlled mode. **Bone-shaped film-type samples** of 10 x 4 x 0.25 mm^3 of length x width x thickness were used. In Figure II-27(a) the SCE is presented in a "2D" force-strain-temperature plot and in (b) the experimental setup is illustrated.

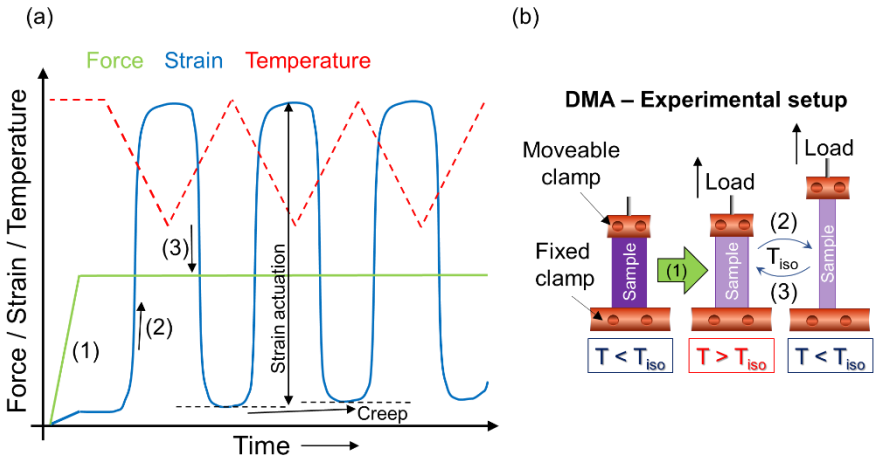

Figure II-27. Thermomechanical cycling process: (a) strain-force-temperature plot and (b) illustration of the experimental setup in the DMA apparatus.

The experiments were performed as follows:

Step 1: Rapid heating up to T_{iso} + 20 °C.

Isothermal step for 5 minutes to ensure thermal stabilization of the sample.

Loading at a force rate of 10 mN/min up to a % of σ_b.

Step 2: Cooling down to $T < T_{iso}$ at 2 °C/min while maintaining the force applied (induced-elongation).

Step 3: Heating up to $T > T_{iso}$ at 2 °C/min while maintaining the force applied (shrinkage).

Repeat **steps 2** and **3** (cycling).

The **SCE** is analysed through the magnitude and evolution of the strain actuation which is measured as the **elongation-shrinkage step** in % units for each cycle (highlighted in Figure II-27(a)). The **creep** or remaining strain after each cycle (highlighted in Figure II-27(a)) is determined as a measure of the performance upon cycling processes.

II.4.2 Non-isothermal fully constrained thermomechanical cycling

Uniaxial constrained experiments were carried out using the DMA apparatus equipped with a Tension Film clamp geometry at force controlled mode (programming step) and iso-strain mode (force generation). **Bone-shaped film-type samples** of 10 x 4 x 0.25 mm^3 of

length x width x thickness were used. In Figure II-28(a), the constrained response is presented in a "2D" force-strain-temperature plot and in (b) the experimental setup is illustrated.

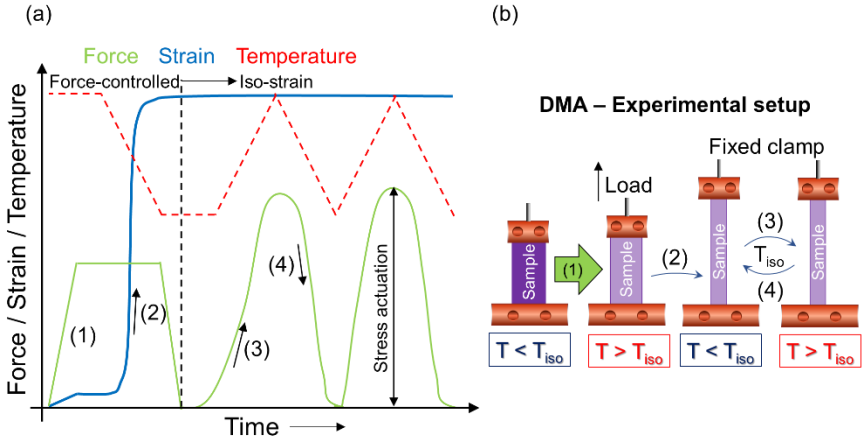

Figure II-28. Thermomechanical fully constrained cycling process: (a) strain-force-temperature plot and (b) illustration of the experimental setup in the DMA apparatus.

The experiments were performed as follows:

DMA (Force-controlled mode): Programming steps

Step 1 / Step 2 were performed as explained in the previous section II.4.1, however, after the cooling process the sample was unloaded down to zero-stress at a force rate of 10 mN/min, and the DMA was set in iso-strain mode.

DMA (Iso-strain mode): Force generation steps

Step 3: Heating up to $T > T_{iso}$ at 2 °C/min

Step 4: Cooling down to $T < T_{iso}$ at 2 °C/min

Repeat **steps 3** and **4**.

The constrained response is analysed through the magnitude and evolution of the mechanical actuation which is measured as the force or stress step for each cycle (highlighted in Figure II-28(a)).

II.5 Characterization of free-standing actuators

Free-standing actuators undergo reversible dimensional changes upon stimulation. Unlike LCNs, the shape-change is induced without any external load. In this investigation, free-standing actuators **working in flexural mode** are studied. The actuation was recorded in a conventional

oven under heating-cooling processes and analysed in the DMA apparatus following the experimental setup for the flat-to-bent recovery of bent-shaped SMPs obtained via dual-curing processing (see in section II.3.3). The experiments were carried out at *Departament de Química Orgànica i Química Analítica* of *Universitat Rovira i Virgili* and at *Institute for Polymers, Composites and Biomaterials, National Council of Research of Italy.*

II.5.1 Analysis of the flexural actuation

The **flexural actuation** was visually recorded with a high-resolution camera in a conventional oven under rapid heating above T_{iso} and naturally cooling below T_{iso} cyclic processes. In Figure II-29 the analysis of the flexural actuation is presented.

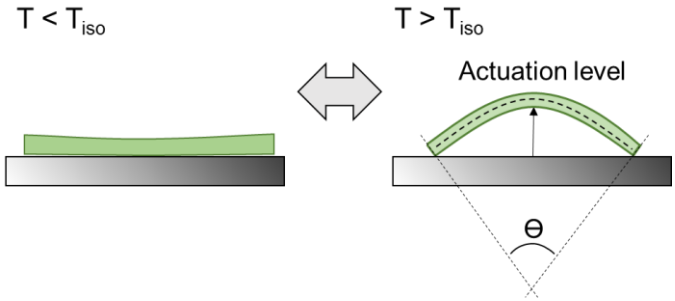

Figure II-29. Analysis of the flexural actuation upon heating-cooling processes in free-standing actuators.

The **actuation level**, which is determined as the maximum deflection achieved after the bending process ($T > T_{iso}$) is the main quantifier. The **bending angle**, Θ, which is calculated considering the length and radius of curvature of the sample as indicated in Figure II-29, is further compared with the predicted values obtained through an analytical model for multi-layered beams subject to stress-free strains developed in section V.3.

II.5.2 Non-isothermal flexural actuation analysis

Non-isothermal experiments were carried out using the TA Instruments DMA Q800 apparatus equipped with a custom-made clamp (see in Figure II-30(a)) at force-controlled mode. A minimal force of 0.01 N was applied to ensure the contact of the clamp with the sample. Heating-cooling procedures at a constant rate of 2 °C/min were imposed, and the flexural actuation, both bending and unbending processes, was recorded through the displacement of the clamp in the "y" axis as explained in

section II.3.3 for flat-to-bent recovery processes. The actuation is defined according to equation (II-32):

$$Acutation(t) = \frac{d_y(t)}{d} \cdot 100 \qquad \text{(II-32)}$$

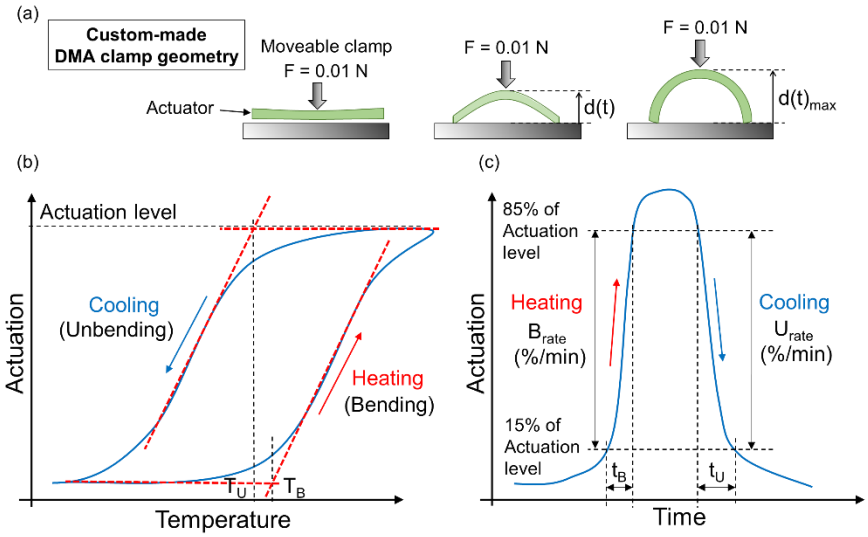

Figure II-30. Non-isothermal flexural actuation: (a) experimental setup in the DMA and (b) actuation-temperature and actuation-time plots.

The **flexural actuation** is analysed through the actuation-temperature and actuation-time plots illustrated in Figure II-30(b) and Figure II-30(c). As it can be seen, the actuation follows a hysteresis cycle in respect to the temperature and a bell-shape peak in respect to the time. The actuation level can be determined as the maximum value of the actuation-temperature curve (b) or the peak of the actuation-time curve (c). In general, the actuation is divided in two processes: the bending and unbending. From Figure II-30(b), the temperature at which the bending takes place, the **bending temperature** (T_B), is determined as the onset point of the lower increase and the **unbending temperature** (T_U) is determined as the onset point of the higher decrease of the hysteresis cycle. From Figure II-30(c), the bending and unbending rates and total times are determined according to expressions (II-33) and (II-34):

$$B_{rate} = \frac{B_{actuation}\ (15\% - 85\%)}{t_B\ (15\% - 85\%)}\ (\%/min) \qquad \text{(II-33)}$$

$$U_{rate} = \frac{U_{actuation}\ (15\% - 85\%)}{t_U\ (15\% - 85\%)}\ (\%/min) \quad \text{(II-34)}$$

Where $B_{actuation}$ and $U_{actuation}$ are the Actuation range from the 15% to the 85% of the actuation level (maximum actuation value) corresponding to the bending and unbending processes respectively, and both, t_B and t_U, are the associated times.

II.6 Materials

II.6.1 Epoxy-based thermosetting polymers

In chapter III "**thiol-epoxy" glassy SMPs** obtained via **click chemistry** were thoroughly studied. The SMPs were prepared at *Departament de Quimica Analítica i Química Orgànica* of *Universitat Rovira i Virgili*. The compounds used were:

- A commercial epoxy resin, **Diglycidyl ether of bisphenol A** (**DGEBA**, GY240, Huntsman, Everberg, Belgium) with a molecular weight per epoxy equivalent unit of 182 g/eq was used as the main epoxy resin.
- **Pentaerythritol tetrakis (3-mercaptopropionate) (S4)**, with a molecular weight per thiol equivalent unit of 122.17 g/eq (Sigma-Aldrich, St. Louis, MO, USA) and **trimethylolpropane tris(3-mercaptopropionate) (S3)**, with a molecular weight per thiol equivalent unit of 132.85 g/eq (Sigma-Aldrich, St. Louis, MO, USA) were used separately as crosslinking agents.
- **Tri(2,3-epoxypropyl)isocyanurate (iso)**, with a molecular weight per epoxy equivalent unit of 99.09 g/eq (Sigma-Aldrich, St. Louis, MO, USA) was used as network modifier in different weight proportions: 10%, 20%, 30% and 40% (i.e., 10:90 wt % ISO:DGEBA), maintaining a stoichiometric proportion of thiol and epoxy groups (epoxy:thiol ratio equal to 1:1).
- An **encapsulated imidazole** (**LC80**, AC Catalysts) was used as a latent catalyst in a proportion of 0.5 phr (parts of catalyst per hundred parts of epoxy resin).

In chapter IV **"thiol-epoxy" glassy SMPs** obtained via **dual-curing processing** were studied. The SMPs were prepared at *Departament de Quimica Analítica i Química Orgànica* of *Universitat Rovira i Virgili*. Besides the reactants used in chapter III the following compounds were used:

- An **EPON™ resin SU8** with an epoxy equivalent average weight of 215 g/eq was used as a highly functional network modifier (average functionality of 8 epoxy groups per molecule) in a molar proportion of 3:7 (SU8:DGEBA).

- **1-methylimidazole (1MI)** with a molecular weight of 82.1 g/mol (Sigma-Aldrich, St. Louis, MO, USA) was used as catalyst in a proportion of 1 phr (parts of catalyst per hundred parts of the whole mixture).

The DGEBA was previously dried under vacuum at 80 °C overnight, and the other reagents were used without further purifications. The chemical structures and proportions are specified in the corresponding chapters.

II.6.2 Epoxy-based liquid-crystalline networks

In chapter V **free-standing actuators** were prepared combining the **"thiol-epoxy" dual-curing systems** and the **LCNs**. The LCNs were synthesized and prepared at *Dipartimento di Ingegneria chimica, dei Materiali e della Produzione Industriale*, of *Universitá degli Studi di Napoli Federico II* and at *Institute for Polymers, Composites and Biomaterials (National Council of Research of Italy)*. The compounds used were:

- A commercial diphenol compound (**4,4'- dihydroxybiphenyl**, 97% purity, 186.21 g/mol), epichlorohydrin (99% purity, 1.183 g/mL, 92.52 g/mol), isopropyl alcohol, and sodium hydroxide were used for the synthesis of the **epoxy-based mesogen**.
- Commercial **dicarboxylic acids** with different aliphatic chain length $(CH_2)_n$ were used as curing agents for the synthesis of the **epoxy-based LCNs**: **adipic acid** (n = 4, C4), **pimelic acid** (n = 5, C5), **suberic acid** (n = 6, C6), **azelaic acid** (n = 7, C7), **sebacic acid** (n = 8, C8), and **dodecandioic acid** (n = 10, C10).
- **Tricaprylyl methylammonium chloride** was used as catalyst for the epoxy-carboxylic reaction.

All chemicals were supplied by Sigma-Aldrich and used as received.

II.7 Sample preparation methods

In chapter III, for the characterization of the "thiol-epoxy" SMPs, bone-shaped and prismatic-shaped samples were prepared. **Bone-shaped samples** of 15 x 1.4 x 0.5 mm^3 (length x width x thickness) were prepared using an open custom-made mould consisting of a Teflon metallic plate as support, and a thin metallic plate (0.6 mm) with ten parallel-placed bone-shaped casts along the width as matrix. The preparation process is illustrated in Figure II-31: the thin metallic plate is stick onto the support using liquid silicone and fastened with holders. The unreacted mixtures are poured over the bone-shaped casts, and the samples are cured in a

conventional oven. The curing conditions are specified in the corresponding chapter. After curing, the samples are released from the mould, and polished to fit the specific dimensions and erase any defects on the surfaces.

The **prismatic-shaped samples** were prepared following the same procedure sketched in Figure II-31. In this case, a thick and tough Teflon layer (2 mm) with three parallel-placed prismatic casts was used as matrix.

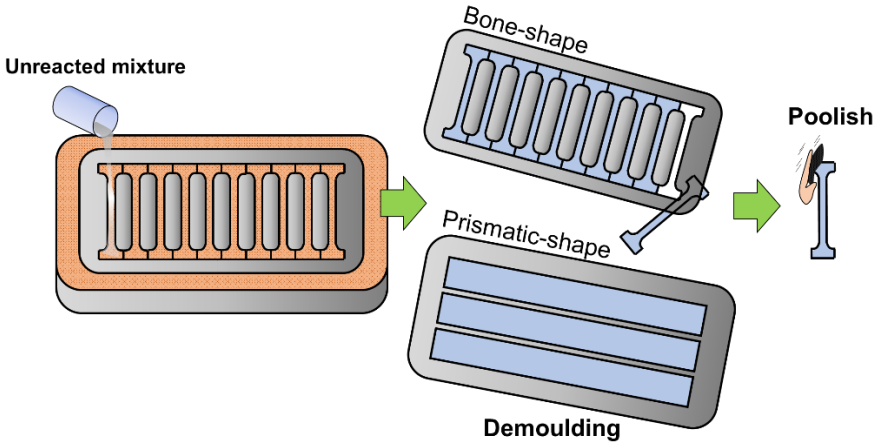

Figure II-31. Illustration of the bone-shaped and prismatic-shaped samples preparation.

In chapter IV **planar, circular, plaited, spring and bent shaped samples** were prepared via dual-curing processing. All the samples were pre-processed in **thin (film)** or **thick layers** of specific dimensions after the 1st curing stage.

The pre-processing of **thick layers** was carried out following the same procedure for prismatic samples sketched in Figure II-31. In this case, different matrixes were used depending on the shape dimensions (prismatic and square casts). **Film-type layers** were prepared using two Teflon-coated glass plates and metallic spacers of different thickness (depending on the desired thickness of the film). The process is sketched in Figure II-32: first, the spacers are stick onto one of the Teflon-coated glass plates using liquid silicone. Then, the unreacted mixture is poured in between the spacers. Afterwards, the second plate is carefully placed onto the prepared plate, flattening and spreading the mixture over the whole surface. The device is slightly fastened using holders. The curing process is performed according to the conditions specified in the corresponding chapter. Once the material is cured, the film is released from the mould

using a tweezer after separating the two plates (the Teflon avoid the adhesion of the cured material onto the surface).

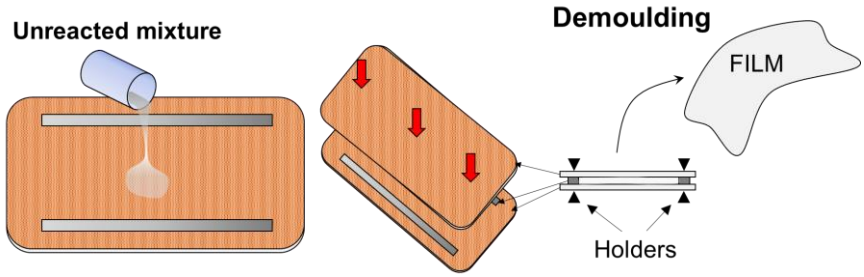

Figure II-32. Illustration of the film-type samples preparation.

Circular, bent and plaited samples were prepared from thick prismatic pre-processed layers: the circular and bent shapes were achieved by bending the sample onto a Teflon-coated metallic cylinder (40 mm of diameter), and slightly fastening it onto the surface (the process is sketched in Figure II-33); the plaited sample was attained by manually plaiting and fastening it from the edges, and the spring sample was obtained by rolling up a pre-processed film sample into a fibber and then curling it along a thin Teflon-coated glass cylinder (3 mm of diameter). All the shapes were fixed through the 2nd curing stage according to the curing conditions detailed in the corresponding chapter.

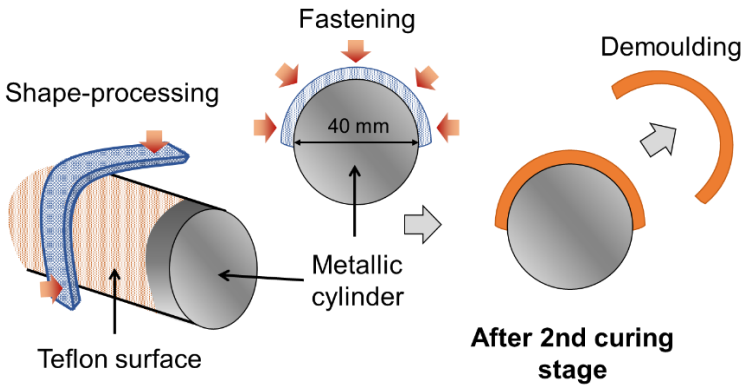

Figure II-33. Illustration of the bent-shaped samples preparation

In chapter V films of both, the LCNs and the “thiol-epoxy” glassy materials (obtained from the dual-curing), of different thickness were prepared as sketched in Figure II-32. The samples were cut from the film using conventional scissors.

II.8 References

[1] J-P. Pascault, H-J. Sautereau, R. Verdu, J. J. Williams, *Thermosetting Polymers*, CRC Press, Florida, USA, **2002**.

[2] J-P. Pascault, H-J. Sautereau, R. Verdu, J. J. Williams, *Rheological and Dieletric Monitoring of Network formation in Thermosetting Polymers*, Marcel Dekker, New York, USA, **2002**.

[3] I. Emri, M. Gergesova, *Rheology, chapter: Time-dependent behaviour of Solid Polymers,* EOLSS. Paris, France, **2010**.

[4] B. Atli, F. Gandhi, G. Karst, *Thermomechanical characterization of shape memory polymers*, Proceedings of SPIE - The International Society for Optical Engineering, San Diego, USA, vol. 6524, **2007.**

[5] A. Turi, *Thermal Characterization of Polymeric Materials,* 2nd Edition, Academic Press, San Diego, USA, **1997**.

[6] H. E. Bair, A. E. Akinay, J. D. Menczel, R. B. Primer, M. Jaffe, *Chapter 4: Thermal Analysis of Polymers*, John Wiley & Sons, Hoboken, USA, **2008**.

[7] E. A. Turi, Y. P. Khanna, T. J. Taylor, J. B. Sibilia, *Chapter 9: A guide to Materials Characterization and Chemical Analysis*, VCH, New York, USA, **1988**.

[8] L. Núñez-Regueira, C.A. Gracia-Fernández, S. Gómez-Barreiro, *Use of rheology, dielectric analysis and differential scanning calorimetry for gel time determination of a thermoset*, Polymer. **2005**, 46, 5979-5985.

[9] I. M. Ward, J. Sweeney, *Mechanical Properties of Solid Polymers*, 3rd Edition, Wiley, New York, USA, **2012**.

[10] J. Goldstein, D. E. Newbury, D. C. Joy, C. E. Lyman, P. Echlin, E. Lifshin, L. Sawyer, J. R. Michael, *Scanning Electron Microscopy and X-ray Microanalysis*, Springer, New York, USA, **2007**.

[11] R-J. Roe, *X-ray Diffraction by Polymers*, Wiley, New York, USA, **2015**.

[12] P. Mather, T. L. Xiaofan, I. a. Rousseau, *Shape-memory Polymers Research,* Annual Rev. Mater. Res. **2009**, 39, 445-471.

[13] A. Wang, G. Li, *Stress memory of a thermoset shape memory polymer*. J. Appl. Polym. Sci. **2015**, 132, 42112– 42123.

UNIVERSITAT ROVIRA I VIRGILI
DESIGN AND CHARACTERIZATION OF ACTIVELY-MOVING POLYMERS OBTAINED VIA DUAL-CURING PROCESSING
Alberto Francisco Belmonte Parra

Chapter III

Shape-memory polymers based on thiol-click chemistry

III

UNIVERSITAT ROVIRA I VIRGILI
DESIGN AND CHARACTERIZATION OF ACTIVELY-MOVING POLYMERS OBTAINED VIA DUAL-CURING PROCESSING
Alberto Francisco Belmonte Parra

III.1 Introduction and scope

Shape-memory thermosets have been lately the focus of interest for many researchers because of their strength, large durability, high performance retaining the temporary shape and fast recovery of the original shape. New technologies involving SMPs must, in most cases, deal with aggressive environmental conditions, thus demanding materials with excellent mechanical properties, high resistance to thermal gradients and chemicals and electrical isolation. To this end, **epoxy-based thermosets** are great candidates due to their excellent properties regarding the mentioned application requirements. Nevertheless, the inherent fragility emerging from their densely crosslinked network structures is a common drawback that must be overcome.

Researchers employ different approaches to reduce the fragility while maintaining, as much as possible, the original properties of the epoxy thermoset in terms of structural, mechanical and thermal properties. The most common approach is to use **curing agents with long aliphatic chains or aromatic amines** that effectively increase the flexibility of the network. Rousseau et al.[1], used curing agents of different nature (propylene-oxide based and ethylene-oxide based) to enhance the deformation limits of the epoxy thermoset. The results indicated the possibility to increase the deformation while maintaining high values of T_g and overall good shape-memory response. Leonardi et al.[2] developed an epoxy-amine SMP using n-dodecylamine and m-xylylenediamine, that is, combining chemical and physical crosslinks. The results demonstrated a great improvement in deformability and the capability to release the stress during the recovery process.

Nevertheless, whereas the deformability is enhanced, the tensile strength is considerably reduced due to the weaker nature of the modified network. This narrows their scope to less mechanically-demanding applications. An efficient solution is the incorporation of **hyperbranched polymers** with aliphatic/functionalized arms that enhances the network mobility, thus, the deformability, while preserving the strength. The high densely branched nature of the hyperbranched polymers makes them excellent mechanisms to absorb and dissipate energy, thus, increasing the impact resistance and overall the strength. Our research group, with the work done by Santiago et al.[3] used a hyperbranched poly(ethyleneimine) polymer to modify a diglycidyl ether of bisphenol A epoxy resin. The results demonstrated good control on the structural, mechanical and thermal

properties, achieving high deformation/strength pair limits and good shape-memory response.

An inconvenient is found in the **network homogeneity**: increasing too much the amount of hyperbranched results in heterogeneous network structures that means, broadening of the relaxation process, inefficient fixation of the temporary shape and slow recovery processes. The control of the network homogeneity is of utmost relevance to tailor the properties of thermoset-based SMPs in an easy and efficient manner. Therefore, other solutions must be explored to reduce the fragility while controlling the structural properties of the resulting SMPs. To this end, **click chemistry** comes out as a great solution. As explained in section I.2 **click reactions** are a set of **selective, efficient and versatile reactions** that take place rapidly in a controlled way. Nair et al.[4] reported excellent shape-memory response and precise control of the mechanical and thermomechanical properties using UV-induced thiol-ene click polymerization. Sunitha's et al.[5] used azyde-alkine–CuAAC "click" chemistry to synthesize SMPs. The results demonstrated the advantages on using almost ideal step-growth reaction in comparison with chain-growth to obtain better shape-memory response in terms of fixation, recovery and velocity.

Among the different click systems, the **"thiol-epoxy" click reaction** is interesting due to the formation of "thio-ether" and hydroxyl groups in one-single step that can be further transformed in other polymeric structures. **Tertiary amines** are used to catalyse the reaction; however, they are usually too fast decreasing the pot-life. The control of the pot-life is of utmost importance in industrial processing to allow a large chain of production. As mentioned in section I.2 **latent catalysts** are effective mechanism to extend the latency of a reactive mixture until the catalyst is activated. In this investigation, **thermally-activated encapsulated latent catalysts** are used. The catalyst is released when the capsule degrades, thus, the polymerization process is triggered at high temperature enhancing the kinetics and leading to more homogeneous network structures.

To the best of our knowledge, the use of **"thiol-epoxy" click chemistry** combined with **latent catalyst** for the development of **SMPs** have not been reported yet and could open a new line of production of SMPs with precise control of the structural properties and shape-memory response.

In this chapter, **thiol and epoxy compounds with different functionality and chemical structure** (as shown in section II.6.1) **have been proposed to investigate the possibility to develop SMPs** with

precise control of the structural and thermomechanical properties. The potential capabilities of this system to obtain enhanced SMPs and the effect of varying the thermomechanical and structural properties, as well as T_{prog}, with the efficiency fixing the temporary shape and recovering the original shape are studied in **section III.2**.

Then, in order to understand and link the network relaxation dynamics with the time, temperature and velocity of the recovery process, **the proposed "thiol-epoxy" SMPs have been studied under different isothermal-recovery temperatures in flexural mode**. The results and discussion of this study is presented in **section III.3**.

Finally, to provide useful and simple-to-use tools for the operational design of SMPs, a **thorough study on the relation between the stress/strain response with T_{prog} and the effect on the recovery process** is analysed using a new "data-treatment" methodology proposed by our groups of research. This methodology permits to compare raw data regardless the programming and recovery conditions. For this purpose, the proposed "thiol-epoxy" SMPs have been tested under different T_{prog} and stress/strain limits. The results and discussion of this study is presented in **section III.4**.

References

[1] D.M. Feldkamp, I. a. Rousseau, *Effect of Chemical Composition on the Deformability of Shape-Memory Epoxies*, Macromol. Mater. Eng. **2011**, 296, 1128–1141.

[2] A.B. Leonardi, L. a. Fasce, I. a. Zucchi, C.E. Hoppe, E.R. Soulé, C.J. Pérez, R.J.J. Williams, *Shape memory epoxies based on networks with chemical and physical crosslinks*, Eur. Polym. J. **2011**, 47, 362–369.

[3] D. Santiago, A. Fabregat-Sanjuan, F. Ferrando, S. De la Flor, *Recovery stress and work output in hyperbranched poly(ethyleneimine)-modified shape-memory epoxy polymers*, J. Polym. Sci. Part B Polym. Phys. **2016**, 54, 1002–1013.

[4] D.P. Nair, N.B. Cramer, T.F. Scott, C.N. Bowman, R. Shandas, *Photopolymerized thiol-ene systems as shape memory polymers*, Polymer. **2010**, 51, 4383–4389.

[5] K. Sunitha, K.S.S. K. Santhosh, D. Mathew, C.P.P. N. Reghunadhan, *Shape Memory Polymers (SMPs) derived from phenolic cross-linked epoxy resin via click chemistry,* Mater. Letters. **2013**, 99, 101-104.

III.2 Effect of the network structure and programming temperature on the shape-memory response of thiol-epoxy "click" systems

Polymers, **2015**, 7, 2146 – 2164

Alberto Belmonte[1], Dailyn Guzmán[2], Xavier Fernández-Francos[3] and Silvia De la Flor[1]

1) Department of Mechanical Engineering, Universitat Rovira i Virgili, Av. Països Catalans 26, 43007, Tarragona, Spain.

2) Department of Analytical and Organic Chemistry, Universitat Rovira i Virgili, C/Marcel·lí Domingo s/n, 43007, Tarragona, Spain.

3) Thermodynamics Laboratory, ETSEIB, Universitat Politècnica de Catalunya, Av. Diagonal 647, 08028, Barcelona, Spain.

UNIVERSITAT ROVIRA I VIRGILI
DESIGN AND CHARACTERIZATION OF ACTIVELY-MOVING POLYMERS OBTAINED VIA DUAL-CURING PROCESSING
Alberto Francisco Belmonte Parra

Polymers. 2015, 7, 2146-2164 **107**

Abstract

This paper presents a new methodology to develop "thiol-epoxy" shape-memory polymers (SMPs) with enhanced mechanical properties in a simple and efficient manner via "click" chemistry by using thermal latent initiators. The shape-memory response (SMR), defined by the mechanical capabilities of the SMP (high ultimate strength and strain), the shape-fixation and the recovery of the original shape (shape-recovery), was analysed on thiol-epoxy systems by varying the network structure and programming temperature. The glass transition temperature (T_g) and crosslinking density were modified using 3- or 4- functional thiol curing agents and different amounts of a rigid triglycidyl isocyanurate compound. The relationship between the thermomechanical properties, network structure and the SMR was evidenced by means of qualitative and quantitative analysis. The influence of the programming temperature (T_{prog}) on the SMR was also analysed in detail. The results demonstrate the possibility of tailoring SMPs with enhanced mechanical capabilities and excellent SMR, and intend to provide a better insight into the relationship between the network structure properties, programming temperature and the SMR of unconstrained (stress-free) systems; thus, making it easier to decide between different SMP and to define the operative parameters in the useful life.

Keywords: epoxy; thiol; shape-memory polymer; click chemistry.

1. Introduction

Shape-memory polymers (SMPs) are materials that can change from a temporary shape to their original shape through an external stimulus. The original shape is given by the curing process and it is permanent while the temporary shape is imposed by a programming process, which depends on the physical nature of the shape-memory polymer (SMP)[1–4]. The most common type are the thermo-responsive SMPs[5]. The efficiency of a SMP is defined by the shape-memory response (SMR), which includes the mechanical capabilities (high ultimate strength and strain), good fixation and retention of the temporary shape and well-controlled shape-recovery process. Shape-memory thermosets are recently the focus of several researchers due to the higher strength, larger durability, better retention of the temporary shape and faster recovery of the original shape than those SMPs based on thermoplastics. Specifically, epoxy-based SMPs are interesting because of their excellent mechanical properties, electrical insulation and high thermal stability, being potentially interesting in structural applications[3,6]. Nevertheless, the inherent rigidity

of common epoxy resins, their low strain and stress at break, narrows their application range.

Many researchers employ curing agents characterized by flexible and long aliphatic chains to overcome the deformability limitations. Wei et al.[7] enhanced the segmental mobility by introducing a long flexible chain of poly(propylene glycol) diglycidyl ether (PPGDGE) in epoxy-amine formulations. Rousseau et al.[8] used curing agents of different nature (aliphatic-based, propylene oxide (PO)-based, ethylene oxide (EO)-based, PO/EO) on a DGEBA (epoxy resin) and studied the influence of the network structure on the ultimate strain and the impact on the shape-recovery. The results indicated that by carefully varying the network structure it was possible to increase the tensile elongation while maintaining high values of glass transition temperature (T_g) and obtaining excellent shape-recovery performances. On the other hand, another approach to enhance the ultimate strain based on the effect of the programming temperature (T_{prog}) was investigated by Yakacki et al.[9] working with acrylates and Rousseau et al.[10] using epoxy-based systems. The results demonstrated an improvement of the strain at break of three- to five-fold, when deforming at a temperature slightly below the T_g, corresponding to the onset point of the network relaxation process (measured by dynamic-mechanical analyses). Recently, Zheng et al.[11] presented a high strain two component epoxy-amine (up to 210% of strain at break when deforming at the onset temperature) with tailorable T_g and excellent shape-fixity and shape-recovery performances.

Nevertheless, while the ultimate strain is highly enhanced by varying the network structure, both the ultimate strength and the shape-recovery process are affected by these changes. In structural and aerospace applications[12,13] the capability to perform a mechanical work and the control of the shape-recovery process are highly demanded to properly tailor materials for specific conditions. However, one of the major drawbacks is to fulfil both, high ultimate strength and strain. Moreover, the enhancement of the strain limits leads to uncontrolled modifications of the shape-recovery process. To this end, very few works have focused on the study of the relation between the network structure and, either the strength or the shape-recovery process. Williams et al.[14] improved the tensile strain of an epoxy-based system and reported a great strength by combining chemical and physical crosslinking through a long aliphatic chain (n-dodecylamine) and a compact rigid structure (m-xylylenediamine). Our group developed hyperbranched poly(ethyleneimine)-modified epoxy SMPs with enhanced ultimate strength (up to 12 MPa of stress at break), maintaining high ultimate

strain[15]. On the other hand, Yakacki et al.[16,17] studied the dependence of the shape-recovery process on the network structure in constrained and unconstrained (stress-free) conditions. The results evidenced the relationship between the network relaxation dynamics and the unconstrained (stress-free) recovery process, and the dependence on the crosslinking density for the constrained ones. Chen et al.[18] evidenced the influence of the network relaxation dynamics in unconstrained recovery processes by means of numerical simulations. However, the enhanced ultimate strength and strain reported are not sufficiently high, and the knowledge of the network structure role on the shape-recovery process is not yet well-defined. More efforts to better understand the relation of the network structure properties with the shape-recovery process and ultimate mechanical properties are required to advance in the development of smart materials.

The so-called click chemistry is a new generation of reactions based on efficiency, versatility and selectivity[19–21]. Among the different "click" mechanisms, the thiol-epoxy systems[22] are especially interesting due to the formation of hydroxyl and thioether groups in a single step during the polymerization process, which can be further transformed into other polymeric structures[23,24]. Tertiary amines are commonly used as base catalysts in thiol-epoxy formulations, but they are usually too reactive, making it hard to control the reaction and shortening their pot-life. It was recently shown[25,26] that it is possible to increase the pot life of thiol-epoxy formulations by means of polymer-encapsulated amines or thermally stable aromatic-aliphatic urea's, being the former the most effective way. Thus, it is possible to prepare formulations, store them safely before application, and process them at temperatures high enough to quickly release the amine catalyst and produce a completely cured material in a short period of time.

Over the last few years, some reports have been published on the use of the "click" concept to synthesize SMPs. Shandas et al.[27] used UV-induced thiol-ene polymerization to develop SMPs with a wide range of mechanical and thermomechanical properties with excellent SMR. Afterwards, Sunitha et al.[28] and McBride et al.[29] synthesized SMPs based on azyde-alkine–CuAAC "click" chemistry with high shape-recovery and shape-fixation performances. To the best of our knowledge, though, the "click" chemistry via nucleophilic attack to strained heterocycles (i.e. the thiol-epoxy mechanism), using thermal latent initiators, has not been yet investigated on the development of SMPs.

In this paper, we combine the advantages of using "click" thiol-epoxy reaction with latent catalysis to produce SMPs with enhanced mechanical properties (high ultimate strength and strain) in a simple and efficient manner. This study expects to provide, by means of a detailed thermal and mechanical characterization of these materials, a better understanding on the relationship between the network structure and thermomechanical properties with the SMR, and to establish sound criteria for material choice depending on the expected application or certain operation conditions. In this sense, it is expected to clarify as much as possible the parameters one should consider depending on the desired applications. On the other hand, by varying the programming temperature, it is intended to link both the enhancement on the mechanical properties[9,10] with the effect on the SMR. For this purpose, in this work, (3- and 4- functional) thiol components have been used as curing agents for a commercial diglycidyl ether of bisphenol A (DGEBA) via "click" chemistry using encapsulated amines as latent initiators. In addition, different amounts of triglycidyl isocyanurate (iso) have been used as network structure modifiers in order to increase the T_g and the crosslinking density of the material. The SMR has been analysed using different programming temperatures (below, at and above the T_g), and has been related to the network structure changes induced by the addition of isocyanurate and the use of thiol components of different functionality.

2. Experimental section

Materials

A commercial epoxy resin, Diglycidyl ether of bisphenol A (DGEBA, GY240, Huntsman, Everberg, Belgium) with a molecular weight per epoxy equivalent unit of 182 g/eq was used as the main epoxy resin. Pentaerythritol tetrakis (3-mercaptopropionate) (4thiol), with a molecular weight per thiol equivalent unit of 122.17 g/eq (Sigma-Aldrich, St. Louis, MO, USA) and trimethylolpropane tris(3-mercaptopropionate) (3thiol), with a molecular weight per thiol equivalent unit of 132.85 g/eq (Sigma-Aldrich, St. Louis, MO, USA) were used separately as crosslinking agents. In addition, a tri(2,3-epoxypropyl)isocyanurate (iso), with a molecular weight per epoxy equivalent unit of 99.09 g/eq (Sigma-Aldrich, St. Louis, MO, USA) was used as a modifier in different weight proportions: 10%, 20%, 30% and 40% (i.e. 10:90 wt % ISO:DGEBA), maintaining a stoichiometric proportion of thiol and epoxy groups (epoxy:thiol ratio equal to 1:1). An encapsulated imidazole (LC80, AC Catalysts) was used as a latent initiator in a proportion of 0.5 phr) (parts of catalyst for hundred

parts of epoxy resin). The reagents were used as received, without further purification.

The formulations were prepared by manually stirring the components in a glass vial and carefully pouring the mixtures in an open Teflon mould. The curing process was carried out in an oven, one hour at 120 °C followed by one hour at 150 °C to allow the completion of the process. Scheme III-1 shows the expected network for the mixtures without iso and Scheme III-2 the expected changes introduced by the iso (the crosslinking points have been highlighted).

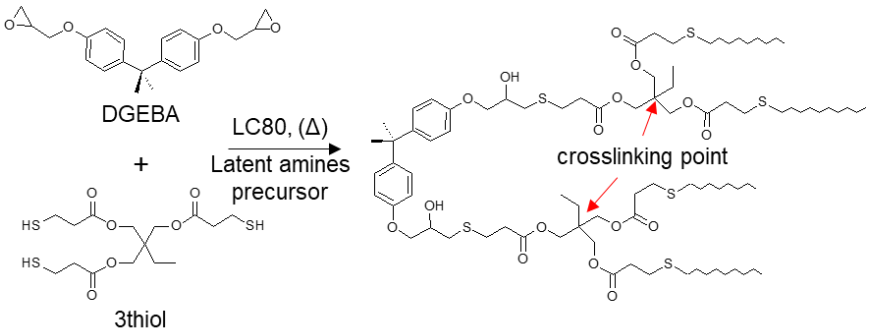

Scheme III-1. Reaction scheme and expected network structure of the mixture containing 3thiol as curing agent, DGEBA as epoxy resin and LC-80 as initiator (3thiol-DGEBA-LC80) formulation.

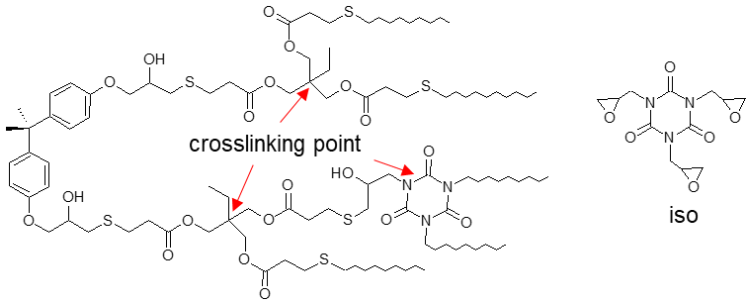

Scheme III-2. Expected network structure of the 3thiol-DGEBA-LC80 modified with the (iso) component.

The composition of the different formulations considered is detailed in Table III-1.

Table III-1. Composition of the different formulations of study.

Formulation	DGEBA (wt %)	Thiol (wt %)	Iso (wt %)	LC80 (wt %)
3thiol-NEAT	57.64	42.07	0.00	0.29
3thiol-(10%)iso	50.11	44.04	5.57	0.28
3thiol-(20%)iso	43.08	45.88	10.77	0.27
3thiol-(30%)iso	36.49	47.61	15.64	0.26
3thiol-(40%)iso	30.31	49.22	20.21	0.25
4thiol-NEAT	59.66	40.04	0.00	0.30
4thiol-(10%)iso	51.95	41.99	5.77	0.29
4thiol-(20%)iso	44.73	43.81	11.18	0.28
4thiol-(30%)iso	37.95	45.52	16.26	0.27
4thiol-(40%)iso	31.56	47.13	21.04	0.26

Network structure and thermomechanical properties

The network structure and thermomechanical properties of the different materials were studied by thermo dynamic-mechanical analyses using a DMA Q800 (TA instrument) equipped with a Single-Cantilever (10 mm) clamp. The samples were thoroughly polished until a prismatic rectangular shape (≈ 20 × 7.5 × 1.8 mm^3) was obtained. The samples were analysed at 1 Hz with oscillation amplitude of 10 µm at a heating rate of 3 °C/min. Figure III-1 shows a typical representation of the curves obtained by DMA. The T_g was determined by the peak of the tanδ curve, both, the modulus at room temperature (E_g') and above the glass transition (E_r'), were determined directly from the storage modulus curve (E'). The onset point ($T_g^{E'}$) was determined as the intersection of the lines corresponding to the plateau in the glassy state and the modulus fall. In addition, the width of the tanδ curve at the half-height (FWHM) and the tanδ peak have been determined as shown in Figure III-1.

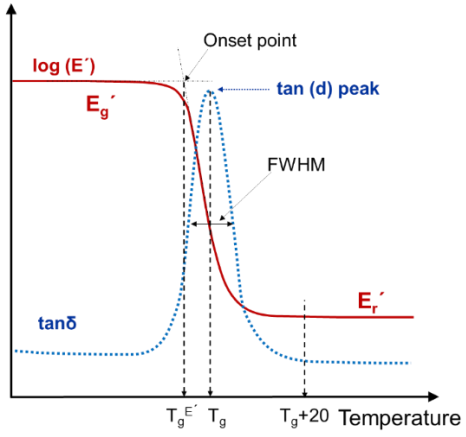

Figure III-1. Schematic representation of the relevant parameters obtained from DMA analysis: storage modulus (E') and tanδ curve for a typical thermoset. The parameters of interest have been pointed out.

According to the Affine model for ideal rubbers, the relaxed modulus E_r' at low strain rates is related to the strand density of the crosslinked network by equation (III-1).

$$E_r' = 3 \cdot R \cdot T \cdot \rho \cdot v_e \quad \text{(III-1)}$$

where R is the universal gas constant, T is the temperature at which the modulus E_r' is calculated, ρ is the density of the material at the temperature T and v_e is the network strand density. Usually, the network strand density v_e is considered to depend on the crosslink density and functionality as:

$$v_e = \sum_{f \geq 3} \left(n_f \cdot \frac{f}{2} \right) \quad \text{(III-2)}$$

where n_f is the density of crosslinking junctions with functionality f. However, it has been shown that the mobility of the network strands and their deformation is further affected by the functionality of the crosslinking points[30] due to the fluctuation of crosslinks in the network, so that modifications to the ideal expression have been proposed such as[31]:

$$v_e = \sum_{f \geq 3} \left(n_f \cdot \frac{f-2}{2} \right) \quad \text{(III-3)}$$

For the correct evaluation of this parameter, one has to take into account the composition of the formulation and that, in the fully cured materials, 3thiol and iso contribute with trifunctional crosslinks, and 4thiol with tetrafunctional crosslinks.

Other non-idealities should have an influence in the value of E_r', such as the presence of permanent physical entanglements[31] or the non-Gaussian deformation of the network strands[32].

Lesser and Crawford[33] studied the dependence of the glass transition temperature on the crosslinking density and the crosslinking functionality, and proposed the following modification of the classical free-volume based relationship taking into account the effect of crosslink fluctuation, as:

$$T_{g,x} = T_{g\infty} + \frac{2 \cdot (f_{ave} - 2)}{f_{ave}} \cdot \frac{\zeta}{M_c} \quad \text{(III-4)}$$

where $T_{g,x}$ is the glass transition temperature at a conversion x, f_{ave} is the average crosslink functionality, ζ is proportional to the molecular weight of the unreacted resin and to the ratio of incremental free volume contributions from the resin and the curing agent, and M_c is the average mass between crosslinks. This expression can be conveniently rearranged and adapted for the present case of comparison between similar materials with differing crosslinking density and functionality. It can be shown that the T_g is approximately proportional to an effective crosslinking density, in a similar way to the Fox-Loshaek equation[34] yielding:

$$T_g = a + b \cdot v_e \quad \text{(III-5)}$$

where a and b are constants and v_e is calculated using expression (III-3), taking into account crosslink fluctuation and functionality. Other expressions have been proposed to account for other non-idealities[35,36] but they are not considered for simplicity purposes.

Mechanical characterization

The mechanical response was analysed through stress-strain experiments using the DMA Q800 (TA instrument, New Castle, DE, USA) equipped with a Tension-Film clamp in Force-controlled mode at a range of temperatures (from T_{room} to T_g + 20). Dog-bone shaped samples were polished thoroughly with sandpaper in order to obtain controlled size samples (length × thickness × width ≈ 15 × 0.5 × 1.4 mm^3, see Figure III-2) and were annealed during 10 min at 120 °C in an oven before testing. The samples were mounted and carefully held between the grips of the clamp to ensure an initial testing length of 10–11 mm. The pressure applied in both grips was sufficiently low to avoid cutting the sample, and sufficiently high to avoid slipping. The experiments were carried out at 3 N/min. The stress and strain at break (σ_b and ε_b respectively) were determined as the failure point from the curves obtained.

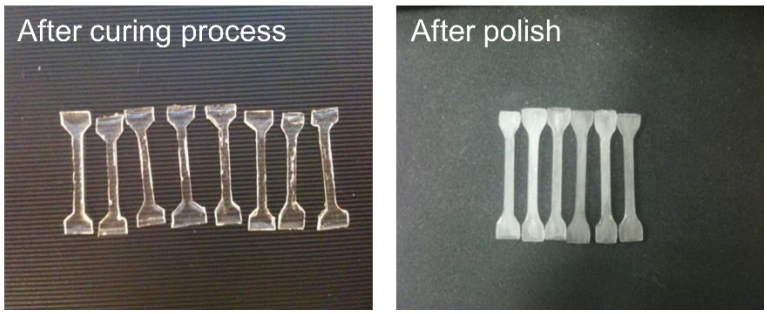

Figure III-2. Dog-bone shaped samples preparation process.

Shape-memory response (SMR)

The SMR of all the formulations was investigated through a visual methodology (qualitative study) for comparison purposes and as a means of choosing the best candidates for further analysing the effect of the programming temperature in the SMR (quantitative study).

Qualitative study

The SMR was analysed using a visual methodology to monitor isothermal-recovery processes. Prismatic rectangular samples of 40 × 8 × 2.5 mm^3 (length × width × thickness) were polished to flat parallel surfaces. The programming process was performed following the next steps: the sample was heated up to the programming temperature (T_{prog}) stipulated as its T_g to make possible the comparison among the different formulations under study, and then deformed to a U-shape using the bending device shown in Figure III-3(a). The device and the sample were rapidly cooled down with cold water while maintaining the force applied. The sample was unloaded and was placed in an oven at the isothermal recovery temperature (T_{rec}) corresponding to its T_g (following the same line of reasoning as for the T_{prog}) as shown in Figure III-3(b). The process was recorded using a high-resolution camera and further analysed frame by frame (one frame per second of the video), measuring the angles as shown in Figure III-3(b) and applying equation (III-6) on each frame. The time needed to recover from the 15% to the 85% of the original shape (t_{sr}) was determined using the equation (III-7) (the beginning and the end of the process were neglected to avoid possible experimental errors since it is a visual methodology).

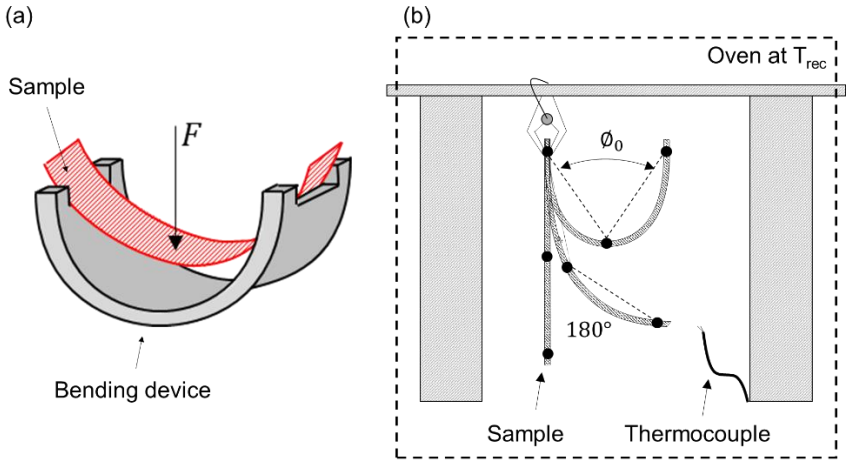

Figure III-3. Schematic representation of the bending device; (a) and the shape-recovery scenario; (b) for the isothermal-recovery experiments.

$$(\%\,SR)_{\emptyset} = \frac{\Delta\emptyset_t}{180° - \emptyset_0} \cdot 100 \quad \text{(III-6)}$$

$$t_{sr} = t_{(\%\,SR)_{85}} - t_{(\%\,SR)_{15}} \quad \text{(III-7)}$$

where *%SR* is the shape-recovered in percentage, Φ_0 is the initial angle and $\Delta\Phi_t$ is the difference between the angle at a time *t*, Φ_t, and Φ_0. t_{sr} is the shape-recovery time.

Quantitative study

In the quantitative study, the SMR was analysed through a customized experimental method using the DMA Q800 (TA Instrument) equipped with the Tension-Film clamp. The samples were prepared in the same way as for their mechanical characterization (see Figure III-2). The experiments were performed following the steps shown in Figure III-4. Three T_{prog} were chosen: $T_g^{E'}$, T_g and T_g + 20, to quantify the SMR at the optimal mechanical point ($T_g^{E'}$)[9,10] and along the glass transition process (T_g and T_g + 20). The samples were heated up to T_{prog} and held during 5 min at this temperature to ensure thermal equilibrium (point 1 in Figure III-4). A uniaxial tensile deformation at a constant force rate of 1 N/min was applied until the 75% of ε_b (ε_D) was reached (line a to point 2 in Figure III-4). This limit of 75% of ε_D was used in order to make comparisons between the formulations regardless of their different network structure and mechanical properties, also depending on T_{prog}, as well as to quantify the SMR near the maximum elongation allowed. Once ε_D was reached, the force applied was held constant while rapidly cooling to setting temperature (T_s) (line b to point 3). Subsequently, the force applied was released at the same force rate of 1 N/min (line c to point 4). Afterwards, a heating rate of 3 °C/min was imposed until the original shape was recovered (line d to point 5). All the other experimental conditions and parameters remained unchanged.

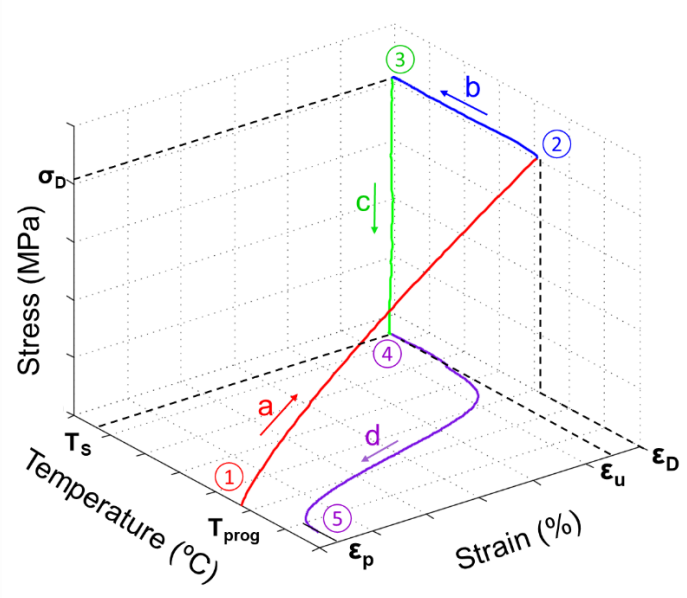

Figure III-4. Thermo-responsive SMPs; 3D representation of the programming process.

The SMR was analysed as the average of the results through three consecutive cycles (it was not appreciated any worsening of the SMR during the cycling until the sample broke). The capability of the material to recover its original shape was determined by the shape-recovery ratio (R_r), using the equation (III-8) and the capability to retain the imposed shape (temporary shape) was determined by the fixation-ratio (R_f), using equation (III-9).

$$R_r(\%) = \frac{\varepsilon_D - \varepsilon_p}{\varepsilon_D} \cdot 100 \quad \text{(III-8)}$$

$$R_f(\%) = \frac{\varepsilon_u}{\varepsilon_D} \cdot 100 \quad \text{(III-9)}$$

where ε_D is the deformation reached after loading, ε_u is the deformation after unloading and ε_p is the permanent strain after the shape-recovery. All these parameters are represented in Figure III-4.

The shape-recovery rate (V_r) was calculated using the equations (III-10) and (III-11), enclosing the whole process (from 1% to 100% of the original shape recovered) and avoiding the early and final stages (from 15% to 85%).

$$\%SR = 100 - \frac{\varepsilon - \varepsilon_p}{\varepsilon_u - \varepsilon_p} \cdot 100 \quad \text{(III-10)}$$

$$V_r(\%/°C) = \frac{\Delta\%SR}{\Delta T_{\Delta\%SR}} \quad \text{(III-11)}$$

where *%SR* is the percentage of original shape recovered normalized to the permanent strain (ε_p), Δ*%SR* is the range tested (*%SR* = 1%–100% and 15%–85%) and $\Delta T_{\Delta\%SR}$ is the temperature increment corresponding to the Δ*%SR*.

3. Results and discussion

Thermomechanical and network structure properties

The thermomechanical and network structure properties were analysed by dynamic-mechanical analyses. The results for the 3thiol and 4thiol systems are shown in Figure III-5 and Figure III-6, and some characteristic parameters of the network relaxation process (see Figure III-1) are summarized in Table III-2.

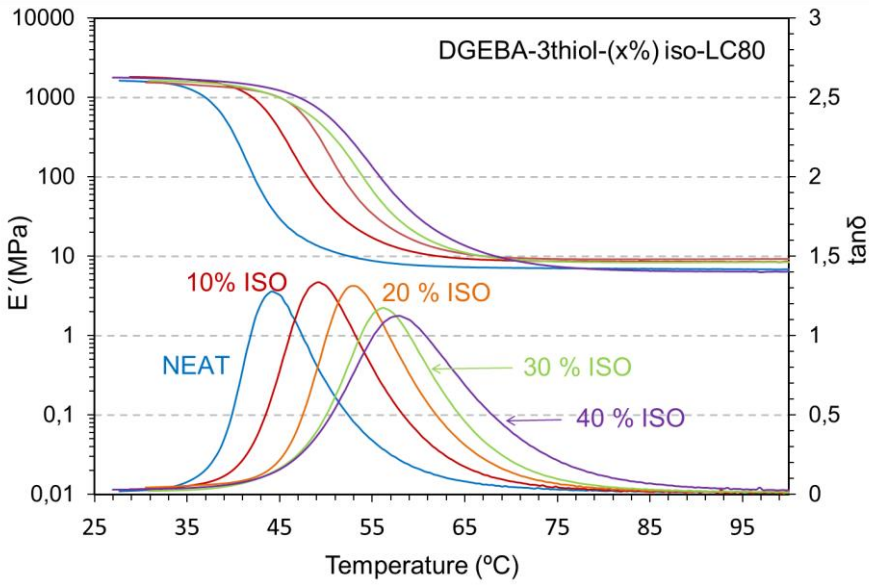

Figure III-5. Dynamic-mechanical analyses for the (3thiol) different formulations.

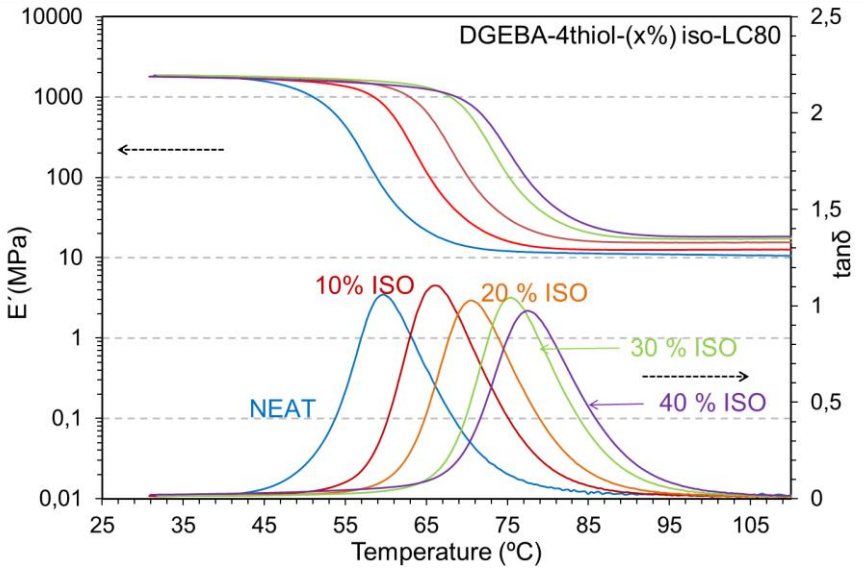

Figure III-6. Dynamic-mechanical analyses for the (4thiol) different formulations.

In general, the formulations with 3thiol have lower T_g than those with 4thiol because of the reduction of free volume and hindrance of the molecular motion caused by the presence of crosslink junctions[36], which becomes more relevant with increasing crosslink functionality[33], as seen for other shape-memory materials[37,38]. On the other hand, adding the iso compound to the different systems tend to increase the T_g. According to the expected network of the Scheme III-2, the iso component acts as a 3-functional crosslinking point, increasing the functionality of the system, thus, creating a more hindered network. Nevertheless, the T_g increment tends to become less relevant especially above an iso content up to 30% for formulations containing 3thiol. Figure III-7 shows a good correlation between the T_g and the effective strand density ν_e (calculated taking into account crosslink functionality and fluctuation, using equation (III-3)), showing a fairly linear trend as predicted by equation (III-5). However, some non-idealities appear for both 3thiol and 4thiol formulations with increasing iso content and, consequently, ν_e. It must be taken into account that the increase in the content of iso also changes the type of network structure, introducing crosslinks with a non-negligible mass, and the size and rigidity of the network strands[25].

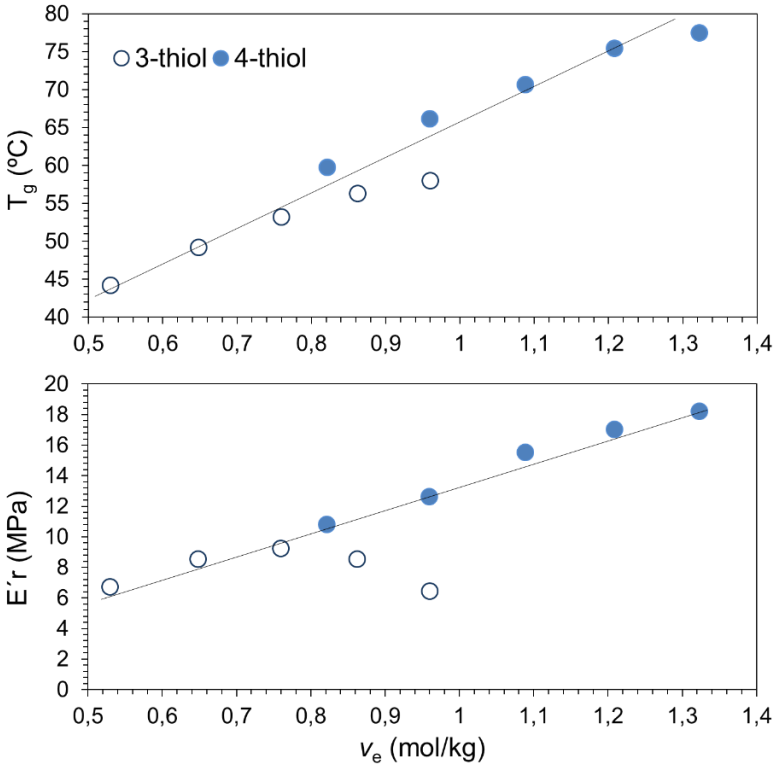

Figure III-7. (T_g) and (E_r') with respect to the effective strand density (v_e) corresponding to each % of iso content.

FWHM and tanδ peak values are characteristics of the relaxation and can be related to the crosslinking density and the network homogeneity of the material. It is commonly observed that the relaxation peaks broaden and decrease its intensity with increasing crosslinking density[15] a phenomenon that is inherently related to the increase in crosslinking density and T_g[34]. Although the trend is not well defined, because of the discrete increase in crosslinking density, the same is observed in the present case. The effect of iso on the shape of the relaxation in 4thiol systems is very limited in comparison with 3thiol and, in fact, the broadening of the relaxation when 40% of iso is used with 3thiol is too large and may have a detrimental effect on the SMR of the material.

Table III-2. Network structure and thermomechanical properties of the different materials of study.

Formulation	E_g' (MPa)	E_r' (MPa)	E_g'/E_r'	FWHM (°C)	tanδ peak	T_g (°C)	$T_g^{E'}$ (°C)	v_e[a] (mol/kg)
3thiol-NEAT	1,590	6.7	237	10.3	1.28	44.1	37.7	0.530
3thiol-(10%)iso	1,804	8.5	211	11.9	1.34	49.1	42.0	0.649
3thiol-(20%)iso	1,540	9.2	167	11.7	1.31	53.1	46.3	0.760
3thiol-(30%)iso	1,616	8.5	191	12.5	1.18	56.2	46.6	0.863
3thiol-(40%)iso	1,744	6.4	271	15.7	1.13	57.9	47.9	0.961
4thiol-NEAT	1,850	10.8	171	12.0	1.06	59.7	52.0	0.822
4thiol-(10%)iso	1,815	12.6	145	12.1	1.11	66.1	58.8	0.960
4thiol-(20%)iso	1,855	15.5	120	12.1	1.03	70.6	62.9	1.089
4thiol-(30%)iso	1,870	17.0	110	11.8	1.05	75.4	68.2	1.209
4thiol-(40%)iso	1,800	18.2	99	12.6	0.98	77.4	69.7	1.323

[a] Calculated using equation (III-3).

The effective strand density v_e (calculated taking into account crosslink functionality and fluctuation, using equation (III-3)) shows an increasing trend with the addition of iso and with the increase in the thiol functionality from 3thiol to 4thiol, as expected. The measured values of the relaxed modulus E_r' have a very good agreement with this trend except 3thiol formulations with 30% and 40% of iso, that show decreasing values of E_r'. Such discrepancies are in line with the non-idealities observed in the T_g and the broadening of the relaxation peak in 3thiol formulations with higher iso content.

Differences between 3thiol and 4thiol formulations may be consequence of the different structure of both crosslinking agents. Setting aside the different functionality, 3thiol has a pendant ethyl group that may produce a certain distortion in the network structure and the network relaxation dynamics, thus affecting the whole of the measured parameters. In addition, one must consider that the introduction of iso produces not only an increase in crosslinking density but also a significant change in the network structure. Such considerations fall out the scope of the simple theoretical expressions used in this work. Furthermore, it is possible that this also results from a certain incompatibility between iso and 3thiol or a difference in the reactivity of the epoxy groups of iso and DGEBA, leading to an inhomogeneous distribution of the different types of network strands and crosslinking points.

SMR qualitative study: comparison with thermomechanical properties and network structure

From the previous thermomechanical analysis, a series of general considerations can be made in terms of the SMR of the different materials. The capability of a material to show shape-recovery is usually quantified

by the E_g'/E_r' ratio[15]. Table III-2 shows that the E_g'/E_r' ratio is over 2 orders of magnitude or above for all the formulations, a high enough value. The drop of the modulus from E_g' to E_r' during the network relaxation is steep enough to expect high rates during the shape-recovery process (see Figure III-5 and Figure III-6). In addition, there is a plateau zone of E_g' at the T_s (temperature at which the temporary shape is fixed) sufficiently away from the modulus drop zone to avoid premature shape-recovery and consequently allow good shape-fixation. Overall, the shape of the network relaxation process, represented by the tanδ curve, is well-defined along the glass transition (no noise is noticed) and it is similar for all the formulations, expecting a similar SMR.

In the qualitative study, the SMR has been analysed through the t_{sr} parameter (see equation (III-7)), since no losing of the temporary shape was visually appreciated after cooling and releasing the stress applied to the sample. In addition, the programmed samples showed good retention of the temporary shape during the 5–10 min of holding time at room temperature before the shape-recovery was triggered inside the oven. Moreover, at the end of the process, the recovery of the original shape was quantitative %SR ≈ 100% (equation (III-8)), leaving no appreciable permanent strain.

As it can be seen in Figure III-8, overall the t_{sr} is excellent for all the formulations as expected from the E_g'/E_r' ratio and the sharp relaxation. The materials are capable of recovering from the 15% to the 85% of their original shape in less than 14 s when heated on air (note that, in many applications such as security devices, the heating process is on air through isothermal conditions). The NEAT formulations show a similar response, about 12 s of t_{sr}, while the addition of 10% of iso accelerates the shape-recovery process for both systems (t_{sr} falls to 10–9 s). In contrast, increasing the amount of iso from 10% to 40% slows down the process in the case of the 3thiol formulations (t_{sr} increases from 10 s at 10% of iso up to 13 s at 40% of iso), while for the 4thiol ones it remains almost constant. Figure III-8 compares the t_{sr} along with the tanδ peak (a) and FWHM (b) values in order to relate the SMR with the network structure. As it can be seen, t_{sr} decreases when the tanδ peak increases and when FWHM decreases. These results point at a strong relationship between the sharpness of the relaxation process and the rate of the shape-recovery process. Materials with a more heterogeneous network structure and a broader relaxation profile (higher FWHM and lower tanδ peak) have a slower relaxation process, thus limiting the chain motion and shape-recovery. This trend is well-appreciated in the case of 3thiol formulations between 20% and 40% of iso, showing an increase in FWHM from 11.7 to

15.7 °C and an increase in t_{sr} from 11 to 13 s. In the case of the 4thiol formulations this trend is also observed from 30% to 40% of iso. The value of the tanδ peak clarifies the situation when FHWM values are similar. In Figure III-8(c) it is seen that t_{sr} decreases when the tanδ peak increases showing a linear correlation for both the 3thiol and 4thiol systems with isocyanurate. In contrast, other network structure parameters, such as the crosslinking density given by v_e or E_r', do not have an influence on the recovery rate. As discussed in the preceding section, v_e increases with the amount of iso (see Table III-2), but changes in t_{sr} follow the trend dictated by FWHM and tanδ peak instead, regardless of the values of v_e or E_r'. These results are in agreement with Yakacki et al. suggesting that on unconstrained experiments the main responsible of the shape-recovery process is the network relaxation process[17].

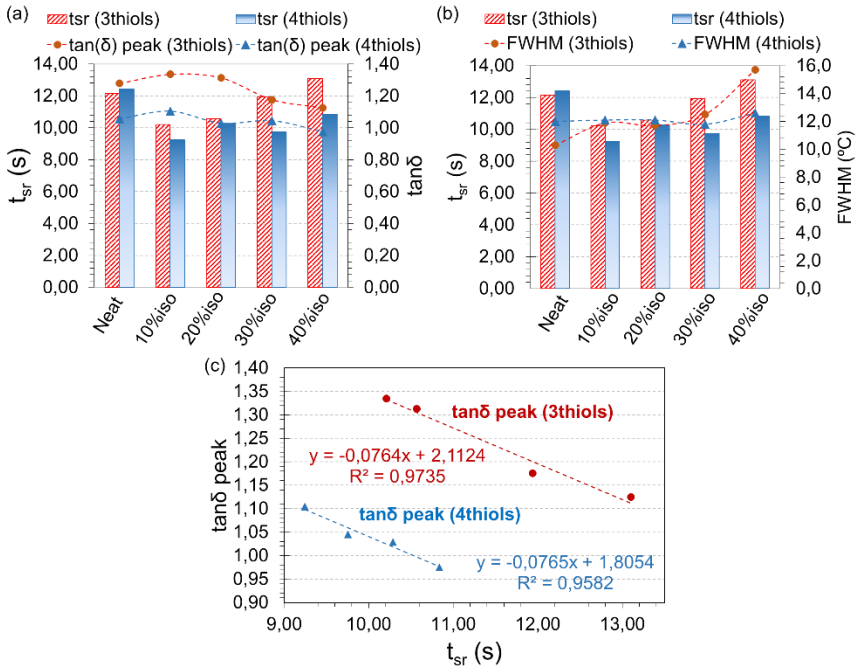

Figure III-8. Relation between the shape-memory response (in terms of t_{sr}) and the network relaxation dynamics; (a) t_{sr} against tanδ peak as a function of the composition; (b) t_{sr} against FWHM as a function of the composition; (c) tanδ peak against the t_{sr} for both, 3thiol and 4thiol with isocyanurate formulations (10%, 20%, 30% and 40%).

To sum up, these results evidence the dependence of the shape-recovery with the network relaxation on unconstrained experiments, suggesting that FWHM and tanδ peak can be used to estimate, at least from a comparative point of view, the velocity of the shape-recovery process[39]. From the shape of the modulus curve (the steepness of the

drop and the plateau zone at the glassy state), one can also obtain a qualitative view of the speed of the recovery process and the capability of the material to retain the temporary shape.

Finally, the best candidates have been chosen by applying the next criteria: the higher glass transition reached by adding the iso component to maximize temporary shape retention along with a homogeneous network structure to have fast recovery process. Therefore, the 3thiol-30%iso and 4thiol-30%iso formulations, along with the NEAT ones, have been chosen for further analysis in the quantitative study. While there is no doubt in the case of 4thiol formulations, the decision was more complicated in the case of the 3thiol ones. The formulations with 10% and 20% of iso are better candidates from the point of view of the recovery speed, but the formulation with 30% of iso has shown a higher T_g value and its t_{sr} is similar to the NEAT formulation which, overall, is excellent. In addition, as commented above, the R_r and R_f, as well as the shape-fixation were excellent for all the formulations. Therefore, for a proper comparative study, the same amount of isocyanurate should be used for both systems.

Mechanical analysis: influence of the network structure and programming temperature

One of the most important capabilities of a SMP during the programming process is the mechanical response (in terms of ultimate strain and stress), described by the σ_b and ε_b parameters. Figure III-9 summarizes the σ_b and ε_b values obtained for the different formulations and the relation with the crosslinking density as a function of the T_{prog}. In general, both parameters have shown a high dependence on temperature and network structure. In accordance with Rousseau and Yakacki[9,10], the optimal mechanical point for all the formulations is found at the onset point ($T_g^{E'}$), where the material combines both properties: high resistance and molecular mobility, therefore leading to higher values of σ_b and ε_b. As the T_{prog} increases from $T_g^{E'}$ to T_g + 20, the σ_b and ε_b tend to decrease because of the material becomes weaker (i.e. for the 4thiol-NEAT system, σ_b and ε_b are 39 MPa and 66% respectively, when programming at $T_g^{E'}$, while programming at T_g decreases σ_b and ε_b down to 9 MPa and 42%, respectively). On the other hand, the effect of the crosslinking density of the materials on the σ_b and ε_b is clearly appreciated when T_{prog} is well above the T_g. At this temperature, conformational rearrangement of network chains take place quickly in response to the stress applied, and therefore the deformation achieved ε_b is mainly limited by the crosslinking density. As can be seen, the higher the molecular weight between

crosslinking points (lower v_e), the higher the strain at break. In contrast, the trend is not well-defined for the σ_b. The explanation must be connected with the heterogeneity of the crosslinking points and thus the differences on the physical nature of the chains created among the different formulations[8].

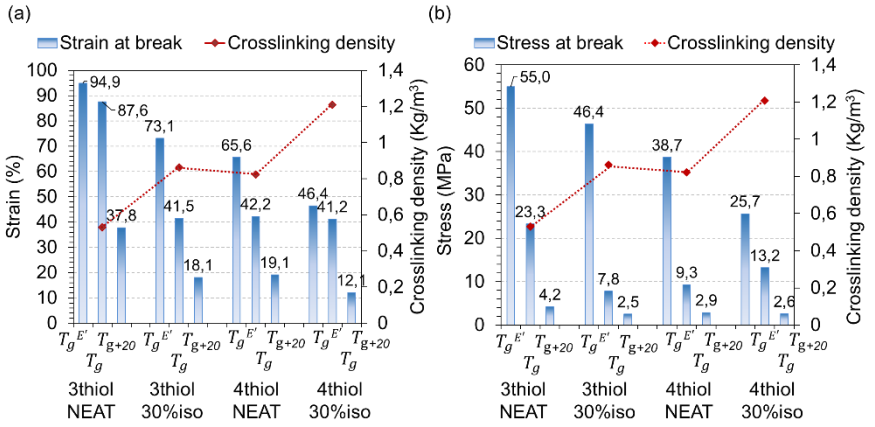

Figure III-9. Mechanical response and crosslinking density as a function of the programming temperature for all the formulations of study; (a) strain at break values; (b) stress at break values.

Overall, it should be pointed out the mechanical performance of these materials, in terms of σ_b and ε_b, they are superior to other epoxy-based SMPs. Williams et al.[14] reported an epoxy-amine system (based on a long aliphatic chain *n*-dodecylamine) with large tensile elongations (up to 75%) and high recovered stresses (over 4 MPa), when programming at a temperature close to the T_g. Rousseau et al.[10] reported epoxy-amine systems (based on long flexible polyetheramines) with higher values of σ_b (up to 8 MPa) and large ultimate strain (over 60%), when programming at $T_g^{E'}$, the optimal mechanical point. In addition, our group[15] reported epoxy-amine materials (based on polyetheramines and hyperbranched poly(ethyleneimines) with σ_b over 12 MPa while maintaining large ultimate strain (ε_b up to 60%). In general terms, while the tensile elongation is enhanced by adjusting the programming temperature and the network structure, the mechanical work remains limited by the low tensile strength obtained. In the present case, the thiol-epoxy materials under study fulfil both the requirements of high tensile strain and enhanced tensile stress, thus, enhancing the energy storage capacity and therefore the expected performance on constrained experiments[40]. The 3thiol-NEAT system reaches values of almost 100% of ε_b (comparable with those reports by the mentioned authors[10,14,15]) and 55 MPa of σ_b (which

is over 4 times higher than those reported by[15]) when programming at $T_g^{E'}$. Furthermore, when programming at T_g, the σ_b (over 23 MPa) is still higher than those reported by the mentioned authors[10,14,15] and ε_b is considerably high (up to 82%). The excellent mechanical properties found between $T_g^{E'}$ and T_g + 20 broaden the applicability of our materials, since T_{prog} not only modifies the mechanical response, but also affects the SMR[41]. In this sense, it is possible to obtain materials with specific SMR maintaining and excellent mechanical response.

SMR quantitative study: influence of the programming temperature

In the quantitative study, the SMR has been investigated through the R_r and R_f ratios (see equations (III-8) and (III-9)). The results are represented in Figure III-10.

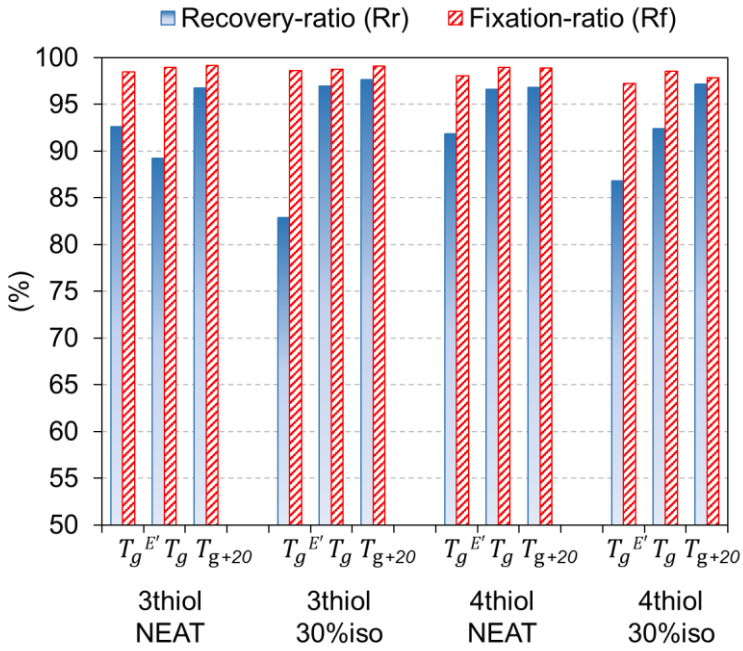

Figure III-10. Recovery-ratio and fixation-ratio as a function of the programming temperature for all the formulations of study.

The capability to retain the temporary shape, quantified by the fixation-ratio, R_f, is excellent for the different materials of study with values of almost 100% regardless of the T_{prog} applied. The R_f basically depends on the mechanical response of the material during the unloading process, which occurs at T_s (the temperature at which the temporary shape is fixed). At T_s the material is in the glassy state and the modulus (E_g') is higher than 1500 MPa for all the formulations (see in Table III-2)

thus, the chain mobility is strongly hindered and the differences in the network structure do not affect the mechanical response. Accordingly, the T_{prog}, which probably introduces changes in the network structure after loading and fixing the temporary shape, does not affect the R_f for the same reason. In contrast, the recovery of the original shape, quantified by the recovery-ratio, R_r, depends on the T_{prog}: when programming at T_g or T_g + 20 the values are higher (over 90%–96% at T_g and almost 100% at T_g + 20) than those when programming at $T_g^{E'}$ (falling down to 83% for 3thiol-30%iso and 87% for 4thiol-30%iso). Furthermore, the differences in R_r between the different formulations when they are programmed at $T_g^{E'}$ are higher than when they are programmed at T_g + 20. According to Pandini et al.[41], loading at a temperature below the T_g involves more energetic changes (elastic and hardening processes) while loading at a temperature above the T_g involves mostly entropic changes. The energy lost during the loading process is higher when the loading involves more energetic molecular changes (at $T_g^{E'}$)[42] because of molecular friction. The low initial chain mobility and the activation of the chain relaxation during programming at this temperature, result in some inter-molecular flow friction. Part of the deformation work corresponds to viscous flow and cannot be recovered, therefore the energy available for the recovery process is not enough to lead it to completion, resulting in a decrease in R_r. In addition, depending on the nature of the chains (molecular structure), the energy lost during the loading process at $T_g^{E'}$ is different. In the case of the NEAT formulations, the R_r is higher and similar for both systems, 3thiol and 4thiol, while adding the isocyanurate decreases the R_r in both systems probably due to the increase in the rigidity of the chains. Moreover, the 3thiol-30%iso shows a lower value of R_r than the 4thiol-30%iso. This must be connected with the previous results of the thermomechanical characterization of the materials. Both the presence of the side ethyl chain in the structure of 3thiol and some reactivity and compatibility issues, resulting in a distortion of the network structure and mobility and a broadening of the relaxation, may explain the higher energy losses in the 3thiol formulation with 30% iso. These results suggest that by properly varying the T_{prog} a balance enhancing both, the mechanical response and the shape-recovery capability is possible.

In Figure III-11, the shape-recovery process is analysed by means of V_r (through 3 consecutive cycles), enclosing the whole process (from 1% to 100% of the original shape recovered), or avoiding the early and final stages (from 15% to 85%). In general, as it was expected from the results of the qualitative study, all the formulations have shown very high values. If one focuses on the middle stage (15%–85%), the values range from

6.3 %/°C to 8 %/°C which are comparable with those reported by[15], thus, allowing almost fully recover of the original shape in very few minutes. On the other hand, using the average (1%–100%), the effect of both the early and final stages is incorporated. As it can be seen, the time needed to fully recover the original shape is 2 or 3 times higher. These results evidence that the shape-recovery process is limited by the early and final stages and therefore the control of these stages is crucial to adjust the shape-recovery process as desired.

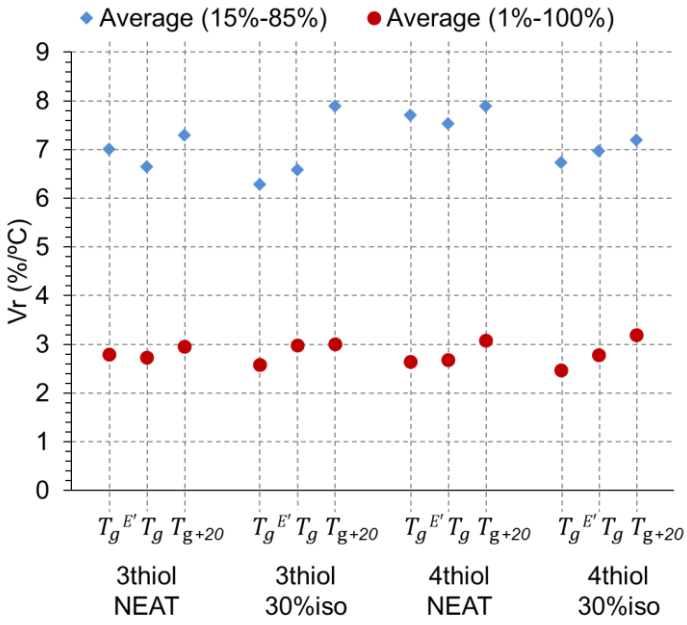

Figure III-11. Shape-recovery rate (%/°C), enclosing the whole shape-recovery process (1%–100%) and avoiding the early and final stages (15%–85%), as a function of the programming temperature for all the formulations of study.

On analysing the effect of the programming temperature with the V_r, it is seen an increment of the V_r with the temperature. This phenomenon is well appreciated if one encloses the whole process (1%–100%) (i.e. the 4thiol-30%iso increases the V_r from 2.5 %/°C up to 3.2 %/°C and the 3thiol-30%iso from 2.6 %/°C up to 3.0 %/°C). This is probably connected with the lower recovery ratio R_r when programming at T_g^E (see Figure III-10). Following the same line of reasoning as above, the lower amount of energy that is effectively stored and available for the recovery process (due to molecular friction losses) decreases both the recovery ratio R_r and the V_r, thus increasing the time needed to fully recover the original shape. It may be speculated that the resulting stretched network structure of the temporary shape is somewhat altered when programming

at T_g^E and this may also have an effect on the recovery rate. Whatever the specific cause, this is of particular importance in the case of the 3thiol-30%iso, being the effect of the programming temperature very strong in the central part of the process (15%–85%), and this may be connected with the lowering and broadening of the relaxation described above for the 3thiol-30% (see Table III-2 and Figure III-8).

In spite of the differences in the relaxation process of the different formulations described in the previous sections, the average recovery speed is similar among the different formulations, especially if one encloses the whole process (1% to 100%). The overall trends with respect to the network structure and the shape of the relaxation process are not as clearly defined as in the qualitative study and depend also on the programming temperature. The recovery process in the qualitative study was analysed under isothermal conditions, using a fixed programming and recovery temperature relative to the network relaxation determined by DMA. Therefore, the time/velocity effect, which is connected with the relaxation dynamics, could be analysed independently. In contrast, the shape-recovery takes place with increasing temperature in the quantitative study. In this case, there is a time-temperature coupling that adds complexity to the process and makes it more difficult to interpret the average recovery speed data, especially taking into account that there are small differences in terms of relaxation shape but clearly different relaxation temperatures. However, it has been observed that during the recovery process there is indeed a strong effect of the network relaxation dynamics, especially when temperature is still below T_g. There is an excellent correspondence between the early stage of the recovery process and the early stage of the relaxation process determined from the DMA experiments (data not shown). Afterwards, at some point, the temperature enhances the molecular mobility and the recovery process is able to proceed more freely causing acceleration and minimizing the effect of the network structure. Therefore, enclosing the whole process, the effect of the relaxation process is clearly minimized, while focusing on the central part (15%–85%) this effect on the early stage has a major role. To this end, by properly tailoring the network structure and programming temperature, the effect at the early stage of the shape-recovery process can be tuned as desired, obtaining higher or lower rates which at the end of the process will be adjusted.

In conclusion, these results evidence the possibility to tailor the early stage and eventually the whole shape-recovery process by properly modifying the network structure and its relaxation dynamics, and the programming temperature. Moreover, the effect on the mechanical

properties (stress and strain at break) is also investigated, thus, making possible a balance between mechanical performance and shape-memory performance.

4. Conclusions

Materials based on epoxy-thiol "click" chemistry have been obtained, with enhanced mechanical properties and well-defined network structures. The different materials have been characterized by dynamic-mechanical analysis and been tested as SMPs from a qualitative and quantitative point of view. The effect of the material network structure and the programming temperature T_{prog} on the SMR in unconstrained shape-recovery scenarios has been discussed and analysed in detail.

It has been seen that the network structure of epoxy-thiol materials can be finely tuned by changing both the thiol crosslinker functionality and by introducing a rigid trifunctional epoxy resin. In general, a good agreement between the experimental data and the expected network structure has been obtained. From the results of the dynamic-mechanical analysis and a qualitative visual methodology for the analysis of the SMR it has been found that the shape-recovery process is highly dependent on the network relaxation dynamics. Thus, the sharpness in the relaxation peak tanδ or the shape of the drop in elastic modulus, can be used to predict, at least from a comparative point of view, the shape-memory response of the materials.

Prior to the quantitative analysis, the stress and strain at break values have been determined for a range of temperatures and an optimal point has been found at the onset point of the relaxation process. Values of stress and strain that break as high as 100% and 55 MPa, respectively, have been reached. A strong dependence of the crosslinking density with the strain at break at T_g + 20 has been found, when the network structure rapidly reaches a relaxed state while the deformation is occurring. As the crosslinking density increases, the strain at break decreases.

From the quantitative analysis, it has been seen that some parameters such as the ratio of fixation are not affected by programming conditions or network structure, reaching values around 100%. In contrast, the recovery ratio has a strong dependence on both the programming temperature and the network structure: the energy lost during the loading process is significantly reduced due to the decrease in chain friction produced by the network relaxation as the programming temperature is increased. At lower temperatures ($T_g^{E'}$), the amount of energy lost during the loading process is strongly related to the network

structure. Following the same reasoning as above, the shape-recovery rate of the shape-recovery process increases by the reduction of energy lost during the loading process on increasing programming temperature. There is a complex time-temperature superposition during the recovery process with increasing temperature, but it has been found a close relationship between the relaxation process determined with DMA and the measured shape-recovery process.

In conclusion, the network structure properties give us an idea of the expected shape-fixation and -retention of the temporary shape during the fixation and storage processes, while the network relaxation process is a powerful tool to define the shape-recovery process on unconstrained experiments. In addition, the T_{prog} has an important impact on the SMR, being a crucial parameter during loading stage and the shape-recovery process: not only the σ_b and ε_b can be adjusted by varying the T_{prog}, but also the shape-recovery process (enclosing the whole-process path) can be tuned as desired.

Acknowledgements

The authors would like to thank MINECO (MAT2014-53706-C03-01) and Generalitat de Catalunya (2014-SGR-67) for its financial support.

References

[1] Lendlein, A.; Sauter, T. Shape-memory effect in polymers. *Macromol. Chem. Phys.* **2013**, *214*, 1175–1177.

[2] Julich-Gruner, K.K.; Löwenberg, C.; Neffe, A.T.; Behl, M.; Lendlein, A. Recent trends in the chemistry of shape-memory polymers. *Macromol. Chem. Phys.* **2013**, *214*, 527–536.

[3] Santhosh Kumar, K.S.; Biju, R.; Reghunadhan Nair, C.P. Progress in shape memory epoxy resins. *React. Funct. Polym.* **2013**, *73*, 421–430.

[4] Mather, P.T.; Luo, X.; Rousseau, I.A. Shape memory polymer research. *Annu. Rev. Mater. Res.* **2009**, *39*, 445–471.

[5] Sun, L.; Huang, W.M.; Ding, Z.; Zhao, Y.; Wang, C.C.; Purnawali, H.; Tang, C. Stimulus-responsive shape memory materials: A review. *Mater. Des.* **2012**, *33*, 577–640.

[6] Rousseau, I.A.; Xie, T. Shape memory epoxy: Composition, structure, properties and shape memory performances. *J. Mater. Chem.* **2010**, *20*, 3431–3441.

[7] Wei, K.; Zhu, G.; Tang, Y.; Niu, L. Shape-memory effects of a hydro-epoxy resin system. *J. Polym. Res.* **2013**, *20*, 123.

[8] Feldkamp, D.M.; Rousseau, I.A. Effect of chemical composition on the deformability of shape-memory epoxies. *Macromol. Mater. Eng.* **2011**, *296*, 1128–1141.

[9] Yakacki, C.M.; Willis, S.; Luders, C.; Gall, K. Deformation limits in shape-memory polymers. *Adv. Eng. Mater.* **2008**, *10*, 112–119.

[10] Feldkamp, D.M.; Rousseau, I.A. Effect of the deformation temperature on the shape-memory behavior of epoxy networks. *Macromol. Mater. Eng.* **2010**, *295*, 726–734.

[11] Zheng, N.; Fang, G.; Cao, Z.; Zhao, Q.; Xie, T. High strain epoxy shape memory polymer. *Polym. Chem.* **2015**, *6*, 3046–3053.

[12] Arrieta, S.; Diani, J.; Gilormini, P. Experimental characterization and thermoviscoelastic modeling of strain and stress recoveries of an amorphous polymer network. *Mech. Mater.* **2014**, *68*, 95–103.

[13] Arrieta, J.S.; Diani, J.; Gilormini, P. Cyclic and monotonic testing of free and constrained recovery properties of a chemically crosslinked acrylate. *J. Appl. Polym. Sci.* **2014**, doi:10.1002/app.39813.

[14] Leonardi, A.B.; Fasce, L.A.; Zucchi, I.A.; Hoppe, C.E.; Soulé, E.R.; Pérez, C.J.; Williams, R.J.J. Shape memory epoxies based on networks with chemical and physical crosslinks. *Eur. Polym. J.* **2011**, *47*, 362–369.

[15] Santiago, D.; Fernández-Francos, X.; Ferrando, F.; de la Flor, S. Shape-memory effect in hyperbranched poly(ethyleneimine)-modified epoxy thermosets. *J. Polym. Sci. Polym. Phys.* **2015**, 924-933.

[16] Yakacki, C.M.; Shandas, R.; Lanning, C.; Rech, B.; Eckstein, A.; Gall, K. Unconstrained recovery characterization of shape-memory polymer networks for cardiovascular applications. *Biomaterials* **2007**, *28*, 2255–2263.

[17] Yakacki, C.M.; Shandas, R.; Safranski, D.; Ortega, A.M.; Sassaman, K.; Gall, K. Strong, tailored, biocompatible shape-memory polymer networks. *Adv. Funct. Mater.* **2008**, *18*, 2428–2435.

[18] Chen, X.; Nguyen, T.D. Influence of thermoviscoelastic properties and loading conditions on the recovery performance of shape memory polymers. *Mech. Mater.* **2011**, *43*, 127–138.

[19] Binder, W.H.; Sachsenhofer, R. "Click" chemistry in polymer and materials science. *Macromol. Rapid Commun.* **2007**, *28*, 15–54.

[20] Moses, J.E.; Moorhouse, A.D. The growing applications of click chemistry. *Chem. Soc. Rev.* **2007**, *36*, 1249–1262.

[21] Kolb, H.C.; Finn, M.G.; Sharpless, K.B. Click chemistry: Diverse chemical function from a few good reactions. *Angew. Chem. Int. Ed.* **2001**, *40*, 2004–2021.

[22] Brändle, A.; Khan, A. Thiol–epoxy "click" polymerization: Efficient construction of reactive and functional polymers. *Polym. Chem.* **2012**, *3*, 3224–3227.

[23] Flores, M.; Tomuta, A.M.; Fernández-Francos, X.; Ramis, X.; Sangermano, M.; Serra, A. A new two-stage curing system: Thiol-ene/epoxy homopolymerization using an allyl terminated hyperbranched polyester as reactive modifier. *Polymer* **2013**, *54*, 5473–5481.

[24] Carlborg, C.F.; Vastesson, A.; Liu, Y.; van der Wijngaart, W.; Johansson, M.; Haraldsson, T. Functional off-stoichiometry thiol-ene-epoxy thermosets featuring temporally controlled curing stages via an UV/UV dual cure process. *J. Polym. Sci. Polym. Chem.* **2014**, *52*, 2604–2615.

[25] Guzmán, D.; Ramis, X.; Fernández-Francos, X.; Serra, A. New catalysts for diglycidyl ether of bisphenol A curing based on thiol-epoxy click reaction. *Eur. Polym. J.* **2014**, *59*, 377–386.

[26] Guzmán, D.; Ramis, X.; Fernández-Francos, X.; Serra, A. Enhancement in the glass transition temperature in latent thiol-epoxy click cured thermosets. *Polymers* **2015**, *7*, 680–694.

[27] Nair, D.P.; Cramer, N.B.; Scott, T.F.; Bowman, C.N.; Shandas, R. Photopolymerized thiol-ene systems as shape memory polymers. *Polymer* **2010**, *51*, 4383–4389.

[28] Sunitha, K.; Santhosh Kumar, K.S.; Mathew, D.; Reghunadhan Nair, C.P. Shape memory polymers (SMPs) derived from phenolic cross-linked epoxy resin via click chemistry. *Mater. Lett.* **2013**, *99*, 101–104.

[29] McBride, M.K.; Gong, T.; Nair, D.P.; Bowman, C.N. Photo-mediated copper(I)-catalyzed azide-alkyne cycloaddition (CuAAC) “click” reactions for forming polymer networks as shape memory materials. *Polymer* **2014**, *55*, 5880–5884.

[30] Graessley, W.W. Statistical mechanics of random coil networks. *Rubber Chem. Technol.* **1975**, *48*, 1008–1017.

[31] Miller, D.R.; Macosko, C.W. A new derivation of postgel properties of network polymers. *Rubber Chem. Technol.* **1976**, *49*, 1219–1231.

[32] Charlesworth, J.M. Effect of crosslink density on molecular relaxations in diepoxide-diamine network polymers. Part 2. The rubbery plateau region. *Polym. Eng. Sci.* **1988**, *28*, 230–236.

[33] Lesser, A.; Crawford, E. The role of network architecture on the glass transition temperature of epoxy resins. *J. Appl. Polym. Sci.* **1997**, *66*, 387–395.

[34] Pascault, J.-P.; Sautereau, H.; Verdu, J.; Williams, R.J.J. *Thermosetting Polymers*; CRC Press: New York, NY, USA, 2002.

[35] Charlesworth, J.M. The glass transition temperature for non-gaussian network polymers. *J. Macromol. Sci.* **1987**, *26*, 105–133.

[36] Hale, A.; Macosko, C.W.; Bair, H.E. Glass transition temperature as a function of conversion in thermosetting polymers. *Macromolecules* **1991**, *24*, 2610–2621.

[37] Liu, Y.; Han, C.; Tan, H.; Du, X. Thermal, mechanical and shape memory properties of shape memory epoxy resin. *Mater. Sci. Eng. A* **2010**, *527*, 2510–2514.

[38] Fan, M.; Yu, H.; Li, X.; Cheng, J.; Zhang, J. Thermomechanical and shape-memory properties of epoxy-based shape-memory polymer using diglycidyl ether of ethoxylated bisphenol-A. *Smart Mater. Struct.* **2013**, doi:10.1088/0964-1726/22/5/055034.

[39] Rousseau, I.A.; Xie, T. Relationship between materials properties and shape memory behavior in epoxy-amine polymers. *MRS Proc.* **2009**, *1190*, 31–36.

[40] Anthamatten, M.; Roddecha, S.; Li, J. Energy storage capacity of shape-memory polymers. *Macromolecules* **2013**, *46*, 4230–4234.

[41] Pandini, S.; Bignotti, F.; Baldi, F.; Passera, S. Network architecture and shape memory behavior of cold-worked epoxies. *J. Intell. Mater. Syst. Struct.* **2013**, *24*, 1583–1597.

[42] Gu, Y.; Li, S.X. Thermo-mechanical behavior of epoxy shape memory polymer. *Adv. Mater. Res.* **2013**, *721*, 169–172.

UNIVERSITAT ROVIRA I VIRGILI
DESIGN AND CHARACTERIZATION OF ACTIVELY-MOVING POLYMERS OBTAINED VIA DUAL-CURING PROCESSING
Alberto Francisco Belmonte Parra

III.3 Network structure dependence on unconstrained isothermal-recovery processes for shape-memory thiol-epoxy "click" systems

Mechanics of Time-Dependent Materials, **2017**, 21, 133-149

Alberto Belmonte[1], Xavier Fernández-Francos[2], Silvia De la Flor[1] and Àngels Serra[3]

1) Department of Mechanical Engineering. Universitat Rovira i Virgili. Av. Països Catalans 26, 43007 Tarragona, Spain.

2) Thermodynamics Laboratory, ETSEIB, Universitat Politècnica de Catalunya. Av. Diagonal 647, 08028 Barcelona, Spain.

3) Department of Analytical and Organic Chemistry, Universitat Rovira i Virgili, C/Marcel·lí Domingo s/n, 43007, Tarragona, Spain.

UNIVERSITAT ROVIRA I VIRGILI
DESIGN AND CHARACTERIZATION OF ACTIVELY-MOVING POLYMERS OBTAINED VIA DUAL-CURING PROCESSING
Alberto Francisco Belmonte Parra

Mech. Time-Depend. Mater. 2017, 21, 133-149

Abstract

The shape-memory response (SMR) of "click" thiol-epoxy polymers produced using latent catalysts, with different network structure and thermomechanical properties, was tested on unconstrained shape-recovery processes under isothermal conditions. Experiments at several programming temperatures (T_{prog}) and isothermal-recovery temperatures (T_{iso}) were carried out, and the shape-memory stability was analysed through various consecutive shape-memory cycles. The temperature profile during the isothermal-recovery experiments was monitored, and it showed that the shape-recovery process takes place while the sample is becoming thermally stable and before stable isothermal temperature conditions are eventually reached. The shape-recovery process takes place in two different stages regardless of T_{iso}: a slow initial stage until the process is triggered at a temperature strongly related with the beginning of network relaxation, followed by the typical exponential decay of the relaxation processes until completion at a temperature below or very close to T_g. The shape-recovery process is slower in materials with more densely crosslinked and hindered network structures. The shape-recovery time (t_{sr}) is significantly reduced when the isothermal-recovery temperature T_{iso} increases from below to above T_g because the network relaxation dynamics accelerates. However, the temperature range from the beginning to the end of the recovery process is hardly affected by T_{iso}; at higher T_{iso} it is only slightly shifted to higher temperatures. These results suggest that the shape-recovery process can be controlled by changing the network structure and working at $T_{iso} < T_g$ to maximize the effect of the structure and/or by increasing T_{iso} to minimize the effect but increasing the shape-recovery rate.

Keywords: thiol-epoxy; shape-memory polymer; isothermal-recovery; click chemistry.

1. Introduction

Shape-memory polymers (SMP) are materials that can retain a temporary shape and recover their original shape through an external stimulus which depends on the physical nature of the polymer[1-3]. Temperature is one of the most common stimuli for the shape-memory effect because it either relaxes the network or melts one of the components, which leads to the recovery of the original shape[4-5]. Recently, the increasing demand for smart materials in aerospace engineering, electronic devices and structural applications has redirected the focus of a great deal of research to thermoset-based SMPs[6-8].

Thermoset-based SMPs are more thermally stable, stronger and more durable than thermoplastic-based SMPs. They also fix the temporary shape better (almost 100%), have higher shape-recovery rates and can perform mechanical work[9-12]. Of all the different types, epoxy-based SMPs are worthy of special mention because of their excellent mechanical, electrical, optical and thermal properties[13-14]. However, the rigid structure and fragility of common epoxy thermosets means that they are less deformable and less applicable. One way of overcoming this limitation is to use curing agents with long, aliphatic chains[15-16]. This can significantly enhance the deformability of the materials, but it reduces the glass transition temperature (T_g) quite considerably and may worsen the strength. A different strategy is to program the temporary shape at the onset point of the glass transition process ($T_g^{E'}$) measured by DMA[17-18], thereby increasing the deformability three-to-five-fold and enhancing the mechanical strength of the material. Therefore, by properly combining curing agents and programming conditions, both the deformability and strength can be improved. Recently, Santiago et al.[19] reported SMPs with enhanced strength in comparison with other works[20, 15-16], when hyperbranched poly(ethyleneimine) polymers were combined with simple monomeric aliphatic amine curing agents reacted with an epoxy resin. In a previous study[21], we developed thiol-epoxy materials with tailored network structures and, in combination with optimal programming conditions at $T_g^{E'}$, the strain and stress at break were as high as 96% and 55 MPa.

"Click" chemistry makes it possible to develop materials easily and efficiently[22]. Of all the various "click" systems, the thiol-epoxy mechanism is particularly interesting because hydroxyl and thioether groups can be formed in a single step and then further transformed into other polymeric structures[23-24]. Tertiary amines are commonly used to catalyse the thiol-epoxy reaction[25-26] but they are usually too reactive to prepare stable one-pot formulations. Latent catalysts such as encapsulated imidazoles or urones have been shown to significantly increase the pot-life of thiol-epoxy formulations allowing an easily handling and processing of the reactive mixture[27-28]. Another advantage of using latent initiators is that the curing process occurs rapidly at a higher temperature and leads to materials with well-defined network structures and enhanced mechanical properties[29].

Nevertheless, since the material and the programming process are optimized to obtain the desired thermal and mechanical properties, the shape-recovery process is inherently modified by changes in the network structure. Therefore, it is of key importance to establish a well-defined

relation between the network structure and the expected shape-recovery process. Understanding these relations is essential in structural applications in which the control and the stability of the shape-recovery process are of utmost importance in defining how the material will be applied. As is well-known, all viscoelastic materials follow a time-temperature relation during relaxation processes which depends on their network structure. The shape-recovery process occurs during network relaxation. Although it is widely acknowledged that, in unconstrained experiments, network relaxation dynamics are more important to the shape-recovery process than other network parameters such as crosslinking density and modulus decrease (from the glassy to the rubbery state)[30-31], further studies are required if this is to be confirmed[32-34].

Following our previous work on the characterization of thiol-epoxy materials with shape-memory properties[21], here we focus on how the network structure affects unconstrained shape-recovery processes under isothermal conditions. Materials with different network structures and therefore different transition temperatures and mechanical properties are obtained by combining epoxy monomers and thiol crosslinkers with different functionalities. The materials are programmed at $T_g^{E'}$ but tested at different isothermal-recovery temperatures (T_{iso}) with the purpose of elucidating the network structure–shape-recovery relation. By analysing the time-temperature dependence on the shape-recovery process, we expect to identify and highlight the parameters of the network structure that are most important to the shape-recovery process and define qualitative and quantitative criteria for the dependence so that tools can be designed for the operational design of SMPs.

2. Materials and methods

Materials

A commercial epoxy resin, diglycidyl ether of bisphenol A (DGEBA, GY240, Huntsman, Everberg, Belgium), with a molecular weight per epoxy equivalent unit of 182 g/eq was used as the main epoxy resin. Pentaerythritol tetrakis(3-mercaptopropionate) (4thiol), with a molecular weight per thiol equivalent unit of 122.17 g/eq and trimethylolpropane tris(3-mercaptopropionate) (3thiol), with a molecular weight per thiol equivalent unit of 132.85 g/eq (Sigma-Aldrich, St. Louis, MO, USA) were used separately as thiol crosslinking agents. In addition, tris(2,3-epoxypropyl)isocyanurate (iso), with a molecular weight per epoxy equivalent unit of 99.09 g/eq (Sigma-Aldrich, St. Louis, MO, USA) was used as a modifier (30:70 %wt. iso:DGEBA), while keeping the 1:1 stoichiometric ratio between epoxy and thiol groups in the formulations. An

encapsulated imidazole (LC80, AC Catalysts) was used as a latent initiator in a quantity of 0.5 parts of catalyst per hundred parts of epoxy resin (phr). The composition of the different formulations considered are listed in Table III-3.

The formulations were prepared by manually stirring the components in a glass vial and carefully pouring the mixtures into an open Teflon mould. The curing process was carried out in an oven for one hour at 120 °C followed by one hour at 150 °C to ensure that the process was completed. Scheme III-3 shows the expected network for the mixtures without iso, and Scheme III-4 presents the changes expected in mixtures with iso (the crosslinking points have been highlighted).

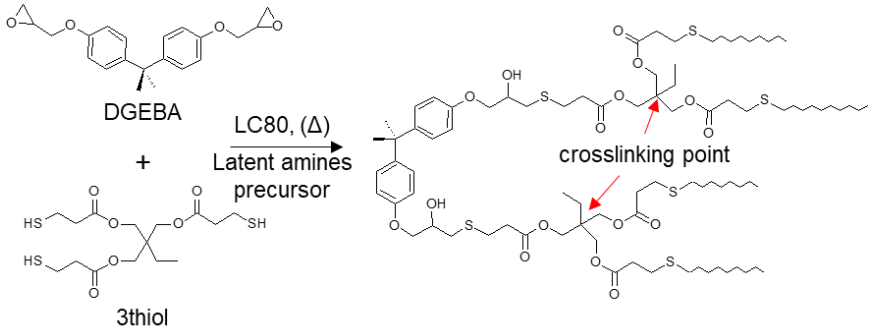

Scheme III-3. Reaction scheme and expected network structure using DGEBA as epoxy resin, 3thiol as curing agent and LC-80 as initiator (3thiol-DGEBA-LC80).

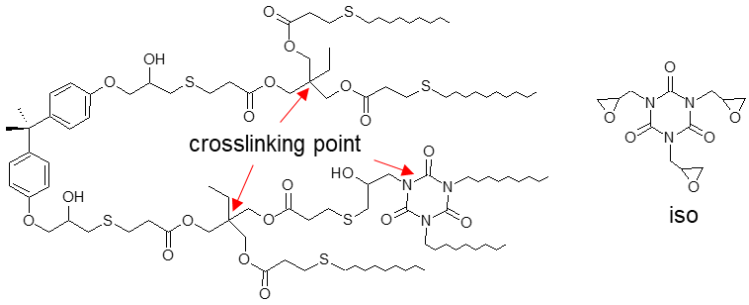

Scheme III-4. Expected network structure of the 3thiol-DGEBA-LC80 formulation modified with the iso component.

Table III-3. Composition of the different formulations of study.

Formulation	DGEBA (wt.%)	Thiol (wt.%)	Iso (wt.%)	LC80 (wt.%)
3thiol-NEAT	57.64	42.07	0.00	0.29
3thiol-(30%)iso	36.49	47.61	15.64	0.26
4thiol-NEAT	59.66	40.04	0.00	0.30
4thiol-(30%)iso	37.95	45.52	16.26	0.27

Thermomechanical characterization

A DMA Q800 (TA instrument) equipped with a single-cantilever (10 mm) clamp was used for the dynamic-mechanical thermal analysis. The experiments were performed at a controlled heating rate (3 °C/min), from 30 °C to 120 °C, at 1 Hz and 10 μm of amplitude. The samples were thoroughly polished until they were shaped like a prismatic rectangle (≈ 20 x 7.5 x 1.5 mm^3). The T_g was determined by the peak of the tanδ curve. The $T_g^{E'}$ was calculated as the onset point of the decrease in storage modulus due to the mechanical relaxation of the network. The width at half-height (FWHM) and the peak of the tanδ curve were used as an indication of the heterogeneity of the relaxation process. An onset period of the network relaxation process was determined by integrating the tanδ curve and calculating the temperature range (ΔT_{net}) (°C) between 0.1% and 2% of the whole relaxation process (100% being the end of the relaxation process). According to the Affine model for ideal rubbers (see equation (III-12)), the network strand density (v_e) is related to the relaxed storage modulus (E_r') at low strain rates. The Affine model needs to be modified (see equation (III-13)) to account for the different functionality and fluctuation of the crosslinking points (a detailed explanation can be found in our previous study[21]).

$$E_r' = 3 \cdot R \cdot T \cdot v_e \qquad \text{(III-12)}$$

$$v_e = \sum_{f \geq 3} \frac{f-2}{2} \cdot n_f \qquad \text{(III-13)}$$

where R is the universal gas constant, T is the temperature at which the modulus E_r' is calculated and n_f is the density of crosslinking points with functionality f.

Shape-memory response (SMR)

Isothermal-recovery experiments were performed to analyse the SMR using the "U" bending test methodology. Prismatic rectangular shaped samples of 40 x 7.5 x 1.5 mm^3 (length x width x thickness) were polished to flat parallel surfaces (original shape). The U-shaped programming process was performed as follows: the samples were heated up to the programming temperature and then deformed to the U-shape using the bending device shown in Figure III-12(a). Both the device and the sample were rapidly cooled using ice water while the stress was maintained for one minute. Afterwards, the stress was released and the U-shape was fixed. The shape-recovery process was performed by placing the programmed sample inside the preheated oven at an isothermal-

recovery temperature (T_{iso}). The experimental shape-recovery process is illustrated in Figure III-13: the use of a thermocouple positioned very close to the sample allowed us to control the T_{iso} in the oven. The process was recorded using a high-resolution camera and analysed frame by frame (one frame per second of the video). The opening angle was measured as shown in Figure III-12(b). The percentage of the original shape recovered (%SR) was obtained for each frame using equation (III-14), where Ø is the opening angle, $Ø_0$ is the initial angle and $\Delta Ø_t$ is the angle increase at a time t ($\Delta Ø_t = Ø_t - Ø_0$).

The shape-recovery time (t_{sr}) was calculated as the time between the onset point (t_{onset}) and the end point (t_{end}) of the shape-recovery curve using equation (III-15).

$$(\%SR)_t = \frac{\Delta Ø_t}{180° - Ø_0} \cdot 100 \qquad \text{(III-14)}$$

$$t_{sr} = t_{end} - t_{onset} \qquad \text{(III-15)}$$

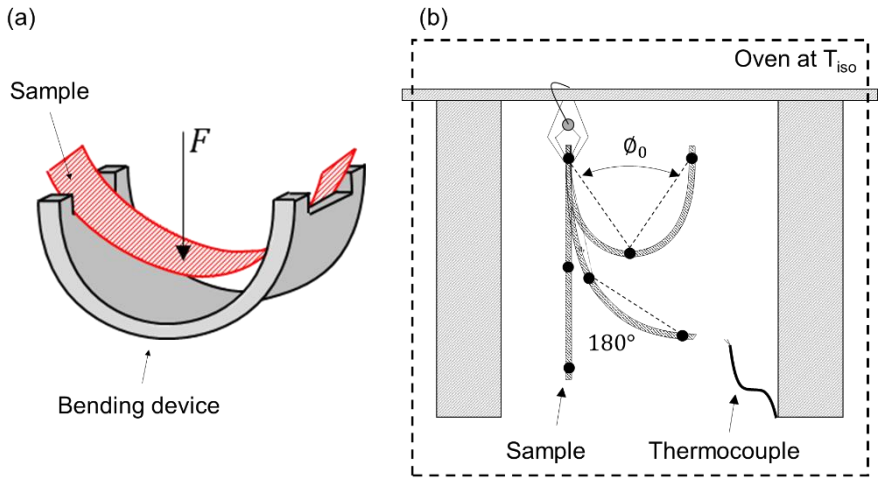

Figure III-12. (a) Schematic representation of the bending device; (b) shape-recovery scenario.

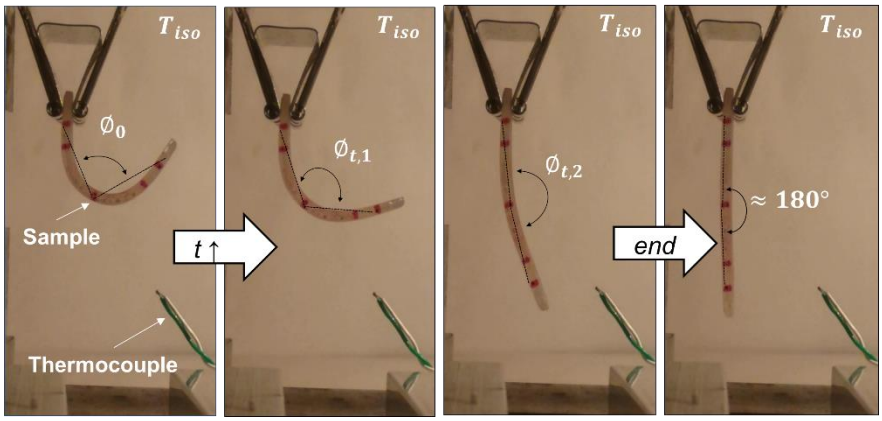

Figure III-13. Images of the shape-recovery process at different shape-recovery times (from the beginning to the end).

Determination of the sample temperature profile

Overall, the isothermal-recovery experiments are limited by the sample temperature stabilization. Depending on the sample's dimensions and the heating conditions, the stabilization time can exceed the shape-recovery time, in which case the experiment becomes non-isothermal. To this end, in order to correctly analyse the shape-recovery process, the temperature on the surface of the sample was measured using a thermocouple stuck to the surface of one testing sample. The temperature was monitored from the initial time (placement of the sample inside the preheated oven) until the isothermal-recovery temperature was reached. Different T_{iso} (50, 60 and 70 °C) were chosen to experimentally determine the coefficient of convection (h) inside the oven and, therefore, to obtain the sample temperature profile. Assuming the sample is sufficiently thin and the heat resistance inside the sample sufficiently low, that is, the temperature profile is uniform throughout the sample thickness, the energy balance shown in equation (III-16) for the heating of the sample would hold true. Parameter m is the mass of the sample, C_p is the heat capacity of the material, h is the coefficient of convection, A is the area of the surface receiving the heat flow, T is the sample surface temperature and T_∞ is the isothermal temperature inside the oven.

$$m \cdot C_p \cdot \frac{dT}{dt} = -h \cdot A \cdot (T - T_\infty) \qquad \text{(III-16)}$$

Integration of equation (III-16) with initial conditions of T_0 equal to the sample temperature at time 0, before the sample is placed inside the oven, and boundary condition T_∞ is constant and equal to the temperature inside the preheated oven, leads to equation (III-17). Note that the

experiments were performed inside an air-controlled room, with T_0 = 18 °C. Constant *"C"* can be calculated from the slope of the plot ln(T-T_∞/T_0-T_∞) against time:

$$ln\left(\frac{T-T_\infty}{T_0-T_\infty}\right) = -\frac{h\cdot A}{m\cdot C_p}\cdot t = -C\cdot t \qquad \text{(III-17)}$$

Nevertheless, the assumption of uniform temperature inside the sample should be validated using the Biot number Bi (see equation (III-18)), which should be less than 0.1. After constant C has been determined, the convection coefficient h and the Biot number can be estimated, using typical properties for epoxy systems[35] (thermal conductivity of the sample $k = 0.2$ W/m·K, specific heat capacity C_p = 1300 J/kg·K and density ρ = 1200 Kg/m^3) and the sample dimensions, which are measured:

$$Bi = \frac{h\cdot L}{k} \qquad \text{(III-18)}$$

3. Results and discussion

Thermomechanical properties

The results of the dynamic-mechanical thermal analysis are shown in Figure III-14, and the parameters of interest are summarized in Table III-4. As discussed in our previous study[21], by using curing agents of higher functionality (4thiol instead of 3thiol), the T_g can be increased. Although the network strands have the same length, the higher functionality of the crosslinking points leads to a higher concentration of effective network strands in the system ν_e, therefore increasing T_g. In addition, the incorporation of isocyanurate into the system also increases the T_g because it acts as a crosslinking point by itself, increasing the crosslinking density and reducing the network strand length. As it was reported in the previous work[21], the use of iso in the 3thiol formulations led to some incompatibility issues, producing a broadening of the relaxation at >30% of iso content. In order to avoid erroneous relationships between the shape-memory response and the network structure, we have chosen formulations with homogeneous network structures (as it can be deduced from the FHWM and tanδ peak values in Table III-4).

Table III-4. Network structure and thermomechanical properties of the different materials of study.

Formulation	T_g (°C)	$T_g^{E'}$ (°C)	FWHM (°C)	tanδ peak	ν_e[a] (mol/kg)	ΔT_{net} (°C) = ($T_{0.1\%}$ - $T_{2\%}$)[b]
3thiol-NEAT	44.1	37.7	10.3	1.28	0.530	5.3 = (31.6 – 36.9)
3thiol-(30%)iso	56.2	46.6	12.5	1.18	0.863	8.0 = (35.6 – 43.6)
4thiol-NEAT	59.7	52.0	12.0	1.06	0.822	8.7 = (35.3 - 44.0)
4thiol-(30%)iso	75.4	68.2	11.8	1.05	1.209	16.5 = (46.6 – 63.1)

[a] Calculated using equation (III-13).
[b] Calculated by integrating the tanδ curve into the temperature range corresponding to 0.1% and 2% of the completion (explained in the materials and methods section).

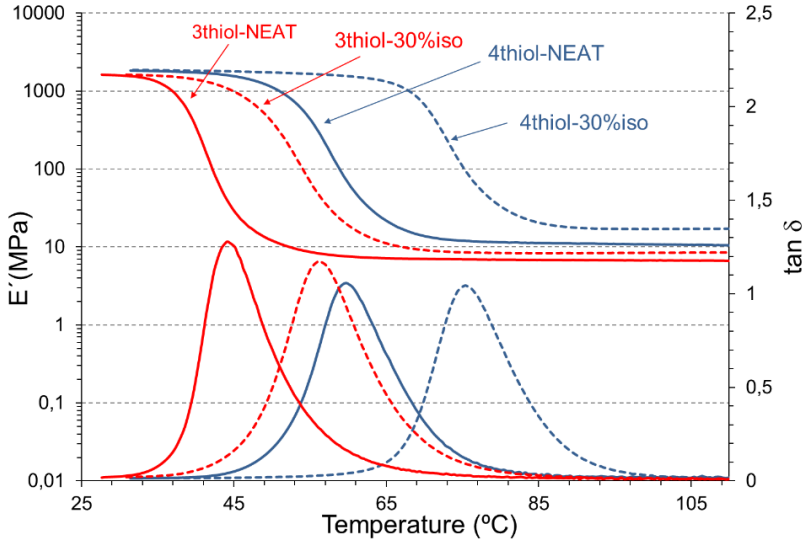

Figure III-14. Dynamic-mechanical thermal analyses of the different formulations of study.

Sample temperature profile

Before discussing the results of the isothermal-recovery experiments, the temperature profile should be determined so that the shape-recovery process can be correctly analysed. Following the experimental procedure described in the materials and methods section, various T_{iso} were tested to calculate the constant C in the oven and to get the temperature profile. In Figure III-15, the plot $\ln(T-T_\infty/T_0-T_\infty)$ against time is shown for different T_{iso}. The data obtained show a very good correlation above t = 7 s, with only slight deviations at the beginning. Since the shape-recovery processes (mostly those at higher T_{iso}) took place rapidly after the sample had been placed in the oven, the temperature profile was divided into two different sections, equations (III-19) and (III-20), and the slope calculated separately for $t < 7$ s and $t \geq 7$ s. The result was C_0 ($t < 7$) = 0.04 s^{-1} and C ($t \geq 7$) = 0.0243 s^{-1}:

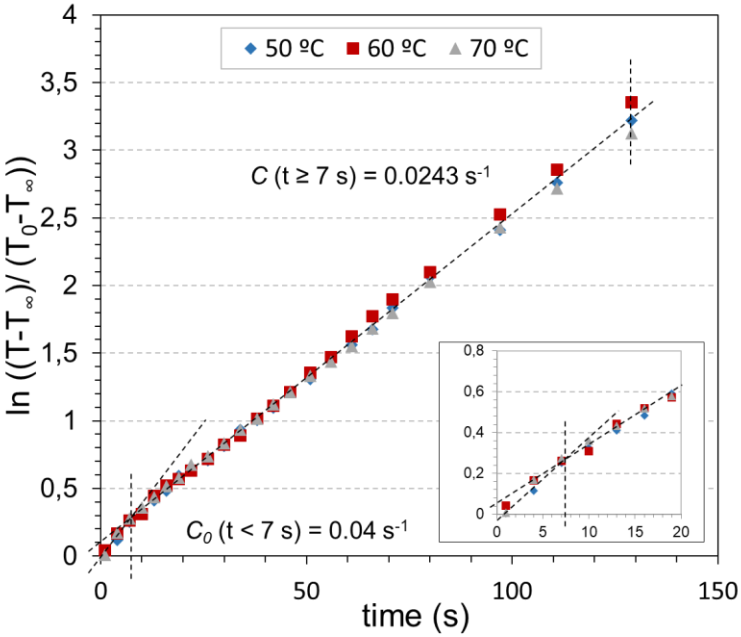

Figure III-15. Curve fitting and determination of the constant *C* for each section of the temperature profile.

$$ln\left(\frac{T-T_\infty}{T_0-T_\infty}\right) = -\frac{h\cdot A}{m\cdot C_p}\cdot t = -C_0\cdot t \qquad \text{(III-19)}$$

$$ln\left(\frac{T-T_\infty}{T_0-T_\infty}\right) = -\frac{h\cdot A}{m\cdot C_p}\cdot t = -C\cdot (t-7) \qquad \text{(III-20)}$$

Finally, in order to validate the assumption that temperature is uniform throughout the thickness of the sample, *Bi* should be less than 0.1. The coefficient of convection *h* was calculated from constant *C* by using values typical for epoxy systems[35]. The result was h = 28.4 W/m^2·K, so by applying the equation (III-18), *Bi* ≈ 0.1. Therefore, the error committed by assuming uniform temperature is minimal and fairly acceptable.

Effect of shape-memory cycling on stability

Once the temperature profile had been defined, experiments consisting of 10 consecutive cycles (programming the U-shape and recovering the original shape each time) were performed following the experimental setup shown in Figure III-12 and Figure III-13. In the programming process, two different T_{prog} were chosen, the $T_g^{E'}$ (shown to

be the optimal mechanical point in our previous study[21] and other studes[17-18]) and the T_g. For the shape-recovery process, T_{iso} was chosen to be equal to T_g. Because the same reference temperatures were used for each sample (in terms of the thermomechanical properties and network relaxation behaviour), the results were meaningful. The curves obtained are shown in Figure III-16 and Figure III-17, which also show the corresponding temperature profile. In addition, various parameters of interest are highlighted in the curves in Figure III-16(a) and summarized in Table III-5: the temperature at which the shape-recovery process starts (stipulated as the onset point of the decrease in shape recovery) (T_{onset}), the shape-recovery time t_{sr}, and the temperature range corresponding to the shape-recovery time (ΔT_{sr}) obtained using the sample temperature profile.

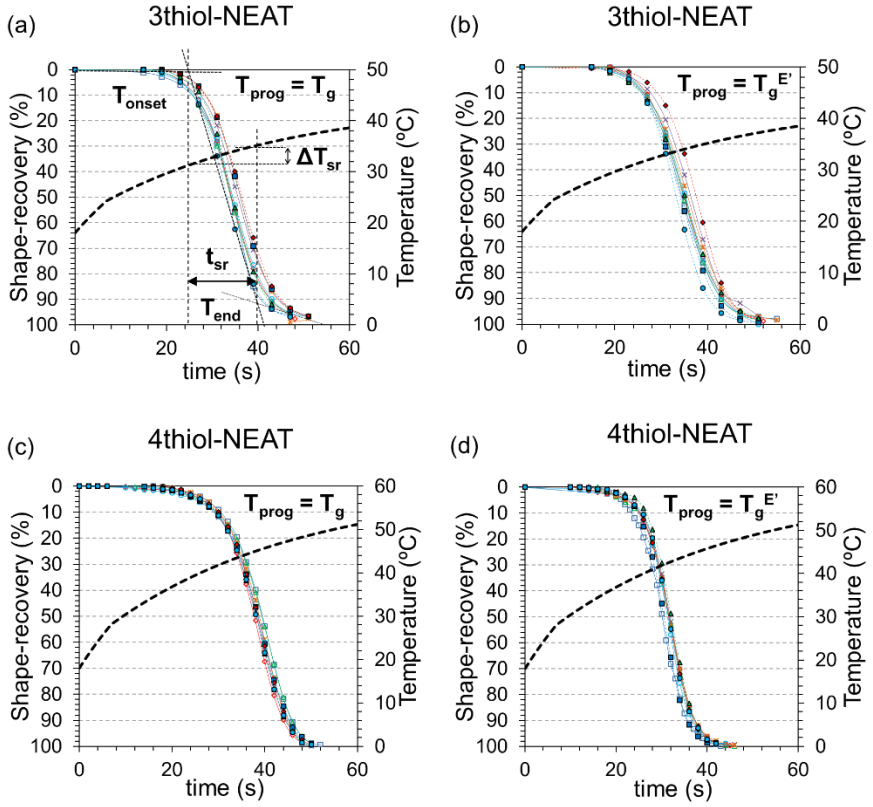

Figure III-16. % Of shape recovery and the corresponding temperature profile (in discontinuous lines) as a function of the time over 10 consecutive cycles; (a, b) 3thiol-NEAT programmed at $T_{prog} = T_g$ and $T_g^{E'}$; (c, d) 4thiol-NEAT programmed at $T_{prog} = T_g$ and $T_g^{E'}$. In all experiments, $T_{iso} = T_g$.

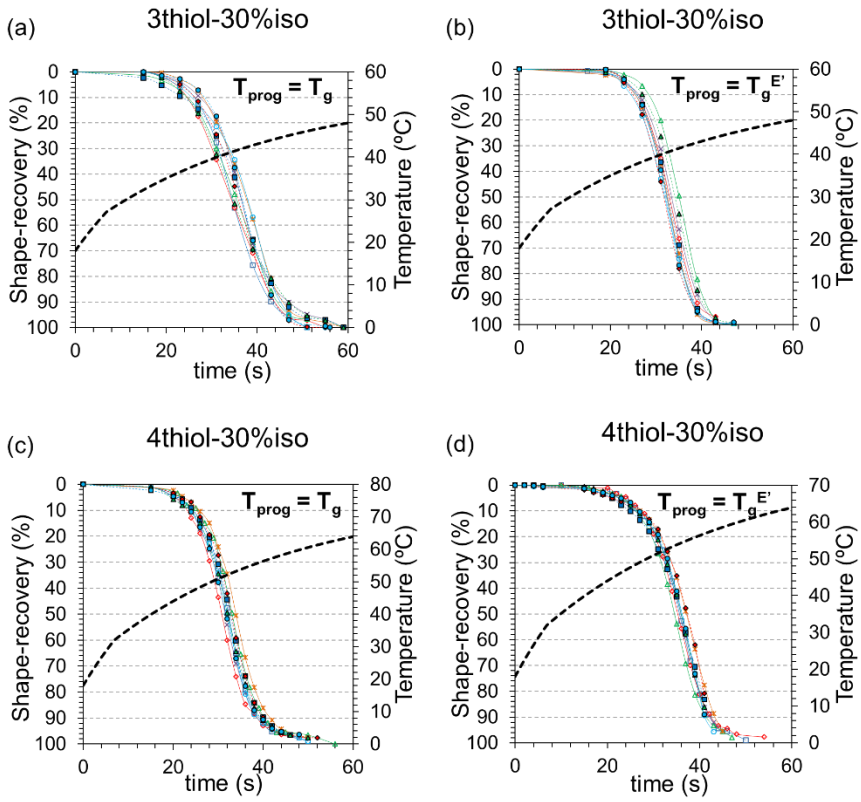

Figure III-17. % Of shape recovery and the corresponding temperature profile (in discontinuous lines) as a function of the time over 10 consecutive cycles; (a, b) 3thiol-30%iso programmed at $T_{prog} = T_g$ and $T_g^{E'}$; (c, d) 4thiol-30%iso programmed at $T_{prog} = T_g$ and $T_g^{E'}$. In all experiments, $T_{iso} = T_g$.

Table III-5. Mean value and its deviation of the shape-recovery parameters for all the formulations studied.

	T_{onset} (°C)		ΔT_{sr} (°C)		t_{sr} (s)	
Formulation	$T_{prog} = T_g$	$T_{prog} = T_g^{E'}$	$T_{prog} = T_g$	$T_{prog} = T_g^{E'}$	$T_{prog} = T_g$	$T_{prog} = T_g^{E'}$
3thiol-NEAT	32 ± 0.9	32 ± 1.1	3.0 ± 0.2	3.4 ± 0.2	12.0 ± 0.8	14.0 ± 0.9
3thiol-30%iso	38 ± 1.0	38 ± 1.0	5.9 ± 0.3	5.6 ± 0.1	19.0 ± 1.1	15.0 ± 0.4
4thiol-NEAT	42 ± 0.4	40 ± 0.4	5.0 ± 0.1	4.6 ± 0.1	14.3 ± 0.4	11.0 ± 0.4
4thiol-30%iso	48 ± 0.7	50 ± 0.7	6.1 ± 0.1	6.7 ± 0.1	11.0 ± 0.3	13.0 ± 0.4

Figure III-16 and Figure III-17 clearly show that the shape-recovery process starts before the temperature of the sample stabilizes, so it is not isothermal. The temperature of the sample takes at least 2 minutes to stabilize, when the shape-recovery has already finished. This drawback is common when testing at isothermal-recovery temperatures near or above T_g. Pandini et al.[33] observed the same phenomenon with epoxy-amine

based SMPs, and stated that only the samples tested at $T_{iso} < (T_g - 15\ °C)$ proceed isothermally. Nevertheless, very few studies have taken into account the real temperature of the sample when analysing isothermal-recovery experiments. The temperature profile can be used to analyse the different stages during the shape-recovery process and determine the real temperature of the sample at which the shape-recovery process starts T_{onset} (see Figure III-16(a)). As can be seen in Table III-5, T_{onset} increases as T_g increases (see Table III-4 from 3thiol-NEAT to 4thiol-30%iso), and does not vary with T_{prog} (± 2 °C with no defined trend among the different formulations). It can also be seen that T_{onset} is within the temperature range of the onset of network relaxation ΔT_{net} (see Table III-4), thus suggesting that this onset triggers the shape-recovery process. Shape-recovery takes place in the temperature interval ΔT_{sr}, and it can be seen that it is completed below T_g ($T_{onset} + \Delta T_{sr} < T_g$). It must be remembered that the nominal value of T_g determined in this study corresponds to the tanδ peak temperature, which is frequency dependent. The network relaxation process obviously starts before this temperature is reached. In overall terms, the shape-recovery curves can be divided into two different stages. At the beginning, when the sample is placed in the oven, the process is very slow because the sample temperature is well below the T_g during this initial period. Once the sample has reached T_{onset} and network relaxation starts to take place, the curves show an exponential decay of relaxation processes[36-37], further enhanced by the progressive temperature increase.

All the samples fully recovered their original shape through the cycling procedure and there was no loss of temporary shape after each cycle. The shape-fixation and shape-recovery performances were excellent regardless of T_{prog}, and stable over the 10 consecutive cycles. It should be pointed out that no differences were appreciated between the first cycle and the second cycle, thus suggesting that the network structure created after the curing process is stable from a mechanical and energy point of view, that no training procedure[38] (thermomechanical accommodation) was necessary, and that no plastic and irreversible rearrangements within the network occur after the first cycle. On the other hand, focusing on the shape-recovery process, the t_{sr} ranges from 11 to 19 seconds and shows great stability over the 10 consecutive cycles (± 1.1 s in the worst case) irrespective of T_{prog}. The differences between programming at T_g or $T_g^{E'}$ do not follow any specific trend, and no cracking of the sample was observed. This high thermomechanical stability is provided by the excellent stability of the epoxy-based materials[39]. As can be seen in Figure III-16, the differences caused by the curing agent are

almost negligible, so crosslinking points with different functionalities have little impact on stability. Likewise, introducing isocyanurate into the system (Figure III-17) is also negligible in terms of stability. These results reveal the good shape-memory response of these materials, which adds to the advantages of developing SMPs by thiol-epoxy "click" chemistry. Taking into account these results and the excellent mechanical properties of the materials (high ultimate stress and strain observed in our previous study[21]), these materials seem to be excellent candidates for actuator devices.

Effect of the isothermal-recovery temperature on the shape-recovery process

The effect of the isothermal-recovery temperature T_{iso} on the shape-recovery process was analysed using the same experimental setup as in the previous section. Various T_{iso}, ranging from (T_g-10 to T_g+20), were chosen to further analyse the effect of the network relaxation dynamics on the shape-recovery process. For all the experiments, given the results obtained in the previous section, T_{prog} was chosen as the optimal mechanical point ($T_g^{E'}$). All the experiments were performed three times, and the average value is presented. The curves obtained are shown in Figure III-18. Taking into account that the experiments proceed non-isothermally, besides the parameters in the previous section, the times for the onset and end points (t_{onset} and t_{end}, respectively) and the temperature associated to the end point (T_{end}) were determined to properly analyse each stage of the process. All these parameters are summarized in Table III-6 or represented in Figure III-19 with respect to T_{iso}.

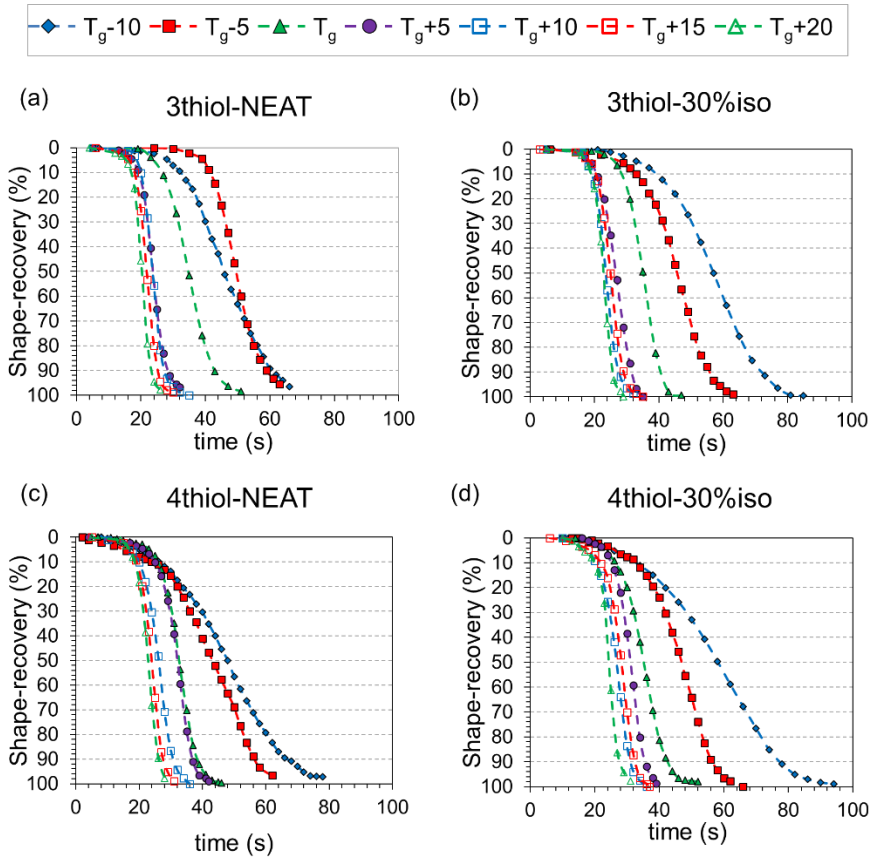

Figure III-18. Shape-recovery curves for all the formulations at different T_{iso} (from T_g – 10 to T_g + 20). All the samples were programmed at $T_g^{E'}$.

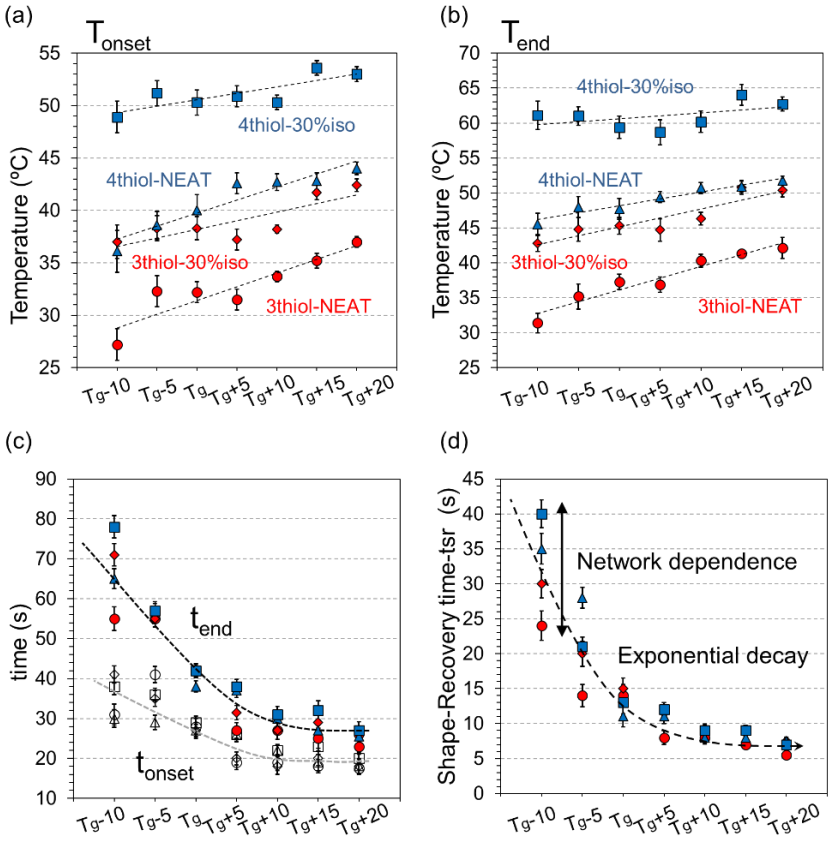

Figure III-19. (a) Temperature corresponding to the onset point; (b) temperature corresponding to the end point; (c) times corresponding to the onset and end points; (d) shape-recovery time (t_{sr}). All data is shown including the standard deviation.

Table III-6. Average value of the parameters of interest determined at different T_{iso} for all the formulations of study: the time corresponding to the onset point, t_{onset}, the temperature range for the shape-recovery, ΔT_{sr}, and the shape-recovery time, t_{sr}. Maximum standard deviation of ± 2 °C in T_{onset} and T_{end}, ± 3 seconds in t_{sr}, ± 0,8 °C in ΔT_{sr} and ± 3 seconds in t_{onset}.

	3thiol-NEAT			**3thiol-30%iso**			**4thiol-NEAT**			**4thiol-30%iso**		
	t_{onset} (s)	ΔT_{sr} (°C)	t_{sr} (s)	t_{onset} (s)	ΔT_{sr} (°C)	t_{sr} (s)	t_{onset} (s)	ΔT_{sr} (°C)	t_{sr} (s)	t_{onset} (s)	ΔT_{sr} (°C)	t_{sr} (s)
T_g-10	31	4.2	24.0	41	5.8	30.0	30	9.4	35.0	38	12.2	40.0
T_g-5	41	2.9	14.0	35	6.5	20.0	29	9.4	28.0	36	9.8	21.0
T_g	28	5.1	14.0	27	7.0	15.0	27	7.7	11.0	29	9.1	13.0
T_g+5	19	5.4	8.0	20	7.5	11.5	26	6.8	11.0	26	7.8	12.0
T_g+10	19	6.6	8.0	18	8.1	9.0	22	8.0	8.0	22	9.9	9.0
T_g+15	18	6.1	7.0	20	9.1	9.0	19	8.1	8.0	23	10.4	9.0
T_g+20	17	5.1	5.5	18	8.0	7.5	18	7.8	7.5	20	9.7	7.0

In general, regardless of T_{iso}, all the curves go through two different stages as discussed above: the initial, slow stage until T_{onset} is reached followed by the typical exponential decay of the relaxation processes. The time for this initial stage t_{onset} decreases as T_{iso} increases (see Table III-6, t_{onset} decreases by 23 s in the case of 3thiol-30%iso from T_g-10 to T_g+20) because the temperature increases more quickly when the sample is placed in the oven preheated to a higher temperature. As a consequence of this quick increase in the sample temperature in the early stage, T_{onset} is also slightly displaced to higher temperatures as T_{iso} increases in a linear fashion (see Figure III-19(a), the increase is maximum for the 3thiol-NEAT formulation, from 26 to 37 °C). Nevertheless, it should be pointed out that in all cases, these temperatures are within the temperature range given by ΔT_{net}, so the shape-recovery process takes place because the network relaxation is activated. The shape-recovery time, t_{sr}, naturally decreases due to the enhancement of the network relaxation dynamics as T_{iso} increases[40], which leads to a faster temperature increase in the sample taking place below and during the glass transition process. This phenomenon can be observed in Figure III-19(d), where t_{sr} decreases as T_{iso} increases and decays exponentially (as expected from the shape-recovery curves). In contrast, as can be seen in Table III-6, the temperature range in which recovery takes place, ΔT_{sr}, does not show any specific trend. As is observed in Figure III-19(b), the trend in the temperature T_{end} (which corresponds to $T_{onset} + \Delta T_{sr}$) is very similar to that of T_{onset} (Figure III-19(a)): it slightly increases as T_{iso} increases, but is still below T_g. It should be pointed out that all the materials complete the shape-recovery process at $T_{iso} < T_g$. However, it must be remembered that the nominal value of T_g corresponding to the tanδ peak temperature is frequency-dependent and is only taken as a reference: it does not mean that network relaxation cannot take place below this temperature; it is just a question of time. To sum up, an increase in T_{iso} produces a faster temperature increase in the samples, leading to faster network relaxation and recovery and a shift in the shape-recovery curve to higher temperatures. However, this takes place in narrow temperature ranges.

Differences in the shape-recovery time in the various formulations (see Figure III-19(d)) are negligible at $T_{iso} >> T_g$ because the fast temperature increase taking place before and during the glass transition process leads to very fast relaxation dynamics in all cases. In contrast at $T_{iso} < T_g$, the fast temperature increase (mostly taking place in the formulations with the highest T_g) happens well-below the glass transition and therefore has a minor role, whereas the differences due to the network structure are considerable. The formulations with 3thiol show

lower values of t_{sr} than those with 4thiol. This may be caused by the higher functionality of the 4thiol which leads to a more hindered spatial structure and more difficult relaxation, while the 3thiol crosslinker leads to a less packed structure with higher free volume, thus, accelerating the network relaxation process[33]. As a result, the t_{sr} differences increase to 16 s from 3thiol-NEAT to 4thiol-30%iso formulations. In terms of tuning the shape-recovery process, differences in shape-recovery time between the formulations are maximized by working at $T_{iso} < T_g$. Recovery is fast in all cases at $T_{iso} > T_g$ for all the formulations, so the difference comes from the different network structure which leads to different transition temperatures. The materials studied here are promising not only because they ensure that shape recovery can be completed at low temperatures (i.e. if a slow ending is desired), but also because of their tuneable network structure properties and shape-recovery behaviour.

4. Conclusions

Shape-memory polymers based on "thiol-epoxy" networks with tailorable glass transition and crosslinking density have been developed by "click" chemistry and using latent initiators (encapsulated imidazoles). These materials have homogeneous network structures and narrow relaxation processes, a significant advantage in terms of shape-recovery behaviour.

The results of the shape-memory cycling of the samples revealed a highly stable thermomechanical and shape-recovery time for all the materials regardless of the programming temperature ($T_g^{E'}$ or T_g), which suggests that the mechanical response can be optimized (by programming at $T_g^{E'}$) while high stability can be maintained for applications involving repetitive use of an actuator.

Shape recovery could not be activated under strictly isothermal conditions because the time the sample took to reach the isothermal-recovery temperature T_{iso} inside the oven was much longer than the time taken to complete the shape recovery. The shape-recovery process takes place in two well-defined stages: initially, when the sample temperature is still low, the temporary shape remains stable, but when the sample temperature increases and network relaxation is activated, shape recovery takes place very fast and follows the typical exponential decay of the relaxation processes until completion. The shape-recovery process is accelerated but shifted to slightly higher temperatures when the isothermal-recovery temperature T_{iso} was increased due to the faster and higher increase in the sample temperature, leading to faster relaxation dynamics. At isothermal-recovery temperatures T_{iso} well above the T_g of

the samples, the effect of the temperature on the shape-recovery time was negligible. The effect of the different network structures of the materials was found to be greater when recovering at $T_{iso} < T_g$. Formulations with higher crosslinking densities and more hindered network structures have slower shape-recovery rates due to slower relaxation dynamics at low temperatures. These results suggest that the shape-recovery process can be controlled by changing the network structure and working at $T_{iso} < T_g$ to maximize the effect of the structure and/or by increasing T_{iso} to minimize the effect but increase the shape-recovery rate.

Acknowledgements

The authors would like to thank MINECO (MAT2014-53706-C03-01 and MAT2014-53706-C03-02) and Generalitat de Catalunya (2014-SGR-67) for financial support.

References

[1] Hager, M.D., Bode, S., Weber, C., Schubert, U.S.: Shape memory polymers: Past, present and future developments. Prog. Polym. Sci. 49-50, 3–33 (2015).

[2] Scalet, G., Auricchio, F., Bonetti, E., Castellani, L., Ferri, D., Pachera, M., Scavello, F.: An experimental, theoretical and numerical investigation of shape memory polymers. Int. J. Plast. 67, 127–147 (2015).

[3] Zhao, Q., Qi, H.J., Xie, T.: Recent progress in shape memory polymer: New behavior, enabling materials, and mechanistic understanding. Prog. Polym. Sci. 49-50, 1–42 (2015).

[4] Lendlein, A., Sauter, T.: Shape-memory effect in polymers. Macromol. Chem. Phys. 214, 1175–1177 (2013).

[5] Sun, L., Huang, W.M., Ding, Z., Zhao, Y., Wang, C.C., Purnawali, H., Tang, C.: Stimulus-responsive shape memory materials: A review. Mater. Des. 33, 577–640 (2012).

[6] Leng, J., Yu, K., Sun, J., Liu, Y.: Deployable morphing structure based on shape memory polymer. Aircr. Eng. Aerosp. Technol. 87, 218–223 (2015).

[7] Song, J.J., Chang, H.H., Naguib, H.E.: Biocompatible shape memory polymer actuators with high force capabilities. Eur. Polym. J. 67, 186–198 (2015).

[8] Tandon, G.P., McClung, A.J., Bauer, J.W.: Shape-Memory Polymers for Aerospace Applications. DEStech Publications (2016).

[9] Arrieta, J.S., Diani, J., Gilormini, P.: Cyclic and monotonic testing of free and constrained recovery properties of a chemically crosslinked acrylate. J. Appl. Polym. Sci. 131, 9813-39820 (2014)(a).

[10] Arrieta, S., Diani, J., Gilormini, P.: Experimental characterization and thermoviscoelastic modeling of strain and stress recoveries of an amorphous polymer network. Mech. Mater. 68, 95–103 (2014)(b).

[11] Lakhera, N., Yakacki, C.M., Nguyen, T.D., Frick, C.P.: Partially constrained recovery of (meth)acrylate shape-memory polymer networks. J. Appl. Polym. Sci. 126, 72–82 (2012).

[12] Santiago, D., Fabregat-Sanjuan, A., Ferrando, F., De la Flor, S.: Recovery stress and work output in hyperbranched poly(ethyleneimine)-modified shape-memory epoxy polymers. J. Polym. Sci. Part B Polym. Phys. 54(10), 1002-1013 (2016).

[13] Santhosh Kumar, K.S., Biju, R., Reghunadhan Nair, C.P.: Progress in shape memory epoxy resins. React. Funct. Polym. 73, 421–430 (2013).

[14] Tandon, G.P., Gibson, T., Shumaker, J., Coomer, R., Baur, J., Justice, R.S.: Processing and characterization of novel bismaleimide-based shape memory polymer composites. ASME 2012 Conference on Smart Materials, Adaptive Structures and Intelligent Systems, SMASIS 2012. 1,19-25 (2012).

[15] Feldkamp, D.M., Rousseau, I. A.: Effect of Chemical Composition on the Deformability of Shape-Memory Epoxies. Macromol. Mater. Eng. 296, 1128–1141 (2011).

[16] Leonardi, A.B., Fasce, L. A., Zucchi, I. A., Hoppe, C.E., Soulé, E.R., Pérez, C.J., Williams, R.J.J.: Shape memory epoxies based on networks with chemical and physical crosslinks. Eur. Polym. J. 47, 362–369 (2011).

[17] Feldkamp, D.M., Rousseau, I. A.: Effect of the deformation temperature on the shape-memory behavior of epoxy networks. Macromol. Mater. Eng. 295, 726–734 (2010).

[18] Yakacki, C.M., Willis, S., Luders, C., Gall, K.: Deformation limits in shape-memory polymers. Adv. Eng. Mater. 10, 112–119 (2008)(b).

[19] Santiago, D., Fernández-Francos, X., Ferrando, F., De la Flor, S.: Shape-memory effect in hyperbranched poly(ethyleneimine)-modified epoxy thermosets. J. Polym. Sci. Part B Polym. Phys. 924–933 (2015).

[20] Fan, M., Yu, H., Li, X., Cheng, J., Zhang, J.: Thermomechanical and shape-memory properties of epoxy-based shape-memory polymer using diglycidyl ether of ethoxylated bisphenol-A. Smart Mater. Struct. 22, 055034 (2013).

[21] Belmonte, A., Guzmán, D., Fernández-Francos, X., De la Flor, S.: Effect of the Network Structure and Programming Temperature on the Shape-Memory Response of Thiol-Epoxy “Click” Systems. Polymers. 2146–2164 (2015).

[22] Binder, W.H., Sachsenhofer, R.: “Click” chemistry in polymer and materials science. Macromol. Rapid Commun. 28, 15–54 (2007).

[23] Carlborg, C.F., Vastesson, A., Liu, Y., Van Der Wijngaart, W., Johansson, M., Haraldsson, T.: Functional off-stoichiometry thiol-ene-epoxy thermosets featuring temporally controlled curing stages via an UV/UV dual cure process. J. Polym. Sci. Part A Polym. Chem. 52, 2604–2615 (2014).

[24] Flores, M., Tomuta, A.M., Fernández-Francos, X., Ramis, X., Sangermano, M., Serra, A.: A new two-stage curing system: Thiol-ene/epoxy homopolymerization using an allyl terminated hyperbranched polyester as reactive modifier. Polymer. 54, 5473–5481 (2013).

[25] Jin, K., Heath, W.H., Torkelson, J.M.: Kinetics of multifunctional thiol-epoxy click reactions studied by differential scanning calorimetry: Effects of catalysis and functionality. Polymer. 81, 70–78 (2015).

[26] Loureiro, R.M., Amarelo, T.C., Abuin, S.P., Soulé, E.R., Williams, R.J.J.: Kinetics of the epoxy–thiol click reaction initiated by a tertiary amine: Calorimetric study using monofunctional components. Thermochim. Acta. 616, 79–86 (2015).

[27] Brändle, A., Khan, A.: Thiol–epoxy “click” polymerization: efficient construction of reactive and functional polymers. Polym. Chem. 3, 3224 (2012).

[28] Guzmán, D., Ramis, X., Fernández-Francos, X., Serra, A.: New Catalysts For Diglycidyl Ether Of Bisphenol A Curing Based On Thiol-Epoxy Click Reaction. Eur. Polym. J. (2014).

[29] Berg, G.J., McBride, M.K., Wang, C., Bowman, C.N.: New directions in the chemistry of shape memory polymers. Polymer. 55, 1–24 (2014).

[30] Yakacki, C.M., Shandas, R., Safranski, D., Ortega, A.M., Sassaman, K., Gall, K.: Strong, tailored, biocompatible shape-memory polymer networks. Adv. Funct. Mater. 18, 2428–2435 (2008)(a).

[31] Yakacki, C.M., Shandas, R., Lanning, C., Rech, B., Eckstein, A., Gall, K.: Unconstrained recovery characterization of shape-memory polymer networks for cardiovascular applications. Biomaterials. 28, 2255–2263 (2007).

[32] Chen, X., Nguyen, T.D.: Influence of thermoviscoelastic properties and loading conditions on the recovery performance of shape memory polymers. Mech. Mater. 43, 127–138 (2011).

[33] Pandini, S., Bignotti, F., Baldi, F., Passera, S.: Network architecture and shape memory behavior of cold-worked epoxies. J. Intell. Mater. Syst. Struct. 24, 1583–1597 (2013).

[34] Rousseau, I. A., Xie, T.: Relationship between materials properties and shape memory behavior in epoxy-amine polymers. In: Materials Research Society Symposium Proceedings. pp. 31–36 (2009).

[35] Pascault, J.-P., Sautereau, H., J, V., R, W.J.J.: Thermosetting Polymers. CRC Press (2002).

[36] Diani, J., Gilormini, P., Frédy, C., Rousseau, I.: Predicting thermal shape memory of crosslinked polymer networks from linear viscoelasticity. Int. J. Solids Struct. 49, 793–799 (2012).

[37] Ge, Q., Yu, K., Ding, Y., Jerry Qi, H.: Prediction of temperature-dependent free recovery behaviors of amorphous shape memory polymers. Soft Matter. 8, 11098 (2012).

[38] Rousseau, I.A.: Challenges of shape memory polymers: A review of the progress toward overcoming SMP's limitations. Polym. Eng. Sci. 48, 2075–2089 (2008).

[39] Liu, Y., Han, C., Tan, H., Du, X.: Thermal, mechanical and shape memory properties of shape memory epoxy resin. Mater. Sci. Eng. A. 527, 2510–2514 (2010).

[40] Williams, M.L., Landel, R.F., Ferry, J.D.: The Temperature Dependence of Relaxation Mechanisms in Amorphous Polymers and Other Glass-forming Liquids. J. Am. Chem. Soc. 77, 3701–3707 (1955).

UNIVERSITAT ROVIRA I VIRGILI
DESIGN AND CHARACTERIZATION OF ACTIVELY-MOVING POLYMERS OBTAINED VIA DUAL-CURING PROCESSING
Alberto Francisco Belmonte Parra

III.4 New understanding of the shape-memory response in thiol-epoxy click systems: towards controlling the recovery process

Journal of Materials Science, **2017**, 52, 1625-1638

Alberto Belmonte[1], Xavier Fernández-Francos[2] and Silvia De la Flor[1]

1) Department of Mechanical Engineering. Universitat Rovira i Virgili, Campus Sescelades, Av. dels Països Catalans, 26, 43007 Tarragona, Spain.

2) Thermodynamics Laboratory, ETSEIB, Universitat Politècnica de Catalunya, Av. Diagonal 647, 08028 Barcelona, Spain.

UNIVERSITAT ROVIRA I VIRGILI
DESIGN AND CHARACTERIZATION OF ACTIVELY-MOVING POLYMERS OBTAINED VIA DUAL-CURING PROCESSING
Alberto Francisco Belmonte Parra

J. Mater. Sci. 2016, 52, 1625-1638

Abstract

Our research group has recently found excellent shape-memory response in "thiol-epoxy" thermosets obtained with click-chemistry. In this study, we use their well-designed, homogeneous and tailorable network structures to investigate parameters for better control of the shape-recovery process. We present a new methodology to analyse the shape-recovery process, enabling easy and efficient comparison of shape-memory experiments on the programming conditions. Shape-memory experiments at different programming conditions have been carried out to that end. Additionally, the programming process has been extensively analysed in uniaxial tensile experiments at different shape-memory testing temperatures. The results showed that the shape-memory response for a specific operational design can be optimized by choosing the correct programming conditions and accurately designing the network structure. When programming at a high temperature ($T >> T_g$), under high network mobility conditions, high shape-recovery ratios and homogeneous shape-recovery processes are obtained for the network structure and the programmed strain level (ε_D). However, considerably lower stress and strain levels can be achieved. Meanwhile, when programming at temperatures lower than T_g, considerably higher stress and strain levels are attained but under low network mobility conditions. The shape-recovery process heavily depends on both the network structure and ε_D. Network relaxation occurs during the loading stage, resulting in a noticeable decrease in the shape-recovery rate as ε_D increases. Moreover, at a certain level of strain, permanent and non-recoverable deformations may occur, impeding the completion and modifying the whole path of the shape-recovery process.

Keywords: thiol-epoxy; shape-memory polymer; click-chemistry; shape-recovery process; programming conditions.

1. Introduction

Shapes-memory polymers (SMPs) enclose materials capable of storing large strain energy upon external programming (in the form of a temporary shape), and recovering the original (or releasing the energy stored as mechanical work[1-7]) upon external stimulus (i.e. heat, magnetic field or light)[8-12]. The increasing demand for shape-memory materials for aerospace, structural applications, electronic devices and biomechanical applications (i.e. artificial muscles), has recently redirected the focus to the development of materials with large recoverable deformation limits, high levels of strength, the ability to perform mechanical work (work

output) and high resistance to aggressive environments. The easy processing and tailorability of the thermoset-based SMPs make them suitable materials for demanding applications. Specifically, epoxy-based systems are very important not only because of the excellent thermal, chemical and mechanical resistance of the epoxy resin, but mostly because of the great shape-memory capabilities: high stress and strain levels are achieved by properly varying the network structure and accurately choosing the shape-memory programming conditions. Moreover, excellent shape-fixation and shape-recovery performance is achieved by the drastic entropic change that takes place during the glass transition process of these thermosets[13].

In our previous works[14,15], we developed SMPs based on "click" thiol-epoxy thermosets, and found a promising response for demanding applications (i.e. complex actuators or bio-inspired artificial movements). These materials showed enhanced stress levels in comparison with other epoxy-based SMPs[16] as well as high strain levels. Moreover, it was possible to produce materials with homogeneous network relaxation dynamics, leading to very good shape-memory response. "Click" chemistry is a curing methodology based on the efficiency, versatility and selectivity of the reactions[17]. The thiol-epoxy "click" mechanism is interesting due to the formation of hydroxyl and thioether groups in a single step, which can be further transformed into other polymeric materials[18,19]. Tertiary amines are commonly used as base catalysts in thiol-epoxy formulations, but their high reactivity makes it difficult to control the reaction. Recently, the use of encapsulated latent imidazoles has been shown to significantly enhance the stability of the uncured mixture[20,21]. Upon heating, the catalyst is released and the reaction occurs rapidly, resulting in homogeneous and well-defined network structures. This enhances the mechanical properties (strength and deformability) of the shape-memory materials developed[22].

An important issue for the effective application of SMPs is to define suitable operational conditions in order to have a safe and reproducible control of the shape-recovery process. The shape-recovery and -fixation ratios (R_r and R_f) and the shape-recovery rate (V_r) are commonly used parameters for assessment of the shape-memory response. However, the information they provide on the dynamics of the shape-recovery process is limited. In certain applications, such as opening mechanisms for security systems, fast recovery is required once the shape-recovery process is triggered in order to avoid initial and compromising damage to the device, rather than a high R_r at the end. Other applications such as artificial muscles require a high R_r, but control of the whole shape-

recovery process is also necessary to properly define the artificial movements. Nevertheless, detailed modelling of the mechanical behaviour of polymers requires time-consuming procedures to give relatively accurate and convincing results that in addition, are limited to certain experimental conditions[9,23-25]. More efforts are therefore necessary in order to find methodologies that can easily produce relevant parameters and relationships useful for the specific control of the shape-recovery process.

In this study, we take advantage of the well-defined and tailorable network structures of the thiol-epoxy SMPs, in order to produce materials with different crosslinking densities and network hindrances. Thiol curing agents and epoxy resin monomers with different structures and functionalities were used. In order to investigate the potential capabilities of these shape-memory materials, the study has been divided into an initial analysis of the programming process by uniaxial tensile experiments at room temperature (the temperature at which the temporary shape is fixed) and at different programming temperatures, followed by the study of the shape-recovery process. The generic ratios R_r, R_f and V_r have been determined and related with stress-strain behaviour under different programming conditions. A new, simple and efficient methodology to analyse the shape-recovery process has also been presented. This methodology is based on a series of mathematical transformations of the original data, enabling comparison and analysis of experiments on various materials in terms of the programming conditions. Shape-memory experiments at different programming temperatures and programming strain levels have been carried out and analysed to that end. A more complete understanding of the role of the network structure and programming conditions in the control of the shape-memory response is anticipated, enabling accurate predictions of generic parameters such as R_f, R_r and V_r, as well as extensive control of the shape-recovery process. Furthermore, we aim to analyse optimal programming conditions for these promising thiol-epoxy materials in order to strengthen their shape-memory capabilities and broaden their range of application.

2. Experimental section

Materials

A commercial epoxy resin, Diglycidyl ether of bisphenol A (DGEBA, GY240, Huntsman, Everberg, Belgium), with a molecular weight per epoxy equivalent unit of 182 g/eq was used as the main epoxy resin. Pentaerythritol tetrakis(3-mercaptopropionate) (4thiol), with a molecular weight per thiol equivalent unit of 122.17 g/eq and trimethylolpropane

tris(3-mercaptopropionate) (3thiol), with a molecular weight per thiol equivalent unit of 132.85 g/eq were used separately as curing agents. In addition, a tris(2,3 epoxypropyl)isocyanurate (iso), with a molecular weight per epoxy equivalent unit of 99.09 g/eq was used as a modifier in a 30 wt.% proportion with respect to the total epoxy content (30:70 %wt. iso:DGEBA). The epoxy:thiol equivalent ratio was stoichiometric (1:1). The 3thiol, 4thiol and iso were purchased from Sigma-Aldrich, St. Louis, MO, USA). An encapsulated imidazole, 1-methylimidazole (LC80, AC Catalysts), was used as a latent initiator at 0.5 parts of catalyst per one hundred parts of epoxy resin (phr).

The formulations were prepared by manually stirring the components in a glass vial and carefully pouring the mixtures into an open Teflon mould. The curing process was carried out in an oven, at 120 °C for one hour, followed by one hour at 150 °C to allow the completion of the process. Scheme III-5 shows the expected network structure after polymerization in mixtures containing iso and 3thiol (the structure using 4thiol would lead to a new chain growing from the fourth arm and the lack of iso in the mixture would be replaced by DGEBA bodies). The crosslinking points and the presence of hydroxyl groups have been highlighted.

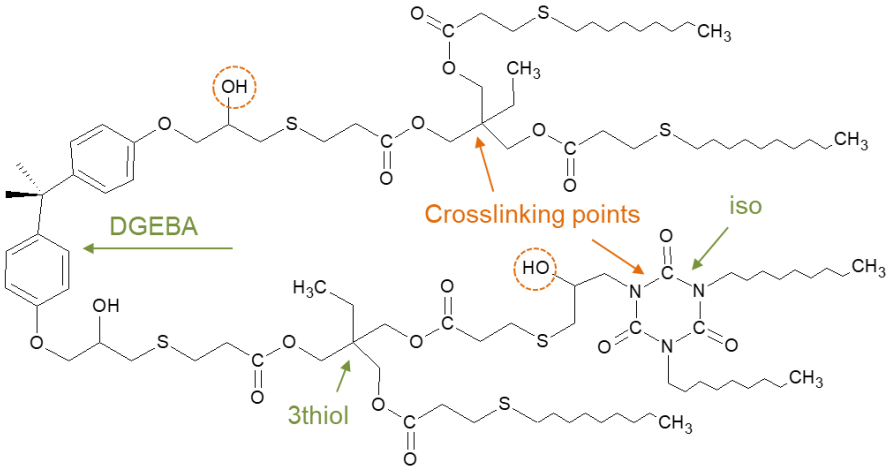

Scheme III-5. Expected network structure of the 3thiol-DGEBA-LC80 modified with the iso component.

The composition of the different formulations of study is shown in Table III-7.

Table III-7. Composition of the different formulations of study in weight percentage.

Formulation	DGEBA (wt.%)	Thiol (wt.%)	Iso (wt.%)	LC80 (wt.%)
3thiol-NEAT	57.64	42.07	0.00	0.29
3thiol-(30%)iso	36.49	47.61	15.64	0.26
4thiol-NEAT	59.66	40.04	0.00	0.30
4thiol-(30%)iso	37.95	45.52	16.26	0.27

Thermomechanical properties

The network structure and thermomechanical properties of the different materials were studied by dynamic-mechanical thermal analysis using a DMA Q800 (TA instrument, New Castle, DE, USA) equipped with a Single-Cantilever (10 mm) clamp. The samples were thoroughly polished to a prismatic rectangular shape (≈ 20 x 7.5 x 1.5 mm^3) and were analysed at 1 Hz with an oscillation amplitude of 10 µm at a heating rate of 3 °C/min. The T_g was determined by the peak of the tanδ curve, and the glassy modulus (E_g) and the rubbery modulus (E_r) were determined directly from the storage modulus curve (E). The $T_g^{E'}$ was determined as the onset point of the drop in modulus. The width of the tanδ curve at half-height (FWHM) and the tanδ peak were also determined.

The network strand density (v_e) in mol/kg was determined following a modification of the ideal theory of elasticity for elastomeric polymers at low strain rates shown in equation (III-21), defined by the equation (III-22), which takes into account the deviations due to the fluctuations of the functionality of the crosslinking points[26-30].

$$E_r = 3 \cdot R \cdot T \cdot v_e \quad \text{(III-21)}$$

$$v_e = \sum_{f \geq 3} \frac{f-2}{2} \cdot n_f \quad \text{(III-22)}$$

Where R is the universal gas constant, T is the temperature at which E_r is determined and n_f is the density of crosslinks with functionality f.

Shape-memory: thermomechanical programming characterization

The uniaxial tensile experiments were carried out at the different testing temperatures. The DMA Q800 equipped with a Tension-Film clamp was used to perform the experiments at $T_g^{E'}$, T_g and T_g+20 at a controlled-force rate of 3 N/min. Due to the force limitations of the DMA, an electromechanical universal testing machine (Hounsfield H 10k-S) with specially designed grips was used to perform the experiments at T_{room}. For the DMA experiments, the samples were thoroughly polished until a dog-

bone shape of 15 x 1.4 x 0.5 mm^3 (length x width x thickness) was obtained. For the experiments at room temperature, the size of the specimens was adapted from ASTMD638 requirements, adopting a Type IV dog-bone shape. All the experiments were performed at a crosshead speed of 1 mm/min.

From the σ-ε curves, the stress and strain at break values (σ_b and ε_b respectively) were determined as the failure point of the curves, and the mean value of at least three different samples were reported. The tensile elastic modulus (E_t) was determined as the slope of the curve at the initial and proportional part of the curve.

Shape-memory: response

The shape-memory response was analysed using the DMA Q800 equipped with a Tension-Film clamp in the controlled-force mode. The experiments were carried out as explained in our previous study[14]: first, the sample was heated up to the programming temperature (in accordance with the mechanical analysis, different T_{prog} were chosen: $T_g^{E'}$, T_g and T_g+20). After 5 minutes of temperature stabilization, the sample was loaded at 3 N/min using a controlled-force ramp until a strain level ε_D equal to 75% of ε_b was reached (some additional experiments were carried out at ε_D = 15, 30 and 50% of ε_b when specified). At this point, the sample was rapidly cooled down to T_{room} while maintaining the force applied (the holding time at T_{prog} has been reduced to "0" in order to avoid creep processes affecting the shape-memory response[31]). The sample was then unloaded at the same force rate (3 N/min) and the temporary shape was fixed. Afterwards, a temperature ramp of 3 °C/min was imposed until the shape-recovery was completed. All the experiments were repeated three times to ensure reproducible results, and the mean value has been presented.

The shape-fixation and shape-recovery ratios were quantified using common expressions; see equations (III-23) and (III-24).

$$R_f = \left(\frac{\varepsilon_U}{\varepsilon_D}\right) \cdot 100 \qquad \text{(III-23)}$$

$$R_r = \left(\frac{\varepsilon_D - \varepsilon_P}{\varepsilon_D}\right) \cdot 100 \qquad \text{(III-24)}$$

Where R_f is the shape-fixation ratio, R_r is the shape-recovery ratio, ε_D is the programmed strain level (defined as a % of the strain at break, ε_b), ε_U is the remaining strain after unloading and ε_P is the permanent strain after the shape-recovery process takes place. It must be acknowledged that the time after programming and before the recovery-process begins,

is not taken into account. During this period of time, shape-recovery may take place slowly depending on the programming conditions[32]. In the present study the temperature ramp begins just after unloading, and there is indeed some time elapsed during heating before the recovery starts, but this time depends on the T_g of the material and would be also affected by the temperature increase. Therefore, in this study we have chosen to overestimate the shape-recovery ratio using equation (III-24), taking into consideration the overall process from ε_D to ε_P. The shape-recovery rate (V_r) was quantified from 15% to 85% of the shape-recovery process as a measure of the average shape-recovery speed; see equation (III-25).

$$V_r(\%/min) = \frac{\Delta\%_{SR}}{\Delta t_{\Delta\%SR}} \qquad \text{(III-25)}$$

Where *SR* refers to the shape-recovery curve normalized to ε_U. $\Delta\%_{SR}$ is the chosen shape-recovery range (in this case it is from 15% to 85%, that is, 70%), and $\Delta t_{\Delta\%SR}$ is the time elapsed from 15% to 85% of *SR*.

In order to analyse and compare the shape-recovery process in different formulations and experiments, the shape-recovery curves have been differentiated and normalized as illustrated in Figure III-20. These transformations allow us to properly compare different formulations in terms of the programming conditions. In Figure III-20(b), SR is the normalized shape-recovery curve (0 means no recovery, 1 means that the shape-recovery is completed). The curves were normalized to their ε_P, and thus 1 does not mean full-recovery of the original shape but the completion of the shape-recovery process. In Figure III-20(c), the shape-recovery speed is defined as ∂SR/∂T (%/°C) as a measure of the instantaneous recovery rate[33].

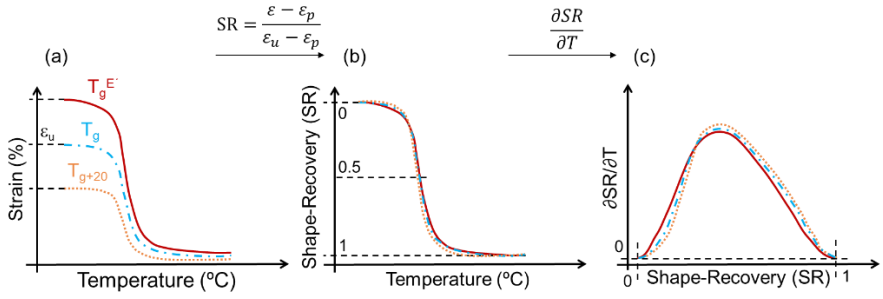

Figure III-20. Illustration of the mathematical transformation of the shape-recovery curves. "∂SR/∂T" is the derivative of the shape-recovery process over the temperature.

3. Results and discussion

Thermomechanical properties

The results of the thermo dynamic-mechanical analysis are shown in Figure III-21 and the parameters of interest are listed in Table III-8.

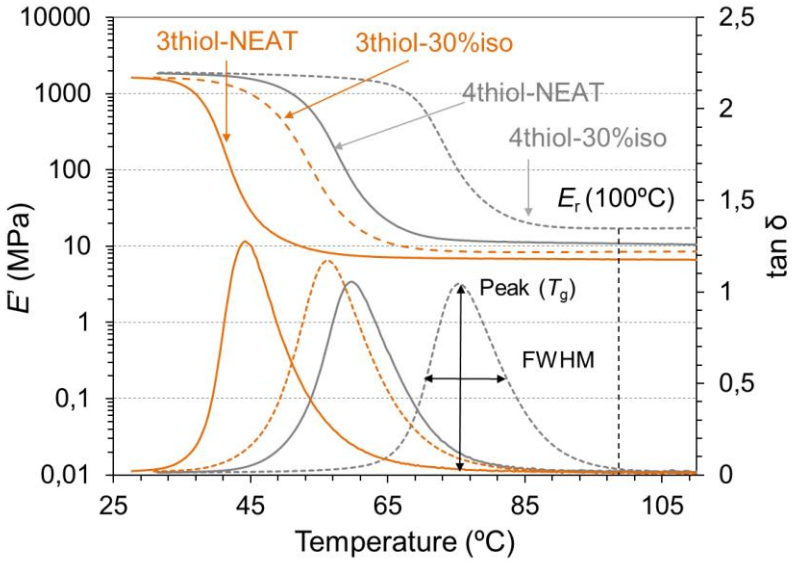

Figure III-21. Dynamic-mechanical thermal analysis of the different formulations of study. The relaxed modulus (E_r) determination has been highlighted.

Table III-8. Network structure and thermomechanical properties of the different formulations of study.

	3thiol-NEAT	3thiol-30%iso	4thiol-NEAT	4thiol-30%iso
T_g (°C)	44.1	56.2	59.7	75.4
$T_g^{E'}$(°C)	37.7	46.6	52.0	68.2
FWHM (°C)	10.3	12.5	12.0	11.8
tanδ peak	1.28	1.18	1.06	1.05
E_r (MPa)	6.7	8.5	10.8	17.0
v_e[a] (mol/kg)	0.530	0.8633	0.822	1.209

[a] Calculated using equation (III-22).

The results of the dynamic-mechanical thermal analysis were thoroughly discussed in our previous work[14]. By using curing agents with a different functionality but a similar structure (3thiol and 4thiol) and the mixture of rigid epoxy resins of different functionality and structure (DGEBA and iso), it was possible to obtain materials with a homogeneous and tailorable network structure (T_g values ranging from 44.1 °C to 75.4 °C and rubbery modulus ranging from 6.7 MPa to 17.0 MPa), as well as a narrow and steep relaxation process (low values of FWHM and high values

of tanδ peak). The increased functionality in the system leads to a higher crosslinking density and to the formation of more hindered network structures. Systems containing 4thiol instead of 3thiol therefore showed higher T_g and crosslinking density values (see T_g and ν_e in Table III-8). On the other hand, introducing the isocyanurate in the system increases the functionality, as well as incorporates different types of crosslinking points. The increase in the functionality leads as expected to higher values of T_g and crosslinking density, but the presence of crosslinks of different mass, size and rigidity leads to some incompatibilities when the amount of iso is too high (> 30%). This phenomenon is more relevant in the case of the 3thiol systems, probably as a result of the presence of an ethyl side chain in the 3thiol structure, which leads to a more heterogeneous and less packed network structure.

Shape-memory characterization

The data obtained from the uniaxial tensile experiments (σ-ε curves) at the different shape-memory testing temperatures is shown in Figure III-22: at room temperature T_{room} (the temperature at which the temporary shape is fixed), at $T_g^{E'}$, T_g and at T_g+20 (the programming temperatures). The stress and strain at break values achieved are summarized in Table III-9. For comparison purposes, the shape-recovery ratios, R_r, of the shape-memory experiments carried out at the corresponding programming temperatures and up to ε_D = 75 % are also shown in Table III-9.

First of all, as explained in our previous work[14], the optimal mechanical point was found at $T_g^{E'}$, in which both the stress and strain at break values where enhanced, a physical effect called viscoelastic toughening[34,35]. Moreover, the values obtained are higher than those reported by other authors with epoxy-based systems, especially for the stress at break (up to 55 MPa on the 3thiol-NEAT formulation with 95% of ε_b at $T_g^{E'}$)[36,37]. On analysing the σ-ε curves in Figure III-22(a), all the formulations were in the glassy state, so that the σ-ε response was similar and only the 3thiol-NEAT formulation differed. The tensile elastic modulus, E_t, is high in all the formulations (around 1 GPa) but the 3thiol-NEAT formulation shows higher ductility (up to 55.5% of strain at break). This is probably caused by the lower T_g-T_{room} difference and crosslinking density, which enhances the dynamics of the network structure. In terms of shape-memory response, the high elastic modulus and lower ductility of almost all the formulations at room temperature (greater resistance to stretching and hindered mobility of the chains) leads to high shape-fixation (R_f values were almost 100%) and shows that the material is able

to maintain the temporary shape for long periods of time, a useful characteristic for storage purposes, even under constant load (i.e. in certain applications such as security valves, where the temporary shape is constantly subject to a pressure until the shape-recovery is triggered).

Table III-9. Stress and strain at break values (σ_b and ε_b respectively), tensile elastic modulus (E_t) and the shape-recovery ratio (R_r) at the shape-memory testing temperatures (T_{room}, $T_g^{E'}$, T_g and T_g+20) of the different formulations of study programmed at ε_D = 75%. The mean value of three different samples tested is shown. Standard deviation of ± 0.2 on the stress and strain at break values, ± 30 MPa on the elastic modulus at T_{room}. ± 1% on the R_r.

	T_{room}			$T_g^{E'}$		
	σ_b (MPa)	ε_b (%)	E_t (MPa)	σ_b (MPa)	ε_b (%)	R_r (%)
3thiol-NEAT	21.0	55.5	1056	55.0	94.9	92.6
3thiol-(30%)iso	37.6	22.9	1248	46.4	73.1	82.9
4thiol-NEAT	35.7	17.6	1145	38.7	65.6	92.8
4thiol-(30%)iso	47.0	15.5	1353	28.8	50.3	88.7
	T_g			T_g+20		
	σ_b (MPa)	ε_b (%)	R_r (%)	σ_b (MPa)	ε_b (%)	R_r (%)
3thiol-NEAT	23.3	87.6	89.2	4.17	37.8	96.8
3thiol-(30%)iso	7.8	41.5	96.9	2.46	18.1	97.6
4thiol-NEAT	9.3	42.2	96.6	2.89	19.1	96.8
4thiol-(30%)iso	13.2	41.2	89.2	2.55	12.1	97.1

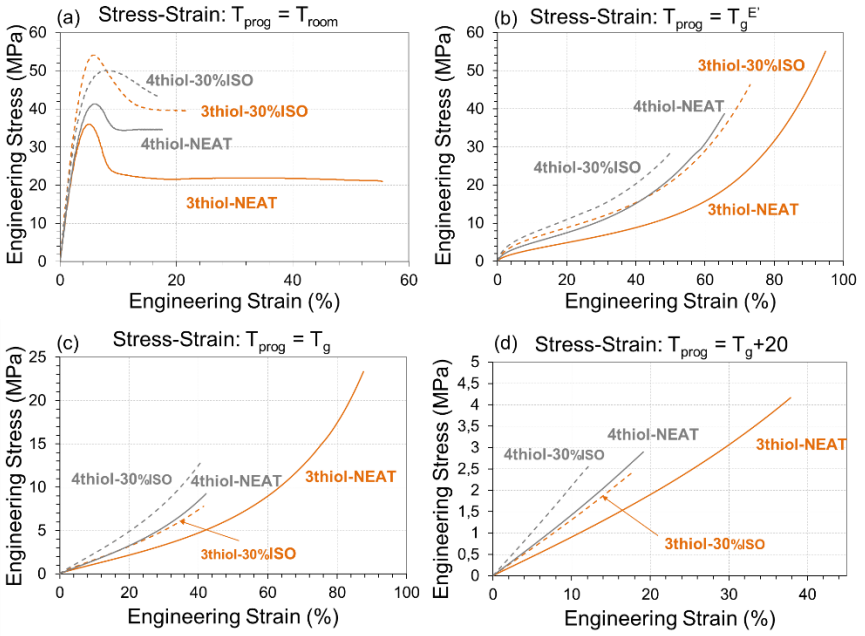

Figure III-22. Stress-strain curves for the different formulations of study at the shape-memory testing temperatures; (a) at room temperature; (b) at $T_g^{E'}$; (c) at T_g; (d) at T_g+20.

On analysing the σ-ε curves at the optimal mechanical point, $T_g^{E'}$ (see Figure III-22(b)), the stress and strain at break values are higher in the case of the 3thiol systems (up to 55 MPa and 95% respectively). The lower crosslinking density and enhanced mobility of the network chains in the 3thiol systems greatly improve the stress and strain at break values. However, from the change in slope at the beginning of these σ-ε curves, it can be deduced that stress relaxation occurs during this deformation process, because the characteristic relaxation time of the network structure is within and comparable to the time scale of the experiment. Consequently, significant energy losses take place due to viscous friction by network relaxation. Moreover, a strain hardening process is clearly observed at high strain levels in all the formulations studied (mostly in the 3thiol formulations), which may be indicative of damage in the material and a cause of permanent deformation in the network structure after programming the temporary shape. By contrast, on increasing the temperature to T_g+20 (see Figure III-22(d)), the network structure relaxation times are highly reduced, and the chains are thus able to quickly reach a stable equilibrium conformational state during loading, with little friction losses. As can be seen in Table III-9, the shape-recovery ratio, R_r, in free shape-recovery experiments of samples programmed at ε_D = 75%, considerably decreases when T_{prog} decreases from above to below the T_g (i.e. for 3thiol-30%iso, R_r falls from 97.6% at T_g*+20* to 82.9% at $T_g^{E'}$, and the same trend is apparent in all the formulations). This could be related to permanent deformation and network damage produced during the loading process at such high deformation levels (higher than the strain at break in the relaxed state), taking place at the same time as the strain hardening that is observed at higher strain levels (see Figure III-22(b)). In contrast, in those samples programmed at T_g+20, the network structure was already relaxed and therefore under equilibrium conditions during the loading process, leading to no energy losses. The lower strain levels achieved (no strain hardening observed, see Figure III-22(d)) might have also prevented permanent deformation.

Table III-10. Shape-recovery ratio (R_r) and shape-recovery rate (V_r) as a function of the programming temperature and strain level.

T_{prog}		$T_g^{E'}$				T_g	T_g+20
ε_D (%)		15%	30%	50%	75%[a]	75%[a]	75%[a]
3thiol-NEAT	R_r (%)	97.1	97.9	97.5	92.6	89.2	96.8
	V_r (%/min)	33.3	27.8	26.1	22.0	20.1	21.8
3thiol-30%iso	R_r (%)	96.8	97.5	94.7	83.7	96.9	97.6
	V_r (%/min)	29.2	26.9	24.3	18.9	19.8	26.0
4thiol-NEAT	R_r (%)	97.0	98.3	98.1	92.8	96.6	96.8
	V_r (%/min)	32.6	30.4	26.6	23.3	22.7	23.7
4thiol-30%iso	R_r (%)	96.5	95.9	94.0	88.7	92.4	97.1
	V_r (%/min)	25.3	23.5	22.3	20.3	21.0	21.8

[a] For comparison purposes, the R_r at ε_D = 75% have been also included in this table.

In order to clarify the role of T_{prog} and strain level on the shape-recovery performance, shape-memory experiments were carried out at $T_g^{E'}$, at the same loading rate (1 N/min), but at different programming strain levels (ε_D = 15, 30 and 50%). The thermomechanical cycles for all the experiments performed are presented in Figure III-23 in combined stress-time and strain-time graphs. In Figure III-24, the thermomechanical cycles performed at ε_D = 75% and different T_{prog} are also represented in combined stress-time and strain-time graphs. The shape-recovery ratios, R_r, and shape-recovery rates, V_r, obtained are presented in Table III-10 (the results obtained at ε_D = 75% have been also included for comparison purposes) and are shown in Figure III-25. As it can be seen, R_r is highly enhanced at low strain levels (almost constant and nearly 100%) while it suddenly decreases at a certain strain level in all the formulations studied. This means that the energy lost due to viscous friction during network relaxation plays a minor role in terms of maximum recoverable strain (R_r), and therefore the lower recovery ratio R_r is probably caused by the damaging processes and permanent deformation taking place during the loading process. The shape-recovery rate V_r of the samples programmed at $T_g^{E'}$ also follows a decreasing trend as ε_D increases, but this can be interpreted in terms of the network relaxation dynamics during the programming at different ε_D, resulting in materials with different states of network relaxation. In terms of strain recovery velocity, the velocity is higher with increasing strain, but the time required is longer; hence the decrease in the relative recovery rate V_r. The presence of isocyanurate in the network structure tends to decrease R_r and the recovery rate V_r of samples programmed at $T_g^{E'}$, in comparison with the neat formulations, at any ε_D, but especially at ε_D = 50% and above. This may be due to the presence of isocyanurate, leading to heterogeneities in the network structure resulting in earlier non-recoverable deformations during the loading stage. In addition, experiments at different ε_D were carried out at

T_g+20 and these confirmed that the R_r obtained were almost 100% because the strain levels were moderate and there was therefore no damage in the network structure. Likewise, the relative recovery rate V_r regarding ε_D remained almost constant. As explained above, at this temperature, the chains are able to reach a stable configuration during the loading stage, and similar states of network relaxation are therefore eventually achieved.

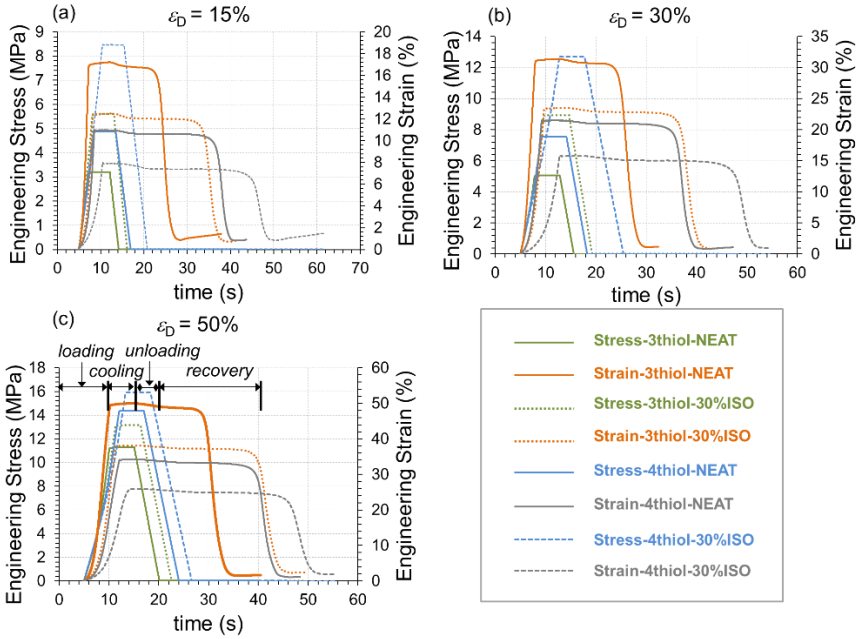

Figure III-23. Thermomechanical cycles for all the formulations of study programmed at $T_g^{E'}$ and at different strain levels (ε_D = 15, 30 and 50%).

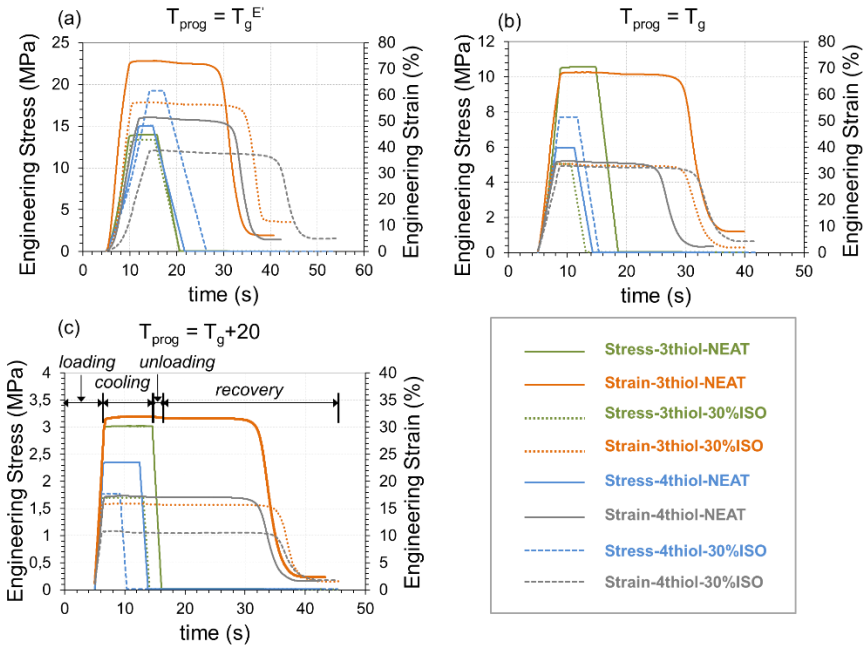

Figure III-24. Thermomechanical cycles for all the formulations of study programmed at ε_D = 75% and at programming temperatures ($T_g^{E'}$, T_g and T_g+20).

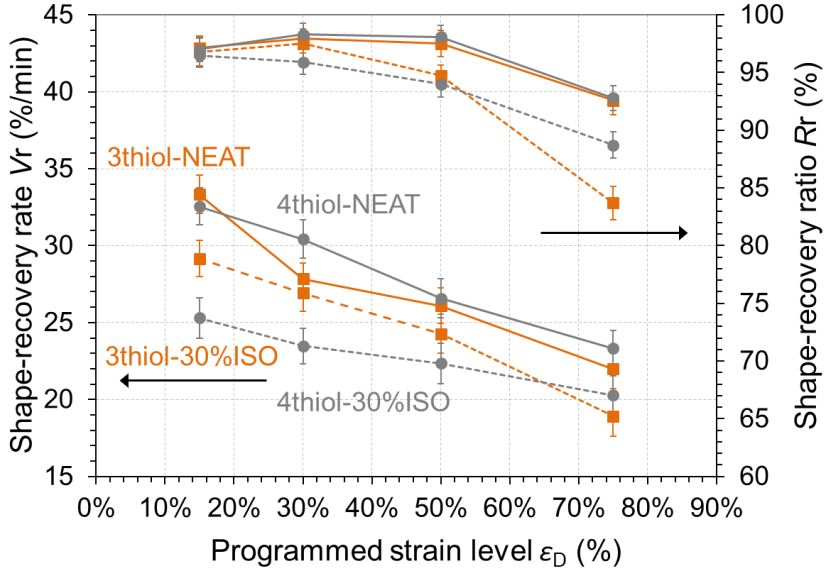

Figure III-25. Shape-recovery ratio (R_r) and shape-recovery rate (V_r) for all the formulations of study programmed at $T_g^{E'}$ and at different strain levels.

As explained in the introduction, generic parameters as the shape-recovery ratio or the shape-recovery rate are not sufficient to design

shape-memory materials for smart applications in which full control of the shape-recovery process is of high relevance. For this purpose, the shape-recovery process is analysed by means of the mathematical transformations of the original shape-recovery curves (as illustrated in Figure III-20), which enables comparison of experiments in terms of the programming conditions and formulations of study. First of all, the effect of T_{prog} at the same programmed strain level (ε_D = 75%) is shown in Figure III-26 for all the formulations of study.

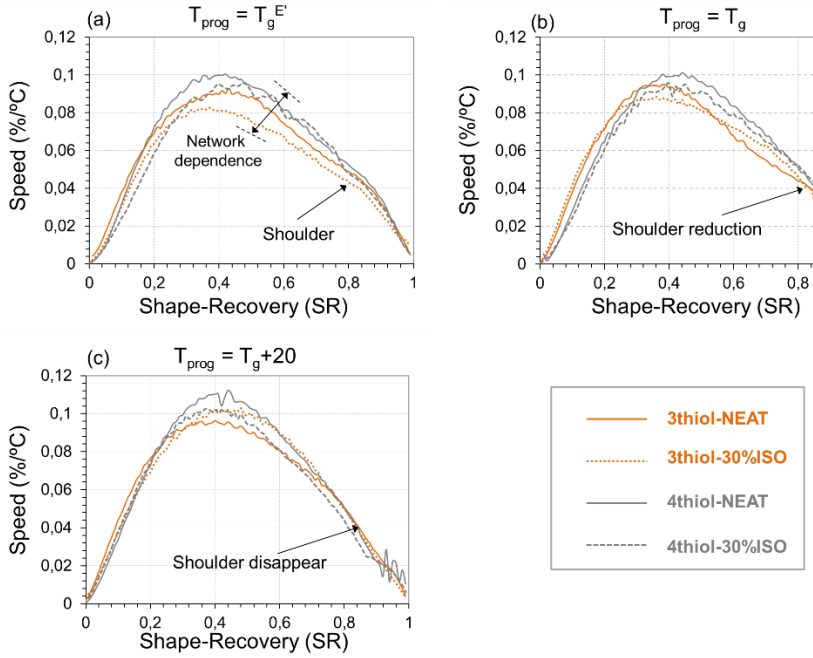

Figure III-26. Mathematical transformation of the shape-recovery curves (%/°C) for all the formulations of study at the different programming temperatures and fixed strain level (ε_D = 75%).

Characteristic bell-shaped curves are obtained in all cases, similar to that of the network relaxation process, but some relevant differences between the different formulations are found. The materials behave in a similar way when programming at T_g+20. At this temperature, the chains easily reach equilibrium during the loading stage, leading to a more stable stretched network architecture as explained above. In consequence, the differences due to the network structure during the shape-recovery process are minimized. However, when programming at $T_g^{E'}$ a noticeable shoulder is appreciated in the final stage of the shape-recovery process. This suggests that the shape-recovery process slows down at some point, but it finally accelerates as the temperature increases. As mentioned

above, programming at this temperature, and with such a high level of strain (ε_D = 75%), may cause some damage to the material, resulting in low shape-memory performance and, in addition, changing the network relaxation dynamics. When programming at higher temperatures, lower strain levels are achieved, and this leads to the progressive disappearance of this shoulder. Some differences are also observed between 3thiol and 4thiol formulations. In 3thiol formulations the onset of the shape-recovery process is accelerated when programming at T_g and $T_g^{E'}$ and the presence of this shoulder at the end is more evident. As explained previously, this may be due to the presence of a side ethyl chain in the 3thiol systems, which results in a less packed and unstable network structure after programming. This facilitates the beginning of the shape-recovery process[33]. However, differences vanish when programming at T_g+20, indicating that differences in network structure become irrelevant at higher temperatures, from a qualitative point of view.

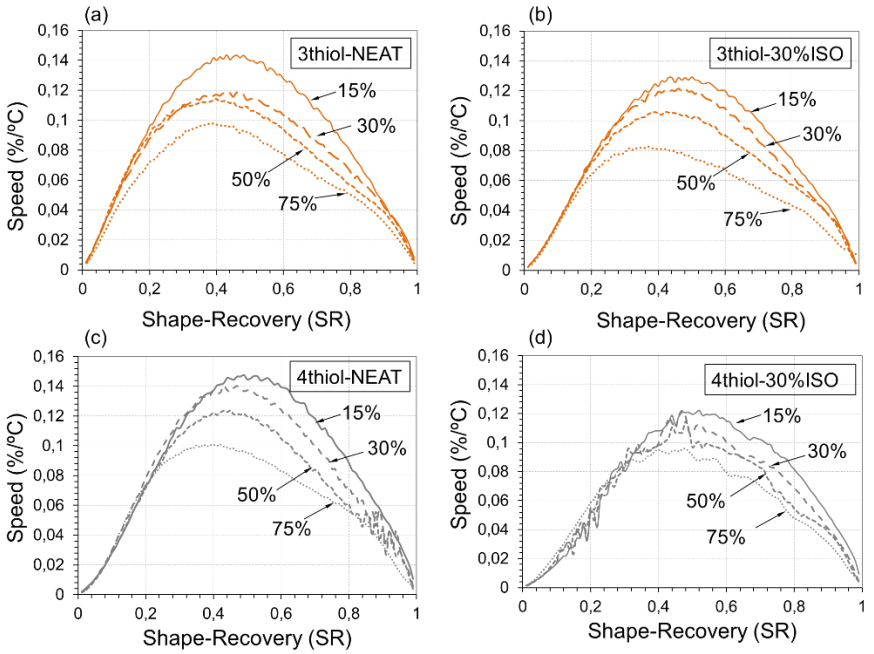

Figure III-27. Mathematical transformation of the shape-recovery curves (%/°C) for all the formulations programmed at $T_g^{E'}$ and at different strain levels (ε_D = 15, 30, 50 and 75%).

Using the same methodology, Figure III-27 shows the effect of ε_D on samples programmed at $T_g^{E'}$. It can be observed that the shoulder mentioned above appears at a certain level of strain, while the maximum speed (the peak of the curve) progressively decreases as the strain level ε_D increases. This suggests that the shoulder is mainly related with the

damage in the network structure caused by the strain hardening process at high levels of strain, while the decrease in the maximum speed (which eventually becomes in an overall lowering of the shape-recovery rate, see V_r in Table III-10) is mostly related to the increasing viscoelastic recovery time on increasing ε_D due to a change in the network relaxation dynamics.

These results suggest that it is possible to use the high stress levels reached when programming at $T_g^{E'}$, at a certain strain level (i.e. ε_D = 50%) with no relevant damage in the sample and excellent shape-memory performance: nearly 100% of R_r and equal or even higher V_r in comparison with that obtained when programming at T_g+20. For example, programming the 3thiol-NEAT formulation at 47.5% of strain (ε_D = 50%), leads to around 10 MPa of stress, being both the stress and strain programmed values higher than those reached at T_g+20 (in the 3thiol-NEAT formulation the strain and stress at break values are 37.8% and around 4 MPa respectively). This is of crucial importance for applications in which not only enhanced mechanical work is required, but also repeatability without damage is necessary (i.e. in actuators). In this respect, knowledge of the σ-ε programming curves of the shape-memory materials enables a more complete prediction of the shape-recovery process and its performance than when only using common ratios (R_r, R_f and V_r). Through well-designed network structures and properly chosen programming conditions, it is possible to tailor the shape-recovery process as desired: on increasing the programming temperature (or otherwise decreasing the loading rate to allow chains relaxation) the σ-ε curves become flatter, the network structure is able to completely relax the changes induced while the loading process is taking place, minimizing the energy lost due to viscous friction and therefore changes in the network relaxation dynamics, as well as avoiding permanent and non-recoverable deformations in the sample. This leads to high R_r values and more homogeneous shape-recovery processes, but low stress and strain levels are achieved. However, when working at low programming temperatures (in which network relaxation takes place during the loading stage), on increasing the strain level, the energy lost progressively increases due to viscous friction, and damage to the sample may occur, leading to non-recoverable strain (lowering the R_r) and modifying the overall path of the shape-recovery process. In conclusion, it is possible to efficiently optimize the programming conditions in order to adapt the operational design of the shape-memory material to the application requirements.

4. Conclusions

Materials with homogeneous and well-defined network structures were obtained by a thiol-epoxy "click" reaction catalysed by latent initiators. From the uniaxial tensile experiments at different T_{prog}, useful predictions of the shape-memory response are possible, not only in terms of common ratios (R_r and R_f) but also of the entire shape-recovery process. The σ-ε curves give us relevant information concerning different stages of the shape-memory response. The high elastic modulus of these materials at the shape-fixation temperature (T_{room}) highlights the good performance in fixing the temporary shape (R_f was almost 100%). From the initial change in the slope in the σ-ε curves at the optimal mechanical point ($T_g^{E'} < T_g$), it can be deduced that network relaxation takes place during the loading process, leading to a loss of energy due to viscous friction of the chains. Moreover, at the end of the curves, an increase in the slope shows hardening and therefore damaging processes, which may cause permanent and non-recoverable deformations. The shape-memory experiments show that the network relaxation during programming does not modify the shape-recovery ratio (the sample is able to fully recover its original shape) at moderate strain levels, but decreases the shape-recovery rate V_r. However, exceedingly high programming strain leads to damaging processes, and/or permanent deformations may take place, modifying the whole shape-recovery process and impeding the completion (i.e. low values of R_r). In contrast, when programming at higher temperatures ($T_{prog} >> T_g$), the curves are flatter and no changes in the slope are appreciated. The chains are able to completely reorganize the changes induced during the loading process, and therefore no network relaxation and energy losses take place. Because of the lower strain level, no permanent or non-recoverable deformation occurs, leading to R_r of nearly 100% and homogeneous shape-recovery process regardless of the strain level. In addition, the network structure has a minor role at this temperature and there are no differences between formulations. Nevertheless, the major drawback is the low stress and strain values achieved at this temperature, which may be overcome by well-designed network structure architectures and by an appropriate choice of programming conditions at lower programming temperatures.

Acknowledgements

The authors would like to thank MINECO (MAT2014-53706-C03-01 and MAT2014-53706-C03-02) and Generalitat de Catalunya (2014-SGR-67) for its financial support.

References

[1] Lewis CL, Meng Y, Anthamatten M (2015) Well-Defined Shape-Memory Networks with High Elastic Energy Capacity, Macromolecules. 48(14): 4918-4926.

[2] Wang A, Li G (2015) Stress memory of a thermoset shape memory polymer, J Appl Polym Sci. 132(24): 42112.

[3] Arrieta JS, Diani J, Gilormini P (2014) Cyclic and monotonic testing of free and constrained recovery properties of a chemically crosslinked acrylate, J Appl Polym Sci. 131 (2): 39813.

[4] Arrieta JS, Diani J, Gilormini P (2014) Experimental characterization and thermoviscoelastic modeling of strain and stress recoveries of an amorphous polymer network, Mech Mater. 68: 95-103.

[5] Anthamatten M, Roddecha S, Li J (2013) Energy storage capacity of shape-memory polymers, Macromolecules. 46:42304234.

[6] Yakacki CM, Shandas R, Safranski D, Ortega AM, Sassaman K, Gall K (2008) Strong, tailored, biocompatible shape-memory polymer networks, Adv Funct Mater. 18:2428-2435.

[7] Lakhera N, Yakacki CM, Nguyen TD, Frick CP (2012) Partially constrained recovery of (meth)acrylate shape-memory polymer networks, J Appl Polym Sci,126:72-82.

[8] Hager MD, Bode S, Weber C, Schubert US (2015) Shape memory polymers: Past, present and future developments, Prog Polym Sci, 49-50: 3-33.

[9] Scalet G, Auricchio F, Bonetti E, Castellani L, Ferri D, Pachera M, Scavello F (2015) An experimental, theoretical and numerical investigation of shape memory polymers, Int J Plasticity, 67:127-47.

[10] Lendlein A, Sauter T (2013) Shape-memory effect in polymers, Macromol Chem Phys, 214:1175-7.

[11] Anis A, Faiz S, Luqman M, Poulose AM, Gulrez SKH, Shaikh H, Al-Zahrani SM (2013) Developments in Shape Memory Polymeric Materials, Polym Plast Technol Eng. 52:1574-1589.

[12] Habault D, Zhang H, Zhao Y (2013) Light-triggered self-healing and shape-memory polymers, Chem Soc Rev. 42:7244-7256.

[13] Santhosh Kumar KS, Biju R, Reghunadhan Nair CP (2013) Progress in shape memory epoxy resins, React Funct Polym.73:421-30.

[14] Belmonte A, Guzmán D, Fernández-Francos X, De la Flor S (2015) Effect of the Network Structure and Programming Temperature on the Shape-Memory Response of Thiol-Epoxy " Click " Systems, Polymers. 7(10): 2146–64.

[15] Belmonte A, Fernández-Francos X, De la Flor S, Serra À (2016) Network structure dependence on unconstrained isothermal-recovery processes for shape-memory thiol-epoxy "click" systems, Mech Time Depend Mater. DOI 10.1007/s11043-016-9322-z.

[16] Feldkamp DM, Rousseau IA (2011) Effect of Chemical Composition on the Deformability of Shape-Memory Epoxies, Macromol Mater Eng. 296: 1128-1141.

[17] Binder WH, Sachsenhofer R (2007) "Click" chemistry in polymer and materials science, Macromol Rapid Commun. 28: 15-54.

[18] Carlborg CF, Vastesson A, Liu Y, Van Der Wijngaart W, Johansson M, Haraldsson T (2014) Functional off-stoichiometry thiol-ene-epoxy thermosets featuring temporally controlled curing stages via an UV/UV dual cure process, J Polym Sci Part A Polym Chem. 52:2 604-2615.

[19] Flores M, Tomuta AM, Fernández-Francos X, Ramis X, Sangermano M, Serra À (2013) A new two-stage curing system: Thiol-ene/epoxy homopolymerization using an allyl terminated hyperbranched polyester as reactive modifier, Polymer. 54: 5473-5481.

[20] Guzmán D, Ramis X, Fernández-Francos X, Serra À (2014) New Catalysts For Diglycidyl Ether Of Bisphenol A Curing Based On Thiol-Epoxy Click Reaction, Eur Polym J. 59: 377-396.

[21] Brändle A, Khan A (2012) Thiol-epoxy "click" polymerization: efficient construction of reactive and functional polymers, Polym Chem. 3: 3224- 3227.

[22] Berg GJ, McBride MK, Wang C, Bowman CN (2014) New directions in the chemistry of shape memory polymers, Polymer, 55:1-24.

[23] Xiao R, Guo J, Nguyen TD (2015) Modeling the multiple shape memory effect and temperature memory effect in amorphous polymers, RSC Adv. 5: 416-423.

[24] Barot G, Rao IJ (2006) Constitutive modeling of the mechanics associated with crystallizable shape memory polymers, Zeitschrift Fur Angew Math Und Phys. 57: 652-681.

[25] Diani J, Gilormini P, Frédy C, Rousseau IA (2012) Predicting thermal shape memory of crosslinked polymer networks from linear viscoelasticity, Int J Solids Struct. 49: 793-799.

[26] Graessley WW (1975) Statistical Mechanics of Random Coil Networks. Rubber, Chem Technol. 48: 1008-1017.

[27] Miller DR, Macosko CW (1976) A New Derivation of Postgel Properties of Network Polymers, Rubber Chem Technol. 49: 1219-1231.

[28] Charlesworth JM (1988) Effect of crosslink density on molecular relaxations in diepoxide-diamine network polymers. Part 2. The rubbery plateau region, Polym Eng Sci. 28: 230-236.

[29] Lesser A, Crawford E (1997) The role of network architecture on the glass transition temperature of epoxy resins, J Appl Polym Sci. 66: 387-395.

[30] Pascault JP, Sautereau H, Verdu J, Williams RJJ (2002) Thermosetting Polymers. 1st edn. CRC Press; New York

[31] Li G, Xu W (2011) Thermomechanical behavior of thermoset shape memory polymer programmed by cold-compression: Testing and constitutive modeling. J Mech Phys Solids 59:1231–50. doi:10.1016/j.jmps.2011.03.001.

[32] Li G, Wang A (2016) Cold, warm, and hot programming of shape memory polymers. J Polym Sci Part B Polym Phys 54: 1319–39. doi:10.1002/polb.24041.

[33] Pandini S, Bignotti F, Baldi F, Passera S. Network architecture and shape memory behavior of cold-worked epoxies. J Intell Mater Syst Struct 2013;24:1583–97. doi:10.1177/1045389X13478275.

[34] Feldkamp DM, Rousseau IA (2010) Effect of the deformation temperature on the shape-memory behavior of epoxy networks, Macromol Mater Eng. 295: 726-734.

[35] Yakacki CM, Willis S, Luders C, Gall K (2008) Deformation limits in shape-memory polymers, Adv Eng Mater. 10: 112-119.

[36] Leonardi AB, Fasce LA., Zucchi IA., Hoppe CE, Soulé ER, Pérez CJ, Williams JJ (2011) Shape memory epoxies based on networks with chemical and physical crosslinks, Eur Polym J. 47(3): 362-369.

[37] Santiago D, Fernández-Francos X, Ferrando F, De la Flor S (2015) Shape-memory effect in hyperbranched poly(ethyleneimine)-modified epoxy thermosets, J Polym Sci Part B Polym Phys. 53(13): 924-933.

Chapter IV

Shape-memory polymers based on dual-curing processing

IV

UNIVERSITAT ROVIRA I VIRGILI
DESIGN AND CHARACTERIZATION OF ACTIVELY-MOVING POLYMERS OBTAINED VIA DUAL-CURING PROCESSING
Alberto Francisco Belmonte Parra

IV.1 Introduction and scope

As introduced in chapter III new technologies require **intelligent materials** capable to adapt to aggressive environments. In many cases, the design of these materials demands **complex shapes**. For example, in aerospace, the pieces show curved shapes rather than edges. In bio-inspired mechanisms, including soft robotics, complex shapes are required from micro to macroscale.

The **"thiol-epoxy" click SMPs** have demonstrated precise control of the structural and thermomechanical properties. SMPs with homogeneous network structures, excellent mechanical and thermal properties, and enhanced shape-memory response have been obtained. Nevertheless, thermosets cannot be processed after polymerization, thus, the design of the initial shape must be approached during the curing process. The curing of thermosets is a complex process involving drastic changes in the physical response of the material that take place in tight time-temperature constraints, thus making difficult the development of complex-shaped designs. The straight approach is the use of complex moulding techniques that, in many cases, lead to inefficient results in terms of macroscopic structure (bubble formation) and curing kinetics control (inefficient dissipation of the heat released during the reaction).

An approach to overcome this limitation is the use of **B-stage curing techniques**. B-stage essentially consists on partially cure a resin (commonly known as pre-dried stage) to obtain an initial, solid-like and stable material that can serve as precursor of the final shape after fully curing the resin. The main advantage lies on the processing from solid-like materials instead of the initial liquid mixture. However, this technique is limited to one single polymerization process, thus, narrowing the properties design. Moreover, the control of phenomenon's, such as, gelation and vitrification are rather complex.

Recently, the concept of **dual-curing** has come out as an effective and versatile solution to enhance the **processing of thermosets**. As explained in section I.2, dual-curing processing is based on the combination of two polymerization processes that are compatible and can be triggered in a sequential way. The polymerization processes can be separated by different stimuli, reaction kinetics or the presence of latent catalysts. Our research group, with the work done by Guzmán et al.[1] combined "click" thiol-ene/thiol-epoxy reactions, thus, a UV-activated/thermally-activated sequential dual-curing process. Effective separation of both processes was achieved by using a photoinitiator for

the thiol-ene reaction and a latent amine precursor to activate the thiol-epoxy reaction at high temperature. Another example from our research group is the work done by Gustavo et al.[2] who prepared off-stoichiometric amine-acrylates systems with an excess of acrylates to combine a self-limiting aza-Michael addition between amines and acrylates groups and the further photoinduced radical polymerization of the remaining acrylates. The results showed the possibility to obtain, **from liquid-like to solid-like stable intermediate materials, to lightly or densely crosslinked final materials**.

Considering the above, the use of **"thiol-epoxy" click chemistry** in dual-curing processing is expected to add value in the development of AMPs. On the one side, the thiol-epoxy click reaction ensures the formation of enhanced SMPs, on the other side, the processing through dual-curing makes possible to achieve complex shaped designs. Our research group, with the work done by Fernández-Francos et al.[3] demonstrated the possibility to attain sequential dual-curing processing with **off-stoichiometric "thiol-epoxy" mixtures with an excess of epoxy groups**. The catalysis of this system with tertiary amines promotes the "thiol-epoxy" click reaction to take place at low temperature, while maintaining the epoxy homopolymerization latent. The further increase of the temperature leads to the formation of the epoxy homopolymer network with the remaining unreacted epoxy groups. Therefore, a sequential dual-curing processing separated by means of kinetics was achieved. Similar to the system presented by Gustavo et al.[2], this system makes possible to obtain intermediate and solid-like materials that can be processed into complex shape designs.

To the best of our knowledge, the use of **"thiol-epoxy" dual-curing systems** for the development of **AMPs** have not been investigated yet. The potential capabilities of these dual-curing systems and the possibility to control and enhance the AMPs through the variation of the "thiol" and "epoxy" compounds in an easy and efficient manner makes these systems attractive in many applications.

In this chapter, **we investigate the "thiol-epoxy" dual-curing systems from a processing point of view**. The evolution of the physical properties during both, the intermediate and final stages is studied by means of rheological and calorimetric analyses. The gelation and vitrification phenomena are detected and discussed. The processing of complex shapes is studied considering different mixtures and "thiol-epoxy" off-stoichiometric ratios. Qualitative and quantitative analyses of the wetting, deformability, colour, transparency and efficiency achieving

complex shape designs are performed. Finally, the thermomechanical and structural properties of both the intermediate and final materials are studied and presented considering the physical state (liquid-like or solid-like) as a tool to design accurate processing methods. The results and discussion of this study are presented in **section IV.2**.

Once the proposed "thiol-epoxy" dual-curing systems have been completely characterized, **SMPs with initial bent shapes are designed and characterized in "flat-to-bent" (flexural) recovery mode**. Flat shapes are programmed as explained in section II.7 and tested under unconstrained, partially-constrained and fully constrained conditions, to study their potential capabilities as smart mechanical actuators. The results and discussion of this study are presented in **section IV.3**.

References

[1] D. Guzmán, X. Ramis, X. Fernández-Francos, A. Serra, *Preparation of click thiol-ene/thiol-epoxy thermosets by controlled photo/thermal dual curing sequence*, RSC Adv. **2015**, 5, 101623–101633.

[2] G. González, X. Fernández-Francos, A. Serra, M. Sangermano, X. Ramis, *Environmentally-friendly processing of thermosets by two-stage sequential aza-Michael addition and free-radical polymerization of amine–acrylate mixtures*, Polym. Chem. **2015**, 6, 6987-6997.

[3] X. Fernández-Francos, A-O. Konuray, A. Belmonte, S. De la Flor, A. Serra, X. Ramis, *Sequential curing of off-stoichiometric thiol–epoxy thermosets with a custom-tailored structure*, **2016**, 7, 2280-2290.

IV.2 Phenomenological characterization of sequential dual-curing of off-stoichiometric "thiol-epoxy" systems: Towards applicability

Materials and Design, **2017**, 113, 116-127

Alberto Belmonte[1], Xavier Fernández-Francos[2], Àngels Serra[3] and Silvia De la Flor[1]

1) Department of Mechanical Engineering, Universitat Rovira i Virgili, Av. Països Catalans 26, 43007 Tarragona, Spain.

2) Thermodynamics Laboratory, ETSEIB, Universitat Politècnica de Catalunya, Av. Diagonal 647, 08028 Barcelona, Spain.

3) Department of Analytical and Organic Chemistry, Universitat Rovira i Virgili, C/Marcel·lí Domingo s/n, 43007 Tarragona, Spain.

UNIVERSITAT ROVIRA I VIRGILI
DESIGN AND CHARACTERIZATION OF ACTIVELY-MOVING POLYMERS OBTAINED VIA DUAL-CURING PROCESSING
Alberto Francisco Belmonte Parra

Mater. Des. 2017, 113, 116-127 **189**

Abstract

An extensive characterization of a sequential dual-curing system based on off-stoichiometric "thiol-epoxy" mixtures was carried out using thiol compounds of different functionality. The intermediate and final materials obtained after each curing stages at different thiol-epoxy ratios were studied by means of thermomechanical and rheological experiments. The storage and loss modulus and the loss factor tanδ were monitored during the curing process to analyse gelation and network structure build-up. The critical ratio for gelation was determined making use of the ideal Flory-Stockmayer theory and compared with experimental results. Intermediate materials obtained in the vicinity of the theoretical critical ratio did not have the mechanical consistency expected for partially crosslinked materials, did not retain their shape and even experienced undesired flow upon heating to activate the second curing reaction. The rheological results showed that the critical ratio is higher than the predicted value and that a softening during the second curing stage affects the shape-retention at this ratio. From the thermomechanical results, a wide range of intermediate and final materials with different properties and applicability can be obtained by properly choosing the thiol-epoxy ratio: from liquid-like to highly deformable intermediate materials and from moderately crosslinked (deformable) to highly crosslinked (brittle) final materials.

Keywords: dual-curing; thiol-epoxy; functional materials; rheological analysis; thermomechanical analysis

1. Introduction

Crosslinked polymeric materials (thermosets) are used in many application fields because of their excellent thermal and mechanical properties (i.e. aviation, automobile, structures or coatings)[1]. The possibility of forming network structures with tuneable properties and the presence of reversible network relaxation processes make them suitable materials for more demanding applications such as self-healing materials, optical devices or lithographic printing[2,3]. Nowadays, the increasing demand of smart materials with complex shape designs (i.e. aircraft pieces, bio-inspired devices or shape-changing materials[4]), has become a great challenge for thermosets because accurate control of the curing process is necessary to fit the complex processing[5]. The formation of crosslinked network structures is a non-reversible process involving drastic changes in polymer and network structure with tight time-temperature constraints that need to be carefully controlled in order to

produce components with required shapes and properties in complex processing scenarios. Recently, a new concept in crosslinking processes based on the sequential combination of two polymerization processes (dual-curing processing) has come out as an interesting and versatile approach for better controlling of the network structure build-up and properties during processing[6–8].

Dual-curing systems arise from the combination of two compatible and well-controlled polymerization processes taking place simultaneously[9,10] or sequentially[11]. Sequential dual-curing has the advantage of forming an intermediate and stable material after the first polymerization process which is further transformed into the final material after the second polymerization process. This is commonly achieved by combination of polymerization processes triggered by different stimuli, such as UV-light and heat, or else has sufficiently different reaction kinetics. Examples of such processes include photo-curing/thermal-curing click thiol-ene/thiol-epoxy systems[11], aza-Michael addition/free-radical polymerization of amine-acrylate systems[12] and both photo-curing thiol/ene/cationic systems[13].

Click reactions are based on efficiency, versatility and selectivity[14–16], a combination of features that makes them suitable for dual-curing processing[11]. In particular, “thiol-click” reactions are highly interesting because they can react at mild conditions producing radical or anionic species in a controlled and efficient manner by appropriately choosing the catalyst[17–19]. Among them, the thiol-epoxy click reaction, a step-wise reaction mechanism catalysed by tertiary amines, which consists essentially in the nucleophilic attack to the oxirane ring by the thiolate anion, produces functional soft materials with excellent mechanical properties (high resistance and elongation at break) that can be useful in a first-stage life as shape-memory polymers (i.e. for size reduction in transport or storage processes) and further transform into new polymeric structures[20–22]. In our previous work[23], a new sequential dual-curing system based on off-stoichiometric thiol-epoxy mixtures with epoxy excess catalysed by tertiary amines was presented. The combination of the thiol-epoxy click reaction followed by the homopolymerization of the epoxy excess produces two-stage materials with tuneable thermomechanical and structural properties with the advantage of a single-pot reaction mechanism. Dual-curing processing is achieved in this case by the kinetics control of both curing reactions: the thiol-epoxy addition takes place rapidly at low temperature while the epoxy homopolymerization remains almost latent due to the slow kinetics at this temperature[24–27]. The intermediate and final material properties depend

on the functionality and structure of the thiol and epoxy monomers or oligomers and the thiol-epoxy ratio or epoxy excess in the system. In our previous work[23], the network structure build-up during the thiol-epoxy reaction was analysed from a theoretical point of view assuming ideal step-wise behaviour. The critical ratio r_c which defines the minimum thiol-epoxy ratio to form a solid-like and therefore conformable material after the first curing stage was also predicted, a parameter that can be of relevance in the processing of complex shapes. Intermediate and stable materials ranging from highly viscous to solid-like and conformable materials can be obtained after the thiol-epoxy polymerization taking place at low temperature (first curing process). Hereafter, through an easy mechanically processing, complex shapes can be achieved which are further fixed by the formation of the new network structure caused by the epoxy homopolymerization taking place at higher temperature (second curing process).

In this work, thiol-epoxy dual-curing systems using thiol compounds of different functionality are studied in order to analyse their processing capabilities and the thermomechanical and physical properties of the multifunctional materials obtained. Mixtures at thiol-epoxy ratios below, close and above the critical ratio, r_c, were cured and the intermediate and final materials obtained were qualitatively analysed (deformability, consistency, colour, transparency and final shape). Some discrepancies from the theoretical behaviour were found in the processing of materials at the vicinity of r_c: the intermediate materials showed excessive deformation and even flow upon heating to activate the second curing reaction when they were not supposed to. The dual-curing process was therefore studied by means of rheological analysis in order to relate the viscoelastic behaviour during curing and, in particular, of the intermediate materials, with the observed behaviour. Relevant viscoelastic parameters such as the storage and loss modulus, and the loss factor tanδ were monitored at different frequencies. The experimental results were compared with the behaviour expected from the application of the well-known Flory-Stockmayer theory, for ideal step-wise processes, to the thiol-epoxy reaction occurring in the first curing stage. In addition, the thermomechanical and structural properties of the final materials were analysed by means of DMA and the applicability of all materials formed (intermediate and final materials) were discussed in order to optimise the performance of these multifunctional materials.

2. Materials and methodology

The epoxy resin diglycidyl ether of bisphenol A (DGEBA, GY240, Huntsman, Everberg, Belgium) with a molecular weight per epoxy equivalent of 182 g/eq was dried at 80 °C under vacuum during three hours prior to use. The curing agents pentaerythritoltetrakis(3-mercaptopropionate) (S4), with a molecular weight per thiol equivalent unit of 122.17 g/eq and trimethylolpropane tris(3-mercaptopropionate) (S3), with a molecular weight per thiol equivalent unit of 132.85 g/eq (both from Sigma-Aldrich, St. Louis, MO, USA) were used as received and the catalyst 1-methylimidazole (1MI, Sigma-Aldrich, St. Louis, MO, USA) was used as received.

The mixtures were prepared by mixing the compounds in different thiol-epoxy ratios *r* with respect to the epoxy groups. One part per hundred of 1MI of the total mixture (1 phr) was used as catalyst. The mixture was manually stirred in a glass vial and rapidly poured in a Teflon mould. The first curing process was carried out at 50 °C during 3 h to ensure the completion of the thiol-epoxy reaction. Intermediate materials were obtained and the processing of different shapes was carried out using different techniques. Afterwards, the second curing stage was triggered by increasing the temperature up to 120 °C (at 5 °C/min controlled ramp) and maintaining the oven isothermally during 1 h at 120 °C followed by 1 h at 150 °C to ensure the completion of the epoxy homopolymerization. Final materials with different shapes were obtained.

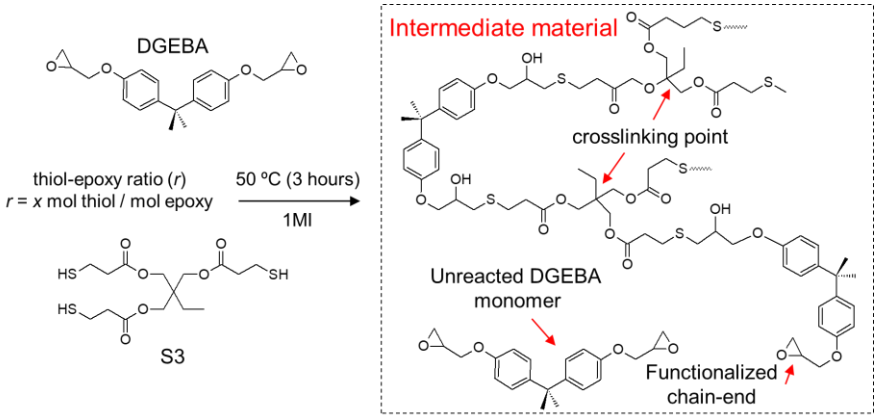

Scheme IV-1. Reaction scheme of the first curing stage and expected network structure of the intermediate material in the S3-DGEBA off-stoichiometric system (thiol-epoxy polymerization).

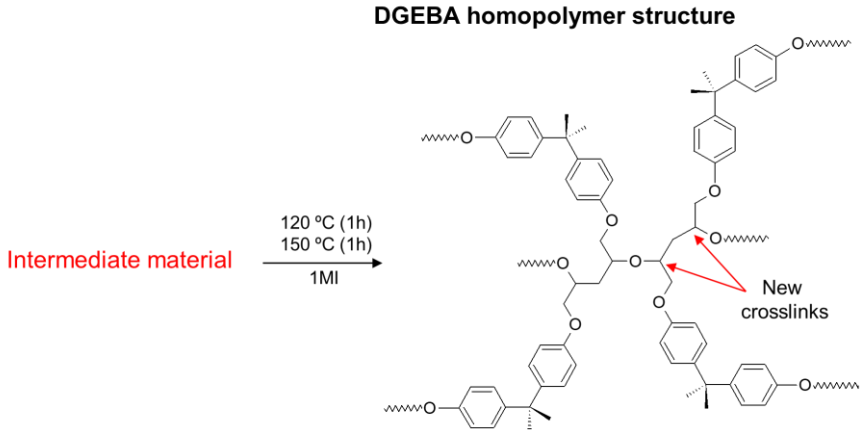

Scheme IV-2. Network structure formed after the second curing stage (epoxy homopolymerization).

In Scheme IV-1, the reaction scheme of the first curing process (thiol-epoxy polymerization) and the expected network structure of the intermediate material for a S3-DGEBA formulation is shown. In Scheme IV-2, the new network structure formed after the second curing stage (homopolymerization of the remaining epoxy) is presented.

Theoretical network build-up parameters

As mentioned in the introduction, one of the main advantages on using sequential dual-curing systems is to get an intermediate solid-like and conformable material. To this end, one approach is to define the thiol-epoxy ratio ensuring the gelation takes place during the first curing stage. The gel point conversion can be calculated, assuming ideal step-growth behaviour for the thiol-epoxy reaction, making use of the well-known theory of Flory-Stockmayer:

$$\alpha_{epoxy,gel} = \sqrt{\frac{r_{thiol:epoxy}}{(f_{epoxy}-1)\cdot(f_{thiol}-1)}} \qquad \text{(IV-1)}$$

In this expression, $\alpha_{epoxy,gel}$ is the conversion of epoxy groups at the gel point, f_{epoxy} and f_{thiol} are the average functionality of epoxy and thiol monomers and $r_{thiol:epoxy}$ is the ratio between thiol and epoxy functional groups. This only produces a valid gel point conversion for values of $r_{thiol:epoxy}$ higher than r_c and lower than $1/r_c$, where r_c is the critical gelation ratio. This parameter can be obtained from the following expression:

$$r_c = \frac{1}{(f_{epoxy} - 1) \cdot (f_{thiol} - 1)} \quad \text{(IV-2)}$$

In the case of formulations with excess of epoxy groups, $r_{thiol:epoxy}$ will be always lower than 1 and therefore only condition for gelation and crosslinking during the first curing stage is that $r_{thiol:epoxy} > r_c$. For lower ratios, the amount of thiol is not sufficient to produce a network during the thiol-epoxy reaction.

Rheological characterization

The dual-curing process was analysed using a rheometer, TA Instruments, New Castle, AR-G2 equipped with an electrical heated plate device (EHP) and parallel plate geometry. Dynamic-mechanical experiments at different frequencies were performed to investigate the evolution of the storage and loss modulus (*G*' and *G*", respectively) during the curing process. The gel point was determined by the crossover of the phase angle δ at different frequencies. The experimental procedure is defined to simulate the curing procedure in the oven: 3 h at 50 °C with oscillation amplitude of 2% (until *G*' has reached a stable plateau) and of 0.5% (until the end of the curing process). Three different frequencies were continuously measured, from 1 to 10 Hz, 2 points per decade in logarithmic scale (1, 3.16 and 10 Hz). Afterwards, the second curing stage was carried out as follows: a heating rate of 5 °C/min from 50 to 120 °C followed by 1 h at 120 °C (same oscillation amplitude and frequencies) and 1 h at 150 °C (same oscillation amplitude but only at 1 Hz).

Thermomechanical characterization

As in our previous work[23], Fox's law for copolymer networks (see equation (IV-3)) can be used to estimate the glass transition temperatures of the intermediate and final materials starting from the experimentally measured values of each component: uncured/cured thiol-epoxy network, uncured/cured epoxy homopolymer network. Such estimation is possible assuming there are no specific interactions between both components[28].

$$\frac{1}{T_{g,m}} = \frac{w_{S-E}}{T_{g,S-E}} - \frac{1 - w_{S-E}}{T_{g,E-E}} \quad \text{(IV-3)}$$

In equation (IV-3) *w* is the mass fraction and subscripts *S-E* refers to the thiol-epoxy network structure, *E-E* to the epoxy homopolymer

network structure, and *m* to the stage of the material (intermediate material, *m* = 1, final material, *m* = 2). For the intermediate material, $T_{g,E\text{-}E}$ is the glass transition temperature of the unreacted DGEBA monomer remaining within the network, while in the final material, $T_{g,E\text{-}E}$ is the glass transition temperature of the DGEBA homopolymer network structure. In both materials, $T_{g,E\text{-}E}$ is the glass transition temperature of the stoichiometric thiol-epoxy network structure.

The $T_{g,S\text{-}E}$ for both, S3 and S4 systems, and the $T_{g,E\text{-}E}$ for both, the intermediate and final materials, were determined by dynamic DSC experiments using a Differential scanning calorimeter Mettler 821e calibrated with indium standards. Neat thiol-epoxy formulations containing S3 or S4 as thiol crosslinker, with $r_{thiol:epoxy}$ = 1, were used to determine the $T_{g,S\text{-}E}$ of each system. The formulations were cured at 10 °C/min from room temperature up to 200 °C. A second DSC run at 10 °C/min up to 120 °C was performed in order to determine their glass transition temperature. A formulation containing only DGEBA and 1MI was used to determine the $T_{g,E\text{-}E}$ of the intermediate materials, that is, the unreacted DGEBA-1MI mixture, and that of the fully crosslinked material. In this case, the mixture was heated at constant heating rate of 10 °C/min from −50 °C to 250 °C to determine the glass transition of the unreacted mixture and cure completely the material. Afterwards, a second DSC scan was performed at 10 °C/min from room temperature to 200 °C to determine the glass transition temperature of the cured material.

In order to verify the predictions made by the Fox equation, dynamic DSC experiments of formulations covering the whole thiol-epoxy ratio ($r_{thiol:epoxy}$ equal to 0.25, 0.5 and 0.75) were performed. The samples were cured in a conventional oven following the procedure explained in the materials section. The intermediate materials were analysed in the DSC at 10 °C/min from −50 to 100 °C. The final materials were analysed at 10 °C/min and from 30 to 200 °C.

A DMA Q800, TA Instruments, equipped with a 3-point-bending clamp (15 mm) was used to analyse the thermomechanical and structural properties of the final materials. Oscillatory experiments were carried out at 15 µm of amplitude, 1 Hz of frequency and at a heating rate of 3 °C/min from 30 °C to 150 °C. The glass transition temperature T_g was determined as the peak of the tanδ curve, the rubbery modulus (E_r) was determined at T_g + 50 °C from the storage modulus curve and the width at half-height (FWHM) and peak value of the tanδ curve were determined to further analyse the heterogeneity of the network relaxation process.

3. Results and discussion

As stated in previous section, it was decided to analyse the materials with thiol:epoxy ratios in the vicinity of the critical gelation ratio r_c; a thiol:epoxy ratio below r_c should lead to uncrosslinked materials with flowing ability at the end of the first curing stage, while a thiol:epoxy ratio above r_c should produce a solid-like and conformable intermediate material. In Table IV-1 the conversion of epoxy groups at gel $\alpha_{epoxy,gel}$, calculated using equation (IV-1), and the thiol-epoxy ratio are shown for both, the S3-DGEBA and S4-DGEBA systems. The point at which both, the thiol-epoxy ratio and the conversion are equal (highlighted in intense grey), determines the minimum thiol-epoxy ratio, r_c, required to form a gelled material and therefore solid-like and conformable. The exact value for the S4-DGEBA system is $r_c = 0.333$, from equation (IV-2), so $r = 0.35$ is only an approximate estimation. As expected, the gel point conversion is lower in systems with higher functionality (S4-DGEBA > S3-DGEBA) for the same thiol-epoxy ratio because formation of the incipient cross-linked network is easier. Likewise, the critical gelation ratio is also lower.

Table IV-1. Determination of the thiol-epoxy critical ratio for the S3-DGEBA and S4-DGEBA systems.

S3-DGEBA		S4-DGEBA	
***r* (thiol-epoxy)**	**$\alpha_{epoxy,gel}$[a]**	***r* (thiol-epoxy)**	**$\alpha_{epoxy,gel}$[a]**
0.70	0.592	0.70	0.483
0.65	0.570	0.65	0.465
0.60	0.548	0.60	0.447
0.55	0.524	0.55	0.428
0.50	0.500	0.50	0.408
0.45	0.474	0.45	0.387
0.40	0.447	0.40	0.365
0.35	0.418	0.35	0.342
0.30	0.387	0.30	0.316

[a] Calculated using equation (IV-1).

Using the values of the determined r_c, intermediate and final materials at $r < r_c$ and $r \geq r_c$ were cured and qualitatively analysed. In Figure IV-1, pictures of different materials obtained with the S3-DGEBA system are presented. As it can be seen, the intermediate materials are completely transparent and colourless regardless of the thiol-epoxy ratio. Moreover, the transparency remains stable from thin samples (≈ 0.1 mm) to thick samples (> 3 mm). At $r < r_c$, highly viscous and sticky materials were obtained, whereas on increasing the ratio up to r_c, solid-like and highly deformable materials were obtained (Figure IV-1(a)). At thiol:epoxy ratios far above r_c, hardly deformable intermediate materials are obtained due to the higher content of thiol-epoxy network structure. After the second

curing stage (Figure IV-1(b)), the final materials remain transparent, but colour changes are appreciated. The anionic epoxy homopolymerization leads to intense brown materials due to the presence of initiator fragments with conjugated double bonds in chain ends[26]. As a consequence, decreasing the thiol-epoxy ratio (higher epoxy excess), leads to darker samples. This is interesting from a qualitative point of view because only through the colour of the sample, one can deduce the amount of epoxy excess present in the material, and also from the application point of view, depending on whether colour is important or not. All the final materials were rigid at room temperature and those formulations containing higher epoxy excess, $r < r_c$, showed higher fragility. This was proved during the sample release from the curing mould: various samples with higher content of epoxy excess broke due to the force applied. The formation of a high densely network structure by the anionic epoxy polymerization leads to brittle materials[29].

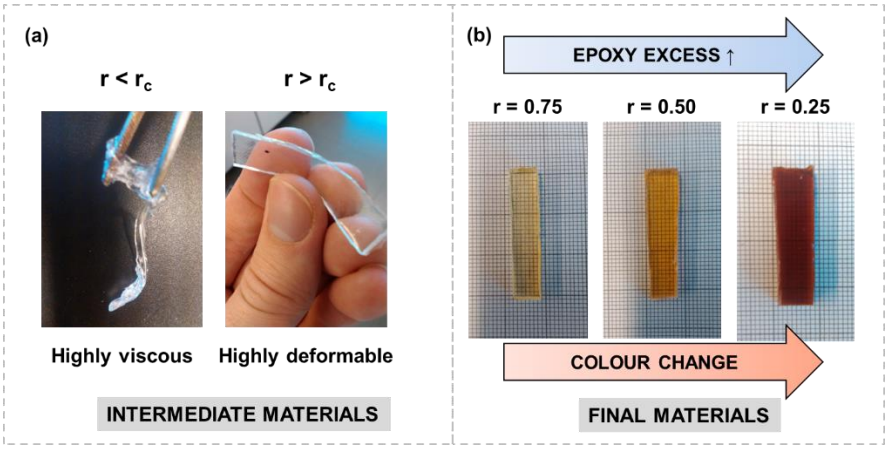

Figure IV-1. Examples of different intermediate and final materials obtained at different thiol-epoxy ratios.

In Figure IV-2 some examples of conformation and processing of complex shapes are shown using formulations with ($r > r_c$). As it can be seen, choosing an appropriate thiol:epoxy ratio makes it possible to form a solid-like and conformable material. This intermediate material (i.e. a thick-type or film-type material) can be deformed into a spring, bent or other complex and uncommon shape through a mechanical or even manual processing. Afterwards, these shapes can be fixed through the second curing stage. Nevertheless, because of the low T_g ($T_g < T_{room}$), viscoelastic relaxation is fast, leading to a recovery of the original shape when temperature starts to increase for the activation of the second curing stage. Therefore, in order to fix the shape, it is necessary to

constrain this shape during the heating and subsequent curing. Therefore, complex shapes were successfully achieved, and no cracking was appreciated over the surface due to shrinkage and internal stresses generated during the epoxy homopolymerization process[30].

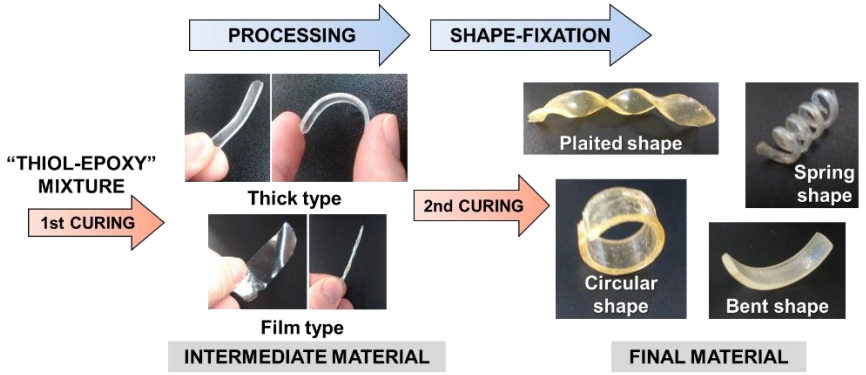

Figure IV-2. Examples of shape-processing (intermediate material) and shape-fixation (final material).

Taking advantage of this process, it is possible to obtain well-defined circular-shapes for structural applications such as opening and closing mechanisms (shape-memory actuators[31]), or otherwise forming complex shape designs (i.e. a plaited-shape or bent-shape) for more demanding applications. In addition, using film-type samples it is possible the processing of long wires by rolling it up and further develop spring-shaped final materials. Moreover, the film-type materials are valuable for bonding pipes or coating purposes because the film can be easily adapted to different types of shapes and elongated as desired.

Nevertheless, as mentioned in the introduction, the imposed final shape is not well-retained when the thiol-epoxy ratio is too close to r_c. The advantage on using these formulations is the enhanced deformability caused by the low modulus and T_g achieved after the first curing stage. In Figure IV-3, the curing of a spring-shaped material using the formulation S3-DGEBA-0.55 (note that r_c is 0.5) is shown. As it can be seen, the shape is lost but, unexpectedly, it was also observed significant dripping, indicative of a liquid-like behaviour. The situation was similar for both S3-DGEBA and S4-DGEBA systems at stoichiometric ratios slightly above r_c.

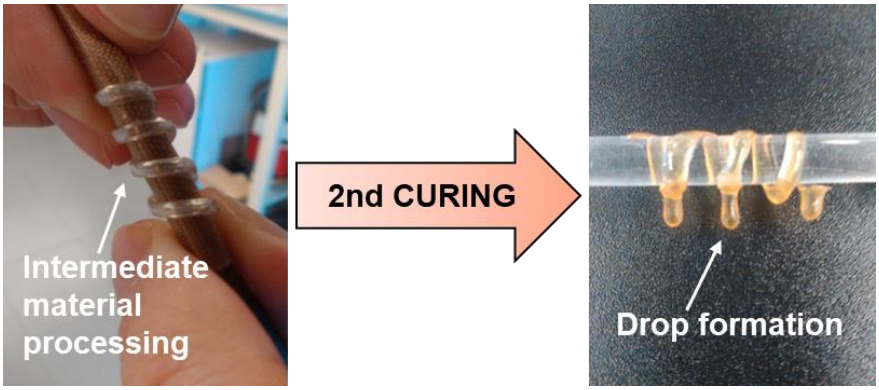

Figure IV-3. Example of the shape-losing after the second curing stage in a formulation with a thiol-epoxy ratio close to the critical ratio (S3-DGEBA-0.55).

Taking into account the above results, an experimental scenario was set up to analyse in depth this phenomenon (from here and so on, we will refer to this phenomenon as "dripping" behaviour). In Figure IV-4, a scheme of the "dripping test" methodology is shown. Different partially cured specimens with $r \geq r_c$ were suspended vertically from one end. This way, elongation is only due to its own weight. Afterwards, the second curing stage is triggered following the same procedure explained in the materials and methods section. Finally, the dripping suffered in the different specimens is qualitative and/or quantitative analysed. It is of key importance to ensure that all the specimens have the same dimensions, thus they were carefully cured in order to obtain the same sizes, 30 × 6 × 1.5 mm^3. In order to further analyse each section of the specimen separately, various equidistant marks were painted along the specimens. As it can be seen in Figure IV-4, the marked specimens were held by the top-side with minimal force onto a Teflon surface in order to avoid the sample being flattened during the experiment.

The dripping behaviour was qualitatively and, when possible, quantitatively analysed through equation (IV-4) (which quantifies the % of elongation suffered during the second curing stage).

$$Dripping(\%) = \frac{\Delta_{l,tot}}{l_0} \cdot 100 \qquad \text{(IV-4)}$$

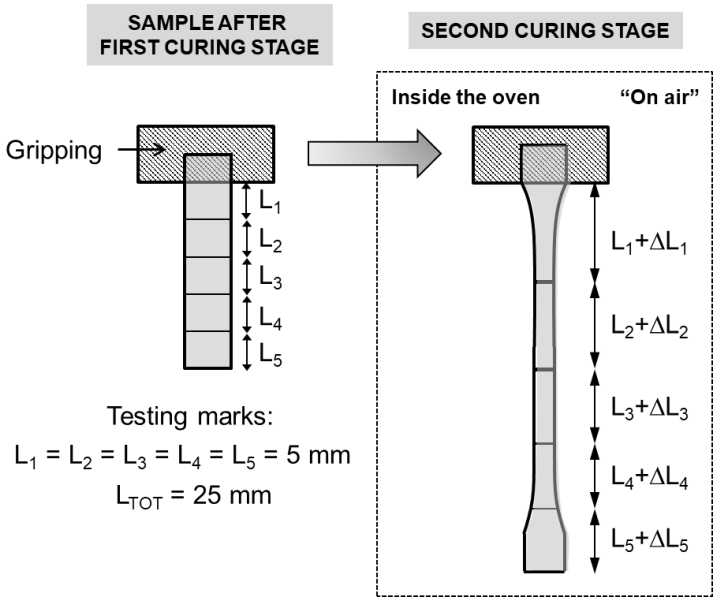

Figure IV-4. Dripping test scenario: on the left side the specimen marked and measured before testing; on the right side the elongation suffered after the second curing stage. All the measured parameters have been highlighted.

In Table IV-2, the results of the dripping test are summarized for the S3-DGEBA and S4-DGEBA systems. The symbol ∞ means that the entire sample fell off the support during the experiment. As it can be seen, both formulations stop dripping at $r = r_c + \approx 0.15$ (considering a % of dripping < 2% as the "no-dripping" point). In Figure IV-5, examples of the dripping test for the S3-DGEBA and S4-DGEBA systems are shown. Overall, samples with ratios close to r_c broke at the fastening point and completely fell off (see S4-DGEBA-0.35 and S3-DGEBA-0.50), whereas with increasing the ratio, the sample did not break but showed high elongation (see S3-DGEBA-0.60). Finally, at a certain ratio (S3-DGEBA-0.65 and S4-DGEBA-0.5), the sample completely retained the shape (no-dripping ratio r_d). According to the theoretical model based on ideal step-wise behaviour[23], the crosslinking density of formulation S3-DGEBA-0.60 was about one-two orders of magnitude lower than that of the stoichiometric material S3-DGEBA-1.0 and it means that it should have a modulus in the range of hundreds of kPa, which should be more than enough to maintain the shape; however, the sample showed high elongation pointing out some discrepancies from the theoretical behaviour.

Table IV-2. Dripping test: quantitative results.

Formulation	L_0	Δl_1	Δl_2	Δl_3	Δl_4	Δl_5	Δl_{total}	Dripping (%)
S3-DGEBA-0.50	25	∞	∞	∞	∞	∞	∞	∞
S3-DGEBA-0.55	25	∞	∞	∞	∞	∞	∞	∞
S3-DGEBA-0.60	25	4	3	2	1	0	12	48
S3-DGEBA-0.65	25	0.2	0.1	0	0	0	0.3	1.2
S4-DGEBA-0.35	25	∞	∞	∞	∞	∞	∞	∞
S4-DGEBA-0.40	25	∞	∞	∞	∞	∞	∞	∞
S4-DGEBA-0.45	25	∞	∞	∞	∞	∞	∞	∞
S4-DGEBA-0.50	25	0	0	0	0	0	0	0

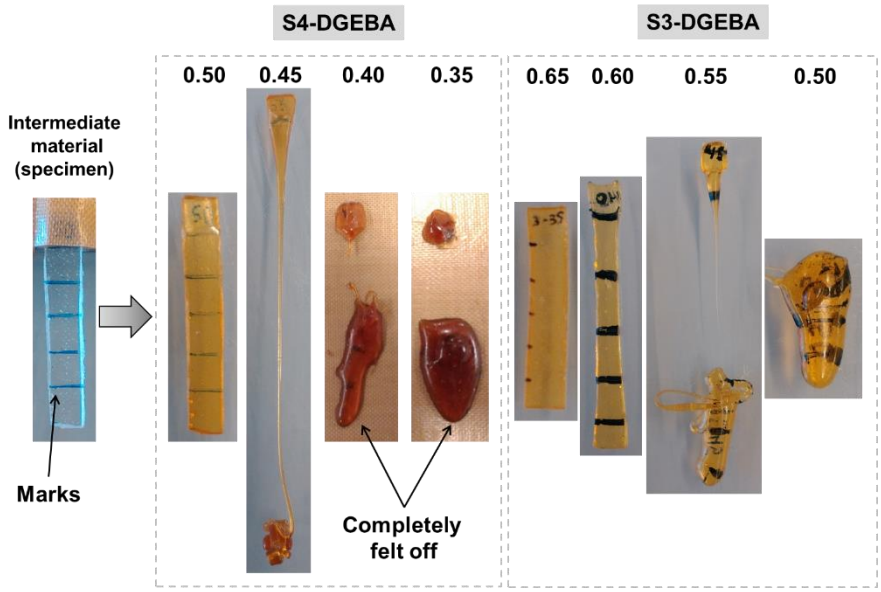

Figure IV-5. In the left side, the specimen of assay (sized and marked intermediate material) and in the right side, the specimens after the dripping test in both systems.

In order to rule out any possible heterogeneity of the samples, DSC analyses were carried out in different parts of the specimen using the same experimental procedure as explained in the materials and methodology section (in this case from 30 °C to 120 °C). The T_g values in Table IV-3 indicate all the formulations were homogeneous regardless of the dripping; the T_g values obtained are almost equal in any part of the specimens.

Table IV-3. Glass transition nominal values obtained from DSC tests of those specimens showing dripping behaviour. Experiments were performed in different sections of the specimen: upper, middle and lower side.

Formulation	$T_{g,2}$ (DSC) (Upper)	$T_{g,2}$ (DSC) (Middle)	$T_{g,2}$ (DSC) (Lower)	$T_{g,2}$ (DSC) (Average)
S3-DGEBA-0.50		73.7 - 72.1[a]		72.9
S3-DGEBA-0.55		70.1 - 69.8[a]		70.0
S3-DGEBA-0.60	65.9	65.6	66.1	65.9
S4-DGEBA-0.35		102.2 - 100.3[a]		101.3
S4-DGEBA-0.40		94.5 - 95.3[a]		94.9
S4-DGEBA-0.45	92.2	[b]	91.6	91.9

[a] The sample completely fell off, two separated pieces were extracted and analysed.
[b] The sample reached the floor, the middle section was mixed with the lower part.

Given that the samples were homogeneous from the structure point of view, it was hypothesized that the assumption of ideal step-wise behaviour for the thiol-epoxy reaction may not be realistic at all. Some of the samples showed a flow-like behaviour, as if they were not gelled, when they should not, indicating that gelation might have been delayed. In consequence, rheological tests were therefore carried out in order to understand the observed behaviour.

Rheology analysis

In basis of the results obtained in the previous section, the rheological analysis of the dual-curing process can provide useful information about the viscoelastic properties of the materials in relation with the dripping phenomenon observed. Two different formulations of each system were analysed: one in which no dripping was appreciated (S3-DGEBA-0.65 and S4-DGEBA-0.50) and one in which "∞" dripping was shown (S3-DGEBA-0.55 and S4-DGEBA-0.40, in both formulations the sample completely fell off). In Figure IV-6, the entire curing process for the S3-DGEBA-0.55 is presented. In order to follow-up the evolution of the curing process, both the storage modulus (G') and loss modulus (G'') at different frequencies are represented against the global time of the experiment (t). In addition, the temperature profile during the experiment is shown. As it can be observed, the evolution of the curing process is frequency-dependent until the material is completely cured (t > 200 min). During polymerization, the material passes through different phases: from a liquid-like material, where both G' and G'', as well as tanδ (the loss factor) are frequency-dependent, up to the formation of a solid-like elastic material where G' becomes independent of the frequency and $G' \gg G''$ (tanδ ≈ 0, elastic mechanical response). During the first curing stage (three hours at 50 °C), the thiol-epoxy polymerization takes place within the first

30–40 min because of the drastic increase in both, *G*′ and *G*″, of about 4 orders of magnitude followed by a stable plateau, in agreement with the previous kinetics analysis[23]. Afterwards, *G*′ slightly increases with the time, because of the epoxy homopolymerization taking place slowly at this temperature[23]. During the temperature increase from 50 °C to 120 °C in the second curing stage, both *G*′ and *G*″ decrease to a certain extent indicating a softening of the material due to the increasing temperature. Finally, the epoxy homopolymerization takes place with a drastic increase in *G*′ up to values in the range of MPa while *G*″ remains at values two orders of magnitude lower, indicating elastic mechanical response (tanδ ≈ 0), and frequency independence.

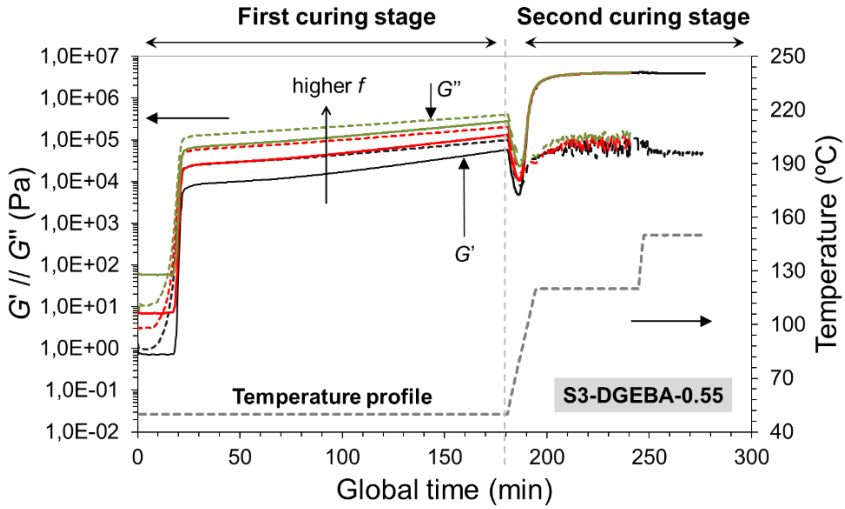

Figure IV-6. Storage modulus (*G*′), loss modulus (*G*′′), and the temperature profile are shown for the whole dual-curing process in the S3-DGEBA-0.55 formulation.

As mentioned above, one of the possible reasons explaining the dripping behaviour is the wrong determination of the gel point from equation (IV-1). The gelation process is frequency-independent and therefore, the most consistent gelation criterion is the crossover of tanδ curves at different frequencies[34] or, equivalently, the crossover of the phase angle δ. In Figure IV-7, the phase angle δ is represented in front of the time during the first curing stage. A typical maximum in δ or tanδ during curing is observed before gelation takes place, because the increase in molecular weight produces an increase in viscosity and therefore in the loss modulus *G*″, while the elastic component *G*′ is hardly affected. Then the phase angles start to decrease due to the increase in *G*′ and, if gelation takes place, a crossover takes place. As it can be seen, in formulations where maximum dripping was shown (S3-DGEBA-0.55 and S4-DGEBA-

0.40), the crossing of δ is not appreciated and therefore the intermediate material formed is not gelled yet. This confirms that network build-up during curing of thiol-epoxy formulations does not follow an ideal step-wise behaviour, and therefore the predictions made using the ideal Flory-Stockmayer expressions are inaccurate. By way of contrast, in formulations where no dripping was shown (S3-DGEBA-0.65 and S4-DGEBA-50), the crossover of δ is clearly appreciated pointing out the formation of a gelled network structure.

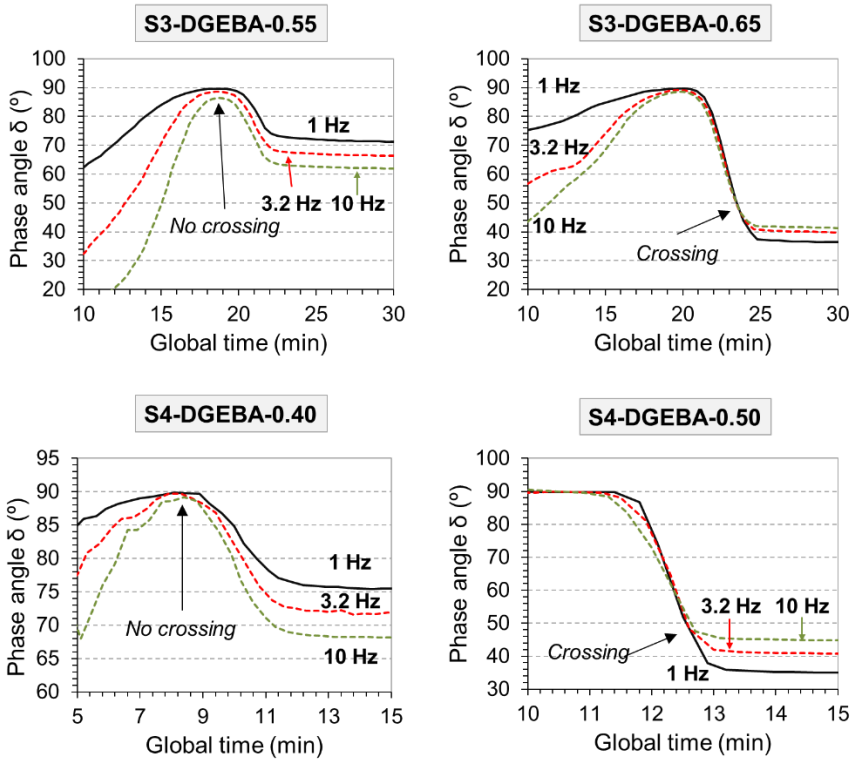

Figure IV-7. Phase angle δ against the experiment global time for all the formulations of study. The crossing of the curves has been highlighted.

In Figure IV-8, δ is represented against the temperature during the temperature increase from 50 °C to 120 °C for those formulations where no gelation took place in the first curing stage. As it was expected, gelation takes place during the early stage of the second curing process. This may explain why the samples completely fell off during the dripping test: the lack of network structure and the softening of the samples (see the decrease in modulus in Figure IV-6) enable the sample to flow as a highly viscous liquid until the shape is completely lost, before the second curing

process is activated and the material starts to build-up a network structure.

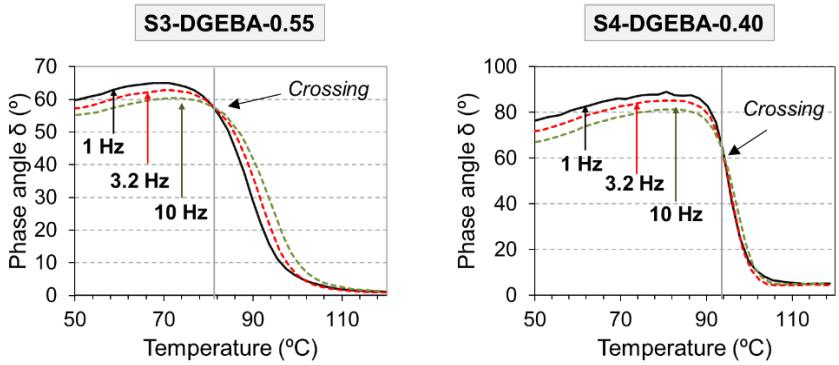

Figure IV-8. Phase angle δ against the temperature for the S3-DGEBA-0.55 and S4-DGEBA-0.40 formulations during the temperature increase (50°C to 120°C) in the second curing stage. The crossing of the curves has been highlighted.

In Figure IV-9, the evolution of *G*' and *G*" during the temperature increase is represented. In formulations where gelation takes place in the first curing stage (S3-DGEBA-0.65 and S4-DGEBA-0.40), *G*' is already above or rapidly overpasses *G*" at low temperature (50–60 °C). On the contrary, formulations without gelled structure have higher *G*" until 80–100 °C, when gelation takes place and the material starts to build-up a network structure with a more elastic character. In the ungelled formulations (S3-DGEBA-0.55 and S4-DGEBA-0.4), the modulus decreases about 1–2 orders of magnitude upon heating due to the softening of the highly viscous structure, reaching values as low as 30 Pa at 1 Hz in the case of the S4-DGEBA-0.40 formulation. This significant change can explain the elongation and flow (the samples are liquid-like) of the sample because of its own weight in the previous experiments. In the case of S3-DGEBA-0.55 the modulus at 1 Hz decreases only down to 5 kPa but, given that the characteristic timescale during the "dripping" experiment may be in the range of minutes, a measurement in the range of 0.01 Hz would lead to an even lower modulus and also explain the considerable elongation and flow observed. In contrast, formulations with already gelled structure (S3-DGEBA-0.65 and S4-DGEBA-0.5) have *G*' values around or above 0.1 MPa, sufficiently high to avoid sample elongation. The explanation of those formulations that elongated but not completely fell down (i.e. S3-DGEBA-0.60) during the dripping test is probably a matter of time. Following the same reasoning as above, the intermediate material is probably not gelled after the first curing stage, making it possible to elongate the sample due to the softening of the material. However, gelation takes place in the early

stage of the second curing process, therefore quickly building up a crosslinked structure preventing further elongation.

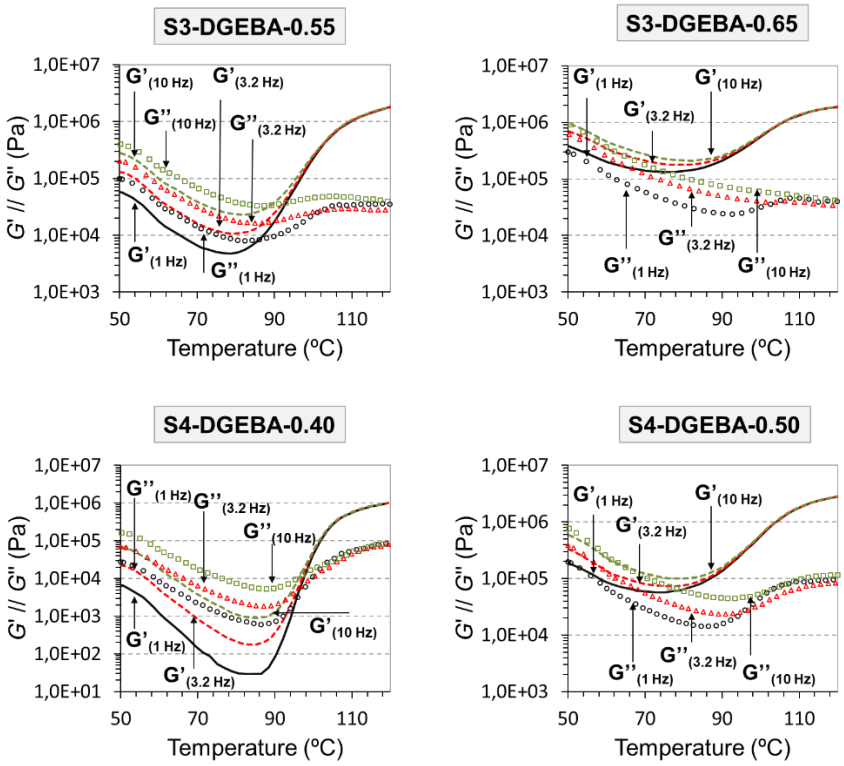

Figure IV-9. Loss modulus (*G''*) and storage modulus (*G'*) during the temperature increase in the second curing stage for all the formulations of study.

From this preliminary analysis, it appears that the effective critical ratio for the S3-DGEBA system should be close to 0.65, and for the S4-DGEBA system should be close to 0.50, and not 0.5 and 0.33 as it is predicted by the Flory-Stockmayer theory. Such departures from the ideal step-wise behaviour are commonly explained by negative substitution effects, which is unlikely in the present case, or better intramolecular cyclization[32,33]. Intra-molecular cyclization would lead to a delayed gel point conversion, a looser network structure with larger deformability, and leading in some cases to no gelation at all and a lack of network structure[34]. On the other hand, the curing agents S3 (purity > 95%) and S4 (purity > 95%) were used as received, and the presence of impurities may result in a lower thiol functionality, hence leading to higher conversion at gelation and looser network structure. A further detailed analysis of gelation and network build-up is out of the scope of this work. Combined calorimetric, rheological and thermomechanical experiments,

as well as solubility measurements, are being done and preliminary results confirm the displacement of the gelation to higher conversion accordingly to the explanation given above. The results of this more detailed analysis will be subject of a future work.

Thermomechanical characterization: towards applicability

In this section, the thermomechanical and structural properties of the different formulations of study are shown in order to evaluate the intermediate and final materials with respect to the potential applicability. In Figure IV-10, the predicted values of $T_{g,1}$ and $T_{g,2}$ (intermediate and final materials) at the different thiol-epoxy ratios (continuous lines) and the experimental values determined by DSC analysis (points) are represented. The apparent critical ratio, determined from the "dripping" experiments (r_d) has also been included, in order to divide the graphic in different sections (A and B) accordingly to the physical state of the sample after each curing stage, liquid-like or solid-like.

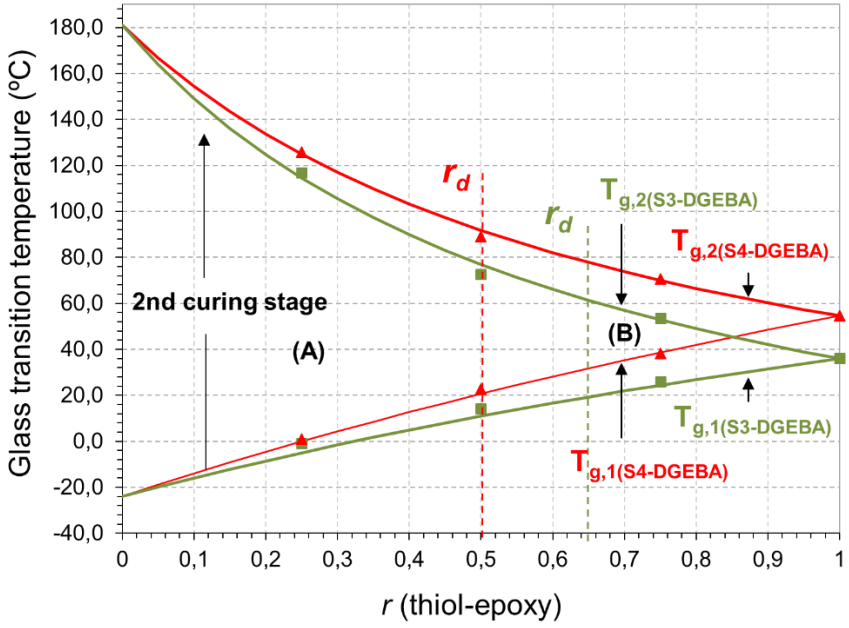

Figure IV-10. Glass transition temperatures and the apparent thiol-epoxy critical ratio of S3 and S4 systems against the thiol-epoxy ratio: comparison between predicted and experimental values.

As it can be observed, the DSC experimental measurements of $T_{g,1}$ and $T_{g,2}$ fit well with the predicted ones using the Fox equation for both systems. Overall, with the increase of the thiol-epoxy ratio, $T_{g,1}$ increases while $T_{g,2}$ decreases. $T_{g,1}$ arises from the formation of a moderately

crosslinked network structure (thiol-epoxy polymerization) and the presence of unreacted epoxy groups (see Scheme IV-1), while $T_{g,2}$ adds a highly densely crosslinked network given by the epoxy homopolymerization and all functional groups have reacted (see Scheme IV-2). The materials with a low thiol:epoxy ratio have little contribution from the thiol-epoxy polymerization and a high contribution from the epoxy homopolymer network, hence the lower $T_{g,1}$ and higher $T_{g,2}$. In contrast, materials with a high thiol:epoxy ratio have a higher contribution from the thiol-epoxy polymerization and lower contribution from the epoxy homopolymer network, hence the higher $T_{g,1}$ and the little increase in $T_{g,2}$. As it is well-known, the T_g of thermosets mainly depends on the network structure hindrance and crosslinking density in such a way that, the higher the T_g due to highly crosslinked and physically hindered network structures, the broader the relaxation process and the stronger the effect on the mechanical properties (brittle materials). This is of high relevance when defining the operational design of the final material. Depending on the application, i.e. coatings, actuation purposes or structural applications, the final material should have specific thermal and mechanical properties. A number of useful parameters such as the storage modulus in the relaxed state of the network, the FWHM (full width at half maximum) and tanδ peak values are an indication of the crosslinking density and the heterogeneity of the network structure. In Figure IV-11, the relaxed modulus, as well as both, the FWHM and tanδ peak values are represented for the different thiol-epoxy ratios of study. In addition, the $T_{g,2}$ is shown to facilitate the comparison between materials. As it is observed, high values of $T_{g,2}$ (low thiol-epoxy ratios) lead to high values of E_r and more heterogeneous network structures (higher FWHM and lower tanδ peak values), whereas lower values of $T_{g,2}$ (increasing the thiol-epoxy ratio), lead to lower values of E_r and more homogeneous network structures.

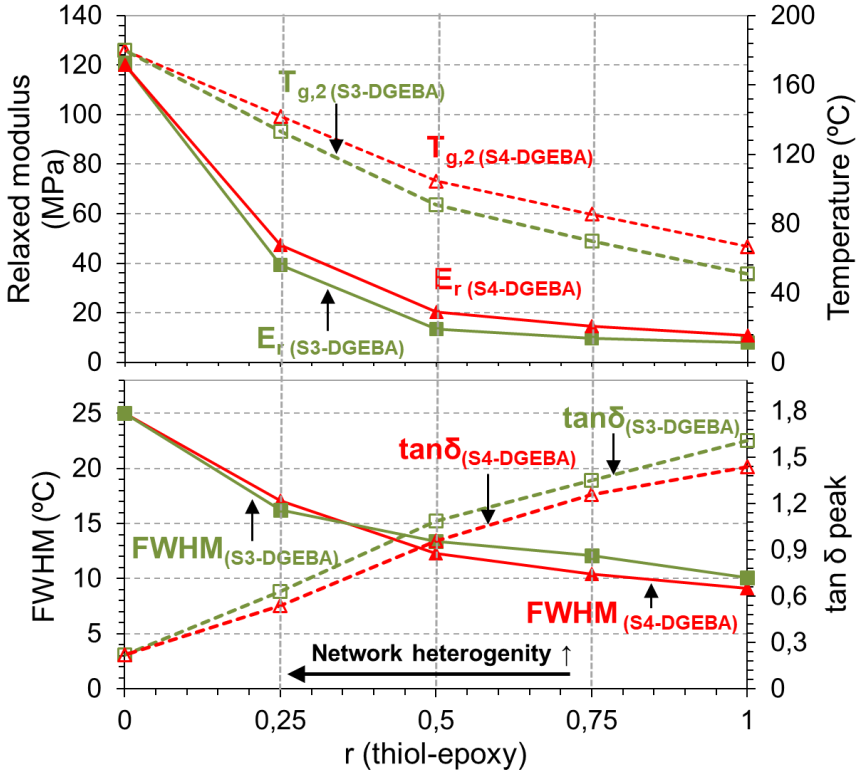

Figure IV-11. Analysis of the network structure properties (heterogeneity, crosslinking density and relaxed modulus) in both systems, S3-DGEBA and S4-DGEBA.

Taking into account the different $T_{g,1}$, $T_{g,2}$ and the rheological properties of the intermediate materials depending on the thiol-epoxy ratio, the graphic in Figure IV-10 can be divided in two sections as previously explained: section (A), from $r = 0$ (DGEBA homopolymerization) to r_d (no-dripping/critical ratio), section (B), from r_d to the stoichiometric ratio. In section (A), the intermediate material is liquid-like and the viscosity increases with increasing the ratio. The final material shows moderate to high T_g values (from 60 to 180 °C depending on the system and the stoichiometric ratio), but may show low impact resistance and higher fragility when the ratio is too close to "0" because of the high content of unreacted epoxy groups forming a highly crosslinked network structure[29]. This type of materials could be of high interest in applications such as adhesives or primer coatings with high temperature resistance, given the good adhesion of the liquid-like intermediate material (see in Figure IV-1) and the high T_g achieved in the final material, or else in applications where the intermediate flowing ability can be controlled or else is irrelevant, such composites or moulded compounds that are

processed in one or two stages. In the vicinity of the critical ratio, the final materials show homogeneous network structures and sufficiently low E_r values (see Figure IV-11) in comparison with materials in section (B), which make them promising in terms of mechanical elongation and strength. The intermediate materials at room temperature behave solid-like and have high conformability (with $T_{g,1}$ values around 20 °C and sufficiently low modulus to reach high elongation, see examples in Figure IV-2) and the final materials still show well-separated T_g values (from 20 °C in the intermediate material to 65–90 °C in the final material). The final shape may not be well-retained below this critical ratio due to the significant elongation during the second curing stage, but applications in which films are required or when a mould is used, can perfectly fit with these materials.

In section (B) the increase in T_g between the intermediate and final stages is more limited, especially as the thiol-epoxy ratio approaches 1. The materials are completely able to retain the imposed final shape but they are hardly processed with increasing the thiol-epoxy ratio. Actually, increasing the ratio worsens the conformation but increases $T_{g,1}$, in such a way that the intermediate material can be exploited for shape-memory applications, i.e. the S4-DGEBA-0.80 has 42 °C of $T_{g,1}$ and 66 °C of $T_{g,2}$ (still separated temperatures to consider them two different materials). Such applications include fold-deploying materials to reduce the volume in storage or transport stages[35]. Furthermore, the shape-memory capability can be used to impose an uncommon complex temporary shape which further will be fixed into a permanent shape through the second curing stage by simply fastening it externally impeding the shape-recovery effect. An example of the fold-deploying and further fixation of a complex shape is shown in Figure IV-12. As it is observed, the intermediate material is easily processed into different reduced temporary shapes, and the original shape can be recovered through the shape-memory effect at low temperature (avoiding the triggering of the second curing stage). After that, a semi-tube shape (for example) can be imposed again through a shape-memory programming process and further fixed through the second curing stage.

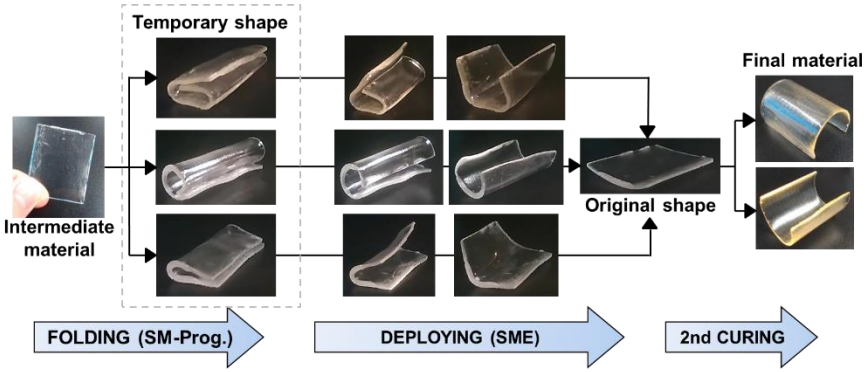

Figure IV-12. Example of fold-deploying and further shape-fixing application taking advantage of the shape-memory capability of the intermediate material in formulation S4-DGEBA-0.8.

In general, all final materials above the critical ratio are promising in shape-memory applications: the possibility to obtain uncommon shaped final materials (see Figure IV-2) and the tailoring capability of the network structural properties (from high to moderately low E_r values with relatively homogeneous relaxation processes) make them suitable materials.

4. Conclusions

Sequential dual-curing of off-stoichiometric thiol-epoxy mixtures has been successfully achieved by using thiol compounds of different functionality and specific curing conditions. Appropriately choosing the thiol-epoxy ratio (higher than the critical ratio, r_c), solid-like and conformable intermediate materials have been obtained after the first curing stage. Temporary shapes can be easily produced and fixed by crosslinking taking place during the second curing stage. Nevertheless, some troubles fixing the final shape were found when using formulations close to the theoretical r_c: after the second curing stage, completely or partially losing of the imposed shape was appreciated in form of drops or elongation of the sample (dripping behaviour). Through a visual study of this phenomenon, r_c has been found higher than expected, pointing out that probably the gelation is taking place at higher conversion than expected. DSC analysis of different parts in the tested samples evidenced that the sample structure remains homogeneous after the second curing stage and therefore no flow of unreacted species is taking place but the whole sample suffers an irreversible elongation.

The rheological analysis verified that, as stated above, gelation takes place at higher conversion than the predicted from the theory

applied. In formulations where dripping was appreciated, the cross of the δ curves does not take place until the second curing stage is triggered, whereas at a certain thiol-epoxy ratio (called "no-dripping" ratio, r_d) the crossing is well-appreciated during the first curing stage. Moreover, the storage modulus dramatically decreases to a minimum value during the temperature increase from 50 °C to 120 °C in the second curing stage that, in the case of samples where "dripping" was appreciated, reaches compromising values that could produce such elongation caused by the own weight of the sample.

The T_g of the intermediate and final materials can be obtained from the application of the Fox equation using the initial and final $T_{g's}$ of the different components. Plotting these glass transitions against the thiol-epoxy ratio, as well as the effective critical ratio, is a useful tool for the analysis of the applicability of the different materials. Possible applications can be defined on the basis of this critical ratio, taking advantage of the flowing ability, the high deformability or the shape-memory properties of the intermediate materials. Final materials with tuneable properties can be achieved: from moderately crosslinked to highly densely crosslinked network structures with T_g ranging from 40 °C (at high thiol-epoxy ratios) up to 180 °C (at low thiol-epoxy ratios) only using two different thiol-epoxy systems. This evidences the potential capability of this system to produce tailor made materials through the use of different thiol and epoxy compounds.

Acknowledgements

The authors would like to thank MINECO (MAT2014-53706-C03-01 and MAT2014-53706-C03-02) and Generalitat de Catalunya (2014-SGR-67) for financial support.

References

[1] J.P. Pascault, H. Sautereau, J. Verdu, R.J.J. Williams, Thermosetting Polymers, 1st edn. CRC Press, New York, 2002.

[2] R.J. Sheridan, C.N. Bowman, Understanding the process of healing of thermoreversible covalent adaptable networks, Polym. Chem. 4 (2013) 4974–4979, http://dx.doi.org/10.1039/C2PY20960H.

[3] C.J. Kloxin, C.N. Bowman, Covalent adaptable networks: smart, reconfigurable and responsive network systems, Chem. Soc. Rev. 42 (2013) 7161–7173, http://dx.doi.org/10.1039/c3cs60046g.

[4] A. Lendlein, Progress in actively moving polymers, J. Mater. Chem. 20 (2010) 3332–3334, http://dx.doi.org/10.1039/C004361N.

[5] B.D. Mather, K. Viswanathan, K.M. Miller, T.E. Long, Michael addition reactions in macromolecular design for emerging technologies, Prog. Polym. Sci. 31 (5) (2006) 487–531, http://dx.doi.org/10.1016/j.progpolymsci.2006.03.001.

[6] C. Decker, F. Masson, R. Schwalm, Dual-curing of waterborne urethane-acrylate coatings by UV and thermal processing, Macromol. Mater. Eng. 288 (1) (2003) 17–28, http://dx.doi.org/10.1002/mame.200290029.

[7] S. Simić, B. Dunjić, S. Tasić, B. Božić, D. Jovanović, I. Popović, Synthesis and characterization of interpenetrating polymer networks with hyperbranched polymers through thermal-UV dual curing, Prog. Org. Coat. 63 (1) (2008) 43–48, http://dx.doi.org/10.1016/j.porgcoat.2008.04.006.

[8] D.P. Nair, N.B. Cramer, J.C. Gaipa, M.K. McBride, E.M. Matherly, R.R. McLeod, R. Shandas, C.N. Bowman, Two-stage reactive polymer network forming systems, Adv. Funct. Mater. 22 (7) (2012) 1502–1510, http://dx.doi.org/10.1002/adfm.201102742.

[9] Q. Lian, Y. Li, T. Yang, K. Li, Y. Xu, L. Liu, J. Zhao, J. Zhang, J. Cheng, Study on the dual-curing mechanism of epoxy/allyl compound/sulfur system, J. Mater. Sci. 51 (17) (2016) 7887–7898, http://dx.doi.org/10.1007/s10853-016-0044-z.

[10] C. Acebo, X. Fernández-Francos, X. Ramis, À. Serra, Multifunctional allyl-terminated hyperbranched poly(ethyleneimine) as component of new thiol–ene/thiol–epoxy materials, React. Funct. Polym. 99 (2016) 17–25, http://dx.doi.org/10.1016/j.reactfunctpolym.2015.12.003.

[11] D. Guzmán, X. Ramis, X. Fernández-Francos, À. Serra, Preparation of click thiol-ene/thiol-epoxy thermosets by controlled photo/thermal dual curing sequence, RSC Adv. 5 (2015) 101623–101633, http://dx.doi.org/10.1039/c5ra22055f.

[12] G. González, X. Fernández-Francos, À. Serra, M. Sangermano, X. Ramis, Environmentally-friendly processing of thermosets by two-stage sequential aza-Michael addition and free-radical polymerization of amine–acrylate mixtures, Polym. Chem. 6 (2015) 6987–6997, http://dx.doi.org/10.1039/c5py00906e.

[13] R.A. Ortiz, A.E.G. Valdéz, L.B. Duarte, R.G. Santos, L.R.O. Flores, M.D. Soucek, Development and study of a coupling agent for photocurable hybrid thiol/ene/cationic formulations, Macromol. Chem. Phys. 209 (20) (2008) 2157–2168, http://dx.doi.org/10.1002/macp.200800305.

[14] H.C. Kolb, M.G. Finn, K.B. Sharpless, Click chemistry: diverse chemical function from a few good reactions, Angew. Chem. Int. Ed. 40 (11) (2001) 2004–2021.

[15] J.E. Moses, A.D. Moorhouse, The growing applications of click chemistry, Chem. Soc. Rev. 36 (2007) 1249–1262, http://dx.doi.org/10.1039/B613014N.

[16] W.H. Binder, R. Sachsenhofer, "Click" chemistry in polymer and materials science, Macromol. Rapid Commun. 28 (1) (2007) 15–54, http://dx.doi.org/10.1002/marc.200600625.

[17] C.E. Hoyle, A.B. Lowe, C.N. Bowman, Thiol-click chemistry: a multifaceted toolbox for small molecule and polymer synthesis, Chem. Soc. Rev. 39 (2010) 1355–1387, http://dx.doi.org/10.1039/b901979k.

[18] J. Shin, H. Matsushima, C.M. Comer, C.N. Bowman, C.E. Hoyle, Thiol-isocyanate-ene ternary networks by sequential and simultaneous thiol click reactions, Chem. Mater. 22 (8) (2010) 2616–2625, http://dx.doi.org/10.1021/cm903856n.

[19] D.P. Nair, M. Podgórski, S. Chatani, T. Gong, W. Xi, C.R. Fenoli, C.N. Bowman, The thiol-Michael addition click reaction: a powerful and widely used tool in materials chemistry, Chem. Mater. 26 (1) (2014) 724–744, http://dx.doi.org/10.1021/cm402180t.

[20] A. Brändle, A. Khan, Thiol–epoxy "click" polymerization: efficient construction of reactive and functional polymers, Polym. Chem. 3 (2012) 3224, http://dx.doi.org/10.1039/C2PY20591B.

[21] K. Jin, W.H. Heath, J.M. Torkelson, Kinetics of multifunctional thiol-epoxy click reactions studied by differential scanning calorimetry: effects of catalysis and functionality, Polymer 81 (2015) 70–78, http://dx.doi.org/10.1016/j.polymer.2015.10.068.

[22] R.M. Loureiro, T.C. Amarelo, S.P. Abuin, E.R. Soulé, R.J.J. Williams, Kinetics of the epoxy-thiol click reaction initiated by a tertiary amine: calorimetric study using monofunctional components, Thermochim. Acta 616 (2015) 79–86, http://dx.doi.org/10.1016/j.tca.2015.08.012.

[23] X. Fernández-Francos, A.O. Konuray, A. Belmonte, S. De la Flor, À. Serra, X. Ramis, Sequential curing of off-stoichiometric thiol–epoxy thermosets with a custom-tailored structure, Polym. Chem. 7 (2016) 2280–2290, http://dx.doi.org/10.1039/C6PY00099A.

[24] M.S. Heise, C. Martin, Curingmechanism and thermal properties of epoxy-imidazole systems, Macromolecules 22 (1) (1989) 99–104, http://dx.doi.org/10.1021/ma00191a020.

[25] S. Vyazovkin, N. Sbirrazzuoli, Mechanism and kinetics of epoxy-amine cure studied by differential scanning calorimetry, Macromolecules 29 (6) (1996) 1867–1873, http://dx.doi.org/10.1021/ma951162w.

[26] R. Sengupta, S. Chakraborty, S. Bandyopadhyay, S. Dasgupta, R. Mukhopadhyay, K. Auddy, A.S. Deuri, A short review on rubber/clay nanocomposites with emphasis on mechanical properties, Engineering 47 (11) (2007) 21–25, http://dx.doi.org/10.1002/pen.20921.

[27] D. Guzmán, X. Ramis, X. Fernández-Francos, À. Serra, New catalysts for diglycidyl ether of bisphenol a curing based on thiol-epoxy click reaction, Eur. Polym. J. 59 (2014) 377–386, http://dx.doi.org/10.1016/j.eurpolymj.2014.08.001.

[28] X. Lu, R.A. Weiss, Relationship between the glass transition temperature and the interaction parameter of miscible binary polymer blends, Macromolecules 25 (12) (1992) 3242–3246, http://dx.doi.org/10.1021/ma00038a033.

[29] D.C. Timm, A.J. Ayorinde, R.F. Foral, Epoxy mechanical properties: function of crosslink architecture, Poylm. Int. 17 (2) (1985) 227–232, http://dx.doi.org/10.1002/pi.4980170226.

[30] M. Shimbo, M. Ochi, Y. Shigeta, Shrinkage and internal stress during curing of epoxide resins, J. Appl. Polym. Sci. 26 (7) (1981) 2265–2277, http://dx.doi.org/10.1002/app.1981.070260714.

[31] D. Santiago, A. Fabregat-Sanjuan, F. Ferrando, S. De la Flor, Recovery stress and work output in hyperbranched poly(ethyleneimine)-modified shape-memory epoxy polymers, J. Polym. Sci. B Polym. Phys. 54 (2016) 1002–1013, http://dx.doi.org/10.1002/polb.24004.

[32] Y. Tanaka, J.L. Stanford, R. Stepto, Interpretation of gel points of an epoxy-amine system including ring formation and unequal reactivity: reaction scheme and gel-point prediction, Macromolecules 45 (17) (2012) 7186–7196, http://dx.doi.org/10.1021/ma300984u.

[33] Y. Tanaka, J.L. Stanford, R. Stepto, Interpretation of gel points of an epoxy-amine system including ring formation and unequal reactivity: measurements of gel points and analyses on ring structures, Macromolecules 45 (17) (2012) 7197–7205, http://dx.doi.org/10.1021/ma3009838.

[34] A. Pizzi, Principles of polymer networking and gel theory in thermosetting adhesive formulations, Handbook of Adhesive Technology, 2nd edn. Marcel Dekker Inc, New York, 2003.

[35] A. Belmonte, D. Guzmán, X. Fernández-Francos, S. De la Flor, Effect of the network structure and programming temperature on the shape-memory response of thiol-epoxy “Click” systems, Polymers 7 (10) (2015) 2146–2164, http://dx.doi.org/10.3390/polym7101505.

UNIVERSITAT ROVIRA I VIRGILI
DESIGN AND CHARACTERIZATION OF ACTIVELY-MOVING POLYMERS OBTAINED VIA DUAL-CURING PROCESSING
Alberto Francisco Belmonte Parra

IV.3 Epoxy-based shape-memory actuators obtained via dual-curing of off-stoichiometric "thiol-epoxy" mixtures

Polymers, **2017**, 9, 113

Alberto Belmonte[1], Claudio Russo[1,2], Veronica Ambrogi[2,3], Xavier Fernández-Francos[4] and Silvia De la Flor[1]

1) Department of Mechanical Engineering, Universitat Rovira i Virgili, Av. Països Catalans 26, 43007 Tarragona, Spain.

2) Department of Chemical, Materials and Production Engineering, University of Naples "Federico II", Piazzale Tecchio, 80, 80125 Napoli, Italy.

3) Institute for Polymers, Composites and Biomaterials, National Research Council of Italy, Via Campi Flegrei, 34, 80078 Pozzuoli, Italy.

4) Thermodynamics Laboratory, ETSEIB, Universitat Politècnica de Catalunya, Av. Diagonal 647, 08028 Barcelona, Spain.

UNIVERSITAT ROVIRA I VIRGILI
DESIGN AND CHARACTERIZATION OF ACTIVELY-MOVING POLYMERS OBTAINED VIA DUAL-CURING PROCESSING
Alberto Francisco Belmonte Parra

Abstract

In this work, epoxy-based shape-memory actuators have been developed by taking advantage of the sequential dual-curing of off-stoichiometric "thiol–epoxy" systems. Bent-shaped designs for flexural actuation were obtained thanks to the easy processing of these materials in the intermediate stage (after the first curing process), and successfully fixed through the second curing process. The samples were programmed into a flat temporary shape and the recovery-process was analysed in unconstrained, partially-constrained and fully constrained conditions using a dynamic mechanical analyser (DMA). Different "thiol–epoxy" systems and off-stoichiometric ratios were used to analyse the effect of the network structure on the actuation performance. The results evidenced the possibility to take advantage of the flexural recovery as a potential actuator, the operation of which can be modulated by changing the network structure and properties of the material. Under unconstrained-recovery conditions, faster and narrower recovery-processes (an average speed up to 80 %/min) are attained by using materials with homogeneous network structure, while in partially- or fully constrained conditions, a higher crosslinking density and the presence of crosslinks of higher functionality lead to a higher amount of energy released during the recovery-process, thus, increasing the work or the force released. Finally, an easy approach for the prediction of the work released by the shape-memory actuator has been proposed.

Keywords: dual-curing; shape-memory polymer; actuator; thiol–epoxy; click chemistry; unconstrained; partially-constrained; fully constrained.

1. Introduction

Shape-memory polymers (SMPs) are those materials capable of attaining and retaining a temporary shape during a long period of time upon a so-called programming process. The programming process usually consists of a thermomechanical process in which the material is firstly heated up to a temperature close to or above a network structural transition (T_{prog}), then mechanically deformed to produce a desired shape, and finally cooled down to a temperature below the network structural transition while keeping the applied deformation so that the programmed shape can be retained after removal of the mechanical load[1]. Therefore, the shape-memory capability of a polymer is not an intrinsic property of the polymer, but an external procedure is necessary. Nevertheless, it demands specific network structural properties. Soft and hard phases must coexist within the network, the hard phase responsible for

memorizing the permanent shape and the soft phase allowing the shape-transformation[2,3]. One of the most usual SMPs are glassy, covalently or physically crosslinked polymers, therefore the crosslinks are the hard phase and the glass transition or melting process responsible for the shape-transformation is driven by the flexible chains or soft phase[4].

Over the last years, two main branches of research have been the focus of the scientific community: on one side, the enhancement and control of the shape-memory response (SMR) by adjusting network structural parameters, changing programming and recovery conditions and modeling the behaviour[5–9]; on the other side, the development of new and challenging SMPs in order to fulfil some inherent issues, such as the need of programming after each cycle[10,11]. Nevertheless, one of the main issues lies in the development of SMPs with complex designs demanded in a wide range of industrial applications, such as structural, aerospace and nautical applications or in the development of bio-inspired devices[12,13]. In such applications, the material is commonly required to work in aggressive environments; thus, high thermal and mechanical resistance are of utmost relevance. Epoxy-based thermosets are widely used in this field of applications due to the high thermal and mechanical resistance, great insulation properties and good chemical resistance[14]. Moreover, epoxy-based SMPs have shown excellent response, with high fixation and recovery ratios as well as rapid and tuneable recovery-processes[15,16]. In this sense, they are excellent candidates to fulfil the operational requirements of such applications. However, the development of complex-shaped designs is a great challenge due to the hard control of the crosslinking during the curing process of epoxy resins making difficult further processing. One approach to overcome the curing limitations lies in the use of the so-called vitrimers[17,18], crosslinked polymers which, upon thermal treatment, can modify their chemical bonds to adopt a new permanent shape. Nevertheless, this process demands high consumption of energy for the network reconfiguration to take place and could lead to undesired final properties. Our research group has recently shown an effective approach to obtain complex-shaped epoxy-based materials through a two-stage curing procedure. The sequential dual-curing of off-stoichiometric “thiol–epoxy” mixtures using tertiary amines as catalyst leads to the formation of an intermediate, stable, solid-like and conformable material after an initial and low energy consuming polymerization process (the “thiol-epoxy” polycondensation), that can be further processed into several complex shapes which are fixed through a second polymerization step triggered at higher temperature (the epoxy homopolymerization of the remaining epoxy groups)[19,20].

The great advantage on using such dual-curing methodology is the possibility of preparing materials with easy and efficient control of the final network structural properties, enhancing the thermomechanical properties of the common click "thiol–epoxy" thermosets. Through different "thiol" and "epoxy" compounds and varying the "thiol–epoxy" ratio of the off-stoichiometric mixture, a wide range of materials are produced: from low to highly crosslinked network structures, homogeneous and tailored glass transition processes and highly deformable glassy materials[19]. Moreover, these materials are potential candidates for shape-memory applications. On the one hand, it has been shown that the "thiol-epoxy" network leads to SMPs with enhanced response: high performance fixing and recovering the original shape, rapid recovery-process, high strength and extended deformation limits[21–23]. On the other hand, thanks to the possibility of forming complex-shaped designs, the final material is an interesting candidate for many of the mentioned applications.

To this end, in this study, we focus on the characterization of these materials as potential shape-memory polymers for actuation purposes. Shape-memory actuators are widely used in industrial applications as smart mechanisms for autonomous control. Taking into account that real operational scenarios usually involve flexural instead of tension or compression actuation designs, bent-shaped SMPs with different network structural properties have been processed from the intermediate material. The performance has been analysed using the DMA equipment, which allows precise analysis and total control in flexural mode. In order to fully characterize the shape-memory response as an actuator, experiments in unconstrained, partially-constrained and fully constrained conditions have been carried out, thus, from completely free-recovery conditions, passing through real situations in which the SMP behaves against an external force, to the fully impeded condition in which a recovery-force instead of shape-transformation is generated. Moreover, in order to enhance and evaluate the actuation performance, a highly functional epoxy resin, Epon™ SU8, has been incorporated in a specific amount to the "thiol-epoxy" networks. It is known that the increase of the crosslinking density and the nature of the crosslinks have a crucial effect in the efficiency storing and releasing the energy associated to the shape-memory effect (SME)[5,24,25]. Taking into account the above, the incorporation of a large and spatially hindered molecule chemically attached to the network is expected to enhance the actuation performance.

2. Experimental section

Materials and methodology

Diglycidyl ether of bisphenol A (DGEBA, GY240, Huntsman, Everberg, Belgium) with an epoxy equivalent weight of 182 g/eq was used as the main epoxy resin. EPON™ resin SU8 with an epoxy equivalent average weight of 215 g/eq was used as a highly functional network modifier (average functionality of 8 epoxy groups per molecule) in a molar proportion of 3:7 (SU8:DGEBA). Pentaerythritoltetrakis (3-mercaptopropionate) (S4) with a thiol equivalent weight of 122.17 g/eq and trimethylolpropane tris(3-mercaptopropionate) (S3) with a thiol equivalent weight of 132.85 g/eq (Sigma-Aldrich, St. Louis, MO, USA) were used as curing agents in an under-stoichiometric proportion with respect to the epoxy groups in the system. 1-methylimidazole (1MI) with a molecular weight of 82.1 g/mol (Sigma-Aldrich, St. Louis, MO, USA) was used as catalyst in a proportion of 1 phr (parts of catalyst per hundred parts of the whole mixture). The DGEBA was dried under vacuum overnight at 80 °C before use. The other reagents were used as received without further purification.

Different off-stoichiometric "thiol–epoxy" systems were chosen in order to study the SMR in relation with the network structural properties. The composition of the different formulations is shown in Table IV-4. According to our previous work[19], mixtures of DGEBA with both S3 and S4 thiol compounds separately, were chosen as the main systems of study. In addition, the SU8 resin was added in a specific proportion to the S3-DGEBA system in order to study the effect of incorporating a highly functional and large molecule in the network structure with the SMR. The SU8:DGEBA weight ratio was 3:7 to ensure a substantial increase of the T_g and crosslinking density while avoiding the formation of extremely brittle materials. The S4-DGEBA system was not considered due to the formation of extremely brittle materials when adding very small amounts of SU8 which do not satisfy the requirements for shape-memory purposes.

Table IV-4. Composition of the different formulations of study.

System	Critical ratio (r_c)[a]	"Thiol-Epoxy" ratio	Thiol (wt. %)	DGEBA (wt. %)	SU8 (wt. %)	1MI (wt. %)
S3-DGEBA	0.65	0.65	31.86	67.15		0.99
		0.75	35.03	63.98		0.99
		0.85	37.91	61.10		0.99
S4-DGEBA	0.5	0.60	28.43	70.58		0.99
		0.70	31.65	67.36		0.99
		0.80	34.59	64.42		0.99
S3-SU8-DGEBA	0.38	0.60	29.14	46.58	23.58	0.99
		0.70	32.42	44.42	22.49	0.99
		0.80	35.42	42.45	21.49	0.99

[a] Experimentally determined from rheological analysis.

For each system, different "thiol–epoxy" ratios were chosen to study the effect of increasing the amount of epoxy excess with the SMR. Taking advantage of the characterization done in our previous work[19], the ratios were selected from the critical ratio (r_c), which is the minimum "thiol-epoxy" ratio to form a gelled and therefore solid-like and conformable intermediate material after the 1st curing stage, up to a ratio in which both, the intermediate and final materials, have very similar properties and therefore the duality of the system is lost in terms of applicability. From the experimental data, it has been considered r = 0.9 the upper limit. In this way, all the formulations of study allow the processing of bent-shaped designs for the further shape-memory characterization as actuators. The r_c of the new system of study (S3-SU8-DGEBA) has been determined following the same experimental procedure as in our previous work[19]: intermediate materials cured from the theoretical r_c (calculated using the Flory equation) were heated up and the physical behaviour observed. Non-gelled networks lead to undesired material flow and therefore shape-loosing. By increasing the "thiol-epoxy" ratio, the flow is reduced until no shape-losing is appreciated. This ratio is then checked through rheological analysis to confirm that gelation is taking place and therefore it is stipulated as the r_c. The r_c of the three systems of study are summarized in Table IV-4.

Once the r_c are determined, the "thiol-epoxy" ratios of study have been experimentally determined by trial and error as follows: starting from $r = r_c$ and increasing by 0.05, bent-shaped samples were prepared, and a flat temporary shape was programmed following the shape-memory programming procedure explained in the next section. In some systems, samples with ratios too close to r_c could not allow such level of deformation during the programming process and broke. The first ratio in which the sample did not break was stipulated as the initial ratio. From

this ratio, increasing by 0.1 each time, the other formulations were defined until $r \leq 0.9$. Therefore, the selected formulations of study are (S3-DGEBA-r = 0.65/0.75/0.85), (S4-DGEBA-r = 0.6/0.7/0.8) and (S3-SU8-DGEBA-r = 0.6/0.7/0.8). As can be seen, the role of the epoxy excess in the deformation level is the crucial parameter in these systems. Regardless of r_c, in both S4-DGEBA and S3-SU8-DGEBA, working at $r < 0.6$ leads to very brittle materials for such deformation level.

The formulations without SU8 were prepared by pouring the compounds in a glass vial and manually stirring until a homogeneous liquid was attained. In the case of the formulation containing SU8, the DGEBA and SU8 resins were previously mixed by dissolving them in dichloromethane to ensure a homogeneous and compatible mixture. The solvent was then released under vacuum, stirring and temperature. Afterwards, the mixture was cooled down to room temperature and the S3 and 1MI reagents were poured in and the whole mixture manually stirred.

Sample processing

Taking advantage of the sequential dual-curing system, it is possible to obtain complex-shaped materials in an easy, efficient and most important, reproducible manner. In this study, bent-shaped SMPs have been processed in order to analyse the SMR in flexural mode; from a flat temporary shape to the original bent-shape, thus, recreating one of the most usual working designs of an actuator. The entire process to obtain the bent-shaped samples is depicted in Figure IV-13. First, the initial mixture is prepared as described in the previous section. Once the mixture is prepared, it is rapidly poured into a mould to obtain an intermediate prismatic-shaped material with specific dimensions. The first curing stage is carried out at 50 °C during 3 h to ensure the completion of the "thiol–epoxy" polycondensation[20]. Afterwards, thanks to the high deformability of the intermediate material, it is easily moulded onto a metallic cylinder of 40 mm diameter covered with a Teflon layer to obtain the desired level of curvature in the sample. The Teflon layer avoids the sample adhesion onto the metallic surface after the second curing stage. Then, in order to impede the recovery of the original shape due to the viscoelastic response during the temperature increase for the second curing stage, the sample is fastened with minimal force (using sticky Teflon film) onto the cylinder surface. Finally, the second curing stage is carried out at 120 ºC for 1 h followed by 1 h at 150 ºC to ensure the completion of the epoxy homopolymerization[20].

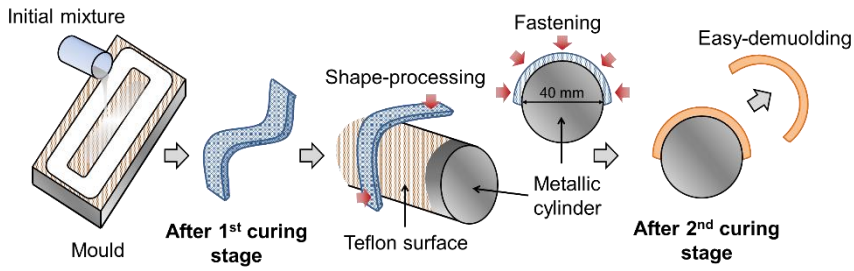

Figure IV-13. Illustration of the bent-shaped sample processing: from the initial liquid mixture to the final solid bent-shaped material.

Once the sample is prepared, it is polished in order to eliminate any defects in the surface and to fit the specific dimensions, thus ensuring reproducibility and making possible a safe and meaningful comparison between samples from different formulations and experimental conditions. In Figure IV-14, a scheme of the sample final dimensions and a photograph of the bent-shaped samples are shown. The deflection, "*d*", is determined from the lower side of the sample and the other dimensional parameters as schematized.

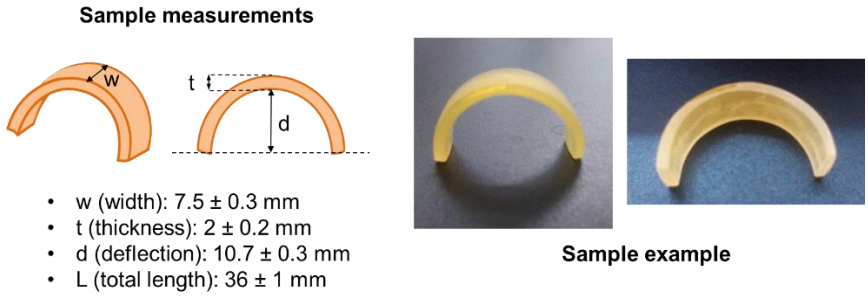

Figure IV-14. Bent-shaped sample measuring definitions and a photograph of the final sample.

Thermomechanical characterization

The S3-SU8-DGEBA system was characterized using a Differential Scanning Calorimeter (DSC) Mettler 821e, calibrated with indium standards. A preliminary characterization of the curing process of S3-SU8-DGEBA formulations was carried at 10 °C/min. Materials with different "thiol-epoxy" ratios ranging from 0 to 1 (0/0.25/0.5/0.75/1) were prepared and analysed following the same procedure as for the S3-DGEBA and S4-DGEBA systems in our previous work[19]. The intermediate materials were cured in a conventional oven at 50 °C during 3 h. Then, a piece of around 5 mg was analysed in the DSC from −50 °C up to 100 °C at 10 °C/min. For the final materials, after the 3 h of curing at 50 °C in the

oven, a post-curing of 1 h at 120 °C followed by 1 h at 150 °C was imposed and then a piece of around 5 mg was analysed in the DSC from 30 °C up to 200 °C at 10 °C/min. The glass transition temperatures of the intermediate and final materials were determined as the halfway point in the heat capacity step taking place during the glass transition.

Dynamic-mechanical analysis of the formulations of study (S3-DGEBA-r = 0.65/0.75/0.85), (S4-DGEBA-r = 0.6/0.7/0.8) and (S3-SU8-DGEBA-r = 0.6/0.7/0.8) were performed using a DMA Q800 TA Instruments, equipped with a 3-point-bending clamp (15 mm), in oscillation mode at 1 Hz and 0.1% of amplitude strain and imposing a temperature ramp of 3 °C/min. The glassy (E_g) and rubbery (E_r) moduli were determined at 40 °C and T_g + 30 °C, respectively. The T_g was determined as the tanδ peak temperature. The height of the peak and width at half-height (FWHM) of the tanδ curve were also determined. The relation between E_g and E_r was calculated as a measure of the SMR (efficiency fixing the temporary shape and recovering the original shape).

Shape-memory characterization

The shape-memory characterization was divided in two steps: programming of the temporary shape and recovery of the original shape. For the programming of the temporary shape, a tailor-made device consisting of male and female stainless-steel plates of 15 x 8 cm^2 of surface was used. In order to produce an equal, homogeneous and controlled pressure over the sample during the programming, the thickness of the female part was fitted to weigh 0.5 kg. The programming procedure is schematized in Figure IV-15: the male part of the device with the bent sample placed on it, and the female part were introduced separately in a preheated oven at the programming temperature T_{prog} = T_g + 30 °C and held during 30 min for thermal stabilization in order to ensure that the network structure of the material is fully relaxed before programming. Afterwards, the female part of the device was fitted to the male part, and its weight produced the flattening of the sample. The whole assembly was placed immediately inside a bath with cold water for 1 min to ensure that the sample temperature decreased below the network relaxation temperature and therefore fix the temporary shape. Finally, the female part was removed, and the flat sample was wiped dry using a paper towel.

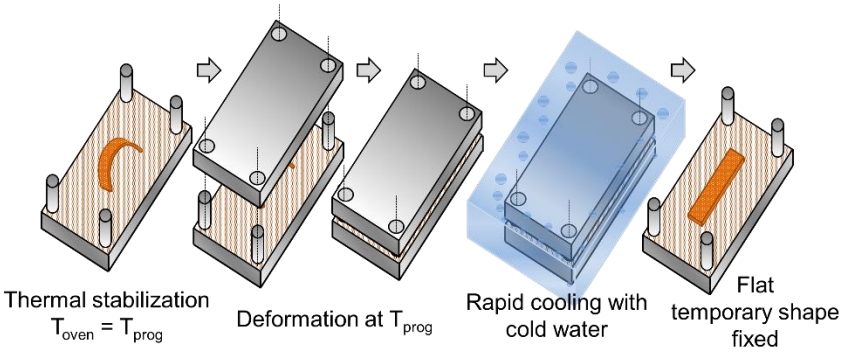

Figure IV-15. Illustration of the shape-memory programming process.

Once the samples were programmed, the recovery of the original shape was carried out using the DMA equipped with the compression clamp (diameter of 40 mm) at different operational modes depending on the experiment performed: unconstrained, partially-constrained or fully constrained recovery conditions. The sample mounting, and the recovery analysis is depicted in Figure IV-16: in unconstrained-recovery experiments, the DMA was set in Force-controlled mode and a minimal force of 0.01 N was imposed to register the recovery-process. The displacement of the moveable clamp, $d_y(T)$, was recorded as a measure of the shape-recovery (SR), which was determined applying equation (IV-5). It should be note that in equation (IV-5) the maximum displacement is defined by the deflection, "d", of the original shape.

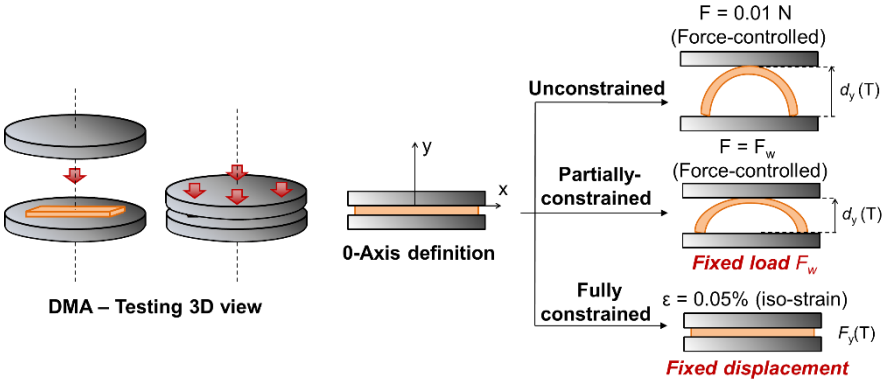

Figure IV-16. Illustration of the DMA testing procedure including the different recovery scenarios.

The instantaneous shape-recovery speed, $SR_{speed}(T)$, was calculated using equation (IV-6) as a measure of the shape-recovery sharpness. Using the $SR_{speed}(T)$ curve, the temperature at which the

maximum recovery speed is found was determined as the peak of the curve (T_{peak}), and the duration of the process as the width of the curve at half-height (ΔT_{peak}). Additionally, common shape-memory quantifiers, such as, the shape-recovery rate (V_r) and the shape-recovery ratio (R_r) were determined for comparison purposes among the different formulations. V_r was determined from $SR(T_1)$ = 0.15 to $SR(T_2)$ = 0.85 applying equation (IV-7) and R_r applying equation (IV-8), where $d_y(T_{end})$ is the displacement reached by the moveable clamp at the end of the recovery-process.

$$SR(T) = 1 - \frac{d - d_y(T)}{d} \quad \text{(IV-5)}$$

$$SR_{speed}(T) = \frac{\partial SR(T)}{dT} \quad \text{(IV-6)}$$

$$V_r = \frac{SR_{15\%-85\%}}{\Delta T_{SR_{15\%-85\%}}} \cdot \frac{dT}{dt} \quad \text{(IV-7)}$$

$$R_r = \frac{d_y(T_{end})}{d} \cdot 100 \quad \text{(IV-8)}$$

The partially-constrained experiments were carried out in Force-controlled mode applying a constant force (F_w) equal in all the experiments. The displacement of the moveable clamp was recorded, and the shape-recovery was measured using equation (IV-5). Applying equation (IV-6), the $SR_{speed}(T)$ curve was calculated and both T_{peak} and ΔT_{peak} were determined as explained above. Additionally, the relative work, W_{rel}, developed by the sample was determined both, experimentally and theoretically, using equation (IV-9) (in mN·mm/mm). In this expression, the final displacement reached, $d_y(T_{end})$, has been normalized with respect to the maximum displacement, "*d*", for comparison purposes.

$$W_{rel} = F_w \cdot \frac{d_y(T_{end})}{d} \quad \text{(IV-9)}$$

For the calculus of the theoretical relative work, W_{rel}^t, it has been taken into account that all the force given by the sample during the SME is equal to the force given to program the sample into the temporary shape (F_{prog}). F_{prog} can be approached using the beam deflection formula for small deformations given by equation (IV-10).

$$F_{prog} = \frac{4 \cdot (d + \frac{t}{2}) \cdot E_{(T_{prog})} \cdot w \cdot t^3}{L^3} \quad \text{(IV-10)}$$

where "*d*" is the deflection of the sample, $E(T_{prog})$ is the modulus at the programming temperature, considered constant and equal to the relaxed modulus E_r, and "*w*", "*t*" and "*L*" are the dimensions of the sample (width, thickness and length, respectively). Once F_{prog} is determined, the theoretical displacement reached, $d_y(T_{end})$, can be determined reordering equation (IV-10) into (IV-11) and taking into account the force applied by the DMA, F_w, behaving in opposite direction during the recovery experiment. Then, by simply applying equation (IV-9), W_{rel}^t is determined.

$$d_y(T_{end}) = \frac{\left(F_{prog} - F_w\right)}{4 \cdot L^3 \cdot E_{(T_{prog})} \cdot w \cdot t^3} - \frac{t}{2} \quad \text{(IV-11)}$$

The fully constrained experiments were performed at Iso-Strain mode imposing 0.05% of strain in order to measure the force generated by the sample, $F_y(T)$, during the recovery-process. In the same way as for the unconstrained and partially-constrained experiments, T_{peak} and ΔT_{peak} were determined from the derivative curve, $\partial F_y(T)/\partial T$. As proposed by Li and Wang[26], $F_y(T)$ can be divided in different components as shown in equation (IV-12). $F_{residual}(T)$ is the force generated due to incomplete stress relaxation during the programming process. In our case, it can be neglected since the programming process is performed at $T_{prog} >> T_g$, thus, the sample is able to relax all the structural changes during the programming. $F_{thermal}(T)$ is the force generated due to the thermal expansion of the sample and it depends on the contact area of the sample with the DMA clamp. $F_{SR}(T)$ is the force generated due to the SME during the mechanical relaxation and it depends on the programming and recovery time-temperature conditions.

$$F_y(T) = F_{SR}(T) + F_{residual}(T) + F_{thermal}(T) \quad \text{(IV-12)}$$

The thermal force, $F_{thermal}(T)$, has a crucial role and, in contrast with common experiments carried out in tension mode, it acts in the same direction of the SME. It can be approached by applying equation (IV-13), which takes into account the variation of the modulus with the temperature.

$$F_{thermal} = E(T) \cdot \alpha(T) \cdot (T - T_0) \cdot S_{eff} \quad \text{(IV-13)}$$

where $E(T)$ is the modulus at temperature "*T*", $\alpha(T)$ is the thermal expansion coefficient which can be considered a constant value in the ranges $T < T_g$ and $T > T_g$ (4.5×10^{-5} and 6.0×10^{-6} °C^{-1} respectively, values obtained from common epoxy materials in the literature[27]). T_0 is the initial

temperature (T_0 = 30 °C in all the experiments) and "S_{eff}" is the effective section (section in contact with the DMA clamp). Theoretically, in a compression experiment "S_{eff}" would be the whole contact surface (width x length) of the sample; however, in spite of the good fixation of the temporary shape, some residual shape-recovery takes place, therefore the effective surface approaches a punctual contact instead. To better calculate "S_{eff}", one can take advantage of the force given by the DMA to keep the imposed ε of 0.05%. This force is applied at room temperature and therefore, by simply applying Hooke's law it is possible to obtain the real surface in which it is being applied (see equation (IV-14)).

$$S_{eff} = \frac{F_{DMA}}{E_g \cdot \varepsilon} \quad \text{(IV-14)}$$

where E_g is the modulus in the glassy state (at T_0 = 30 °C) and ε is the imposed deformation in the experiment (0.05%).

Finally, the force generated due to the SME during the mechanical relaxation, $F_{SR}(T)$, has been determined by subtracting $F_{thermal}(T)$ from $F_y(T)$. From this curve, the total shape-recovery force F_{SR} has been determined as the force gained between the onset and offset points. Note that the force generated in fully constrained experiments shows the typical behaviour of the network relaxation processes, thus, an onset and offset points can be defined.

3. Results and discussion

DSC analysis of the dual-curing process

As it was explained in our previous works[19,20], sequential dual-curing systems are attained by preparing different "thiol-epoxy" mixtures in off-stoichiometric proportions. The use of tertiary amines as catalyst allows the separation of both polymerization processes, the initial polycondensation between thiol and epoxy groups and the following homopolymerization of the remaining unreacted epoxy groups. The monomers and expected networks formed after the "thiol-epoxy" polycondensation (1st curing stage) and epoxy homopolymerization (2nd curing stage) are shown in Figure IV-17. As it can be seen, the "thiol-epoxy" click polycondensation takes places rapidly at low temperature, leading to partially-crosslinked network structures. These intermediate materials are stable at room temperature until the temperature is increased, and the remaining epoxy groups react forming a highly crosslinked and less flexible network structure, enhancing the thermomechanical properties of the material.

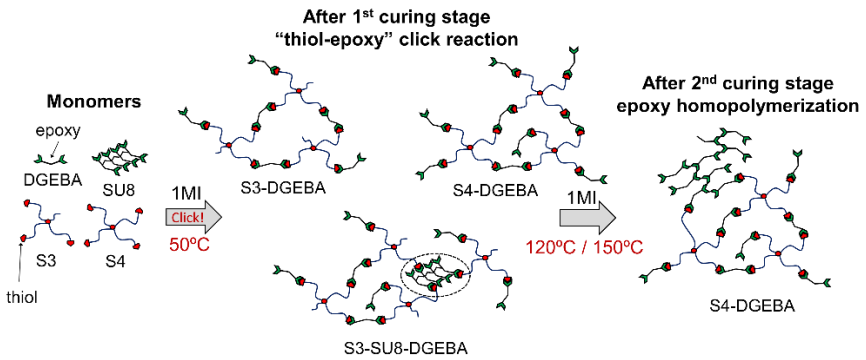

Figure IV-17. Monomers and expected network structures after the first and second curing stages for all the systems of study.

In order to analyse the duality of the new system, the curing process of both S3-SU8-DGEBA and S3-DGEBA systems at different "thiol-epoxy" ratios are illustrated in Figure IV-18. In Figure IV-18(a), the heat flow is plotted as a function of the temperature. The presence of two well-separated peaks is an indication of two sequential polymerization processes taking place, in agreement with our previous results[20]. The first and sharper peak is related to the "click" thiol-epoxy polycondensation, while the broader and smaller peak to the anionic epoxy homopolymerization of the excess epoxy groups. Therefore, the incorporation of SU8 does not affect the duality of the curing process. In Figure IV-18(b) the conversion is plotted as a function of the temperature. Note that the conversion curves (Figure IV-18(b)) have been determined taking into account empirical values of the enthalpy of reaction from the literature: the thiol-epoxy polycondensation (1st curing process) releases around 130 kJ/eq, while the epoxy homopolymerization around 100 kJ/eq[28,29]. Within the experimental error, the contribution of the first process to the total conversion is proportional to the presence of thiol in the mixture and is not affected by the presence of SU8, as could be expected.

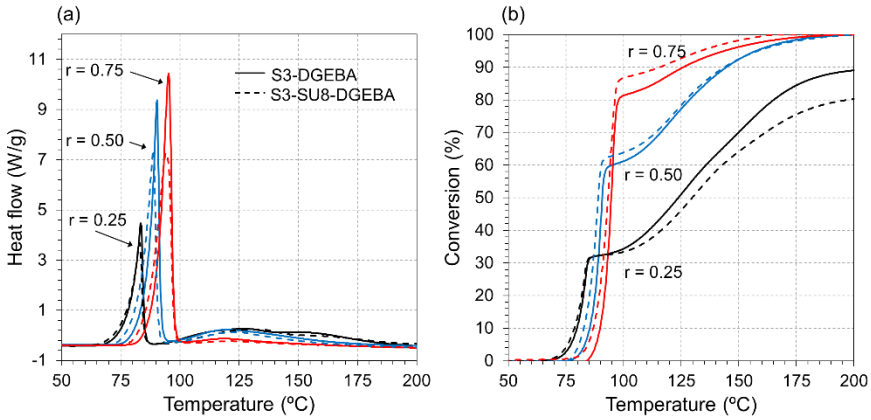

Figure IV-18. DSC traces of the curing process of the S3-SU8-DGEBA system at different "thiol-epoxy" ratios: (a) heat flow trace and (b) conversion trace.

In Table IV-5, the enthalpy values corresponding to each polymerization process are presented. As it can be seen, the "thiol-epoxy" polycondensation (1st curing process) releases around 130 kJ/eq, similar values to the reported one. Nevertheless, during the epoxy homopolymerization, formulations containing high content of epoxy excess (r = 0.25), do not reach the expected enthalpy value. Moreover, this is more evident in the S3-SU8-DGEBA system; the enthalpy per equivalent epoxy is 79.1 kJ/eq, while in the S3-DGEBA system is 84.4 kJ/eq, both of them lower than 100 kJ/eq. This may be caused by topological restrictions in the highly crosslinked homopolymer network, especially in the presence of SU8, leading to incomplete reaction of epoxy groups.

Table IV-5. Reaction heat of the first and second polymerization processes corresponding to the curing of S3-DGEBA and S3-SU8-DGEBA formulations with a thiol:epoxy ratios of 0.25, 0.50 and 0.75.

Formulation	ΔH_{1st} (J/g)	ΔH_{2nd} (J/g)	ΔH_{1st} (kJ/eq)[a]	ΔH_{2nd} (kJ/eq)[a]
S3-DGEBA-0.25	151	291	131.6	84.4
S3-DGEBA-0.50	263	197	132.0	98.7
S3-DGEBA-0.75	348	82	131.9	93.2
S3-SU8-DGEBA-0.25	147	261	133.8	79.1
S3-SU8-DGEBA-0.50	257	190	134.2	99.1
S3-SU8-DGEBA--0.75	347	83	136.3	97.8

[a] Heat flow per equivalent epoxy ($MW_{eq\text{-}epoxy}$ determined as an average value taking into account the DGEBA:SU8 proportion).

Thermomechanical results

In Figure IV-19, the glass transition temperatures (T_g) of the intermediate materials (lower curves) and final materials (upper curves) are shown for all the systems of study at the different "thiol-epoxy" ratios

(the data for S3-DGEBA and S4-DGEBA are taken from our previous work[19]). Overall, two different trends are shown for each material: the T_g of the intermediate materials increase with increasing "thiol-epoxy" ratio due to the decreasing amount of unreacted excess DGEBA at the end of the first stage of the curing process (see schemes in Figure IV-17). In contrast, the T_g of the final materials increases with decreasing "thiol-epoxy" ratio because of the higher contribution of the homopolymerization of the excess epoxy groups. The increase of functionality of the crosslinking agents, S3 and S4, results in somewhat different properties at high "thiol-epoxy" ratios and reduces the critical ratio, r_c. In contrast, the incorporation of the high functional resin SU8 also produces an increase in T_g at lower "thiol-epoxy" ratios and also reduces significantly the critical ratio r_c because of its higher functionality. The T_g of the uncured neat epoxy formulation (without thiol) increases from -23 °C to -1 °C when SU8 is added to the formulation, due to the lower mobility of the highly functional SU8 monomer. The final T_g of the neat epoxy homopolymer increases from 181 °C to 193 °C when SU8 is added. This small increase in the final T_g of the homopolymer can be explained by the fact that conversion of epoxy groups may not be complete due to topological restrictions, as explained in the preceding section. Overall, the possibility to modulate the structural properties of the materials and the critical ratio of the systems by combining different thiol and epoxy compound makes it possible to extend the processing of complex-shaped materials to lower "thiol-epoxy" ratios and therefore makes it possible to get materials with also different structural properties.

Table IV-6 shows the results of the thermomechanical characterization of the cured materials using DMA. In agreement with the above explanation, on decreasing the "thiol-epoxy" ratio, i.e, increasing the amount of epoxy homopolymerization, the T_g of the materials increases significantly. In the same way, the relaxed modulus, E_r, increases and the relaxation process becomes more heterogeneous (FWHM increases and the peak of the tanδ curve decreases). It is well-known that the increase of the crosslinking density leads to higher relaxed modulus and a more heterogeneous network structure with longer relaxation times. The incorporation of a highly functional and rigid epoxy resin (SU8) to the S3-DGEBA system has an evident impact on the structural properties, showing a noticeable increase in E_r and T_g and a significant broadening of the network relaxation process, as deduced from the increase in FWHM (i.e. from 12.1 °C in the S3-DGEBA-0.75 to 22.8 °C in the S3-SU8-DGEBA-0.7) and the decrease in the tanδ peak height.

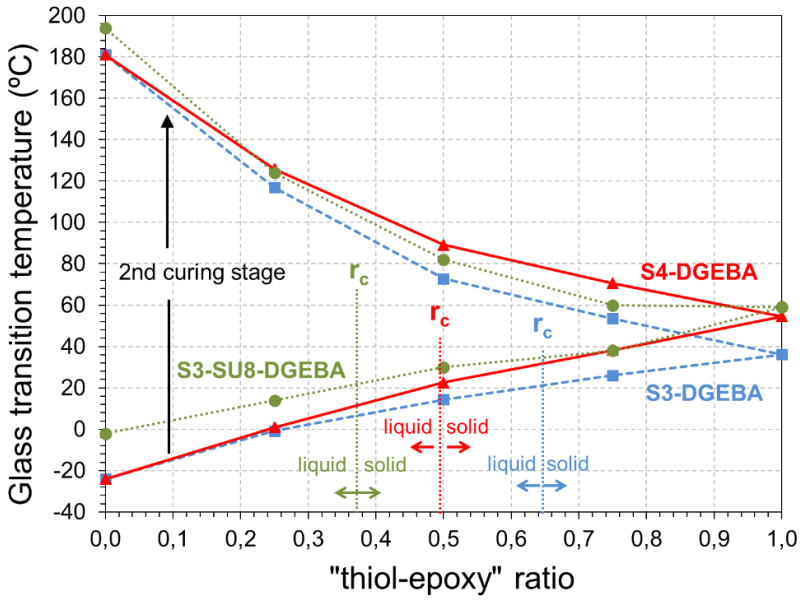

Figure IV-19. Glass transition temperatures and critical ratio for the different systems of study at different "thiol-epoxy" ratios.

In terms of shape-memory properties, the relation E_g/E_r is higher of 100 in all cases; this means two orders of magnitude which is sufficiently high to expect well SMR in terms of shape-fixation and -recovery. This parameter increases with the decrease of E_r on approaching the stoichiometric ratio because, in all these materials, the value of the glassy modulus E_g is similar regardless of the structural differences and therefore the relation is governed by E_r. On the other hand, the homogeneity of the relaxation process (quantified by the breadth of tanδ) gives us an idea of the shape-recovery rate[21]. The S3-SU8-DGEBA materials have broader relaxation processes and therefore it is expected a slower and more gradual recovery-process in comparison with the other systems.

Table IV-6. Thermomechanical and structural properties of the different formulations of study.

Formulation	S3-DGEBA			S4-DGEBA			S3-SU8-DGEBA		
"thiol-epoxy" ratio	0.65	0.75	0.85	0.6	0.7	0.8	0.6	0.7	0.8
E_g (MPa)	2150	2001	2130	2200	2130	2150	2310	2250	2310
E_r (MPa)	10.9	9.6	8.4	18.4	15.1	14.0	19.5	17.3	14.4
T_g^{DMA} (ºC)	80.1	70.0	61.0	98.0	89.0	81.0	96.0	81.0	73.0
FWHM (ºC)	12.8	12.1	11.0	11.5	10.5	10.0	23.0	22.8	21.8
tanδ peak	1.25	1.35	1.46	1.16	1.23	1.30	0.69	0.81	0.92
E_g/E_r	197	208	254	120	141	154	118	130	160

Shape-memory results

As stated in the experimental part, the shape-memory characterization has been studied under three different scenarios (see Figure IV-16). The results of the unconstrained recovery experiments are shown in Figure IV-20 and the parameters of interest summarized in Table IV-7. First, it should be pointed out that all the samples were able to completely recover the original shape, with values of R_r almost equal to 100% in all cases. This can be explained by the safe programming conditions and the sample structural properties of epoxy-based SMPs[16]. The programming was carried out at T_{prog} >> T_g and under mild deformation conditions, therefore completely elastic deformation was imposed, where no damaging processes and no stress relaxation were involved.

Table IV-7. Parameters obtained from the shape-memory analysis (unconstrained, partially-constrained and fully-constrained) of the different formulations studied: Peak temperature (T_{peak}), Width at half-height of the peak (ΔT_{peak}), Recovery-rate (R_r), Relative Work output (W_{rel}) and shape-recovery force (F_{SR}).

	Unconstrained				Fully constrained		
Formulation	R_r (%)	ΔT_{peak} (°C)	T_{peak} (°C)	V_r (%/min)	ΔT_{peak} (°C)	T_{peak} (°C)	F_{SR} (N)
S3-DGEBA-0.65	99.9	2.0	69.7	73.7	5.0	74.0	0.74
S3-DGEBA-0.75	100.0	2.0	62.9	76.7	6.2	64.5	0.76
S3-DGEBA-0.85	99.5	2.3	55.0	80.3	5.4	56.2	0.53
S4-DGEBA-0.60	99.9	1.7	92.3	79.2	7.6	91.0	1.71
S4-DGEBA-0.70	99.9	1.8	81.3	72.1	6.7	81.8	1.42
S4-DGEBA-0.80	99.8	1.8	74.9	79.0	5.6	78.4	1.47
S3-SU8-DGEBA-0.60	99.8	4.9	84.3	34.7	23.9	81.9	2.92
S3-SU8-DGEBA-0.70	99.8	4.8	74.4	37.7	12.4	77.8	1.79
S3-SU8-DGEBA-0.80	99.9	4.1	66.5	45.8	7.0	68.3	0.89

	Partially-constrained		
	ΔT_{peak} (°C)	T_{peak} (°C)	W_{rel} (mN·mm/mm)
S3-DGEBA-0.65	4.0	75.0	57
S3-DGEBA-0.75	4.7	67.2	39
S3-DGEBA-0.85	5.2	56.7	34
S4-DGEBA-0.60	3.7	93.2	187
S4-DGEBA-0.70	4.3	85.7	179
S4-DGEBA-0.80	6.2	79.6	136
S3-SU8-DGEBA-0.60	10.9	87.2	314
S3-SU8-DGEBA-0.70	12.1	77.7	247
S3-SU8-DGEBA-0.80	7.8	67.9	49

The evolutions of the shape-recovery (SR) and recovery speed (SR_{speed}) parameters show a clear difference between the formulations without and with SU8. The shape-recovery process is considerably faster and sharper in the materials without SU8, regardless of the use of S3 or S4

as crosslinking agent. The SR_{speed} curves of S4-DGEBA formulations are slightly taller and narrower than those of S3-DGEBA formulations, but, if one analyses the overall recovery rate V_r (see Table IV-7) it can be seen that they have very similar and high values (70-80 %/min). In contrast, the presence of SU8 leads to lower and broader SR_{speed} curves (ΔT_{peak} increases from 2 °C up to 4-5 °C), and therefore lower V_r values (around 35 %/min). Moreover, the effect of the "thiol-epoxy" ratio is more relevant with the presence of SU8, leading to a clear decrease in V_r from 46% to 35% on increasing the epoxy content from r = 0.8 to r = 0.6 in the S3-SU8-DGEBA system, while this is not that evident in the S3-DGEBA and S4-DGEBA systems. This must be caused by the effect of the strongly hindered homopolymer structure of SU8 in comparison with DGEBA.

Parameters as ΔT_{peak} and T_{peak} are closely related to the glass transition. T_{peak} is commonly close to the T_g nominal value and ΔT_{peak} is related to the breadth of the tanδ curve. As it can be seen, in all the experiments, T_{peak} is placed slightly below T_g^{DMA}: however, it increases with the increase in epoxy content accordingly to the trend observed in the T_g^{DMA}. Moreover, the differences regarding ΔT_{peak} are clearly related to the structural relaxation. As explained above, formulations containing SU8 show higher ΔT_{peak} due to the broader relaxation process as deduced from the FWHM values in Table IV-5. These results point out the close relation between network relaxation and shape-recovery in glassy materials, as previously observed[22].

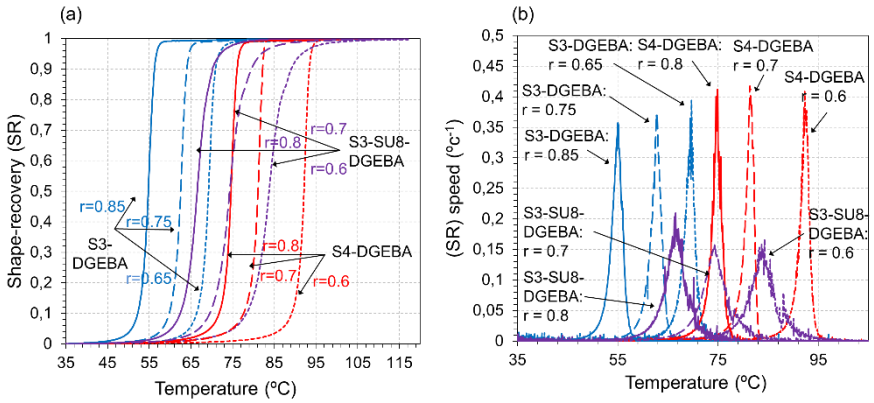

Figure IV-20. Shape-memory unconstrained recovery experiments: (a) shape-recovery as function of temperature; and (b) derivative of shape-recovery with respect to temperature (SR_{speed}) as function of temperature.

Fully constrained experiments were carried out to determine the response of the material under a completely impeded scenario. The DMA was set in Iso-Strain mode and the force, F_y(T), generated by the sample

during the recovery-process was recorded. The results are shown in Figure IV-21 and the parameters of interest summarized in Table IV-7. In a similar way to the SR_{speed} (Figure IV-20(b)), the force rate, $\partial F_y/\partial T$, in (N/°C) has been determined and presented as small side graphics on the right side of the figure for all the formulations under study.

The recovery-process can be divided into three different sections (see Figure IV-21(a)). First, there is a constant increase of the force mostly related to the thermal expansion of the material at temperatures below T_g. Then, on approaching to T_g, the material undergoes an initial relaxation process caused by the lowering of the modulus followed by a drastic increase of the force due to the SME. This is clearly appreciated in the N/°C graphics on Figure IV-21(b), showing an initial and small decreasing peak followed by a drastic increasing peak. Finally, the force slightly increases probably due to the thermal expansion at temperatures above T_g. The effect of the network structure is clearly appreciated in the homogeneity of the recovery-process, as deduced from the shape of the $\partial F_y/\partial_T$ curves (Figure IV-21(b)). Formulations containing SU8 show broader and slower processes, while S3-DGEBA and S4-DGEBA systems have sharper and faster processes. Moreover, the effect of the presence of the SU8 molecule is clearly appreciated; on decreasing the ratio to 0.6 in the S3-SU8-DGEBA system, up to three peaks appears during the SME, pointing out the complex relaxation process produced by the presence of SU8 in the thiol-epoxy and epoxy homopolymer networks.

On analysing the parameters obtained from $\partial F_y/\partial T$, it can be seen that both, ΔT_{peak} and T_{peak}, are clearly related to the glass transition process and network structural properties, in accordance with the unconstrained experiments. Nevertheless, the magnitude of ΔT_{peak} is considerably higher in all the formulations of study. Moreover, the differences regarding the content of SU8 are more evident in the S3-SU8-DGEBA system, ΔT_{peak} increases from 7 °C at r = 0.8 to 23.9 °C at r = 0.6. This suggests that in completely impeded scenarios, differences regarding the crosslinking points are more relevant than in unconstrained experiments[30], and that, overall, the recovery-process is extended longer.

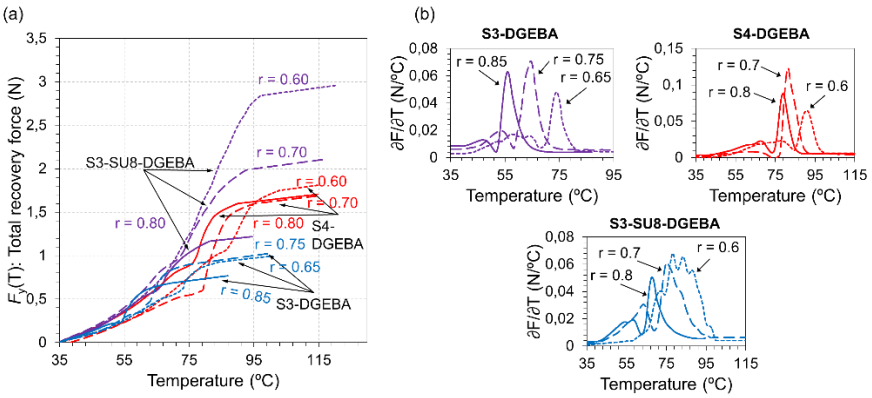

Figure IV-21. Shape-memory fully constrained recovery experiments: (a) force generated as a function of the temperature; and (b) derivative of the force generated with respect to the temperature as a function of the temperature.

The thermal force, $F_{thermal}$(T), and its effect on F_y(T) is shown in Figure IV-22. In Figure IV-22(a), $F_{thermal}$(T) is plotted as a function of the temperature and subtracted from F_y(T) to obtain the shape-recovery force, F_{SR}(T), for the formulation S4-DGEBA-0.7, while, in Figure IV-22(b), the F_{SR}(T) curves are presented for all the formulations studied. As it can be seen in Figure IV-22(a), the higher contribution of $F_{thermal}$(T) takes place at $T < T_g$; $F_{thermal}$(T) increases until a maximum is reached, and then goes down to a minimum and almost constant value. This is caused by the drastic decrease of the modulus as the material becomes a rubber. Having in mind these results, the resulting curves F_{SR}(T) = F_y(T) - $F_{thermal}$ (Figure IV-22(b)) clearly point out that, as stated above, the thermal expansion is the responsible of the initial increase of F_y(T), while F_{SR}(T) is mainly related to the network relaxation and build-up of stress in the fully impeded recovery process taking place during heating. This result emphasizes the relevance of the thermal expansion in fully constrained experiments at temperatures below T_g and should be taken into account in certain applications to avoid an early undesired actuation.

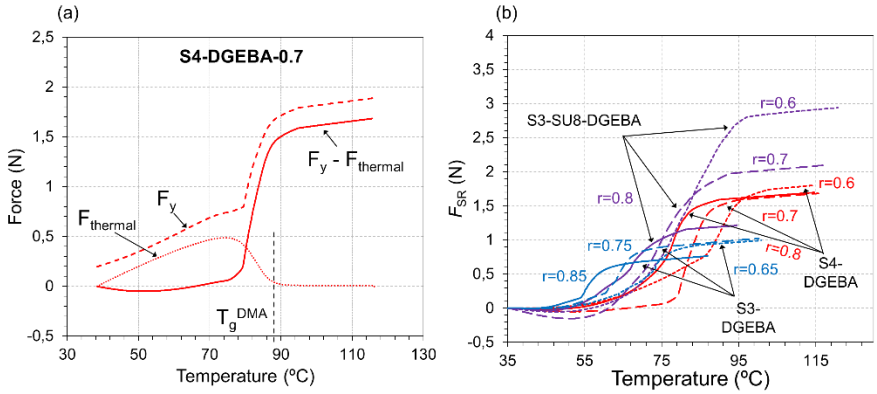

Figure IV-22. Shape-memory fully constrained recovery experiments: (a) thermal force subtraction process; (b) force generated after subtracting the thermal contribution.

The value and evolution of F_{SR} is closely related to the network structural properties. In general, formulations with higher relaxed modulus (see Table IV-5) lead to higher F_{SR} values (SU8 > S4 > S3 see in Table IV-7). However, there is a clear difference in the presence of SU8, which may be connected to its molecular structure. Moreover, on decreasing the ratio in the S3-SU8-DGEBA system, i.e., increasing the epoxy homopolymer content, F_{SR} increases much more than in the other cases.

Partially-constrained experiments were performed to fully characterize the SMR in more realistic applications since most of the SMPs are required to recover their shape working against a force. A constant force, F_w, is applied to the sample and the work done by the sample during the recovery-process is calculated. F_w is fixed to a constant value for all the experiments. As it can be seen in Table IV-7, the minimum force to ensure that all the formulations are able to produce a positive work is 0.5 N (the S3-DGEBA-0.85 gives the minimum F_{SR} value of 0.53 N). The shape-recovery curves (SR) and the shape-recovery instantaneous speed SR_{speed} are shown in Figure IV-23, and the parameters of interest summarized in Table IV-7.

First, it must be noted that all the samples were able to partially recover the original shape, that is, a positive work was produced. The shape of the (SR) curves is similar to that of the unconstrained recovery experiments, but the SR_{speed} curves are broader, as in fully constrained experiments. In contrast, the influence of the crosslinking points is not evident in partially-constrained experiments. ΔT_{peak} is similar or even lower in formulations with higher content of epoxy (i.e. ΔT_{peak} of S3-SU8-DGEBA-0.7 is 12.1, while it goes down to 10.9 in S3-SU8-DGEBA-0.6). In general,

T_{peak} is closely related to T_g^{DMA} in all experimental modes, while ΔT_{peak} increases from unconstrained to fully constrained modes, pointing out an extension of the recovery-process caused by the presence of an external force impeding or making difficult the recovery of the original shape.

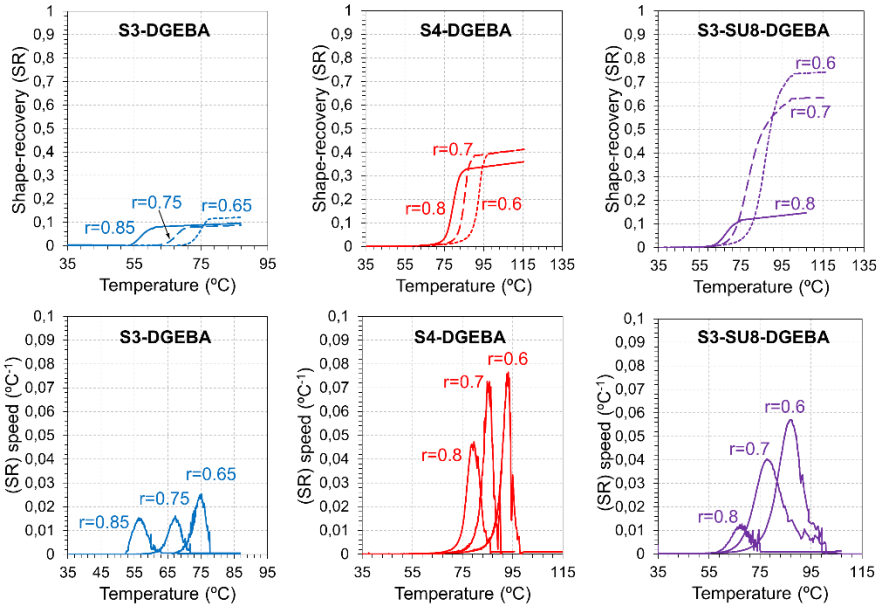

Figure IV-23. Shape-memory partially-constrained recovery experiments: shape-recovery as a function of the temperature.

The experimental relative work and the theoretical relative work, W_{rel}, are shown in Figure IV-24. As mentioned in the experimental section, the work has been normalized to a relative work (mN·mm/mm) in order to allow comparison between samples taking into account the differences in the deflection. The increase in functionality of the crosslinker compound (SU8 > S4 > S3), as well as the presence of the SU8 in the network structure clearly enhance the mechanical performance of the actuator, in line with the results from the fully constrained experiments. W_{rel} increases on increasing F_{SR}, because the sample is able to produce a higher displacement of the clamp during the SME. Moreover, it is clearly appreciated an increasing trend of W_{rel} on decreasing the "thiol-epoxy" ratio in all the systems of study. These results point out that the increase of the crosslinker functionality (the presence of the DGEBA homopolymer) has a positive effect in the force generated during the recovery-process as shown in the fully constrained experiments.

As stated in the experimental part, it is possible to predict the theoretical relative work, W_{rel}^t as follows: the theoretical $d_y(T_{end})$ reached

by the sample during the recovery-process is approached by using expressions (IV-10) and (IV-11) and then W_{relt} is determined by simply applying equation (IV-9) with the predicted $d_y(T_{end})$. Through this methodology, one considers that the sample produces a F_{SR} equal to F_{prog} as no energy losses takes place during the programming and thus, all the programmed force is then released during the recovery-process. In Figure IV-24 the comparison between the experimental relative work generated and the predicted one is presented.

As it can be observed, the use of the beam formula for small deformations gives reliable and good results; the predicted values fit very well with the experimental ones. This can be explained as follows: on one side, during the programming process, the sample is above T_g and the network structure completely relaxed, therefore, the response of the sample to the applied stress is completely elastic. On the other side, the recovery-process takes place in between and above T_g, with a constant force applied, thus, the time-scale of the experiment is high enough to allow almost complete relaxation of the network during the process. This means that the sample response is almost completely elastic to the stress applied in both, the programming and the recovery processes; therefore, the equation is able to predict properly the final deflection and/or force applied.

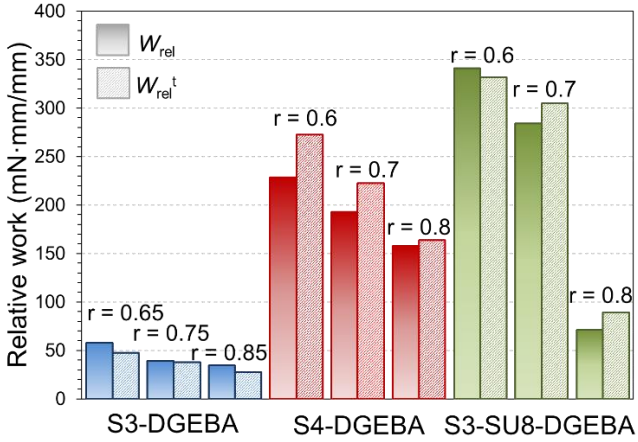

Figure IV-24. Comparison between predicted W_{rel}^t and experimental W_{rel} for all the formulations of study.

4. Conclusions

Bent-shaped shape-memory actuators have been successfully characterized by taking advantage of the sequential dual-curing of off-stoichiometric "thiol-epoxy" mixtures. By appropriately choosing the "thiol-epoxy" ratio, solid-like and conformable materials are formed after the first curing stage that can be easily processed into bent-shaped materials and fixed thanks to the crosslinks formed in the second curing stage. The SMPs have been fully characterized as potential actuators in different shape-memory scenarios: unconstrained, partially-constrained and fully constrained. The unconstrained recovery experiments showed an efficient and tailorable recovery process; the SMPs are able to efficiently fix the temporary shape and completely recover their original shape with high recovery rates. The dependence of the recovery-process on the network structure, in particular on the network relaxation process, has been clearly evidenced in the presence of the high functional epoxy resin SU8 in the S3-DGEBA system, leading to more heterogeneous network structures and thus lower recovery rates.

The fully constrained experiments showed the capability of these materials to release a force instead of recovering the original shape on heating above T_g. This force has been found closely related to the network structure and chemical structure of the crosslinking points. The presence of crosslinks of higher functionality increase the force released during the SME. Moreover, large and spatially impeded crosslinks (SU8 molecule) produce a major effect on the force enhancement.

In partially-constrained experiments, the materials showed the capability to produce a positive work on heating above T_g. The work released shows an increasing trend with the increase of the crosslinks functionality and size (SU8 > S4 > S3), as well as with the increase of epoxy excess accordingly to the force released in the fully constrained experiments. Moreover, it has been shown that it is possible to efficiently predict the work released by applying the beam deflection formula for small flexural deformations only taking into account the relaxed modulus and dimensions of the sample.

In general, the recovery-process is closely related to the network structure and its relaxation process in all experimental setup. The temperature at which the maximum rate is found (T_{peak}) is closely related to the T_g nominal value, while the heterogeneity of the relaxation process is connected with the length or duration of the recovery-process, which depends on the experimental setup and increases according to the constraint level, from unconstrained to fully constrained experiments.

Acknowledgements

The authors would like to thank MINECO (MAT2014-53706-C03-01 and MAT2014-53706-C03-02) and Generalitat de Catalunya (2014-SGR-67) for financial support. Xavier F.-F. also acknowledges the Serra-Húnter programme from the Generalitat de Catalunya.

References

[1] Hager, M. D.; Bode, S.; Weber, C.; Schubert, U. S. Shape memory polymers: Past, present and future developments. *Prog. Polym. Sci.* **2015**, *49–50*, 3–33, 10.1016/j.progpolymsci.2015.04.002.

[2] Lendlein, A.; Sauter, T. Shape-memory effect in polymers. *Macromol. Chem. Phys.* **2013**, *214*, 1175–1177, 10.1002/macp.201300098.

[3] Wu, X.; Huang, W. M.; Zhao, Y.; Ding, Z.; Tang, C.; Zhang, J. Mechanisms of the shape memory effect in polymeric materials. *Polymers (Basel).* **2013**, *5*, 1169–1202, 10.3390/polym5041169.

[4] Li, G.; Wang, A. Cold, warm, and hot programming of shape memory polymers. *J. Polym. Sci. Part B Polym. Phys.* **2016**, 1319–1339, 10.1002/polb.24041.

[5] Arrieta, S.; Diani, J.; Gilormini, P. Experimental characterization and thermoviscoelastic modeling of strain and stress recoveries of an amorphous polymer network. *Mech. Mater.* **2014**, *68*, 95–103, 10.1016/j.mechmat.2013.08.008.

[6] Xiao, R.; Guo, J.; Nguyen, T. D. Modeling the multiple shape memory effect and temperature memory effect in amorphous polymers. *RSC Adv.* **2015**, *5*, 416–423, 10.1039/C4RA11412D.

[7] Lewis, C. L.; Meng, Y.; Anthamatten, M. Well-Defined Shape-Memory Networks with High Elastic Energy Capacity. *Macromolecules* **2015**, 48, 4918-4926, 10.1021/acs.macromol.5b00763.

[8] Zhao, Q.; Qi, H. J.; Xie, T. Recent progress in shape memory polymer: New behavior, enabling materials, and mechanistic understanding. *Prog. Polym. Sci.* **2015**, *49–50*, 1–42, 10.1016/j.progpolymsci.2015.04.001.

[9] Xiao, X.; Kong, D.; Qiu, X.; Zhang, W.; Zhang, F.; Liu, L.; Liu, Y.; Zhang, S.; Hu, Y.; Leng, J. Shape-Memory Polymers with Adjustable High Glass Transition Temperatures. *Macromolecules* **2015**, 48, 3582-3589, 10.1021/acs.macromol.5b00654.

[10] Zhou, J.; Sheiko, S. S. Reversible shape-shifting in polymeric materials. *J. Polym. Sci. Part B Polym. Phys.* **2016**, *1*, 1–16, 10.1002/polb.24014.

[11] Lewis, C. L.; Dell, E. M. A Review of Shape Memory Polymers Bearing Reversible Binding Groups. *J. Polym. Sci. Part B Polym. Phys.* **2016**, 1340–1364, 10.1002/polb.23994.

[12] Tandon, G. P.; McClung, A. J.; Baur, J. W. Shape-Memory Polymers for Aerospace Applications; DEStech Publications: Lancaster, Pennsylvania, USA, 2015; pp. 658.

[13] Leng, J.; Yu, K.; Sun, J.; Liu, Y. Deployable morphing structure based on shape memory polymer. *Aircr. Eng. Aerosp. Technol.* **2015**, *87*, 218–223, 10.1108/AEAT-06-2013-0118.

[14] Boyle, M. A.; Martin, C. J.; Neuner, J. D. Epoxy Resins. In ASM Handbook Volume 21, Composites (ASM International); Miracle, D. B.; Donaldson, S. L.; ASM International, Ohio, USA, 2001, pp. 78–89.

[15] Santhosh Kumar, K. S.; Biju, R.; Reghunadhan Nair, C. P. Progress in shape memory epoxy resins. *React. Funct. Polym.* **2013**, *73*, 421–430, 10.1016/j.reactfunctpolym.2012.06.009.

[16] Zheng, N.; Fang, G.; Cao, Z.; Zhao, Q.; Xie, T. High strain epoxy shape memory polymer. *Polym. Chem.* **2015**, 6, 3046–3053, 10.1039/C5PY00172B.

[17] Altuna, F. I.; Hoppe, C. E.; Williams, R. J. J. RSC Advances Shape memory epoxy vitrimers based on DGEBA crosslinked with dicarboxylic acids and their blends with citric acid †. *RSC Adv.* **2016**, *6*, 88647–88655, 10.1039/C6RA18010H.

[18] Pei, Z.; Yang, Y.; Chen, Q.; Wei, Y.; Ji, Y. Regional Shape Control of Strategically Assembled Multishape Memory Vitrimers. *Adv. Mater.* **2016**, 28, 156–160, 10.1002/adma.201503789.

[19] Belmonte, A.; Fernández-francos, X.; Serra, À.; De la Flor, S. Phenomenological characterization of sequential dual-curing of off-stoichiometric " thiol-epoxy " systems : Towards applicability. *Mater. Des.* **2017**, *113*, 116–127, 10.1016/j.matdes.2016.10.009.

[20] Fernández-Francos, X.; Konuray, A.-O.; Belmonte, A.; De la Flor, S.; Serra, À.; Ramis, X. Sequential curing of off-stoichiometric thiol–epoxy thermosets with a custom-tailored structure. *Polym. Chem.* **2016**, 7, 2280–2290, 10.1039/C6PY00099A.

[21] Belmonte, A.; Guzmán, D.; Fernández-francos, X.; De la Flor, S. Effect of the Network Structure and Programming Temperature on the Shape-Memory Response of Thiol-Epoxy " Click " Systems. *Polymers*. **2015**, 7, 2146–2164, 10.3390/polym7101505.

[22] Belmonte, A.; Fernández-Francos, X. De la Flor, S. New understanding of the shape-memory response in thiol-epoxy click systems : towards controlling the recovery process. *J Mater Sci.* **2017**, 52, 1625-1638, 10.1007/s10853-016-0456-9.

[23] Belmonte, A.; Fernández-Francos, X.; De la Flor, S.; Serra, À. Network structure dependence on unconstrained isothermal-recovery processes for shape-memory thiol-epoxy "click" systems. *Mech. Time-Dependent Mater.* **2016**, 1-17, 10.1007/s11043-016-9322-z.

[24] Santiago, D.; Fabregat-Sanjuan, A.; Ferrando, F.; De la Flor, S. Recovery stress and work output in hyperbranched poly(ethyleneimine)-modified shape-memory epoxy polymers. *J. Polym. Sci. Part B Polym. Phys.* **2016**, 54, 1002-1013, 10.1002/polb.24004.

[25] Souri, M.; Lu, Y. C.; Erol, A.; Pulla, S. S.; Karaca, H. E. Characterization of unconstraint and constraint shape recoveries of an epoxy based shape memory polymer. *Polym. Test.* **2015**, *41*, 231–238, 10.1016/j.polymertesting.2014.11.006.

[26] Wang, A.; Li, G. Stress memory of a thermoset shape memory polymer. *J. Appl. Polym. Sci.* **2015**, *132*, 42112-42123, 10.1002/app.42112.

[27] Pascault, J.-P.; Sautereau, H.; J, V.; R, W. J. J. *Thermosetting Polymers*; CRC Press: Florida, USA, 2002; pp. 496.

[28] Fernández-Francos X.; Salla J. M.; Mantecón A.; Serra À; Ramis X. Crosslinking of mixtures of DGEBA with 1,6-dioxaspiro[4,4]nonan-2,7-dione initiated by tertiary amines. I. Study of the reaction and kinetic analysis. *J. Appl. Polym. Sci.*, **2008**, 109, 2304–2315, 10.1002/app.28336.

[29] Fernandez-Francos X.; Cook W. D.; Serra A.; Ramis X.; Liang G. G.; Salla J. M. Crosslinking of mixtures of DGEBA with 1,6-dioxaspiro[4,4]nonan-2,7-dione initiated by tertiary amines. Part IV. Effect of hydroxyl groups on initiation and curing kinetics. *Polymer*, **2010**, 51, 26–34, 10.1016/j.polymer.2009.11.013.

[30] Anthamatten M.; Roddecha S.; Li J. Energy storage capacity of shape-memory polymers. *Macromolecules.* **2013**, 46, 4230-4234, dx.doi.org/10.1021/ma400742g.

UNIVERSITAT ROVIRA I VIRGILI
DESIGN AND CHARACTERIZATION OF ACTIVELY-MOVING POLYMERS OBTAINED VIA DUAL-CURING PROCESSING
Alberto Francisco Belmonte Parra

Chapter V

Free-standing mechanical actuators based on dual-curing and liquid-crystalline networks

V

UNIVERSITAT ROVIRA I VIRGILI
DESIGN AND CHARACTERIZATION OF ACTIVELY-MOVING POLYMERS OBTAINED VIA DUAL-CURING PROCESSING
Alberto Francisco Belmonte Parra

V.1 Introduction and scope

In chapters III and IV **enhanced AMPs** with tailored structural, mechanical and thermomechanical properties were obtained. Moreover, thanks to the **dual-curing processing**, it was possible to develop **complex shaped designs** in an easy and efficient manner. Nevertheless, all the AMPs obtained were SMPs that, in practice, have limited application due to the requirement of a programming process. Adaptive mechanisms demand reversible movements and overall self-control. The self-control and self-organization are the characteristics that define an intelligent material. As explained in section I.1.2, **LCNs** can shift from one shape to another without the necessity of a programming process. The shape-shifting takes place under the effect of a mechanical load during the LC transition. Thus, LCNs can emulate mussels or other "actuation" mechanisms with an enhanced self-control in comparison to SMPs.

Many researchers have investigated the **shape-shifting ability in LCNs** with different structural properties and under different loading conditions. Mater et al.[1] synthesized main-chain smectic-C LCNs with varying crosslinking densities using a two-stage hydrosilylation. A controlled increase of the reversible elongation-shrinkage (actuation) up to 30% of the initial size was reported. Yakacki et al.[2] took advantage of a dual-curing thiol-Michael addition click system to develop main-chain LCNs with controlled actuation up to 400% of strain. The load level and amount of thiol crosslinker were found determinant on the modulation of the actuation level.

Considering the above**, LCNs** are an interesting class of AMPs to attain controlled and high actuation levels. Nevertheless, an external mechanical load is required. Moreover, the dimensional change is usually limited by the network design of the LCN and the direction of the external force. To overcome these limitations, two main approaches have recently been shown: **the internal or external incorporation of a mechanical load**. As explained in section I.1.2.3, the internal incorporation consists of fixing an unstable "stretched" LCN through the formation of a new interpenetrated network that is usually achieved via dual-curing processing. In contrast, the external incorporation consists of fixing the "stretched" LCN by embedding an elastomeric matrix onto the surface. In both cases, **free-standing actuation** can be achieved, that is, reversible actuation without the need of an external force. The mismatch between both networks (in the case of the internal incorporation) or both materials (in the case of the external incorporation) upon heating-cooling processes,

leads to stress generation that promotes the elongation-shrinkage response. The first report on external incorporation was done by Westbrook et al.[3,4] who joint a stretched poly(cyclooctene)-based LCN into an acrylate-based matrix through thermal curing of the latter. The resulting material was able to produce small reversible flexural actuation by heating-cooling procedures due to the elastic response of the matrix at the actuation temperature. Afterwards, different reports on internal incorporation were presented by Anthamatten et al.[5] and Yakacki et al.[6], both using dual-curing methodologies.

In the previous chapter IV, we have presented and extensively characterised a versatile **sequential "thiol-epoxy" dual-curing system**. This system allows to cure intermediate materials in form of layers with controlled thickness that can be further fully crosslinked in rigid layers. Considering the **broad range of material properties** that can be achieved, it has been proposed to develop free-standing actuators through the external incorporation methodology carrying out a multi-layer assembling process. The "stretched" LCN layer is placed in between layers of the "thiol-epoxy" intermediate material and embedded through the second curing stage (epoxy homopolymerization). The configuration of the different layers, the stretching level of the LCN and the structural and thermomechanical properties of the different materials are expected to define the actuation type (i.e. bending or torsion) and the actuation level.

To the best of our knowledge, the use of **"thiol-epoxy" dual-curing systems and "epoxy-carboxylic" LCNs for the development of free-standing actuators** have not been investigated yet. The versatility of the proposed methodology makes possible to obtain a wide range of operational designs with precise control of the actuation and more importantly, without the requirement of complex moulding techniques.

In this chapter **free-standing actuators are developed and characterised** in two steps: first, **the LCN is synthesized and characterised in view of the actuator requirements**. As stated in section I.1.2.3, the matrix must response in an elastic way, thus, the T_g of the final "thiol-epoxy" thermoset must be lower than T_{iso} of the LCN. In addition, the second curing temperature of the "thiol-epoxy" intermediate material, that is, the assembling temperature of the actuator, should be lower than T_{iso} to avoid premature shrinkage and therefore inefficient embedding. To this end, LCNs with high isotropization temperature ($T_{iso} > 90$ °C) and stable and controlled actuation are necessary. To accomplish the mentioned requirements, an epoxy-based mesogen is synthesized and cured with diacids of different aliphatic chain length. The structural,

thermomechanical, liquid-crystalline and shape-changing properties have been studied in relation with the aliphatic chain length of the diacid. The results and discussion of this study are presented in **section V.2**.

Once the LCN is designed, the second step lies on the **development of the free-standing actuator**. The actuator has been assembled **following the multi-layer sandwich-like methodology** with the LCN layer displaced to the actuation side in order to achieve controlled flexural actuation. The adhesion and uniformity of the actuator design have been studied through SEM analysis. The actuation response has been investigated under controlled heating-cooling processes in terms of maximum deflection and angle of curvature. In addition, an analytical model based on the multi-layered beam theory which takes into account the materials properties, layers configuration and LCN stretching level has been developed and validated with the experimental results. The results and discussion of this study are presented in **section V.3**.

Finally, an **extensive study of the free-standing actuators towards controlling the times, temperatures and velocity of the actuation** has been carried out. The results have been corroborated with the development of a well-controlled complex 3D motion device. This study is presented in **section V.4**.

References

[1] K.A. Burke, I.A. Rousseau, P.T. Mather, Reversible actuation in main-chain liquid crystalline elastomers with varying crosslink densities, Polymer. **2014**, 55, 5897–5907.

[2] M.O. Saed, A.H. Torbati, D.P. Nair, C.M. Yakacki, *Synthesis of Programmable Main-chain Liquid-crystalline Elastomers Using a Two-stage Thiol-acrylate Reaction*, J. Vis. Exp. **2016**, 107, 1–10.

[3] K.K. Westbrook, P.T. Mather, V. Parakh, M.L. Dunn, Q. Ge, B.M. Lee, H.J. Qi, *Two-way reversible shape memory effects in a free-standing polymer composite*, Smart Mater. Struct. **2011**, 20, 65010.

[4] Q. Ge, K.K. Westbrook, P.T. Mather, M.L. Dunn, H. Jerry Qi, *Thermomechanical behavior of a two-way shape memory composite actuator*, Smart Mater. Struct. **2013**, 22, 55009.

[5] Y. Meng, J. Jiang, M. Anthamattern, *Shape actuation via internal stress-induced crystallization of dual-cure networks*, ACS Macro Lett. **2015**, 4, 115–118.

[6] M.O. Saed, A.H. Torbati, C.A. Starr, R. Visvanathan, N.A. Clark, C.M. Yakacki, *Thiol-Acrylate Main-Chain Liquid-Crystalline Elastomers with Tunable Thermomechanical Properties and Actuation Strain*, J. Polym. Sci. Part B Polym. Phys. 2016, 0, 1–12.

V.2 Synthesis and characterization of liquid-crystalline networks: toward autonomous shape-memory actuation

The Journal of Physical Chemistry C, **2017**, 121, 22403-22414

Alberto Belmonte[1], Giuseppe Cesare Lama[2,3], Gennaro Gentile[3], Xavier Fernández-Francos[4], Silvia De la Flor[1], Pierfrancesco Cerruti[3] and Veronica Ambrogi[2]

1) Department of Mechanical Engineering, Universitat Rovira i Virgili, Av. Països Catalans, 26, 43007 Tarragona, Spain.

2) Department of Chemical, Materials and Production Engineering, University of Naples "Federico II", Piazzale Tecchio, 80, 80125 Napoli, Italy.

3) Institute for Polymers, Composites and Biomaterials, National Council of Research of Italy, Via Campi Flegrei, 34, 80078 Pozzuoli (NA), Italy.

4) Thermodynamics Laboratory ETSEIB, Universitat Politècnica de Catalunya, Av. Diagonal, 647, 08028 Barcelona, Spain.

*** Supplementary information provided in section (V.2.SI)**

UNIVERSITAT ROVIRA I VIRGILI
DESIGN AND CHARACTERIZATION OF ACTIVELY-MOVING POLYMERS OBTAINED VIA DUAL-CURING PROCESSING
Alberto Francisco Belmonte Parra

J. Phys. Chem. C. 2017, 121, 22403-22414

Abstract

In this paper, epoxy-based shape-changing liquid-crystalline lightly crosslinked networks (LCN) are synthesized and characterized with a view to the future development of two-way autonomous shape-memory actuators by coupling the LCN with an external epoxy-matrix. Carboxylic acids of different aliphatic chain lengths are used as curing agents for a rigid-rod epoxy-based mesogen. Thermal and liquid-crystalline (LC) properties of the LCN are investigated through calorimetric and X-ray diffraction analysis on unstretched and stretched samples. Structural and thermomechanical properties are studied by means of tensile and dynamic-mechanical analyses and the shape-changing capabilities are analysed in terms of actuation strain and stress under partially- and fully constrained thermomechanical procedures. The results have shown the possibility to obtain LCN with isotropization temperatures above 100 °C, controlled degree of liquid crystallinity, and high actuation stress and strain by simply varying the aliphatic chain length of the curing agent. Moreover, by properly adjusting the programming conditions (stress level), it is possible to optimize and stabilize the actuation performance. In addition, the effects of the liquid-crystalline domains on the network relaxation and their degree of orientation after programming at the different stress levels have been discussed. Overall, proper design of chain length and stress level allows strain actuation to be modulated from low, ∼60%, to high, ∼160% strain levels. The results evidence the possibility of finely tuning LCN with controlled and stable actuation protocols by balancing the aliphatic chain length and programming conditions.

1. Introduction

Shape-memory polymers (SMP) are a class of mechanically active materials capable of interacting with the environment through the transformation of a temporary shape into the original shape in one or multiple steps. The temporary shape is imposed through a so-called programming process that usually consists of a thermomechanical deformation. The shape-transformation is called shape-memory effect (SME), and it is triggered by one or more external stimuli such as heat, UV-light, pH, or a magnetic field. SMPs are commonly classified by the nature of the polymer: from glassy or semicrystalline covalently crosslinked polymers to glassy or semi-crystalline physically crosslinked copolymers, and by the shape-transformation protocol: one-way (1W) or unidirectional SMPs and two-way (2W) or bidirectional SMPs[1–5].

Other systems belonging to the class of mechanically active polymers are liquid-crystalline elastomers (LCEs). These systems are semi-crystalline, lightly chemically crosslinked materials possessing the ability to change their shape reversibly in response to an external trigger, thanks to a combination of entropic effects and liquid crystal order[6,7]. They are interesting in many fields of application such as industrial actuator[8], artificial muscles[9], lithography[10], and sensors[11]. Despite the fact that several types of LCEs are capable of performing 2W shape-change[12], including smectic or nematic main-chain[13,14] and side-chain LCEs[15], controlling the actuation performance lays on the complex process of developing LCEs with tailor-made network structures and fitted thermal transitions (i.e. glass transition and LC phases). Mather et al.[7] took advantage of a two-stage hydrosilylation reaction to synthesize main-chain LCEs with controlled crosslinking density. Similarly, Yakacki et al.[16,17] used a two-stage acrylate reaction to produce main-chain LCEs with facile control of the structural properties and alignment of the LC domains. Kessler et al.[14] found an easy way to tailor the LC phase and thermomechanical properties by synthesizing epoxy-carboxylic main-chain LCEs with different epoxy-carboxylic ratios. Nevertheless, the increasing demand of LCEs with specific structural and thermal properties requires the development of further effective strategies to synthesize tailored LCEs.

One of the possible major applications of LCEs is the development of responsive smart actuators. However, the main issue is that a constant load in the actuation direction is required to produce the bidirectional shape-change. Recently, some strategies to overcome this limitation and produce autonomous 2W shape-memory actuators have been proposed[18−22]. All of them rely on the retention of an already stretched network, responsible for producing the constant load, within a fixed matrix. One approach is to physically embed the stretched network into a polymeric matrix through the curing of the latter or the adhesion of an already cured material. Another approach is to internally fix the stretched network with new covalent bonds through a two-stage curing process: the network is stretched after the first curing stage and fixed through the second curing stage[16,17]. Nevertheless, both approaches have some inherent limitations that make difficult the control and optimization of the actuation performance: the adhesion efficiency and compatibility of the embedded polymeric matrix, the control of the final network structure formed and its effect on the stretched network in a two-stage process, and finally the development of complex actuation designs.

To this end, new strategies for the development of autonomous 2W shape-memory actuators are of utmost relevance to better control the actuation efficiency and design[23–25]. Recently, our research group presented a new methodology to produce epoxy-based materials via sequential dual-curing of off-stoichiometric "thiol-epoxy" mixtures, with tailored structural and thermal properties and easy processing from the intermediate stage[26]. This methodology can be used for the development of autonomous 2W shape-memory actuators by embedding a stretched liquid-crystalline (LC) lightly crosslinked network into the epoxy matrix through the dual-curing procedure, making easier the control of the final properties of the matrix without affecting the stretched LC network and its efficiency. Moreover, the adhesion can be enhanced by the formation of strong physical bonds during the second curing stage of the matrix and, more interestingly, allowing the processing of complex-shaped designs as previously demonstrated[27,28]. The schematic structure and working mechanism of this autonomous two-way shape memory system is illustrated in Figure V-1[29].

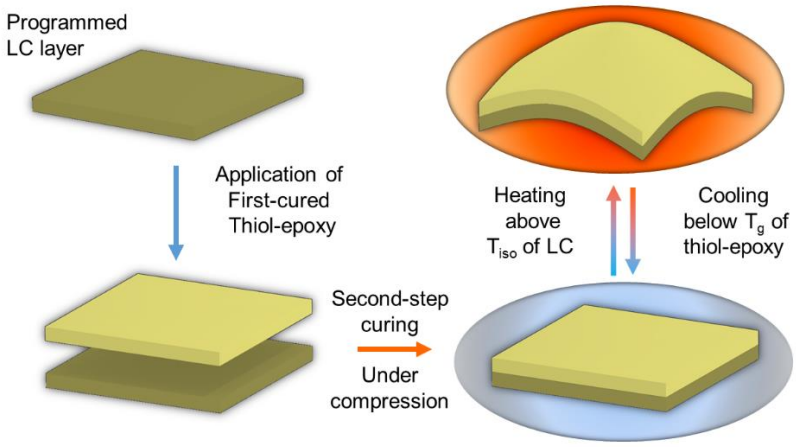

Figure V-1. Schematic structure and working mechanism of the projected two-way actuator[29].

In this work, LC systems are prepared and characterized in view of the requirements for the development of autonomous two-way actuators as proposed above. First, the LC network must be able to retain its stretched shape during the embedding process, which takes place at 80–90 °C (second curing stage of the thiol-epoxy matrix). Other researchers usually overcome this issue by holding the stretched LC layer during the curing process[30]; however, this may damage the LC network or even break it when the force induced by the shrinkage is too high. In order

to embed it under safe conditions, LC crosslinked systems with isotropization temperatures above 100 °C are required. On the other hand, after embedding in the matrix, the LCN must be able to deform the polymer during the shape-change, so a high and controlled actuation stress is required. Taking into account the above, in this work liquid-crystalline systems are prepared by combining an epoxy-based mesogen with dicarboxylic aliphatic acids with different chain length as curing agents: by this approach the isotropization temperature can be controlled by the aliphatic chain length whereas the epoxy-based network can provide high actuation stress to allow deforming the matrix[13,31–33]. The thermal, phase behaviour, and thermomechanical properties of the LC networks have been investigated, and the shape-changing response has been studied in terms of actuation stress and strain through various consecutive cycles under unconstrained and constrained conditions, in order to reproduce the operating conditions of the projected autonomous two-way actuators[29].

2. Experimental section

Materials

A commercial diphenol compound (4,4'-dihydroxybiphenyl, 97% purity, 186.21 g/mol), epichlorohydrin (99% purity, 1.183 g/mL, 92.52 g/mol), isopropyl alcohol, and sodium hydroxide have been used for the synthesis of the epoxy-based mesogen. Commercial dicarboxylic acids with different aliphatic chain length $(CH_2)_n$ have been used as curing agents for the synthesis of the epoxy-based liquid-crystalline polymer: adipic acid (n = 4, C_4), pimelic acid (n = 5, C_5), suberic acid (n = 6, C_6), azelaic acid (n = 7, C_7), sebacic acid (n = 8, C_8), and dodecandioic acid (n = 10, C_{10}). Tricaprylyl methylammonium chloride was used as catalyst. All chemicals were supplied by Sigma-Aldrich and used as received.

Synthesis and characterization of the epoxy-based mesogen (DIF)

The epoxy-based mesogen was synthesized by epoxidation of the 4,4'-dihydroxybiphenyl[34]. The epoxidation was carried out using epichlorohydrin in the presence of NaOH in a two-step reaction mechanism: the formation of a chlorohydrin intermediate and the dehydrohalogenation of the intermediate to the diglycidyl ether[35]. NaOH catalyses the reaction to produce the intermediate, acts as a dehydrohalogenation agent, and neutralizes the formed HCl (the scheme of the reaction is shown in Scheme V-1). Dynamic scanning calorimetry (DSC) confirmed the formation of the epoxy-based mesogen with a melting temperature of 154 °C.

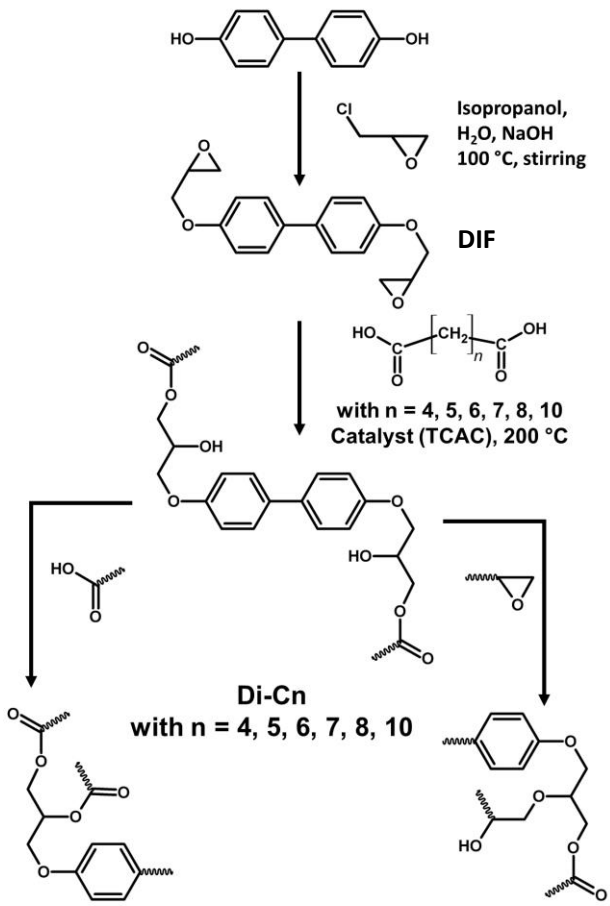

Scheme V-1. Scheme of epoxidation of 4,4′-dihydroxybiphenyl and curing of the diepoxy monomer with dicarboxylic acids C4–C10.

Preparation and characterization of the liquid-crystalline networks (LCN)

Main-chain LCN were prepared by mixing DIF with aliphatic dicarboxylic acids of different chain length "*n*" from 4 to 10 in epoxy-carboxylic stoichiometric proportions, with and without catalyst. The curing process and liquid-crystalline transitions were determined by means of DSC analysis following the same procedure as for the characterization of DIF in the previous section. Referring to the number of carbon atoms in the acids aliphatic chain, the obtained LCN were coded as Di-C4, Di-C5, Di-C6, Di-C7, Di-C8, and Di-C10, respectively (see Scheme V-1).

LCN films of 250−300 µm thickness and 50 × 50 mm^2 surface area were prepared in an oven as follows: first, melting the epoxy-acid mixture

at 180 °C under magnetic stirring, then, pouring the catalyst in and mixing under stirring during 30 s to ensure homogeneity, and finally, pouring the mixture into a preheated mould and placing it inside the oven at 200 °C for 150 min, to ensure the completion of the polymerization.

The LCN samples were analysed by means of DSC analysis, using a TA Instruments DSC Q2000 calorimeter, under N_2 atmosphere with heating and cooling ramps from 0 up to 200 °C at 10 °C/min. The nominal values of the temperatures corresponding to the melting, crystallization, isotropization, and anisotropization (T_m, T_c, T_{iso}, and T_{aniso}) processes were determined as the peak of the heat flow, while the temperature corresponding to the glass transition (T_g) was determined as the midpoint of the step change in the heat flow (see Figure V-12 and Figure V-13 in the V.2.SI Supplementary Information). The enthalpy changes due to reaction between epoxy and carboxylic acid, crystallization, and isotropization (ΔH_r, ΔH_c, and ΔH_{iso}) were measured by integrating the corresponding peak areas of the heat flow signal.

Liquid-crystalline properties characterization

X-ray diffraction (XRD) measurements were carried out using a Bruker-AXS D8-Discover diffractometer equipped with parallel incident beam (Göbel mirror), vertical θ−θ goniometer, XYZ motorized stage, and a GADDS (General Area Diffraction System). The X-ray diffractometer was operated at 40 kV and 40 mA to generate Cu Kα radiation. Unstretched and stretched samples after shape-memory programming (see the stress programming levels in following sections) were analysed. The orientation degree of samples after shape-memory programming was measured with the order parameter *S*, determined by numerical analysis of the scattering profile *I*(γ), according to Hermann's method (equations (V-1) - (V-4))[36]:

$$\cos\alpha = \cos\gamma \cdot \cos\theta \tag{V-1}$$

$$\langle\cos^2\alpha\rangle = \frac{\int_0^{\frac{\pi}{2}} I(\alpha)\cdot\sin\alpha\cdot\cos^2\alpha\cdot\partial\alpha}{\int_0^{\frac{\pi}{2}} I(\alpha)\cdot\sin\alpha\cdot\partial\alpha} \tag{V-2}$$

$$\langle\cos^2\varphi\rangle = 1 - 2\cdot\langle\cos^2\alpha\rangle \tag{V-3}$$

$$S = \frac{1}{2}\cdot(3\cdot\langle\cos^2\varphi\rangle - 1) \tag{V-4}$$

where θ is the scattering angle, γ is the azimuthal angle, α is the angle between the normal and the scattering planes, φ is the inclination

angle (angle of the ordered phase normal to the stretching direction), and $I(\alpha)$ is the distribution function.

Mechanical characterization

Tensile tests at break were performed using a PerkinElmer Pyris Diamond DMA apparatus equipped with a tension film clamp and operating in force-controlled mode in order to evaluate the mechanical response of the LCN. Bone-shaped samples with effective length x width x thickness of 15 × 3 × 0.25 mm^3 were cut from the film and tested at T_{iso} + 20 °C and a constant force rate of 10 mN/min. The engineering stress was transformed into true stress by applying a constant Poisson ratio of 0.4 (typical of common LCN[37]). Mean and standard deviation values of tensile modulus (E_T), stress at break (σ_b), and strain at break (ε_b) were determined from the true stress−strain curves registered on at least three different samples. Furthermore, stress−strain curves of Di-C7, Di-C8, and Di-C10 between T_g and T_{iso} were obtained according to the same procedure, at a temperature T = 75 °C.

Dynamic-mechanical characterization

Dynamic-mechanical analyses were performed using a TA Instruments DMA Q800 equipment operating in oscillation mode and equipped with a tension film clamp geometry. Strips with effective length × width × thickness of 12 × 4 × 0.25 mm^3 were cut from the film and tested in the apparatus at a frequency of 1 Hz, strain amplitude of 0.1%, and a heating rate of 3 °C/min from 30 up to 180 °C. T_g and T_{iso} temperatures were determined as the peak of the tanδ curve in the corresponding transition region. Mean and standard deviation values of the glassy modulus, E_g ($T < T_g$), and rubbery modulus, E_r ($T > T_{iso}$), were determined from the storage modulus curves registered on at least three different samples. In particular, E_r was determined at T_{iso} + 20 °C, analogously to mechanical tensile experiments, as the modulus constantly increases above T_{iso}.

Shape-changing characterization

Thermomechanical experiments were performed using a PerkinElmer Pyris Diamond DMA apparatus equipped with a tension film clamp and operating in both force-controlled and strain-controlled modes. In order to evaluate the actuation capacity, shape-changing cycles were carried out at two different levels of stress (25% and 75% of σ_b). On the one hand, the strain actuation and creep response were analysed by thermomechanical cycling under constant load (DMA in force-controlled mode). On the other hand, the actuation stress was analysed by fully

constrained thermomechanical cycling (DMA in iso-strain mode). Bone-shaped samples with effective length × width × thickness of 10 × 4 × 0.25 mm^3 were cut and used in both experimental setups.

Thermomechanical cycling under constant load

The experiments were carried out as follows: first, programming the sample by heating up to T_{iso} + 20 °C, holding during 5 min for thermal stabilization, loading at 10 mN/min up to 25% or 75% of σ_b, and cooling to room temperature while keeping the load applied (elongation induced by the ordering of the liquid-crystalline domains). Afterward, the shape-change was triggered by heating–cooling steps at 2 °C/min while maintaining the load applied (each cycle is defined by one heating–cooling step). The strain actuation is defined by the strain step from the stretched state to the strain after elongation and the strain after shrinkage. The creep response is determined by the residual strain after each cycle.

Fully constrained thermomechanical cycling

The experiments were carried out as follows: first, programming the sample as explained above and, then, the DMA was set to iso-strain mode and the shape-change triggered by heating–cooling steps at 2 °C/min. The stress generated during the shape-change was recorded and plotted against the temperature.

3. Results and discussion

Thermal properties

The synthesis of the epoxy-based mesogen (DIF) is explained and discussed in the V.2.SI. As stated in the experimental section, main-chain LCN were prepared by using dicarboxylic aliphatic acids of different chain length (see Scheme V-1) and DIF. A preliminary study of the curing process using the DSC at a constant heating rate of 10 °C/min was carried out. The DSC traces are shown in the V.2.SI: in Figure V-12 and Figure V-13, the curing process and liquid-crystalline transitions are shown for mixtures without catalyst, while mixtures with catalyst are reported in Figure V-14 and Figure V-15. The parameters of interest are summarized in Table V-1.

Table V-1. Thermal properties of the different LCN cured with and without catalyst.

Formulation	T_m[a] (ºC)	T_g (ºC)	T_{aniso} (ºC)	T_{iso} (ºC)	ΔH_{iso} (J/g)	ΔH_r (J/g)	ΔH_r (no cat.) (J/g)
Di-C4	131.9	---	111.2	132.6	14.8	261	67.9
Di-C5	100.2	53.0	91.4	104.6	23.1	276	51.3
Di-C6	127.3	52.0	103.0	112.7	17.4	268	87.5
Di-C7	104.2	55.3	104.4	113.4	15.7	264	55.9
Di-C8	125.5	54.1	122.9	137.3	19.3	292	68.2
Di-C10	123.5	53.2	141.8	150.6	21.2	259	62.7

[a] Melting temperature of the carboxylic acid.

As can be seen, all of the curing agents led to the formation of a LCN as deduced by the presence of liquid-crystalline transitions on both cooling and heating, with an enthalpy (ΔH_{iso}) of 17−30 J/g[31]. The use of a quaternary ammonium salt as catalyst clearly enhances the reaction kinetics and the formation of the network structure as deduced by the increase of the reaction enthalpy (ΔH_r) from ∼50 up to ∼260 J/g in all cases. The reaction mechanism generally involves an initial epoxy ring-opening step, which reacts with a carboxylic group to produce the first product, a β-hydroxypropyl ester, which further reacts with a second mole of carboxylic acid through the hydroxyl group to yield an ester or with an epoxy group to yield an ether. The presence of the ammonium salt as catalyst helps the epoxy ring-opening, thus the crosslinking of the final network[38,39].

On analysing the liquid-crystalline parameters, T_{iso} follows an odd−even effect with the increase of the aliphatic chain length. This was previously observed by Carfagna et al.[31,40] in similar epoxy-carboxylic LCN. Usually, longer flexible segments act as spacers promoting the stabilization of the anisotropic phase: indeed, it has been reported that, in low molecular weight liquid crystals, the crystalline structure can incorporate flexible chain segments[41]. In addition, as reported for other LC systems[42], dicarboxylic acids with an odd number of methylene groups valence angles force the chain to adopt a less extended conformation with respect to dicarboxylic acids with an even number of methylene groups, thus negatively affecting the stability of the mesophase. The anisotropization temperature, T_{aniso}, is about 10−20 °C lower than T_{iso}, as commonly observed for liquid-crystalline elastomers[43].

In view of the results, Di-C7, Di-C8, and Di-C10 have been chosen for the characterization as potential LCN for the future development of autonomous 2W shape-memory actuators. All of them have higher T_{iso} than 100 °C, thus making easier the further incorporation in the epoxy matrix through the dual-curing procedure as stated in the Introduction[27]. The odd−even effect is reduced by the longer chain length as deduced

from an almost linear increasing trend of T_{iso} from Di-C7 to Di-C10. Finally, from tensile tests it can be expected that longer chain length results in higher strain actuation in shape-changing experiments (see Figure V-5(b)).

Films of the selected formulations were prepared following the curing protocol described in the experimental section, and they were analysed by DSC. The traces are shown in Figure V-2 and the parameters of interest summarized in Table V-2. In addition, an image of the samples transparency has been included in Figure V-2.

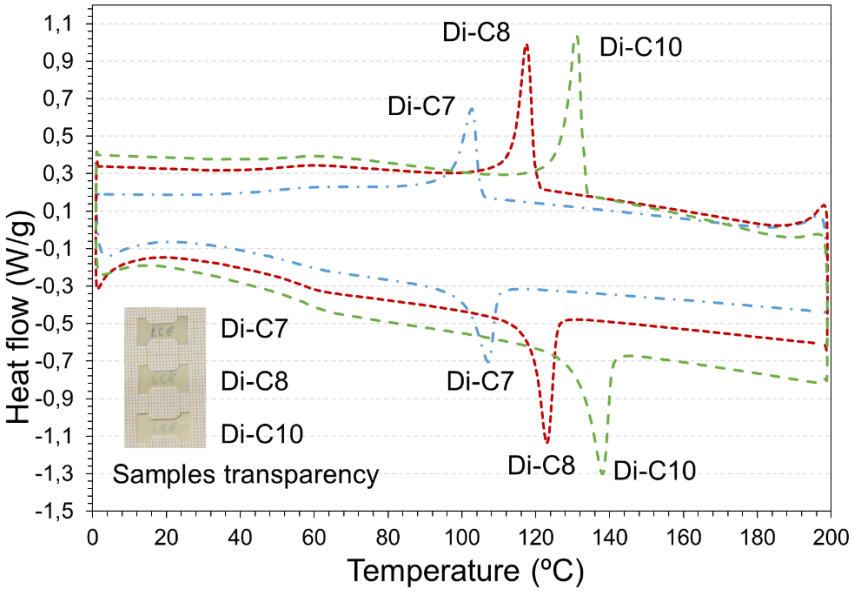

Figure V-2. DSC heating-cooling traces of the different LCN studied.

As can be observed, the proposed curing protocol leads to well-defined materials, with sharp and uniform liquid-crystalline transitions in comparison with those obtained for the samples cured directly in the DSC from the preliminary analysis. T_{iso} and ΔH_{iso} increased with increasing length of the aliphatic chain of the curing agent, denoting higher degree of liquid crystallinity and the formation of a more stable mesophase. As also deduced from the samples transparency in the inset, samples with a higher degree of crystallinity were cloudy since they scattered light to a larger extent (Di-C10 < Di-C8 < Di-C7). On the other hand, the glass transition temperature is similar for all LCN (around 57 °C) and does not follow any specific trend. Overall, systems with shorter aliphatic chain length would lead to network structures with higher crosslinking density and, thus, higher T_g[44]. However, it was reported that, in semi-crystalline networks, LC domains can play the role of physical crosslinks increasing

the expected T_g[45,46]. This would explain the similar T_g values recorded regardless the chain length.

Table V-2. Thermal properties of the different LCN.

Formulation	T_g (ºC)	T_{iso} (ºC)	T_{aniso} (ºC)	ΔH_{iso} (J/g)	ΔH_{aniso} (J/g)
Di-C7	55.3	107.2	102.7	17.2	18.8
Di-C8	57.8	123.1	117.4	23.9	24.6
Di-C10	58.1	137.9	131.0	28.7	28.2

Liquid-crystalline properties of LCN

The results of the low and wide-angle X-ray diffraction characterization are presented in Figure V-3 and Figure V-4, respectively, with images of the scattering rings and the intensity distribution of the scattering angle (2θ). The parameters of interest are summarized in Table V-3. On analysing the scattering rings, the formation of a smectic-A LC phase can be deduced: the scattering rings in Figure V-4 ($2\theta_1$ = 20.3° and d_1 = 4.3 Å) are related to the alignment of the mesogens within the LC domains (almost equal in all formulations), the outer ring in Figure V-3 (i.e. $2\theta_2$ = 6.3° and d_2 = 13.8 Å in the Di-C7 formulation), is attributed to the ordered layers of a smectic phase as deduced from the length of the epoxy-based mesogen (∼14 Å). Finally, the inner ring in Figure V-3, which is clearly appreciated in Di-C7 ($2\theta_3$ = 3.2°, d_3 = 27.6 Å) and becomes diffuse in Di-C8 and almost disappears in Di-C10, can be related to an ordered superstructure of the smectic LC domains.

On analysing unstretched samples, important differences are appreciated at low-angle level: in Figure V-3(a), formulations containing longer flexible chains lead to a smectic phase with longer distance between layers and higher degree of order, as deduced from the increase of d_2 and decrease of full width at half maximum ($fwhm_2$), respectively. In contrast, they show lower order among LC domains in the superstructure level ($fwhm_1$ broadens and the peak progressively disappears from Di-C7 to Di-C10). As stated above, the increase of effective flexible segments promotes the formation of crystalline domains during the LC phase, that is, higher order and increased space between layers. However, the longer spacer promotes the growth of LC domains in all directions, decreasing the order in the superstructure level.

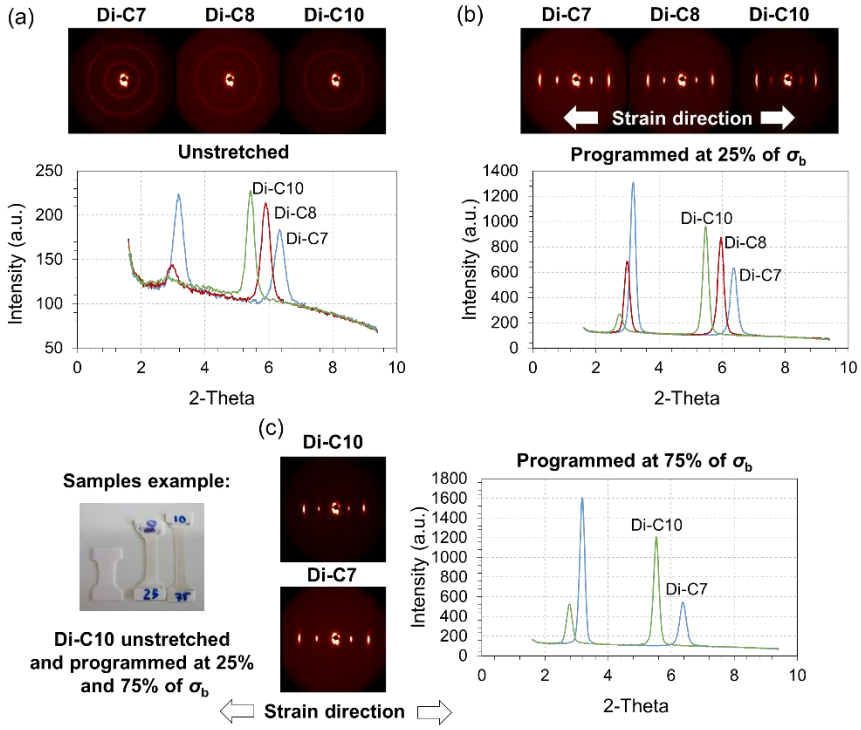

Figure V-3. Low-angle XRD analysis: (a) Unstretched samples; (b) stretched samples after shape-memory programming at 25% of σ_b and (c) Di-C7 and Di-C10 after shape-memory programming at 75% of σ_b.

On stretching the samples under a shape-memory programming (see XRD results in Figure V-3(b) and Figure V-4(b)), the liquid-crystalline domains are aligned in the stretching direction, leading to a highly oriented mesophase as indicated by the presence of the scattering arcs in all of the studied formulations. The peaks tend to narrow and increase their intensity, but they appear at the same 2θ and d-spacing in all cases. This means an increase of the orientation degree caused only by the rotation of the crystalline domains toward the stretching direction without deforming them. The orientation degree is quantified by the order parameter *S*, determined from the azimuthal distribution of the peak corresponding to the order of the smectic layers (S_2, the azimuthal distribution is shown in Figure V-16 of the V.2.SI). As it can be seen, S_2 decreases on increasing the flexible chain length (i.e. S_2 = 0.87 in Di-C7, while S_2 = 0.51 in Di-C10 at 25% of stress level). In order to further analyse this phenomenon, Di-C7 and Di-C10 have been analysed at 75% of programmed stress level (see results in Figure V-3(c)). As expected, on increasing the stress level, S_2 increases; however, the increase is more

pronounced in Di-C10 (from 0.51 to 0.60) than in Di-C7. This is caused by the higher order of orientation achieved in formulations with shorter chain length at lower stress level.

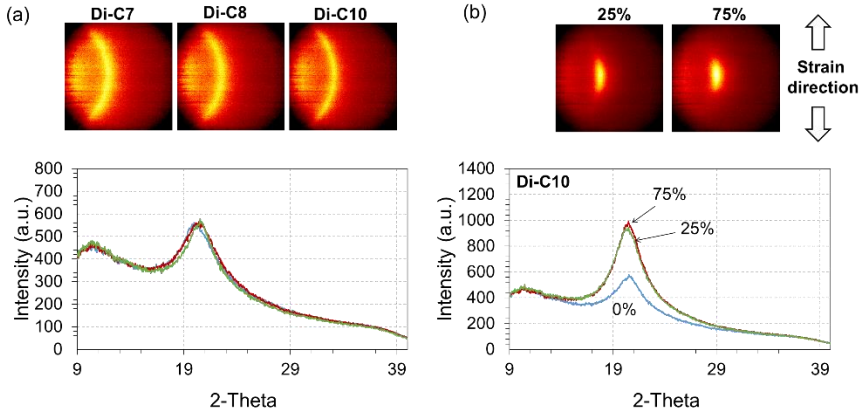

Figure V-4. Wide angle XRD analysis: (a) Unstretched samples and (b) Di-C10 after shape-memory programming at 25% and 75% of σ_b.

Table V-3. Parameters of interest of the XRD characterization.

	Unstretched			25% of σ_b			75% of σ_b	
	Di-C7	**Di-C8**	**Di-C10**	**Di-C7**	**Di-C8**	**Di-C10**	**Di-C7**	**Di-C10**
d_1 (Å)[a]	27.6	29.5		27.6	29.5	32.2	27.6	32.2
d_2 (Å)[a]	13.8	14.8	16.2	13.8	14.8	16.2	13.8	16.2
d_3 (Å)[b]	4.4	4.3	4.3			4.3		4.3
$2\Theta_1$ (deg)[a]	3.2	3.0		3.2	3.0	2.7	3.2	2.7
$2\Theta_2$ (deg)[a]	6.3	6.0	5.4	6.4	6.0	5.4	6.4	5.4
$2\Theta_3$ (deg)[b]	20.1	20.3	20.5			20.5		20.5
$fwhm_1$ (deg)[a]	0.38	0.39		0.21	0.21	0.25	0.19	0.21
$fwhm_2$ (deg)[a]	0.39	0.34	0.30	0.26	0.23	0.21	0.25	0.20
$fwhm_3$ (deg)[b]	3.0	3.0	3.0			3.2		3.2
S_2	0.00	0.00	0.00	0.87	0.75	0.51	0.89	0.60

[a] Determined from low-angle XRD analysis.
[b] Determined from wide-angle XRD analysis.

Thermomechanical properties

Figure V-5(a) plot the evolution of the storage modulus, E', and the loss tangent, tanδ, as a function of the temperature, resulting from the DMA analysis of the materials. The parameters of interest are summarized in Table V-4. As can be observed, all of the LCN exhibit similar behaviour: at temperatures below T_g the material is in the glassy region, the response is completely elastic, and E' remains stable with values > 1 GPa. When the materials approach their glass transition, the mechanical relaxation of the network structure takes place, E' falls down to 100−10 MPa, and tanδ reaches a maximum peak associated with the nominal T_g value. After the tanδ peak, the material is in the smectic region; tanδ remains constant and

higher than 0 pointing out the presence of a single liquid-crystalline mesophase, and E' slowly decreases on approaching the isotropization transition. Finally, a drastic decrease of E' (called dynamic softening elasticity) takes place during the isotropization relaxation, and E' reaches a stable plateau refereed to the rubbery region. In this region, the response is completely elastic and basically depends on the crosslinking density of the material[47].

On analysing the differences among LCN, the increase of the aliphatic chain length enhances the stability of the mesophase, as deduced by the increase of ΔH_{iso} and T_{iso}. Literature data on similar main-chain LC systems pointed out that the chain length (in terms of methylene units n) in dicarboxylic acids does not influence T_{iso} for $n < 7$. However, for higher n values, both clearing temperatures and enthalpies increase significantly as n increases, as also evidenced in the present paper[40]. Furthermore, the longer distance between crosslinks leads to less crosslinked network structures, as confirmed by the lowering of the rubbery modulus from Di-C7 to Di-C10. The values of T_{iso} reported in Table V-4 are in good agreement with those shown in Table V-2 from the DSC experiments. On the other hand, the T_g values are similar accordingly to the DSC results, but a narrower glass transition process is observed in formulations with longer aliphatic chains (fwhm narrows from 19.7 to 15.4 °C). This may be related to the differences between the size and number of the LC domains that, as explained above, can participate as physical crosslinks, affecting the glass transition process.

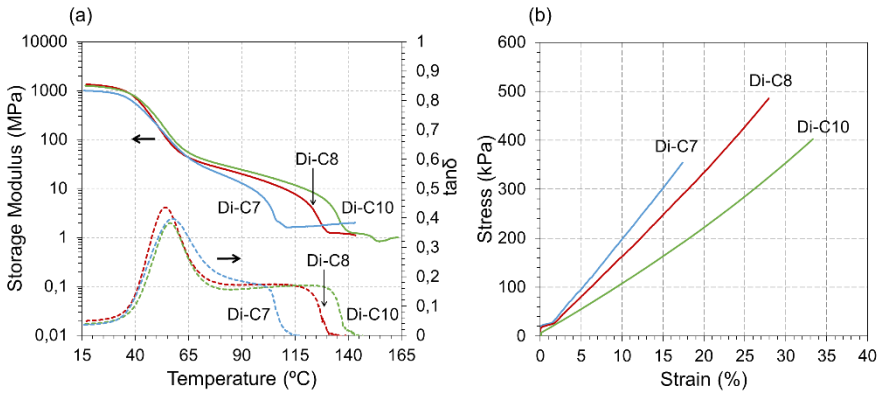

Figure V-5. (a) DMA curves and (b) tensile stress-strain curves of the different LCN studied above isotropization temperature.

Table V-4. Thermomechanical properties of the different LCN.

	DMA characterization				
Formulation	**E_g (MPa)**	**E_r (MPa)**	***fwhm* (°C)**	**T_g (°C)**	**T_{iso} (°C)**
Di-C7	1000 ± 20	1.6 ± 0.1	19.7 ± 0.3	57.4 ± 1	107 ± 2
Di-C8	1340 ± 50	1.3 ± 0.2	16.2 ± 0.5	54.1 ± 2	127 ± 3
Di-C10	1250 ± 50	1.2 ± 0.2	15.4 ± 0.5	57.3 ± 2	136 ± 3
	Mechanical characterization				
	E_T (MPa)		**σ_b (kPa)**		**ε_b (%)**
Di-C7	2.1 ± 0.1		350 ± 10		17 ± 2
Di-C8	1.6 ± 0.15		560 ± 15		31 ± 3
Di-C10	1.1 ± 0.15		430 ± 20		35 ± 4

The results of the mechanical characterization above the isotropization temperature is presented in Figure V-5(b), and the parameters of interest are summarized in Table V-4. Based on the DMA results, stress–strain experiments were performed in the rubbery state (T_{iso} + 20 °C), thus the straight curve (elastic response) in all tested formulations. The slope of the curves defines the tensile modulus, E_T, of the material which is related with the rubbery modulus (E_r) obtained from the DMA. As it can be seen, the E_T values are slightly higher in comparison with those of the DMA for the same formulation; however, the trend is the same (Di-C7 > Di-C8 > Di-C10), pointing out the effect of longer aliphatic chains in the crosslinking density. With regards to the stress–strain limits, ε_b is clearly related to the aliphatic chain length: the extended configuration of the network structure in the relaxed state (rubbery region) is longer when the effective chain length increases (length between crosslinking points). Therefore, Di-C10, with 10 repeating units in the aliphatic chain, shows the higher elongation at break value, while Di-C7 with 7 repeating units shows the lower. In contrast, σ_b does not show any specific trend. Di-C8 shows the higher value, similar to that of Di-C10, while it considerably drops with Di-C7. A different trend was found when tensile tests were performed on the LCN samples in their LC phase (75 °C). As reported in Figure V-17 in the V.2.SI, for all samples the stress–strain curves were characterized by the presence of three regions: a linear deformation at small strains was followed by a plateau in the stress–strain curve, due to the soft elastic response related to the polydomain-to-monodomain (P-M) transition[32]. Finally, the stress increased again up to the sample failure. Di-C7 showed the highest tensile strength ahead of the P-M transition, since an odd number of methylene groups resulted in a less extended conformation with respect to dicarboxylic acids with an even number of methylene groups. Moreover, Di-C7 displayed the highest length of the soft elastic plateau, likely connected to the higher order of orientation achieved under straining, as also revealed by XRD analysis. As

for the LCN samples based on even number of methylene groups, larger stress values were displayed by Di-C10 with respect to Di-C8, since tensile strength of crosslinked rubbers increases with number-average molecular weight of the starting un-crosslinked polymer[32].

It is worth noting that, from both the DMA and tensile results, the differences due to the chain length do not follow a linear trend: from Di-C7 to Di-C8 the variation of T_{iso}, crosslinking density, and mechanical properties (σ_b and ε_b) are much higher than from Di-C8 to Di-C10. This endorses the explanation given above, the network structure is somewhat affected by the less extended chain conformation obtained by the azelaic acid with an odd-number of repeating units, affecting the thermomechanical properties of the final material.

Shape-changing actuation response

As stated in the experimental section, the shape-changing characterization has been divided in two different experimental setups. On the one hand, the strain actuation and creep response have been investigated through shape-changing cycles under constant load. On the other hand, the actuation stress has been evaluated through fully constrained experiments.

In Figure V-6, the results of four consecutive shape-changing cycles under a constant load of 25% of σ_b for one single formulation (Di-C7) are presented in two different graphics: (a) temperature−strain-time and (b) stress−strain, respectively. The steps of the shape-changing cycles are highlighted with numbers (from 1 to 3) and the strain actuation and creep response are indicated in both graphics.

In order to follow up the evolution of the strain actuation and creep response, it is worth focusing on Figure V-6(a). First, the sample is loaded up to 25% of σ_b (∼5% of strain) at $T > T_{iso}$ (step 1). Then, on cooling below the anisotropization temperature T_{aniso}, the sample elongates due to the formation and alignment of the liquid-crystalline domains in the stretching direction as deduced from the X-ray diffraction analysis (step 2). Afterward, on heating up to T_{iso}, the sample undergoes a gradual contraction, followed by a drastic shrinkage produced by the disordering of the liquid-crystalline domains and the elastic response of the amorphous network above T_{iso} (step 3). Steps 2 and 3 are repeated in order to evaluate the effect of cycling in the strain actuation and creep response. Figure V-6(a) also shows that the elongation and stretching steps due to alignment and disordering of the liquid-crystalline domains take place in all cases at T_{aniso} and T_{iso}, respectively (see Table V-2), with no differences between the different cycles (highlighted with arrows in the graphic). In

Figure V-6(b), the stress–strain behaviour during the shape-changing cycles is presented. During the loading stage (1), the sample follows the expected linear/elastic stress–strain behaviour until the 25% of σ_b is reached. Afterward, during the elongation-shrinkage cycle, the behaviour is completely different: while for the initial loading the response is completely elastic, during the induced stretching and shrinkage the material undergoes a softening process usually called soft elasticity[32,48,49]. On cooling, the formation of the monodomain aligned along the stress direction causes drastic elongation with minimal force, whereas on heating, the disordering of the LC domains causes the elastic recovery of the amorphous network driven by the crosslinking points (note that the experiments were carried out at constant force, the initial stress is the programming stress while the final stress depends on the elongation level of the sample).

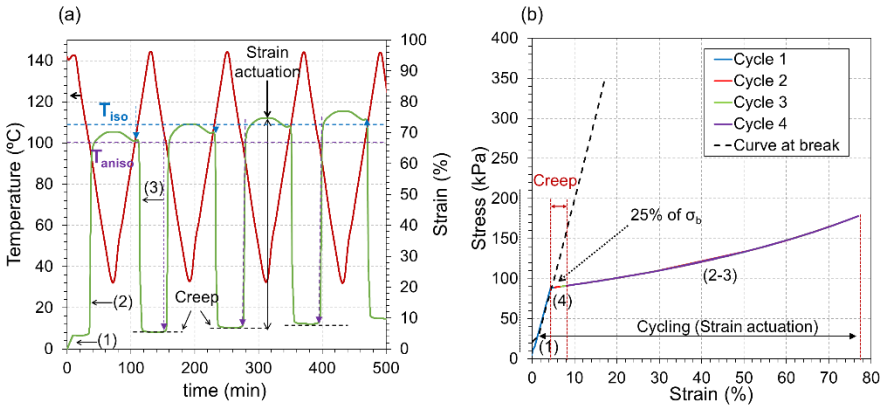

Figure V-6. Shape-changing four cycles of the Di-C7 at 25% of σ_b: (a) Temperature-strain-time graphic and (b) stress-strain graphic including the tensile at break curve (dashed line).

Taking into account the explanation above, in Figure V-7 the strain actuation (a) and creep response (b) are shown for the different formulations studied. On analysing the effect of cycling, the strain actuation considerably increases with the stress level but depends strongly on the number of cycles: at low stress level, it remains almost constant during the four consecutive cycles while at 75% of σ_b it worsens after the first cycle (i.e. Di-C7 and Di-C10) or in few cycles (i.e. Di-C8). On the other hand, the creep (or residual strain after each cycle) increases with both the stress level and after each cycle. Moreover, the increase in creep after each cycle appears to be constant and dependent on the stress level. In order to further analyse this phenomenon, 20 consecutive cycles have been performed for one single formulation (Di-C7) at 25% and 75% of σ_b, and the results are shown in Figure V-8. As it can be observed, the

stability of the strain actuation depends on both the stress level and the number of cycles; at 25% it reaches a maximum value after eight cycles and then begins to worsen, while at 75% it rapidly worsens after the first cycle. In contrast, the creep constantly increases during the 20 cycles, reaching a permanent strain of 25% at 25% of σ_b and 47% at 75% of σ_b. This can be rationalized as follows: after the curing process, some residual stress remains within the network structure that is accommodated after each cycle and, hence, the initial increase of the actuation strain. At some point, the network structure is completely relaxed, and therefore the constant increase of the creep eventually worsens the strain actuation performance. This is clearly appreciated at low stress level (a maximum is reached and then it begins to worsen). However, at 75% of σ_b, the material is subject to very high strain levels, resulting in irreversible deformation, either due to partial disruption of liquid crystallinity or to some damage of the network structure.

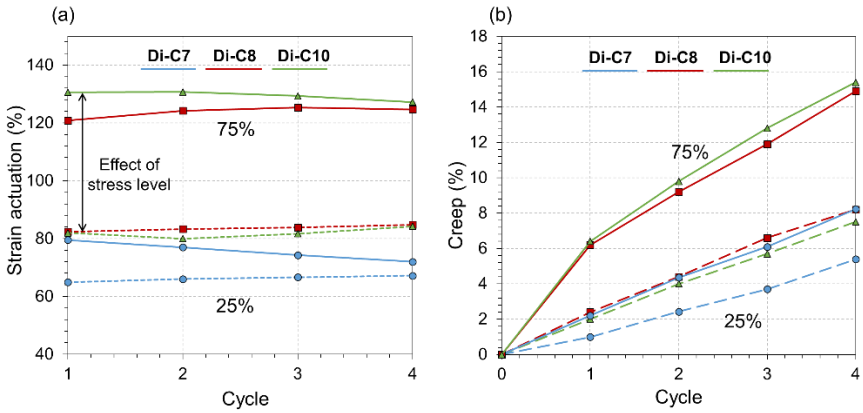

Figure V-7. (a) Four-cycle strain actuation and (b) creep response of the different LCN studied at 25% (dashed lines) and 75% (full lines) of σ_b.

In order to evaluate the influence of thermomechanical cycling on LC phase behaviour, DSC analysis was performed on Di-C7 before and after 20-cycle thermomechanical testing at 75% of σ_b. Results of the first heating runs (Figure V-18 in the V.2.SI) showed that thermomechanical cycling resulted in a more stable mesophase, as deduced by the slight increase in ΔH_{iso} and T_{iso}. Therefore, a damage of the network structure due to very high straining seems to be more plausible.

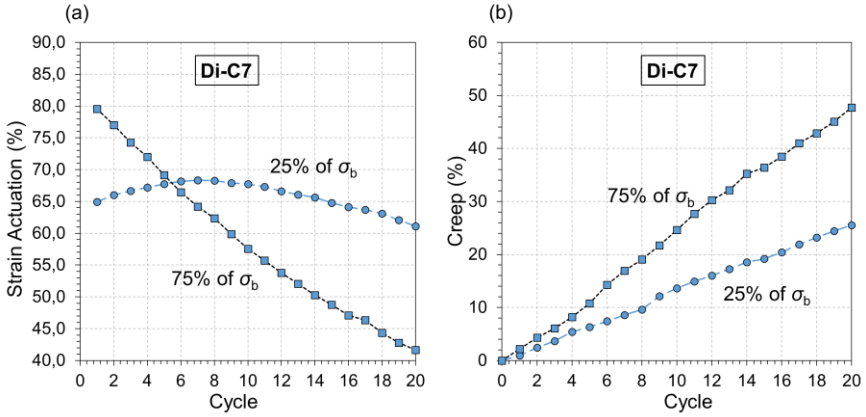

Figure V-8. Twenty-cycle strain actuation and creep response of Di-C7 at 25% and 75% of σ_b.

In order to further endorse the explanation above, in Figure V-9 the stress–strain response for all of the formulations at 25% and 75% of σ_b is shown in both a 2D (stress–strain) plot as in Figure V-6(b) and a 3D (stress–strain-cycle) plot. As it can be seen, the increase of the stress level not only leads to an increase of the strain actuation but considerably increases the maximum stress reached (i.e. from 0.5 to 3 MPa for the Di-C8 formulation at 75% of σ_b). Moreover, the slope notoriously increases at certain strain value (higher than 100%), mostly for those formulations with higher strain actuation performance (Di-C8 and Di-C10), pointing out a hardening process caused by the proximity of the aligned LC domains. Such a high stress/strain level could result in the appearance of defects and damage in the network structure, producing an unrecoverable and permanent deformation, as observed in other shape-memory applications[50], increasing gradually after each cycle.

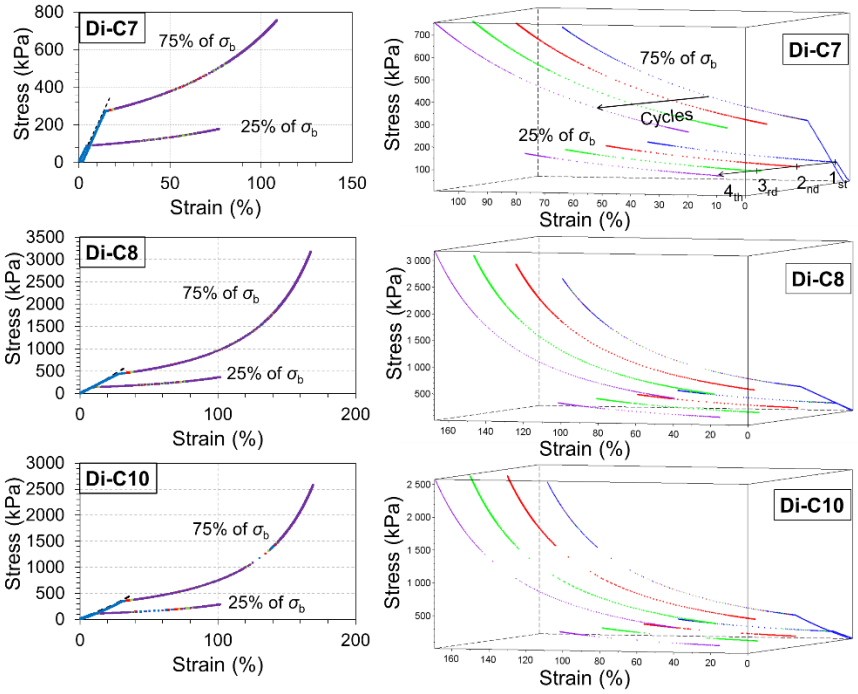

Figure V-9. 2D (stress–strain) and 3D (stress–strain-cycle) plots of four shape-changing cycles for the different formulations at 25% and 75% of σ_b.

If one compares the different materials, it is clear to see that an increase of the aliphatic chain length leads to higher strain actuation values. However, there is no linear trend observed. As discussed in the previous section, an important difference between Di-C7 and the other formulations comes from the odd number of repeating units, leading to differences in the network structure that would explain the notoriously lower strain actuation. On the other hand, from Di-C8 to Di-C10 there is a clear effect of the stress level: at 25% of σ_b Di-C8 elongates further than Di-C10 regardless of the shorter chain length, while at 75% of σ_b, Di-C10 overpasses Di-C8. This can be attributed to the considerably lower orientation parameter "*S*" of Di-C10 at 25% of σ_b as deduced form X-ray diffraction experiments. Regardless of the shorter chain length, the higher orientation achieved by the LC domains allows further elongation. The same trend is observed for the creep response: it increases with the chain length and stress level.

In Figure V-10, the results of the fully constrained experiments are shown for all of the formulations studied. In Figure V-10(a), the stress generated is plotted as a function of the temperature throughout heating

(from 20 °C, below T_g, up to 160 °C, above T_{iso}). Note that it was only possible to record one cycle per formulation programmed at 25% of σ_b due to the failure of the sample during the shrinkage step. One must take into account that these materials will be eventually incorporated inside a thiol-epoxy-based matrix in order to work as autonomous actuators, so that their final mechanical properties and failure limits are expected to be enhanced. On analysing the evolution of the stress, it increases up to a maximum value at a temperature around 90 °C in all of the formulations and then decreases to a minimum value closely related to T_{iso}. After that, the stress increases again until the sample is not able to resist, and it breaks.

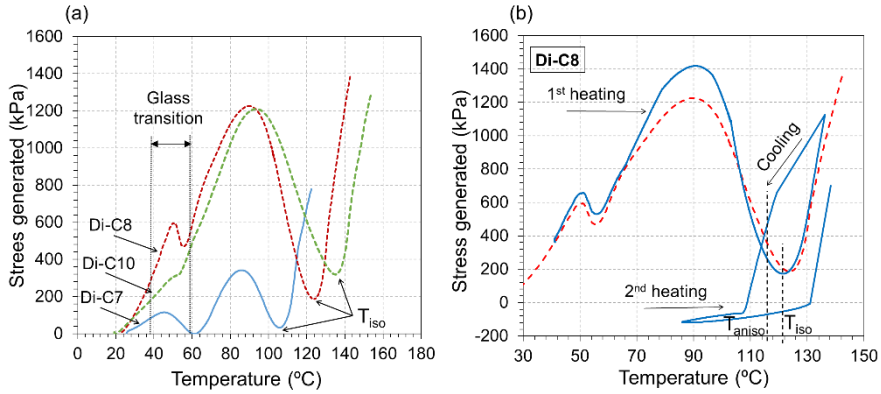

Figure V-10. Shape-changing fully constrained recovery processes: (a) stress generated as a function of the temperature for all of the formulations of study and (b) stress generated as a function of the temperature for the Di-C8 formulation (heating–cooling procedure).

First of all, one may notice that the stress increases on approaching the different relaxation processes. In uniaxial-constrained experiments, it is common to observe a decrease of the stress associated with the thermal expansion of the sample (the sample expands against the clamp generating a negative force)[51,52]. In our case, there is an apparent shrinkage effect, prevailing over the effect of thermal expansion which may be related to a residual recovery process taking place on heating up to T_{iso}. During the induced-elongation and further cooling below T_g, an unstable LC monodomain was formed and stabilized below T_g. On heating up again, the network structure gradually relaxes leading to such residual recovery process which takes over at $T \approx 90$ °C, the point at which the stress relaxes due to the thermal expansion of the sample. Afterward, once the material reaches T_{iso}, the entropic change associated with the isotropic phase transition (disordering of the LC domains) plus the induced-elongation (elastic recovery) causes the stress generation as

reported by Thomsen III et al.[53] for side-chain LCN and Giamberini et al.[32] using main-chain LCN. Moreover, if one analyses the strain evolution in Figure V-6(a), after the induced-elongation (step 2), there is a slight increase of the strain (creep process) until $T < T_g$, the point at which the maximum value is found, and then, on heating again for the shape-recovery to take place, this strain is slowly recovered until T_{iso} is reached, where the strain stabilizes (small plateau zone) before the drastic shrinkage (step 3). The appearance of such creep process during the cooling process may explain the residual recovery-process on heating up.

In order to endorse the explanation above, another sample of Di-C8 was programmed at 25% of σ_b and subject to a different heating-cooling procedure in order to avoid failure of the sample: from 30 °C, below T_g, up to 130 °C, above T_{iso}, down to 80 °C and up to 130 °C again at 2 °C/min. The results are shown in Figure V-10(b) together with the Di-C8 curve from Figure V-10(a). As it can be seen, on cooling from 130 to 80 °C after the first heating trace, the stress generated in the last step relaxes in a two-step process as deduced by the change in the slope at $T \approx T_{aniso}$: at higher temperature, the stress relaxation is influenced by the unstable state of the stretched network above T_{iso}, hence the high slope. On approaching T_{aniso} the slope increases because of the relaxation associated with the ordering of the LC domains. Once the LC transition is completed, the stress slowly decreases down to a negative value of −110 kPa pointing out that the network structure is almost completely relaxed. On heating again, the stress follows a linear trend with an increase at a temperature slightly above T_{iso} related to the disorder of the LC domains. This clearly points out the presence of a structural relaxation or residual recovery during the first heating trace due to the processing of the stretched shape (programming process) that is eventually erased after the first cycle. It is worth noting that the thermal hysteresis associated with the ordering/disordering of the LC domains is wider than the observed in Figure V-6(a) and thus than the expected from DSC experiments ($T_{iso} - T_{aniso}$ difference). This could be related to the imposed constant strain that somewhat makes difficult the ordering/disordering processes as it was observed in a previous work[28], where the shape-recovery process was extended under completely impeded recovery scenarios.

Finally, the actuation stress or stress associated with the recovery of the original shape is calculated as the difference between the minimum value achieved at T_{iso} and the maximum in which the sample breaks (see in Figure V-10(a)). As explained above, from the minimum stress value at T_{iso} to the failure point, the sample undergoes disordering of LC domains and then elastic shrinkage. The effective actuation stress would be that of

the elastic shrinkage, in which the sample shrinks about 95% in the case of Di-C8 (see actuation strain in Figure V-6 and Figure V-7), whereas the disordering of LC domains does not produce any remarkable displacement. However, it is not possible to correctly separate both processes, and thus, the whole step has been considered. The calculated actuation stress values are 746, 1195, and 966 kPa for Di-C7, Di-C8, and Di-C10, respectively. One may notice that in all of the formulations the actuation stress is higher than the programmed stress. For example, the programmed stress of Di-C8 is 350 kPa, and the same is observed for all of the formulations of study (note that the programmed stress corresponds to the maximum value of stress reached after the elongation, see in Figure V-9 the curves corresponding to 25% of σ_b). This can be explained as follows: the programming process involves a phase transition phenomenon in which the material undergoes a large softening process (soft elasticity), that is, a large entropic change with minimal force. Once the temperature rises again and the disordering of the LC domains take place (above isotropization), the material behaves as a rubber and all of this entropic change is elastically recovered, leading to considerably higher stress values.

4. Conclusions

Epoxy-based LCN as potential materials for the development of autonomous actuators have been successfully synthesized starting from dicarboxylic acids of different aliphatic chain lengths and a stiff rod-like epoxy-based mesogen. LCN with liquid-crystalline transitions above 100 °C and controlled strain and stress actuation have been obtained. The liquid-crystalline transitions have been checked by DSC analysis, pointing out an odd−even effect of T_{iso} with the increase of the aliphatic chain length. The degree of crystallinity and degree of orientation after shape-memory programming have been studied by means of X-ray diffraction analysis. All of the formulations have shown a smectic polydomain structure before programming and a highly oriented monodomain after programming. In formulations containing longer flexible chains a higher degree of crystallinity but lower degree of orientation after programming have been observed.

The effect of the liquid-crystalline domains in the network structural properties has been studied by means of thermomechanical analysis. The presence of liquid-crystalline domains decreases the mobility of the amorphous phase leading to materials with a partially relaxed modulus after T_g before the isotropization takes place. After isotropization ($T > T_{iso}$), the material relaxes completely, and the elastic modulus is

proportional to the crosslinking, as predicted by the theory of rubber elasticity. Formulations containing longer flexible segments (i.e. Di-C10) have lower relaxed modulus, that is, lower crosslinking density, and have higher strain at break above T_{iso}.

The shape-changing characterization has demonstrated the potential capabilities of these LCN as shape-memory actuators. On one side, the strain actuation can be modulated from low, ∼60%, to high, ∼160% strain level, by properly adjusting the length of the flexible segments, and varying the stress level. On the other side, these materials are capable of producing very high actuation stress values during the shape-changing. It is expected to control and stabilize the actuation performance in view of the actuator requirements and broaden the application range from micro to industrial scale applications.

Acknowledgements

The authors would like to thank MINECO (MAT2014-53706-C03-01 and MAT2014-53706-C03-02) and Generalitat de Catalunya (2014-SGR-67) for their financial support. X.F.F. also acknowledges the Serra-Húnter programme from the Generalitat de Catalunya. The authors also thank Dr. Francesc Guirado for recording XRD diffractograms.

References

[1] Du, H.; Lei, X.; Xu, Y.; Liang, Z.; Wang, Y. Multi-Stimuli Induced Shape Memory Effect of Polymers Based on Poly(Vinyl Alcohol). Prog. Chem. 2016, 28, 1648−1657.

[2] Li, G.; Wang, A. Cold, Warm, and Hot Programming of Shape Memory Polymers. J. Polym. Sci., Part B: Polym. Phys. 2016, 54, 1319−1339.

[3] Zhao, Q.; Qi, H. J.; Xie, T. Recent Progress in Shape Memory Polymer: New Behavior, Enabling Materials, and Mechanistic Understanding. Prog. Polym. Sci. 2015, 49−50, 79−120.

[4] Hager, M. D.; Bode, S.; Weber, C.; Schubert, U. S. Shape Memory Polymers: Past, Present and Future Developments. Prog. Polym. Sci. 2015, 49−50, 3−33.

[5] Lendlein, A.; Sauter, T. Shape-Memory Effect in Polymers. Macromol. Chem. Phys. 2013, 214, 1175−1177.

[6] García-Márquez, A. R.; Heinrich, B.; Beyer, N.; Guillon, D.; Donnio, B. Mesomorphism And Shape-Memory Behavior of Main-Chain Liquid-Crystalline Co-Elastomers: Modulation by the Chemical Composition. Macromolecules 2014, 47, 5198−5210.

[7] Burke, K. A.; Rousseau, I. A.; Mather, P. T. Reversible Actuation in Main-Chain Liquid Crystalline Elastomers With Varying Crosslink Densities. Polymer 2014, 55, 5897−5907.

[8] Ohm, C.; Brehmer, M.; Zentel, R. Application of Liquid-Crystalline Elastomers. Adv. Polym. Sci. 2012, 250, 49−94.

[9] Li, M.; Keller, P. Artificial Muscles Based on Liquid Crystal Elastomers. Philos. Trans. R. Soc., A 2006, 364, 2763−2777.

[10] Yu, Y.; Ikeda, T. Soft Actuators Based on Liquid-Crystalline Elastomers. Angew. Chem., Int. Ed. 2006, 45, 5416−5418.

[11] Ohm, C.; Brehmer, M.; Zentel, R. Liquid Crystalline Elastomers as Actuators and Sensors. Adv. Mater. 2010, 22, 3366−3387.

[12] Kolesov, I. Shape-Memory Behavior of Cross-Linked Semi-Crystalline Polymers and Their Blends. eXPRESS Polym. Lett. 2015, 9, 255−276.

[13] Lama, G. C.; Cerruti, P.; Lavorgna, M.; Carfagna, C.; Ambrogi, V.; Gentile, G. Controlled Actuation of a Carbon Nanotube/Epoxy Shape-Memory Liquid Crystalline Elastomer. J. Phys. Chem. C 2016, 120, 24417−24426.

[14] Li, Y.; Pruitt, C.; Rios, O.; Wei, L.; Rock, M.; Keum, J. K.; Mcdonald, A. G.; Kessler, M. R. Controlled Shape Memory Behavior of a Smectic Main-Chain Liquid Crystalline Elastomer. Macromolecules 2015, 48, 2864−2874.

[15] Chen, S.; Yuan, H.; Chen, S.; Yang, H.; Ge, Z.; Zhuo, H.; Liu, J. Development of Supramolecular Liquid-Crystalline Polyurethane Complexes Exhibiting Triple-Shape Functionality Using a One-Step Programming Process. J. Mater. Chem. A 2014, 2, 10169−10181.

[16] Saed, M. O.; Torbati, A. H.; Starr, C. A.; Visvanathan, R.; Clark, N. A.; Yakacki, C. M. Thiol-Acrylate Main-Chain Liquid-Crystalline Elastomers with Tunable Thermomechanical Properties and Actuation Strain. J. Polym. Sci., Part B: Polym. Phys. 2017, 55, 157−168.

[17] Saed, M. O.; Torbati, A. H.; Nair, D. P.; Yakacki, C. M. Synthesis of Programmable Main-chain Liquid-crystalline Elastomers Using a Two-stage Thiol-acrylate Reaction. J. Visualized Exp. 2016, 107, 1−10.

[18] Zhou, J.; Sheiko, S. S. Reversible Shape-Shifting in Polymeric Materials. J. Polym. Sci., Part B: Polym. Phys. 2016, 54, 1365−1380.

[19] Wang, W.; Liu, Y.; Leng, J. Recent Developments in Shape Memory Polymer Nanocomposites: Actuation Methods and Mechanisms. Coord. Chem. Rev. 2016, 320−321, 38−52.

[20] Lewis, C. L.; Dell, E. M. A Review of Shape Memory Polymers Bearing Reversible Binding Groups. J. Polym. Sci., Part B: Polym. Phys. 2016, 54, 1340−1364.

[21] Song, S. H.; Lee, H.; Lee, J. G.; Lee, J. Y.; Cho, M.; Ahn, S. H. Design and Analysis of a Smart Soft Composite Structure for Various Modes of Actuation. Composites, Part B 2016, 95, 155−165.

[22] Kumar, B.; Hu, J.; Pan, N.; Narayana, H. A Smart Orthopedic Compression Device Based on a Polymeric Stress Memory Actuator. Mater. Des. 2016, 97, 222−229.

[23] Ware, T. H.; Perry, Z. P.; Middleton, C. M.; Iacono, S. T.; White, T. J. Programmable Liquid Crystal Elastomers Prepared by Thiol−Ene Photopolymerization. ACS Macro Lett. 2015, 4, 942−946.

[24] Ware, T. H.; McConney, M. E.; Wie, J. J.; Tondiglia, V. P.; White, T. J. Voxelated Liquid Crystal Elastomers. Science 2015, 347, 982−984.

[25] Ahn, S.-k.; Ware, T. H.; Lee, K. M.; Tondiglia, V. P.; White, T. J. Photoinduced Topographical Feature Development in Blueprinted Azobenzene-Functionalized Liquid Crystalline Elastomers. Adv. Funct. Mater. 2016, 26, 5819−5826.

[26] Fernández-Francos, X.; Konuray, A.-O.; Belmonte, A.; De la Flor, S.; Serra, À.; Ramis, X. Sequential Curing of Off-Stoichiometric Thiol−Epoxy Thermosets with a Custom-Tailored Structure. Polym. Chem. 2016, 7, 2280−2290.

[27] Belmonte, A.; Fernández-Francos, X.; Serra, À.; De la Flor, S. Phenomenological Characterization of Sequential Dual-Curing of Off-Stoichiometric "Thiol-Epoxy" Systems: Towards Applicability. Mater. Des. 2017, 113, 116−127.

[28] Belmonte, A.; Russo, C.; Ambrogi, V.; Fernández-Francos, X.; De la Flor, S. Epoxy-Based Shape-Memory Actuators Obtained Via Dual-Curing of Off-Stoichiometric "Thiol-Epoxy" Mixtures. Polymers 2017, 9, 113.

[29] Belmonte, A.; Lama, G. C.; Gentile, G.; Cerruti, P.; Ambrogi, V.; Fernández-Francos, X.; De la Flor, S. Thermally-Triggered Autonomous Shape-Memory Actuators. Eur. Polym. J. 2017, under review.

[30] Westbrook, K. K.; Mather, P. T.; Parakh, V.; Dunn, M. L.; Ge, Q.; Lee, B. M.; Qi, H. J. Two-Way Reversible Shape Memory Effects in a Free-Standing Polymer Composite. Smart Mater. Struct. 2011, 20, 065010.

[31] Carfagna, C.; Amendola, E.; Giamberini, M. Liquid Crystalline Epoxy Based Polymers. Prog. Polym. Sci. 1997, 22, 1607−1647.

[32] Giamberini, M.; Cerruti, P.; Ambrogi, V.; Vestito, C.; Covino, F.; Carfagna, C. Liquid Crystalline Elastomers Based on Diglycidyl Terminated Rigid Monomers and Aliphatic Acids. Part 2. Mechanical Characterization. Polymer 2005, 46, 9113−9125.

[33] Giamberini, M.; Ambrogi, V.; Cerruti, P.; Carfagna, C. Viscoelasticity of Main Chain Liquid Crystalline Elastomers. Polymer 2006, 47, 4490−4496.

[34] Giamberini, M.; Amendola, E.; Carfagna, C. Liquid Crystalline Epoxy Thermosets. Mol. Cryst. Liq. Cryst. Sci. Technol., Sect. A 1995, 266, 9−22.

[35] Lee, H.; Neville, K. Handbook of epoxy resins; McGraw-Hill: New York, 1967.

[36] Leroy, E A. X-ray diffraction methods in polymer science; Robert, A. K., Ed.; Huntington: New York, 1979.

[37] Liquid Crystalline Polymers; Carfagna, C., Ed.; Elsevier: Capri, 1993.

[38] Madec, P. J.; Marechal, E. Kinetics and Mechanisms of Polyesterifications. II Reactions of Diacids and Diepoxides. Adv. Polym. Sci. 1985, 71, 153−228.

[39] Heise, M. S.; Martin, C. Curing Mechanism and Thermal Properties of Epoxy-Imidazole Systems. Macromolecules 1989, 22, 99−104.

[40] Giamberini, M.; Cerruti, P.; Ambrogi, V.; Vestito, C.; Covino, F.; Carfagna, C. Liquid Crystalline Elastomers Based on Diglycidyl Terminated Rigid Monomers and Aliphatic Acids. Part 1. Synthesis and Characterization. Polymer 2005, 46, 9113−9125.

[41] Finkelmann, H.; Happ, M.; Portugal, M.; Ringsdorf, H. Liquid Crystalline Polymers with Biphenyl-Moieties as Mesogenic Group. Makromol. Chem. 1978, 179, 2541−2544.

[42] Finkelmann, H. Liquid Crystalline Polymers. Angew. Chem., Int. Ed. Engl. 1987, 26, 816−824.

[43] Zentel, R. Liquid Crystalline Elastomers. Angew. Chem., Int. Ed. Engl. 1989, 28, 1407−1415.

[44] Pizzi, A. Principles of Polymer Networking and Gel Theory in Thermosetting Adhesive Formulations; Taylor & Francis Group: London, 2003.

[45] Askadskii, A.; Popova, M.; Matseevich, T.; Kurskaya, E. The Influence of the Degree of Crystallinity on the Glass Transition Temperature of Polymers. Adv. Mater. Res. 2013, 864−867, 751−754.

[46] Askadskii, A.; Popova, M.; Matseevich, T.; Afanasyev, E. The Influence of the Degree of Crystallinity on the Elasticity Modulus of Polymers. Adv. Mater. Res. 2013, 864−867, 640−643.

[47] Pascault, J.-P.; Sautereau, H.; Verdu, J.; Williams, R. J. J. Thermosetting Polymers; CRC Press: Boca Raton, FL, 2002.

[48] Ware, T. H.; Biggins, J. S.; Shick, A. F.; Warner, M.; White, T. J. Localized Soft Elasticity in Liquid Crystal Elastomers. Nat. Commun. 2016, 7, 10781.

[49] Ishige, R.; Osada, K.; Tagawa, H.; Niwano, H.; Tokita, M.; Watanabe, J. Elongation Behavior of a Main-Chain Smectic Liquid Crystalline Elastomer. Macromolecules 2008, 41, 7566−7570.

[50] Belmonte, A.; Guzmán, D.; Fernández-Francos, X.; De la Flor, S. Effect of the Network Structure and Programming Temperature on the Shape-Memory Response of Thiol-Epoxy “Click” Systems. Polymers 2015, 7, 2146−2164.

[51] Arrieta, S.; Diani, J.; Gilormini, P. Experimental Characterization and Thermoviscoelastic Modeling of Strain and Stress Recoveries of an Amorphous Polymer Network. Mech. Mater. 2014, 68, 95−103.

[52] Santiago, D.; Fabregat-Sanjuan, A.; Ferrando, F.; De la Flor, S. Recovery Stress and Work Output in Hyperbranched Poly-(Ethyleneimine)-Modified Shape-Memory Epoxy Polymers. J. Polym. Sci., Part B: Polym. Phys. 2016, 54, 1002−1013.

[53] Thomsen, D. L., III; Keller, P.; Naciri, J.; Pink, R.; Jeon, H.; Shenoy, D.; Ratna, B. R. Liquid Crystal Elastomers with Mechanical Properties of a Muscle. Macromolecules 2001, 34, 5868−5875.

V.2.SI - Supplementary Information

The synthesis of the epoxy-based mesogen, DIF, was carried out in three different batches of ≈ 30 g of product each one. Each batch was checked by means of calorimetric analysis in order to verify the formation of the desired monomer and to check the homogeneity. As it can be seen in Figure V-11, both the melting and crystallization transitions are almost equal for all the different DIF batches and the endothermic peak associated to the melting point is placed around 154 °C, similar to the values reported in the literature for this specific monomer[1]. Therefore, it has been decided to mix all batches in a single pot and use it as DIF for the synthesis of all the LCNs.

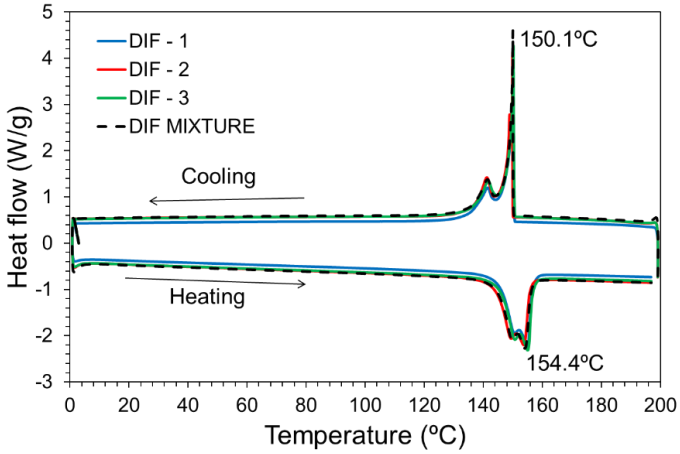

Figure V-11. DSC heating-cooling procedures of the different batches of epoxy monomer.

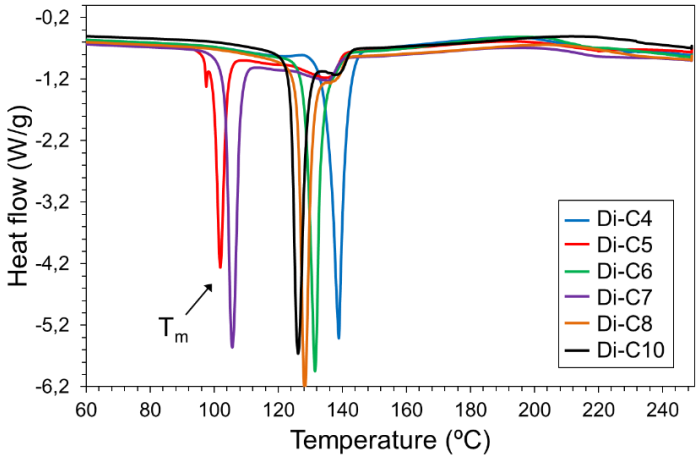

Figure V-12. DSC heating trace: melting of the acid and DIF compounds and curing.

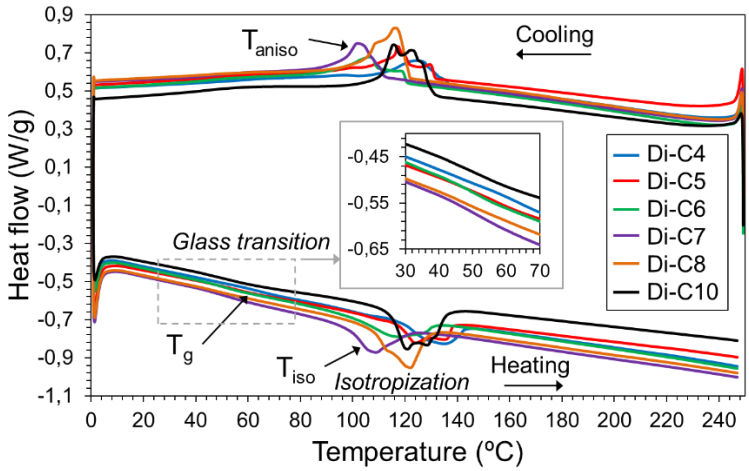

Figure V-13. DSC heating and cooling final traces: glass transition, isotropization and anisotropization processes without catalyst.

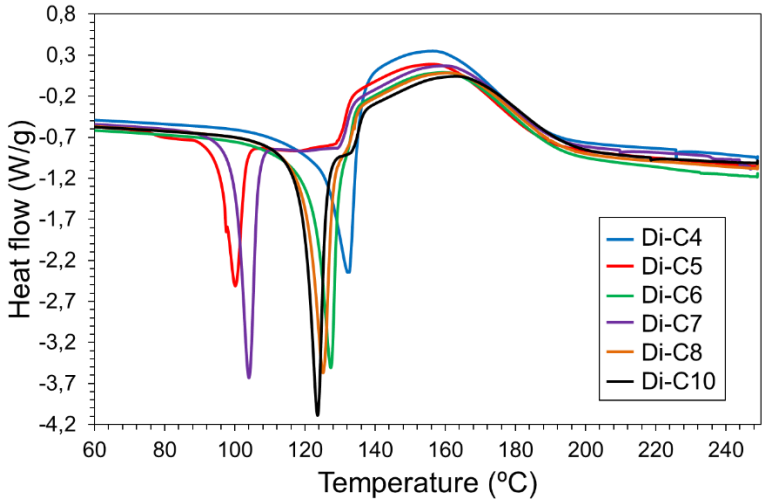

Figure V-14. DSC heating trace: melting of the acid and DIF compounds and curing process with catalyst.

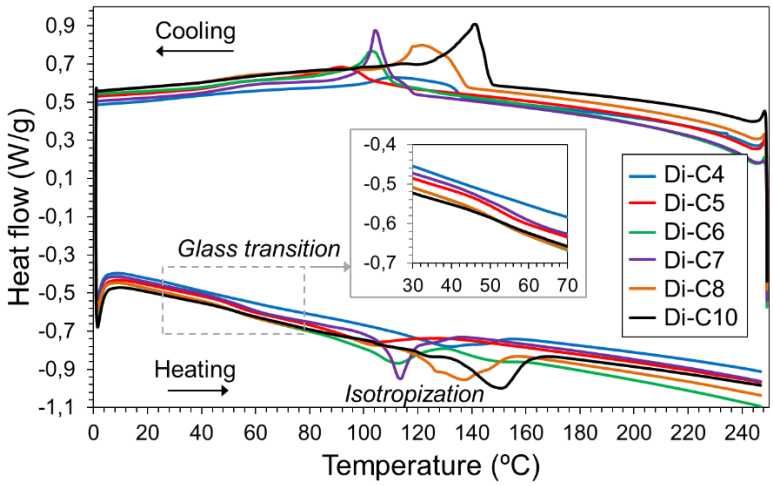

Figure V-15. DSC heating and cooling final traces: glass transition, isotropization and anisotropization processes with catalyst.

Table V-5. Thermal properties of the different LCN cured with catalyst and the enthalpy of reaction of the mixtures without catalyst.

Formulation	T_m (°C)	T_g (°C)	T_{aniso} (°C)	T_{iso} (°C)	ΔH_{iso} (J/g)	ΔH_c (J/g)	ΔH_r (J/g)	ΔH_r (no cat.) (J/g)
Di-C4	131.9	[a]	111.2	132.59	14.82	29.58	261.3	67.94
Di-C5	100.2	53.0	91.4	104.6	23.1	31.26	276.0	51.26
Di-C6	127.3	52.0	103.0	112.7	17.38	13.55	267.8	87.49
Di-C7	104.2	55.3	104.4	113.38	15.7	17.54	264.4	55.85
Di-C8	125.5	54.1	122.9	137.3	19.25	25.17	292.3	68.22
Di-C10	123.5	53.2	141.8	150.6	21.18	17.8	259.0	62.69

[a] Glass transition non-observed.

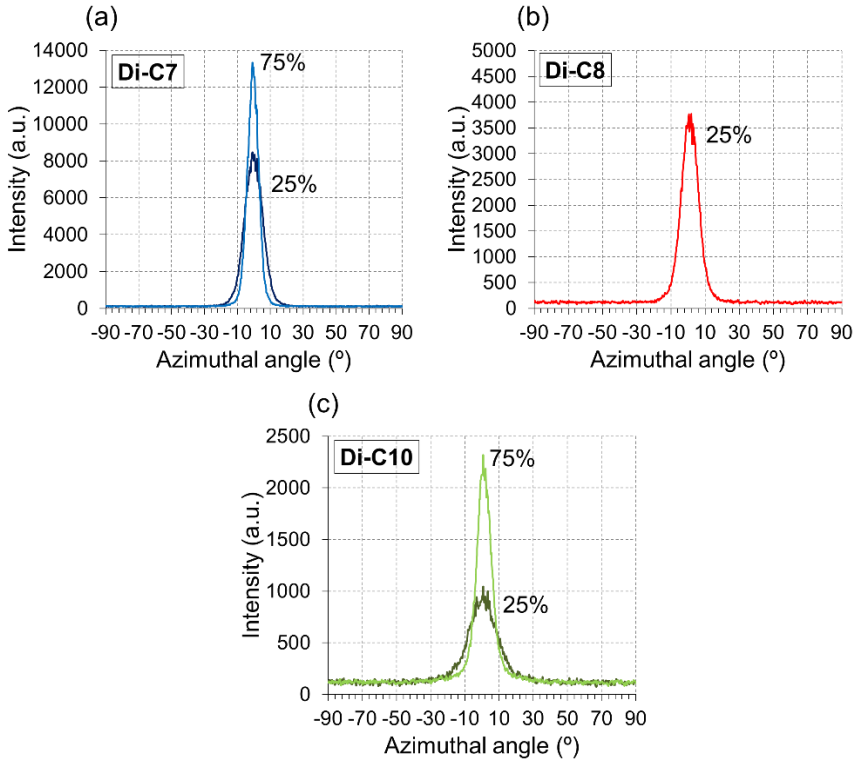

Figure V-16. Azimuthal intensity distribution of the peak corresponding to the order of the smectic layers for all the formulations of study at the 25% and for Di-C7 and Di-C10 at 75% of stress level.

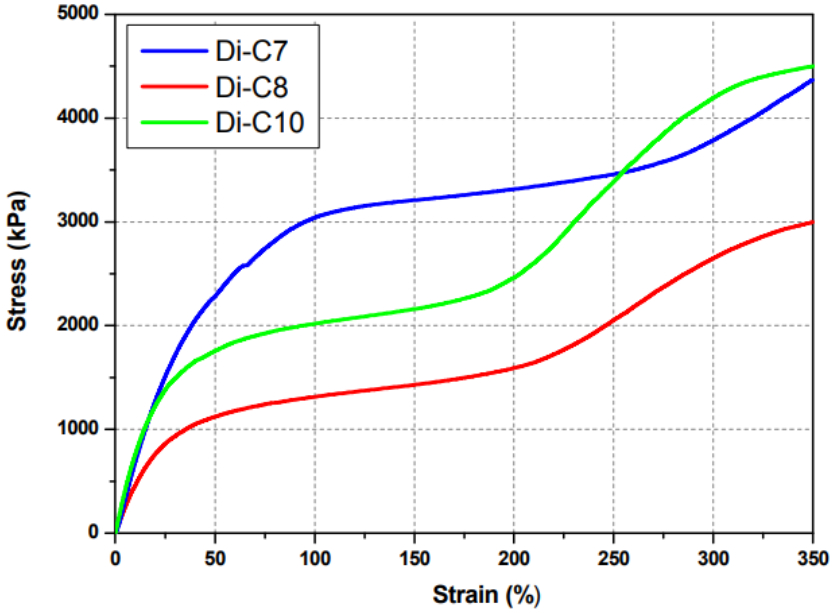

Figure V-17. Stress-strain curves of the LCN samples in the LC phase (*T* = 75 °C). Due to equipment experimental limitations, it was not possible to stretch the samples up to their respective strain at break values.

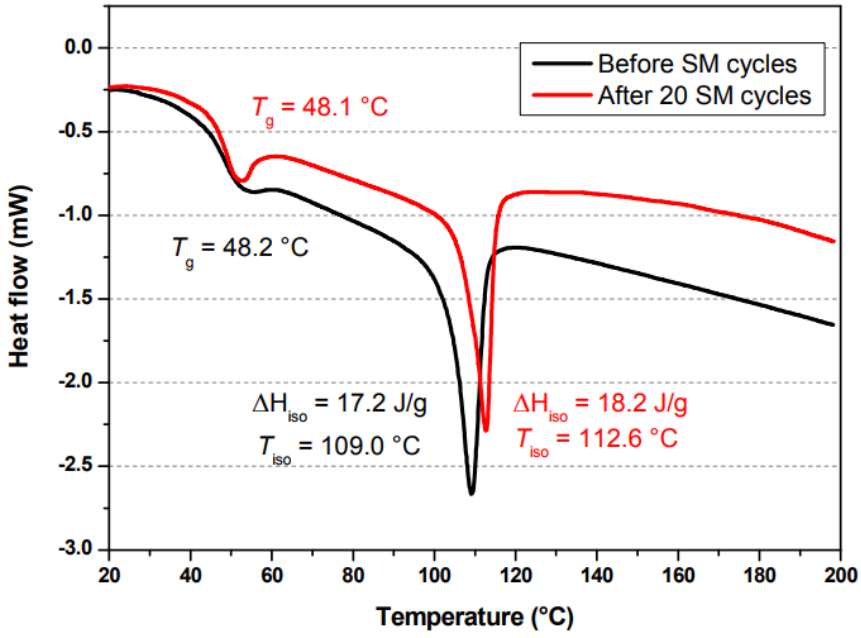

Figure V-18. DSC first heating scan performed on Di-C7 before and after thermomechanical shape-memory test.

References

[1] Li, Y.; Badrinarayanan, P.; Kessler, M. R. Liquid crystalline epoxy resin based on biphenyl mesogen: Thermal characterization. *Polym. (United Kingdom)* **2013**, *54*, 3017–3025.

UNIVERSITAT ROVIRA I VIRGILI
DESIGN AND CHARACTERIZATION OF ACTIVELY-MOVING POLYMERS OBTAINED VIA DUAL-CURING PROCESSING
Alberto Francisco Belmonte Parra

V.3 Thermally-triggered free-standing shape-memory actuators

European Polymer Journal, **2017**, 97, 241-252

Alberto Belmonte[1], Giuseppe C. Lama[2,3], Gennaro Gentile[3], Pierfrancesco Cerruti[3], Veronica Ambrogi[2,3], Xavier Fernández-Francos[4] and Silvia De la Flor[1]

1) Department of Mechanical Engineering, Universitat Rovira i Virgili, Av. Països Catalans, 26, 43007, Tarragona (Spain).

2) Department of Chemical, Materials and Production Engineering, University of Naples "Federico II", Piazzale Tecchio, 80, 80125, Napoli (Italy).

3) Institute for Polymers, Composites and Biomaterials, National Council of Research of Italy, Via Campi Flegrei, 34, 80078, Pozzuoli (NA) (Italy).

4) Thermodynamics Laboratory ETSEIB, Universitat Politècnica de Catalunya, Av. Diagonal, 647, 08028, Barcelona (Spain).

*** Supplementary information provided in section (V.3.SI).**

UNIVERSITAT ROVIRA I VIRGILI
DESIGN AND CHARACTERIZATION OF ACTIVELY-MOVING POLYMERS OBTAINED VIA DUAL-CURING PROCESSING
Alberto Francisco Belmonte Parra

Eur. Polym. J. 2017, 97, 241-252 **291**

Abstract

This investigation presents a new approach to obtain free-standing thermally-triggered "two-way" shape-memory actuators by realizing multilayer structures constituted by glassy thermoset (GT) films anchored to a previously programmed liquid-crystalline network (LCN) film. The GT is obtained via dual-curing of off-stoichiometric "thiol-epoxy" mixtures, thus enabling the development of complex actuator configurations thanks to the easy processing in the intermediate stage, and a compact and resistant design due to the strong adhesion between the layers obtained upon the final curing stage of the GT. A model based on the classical multi-layered beam theory to predict the maximum deflection of a "beam-like" design is proposed, and its reliability is verified by experimental investigation of actuators with different configurations and LCN stretching levels. The results show the capability of these actuators to bend and unbend under various consecutive heating-cooling procedures in a controlled way. The maximum deflection can be modulated through the configuration and the LCN stretching level, showing an excellent fitting with the model predictions. The model is able to predict high actuation levels (angles of curvature ≈ 180°) and the bidirectional shape-memory behaviour of the device as a function of the thickness, configuration of the layers, and the LCN stretching level. This approach enables the design of free-standing two-way actuators covering a range of bending actuation from 27 to 98% of the theoretical maximum deflection.

Keywords: shape memory polymers, thermally-triggered actuators, click chemistry, dual-curing, liquid-crystalline network.

1. Introduction

Shape-memory polymers (SMPs) are a class of responsive materials capable to shift under an external stimulus from one temporary shape to the original shape, usually fixed during the curing process[1-3]. The shape-transformation, commonly referred to shape-memory effect (SME), is not an intrinsic property of the polymer, but a consequence of an external treatment (programming process). The material must undergo a transformation from a stable state of the network (original shape) to one or more unstable states (temporary shapes) usually through thermomechanical procedures. These temporary shapes are stabilized by the formation of strong interactions within the network that impede the recovery of the original shape until an external stimulus, such as heat, is applied[4,5]. During this process, the material stores an amount of energy

that is then released in form of shape-transformation or force[6-10]. This makes this class of materials attractive in many fields of applications, such as industrial applications (i.e. opening-closing mechanisms[11]), aviation (i.e. morphing structures[12]) and robotics (i.e. artificial muscles[13]).

Liquid-crystalline networks (LCN) are another class of stimuli-responsive materials capable of shifting from one to another temporary shape in a reversible way under the effect of a constant load and an external stimulus, thus, only an initial programming process is required[14,15]. The reversible transformation is caused by the formation and alignment of liquid-crystalline (LC) domains in the load direction (induced-elongation) and further disordering of the LC domains (shrinkage) during the LC transition[16,17]. LCNs are potential candidates for actuation purposes due to their shape-shifting capability[18-20], but the need of a constant load in the shifting direction limits considerably their application. Recently, some strategies to overcome this limitation have been proposed. All of them depend on the incorporation of an internal or external stress-applying component into an already stretched LCN network (microscopic[21,22] or macroscopic[23,24] composites, respectively), hindering the recovery of the original shape, but adopting a metastable shape "state-of-ease" after the LCN shrinkage. This state can help to further elongate back to the original shape thanks to the internal stress generated between both the stress-applying component and the LCN[25,26]. In general words, combining a stress-applying component with a shape-shifting component leads to free-standing reversible actuation when compatibility between them is attained. The external incorporation of the stress-applying component was first reported by Westbrook et al.[27,28], who embedded a stretched poly(cyclooctene)-based LCN into an elastomeric matrix through thermal curing of the latter. The resulting material was able to produce small reversible flexural actuation by heating-cooling procedures. The internal approach could be achieved by taking advantage of two-stage curing procedures[22,29,30]. Anthamatten et al.[22] cured partially-crosslinked semi-crystalline poly(ε-caprolactone) networks after the 1st curing stage, stretched them up to 650% of strain and fixed the shape by UV-crosslinking (2nd curing stage). However, the actuation strain was lower than 15%. Yakacki et al.[29,30], enhanced the actuation strain up to 110% (with a programmed strain of 400%) by using a "thiol-acrylate" two-stage curing procedure with crosslinks of different functionality. Other approaches consisting of semi-crystalline networks with two crystalline domains or confined crystalline domains have been reported[31].

To this end, novel strategies to develop free-standing "two-way" shape-memory actuators are necessary to fulfil the increasing demand of smart actuators. Nowadays, their actuation response is limited to common designs and their performance is too low in comparison with common LCNs. In this work, a new methodology to develop free-standing "two-way" shape-memory actuators with an enhanced control of the actuation response is presented. An epoxy-based glassy thermoset (GT) obtained via sequential dual-curing of stoichiometrically imbalanced "thiol-epoxy" mixtures is used as external stress-applying component[32]. An epoxy-based lightly crosslinked LCN with high isotropization temperature (T_{iso}) is used as shape-shifting component[33]. The assembly of actuators with different configuration and actuation response is attained thanks to the possibility of pre-designing the GT component in the shape of solid-like and sticky layers with controllable thickness after the 1st curing stage that are further attached to the stretched LCN (shape-shifting component) through the 2nd curing stage of the former (multi-layer assembling methodology)[34]. The actuator response depends on the capability of the LCN to deform the device during the shrinkage (heating above T_{iso}) and the capability of the GT to stress back the LCN during the induced-elongation (cooling below T_{iso}). This can be achieved thanks to the rubbery elastic mechanical response of the GT material above T_g[35]. If the T_g of the GT is lower than T_{iso}, and operation of the GT-LCN assembly takes place only above this T_g, the GT will be in the rubbery state during both cooling and shrinkage processes, thus, making possible the elastic response. The way in which the actuator works is defined by the thermomechanical properties of the materials, the stretching level of the LCN, the adhesion between layers and the assembled configuration. In the present work, all these parameters are investigated and an analytical model to predict the actuation response is proposed. Experimental analyses are carried out with different actuator configurations and LCN stretching levels and the results are compared with the model predictions.

2. Experimental section

Materials

Actuator shape-shifting component: epoxy-based LCN

A commercial diol (4,4'-dihydroxybiphenyl, DIF, 97% purity, 186.21 g/mol), epichlorohydrin (Sigma-Aldrich, 99% purity, 1.183 g/ml, 92.52 g/mol), isopropanol and sodium hydroxide were used for the preparation of the epoxy-based mesogenic compound by epoxidation of the DIF monomer[36]. A commercial acid (1,8-octanedicarboxylic acid, sebacic acid, 98% purity, 202.25 g/mol) was used as curing agent of the

mesogenic compound for the synthesis of the LCN. Trycaprylyl methylammonium chloride was used as catalyst of the reaction. As it was reported[33], the use of sebacic acid as curing agent of this epoxy-based mesogen leads to the formation of a LCN material with isotropization temperature, T_{iso}, around 123 °C (the formulation is referred to as Di-C8, being C8 the number of (CH_2) units in the aliphatic chain of sebacic acid[33]). The curing process was carried out as already reported[33]: the mesogenic and the acid were mixed and melted at 180 °C under magnetic stirring during 10 minutes. Then, the catalyst was added and the whole mixture was rapidly poured in a preheated mould placed inside an oven at 200 °C. The mould consists of two Teflon-coated metallic plates and a thin Teflon layer placed in between as spacer. A square of 8 x 8 cm^2 with an exit channel of 2 cm of width to allow gas release was cut in the middle of the Teflon layer. The mixture was left 2 hours and a half to react. After that, films of 250 µm thick were obtained. The reaction scheme and expected network structure of the LCN are shown in Scheme V-2.

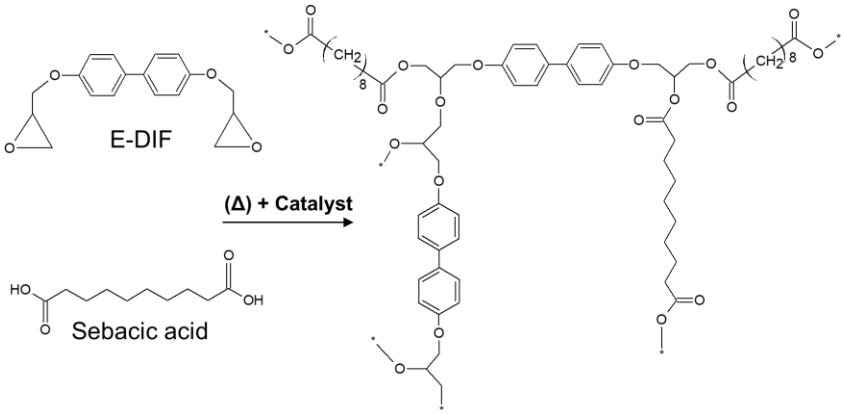

Scheme V-2. Reaction scheme and expected network structure of Di-C8 liquid-crystalline network.

Actuator stress-applying component: epoxy-based glassy thermoset (GT)

Diglycidyl ether of bisphenol A (DGEBA, GY240, Huntsman, Everberg, Belgium) with an epoxy equivalent weight of 182 g/eq was used as epoxy resin. Trimethylolpropane tris (3-mercaptopropionate) (S3, Sigma-Aldrich, St. Louis, MO, USA) with a thiol equivalent weight of 132.85 g/eq was used as curing agent in an under-stoichiometric proportion with respect to the epoxy groups in the system. 1-methylimidazole (1MI, Sigma-Aldrich, St. Louis, MO, USA, 82.1 g/mol) was used as catalyst in a proportion of 1 phr (parts of catalyst per hundred parts of the whole mixture). The DGEBA was dried under vacuum overnight at 80 °C before

use. The other reagents were used as received without further purification.

As it was reported in our previous work, off-stoichiometric "thiol-epoxy" mixtures with epoxy excess catalyzed by tertiary amines can lead to sequential dual-curing systems under the following curing conditions[32,34]. First, the mixture was allowed to react for 1 hour and 45 minutes at 50 °C for the "thiol-epoxy" polycondensation to take place (1st curing stage). After that, the temperature was increased up to 120 °C to trigger the homopolymerization of the epoxy excess (2nd curing stage) and was kept at that temperature for 2 hours for the reaction to be completed. In this work, the "intermediate" material (after 1st curing stage) is joined to the shape-shifting component through the 2nd curing stage, thus, the 2nd curing temperature has been lowered to 90 °C and the time extended to 6 hours to ensure the completion of the epoxy homopolymerization, in order to avoid overpassing T_{iso} (shape-shifting temperature), and therefore making the embedding process under safe conditions. This system is referred to as S3-DGEBA-1MI-r, where "*r*" is the thiol-epoxy ratio[32,34]. The reaction scheme of both, 1st and 2nd curing stages, and the expected networks of both, intermediate and final materials, are shown in Scheme V-3.

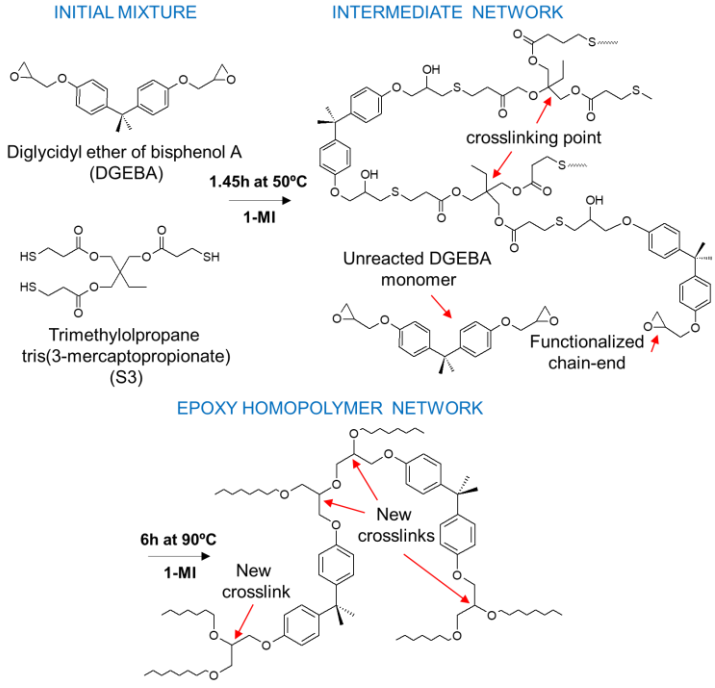

Scheme V-3. Reaction scheme and expected network of the intermediate and final materials obtained from the off-stoichiometric "thiol-epoxy" system studied.

Actuator assembling process

In Figure V-19 the assembling process of the actuator is schematized. The shape-shifting component is set up by programming the LCN material and fixing the final stretched shape (Figure V-19(a)). A Q800 DMA device (TA Instruments, New Castle "DE") equipped with a tension-film clamp in force-controlled mode is used for that purpose, following the same procedure as in our previous work[33]: a temperature of T_{iso}+20 °C is imposed during 5 minutes for thermal stabilization, followed by a ramp of 10 mN/min up to a specific % value of the stress at break (programming level, σ_{prog}); afterwards, the temperature is decreased down to 40 °C at 2 °C/min while maintaining the force applied (induced-elongation); finally, the shape is fixed by unloading at 10 mN/min. The programmed LCN is then cut in strips of 20 x (3.5 – 4) mm^2 effective length x width. Films of the GT "intermediate" material of different thickness (120 and 240 µm) are obtained after the 1st curing stage (Figure V-19(b)) as explained in the previous section, and are cut in strips longer and wider than the LCN ones (25 x 5 mm^2) to ensure that the whole surface of the LCN is in contact with the GT after joining the two materials (Figure V-19(c), top). In Figure V-19(c), bottom, an assembly consisting of one layer of GT of 120 µm placed at the bottom (Layer 1), the programmed LCN layer placed in the middle (Layer 2) and a combination of GT layers of 120 and 240 µm up to the desired thickness placed on top (Layer 3) are assembled. The assembly is then confined using Teflon layers and slightly fastened between Teflon-coated glass plates. Finally, the 2nd curing stage of the GT material is carried out and the resulting material is cut and polished Figure V-19(d), top, until all layers have equal width x length dimensions leading to the desired actuator configuration (Figure V-19(d), bottom). Note that the combination of GT layers on the top is referred to one thick layer (Layer 3) after the 2nd curing stage.

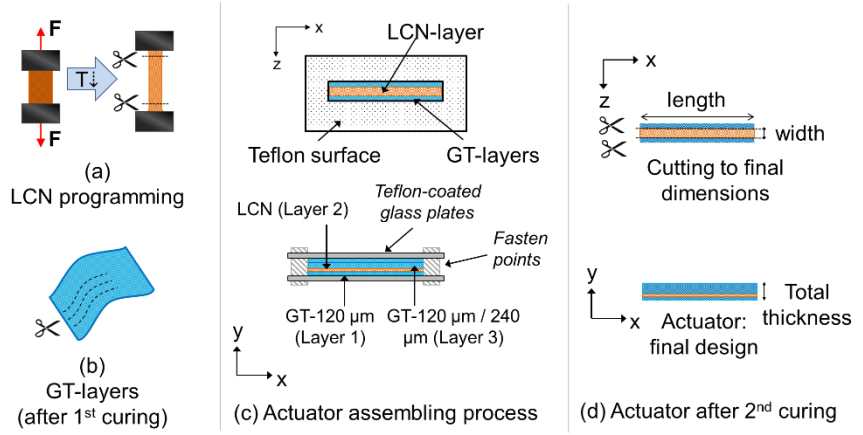

Figure V-19. Actuator assembling process: (a) programming and design of the LCN-layer; (b) curing and design of thin GT-layers; (c) configuration and (d) actuator assembly after final curing of the GT.

Characterization of the actuator response

In Figure V-20(a), the actuator design is presented in 3D and in the XY plane views. Several actuators, with different configurations and LCN programmed strain levels, were studied. The different configurations were obtained by increasing the thickness of the GT layers on the top (t_{L3}) and the volume fraction, v_F, is calculated as the relation between the GT material ($V_{GT} = V_{L1}+V_{L3}$) and the actuator ($V = V_{L1}+ V_{L2}+V_{L3}$).

$$v_F = \frac{V_{GT}}{V} = \frac{t_{GT}}{t} \qquad \text{(V-5)}$$

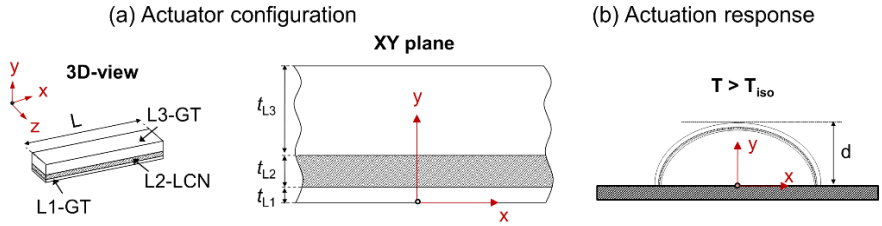

Figure V-20. (a) Actuator configuration (3D and XY plane views) and (b) actuation response.

Assuming the actuator as a multi-layered beam (a detailed explanation is provided in the analytical model section), the actuator will bend upon LCN shrinkage ($T > T_{iso}$) and unbend during the LCN induced-elongation ($T < T_{iso}$), according to Figure V-20(b). The *Actuation* can be defined as the quotient between the deflection reached after bending, d, and the theoretical maximum deflection (d_{max}) as follows:

$$Actuation = \frac{d}{d_{max}} \quad \text{(V-6)}$$

$$d_{max} = \frac{L}{\pi} \quad \text{(V-7)}$$

Where *L* is the length of the actuator and the maximum deflection is that corresponding to an angle of curvature of 180º.

The deflection reached, *d*, was determined experimentally and under an analytical method. The experimental analyses were carried out using the DMA equipment in the force-controlled mode equipped with a custom-made clamp geometry (see Figure V-31 in V.3.SI Supplementary Information). A constant force of 0.01 N was imposed in order to follow up the actuator motion. Ten heating-cooling consecutive cycles (1st heating from 30 °C up to T_{iso}+20 °C, then heating-cooling from 80 °C to 140 °C (≈T_{iso}+20 °C)) were carried out at a constant rate of 2 °C/min and the displacement of the clamp was recorded as a measure of the instantaneous deflection. In addition, the actuation capability of some of the prepared devices was tested using an oven, by heating up to 150 °C and naturally cooling down (low cooling rate). The process was visualized by a camera placed in front of the oven door (equipped with a transparent glass window) and the recorded images of the actuator motion are presented in the results section. For actuators with angles of curvature > 180º, the deflection was determined from the visual test, through the angle of curvature (the DMA was unable to follow the actuator motion). Finally, an illustrative video of the response of various actuators upon a heating-cooling cycle is presented in V.3.SI (Video V-1).

For developing the analytical model, the thermomechanical properties of both GT and LCN materials have been determined through dynamic-mechanical and thermomechanical analyses using the DMA equipment in tension-film clamp geometry. The dynamic-mechanical analyses were performed at a frequency of 1 Hz and 0.1% of strain amplitude. The glass transition temperature, T_g, and isotropization temperature, T_{iso}, were determined as the peaks of the tanδ curve after each relaxation process. The glassy, E_g, liquid-crystalline, E_{lc}, and rubbery, E_r, moduli were determined from the storage modulus plateau in each thermal region. The coefficients of thermal expansion (α) of the materials were also determined by DMA in the force-controlled mode. The samples were heated up to T_g + 30 °C (for the GT material) and T_{iso} + 30 °C (for the LCN material), cooled down rapidly and heated up again at 2 °C/min at a constant force of 0.001 N. The CTEs were determined as the slope of the

strain-temperature curve (%/°C) at the different thermal regions (α_g, α_{lc} and α_r) of the second heating curve.

Morphological analysis

Scanning Electron Microscopy (SEM) analysis have been carried out with a FEI Quanta 200 FEG (Hillsboro "OR" Eindhoven, The Netherlands) in high vacuum mode, using a secondary electron detector and an accelerating voltage ranging between 15 and 20 kV. The cryogenic fractures of different actuators have been analysed in order to investigate the adhesion between the layers. The most relevant images have been presented and discussed.

3. Analytical model

Considering the actuator as a multi-layered beam with "*n*" layers subject to a thermal load (ΔT), the mismatch between the layers produced by the generation of different "stress-free" strains is accommodated through a bending deformation according to the multi-layered beam theory (see illustration in Figure V-21(b))[37,38].

In the present case, "stress-free" strains (ε^0) are given by the combination of the thermal expansion (ε^{th}) and the LCN-shrinkage (ε^{prog}). The "stress-free" strains are additive and define the change in volume of each layer. The thermal expansion is a growing-strain that depends on the material thermal properties. Assuming that the coefficients of thermal expansion "α" are constant in each thermal region "*j*"[35] (i.e. glassy and rubbery regions), the total ε^{th} suffered by each layer "*i*" can be expressed as follows (equation (V-8)):

$$\varepsilon_i{}^{th} = \sum_{j=1}^{m} \alpha_{j,i} \cdot \Delta T_{j,i} \qquad \text{(V-8)}$$

On the other hand, ε^{prog} is associated to an external strain and therefore is a built-in strain of the layer that must be calibrated externally (in the present case it corresponds to the programmed strain level, thus, the nomenclature refers to "programmed strain"). The total "stress-free" strain suffered by each layer is then expressed as:

$$\varepsilon_i{}^0 = \varepsilon_i{}^{th} + \varepsilon_i{}^{prog} \qquad \text{(V-9)}$$

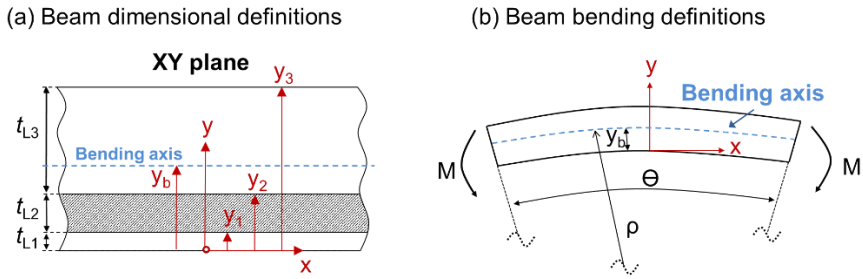

Figure V-21. Geometrical definitions of the layered beam: (a) Dimensional definitions and (b) bending definitions.

Assuming that the actuator is a perfect beam (length » transversal section), that the transversal section remains unchanged after deformation and that the interaction between layers is perfect (the beam behaves as a unity), the study can be reduced to a one-dimensional geometry, in which only variations in the "*x*" direction (length direction) are considered. In Figure V-21(a) the geometrical definitions are presented: the "y-axis" zero position has been placed at the bottom of the beam, thus, the position of each layer, y_i, is defined as the sum of the thickness of all layers below plus its own ($y_i = \sum_i^n t_i$). The position of the bending axis (axis in which the bending strain is null) has been refereed as y_b. After bending, the curvature, κ, the radius of curvature, ρ, and the angle of curvature θ have been defined as indicated in Figure V-21(b). For small deformations, κ, ρ and θ are related through the length "*L*" of the beam as follows:

$$\theta = L\kappa = \frac{L}{\rho} \qquad \text{(V-10)}$$

As detailed in the V.3.SI, the normal strain in each layer can be related to the curvature of the beam through the Euler-Bernoulli theory. Adding the contribution of the "stress-free" strains, the total strain in each layer, ε_i, can be expressed relative to the bending axis as follows:

$$\varepsilon_i = \varepsilon_i^{elastic} + \varepsilon_i^{0} = C + (y - y_b)\kappa \qquad \text{(V-11)}$$

Where super index "*elastic*" refers to the total elastic strain and "*C*" is a constant value related to the uniform strain generated on each layer after geometrical equilibrium (a detailed explanation is provided in the V.3.SI). The stress-strain relation is then approached on applying the Hooke's law to the elastic strain, $\varepsilon_i^{elastic}$:

$$\sigma_i = E_i \cdot \left((y - y_b)\kappa + C - {\varepsilon_i}^0\right) \quad \text{(V-12)}$$

Where E_i is the modulus of each layer (E_i is assumed constant in each thermal region). After applying the equilibrium conditions (force and moment balances) in each layer, κ and y_b are related as follows:

$$\sum_{i=1}^{n} \int_{y_{i-1}}^{y_i} \sigma_i dy = \sum_{i=1}^{n} \left(\int_{y_{i-1}}^{y_i} E_i y dy - \int_{y_{i-1}}^{y_i} E_i y_b dy \right) \cdot \kappa + \int_{y_{i-1}}^{y_i} E_i C dy - \int_{y_{i-1}}^{y_i} E_i {\varepsilon_i}^0 dy = 0 \quad \text{(V-13)}$$

$$\sum_{i=1}^{n} \int_{y_{i-1}}^{y_i} \sigma_i y dy = \sum_{i=1}^{n} \left(\int_{y_{i-1}}^{y_i} E_i y^2 dy - \int_{y_{i-1}}^{y_i} E_i y_b y dy \right) \cdot \kappa + \int_{y_{i-1}}^{y_i} E_i C y dy - \int_{y_{i-1}}^{y_i} E_i {\varepsilon_i}^0 y dy = 0 \quad \text{(V-14)}$$

Solving equations (V-13) and (V-14), the curvature, κ, can be expressed as a function of different constants as follows:

$$\kappa = \frac{A(M_{SR} + M_{th}) - B(F_{SR} + F_{th})}{AB - D^2} \quad \text{(V-15)}$$

where A, B and D refers to the extensional, bending and coupling constants respectively in terms of laminated composite materials. F_{th} and M_{th} denote respectively the force and moment generated by the thermal expansion "stress-free" strain and F_{SR} and M_{SR} to the LCN shrinkage "stress-free" strain (all the constants are developed in the V.3.SI).

Using the κ, ρ and θ relation (see equation (V-10)), the deflection, d, can be approached by trigonometry as follows:

$$d\ (\theta < 180^o) = \rho \cdot (1 - \cos\frac{\theta}{2}) \qquad d\ (360^o > \theta > 180^o) = \rho \quad \text{(V-16)}$$

Note that for an angle of curvature higher than 180º, the deflection is defined as the radius of curvature, meaning that it decreases as the circle (360º) is being formed. It must be acknowledged that such bending level is out of the elastic theory limits (small deflections);

however, it is considered for further discussion with the experimental results. Finally, the *Actuation* is determined using equation (V-6):

$$Actuation = \frac{d}{d_{max}} = \frac{\rho \cdot \left(1 - \cos\frac{\theta}{2}\right)}{L/\pi} \qquad \text{(V-17)}$$

From the equation above it is deduced that the maximum deflection is reached for an angle of 180º by definition, whereas, higher angles of curvature lead to lower *Actuation*.

4. Results and discussion

As stated in the introduction, free-standing, reversible actuation is attained by the incorporation of a compatible stress-applying component into the shape-shifting component[25]. In this work, an epoxy-based glassy thermoset, GT, is used as external stress-applying component and an epoxy-carboxylic LCN stretched up to a certain strain level (programmed strain, ε_{prog}) is used as the shape-shifting component. The thermomechanical compatibility between components is achieved by adjusting the T_g of GT below the T_{iso} of the LCN, to ensure that GT is in the rubbery state ($T > T_g$) during the LCN shrinkage, thus allowing further LCN elongation thanks to the GT elastic response[27].

Taking into account the above, the T_g of the GT material must be lower than 121 °C (T_{iso} of the LCN material). Another important consideration is that the GT intermediate material (after the 1st curing stage) must be solid-like and deformable to allow the processing of strips before the assembling process. As it was reported in our previous work[34], the physical and structural properties of the GT material are controlled with the thiol-epoxy ratio. For this particular system, a ratio $r > 0.65$ (minimum ratio to form a gelled structure after the 1st curing stage) leads to solid-like and deformable intermediate materials that after the 2nd curing stage reach T_g values ranging from 70 °C to 34 °C. In addition, it was demonstrated that using ratios slightly below this critical ratio also leads to solid-like materials, enhancing the deformability and stickiness. These materials are interesting due to their liquid-like behaviour, which is expected to enhance the adhesion between the LCN and GT layers[39].

Therefore, a S3-DGEBA-1MI system with a “thiol-epoxy” ratio of 0.6 has been chosen as the GT material of study. This system leads to a final material with a T_g lower than T_{iso}, as will be later shown.

Determination of the model parameters

Once the stress-applying GT and the LCN have been selected, their structural and thermal properties were determined as detailed in the experimental section. The results are summarized in Table V-6.

Table V-6. Formulation, dynamic-mechanical and thermal properties of the GT and LCN materials.

Material	Nomenclature	E_g (MPa)	E_{lc} (MPa)	E_r (MPa)		
GT	S3-DGEBA-1MI-0.6	2150 ± 50		16.8 ± 0.3		
LCN	Di-C8	1340 ± 50	10 ± 1	2.9 ± 0.2		
		α_g ($^oC^{-1}$)	α_{lc} ($^oC^{-1}$)	α_r ($^oC^{-1}$)	T_g (^oC)	T_{iso} (^oC)
GT	S3-DGEBA-1MI-0.6	$3.4{\cdot}E^{-5}$		$2.0{\cdot}E^{-4}$	71 ± 2	
LCN	Di-C8	$1.0{\cdot}E^{-4}$	$3.0{\cdot}E^{-4}$	$7.6{\cdot}E^{-5}$	54 ± 2	121 ± 3

As stated in the experimental section, the LCN films were stretched up to a certain % of the stress at break, σ_b, in order to program the shape-shifting component. Here, five levels of programming have been chosen for a preliminary analysis of the actuator response with the model (σ_{prog} = 1%, 2%, 5%, 10% and 25% of σ_b). The results are presented in Figure V-22.

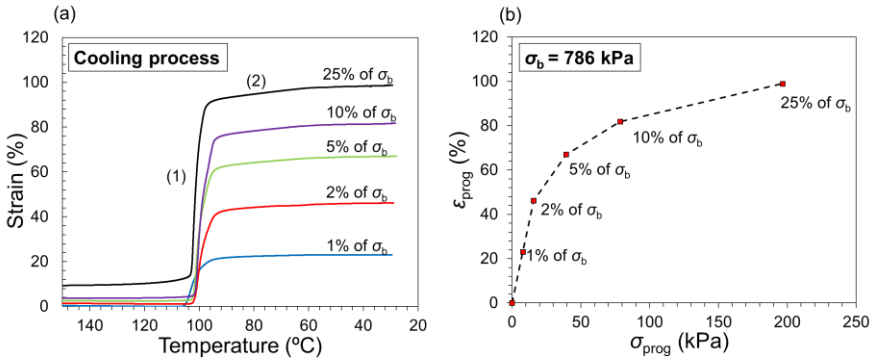

Figure V-22. LCN programming at different stress levels (from 1% to 25% of stress at break); (a) Strain as a function of the temperature and (b) programmed strain as a function of the programming stress.

In Figure V-22(a), the strain evolution is plotted as a function of the temperature during the cooling step, whereas in Figure V-22(b), the relation between the programming stress, σ_{prog}, and programmed strain, ε_{prog}, is shown (σ_b has been highlighted in the graphic). As can be observed, the programmed strain (determined as the maximum strain reached after cooling down) increases with the increase of the programming stress level with no linear trend: at low programming level, from 1% to 5% of σ_b, the

increase in programmed strain is much higher than from 5% to 25% of σ_b as deduced in Figure V-22(b). This can be explained as follows: the induced-elongation (step (1) in Figure V-22(a)) is related to the soft elasticity, where the configurational change of the network (formation of the LC domains) on cooling below T_{iso}, allows stretching with minimal force (formation of a monodomain aligned in the load direction)[40]. Of course, this process is time-temperature dependent. In our case, the cooling rate is fixed, however the force applied depends on the programming level and therefore the stretching rate increases with the programming level (these experiments were carried out in force-controlled mode). High stretching rates may lead to network relaxation phenomena taking place during the stretching process, thus, slowing down the process[33]. If one analyses the strain evolution after the induced-elongation (step (2) in Figure V-22(a)), it is clear that higher programming levels result in a constant increase of the strain associated to some residual relaxation of the network taking place at $T < T_{iso}$. This would explain the incomplete network relaxation during the induced-elongation, step (1), and therefore, the nonlinear trend observed. However, in our previous work[33] we demonstrated that high shape-memory cycling stability is attained when programming at 25% of σ_b, therefore we do not expect a great influence of the programmed stress on the actuator stability.

Model output: preliminary analysis

The model parameters for the case of study are summarized in Table V-7. As stated in the analytical section, the actuator is subject to a thermal load, ΔT, which is responsible for two different phenomena: the thermal expansion of the different layers and the shrinkage of the LCN layer. While the strain related to the LCN shrinkage is a constant parameter in the model, the strain associated to the thermal expansion depends on the thermal load. In the present case, the thermal expansion generated from room temperature up to 90 °C is neglected since the assembling process was carried out at 90 °C, thus, the corresponding thermal history is already included in the actuator at room temperature and eventually erased after reaching 90 °C (the zero point is placed at 90 °C). Therefore, the temperature gradient is defined from 90 °C up to 140 °C (in Table V-7, the thermal load is divided in the different thermal regions according to the transition temperatures of each material).

Table V-7. Model parameters for the case of study: actuator geometry (thickness and length), thermal load and programmed strain.

Layer	Material	t (mm)	L (mm)	ΔT_g[b] (ºC)	ΔT_{lc}[b] (ºC)	ΔT_r[b] (ºC)	ε_{prog}
L1	GT	0.12	20	0	0	50	0
L2	LCN	[0.19 – 0.23][a]	20	0	31	29	[-0.23 – -0.81]
L3	GT	[0.12 – 5]	20	0	0	50	0

[a] The thickness of the LCN layer depends on the programmed strain level.
[b] "g", "lc" and "r" sub-indexes refer to the glassy, liquid-crystalline and rubbery regions, respectively.

Four different programmed strain levels (ε_{prog} = 23%, 43%, 71% and 81%) corresponding to a programming stress level of 1%, 2%, 5% and 10% of σ_b (see Figure V-22) have been used in the model. Each programmed strain level has been applied for different configurations through the variation of t_{L3} (from t_{L3} = 0.12 corresponding to $v_F \approx 0.5$ to t_{L3} = 5 mm, $v_F \approx 1$), in accordance with the proposed actuator design (see Figure V-20(a)) and equation (V-5). The length of the actuator has been defined as 20 mm and the width neglected since it is eventually simplified in the model.

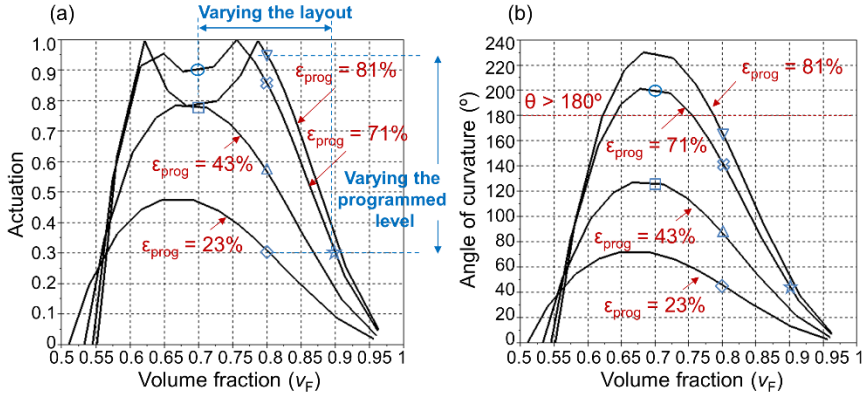

Figure V-23. Model output: (a) Actuation and (b) angle of curvature as a function of the volume fraction at different programmed strain levels. The blue markers indicate the experimental assemblies to be tested (they are not experimental results).

The results of the model are shown in Figure V-23: the Actuation (Figure V-23(a)) and the angle of curvature (Figure V-23(b)) are presented as a function of the volume fraction (different actuator configurations) for the different programmed strain levels (different curves). As it can be observed, the *Actuation* strongly depends on both the programmed strain level and the volume fraction. Starting from a theoretical v_F = 1 ($t_{L3} \approx$ infinite), point at which the *Actuation* would be null, on decreasing v_F, that is, decreasing t_{L3}, the *Actuation* increases up to a maximum value (see Figure V-23(a)). If the sum of the "stress-free" strains is low enough to

avoid angles of curvature > 180º (see in Figure V-23(b)), this maximum is placed at $t_{L3} = t_{L2} + t_{L1}$ (geometrical equilibrium); from this point to lower volume fractions there is a progressive decrease of the *Actuation* as t_{L3} approaches t_{L1} (i.e. at ε_{prog} = 23% and 43%) point at which there is no "bending" *Actuation* (theoretically, the beam would suffer a planar shrinkage). From this v_F (i.e. $v_F \approx 0.55$ for the ε_{prog} = 81% curve) to lower volume fractions the *Actuation* curve would be the same but in the opposite direction (an inversion of the *Actuation* because the curvature of the beam, κ, becomes negative). When the "stress-free" strains produce angles of curvature > 180º (i.e. at ε_{prog} = 71% or higher), the deflection is equal to the radius of curvature (see equation (V-7)), therefore, the *Actuation* is maximum at $\theta = 180^o$ and decreases at higher angles of curvature. Because of the geometrical equilibrium is found at $\theta > 180^o$, there is a minimum instead, and two maximum values appear at $\theta = 180^o$.

Overall, the model predicts that it is possible to control the *Actuation* by modifying the actuator configuration and the LCN programmed strain level. This is of utmost importance when designing the actuator. The thickness of the GT layers defines the stiffness of the actuator, thus, the potential capabilities as a mechanical actuator, as well as the actuation design. Therefore, for a given configuration, the *Actuation* can be optimized by modifying the programmed strain level in an easy and efficient manner. Moreover, this can be extended to the variation of the thermomechanical properties of both materials. The model is able to predict the response depending on the materials properties, thus, it is possible to modulate both the stiffness and *Actuation* thanks to the versatility of the proposed materials: in the GT material, the network structure can be controlled through the "thiol-epoxy" ratio as well as the "thiol-epoxy" system[11,34], whereas, in the LCN material, the rubbery modulus and isotropization temperature can be easily tailored by varying the aliphatic chain length of the acid curing agent as proposed in a previous work[33].

In order to verify the model predictions, an experimental investigation of the actuators varying the configuration and LCN programmed strain level has been carried out. In Figure V-23, the blue markers indicate the experimental actuators assembled and analysed (they are not experimental results). As it can be seen, a wide range of possible responses is covered: from low level of *Actuation* (corresponding to a v_F = 0.9) to high level of *Actuation* (for v_F = 0.7). As stated earlier, angles of curvature > 180º (i.e. the point v_F = 0.7 with ε_{prog} = 71%) are probably out of the model limits of applicability, however, it is worth analysing the real behaviour and compare it with the model predictions.

Actuator response: experimental analysis

The proposed actuator configurations have been assembled as explained in the experimental section. The dimensional parameters and LCN programmed strain levels are summarized in Table V-8. Note that the nomenclature of the actuators refers to the volume fraction (i.e. "07" means v_F = 0.7) and the programming stress (i.e. "1%" is σ_{prog} = 1% of σ_b). In Table V-8, it is worth noting the variation of some parameters, such as the total thickness (t) and the LCN programmed strain level (ε_{prog}). As the purpose of this study is to analyse different geometrical configurations and different LCN programmed strain levels, we had defined the parameter v_F as a non-dimensional factor eliminating the geometrical variation in thickness and making possible to vary the configuration in a controlled way. On the other hand, the variation in programmed strain (ε_{prog}) is similar to the error found in typical stress-strain experiments. The variation of the width is not relevant if the actuator accomplishes the geometrical relation for a beam-like design, and the variation of ± 1 mm in length is taken into account in the model and will be discussed later.

Table V-8. Dimensions and programmed strain for the actuators of study.

Actuator	v_F	t_{L1} (mm)	t_{L2} (mm)	t_{L3} (mm)
A_08_1%	0.808 ≈ 0.8	0.12	0.23	0.85
A_08_2%	0.809 ≈ 0.8	0.12	0.21	0.77
A_08_5%	0.820 ≈ 0.8	0.12	0.20	0.79
A_08_10%	0.805 ≈ 0.8	0.12	0.20	0.69
A_07_2%	0.697 ≈ 0.7	0.12	0.22	0.37
A_07_5%	0.717 ≈ 0.7	0.12	0.21	0.40
A_09_5%	0.903 ≈ 0.9	0.12	0.20	1.72

		t (mm)	w (mm)	L (mm)	ε_{prog} (%)
A_08_1%	0.808 ≈ 0.8	1.20 ± 0.01	3.0 ± 0.1	20.0 ± 0.1	23.0
A_08_2%	0.809 ≈ 0.8	1.10 ± 0.01	3.5 ± 0.1	20.8 ± 0.1	49.3
A_08_5%	0.820 ≈ 0.8	1.11 ± 0.01	3.9 ± 0.1	19.2 ± 0.1	70.0
A_08_10%	0.805 ≈ 0.8	1.00 ± 0.01	4.2 ± 0.1	20.5 ± 0.1	81.0
A_07_2%	0.697 ≈ 0.7	0.71 ± 0.01	3.9 ± 0.1	19.0 ± 0.1	43.0
A_07_5%	0.717 ≈ 0.7	0.72 ± 0.01	3.4 ± 0.1	20.1 ± 0.1	71.0
A_09_5%	0.903 ≈ 0.9	2.03 ± 0.01	4.1 ± 0.1	20.6 ± 0.1	70.1

In Figure V-24, photographs of the assembling process of A_08_5% are shown. As can be observed, after the 2nd curing stage (Figure V-24(c)), the length of the LCN-layer remains unchanged; pointing out that no recovery took place during the 6 hours at 90 °C. After polishing, the position of the LCN layer (indicated in Figure V-24(d)) can be clearly distinguished. If one analyses the frontal view, it can be reasonably said that the desired configuration has been successfully achieved. It is worth

noting that the actuator is slightly bent upwards (see Side view in Figure V-24(d)). This can be rationalized as follows: during the 2nd curing stage of the GT layers (assembling process), the epoxy homopolymerization takes place. As described in[41], this reaction generates internal stresses caused by shrinkage that, under constrained conditions and after cooling down to room temperature, lead to a final bending of the material (Note that $t_{L3} > t_{L1}$, thus the beam contracts on the top).

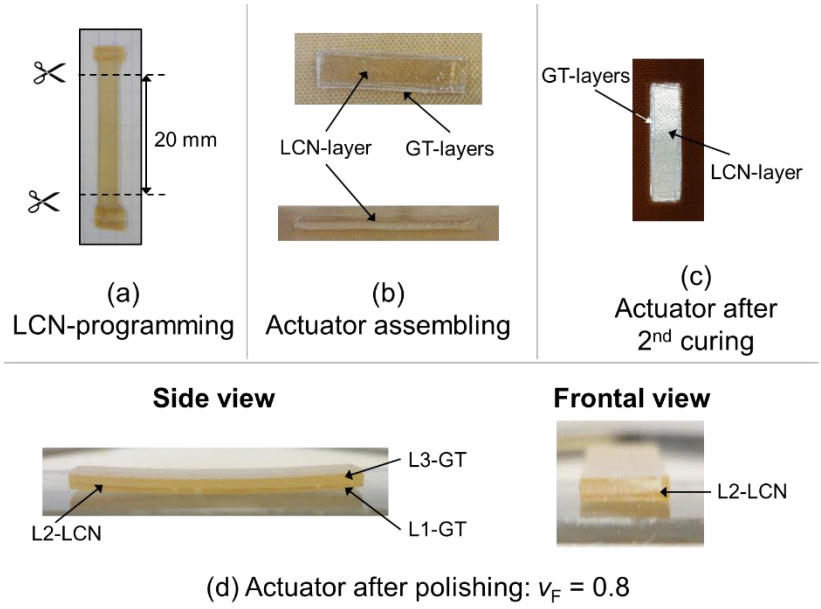

Figure V-24. Photographs of the actuators assembling process.

In order to analyse the adhesion efficiency of the layers, in Figure V-25, SEM images of the cryogenic fracture of A_08_2% are shown. From Figure V-25(a) to Figure V-25(c), the whole thickness (Figure V-25(a)), magnifications of the LCN layer (Figure V-25(b)) and the interface between the LCN and GT layers (Figure V-25(c)) are presented. In Figure V-25(a), it can be confirmed that, after the assembling process the GT layers were completely mixed in one thicker and homogeneous block as deduced from the absence of interface lines between them. The use of "thiol-epoxy" ratios close but slightly below the critical ratio ($r \leq 0.65$) produces an initial and slight softening of the material that, thanks to the slight pressure applied by the glass plates during the assembling process, promotes an efficient wetting of the LCN layer and effective inter-layer adhesion before the reaction takes place, therefore allowing the formation of a unique block[34]. Figure V-25(b) points out the differences between an amorphous network, the GT, where the fracture is homogeneous and smooth, and a

liquid-crystalline network, the LCN layer, where several cracks are formed and deviated due to the presence of LC domains[42]. Finally, in Figure V-25(c) evidences of crack propagation are clearly appreciated: the cracks propagate from the LCN to the GT layers pointing out the strong adhesion between them. Probably, not only physical bonds are formed during the assembling process, but also chemical bonds between the epoxy monomers of both materials are created.

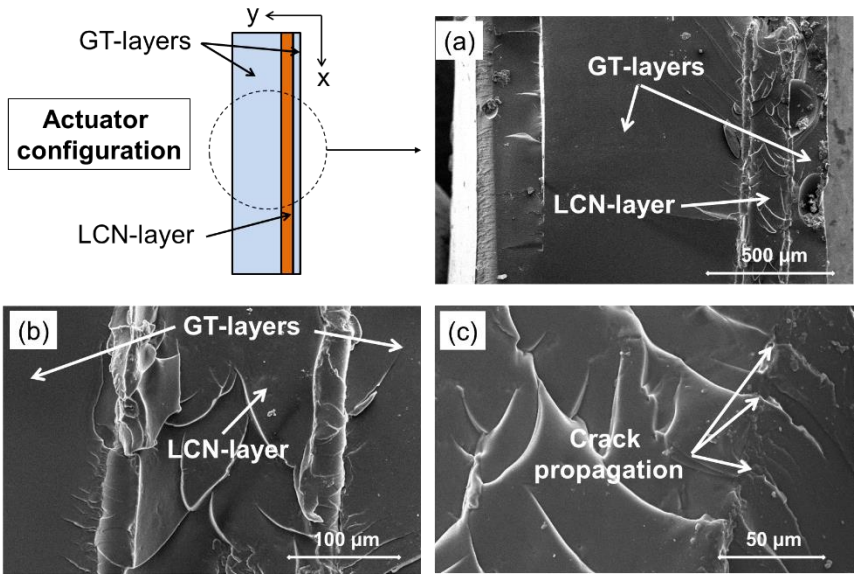

Figure V-25. SEM images of the cryogenic fracture of the actuators.

The results of the actuators response measured by DMA are summarized in Table V-9 and the actuation cycles of A_08_1% are presented in Figure V-31 in the V.3.SI. In addition, images of the actuation process are shown in Figure V-26 and an illustrative video is provided in the V.3.SI (Video V-1). As it can be observed, in all cases, on heating above T_{iso} (Figure V-26(e)), the actuator is able to bend up to a certain deflection level (metastable "state-of-ease" shape), while it goes back to the initial shape on naturally cooling down to T_{room} (Figure V-26(a)). This process is repeated several times until a stable cycling is reached and therefore, the operational design of the actuator is defined (see the actuation stability attained after 8-10 cycles in Figure V-26).

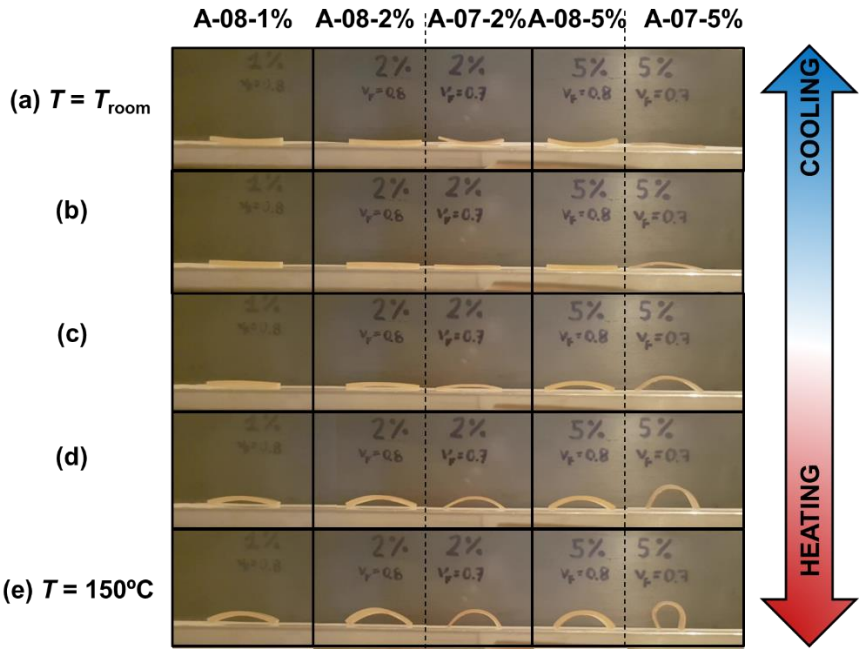

Figure V-26. Actuation response: visual demonstration of the different configurations studied.

Table V-9. Parameters of the actuator response characterization.

Actuator	v_F	L (mm)	d (mm)	d_{max} (mm)	$Actuation_{exp}$ (%)	$Actuation_{model}$ (%)
A_08_1%	0.808	20.0 ± 0.1	1.77	6.37	27.8	28
A_08_2%	0.809	20.8 ± 0.1	3.77	6.62	56.9	56.0
A_08_5%	0.820	19.2 ± 0.1	4.28	6.09	70.2	71
A_08_10%	0.805	20.5 ± 0.1	6.40	6.51	98.3[b]	96.1
A_07_2%	0.697	19.0 ± 0.1	1.77	6.55	71.9	73.0
A_07_5%	0.717	20.1 ± 0.1	4.79[a]	6.39	74.9	91.2
A_09_5%	0.903	20.6 ± 0.1	4.35	6.04	27.0	27.5

[a] Visual determination through the angle of curvature.
[b] The LCN split from the GT layer after the first cycle.

As can be observed, from room temperature (Figure V-26(a)) up to a certain temperature below T_{iso} (Figure V-26(b)), the actuators pass from the initial bent shape to a flat shape. This is related to the explanation given above: the curing process and further cooling down to room temperature generates an initial bending that after heating up again is recovered. In order to thoroughly analyse the exact temperature at which the actuator shape becomes flat, the A_07_2% was tested in the DMA placing it in opposite direction to the actuation, thus, to record the initial unbending until the actuator becomes flat. It was observed that the unbending starts at $T \approx 60$ °C and ends at $T \approx 90$ °C (the 2nd stage curing

Eur. Polym. J. 2017, 97, 241-252 **311**

temperature), thus the assumption in the model of ΔT starting from 90 °C is in agreement with the experimental observations. After that, on approaching T_{iso}, the actuators bend up to certain deflection (Figure V-26(c)-(d)-(e)) that depends on the configuration and LCN programmed strain accordingly to the predictions of the model. It is worth noting that the actuators remain stable until the temperature is lowered below T_{iso} and the flat shape (Figure V-26(b)) is recovered due to the induced-elongation of LCN coupled to the elastic response of the GT material. Further cooling down to room temperature allows the actuator to recover its initial shape (Figure V-26(a)).

If one analyses the deflection reached, *d*, in Table V-9 and the corresponding *Actuation*, it is clear that the length has a crucial role. As can be seen, due to experimental limitations, the length of the actuators has an error of ± 1 mm (see Figure V-26) and the *Actuation* is very sensitive to slight changes in length, as deduced from its definition in equation (V-6). For example, from A_08_2% to A_08_5%, the difference in "*d*" is about 0.5 mm, whereas the *Actuation* increases up to 25%. However, if one compares from A_08_1% to A_08_2%, the difference in deflection is much greater (about 2 mm), but the *Actuation* increases the same level. This is caused by the difference in length (from 20.8 mm to 19.2 mm) between A_08_1% and A_08_5%.

In Figure V-27, the experimental data (lighter points) are compared with the results of the model (darker points). As can be observed, the experimental data fit very well with the model predictions (see also Table V-9): not only is the tendency similar (the *Actuation* increases with the level of programmed strain and with the decrease of v_F), but also the *Actuation* values are closely related to the theoretical ones. In general, the best data fitting is found at low programmed strain levels (i.e. ε_{prog} = 23% and 43%) and high v_F (i.e. v_F = 0.8 and 0.9). This can be explained as follows: on the one side, the reduction of the programmed strain level leads to lower angles of curvature, thus, obeying the model assumptions related to the linear elasticity. On the other side, the increase of v_F reduces the experimental error when assembling the actuator (increasing the thickness of the actuator makes easier the proper positioning of the LCN layer). On analysing the actuator A_07_5%, the experimental *Actuation* clearly differs from the model prediction (0.72 against 0.91). Here, the model predicted an angle of curvature of 200° (see Figure V-23(b)) which considerably overpasses the model limitations (the model is developed under the basis of small deformations), whereas the visual test showed an angle of 240°. High deformation levels lead to the planar deformation of the transversal section along the length, thus, the

model simplifications are not valid anymore. This means that, from a quantitative point of view, the model has no application at such deformation levels; instead, it can be useful to analyse the tendency and avoid such undesired deformation levels.

Although the effect of the structural parameters of the GT and LCN materials with the actuation response is out of the scope of the present paper, it is worth to analyse them from a qualitative point of view. Considering the model predictions, it can be anticipated that increasing the rubbery modulus would lead to lower actuation levels, but increased stiffness of the device during actuation, that means, higher performance as mechanical actuators. However, the variation of the rubbery modulus is related to other parameters such as crosslinking density, network hindrance and T_g. We speculate the possibility to modulate the actuation in terms of rate and stability through the variation of these parameters: whereas the model is able to predict the actuation level, the relaxation dynamics of the GT material, as well as the dynamics of the LC transition in the LCN, could serve to modulate the actuation path (velocity and shape). For example, approaching the T_g of the GT to T_{iso} of the LCN would cause an overlap of network relaxation with the LCN shrinkage that may slow down the actuation. Further studies on this matter will be done and the possibility to incorporate the effect in the model will be considered.

Finally, it must be acknowledged that all the actuators were able to bear the level of deformation in terms of resistance at break. Nevertheless, in terms of layers adhesion, A_08_10% failed, as the LCN layer separated from the GT layers after the 1st cycle (an image of the actuator disassemble is shown in Figure V-27). In contrast, the actuator A_07_5%, with $\theta \approx 240°$, was able to retain the LCN layer. This suggests that the programmed strain level in the LCN layer is the responsible of the actuator disassemble instead of the *Actuation* or angle of curvature achieved. An approach to enhance the layers adhesion, thus, the performance of the LCN in the assembled device, would be the use of "thiol-epoxy" systems with higher content of epoxy excess during the assembling process, that is, stronger interactions between the GT and LCN surfaces. This would effectively increase the adhesion between layers, making possible to use LCNs with a programmed strain higher than 5% with good performance in the assembled device. However, it must be acknowledged that increasing too much the epoxy content may lead to brittle GT materials, decreasing the maximum actuation of the assembled device. In this study, a GT material with 40% of epoxy excess is used and a bending angle of 240° has been achieved as observed in A_07_5%, therefore, an increase of 10% or 20% of epoxy excess would considerably

enhance the layers adhesion, while maintaining sufficient deformability, making possible to attain bending angles of 180° (defined as the maximum operationally effective angle). By increasing the percentage of LCN programmed strain it is expected to modify the actuation response in terms of rate and stability.

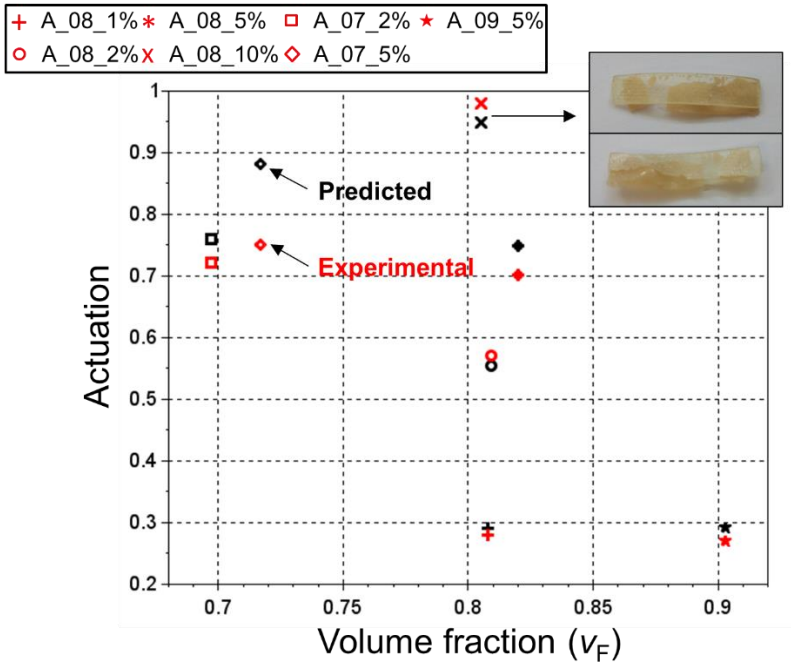

Figure V-27. Predicted deflection as a function of the volume fraction at different internal stresses in front of the experimental data.

5. Conclusions

Actuators with different configurations (GT-LCN-GT) have been successfully assembled through a multilayer methodology. SEM analyses have evidenced strong adhesion between the GT and LCN layers with the presence of crack propagation among them. In addition, from the smooth surface and the absence of layer separation it has been deduced that multiple GT layers forms a single block of GT material after the assembling process, thus, enhancing the actuator mechanical performance.

In all cases, an actuation response has been achieved: the actuator has been able to bend up to a temporary shape on heating above T_{iso} and unbend down to the original shape on cooling down T_{iso}. A model based on the multi-layered beam theory to predict the extent of deflection has been proposed and experimentally verified. All the parameters of the

model have been determined through dynamic-mechanical and thermomechanical analyses and the LCN programmed strain level has been analysed at different programming stress levels. The results have shown that the increase of the programmed strain with the programming level does not follow a linear trend due to the presence of network relaxation when the induced-elongation is driven too fast. The model has been applied to some of the analysed LCN programmed strain levels for all possible configurations. Results have shown that the *Actuation* increases with increasing of the programmed strain level, exhibiting a maximum at the geometrical equilibrium between the layers. Nevertheless, angles of curvature higher than 180º lead to a decrease of the *Actuation*, as the device tended to assume a rounded shape on approaching 360º. The experimental results are in good agreement with the model predictions. As a matter of fact, only actuators with angles of curvature higher than 180º deviate from the model output due to the high deformation level, overpassing the model limits of applicability.

Acknowledgements

The authors would like to thank MINECO (MAT2014-53706-C03-01 and MAT2014-53706-C03-02) and Generalitat de Catalunya (2014-SGR-67) for financial support. Xavier F.-F. also acknowledges the Serra Húnter programme from the Generalitat de Catalunya.

References

[1] A. Lendlein, C. Wischke, K. Kratz, M. Heuchel, J. Zotzmann, B. Hiebl, A.T. Neffe, M. Behl, B. Development, Shape-Memory Polymers, Elsevier Ltd., 2011. doi:10.1016/B978-0-08-055294-1.00271-3.

[2] Q. Zhao, H.J. Qi, T. Xie, Recent progress in shape memory polymer: New behavior, enabling materials, and mechanistic understanding, Prog. Polym. Sci. 49–50 (2015) 1–42. doi:10.1016/j.progpolymsci.2015.04.001.

[3] F. Xie, L. Huang, J. Leng, Y. Liu, Thermoset shape memory polymers and their composites, J. Intell. Mater. Syst. Struct. 27 (2016) 2433–2455. doi:10.1177/1045389X16634211.

[4] J. Leng, X. Lan, Y. Liu, S. Du, Shape-memory polymers and their composites: Stimulus methods and applications, Prog. Mater. Sci. 56 (2011) 1077–1135. doi:10.1016/j.pmatsci.2011.03.001.

[5] A. Lendlein, T. Sauter, Shape-memory effect in polymers, Macromol. Chem. Phys. 214 (2013) 1175–1177. doi:10.1002/macp.201300098.

[6] M. Anthamatten, S. Roddecha, J. Li, Energy storage capacity of shape-memory polymers, Macromolecules. 46 (2013) 4230–4234. doi:10.1021/ma400742g.

[7] C.L. Lewis, Y. Meng, M. Anthamatten, Well-Defined Shape-Memory Networks with High Elastic Energy Capacity, Macromolecules. 48 (2015) 4918-4926. doi:10.1021/acs.macromol.5b00763.

[8] D. Santiago, A. Fabregat-Sanjuan, F. Ferrando, S. De la Flor, Recovery stress and work output in hyperbranched poly(ethyleneimine)-modified shape-memory epoxy polymers, J. Polym. Sci. Part B Polym. Phys. 54 (2016) 1002–1013. doi:10.1002/polb.24004.

[9] A. Belmonte, X. Fernández-Francos, S. De la Flor, À. Serra, Network structure dependence on unconstrained isothermal-recovery processes for shape-memory thiol-epoxy “click” systems, Mech. Time-Dependent Mater. (2017) 1–17. doi:10.1007/s11043-016-9322-z.

[10] W. Wang, Y. Liu, J. Leng, Recent developments in shape memory polymer nanocomposites : Actuation methods and mechanisms, Coord. Chem. Rev. 320–321 (2016) 38–52. doi:10.1016/j.ccr.2016.03.007.

[11] A. Belmonte, C. Russo, V. Ambrogi, X. Fernández-Francos, S. De la Flor, Epoxy-based shape-memory actuators obtained via dual-curing of off-stoichiometric “thiol-epoxy” mixtures, Polymers. 9 (2017) 113. doi:10.3390/polym9030113.

[12] J. Leng, K. Yu, J. Sun, Y. Liu, Deployable morphing structure based on shape memory polymer, Aircr. Eng. Aerosp. Technol. 87 (2015) 218–223. doi:10.1108/AEAT-06-2013-0118.

[13] J.J. Song, H.H. Chang, H.E. Naguib, Biocompatible shape memory polymer actuators with high force capabilities, Eur. Polym. J. 67 (2015) 186–198. doi:10.1016/j.eurpolymj.2015.03.067.

[14] Y. Li, C. Pruitt, O. Rios, L. Wei, M. Rock, J.K. Keum, A.G. Mcdonald, M.R. Kessler, Controlled shape memory behavior of a smectic main-chain liquid crystalline elastomer, Macromolecules. 48 (2015) 2864–2874. doi:10.1021/acs.macromol.5b00519.

[15] G.C. Lama, P. Cerruti, M. Lavorgna, C. Carfagna, V. Ambrogi, G. Gentile, Controlled Actuation of a Carbon Nanotube/Epoxy Shape-Memory Liquid Crystalline Elastomer, J. Phys. Chem. C. 120 (2016) 24417–24426. doi:10.1021/acs.jpcc.6b06550.

[16] M. Giamberini, P. Cerruti, V. Ambrogi, C. Vestito, F. Covino, C. Carfagna, Liquid crystalline elastomers based on diglycidyl terminated rigid monomers and aliphatic acids. Part 2. Mechanical characterization, Polymer. 46 (2005) 9113–9125. doi:10.1016/j.polymer.2005.04.093.

[17] B.A. Kowalski, T.C. Guin, A.D. Auguste, N.P. Godman, T.J. White, Pixelated Polymers: Directed Self Assembly of Liquid Crystalline Polymer Networks, ACS Macro Lett. 6 (2017) 436–441. doi:10.1021/acsmacrolett.7b00116.

[18] C. Ohm, M. Brehmer, R. Zentel, Liquid crystalline elastomers as actuators and sensors., Adv. Mater. 22 (2010) 3366–3387. doi:10.1002/adma.200904059.

[19] H. Yang, G. Ye, X. Wang, P. Keller, Micron-sized liquid crystalline elastomer actuators, Soft Matter. 7 (2011) 815–823. doi:10.1039/C0SM00734J.

[20] T.J. White, D.J. Broer, Programmable and adaptive mechanics with liquid crystal polymer networks and elastomers, Nat. Mater. 14 (2015) 1087–1098. doi:10.1038/nmat4433.

[21] J. Zhou, S.A. Turner, S.M. Brosnan, Q. Li, J.M.Y. Carrillo, D. Nykypanchuk, O. Gang, V.S. Ashby, A. V. Dobrynin, S.S. Sheiko, Shapeshifting: Reversible shape memory in semicrystalline elastomers, Macromolecules. 47 (2014) 1768–1776. doi:10.1021/ma4023185.

[22] Y. Meng, J. Jiang, M. Anthamattern, Shape actuation via internal stress-induced crystallization of dual-cure networks, ACS Macro Lett. 4 (2015) 115–118.

[23] M. Behl, K. Kratz, U. Noechel, T. Sauter, A. Lendlein, Temperature-memory polymer actuators, Proc. Natl. Acad. Sci. 110 (2013) 12555–12559. doi:10.1073/pnas.1301895110.

[24] M. Behl, K. Kratz, J. Zotzmann, U. Nöchel, A. Lendlein, Reversible bidirectional shape-memory polymers, Adv. Mater. 25 (2013) 4466–4469. doi:10.1002/adma.201300880.

[25] J. Zhou, S.S. Sheiko, Reversible shape-shifting in polymeric materials, J. Polym. Sci. Part B Polym. Phys. 1 (2016) 1–16. doi:10.1002/polb.24014.

[26] C.L. Lewis, E.M. Dell, A Review of Shape Memory Polymers Bearing Reversible Binding Groups, J. Polym. Sci. Part B Polym. Phys. 54 (2016) 1340–1364. doi:10.1002/polb.23994.

[27] K.K. Westbrook, P.T. Mather, V. Parakh, M.L. Dunn, Q. Ge, B.M. Lee, H.J. Qi, Two-way reversible shape memory effects in a free-standing polymer composite, Smart Mater. Struct. 20 (2011) 65010. doi:10.1088/0964-1726/20/6/065010.

[28] Q. Ge, K.K. Westbrook, P.T. Mather, M.L. Dunn, H. Jerry Qi, Thermomechanical behavior of a two-way shape memory composite actuator, Smart Mater. Struct. 22 (2013) 55009. doi:10.1088/0964-1726/22/5/055009.

[29] M.O. Saed, A.H. Torbati, C.A. Starr, R. Visvanathan, N.A. Clark, C.M. Yakacki, Thiol-Acrylate Main-Chain Liquid-Crystalline Elastomers with Tunable Thermomechanical Properties and Actuation Strain, J. Polym. Sci. Part B Polym. Phys. 55 (2017) 157-168. doi:10.1002/polb.24249.

[30] M.O. Saed, A.H. Torbati, D.P. Nair, C.M. Yakacki, Synthesis of Programmable Main-chain Liquid-crystalline Elastomers Using a Two-stage Thiol-acrylate Reaction, J. Vis. Exp. 107 (2016) 1–10. doi:10.3791/53546.

[31] E. Zharinova, M. Heuchel, T. Weigel, D. Gerber, K. Kratz, Water-blown polyurethane foams showing a reversible shape-memory effect, Polymers. 8 (2016) 412.

[32] X. Fernández-Francos, A.-O. Konuray, A. Belmonte, S. De la Flor, À. Serra, X. Ramis, Sequential curing of off-stoichiometric thiol–epoxy thermosets with a custom-tailored structure, Polym. Chem. 7 (2016) 2280–2290. doi:10.1039/C6PY00099A.

[33] A. Belmonte, L. Giuseppe C., G. Gentile, P. Cerruti, V. Ambrogi, X. Fernández-Francos, S. De la Flor, Synthesis and characterization of liquid-crystalline elastomers: towards autonomous shape-memory actuation, J. Phys. Chem. C. (2017) (in press).

[34] A. Belmonte, X. Fernández-Francos, À. Serra, S. De la Flor, Phenomenological characterization of sequential dual-curing of off-stoichiometric " thiol-epoxy " systems : Towards applicability, Mater. Des. 113 (2017) 116–127. doi:10.1016/j.matdes.2016.10.009.

[35] J.-P. Pascault, H. Sautereau, V. J, W.J.J. R, Thermosetting Polymers, CRC Press, 2002.

[36] M. Giamberini, E. Amendola, C. Carfagna, Liquid Crystalline Epoxy Thermosets, Mol. Cryst. Liq. Cryst. Sci. Technol. Sect. A. Mol. Cryst. Liq. Cryst. 266 (1995) 9–22.

[37] C.-H. Hsueh, Modeling of elastic deformation of multilayers due to residual stresses and external bending, J. Appl. Phys. 91 (2002) 9652–9656.

[38] J. Malzbender, Mechanical and thermal stresses in multilayered materials, J. Appl. Phys. 95 (2004) 1780–1782. doi:10.1063/1.1642289.

[39] A. Pizzi, Principles of Polymer Networking and Gel Theory in Thermosetting Adhesive Formulations, Taylor & Francis Group, 2003.

[40] T.H. Ware, J.S. Biggins, A.F. Shick, M. Warner, T.J. White, Localized soft elasticity in liquid crystal elastomers., Nat. Commun. 7 (2016) 10781. doi:10.1038/ncomms10781.

[41] M. Shimbo, M. Ochi, Y. Shigeta, Srinkage and internal stress during curing of epoxide resins, J. Appl. Polym. Sci. 26 (1981) 2265–2277. doi:10.1002/app.1981.070260714.

[42] J.F. Ban, S.R. Lu, D. Guo, K. Liu, C.X. Luo, Thermomechanical Properties and Morphology of Liquid Crystalline Polyurethane/Epoxy Resin Composites, Adv. Mater. Res. 194–196 (2011) 1421–1425. doi:10.4028/www.scientific.net/AMR.194-196.1421.

V.3.SI – Supplementary Information

Video V-1. Demonstration of the actuation response of different free-standing actuator designs.

URL: *http://www.sciencedirect.com/science/article/pii/S0014305717313241#s0080.*

Detailed development of analytical model

Mechanical and thermal loading in multi-layered materials lead to stress, strain and curvature relationships that can be approached on applying the classical Euler Bernoulli theory. The Euler Bernoulli theory describes the relationship between the deflection and the load of a beam subject to a pure bending process.

Assuming that the multi-layered material is a perfect beam (length » transversal section), that the transversal section remains unchanged after deformation and that the interaction between layers is perfect (the beam behaves as a unity). The case of study is reduced to a one-dimensional geometry, in which only variations in the "x" direction (across the length) are considered.

According to the classical Euler-Bernoulli theory, the bending strain or strain suffered by the beam under a pure bending process, depends on the position along the thickness (y) and the curvature of the beam (κ) and can be expressed relative to the bending axis as follows:

$$\varepsilon^M = \frac{[R + (y - y_b)]\theta - R\theta}{R\theta} = \frac{y - y_b}{R} = (y - y_b)\kappa \qquad \text{(V-18)}$$

where $R\Theta$ is the length of the bending axis which under pure bending is equal to the neutral axis, thus, remains unchanged after bending ($R\Theta = l_0$), the curvature is defined with the radius of curvature, ρ, as $\kappa = 1/\rho$, θ is the angle of curvature and the position of the bending axis is "y_b" (see scheme in Figure V-28).

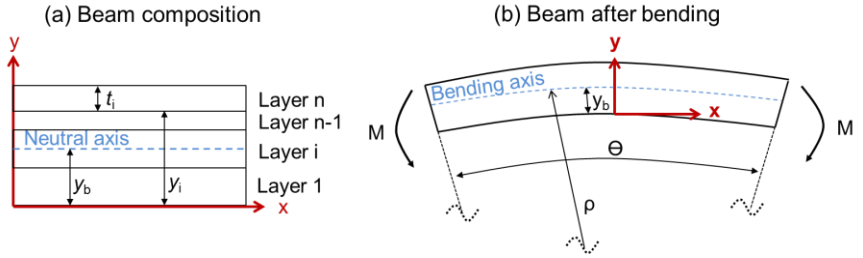

Figure V-28. Scheme of the beam and geometrical definitions: (a) Composition along the thickness and (b) beam after bending.

Eur. Polym. J. 2017, 97, 241-252

Note that, considering the axes definition in Figure V-28, the curvature, κ, will be positive when the beam bends downwards and will be negative when it bends upwards.

Bending in a multi-layered beam is not only caused by external forces, internal forces may take place due to internal volume changes, such as, thermal expansion, humidity absorption or built-in strains, leading to a geometrical mismatch between the layers that is eventually accommodated under a bending process. The strain associated to these phenomena is called "stress-free strain", ε^0, and is defined as the sum of all different stress-free strains "*n*":

$$\varepsilon^0 = \sum_i^n \varepsilon^n \qquad \text{(V-19)}$$

The thermal strain is associated to the change in volume during a thermal load and therefore is considered a growing "stress-free" strain defined as:

$$\varepsilon^{th} = \int \alpha \partial T \qquad \text{(V-20)}$$

where α depends on the material thermal properties and ∂T depends on the thermal load and the thermal gradient along the thickness. Assuming that the temperature is equal along the thickness, that α is constant in the temperature range and that no thermal transitions occur within this range, equation (V-20) is reduced to:

$$\varepsilon^{th} = \alpha(T_f - T_0) \qquad \text{(V-21)}$$

where "*f*" and "*0*" sub-indexes are the final and initial temperatures of the thermal load.

The built-in strain, ε^{bint}, is associated to an external strain (i.e. a shape-memory programming of a stretched temporary shape) that is externally calibrated and incorporated as a nominal value with the corresponding sign.

Conceptual design of the multi-layered beam

In one-layer beams, the "stress-free" strains lead to a linear change in the volume. However, in beams composed by multiple layers of materials with different thermomechanical properties, the change in volume of each layer causes a geometrical mismatch along the thickness, where forces and moments are generated in each layer, leading to a

bending process called Natural Bending after bending and mechanical relaxations.

In Figure V-29, the analysis of a simple bi-layer system in which a positive built-in strain, ε^{bint}, takes place in the layer above (L_1) is schematized. Considering the bi-layer beam with initial length, l_0, the analysis starts by "decomposing" the beam and placing the layers, i, in their final state ($l_{i,f} \neq l_0$). Afterwards, the beam is composed to fit the geometrical equilibrium by applying the necessary forces on each layer (in this case, L_1, will suffer a contractual force and L_2 will remain unchanged). Finally, after balancing the forces and moments generated on each layer, the beam will bend upwards ($\kappa > 0$) due to L_1 tends to expand to its final state.

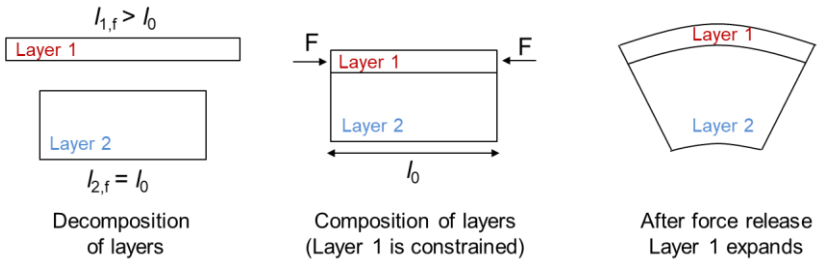

Figure V-29. Conceptual idea of the multi-layer beam theory.

The above can be extended to a beam composed by "n" layers with different properties; "stress-free" strains and thickness (see Figure V-30). Considering the axis definitions in Figure V-28, the position of each layer can be defined as follows:

$$y_n\ (n > 0) = \sum_{i=1}^{n} t_i \qquad \text{(V-22)}$$

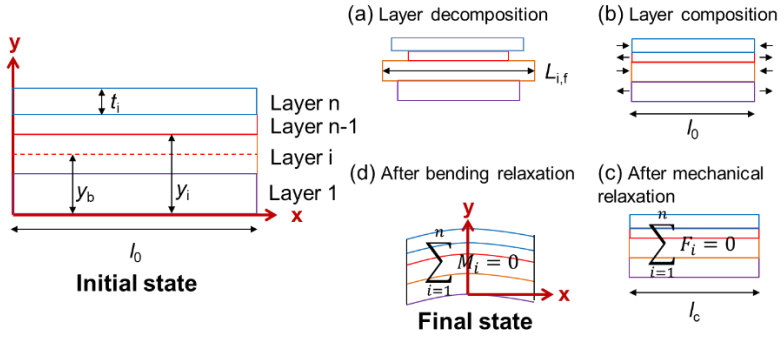

Figure V-30. Scheme of the multi-layer beam theory applied for n-layered beams.

The decomposition of the layers is shown in (a), where $l_{i,f}$ is the final length of layer "*i*". The composition of the layers (b) results in different forces to reach a geometrical equilibrium length which is equal to the initial length of the beam. After mechanical or planar relaxation (c) a final length (composed length, l_c) is eventually reached. At this point, the strain of each layer associated to steps (a-b) and (a-c) can be expressed using the true strain definition as follows:

$$\varepsilon_i{}^0 = \ln l_i - \ln l_0 \quad \text{(V-23)}$$

$$\varepsilon_i{}^F = \ln l_c - \ln l_i \quad \text{(V-24)}$$

where "*F*" refers to the strain of zero-forces or after the force balance. Finally, after bending relaxation (d) the beam will bend with a bending strain defined accordingly to equation (V-18). Here, the strain suffered by each layer can be expressed as a function of both, the mechanical and bending strains, as follows:

$$\varepsilon_i = \varepsilon_i{}^F + \varepsilon_i{}^M \quad \text{(V-25)}$$

On applying the Hooke's law, the stress suffered by each layer can be expressed in two separated terms, the corresponding to the zero-forces strain (uniform term) and the one caused by the bending strain:

$$\sigma_i = E_i\varepsilon_i = E_i\varepsilon_i{}^F + E_i\varepsilon_i{}^M \quad \text{(V-26)}$$

From the force balance ($\sum_{i=1}^{n} F_i = 0$), the uniform term of equation (V-26) ($E_i\varepsilon_i{}^F$) is null by definition of the zero-force strain $\varepsilon_i{}^F$ and therefore can be analysed separately from the bending component, leading to the following relation:

$$\ln l_c = \frac{\sum_{i=1}^{n} E_i t_i \ln l_i}{\sum_{i=1}^{n} E_i t_i} - \ln l_i \quad \text{(V-27)}$$

which in terms of strain (applying equations (V-24) and (V-25)) is expressed as:

$$\varepsilon_i{}^F = \frac{\sum_{i=1}^{n} E_i t_i \varepsilon_i{}^0}{\sum_{i=1}^{n} E_i t_i} - \varepsilon_i{}^0 = C - \varepsilon_i{}^0 \quad \text{(V-28)}$$

From the equation above it is deduced a "Uniform-Strain", *C*, which is equal in all layers and is defined as the weighted average strain of the initial configuration (Figure V-30(b)) weighted by the Bending Stiffness of each layer.

Therefore, the elastic strain of each layer, which is the strain only due to mechanical forces, is written as:

$$\varepsilon_i^{elastic} = C - \varepsilon_i{}^0 + (y - y_b)\kappa \quad \text{(V-29)}$$

and the total strain suffered by each layer, which is the sum of the strain due to mechanical forces, $\varepsilon_i^{elastic}$, and stress-free forces, $\varepsilon_i{}^0$ is:

$$\varepsilon_i = C + (y - y_b)\kappa \quad \text{(V-30)}$$

Applying the Hooke's law to the elastic strain (equation (V-29)), the stress suffered in each layer of the beam is defined as:

$$\sigma_i = E_i\big((y - y_b)\kappa + C - \varepsilon_i{}^0\big) \quad \text{(V-31)}$$

Note that the strain, which must be linear along the thickness, accomplish the contour conditions between layers by the incorporation of the stress-free strain term. On the contrary the stress is not continuous along the thickness. Now, on applying the equilibrium conditions (force and moment balances) in equation (V-31) leads to:

$$\sum_{i=1}^{n} F_i = 0 \rightarrow \sum_{i=1}^{n} \int_{y_{i-1}}^{y_i} \sigma_i dy = 0 \quad \text{(V-32)}$$

$$\sum_{i=1}^{n} M_i = 0 \rightarrow \sum_{i=1}^{n} \int_{y_{i-1}}^{y_i} \sigma_i y dy = 0 \quad \text{(V-33)}$$

The force balance can be expressed as follows:

$$\sum_{i=1}^{n} \int_{y_{i-1}}^{y_i} E_i y dy - \int_{y_{i-1}}^{y_i} E_i y_b dy + \int_{y_{i-1}}^{y_i} E_i C dy - \int_{y_{i-1}}^{y_i} E_i \varepsilon_i{}^0 dy = 0 \quad \text{(V-34)}$$

Substituting the "stress-free" strain term, $\varepsilon_i{}^0$, per equation (V-19) and considering the thermal expansion definition of equation (V-21), equation (V-34) leads to:

$$\sum_{i=1}^{n} \int_{y_{i-1}}^{y_i} E_i y dy - \int_{y_{i-1}}^{y_i} E_i y_b dy + \int_{y_{i-1}}^{y_i} E_i C dy - \left(\int_{y_{i-1}}^{y_i} \left[\sum_{j=1}^{m} E_{i,j} \alpha_{i,j} \Delta T_j \right] dy + \int_{y_{i-1}}^{y_i} E_i \varepsilon^{bin} dy \right) = 0 \quad \text{(V-35)}$$

where "*j*" in the thermal term refers to the thermal region (i.e. a glassy covalently crosslinked thermoset would have two regions, glassy and rubbery regions) and "*m*" the number of regions. Similarly, the moment balance is expressed as follows:

$$\sum_{i=1}^{n}\int_{y_{i-1}}^{y_i} E_i y^2 dy - \int_{y_{i-1}}^{y_i} E_i y_b y dy + \int_{y_{i-1}}^{y_i} E_i C y dy - \left(\int_{y_{i-1}}^{y_i} \left[\sum_{j=1}^{m} E_{i,j}\alpha_{i,j}\Delta T_j \right] y dy + \int_{y_{i-1}}^{y_i} E_i \varepsilon^{bin} y dy \right) = 0 \quad \text{(V-36)}$$

Equations (V-35) and (V-36) are commonly written as a function of constants *A*, *B* and *D* as follows:

$$AC + B\kappa - ABy_b - F_{th} + F_{bin} = 0 \quad \text{(V-37)}$$

$$CB + D\kappa - BDy_b - M_{th} + M_{bin} = 0 \quad \text{(V-38)}$$

where *A*, *B* and *D* are the extensional, coupling and bending constants respectively in terms of laminated composite materials, F_{bin} and M_{bin} denotes respectively the force and moment caused by the built-in strain and, F_{th} and M_{th} are the force and moment caused by the effect of the thermal expansion. Solving equations (V-37) and (V-38) leads to:

$$\kappa = \frac{A(M_{bin} + M_{th}) - B(NF_{bin} + F_{th})}{AB - D^2} \quad \text{(V-39)}$$

All the constants expressed in equations (V-37) and (V-38) can be written in terms of sums as follows:

$$A = \sum_{i=1}^{n} E_i(y_i - y_{i-1}) \quad \text{(V-40)}$$

$$B = \frac{1}{2}\sum_{i=1}^{n} E_i({y_i}^2 - {y_{i-1}}^2) \quad \text{(V-41)}$$

$$D = \frac{1}{3}\sum_{i=1}^{n} E_i({y_i}^3 - {y_{i-1}}^3) \quad \text{(V-42)}$$

$$F_{bin} = \sum_{i=1}^{n} E_i \varepsilon^{bin}(y_i - y_{i-1}) \quad \text{(V-43)}$$

$$M_{bin} = \frac{1}{2}\sum_{i=1}^{n} E_i \varepsilon^{bin} (y_i{}^2 - y_{i-1}{}^2) \quad \text{(V-44)}$$

$$F_{th} = \sum_{i=1}^{n} \left(\sum_{j=1}^{m} E_{i,j} \cdot \alpha_{i,j} \cdot \Delta T_j \right) (y_i - y_{i-1}) \quad \text{(V-45)}$$

$$M_{th} = \frac{1}{2}\sum_{i=1}^{n} \left(\sum_{j=1}^{m} E_{i,j} \cdot \alpha_{i,j} \cdot \Delta T_j \right) (y_i{}^2 - y_{i-1}{}^2) \quad \text{(V-46)}$$

Cyclic behaviour of the shape-memory actuator

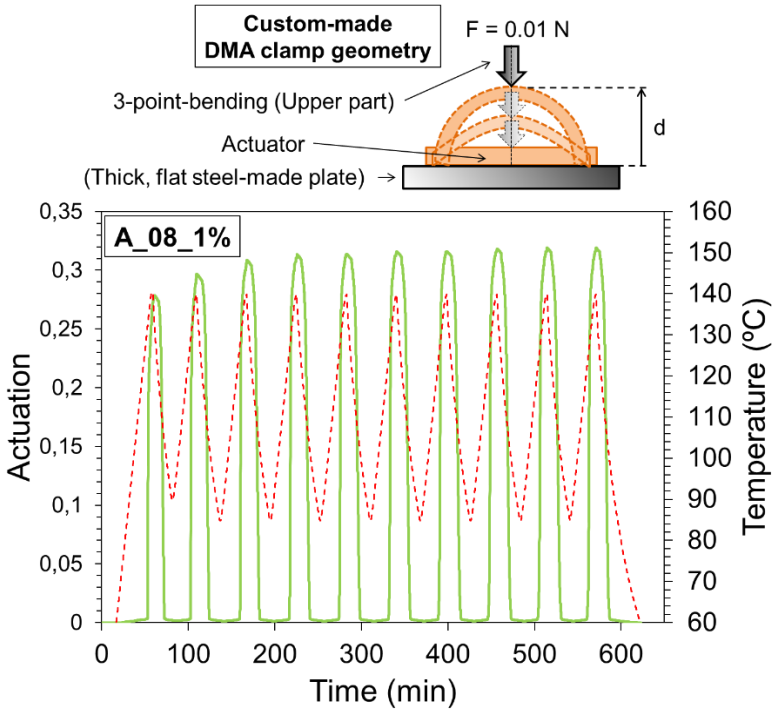

Figure V-31. Cyclic behaviour of the shape-memory actuator in 10 heating-cooling cycles carried out with the DMA.

V.4 Motion control in free-standing shape-memory actuators

Unpublished work

Alberto Belmonte[1], Giuseppe C. Lama[2,3], Pierfrancesco Cerruti[3], Veronica Ambrogi[2,3], Xavier Fernández-Francos[4] and Silvia De la Flor[1]

1) Department of Mechanical Engineering, Universitat Rovira i Virgili, Av. Països Catalans, 26, 43007, Tarragona (Spain).

2) Department of Chemical, Materials and Production Engineering, University of Naples "Federico II", Piazzale Tecchio, 80, 80125, Napoli (Italy).

3) Institute for Polymers, Composites and Biomaterials, National Council of Research of Italy, Via Campi Flegrei, 34, 80078, Pozzuoli (NA) (Italy).

4) Thermodynamics Laboratory ETSEIB, Universitat Politècnica de Catalunya, Av. Diagonal, 647, 08028, Barcelona (Spain).

UNIVERSITAT ROVIRA I VIRGILI
DESIGN AND CHARACTERIZATION OF ACTIVELY-MOVING POLYMERS OBTAINED VIA DUAL-CURING PROCESSING
Alberto Francisco Belmonte Parra

Abstract

In this work, free-standing shape-memory thermally-triggered actuators are developed through lamination of "thiol-epoxy"-based glassy thermoset (GT) and stretched liquid-crystalline network (LCN) films. Sequential curing processing is used to obtain GTs with tailored thermomechanical properties and network relaxation dynamics, and to assemble the final actuator. The actuation extent, rate and time are investigated through the variation of the GT and the heating rate on thermo-actuation. The results demonstrate the possibility to tailor actuation rate and time by designing GT materials with a glass transition temperature close to that of the liquid-crystalline-to-isotropic phase transition of the LCN, thus allowing the coupling of the two processes. At this point, the heterogeneity of the network relaxation has a crucial role on the actuation dynamics. The presence of thermal gradients due to rapid heating can also promote such coupling even when $T_g << T_{iso}$. Interestingly, the variation of the GT network relaxation dynamics does not affect the actuation extent. As predicted by the analytical model developed in our previous work, the modulus of the GT layer is mainly responsible for the actuation extent. Finally, to demonstrate the enhanced control of the actuation, specifically designed actuators are assembled in a 3D actuating device able to make complex motions (including "S-type" bending). Such approach enables the engineering of advanced functional materials for application in self-adaptable structures and soft robotics.

Keywords: free-standing, shape-shifting, dual-curing, liquid-crystalline network, actuator*.*

1. Introduction

Actively moving polymers (AMPs) are a class of stimuli-responsive materials that can undergo large physical changes upon stimulation[1,2]. According to Lendlein and Behl[1], AMPs can be categorized in shape-memory polymers (SMPs) and shape-changing polymers (SCPs) depending on the transformation mechanisms: SMPs are triggered under the well-known shape-memory effect (SME)[3–5], whereas SCPs response is related to the so-called shape-changing effect (SCE)[6,7]. The main difference arises from the requirement of a reiterated programming process in SMPs and the constant stimulation in SCPs to achieve transformation processes. The SME lies on the softening/freezing transition in glassy or semi-crystalline networks that is commonly a glass or melting transition. The softening of the network allows a deformation process towards a temporary shape that is eventually fixed through the vitrification or crystallization process

thanks to the reduction of the network mobility[8–10]. Epoxy-based glassy networks are commonly utilized as SMPs due to the drastic structural changes taking place during the glass transition, leading to enhanced shape-memory performance, but also due to the interesting mechanical and thermal properties of the epoxy resins[11–18]. Nevertheless, the inherent progress in shape-memory materials and the increasing demand of smart applications in which complex and bidirectional motion designs are required, has considerably limited the use of traditional SMPs due to the necessity of programming after each use, leading to unidirectional designs. In contrast, the SCE is caused by structural changes taking place as long as the stimulus is applied and reversed when the stimulus is removed, hence bidirectional actuation is achieved upon stimulation.

Liquid-crystalline networks (LCNs) consisting in lightly crosslinked polymers containing ordered phases called liquid-crystalline domains are a good example of SCPs[19–22]. LCNs can react mechanically to the appropriate stimulus through the reversible anisotropic-to-isotropic transition, that is, the formation and disorder of the liquid-crystalline domains. Commonly, thermomechanical stimulation causes the shape-changing effect in SCPs by means of a stress-alignment of the LC domains into a highly oriented monodomain structure during the isotropic-to-anisotropic transition. At a macroscopic level, this is shown as a large shape change along the stress direction[23]. Unfortunately, the requirement of constant stress application in these SCPs considerably narrows their application range. Moreover, the SCE is limited by the original three-dimensional geometry of the network structure.

In order to overcome this drawback, researchers have focused their efforts on the optimization of the bidirectional actuation in LCNs through the interaction of combined network structures to achieve the required mechanical stimulus for free-standing bidirectional actuation[24,25]. Two lines of research have arisen: the internal incorporation of an elastic network or the external attachment of an elastic material to the SCP[26–28]. Both methodologies lead to stress mismatch between networks or materials during the reversible anisotropic-to-isotropic transition of the LCN, leading to macroscopic changes that are controlled by designing the interaction mechanism.

Yakacki et al.[29,30] demonstrated free-standing unidirectional actuation in main-chain “thiol-acrylate” liquid-crystalline elastomers through internal incorporation of a UV-crosslinked network. After the 1st curing stage, the sample was stretched up to hundreds % of strain. Then, the new network was UV-crosslinked, and the resulting material could

actuate a percentage of the stretching extent. On the other hand, Westbrook et al.[26,31] developed a free-standing flexural actuator through external incorporation of an acrylate-based polymer onto a poly(cyclooctene) based LCN. The embedding was carried out through thermal curing of the elastomeric network directly onto the stretched LCN layer by impeding the shrinkage of the latter. The resulting material could bend and unbend upon heating-cooling processes with a flexural actuation of 6 mm.

As stated above, not only bidirectional motion is demanded, but also complex designs. Emerging techniques like 3D printing has come as a solution to achieve complex spatial designs[32], however, they are still limited to certain materials. Our research group demonstrated the use of sequential dual-curing "thiol-epoxy" systems to achieve thermally-triggered free-standing bidirectional shape-memory actuators with enhanced control of the motion design through a careful design of the device[33]. Multi-layer assemblies were prepared by external bonding of LCN and epoxy-based thermoset (glassy thermoset, GT) layers of controlled thickness. The use of partially-cured GT layers in the assembly process and their subsequent postcuring, following a sequential dual-curing scheme, enhanced the inter-layer adhesion[34–36]. Solid but highly deformable intermediate, partially cured materials can be obtained by appropriately choosing the "thiol-epoxy" ratio and the thiol and epoxy compounds. This also affects the final T_g of the GT material. In general terms, the final T_g of the GT should be lower than T_{iso} of the LCN, so that the assembled actuator will actuate upon the elastic response of the GT which generates the necessary force to promote the alignment of the LC domains during the isotropic-to-anisotropic transition and permits the elastic shrinkage of the LCN during the anisotropic-to-isotropic transition.

In this work, the effect of the thermomechanical properties and network relaxation of the GT material on the actuation extent, time and rate is investigated. GT materials with different modulus, crosslinking density, T_g and network relaxation dynamics are obtained by changing the thiol and epoxy compounds and their ratio. The cyclic response is analysed in detail and the effect of the GT properties and relaxation dynamics are studied under non-isothermal conditions at different heating rates. On the other hand, we demonstrate the possibility to engineer a 3D actuating device by assembling specifically designed actuators with different actuation extent, time and rate. The device is assembled in one single piece, taking advantage of the enhanced processing of the GT material in the intermediate stage. The complex actuation of the resulting 3D device

has been recorded, analysed through visual frames, and compared with the model predictions following our previous work[33].

2. Experimental Section

Materials

Epoxy-based thermoset (GT)

Diglycidyl ether of bisphenol A (DGEBA, GY240, Huntsman, Everberg, Belgium) with an epoxy equivalent weight of 182 g/eq and EPON™ resin SU8 with an epoxy equivalent average weight of 215 g/eq were used as epoxy resins. Pentaerythritol tetrakis(3-mercaptopropionate) (S4) with a thiol equivalent weight of 122.17 g/eq and trimethylolpropane tris(3-mercaptopropionate) (S3) with a thiol equivalent weight of 132.85 g/eq were purchased from Sigma-Aldrich (St. Louis, MO, USA) and used as curing agents in an under-stoichiometric proportion with respect to the epoxy groups in the system. 1-methylimidazole (1MI, Sigma-Aldrich, St. Louis, MO, USA, 82.1 g/mol) was used as catalyst in a proportion of 1 phr (parts of catalyst per hundred parts of the whole mixture). DGEBA was dried overnight under vacuum at 80 °C before use. The other reagents were used as received without further purification. Three different "thiol-epoxy" systems have been investigated according to our previous works[34,35]: DGEBA-S3-1MI, DGEBA-S4-1MI and (DGEBA-SU8)-S3-1MI with a DGEBA-SU8 molar proportion of (7:3). As it was demonstrated, these systems lead to sequential dual-curing processing when under-stoichiometric thiol equivalents are used with respect to the epoxy groups: the "thiol-epoxy" polycondensation (1st curing stage) takes place at low temperature (50 °C) during 1 hour and 45 minutes under the presence of the catalyst, leading to the intermediate and stable material, whereas the homopolymerization of the remaining epoxy groups (2nd curing stage) is triggered at higher temperature (T > 90 °C) under the presence of the catalyst that is regenerated during the 1st curing stage.

Liquid-crystalline network (LCN)

An epoxy-based mesogenic compound was synthesized by epoxidation of a commercial diol (4,4'-dihydroxybiphenyl, DIF, 97% purity, 186.21 g/mol), using epichlorohydrin (Sigma-Aldrich, 99% purity, 1.183 g/ml, 92.52 g/mol), isopropanol and sodium hydroxide. A commercial dicarboxylic acid (1,8-octanedicarboxylic acid, sebacic acid, 98% purity, 202.25 g/mol, Sigma-Aldrich) was used as curing agent. Trycaprylyl methylammonium chloride (Sigma-Aldrich) was used as catalyst in the reaction.

The LCN was prepared as explained in our previous work[37]: first the mesogenic compound and the acid were melted at 180 °C and homogenized under magnetic stirring, then the catalyst was added and the mixture was poured into a Teflon-covered glass mould with 250 µm spacing. Films of 8x8 cm^2 and 250 µm of thickness were obtained.

Preparation of the actuators

The preparation of the LCN-GT actuator (illustrated in Figure V-32) was carried out as explained in our previous work[33]: the GT intermediate material is prepared in form of films with different thickness by pouring the initial "thiol-epoxy" mixture containing all the reactants, including the catalyst, in between Teflon-coated glass plates and carrying out the 1st curing process (see Figure V-32(a)) as explained above. The LCN layer is programmed from a piece of the previously prepared LCN film (see Figure V-32(b)) as follows: first heating up to T_{iso} + 20 °C to elastically deform the network at a constant stress level (σ_p), corresponding to a predetermined % of the stress at break (σ_b = 780 kPa). Then, cooling down to induce the elongation effect caused by the formation and alignment of the LC domains in the stress direction and promoted by the soft elasticity phenomenon of the LCN (see the graphic in Figure V-32(b)). The stress applied is released and the programmed strain (ε_p) is stabilized at low temperature. Once both the LCN and GT intermediate materials are prepared, the actuator is assembled layer-by-layer in a sandwich-like configuration (see Figure V-32(c)). To do that, the LCN and GT materials are firstly cut to fit specific dimensions for a beam-like design of 20 x 3.5 mm^2 (length x width). The total thickness of the assembled actuator is defined through the volume fraction (v_F), a parameter that considers the total thickness of the actuator in relation to the GT total thickness according to equation (V-47). A thinner GT layer (layer 1, t_{L1} = 0.24 mm) is placed on one side, the LCN layer (layer 2, t_{L2} < 0.25 after programming) is placed in the middle, and a thicker GT layer (layer 3) is placed on the other side with the corresponding thickness to fit the specific volume fraction. According to the theory of elasticity for multi-layered beams subject to built-in stresses[38,39], with this configuration, the final actuator will bend downwards with respect to the thinner GT layer (layer 1) due to the contraction of the LCN as it is illustrated in Figure V-32(d).

$$v_F = \frac{V_{GT}}{V_{tot}} = \frac{t_{GT}}{t_{tot}} = \frac{t_{L1} + t_{L3}}{t_{L1} + t_{L2} + t_{L3}} \quad \text{(V-47)}$$

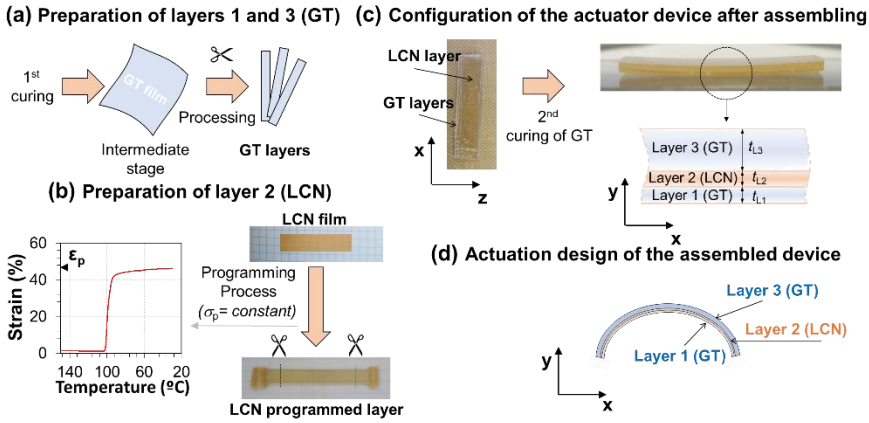

Figure V-32. Preparation of the actuator device: (a) curing and processing of GT layers 1 and 3; (b) programming of the LCN layer 2 (the data of the inner strain-temperature graphic is from our previous work[33] to illustrate the programming process); (c) assembled configuration of the device and (d) actuation schematics of the assembled device.

Once the actuator configuration is built, the 2nd curing stage of the GT material is carried out by placing the actuator in between Teflon-coated glass plates, applying a small constraining force to prevent the LCN shrinkage, and following a specific temperature program. In our previous work[33], a temperature of 90 °C was used to limit the LCN premature shrinkage, however, GT materials with glass transition temperatures close or equal to T_{iso} (120 °C) are used in this work, thus, to allow completion of epoxy homopolymerization (2nd curing stage), the following curing procedure has been used: 3 hours at 90 °C plus 1 hour at 110 °C plus 1 hour at 135 °C. The progressive increase of the curing temperature promotes the formation of the GT network in different steps preventing the LCN shrinkage inside the actuator. At 90 °C, the LCN remains stable, whereas part of the epoxy homopolymer is formed and bound to the LCN surface. LCN shrinkage to some extent cannot be avoided at the higher temperatures, but the LCN displacement is prevented through the adhesion with the homopolymer network already formed during the previous three hours at 90 °C, which reaches its ultimate structure after the higher temperature steps. The application of a constraining force through the glass plates avoids undesired bending of the whole actuator.

Thermomechanical characterization of the GT materials

Dynamic-mechanical analyses were carried out using a TA Instruments Q800 (New Castle, DE, USA) DMA apparatus equipped with a 3-point-bending clamp. The experiments were performed at an oscillation frequency of 1 Hz with a strain amplitude of 0.1% from 35 °C up to 180 °C

at a heating rate of 3 °C/min in samples of the GT final material (after 2nd curing stage). "Thiol-epoxy" ratios ranging from 0.25 up to the stoichiometric proportion (r = 0.25, 0.5, 0.75 and 1) were analysed for the different systems studied (see Table V-10). The T_g was determined from the peak of the tanδ curve, the moduli in the glassy and rubbery regions were obtained from the glassy and rubbery plateaus at 30 °C and T_g + 50 °C. In addition, the tanδ peak value and the width at half-height (FWHM) were also determined as indicators of the network relaxation dynamics.

Table V-10. Composition of the different systems of study.

System	"thiol-epoxy" ratio	DGEBA (%wt.)	SU8 (%wt.)	S3 (%wt.)	S4 (%wt.)	1-MI (%wt.)
DGEBA-S3-1MI	0.25	83.7		15.3		1.0
	0.5	72.5		26.5		1.0
	0.75	64.0		35.0		1.0
	1.0	57.2		41.8		1.0
DGEBA-S4-1MI	0.25	84.8			14.2	1.0
	0.5	74.1			24.9	1.0
	0.75	65.9			33.2	1.0
	1.0	59.2			39.8	1.0
(DGEBA:SU8)-S3-1MI	0.25	56.0	28.4	14.6		1.0
	0.5	48.8	24.7	25.5		1.0
	0.75	43.3	21.9	33.8		1.0
	1.0	38.8	19.7	40.5		1.0

Characterization of the actuation response

The actuation response of the different samples was first stabilized through 20 consecutives "heating-cooling" cycles at a constant heating and cooling rates of 2 °C/min. Afterwards, nine more cycles were carried out varying the heating rate from 0.2 °C/min up to 20 °C/min (0.2, 0.5, 1, 2, 3, 5, 10, 15 and 20 °C/min), and keeping a cooling rate of 2 °C/min, to investigate the effect of the heating rate on the actuation. The thermal cycles were performed using the DMA equipment in force-controlled static mode with a custom-made clamp geometry (see Figure V-33(a)). The sample was placed onto the flat surface producing an upwards displacement of the clamp upon bending of the sample. The displacement of the moveable clamp was registered by applying a small force of 0.01 N centred in the actuator (the process is illustrated in Figure V-33(a)). The actuation extent has been determined as the relation of the instantaneous deflection, d(t), determined through the displacement of the clamp, to the maximum deflection for a bending angle of 180° (the maximum operationally effective angle):

$$Actuation = \frac{d(t)}{d_{max}} = \frac{d(t)}{L/\pi} \quad \text{(V-48)}$$

where *L* is the length of the actuator.

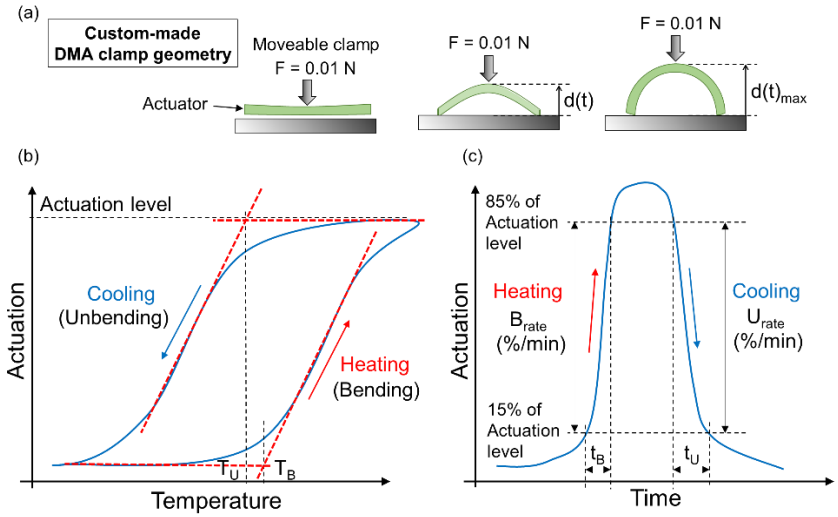

Figure V-33. (a) Scheme of the DMA experimental set up to characterize the actuators; (b) scheme of the actuation-temperature cycle and (c) scheme of the actuation-time cycle.

In Figure V-33, the experimental characterization of the actuation with the DMA is shown according to the explained experimental procedure. The actuation-temperature and actuation-time plots are represented in Figure V-33(b) and (c). First, the actuation extent has been defined as the maximum actuation achieved. From the hysteresis cycle in Figure V-33(b), the temperatures corresponding to the beginning of the bending, T_B, and unbending, T_U, have been determined as the onset point, that is, the intersection between the tangent lines to the hysteresis curve in the high slope and horizontal regions of the curves during the heating (bending) and cooling (unbending) processes, respectively, as indicated in Figure V-33(b). From Figure V-33(c), the rate during the bending (B_{rate}) and unbending (U_{rate}) processes have been determined (in %/min) as the time needed to bend or unbend from the 15% to 85% of the actuation strain. In addition, the time needed to achieve the same actuation range have been considered separately (t_B and t_U) as indicated in Figure V-33(c).

Preparation of the 3D actuating device

To experimentally demonstrate the possibility of obtaining complex motion designs, a planar-to-3D transformation device has been assembled. As shown in Figure V-34(a), the device consists of a central part

made of GT to which six legs made of different actuators are anchored. All the actuators were made using the same stress programming level (σ_p) for the LCN layer and different GTs to produce different motions. The actuation shape and direction of each leg were defined by the vertical positioning of the LCN layer in the sandwich structure, the structural properties of the GT material, and the combination of different actuators along the leg. To properly follow the configuration of the legs, the terminology "below" and "above" is used as concerning the vertical positioning of the LCN layer in the sandwich structure (see also Figure V-39(c)). The shorter legs (Figure V-34(a) legs 1-4) were made of one single LCN positioned below, thus, the actuation direction is the same for the four legs, but each pair of legs (1-2 and 3-4 legs) were made of different GT material, hence different actuation extents are expected. In contrast, the longer legs were divided in two sections along the length (sections 5.1 / 5.2 and 6.1 / 6.2), each one made of a different GT material. In leg (5) a LCN layer was placed below (section 5.2) and no LCN was placed in section (5.1) (to obtain a static section). In leg (6), one LCN was positioned above (section 6.2) and another LCN was placed below (section 6.1), thus, an "S" shaped bending is expected for this leg.

Overall, the device must bend downwards in legs (1-4) and (5), and upwards with an "S" shaped bending in leg (6) at different rates and times for each branch depending on the GT material used. The selected LCN stress programming level and GT materials are presented in the results and discussion section according to the selected materials for the study and the obtained actuation response.

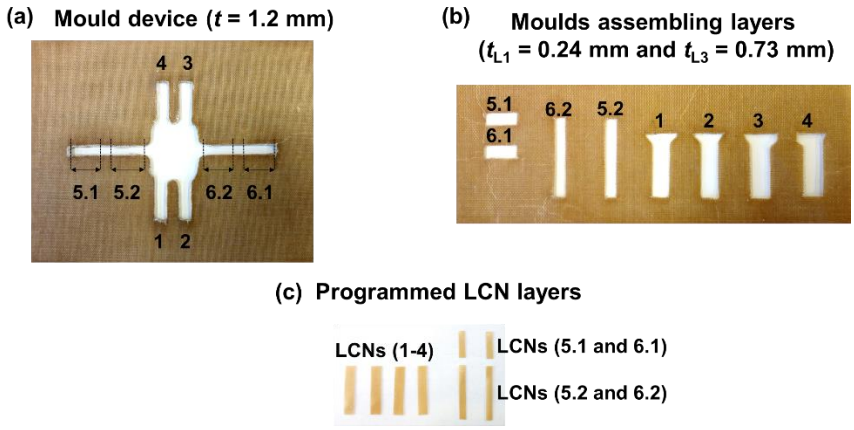

Figure V-34. (a) Mould used for the assembling of the 3D device; (b) mould for the preparation of the GT-layers in the intermediate stage and (c) LCN programmed layers.

The device was built in one single piece using the mould presented in Figure V-34(a). Layers with different shapes of the GT material were prepared using the Teflon mould presented in Figure V-34(b) to fit the design of each leg. Two different moulds were used: for layer 1, a thinner mould ($t = t_{L1}$) and for layer 3 a thicker mould ($t = t_{L3}$). The LCN layers were programmed as explained in the materials section and cut to fit the dimensions of each leg of the device (see Figure V-34(c)). Once intermediate GTs and programmed LCN materials were prepared, the device was mounted with a total thickness of 1.2 mm and a constant v_F = 0.8 in all the actuators. All the LCN were programmed at the same extent and were positioned below or above depending on the leg as explained before. Accordingly, GT thickness of layer (t_{L3}) was defined to meet these requirements. Afterwards, a constraining force was applied using Teflon-coated glass plates, and the same curing process as that adopted for a single actuator was followed: 3 hours at 90 °C plus 1 hour at 110 °C plus 1 hour at 135 °C. Finally, the device was carefully polished to eliminate defects on the edges.

The individual response of all the actuators of the 3D device were previously characterised as explained in the previous section. The motion of the assembled device was tested in a thermal chamber under rapid heating and natural cooling processes from 50 °C up to 160 °C. 20 cycles were performed to achieve stability and, once stabilized, subsequent cycles were recorded with a high-resolution camera. Frames of the device in motion at different times and positions were collected and presented in the results and discussion section. In addition, the bending angles on each actuator were determined using a computational tool and compared with the predicted ones using the analytical model developed in the previous work[33].

3. Results and discussion

Thermomechanical properties of the GT systems

The thermomechanical properties of the different GT systems studied were analysed by means of DMA analysis. The modulus, E_r, glass transition temperature, T_g and tanδ breadth (FWHM and $\tan\delta_{peak}$) are presented in Figure V-35 as a function of the "thiol-epoxy" ratio. As can be seen, the use of a thiol compound with higher functionality (S4 > S3) leads to the formation of network structures with higher rubbery modulus and T_g (see the results for r = 1.0 in Figure V-35(a)). The higher functionality of S4 causes an increase of the crosslinking density, thus, an increase of E_r according to the theory of elasticity[40]. In addition, the absence of the pendant ethyl chain in the S4 compound promotes the formation of a

more homogeneous and packed network, hindering the mobility of the network chains and therefore increasing the T_g. The incorporation of a high functionalized epoxy resin (SU8) does not affect the rubbery modulus in the stoichiometric formulation, but increases the T_g and considerably broadens the relaxation process as deduced by the increase of FWHM and decrease of the $\tan\delta_{peak}$ (see Figure V-35(b)). Moving away from the stoichiometric mixture, that is decreasing the "thiol-epoxy" ratio, the epoxy homopolymerization is extended. Consequently, the crosslinking density and E_r increase, as well as the relaxation process broadens due to the higher functionality of the epoxy homopolymerization in comparison with the thiol-epoxy polycondensation ($f_4 > f_2$).

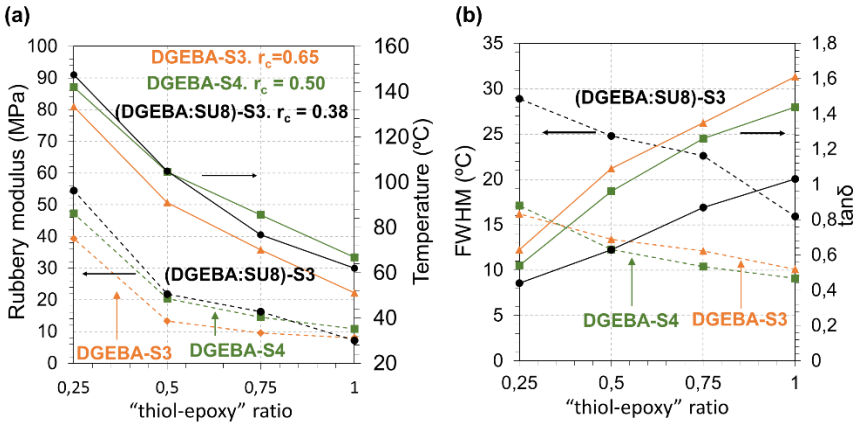

Figure V-35. (a) FWHM and $\tan\delta_{peak}$; (b) rubbery modulus and glass transition temperature as a function of the "thiol-epoxy" ratio for the different systems studied.

As explained in the introduction, the purpose of this investigation is to achieve the control of the actuation extent, rate and time by means of different GT materials. As can be deduced from Figure V-35, a wide range of materials, with different thermomechanical and structural properties, stems from the studied system, however, some requirements for the assembly process and the actuation must be considered. As explained in our previous work[33], in order to facilitate the assembling process and enhance the inter-layer adhesion in the actuator, the GT material should have a "thiol-epoxy" ratio close to or higher than the critical ratio in order to form a gelled structure after the 1st curing stage (in Figure V-35(a), the critical ratio (r_c) of each system is indicated). In addition, the T_g of the final material (after the 2nd curing stage) should be lower than T_{iso} (in this case T_{iso} is equal to 120 °C) to allow an efficient actuation. Consequently, GT materials with T_gs ranging from well-below T_{iso} to very close to T_{iso}, were employed to accomplish these requirements,

and to investigate the effect of approaching both the GT network relaxation and LCN liquid-crystalline transition in the actuation, as well as the impact of the modulus and relaxation processes.

Having in mind the above, four different formulations are proposed. In Table V-11, the thermomechanical properties of these formulations are summarized. Two of the formulations have similar moduli (16.8 and 18.4 MPa) but different T_gs (79 and 94 °C), while the other two have similar T_gs (118 and 120 °C), very close to T_{iso} (120 °C), but with different moduli (37.4 and 42 MPa) and most importantly, different network relaxation dynamics (FWHM varies from 15.8 to 30.1 °C).

Table V-11. Thermomechanical properties of the different GT materials studied.

GT material	E_g (MPa)	E_r (MPa)	T_g (°C)	tanδ (°C)	FWHM (°C)
DGEBA-S3-60	2180	16.8	79	1.1	12.8
DGEBA-S4-60	2105	18.4	94	1.2	11.5
DGEBA-S4-35	2150	37.4	118	0.7	15.8
(DGEBA:SU8)-S3-35	2100	42.0	120	0.5	30.1

In Table V-12, the specifications of the assembled actuators (dimension, LCN programmed strain, ε_p, and volume fraction, v_F) are presented. For the sake of simplicity the nomenclature presented in Table V-12 is slightly different from that used in our previous work[33]. In present case, S3, S4 and SU8 refer to the GT material, and 60 or 35 refers to the "thiol-epoxy" ratio (r = 0.6 or r = 0.35). In all the actuators, the volume fraction has been fixed to 0.8 and the programming stress level to 2% of the corresponding stress at break (σ_b). These parameters were fixed considering actuation extents lower than 30% (predicted by the model developed and presented in the previous work[33]) thus achieving quantifiable bending angles and deformations within the model limits. Moreover, the combination of v_F = 0.8 and σ_p = 2% lead to stiff and tough actuators as it was observed in our previous work (neither failure nor layer delamination were observed for this configuration)[33].

Table V-12. Specifications of the different actuators of study.

Actuator	ε_p (%)	v_F	t (mm)	w (mm)	L (mm)
AS360	49.1	0.8	1.16 ± 0.01	3.5 ± 0.1	20.8 ± 0.1
AS460	51.3	0.8	1.21 ± 0.01	3.5 ± 0.1	21.4 ± 0.1
AS435	50.5	0.8	1.19 ± 0.01	3.5 ± 0.1	21.0 ± 0.1
ASU835	50.8	0.8	1.23 ± 0.01	3.5 ± 0.1	20.3 ± 0.1

Analysis of the cyclic actuation

Before analysing the actuator response, all the actuators have been subject to 20 consecutive cycles to achieve a stable response. In Figure V-36, the cyclic analysis is presented for the actuator AS360 as an example, since the evolution of the different parameters is comparable in terms of stability for all the actuators studied. The evolution of the actuation extent in % is presented as a function of the temperature and time in Figure V-36(a) and (b), respectively. Bending and unbending temperatures (T_B, T_U) and rates (B_{rate}, U_{rate}) are shown in Figure V-36(c) and (d), respectively. To determine whether a sample had reached a steady behaviour, the average value and the standard deviation of all the analysed parameters over 5 successive cycles were calculated. The parameter was considered to be stable when the standard deviation value was under 2%, and this condition was repeated for at least five more consecutive cycles.

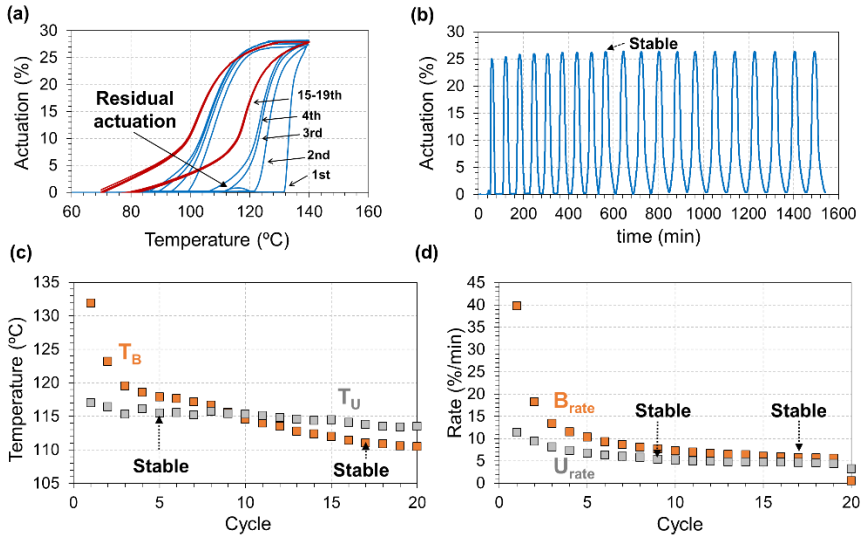

Figure V-36. Stability analysis of actuator AS360: (a) actuation-temperature curves; (b) actuation-time curves; (c) bending and unbending temperatures and (d) bending and unbending rates.

As can be observed in Figure V-36(b), the actuation extent increases slightly up to a stable value found after 9 cycles, and remains constant during the whole process. Similar response was found in our previous work[37] using a LCN (Di-C7) programmed at a considerably higher stress level. In [37] the mechanical response of the LCN showed an increase of the actuation up to a stable value achieved after 8 cycles and slightly decreased in the following cycles. Although the experimental

conditions are not strictly comparable, in the present case, the initial period is very similar, and the stability is further extended. This can be attributed to the state of the network structure after programming: the lower programming stress level in the LCN used for the actuator reduces the presence of internal stresses and unstable structural configurations.

On analysing the bending and unbending processes (Figure V-36(c) and (d)), all the parameters tend to decrease down to a stable value, but stabilization of the parameters corresponding to the bending process is more difficult. From the initial to the second cycle, both B_{rate} and T_B considerably decrease, whereas U_{rate} and T_U only show a slight decrease. Moreover, B_{rate} and T_B require more than 15 cycles to stabilize, whereas U_{rate} and T_U are stabilized after 5-9 cycles. The bending process, which is caused by the shrinkage of the LCN, is more affected during the first cycles and overall stabilizes later due to the structural rearrangements within the network of the LCN after the programming process, and probably due to the stress generated during the assembling process (2nd curing stage of the GT). In contrast, the unbending takes place after a heating procedure, thus, the effect regarding network instabilities is less relevant.

Overall, the width at half-height, FWHM, of the cycle narrows, the bending process starts earlier as deduced by the decrease of T_B (see Figure V-36(c)), and the unbending process starts at similar temperature, thus, the process is extended in temperature range. Similarly, the decrease of the bending and unbending rates, extend the process in time as well. Moreover, it is worth noting that the first cycle shows a residual actuation before the bending process (highlighted in Figure V-36(a) at 115 °C) and both the bending and unbending processes are steeper, pointing out a stress relaxation phenomenon. Various factors contribute to this response: on the one hand, during the assembling process, residual stress is generated by the premature shrinkage of the LCN layer during epoxy homopolymerization. This causes an abrupt stress generation during the first heating procedure, hence, the premature actuation. On the other hand, the programming of the LCN involves heating, deformation and cooling processes, hence, non-relaxed stress is probably present in the final network. This stress is accommodated after each heating procedure, thus, attenuating the drastic response during the bending process and in general, being responsible of the stabilization of the parameters related to the bending process.

The above results remark the requirement of performing controlled cycling procedures to stabilize the actuators response before utilizing them to ensure controlled and repeatable operation.

Effect of the GT structure

In Table V-13, the first stable cycle (the cycle in which stability is accomplished for all the parameters studied), the stable values for the different parameters (Actuation extent, T_B, T_U, B_{rate}, U_{rate}, t_B and t_U) and the analytical model prediction of the actuation extent are summarized.

Table V-13. Stable actuation parameters for the different formulations under study.

Actuator	Stable Cycle	Actuation (%)	Actuation Model (%)
AS360 (T_g = 79 °C)	17	25.6	23.0
AS460 (T_g = 94 °C)	19	23.9	21.0
AS435 (T_g = 118 °C)	18	12.3	11.0
ASU835 (T_g = 120 °C)	19	5.7	8.2

	T_B (°C)	T_U (°C)	B_{rate} (%/min)	t_B (min)	U_{rate} (%/min)	t_U (min)
AS360 (T_g = 79 °C)	111.8	114.2	6.3	11.8	5.1	14.9
AS460 (T_g = 94 °C)	115.0	120.1	6.3	11.1	5.4	13.5
AS435 (T_g = 118 °C)	120.2	119.5	9.8	7.3	7.3	9.7
ASU835 (T_g = 120 °C)	121.8	122.9	12.3	6.9	8.7	9.9

First, it is worth noting that the actuation extent of these actuators fits very well with the predictions of the analytical model developed in our previous work[33]. The model can predict the maximum actuation extent taking into account the actuator configuration (geometrical relation between the layers), materials moduli and the programmed strain extent of the LCN. In the present case, the modulus of the GT and its relaxation dynamics varied whereas the geometrical design (v_F) and the LCN programming stress level were kept constant. It was found that the actuation extent decreased with increasing the rubbery modulus: from 16.8 to 18.4 MPa (AS360 and AS460) the actuation shows comparable values, 25.6% and 23.9%, whereas at 37 MPa (AS435) it drops down to 12.3% and at 42 MPa (ASU835) to 5.7%. This suggests that the key factor to determine the maximum actuation extent is the modulus of the GT material rather than the T_g or the structural relaxation of GT and LCN materials. This makes possible to exploit the effect of varying the relaxation dynamics of the GT network without affecting the actuation extent.

If one analyses the bending and unbending temperatures, it is worth noting that both stabilize at a temperature very close to T_{iso} (T_{iso} = 120 °C), indicating that the actuation takes place within the LCN liquid-crystalline transition. However, both T_B and T_U increase with increasing T_gs of the GT. As the T_g approaches T_{iso}, the relaxation of the GT network takes place later, when the T_g is very close to T_{iso} (formulations AS435 and ASU835), T_B is inherently displaced to higher values due to the hindrance

of the GT material that impedes the LCN shrinkage until the relaxation takes place. Similarly, the unbending process takes place earlier due to the coupling of the GT vitrification with the LC transition on cooling down. Although AS435 has the same T_g as ASU835, this effect is accentuated in the formulation with SU8 probably because of the broader relaxation process that delays the processes towards higher temperatures. Therefore, the beginning of both bending and unbending processes depends not only on the LC transition of the LCN, but is affected by the GT relaxation when coupling between structural transitions takes place.

On the other hand, bending and unbending rates tend to increase on increasing the T_g, suggesting that the processes are faster for those formulations with higher T_g. This is in accordance with the decrease of t_B and t_U. Formulations with higher T_g have broader relaxations processes (mostly the formulation containing SU8), thus, one may expect slower bending-unbending processes. Nevertheless, if the GT relaxation takes place at a temperature close or above T_{iso}, the LCN shrinkage is initially impeded by the high modulus of the GT, thus, when it finally takes place, the force driven by the LCN is higher and the process becomes more drastic and faster.

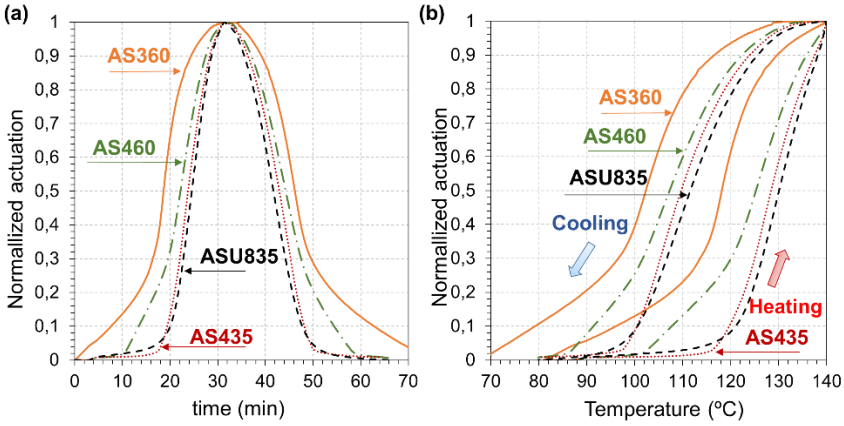

Figure V-37. Normalized actuation as a function of time (a) and temperature (b) for the different formulations studied at a heating and cooling rate of 2 °C/min.

Figure V-37 shows the stable cycles for all the actuators studied, normalized to the actuation extent and presented as a function of time (Figure V-37(a)) and temperature (Figure V-37(b)). As stated above, the increase of the T_g leads to faster bending and unbending processes. This is clearly appreciated in the actuation-time cycles in Figure V-37(a). The formulations with a T_g close to T_{iso} have a narrower cycle, as the total time is considerably reduced due to the shift of T_B and T_U to higher and lower

temperatures, respectively. This implies later bending and earlier unbending processes, coupled with the drastic response of the LCN when the shrinkage-elongation processes are triggered. Moreover, in Figure V-37(b), the effect of the LCN response on increasing the T_g is well-appreciated: there is a two-step actuation process with a lower slope initial part that takes place at 80 °C for AS360, which is shifted to 100 °C for AS460 and almost disappears for AS435 and ASU835 actuators. This early actuation is connected to the glass transition of the GT material that allows a progressive bending associated to the relaxation of the LCN network on approaching T_{iso}. In contrast, when the T_g is close to T_{iso}, this relaxation taking place in the LCN is accumulated in terms of energy that is released when the GT relaxes, hence the sharper response.

Effect of the heating rate

As evidenced in the previous section, the GT relaxation has a crucial impact on the actuation response. It is well-known that the network relaxation dynamics is affected by the heating rate[40], therefore the response of the actuators to different heating rates was investigated. First, the study of the actuator AS360 is presented in Figure V-38(a) with the actuation-time cycles at different heating rates (from 0.2 °C/min to 20 °C/min, with constant cooling rate of 2 °C/min) and the bending parameters, B_{rate} and t_B are shown in Figure V-38(b) and (c) for all the formulations of study. It must be noted that from a rate of 5 °C/min to 20 °C/min the holding time at high temperature (during bending) was extended from 3 to 30 min to allow completion of the process due to the rapid increase of the temperature in the thermal chamber of the DMA and the thermal inertia of the sample.

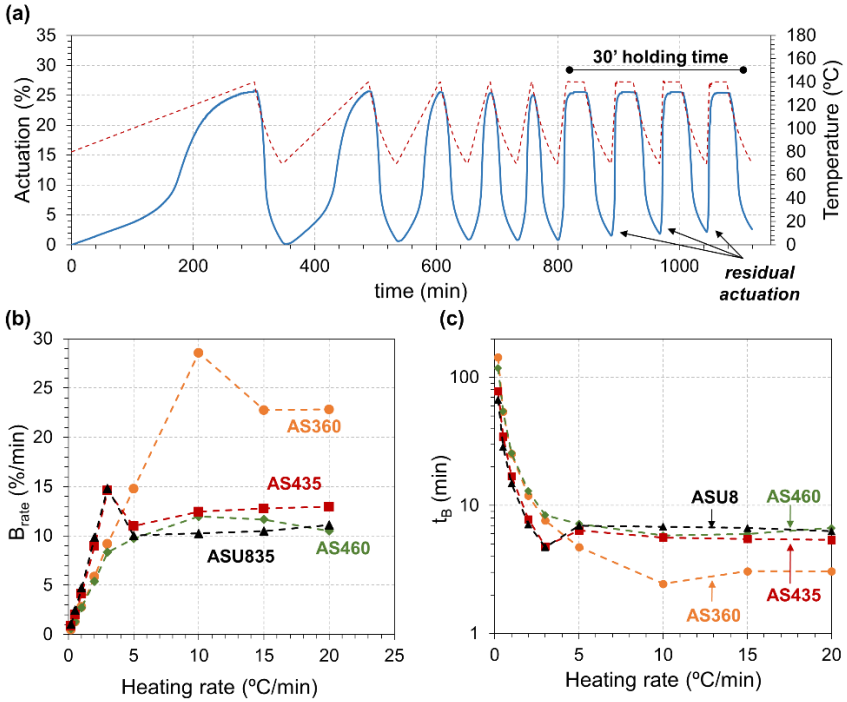

Figure V-38. Effect of the heating rate on the actuation behaviour: (a) actuation-time-temperature cycles in actuator AS360; (b) bending rate and (c) bending time at different heating rates for the different formulations studied.

On analysing the cycles with an extended time at high temperature (heating rates from 5 to 20 °C/min) for the AS360 formulation (Figure V-38(a)), it can be seen that the actuation extent is not affected. However, the capability to recover the original flat shape is slightly worsened as deduced by the appearance of residual actuation. This can be related to the creep phenomenon observed after each shrinkage-elongation cycle of the LCN in our previous work[37]. When the LCN was under free actuation conditions, the creep was attributed to irrecoverable or plastic deformations taking place during each cycle. In present case, the LCN motion is completely impeded, therefore the LCN cannot suffer creep, but stress relaxation. During the 20 consecutive cycles, the actuator performance was excellent, however, on increasing the time at high temperature, the LCN network can suffer stress-relaxation, leading to a new "stable" state that is, losing the original "flat" shape towards a new slightly bent shape promoted by the bending actuation design.

If one analyses the bending parameters (see Figure V-38(b) and (c)) for the AS360 formulation, there is a clear acceleration of the bending process with the increase of the heating rate associated to the enhancement of the relaxation dynamics in both the GT and LCN networks. However, at 10 °C/min a maximum appears and at 15 °C/min this acceleration is attenuated and stabilized. This stable value is related to the coupling of the LCN shrinkage and network relaxation of the GT. When the heating rate is too high, the temperature in the sample is not homogeneous: the outer faces have higher temperature than the inner ones, therefore, the LCN layer, which is placed in the outer face, begins the shrinkage process before or meanwhile the GT relaxation is taking place. As a result, the shrinkage is impeded, and the process is controlled by the relaxation of the GT network. In addition, the network relaxation is also shifted to higher temperatures at higher heating rates[40], but the effect may not be relevant within the experimental range of heating rates tested. This phenomenon is closely related to the explanation given above regarding the proximity of the T_g with T_{iso}. In that case, both processes take place simultaneously, hence a coupling effect is noticed. In the present case, the delay of the GT relaxation when the heating rate is too high causes the same effect. This suggests that the actuation can be controlled with the heating rate by the relaxation of the GT network or by the LCN shrinkage-elongation processes. Moreover, the coupling of the GT relaxation with the LCN shrinkage can promote stress-relaxation due to the constraining forces that are generated favouring the residual actuation observed in those cycles with extended time at high temperature (Figure V-38(a)). To avoid this stress-relaxation phenomenon, the control of the time at high temperature is of outmost importance and must be fit within the necessary time to fully actuate during the bending.

Comparing B_{rate} (Figure V-38(b)) and t_B (Figure V-38(c)) of the different formulations of study, it can be observed that the explanation given above regarding the faster bending and unbending processes in formulations with higher T_g is corroborated when low heating rates are imposed (from 0.2 to 3 °C/min). In that case, the closer T_g to T_{iso}, the faster B_{rate} and the lower t_B. However, on increasing the heating rate, both B_{rate} and t_B are attenuated and stabilized earlier for those formulations with a T_g close to T_{iso} (AS435 and ASU835 stabilizes at 5 °C/min). This can be rationalized as follows: when the heating rate increases, the network relaxation of the GT governs the bending process due to the coupling of both LC and glass transitions. This phenomenon occurs earlier in formulations with a T_g close to T_{iso} (the coupling effect was observed at 2 °C/min in Table V-13 and Figure V-37). Under coupling conditions, the

drastic response caused by the impeded shrinkage of the LCN seems to be affected by the nature of the network structure: formulations with S4 (AS460 and AAS435) show similar behaviour with respect to B_{rate} and t_B probably because of the more homogeneous network structure in comparison with AS360 with the presence of a side ethyl chain. However, the presence of SU8 in the S3 system attenuates the effect of the ethyl chain due to the broadening of the relaxation process.

In conclusion, the modulus of the materials and the configuration of the actuator dictate the actuation extent, whereas the structural relaxation can be used to tailor both the rate and total time needed in the actuation process. Imposing the appropriate heating procedure, rapid heating to promote the GT relaxation, that is, isothermal processes at high temperature, or slower heating to control through the LCN shrinkage-elongation process, the actuation rate can be tailored as desired.

Development of a 3D actuating device

To demonstrate the capability of these materials to be controlled in terms of actuation rate and time, a device made of different designed actuators has been developed in one single element following the curing procedure explained in the experimental section. The top and side views of the device with the specific dimensions are shown in Figure V-39. The code of the different GT materials that form the device have been highlighted in the top view (Figure V-39(a)), as well as the code corresponding to each leg. In addition, the configuration of leg (6) has been highlighted (Figure V-39(c)) to better understand the position of each LCN and GT materials to achieve the "S-type" motion. All the LCNs were programmed at the same level (σ_P).

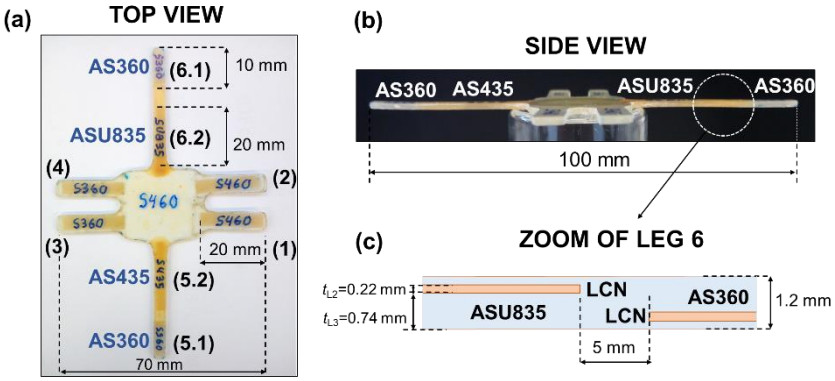

Figure V-39. (a) Top and (b) side view of the device after the assembling process: the GT materials, legs nomenclature and dimensions have been included. (c) Zoom of leg (6) highlighting the materials and configuration.

As can be observed in the TOP view, the device presents different coloration depending on the GT material. Darker coloration in AS435 and ASU835 systems (see legs 5-6) is an indication of a higher contribution of epoxy homopolymerization initiated by 1MI, as observed in our previous work[35]. Regarding the adhesion and assembling of each leg, the proposed methodology led to a compact device without superficial defects or scratches and a constant thickness of 1.2 mm as observed in the side view. The different GT materials have been properly joined (ensuring a solid connection) during the 2nd curing stage as evidenced by the diffusion of the coloured and transparent materials in the joints between the central part and the legs.

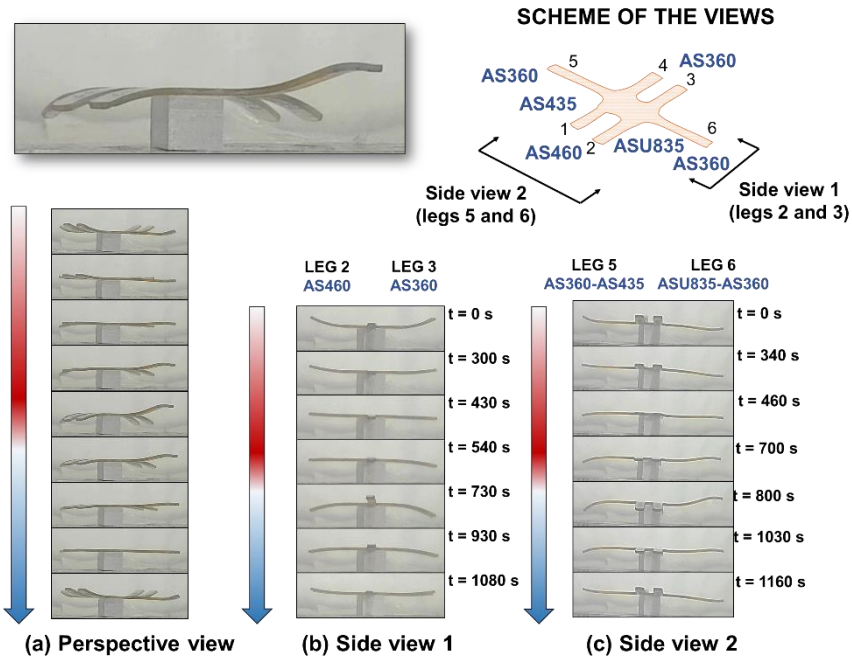

Figure V-40. Visual demonstration of the complex device motion from different perspectives and side views under heating-cooling procedures.

The actuation under heating-cooling procedures is presented in Figure V-40. The scheme of the device and the testing views are shown on top. In the first set of frames (Figure V-40(a)), a perspective view of the actuation response is shown for a rapid heating process and subsequent natural cooling after 20 previous cycles (stabilization of all the actuators). First, it is worth noting that the device starts from an already bent shape. As explained in the previous work[33], after the assembling process, the internal stress generated during the curing process and premature shrinkage of the LCN leads to some curvature in opposite direction to the

actuation. Moreover, this curing process has been carried out at high temperature (above T_{iso}), thus this effect was accentuated.

If one analyses the motion of the device (Figure V-40(b) and (c)), the designed motions has been successfully achieved: legs (1) and (4) bend downwards, whereas leg (6) bend shaping an "S" and leg (5) remains straight and bend downwards only in section (5.1). This is repeated with no appreciable shape-losing as it was observed in the stability section. As deduced in the previous section, when a rapid heating is imposed, the GT relaxation controls the process in all the actuators, thus, the narrower the GT relaxation, the faster the actuation. In addition, the presence of the S3 should accentuate this acceleration. Therefore, the motion sequence should follow the order: AS360 > AS460 > ASU835.

On analysing the second set of frames (Figure V-40(b), side view of legs 1-4), legs (3) and (4) (AS360) bend earlier than legs (1) and (2) (AS460) as deduced in the progressive bending from frames 0 to frame 540 s. This phenomenon is clearer if one analyses legs (5) and (6) (Figure V-40(c)) because ASU835 (section 6.2) is compared against the AS360 (section 6.1 and 5.1). As can be seen, after 460 s AS360 has almost completed the bending process, whereas the ASU835 has just started to bend. The premature beginning of AS360 in section (6.1) is better appreciated in leg (5), section (5.1), because section (5.2) has no LCN (static section), thus, no coupling of the bending processes takes place. After the bending process, during the cooling step the process reverts: ASU835 unbending takes place first (see frame 1030 s) and AS360 starts later (see frame 1160 s) because of the higher T_g of ASU835: as observed in the previous sections, the bending process is delayed with approaching T_g to T_{iso}, but the unbending takes place earlier.

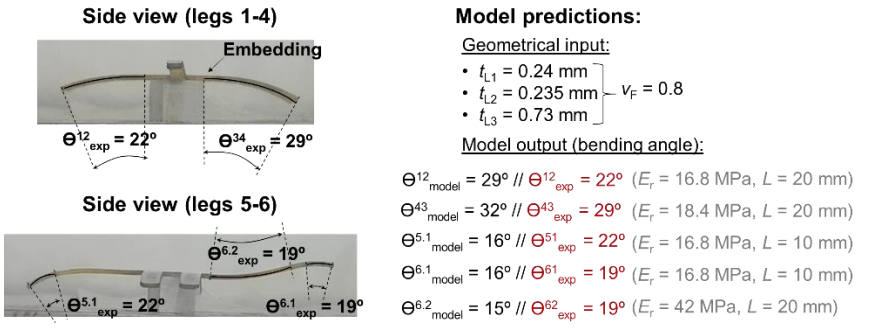

Figure V-41. Determination of the bending angles (actuation) in each leg and comparison with the model predictions.

In Figure V-41, the actuation extent of each actuator in the device has been experimentally calculated and compared with the predictions of the analytical model developed in our previous work[33]. As it can be seen, the experimental actuation extent is slightly lower in legs (1) and (4) in comparison to the model predictions, whereas in legs (5) and (6) the tendency opposite, the experimental values are slightly higher. In general, the experimental and predicted values fit very well considering the experimental limitation when assembling such a complex device (the positioning of the LCN layers and the adjustment of the width, length and thickness of each part of the device). Moreover, in the model the actuator was analysed in free bending (with only two supports), whereas in present case it can be considered as a cantilever beam with an embedded part in the joint between the legs and the central part (highlighted in Figure V-41). This different boundary conditions produce slightly lower bending angles (legs 1-4), and coupled bending in leg (6), thus higher actuation, making difficult the experimental determination of the bending angle.

4. Conclusions

In this work, glassy thermosets with different thermomechanical and structural properties and a liquid-crystalline network with high T_{iso} have been used to develop free-standing shape-memory actuators with enhanced control of the actuation in terms of extent, rate and time. The relevance of the dual-curing processing for the assembling and precise control of the final configuration of the actuators have been demonstrated. Materials with a wide range of structural and physical properties in the intermediate and final stages have been investigated and utilized for the assembling of the actuators. The actuators have shown good stability on cycling: actuation extent, bending and unbending rates and temperatures stabilize after 17-19 cycles. The bending process starts from a drastic response caused by the internal stress generated in the actuator after the assembling process and attenuates as the LCN network structure accommodates internal stresses suffered during its programming process.

The use of GT materials with different moduli allows to control the actuation extent according to the predictions of the analytical model. On the other hand, by using GT materials with a T_g closer to the T_{iso} of the LCN, a coupling effect between the network relaxation of GT and LC transition is noticed. In consequence, the control of the actuation depends on the relaxation of GT rather than the LCN shrinkage-elongation. Since the network relaxation of GT is usually slower than the LC transition, the LCN shrinkage is initially impeded by the high modulus of the GT and therefore

begins later, but once the GT material relaxes, the LCN shrinkage takes place faster due to the accumulated energy in the LCN network.

The heating rate has been found crucial for the control of the actuation through the relaxation of the GT network. At low heating rates, the coupling effect is only appreciated in formulations with $T_g \approx T_{iso}$, therefore the actuation can be controlled by the LCN shrinkage-elongation process. However, if the heating rate is high enough, the coupling effect takes place even with $T_g < T_{iso}$ because of the presence of temperature gradients within the sample and delayed network relaxation at higher heating rates. This leads to the control of the actuation by the GT network relaxation, which is therefore faster when the relaxation process is narrow.

In addition, the possibility to tune actuation extent, rate and time has been experimentally demonstrated through the design and the manufacturing of a 3D actuating device able to make complex motions. The proposed assembling methodology has allowed the development of a compact 3D design in one single piece with a controllable soft motion. The motion has been recorded and the actuation extent of each section of the device compared with the analytical model predictions. The extent achieved fitted very well the model predictions regardless of the coupling of bending processes taking place in the ”S-type” leg and the stress concentration present in the joints between the legs and the middle part. Moreover, the use of the studied GT materials led to different motion times and rates as deduced from the delayed motion in parts of the device.

Acknowledgements

The authors would like to thank MINECO (MAT2014-53706-C03-01 and MAT2014-53706-C03-02) and Generalitat de Catalunya (2014-SGR-67) for financial support. Xavier F.-F. also acknowledges the Serra Húnter programme from the Generalitat de Catalunya.

References

[1] M. Behl, A. Lendlein, Actively moving polymers, Soft Matter. 3 (2007) 58–67. doi:10.1039/B610611K.

[2] J. Hu, S. Chen, A review of actively moving polymers in textile applications, J. Mater. Chem. 20 (2010) 3346. doi:10.1039/b922872a.

[3] A. Lendlein, C. Wischke, K. Kratz, M. Heuchel, J. Zotzmann, B. Hiebl, A.T. Neffe, M. Behl, B. Development, Shape-Memory Polymers, Elsevier Ltd., 2011. doi:10.1016/B978-0-08-055294-1.00271-3.

[4] X. Wu, W.M. Huang, Y. Zhao, Z. Ding, C. Tang, J. Zhang, Mechanisms of the shape memory effect in polymeric materials, Polymers. 5 (2013) 1169–1202. doi:10.3390/polym5041169.

[5] Q. Zhao, H.J. Qi, T. Xie, Recent progress in shape memory polymer: New behavior, enabling materials, and mechanistic understanding, Prog. Polym. Sci. 49–50 (2015) 1–42. doi:10.1016/j.progpolymsci.2015.04.001.

[6] C. Ohm, M. Brehmer, R. Zentel, Liquid crystalline elastomers as actuators and sensors., Adv. Mater. 22 (2010) 3366–3387. doi:10.1002/adma.200904059.

[7] J. Sun, Q. Guan, Y. Liu, J. Leng, Morphing aircraft based on smart materials and structures: A state-of-the-art review, J. Intell. Mater. Syst. Struct. 27 (2016) 2289–2312. doi:10.1177/1045389X16629569.

[8] C.L. Lewis, Y. Meng, M. Anthamatten, Well-Defined Shape-Memory Networks with High Elastic Energy Capacity, Macromolecules, 48 (2015) 4918-4926. doi:10.1021/acs.macromol.5b00763.

[9] X. Xiao, D. Kong, X. Qiu, W. Zhang, F. Zhang, L. Liu, Y. Liu, S. Zhang, Y. Hu, J. Leng, Shape-Memory Polymers with Adjustable High Glass Transition Temperatures, Macromolecules. 48 (2015) 3582–3589. doi:10.1021/acs.macromol.5b00654.

[10] X. Xiao, D. Kong, X. Qiu, W. Zhang, Y. Liu, S. Zhang, F. Zhang, Y. Hu, J. Leng, Shape memory polymers with high and low temperature resistant properties, Sci. Rep. 5 (2015) 14137. doi:10.1038/srep14137.

[11] Y. Gu, S.X. Li, Thermo-Mechanical Behavior of Epoxy Shape Memory Polymer, Adv. Mater. Res. 721 (2013) 169–172. doi:10.4028/www.scientific.net/AMR.721.169.

[12] R. Biju, C.P.R. Nair, Synthesis and characterization of shape memory epoxy-anhydride system, J. Polym. Res. 20 (2013) 82. doi:10.1007/s10965-013-0082-z.

[13] S. Pandini, F. Bignotti, F. Baldi, S. Passera, Network architecture and shape memory behavior of cold-worked epoxies, J. Intell. Mater. Syst. Struct. 24 (2013) 1583–1597. doi:10.1177/1045389X13478275.

[14] N. Zheng, G. Fang, Z. Cao, Q. Zhao, T. Xie, High strain epoxy shape memory polymer, Polym. Chem. 6 (2015) 3046–3053. doi:10.1039/C5PY00172B.

[15] A. Belmonte, D. Guzmán, X. Fernández-Francos, S. De la Flor, Effect of the Network Structure and Programming Temperature on the Shape-Memory Response of Thiol-Epoxy " Click " Systems, Polymers, 7 (2015) 2146–2164. doi:10.3390/polym7101505.

[16] A. Belmonte, X. Fernández-Francos, S. De la Flor, New understanding of the shape-memory response in thiol-epoxy click systems : towards controlling the recovery process, J. Mater. Sci, 52 (2017) 1625-1638. doi:10.1007/s10853-016-0456-9.

[17] D. Santiago, A. Fabregat-Sanjuan, F. Ferrando, S. De la Flor, Recovery stress and work output in hyperbranched poly(ethyleneimine)-modified shape-memory epoxy polymers, J. Polym. Sci. Part B Polym. Phys. 54 (2016) 1002–1013. doi:10.1002/polb.24004.

[18] A. Belmonte, X. Fernández-Francos, S. De la Flor, À. Serra, Network structure dependence on unconstrained isothermal-recovery processes for shape-memory thiol-epoxy "click" systems, Mech. Time-Dependent Mater. (2017) 1–17. doi:10.1007/s11043-016-9322-z.

[19] K.A. Burke, I.A. Rousseau, P.T. Mather, Reversible actuation in main-chain liquid crystalline elastomers with varying crosslink densities, Polymer, 55 (2014) 5897–5907. doi:10.1016/j.polymer.2014.06.088.

[20] S. Chen, F. Mo, S. Chen, Z. Ge, H. Yang, J. Zuo, X. Liu, H. Zhuo, New insights into multi-shape memory behaviours and liquid crystalline properties of

supramolecular polyurethane complexes based on pyridine-containing polyurethane and 4-octyldecyloxybenzoic acid, J. Mater. Chem. A. 3 (2015) 19525–19538. doi:10.1039/C5TA04469C.

[21] Y. Li, C. Pruitt, O. Rios, L. Wei, M. Rock, J.K. Keum, A.G. Mcdonald, M.R. Kessler, Controlled shape memory behavior of a smectic main-chain liquid crystalline elastomer, Macromolecules. 48 (2015) 2864–2874. doi:10.1021/acs.macromol.5b00519.

[22] G.C. Lama, P. Cerruti, M. Lavorgna, C. Carfagna, V. Ambrogi, G. Gentile, Controlled Actuation of a Carbon Nanotube/Epoxy Shape-Memory Liquid Crystalline Elastomer, J. Phys. Chem. C. 120 (2016) 24417–24426. doi:10.1021/acs.jpcc.6b06550.

[23] H. Finkelmann, Liquid Crystalline Polymers, Angew. Chemie Int. Ed. English. 26 (1987) 816–824. doi:10.1002/anie.198708161.

[24] J. Zhou, S.S. Sheiko, Reversible shape-shifting in polymeric materials, J. Polym. Sci. Part B Polym. Phys. 1 (2016) 1–16. doi:10.1002/polb.24014.

[25] C.L. Lewis, E.M. Dell, A Review of Shape Memory Polymers Bearing Reversible Binding Groups, J. Polym. Sci. Part B Polym. Phys. 54 (2016) 1340–1364. doi:10.1002/polb.23994.

[26] K.K. Westbrook, P.T. Mather, V. Parakh, M.L. Dunn, Q. Ge, B.M. Lee, H.J. Qi, Two-way reversible shape memory effects in a free-standing polymer composite, Smart Mater. Struct. 20 (2011) 65010. doi:10.1088/0964-1726/20/6/065010.

[27] Y. Meng, J. Jiang, M. Anthamattern, Shape actuation via internal stress-induced crystallization of dual-cure networks, ACS Macro Lett. 4 (2015) 115–118.

[28] E. Zharinova, M. Heuchel, T. Weigel, D. Gerber, K. Kratz, A. Lendlein, Water-blown polyurethane foams showing a reversible shape-memory effect, Polymers, 8 (2016). doi:10.3390/polym8120412.

[29] M.O. Saed, A.H. Torbati, C.A. Starr, R. Visvanathan, N.A. Clark, C.M. Yakacki, Thiol-Acrylate Main-Chain Liquid-Crystalline Elastomers with Tunable Thermomechanical Properties and Actuation Strain, J. Polym. Sci. Part B Polym. Phys. 55 (2017) 115–118. doi:10.1002/polb.24249.

[30] M.O. Saed, A.H. Torbati, D.P. Nair, C.M. Yakacki, Synthesis of Programmable Main-chain Liquid-crystalline Elastomers Using a Two-stage Thiol-acrylate Reaction, J. Vis. Exp. 107 (2016) 1–10. doi:10.3791/53546.

[31] Q. Ge, K.K. Westbrook, P.T. Mather, M.L. Dunn, H. Jerry Qi, Thermomechanical behavior of a two-way shape memory composite actuator, Smart Mater. Struct. 22 (2013) 55009. doi:10.1088/0964-1726/22/5/055009.

[32] M. Zarek, M. Layani, I. Cooperstein, E. Sachyani, D. Cohn, S. Magdassi, 3D Printing of Shape Memory Polymers for Flexible Electronic Devices, Adv. Mater. 28 (2016) 4449–4454. doi:10.1002/adma.201503132.

[33] A. Belmonte, G.C. Lama, G. Gentile, P. Cerruti, V. Ambrogi, X. Fernández-Francos, S. De la Flor, Thermally-triggered free-standing shape-memory actuators, Eur. Polym. J. (2017). doi:10.1016/j.eurpolymj.2017.10.006.

[34] X. Fernández-Francos, A.-O. Konuray, A. Belmonte, S. De la Flor, À. Serra, X. Ramis, Sequential curing of off-stoichiometric thiol–epoxy thermosets with a custom-tailored structure, Polym. Chem. 7 (2016) 2280–2290. doi:10.1039/C6PY00099A.

[35] A. Belmonte, X. Fernández-Francos, À. Serra, S. De la Flor, Phenomenological characterization of sequential dual-curing of off-stoichiometric " thiol-epoxy "

systems : Towards applicability, Mater. Des. 113 (2017) 116–127. doi:10.1016/j.matdes.2016.10.009.

[36] A. Belmonte, C. Russo, V. Ambrogi, X. Fernández-Francos, S. De la Flor, Epoxy-based shape-memory actuators obtained via dual-curing of off-stoichiometric "thiol-epoxy" mixtures, Polymers. 9 (2017) 113. doi:10.3390/polym9030113.

[37] A. Belmonte, L. Giuseppe C., G. Gentile, P. Cerruti, V. Ambrogi, X. Fernández-Francos, S. De la Flor, G.C. Lama, G. Gentile, X. Fernández-Francos, S. De la Flor, P. Cerruti, V. Ambrogi, Synthesis and Characterization of Liquid-Crystalline Networks: Toward Autonomous Shape-Memory Actuation, J. Phys. Chem. C. 121 (2017) 22403–22414. doi:10.1021/acs.jpcc.7b04610.

[38] C.-H. Hsueh, Modeling of elastic deformation of multilayers due to residual stresses and external bending, J. Appl. Phys. 91 (2002) 9652–9656.

[39] J. Malzbender, Mechanical and thermal stresses in multilayered materials, J. Appl. Phys. 95 (2004) 1780–1782. doi:10.1063/1.1642289.

[40] J.-P. Pascault, H. Sautereau, V. J, W.J.J. R, Thermosetting Polymers, CRC Press, 2002.

UNIVERSITAT ROVIRA I VIRGILI
DESIGN AND CHARACTERIZATION OF ACTIVELY-MOVING POLYMERS OBTAINED VIA DUAL-CURING PROCESSING
Alberto Francisco Belmonte Parra

Chapter VI

Conclusions and Future Work

VI

UNIVERSITAT ROVIRA I VIRGILI
DESIGN AND CHARACTERIZATION OF ACTIVELY-MOVING POLYMERS OBTAINED VIA DUAL-CURING PROCESSING
Alberto Francisco Belmonte Parra

VI.1 Conclusions

The conclusions of this investigation are divided in different categories according to the general and specific objectives listed in section I.3.

(1): Study of thermoset-based SMPs obtained through click chemistry.

- Thiol-epoxy thermosets have been obtained using thiol crosslinkers with different functionality, different amounts of a tri-functional network modifier and a latent "encapsulated" catalyst. The resulting materials have shown homogeneous relaxation processes with an enhanced control of the thermomechanical and structural properties (crosslinking density, T_g and rubbery modulus).
- The tensile mechanical properties at different temperatures within the glass transition region have been found strongly dependent on the structural properties. Formulations containing thiol crosslinkers of lower functionality and low content of the network modifier have shown higher ε_b and σ_b (up to 100% and 55 MPa respectively). This has been attributed to the enhanced network mobility due to the lower crosslinking density and less-packed network structure.
- The T_{prog} have been found crucial on the further response during the unconstrained recovery process. Programming at temperatures below the glass transition enhances the stress/strain limits but leads to energy loosing and even network damage due to the high-frictional state of the network. This worsens the recovery performance of the SMPs making difficult the completion of the process, slowing it and progressively fatiguing the network leading to premature failure. Increasing T_{prog} decreases the mechanical limits but considerably enhances the recovery performance in terms of stability, rate and efficiency.
- In contrast to uniaxial programming, samples programmed under bending conditions have shown higher recovery stability and rate regardless T_{prog}.
- The network relaxation dynamics has been found closely related to the recovery dynamics mostly in the early and intermediate stages. The shape-recovery proceeds accordingly to the time scale of the network relaxation until the mobility of the network is highly enhanced (near to the T_g nominal value) and therefore the recovery can proceed freely and independent of the network relaxation. This means that, formulations with more heterogeneous relaxation processes have shown broader recovery processes.

- The heating conditions have shown a crucial impact on the recovery dynamics due to the time-temperature dependence of the network relaxation: low heating rates or isothermal temperatures enhance the effect of the network structure in the recovery dynamics, that means, the more heterogeneous the network, the broader the recovery process, whereas on increasing the temperature or rate minimizes this effect due to the enhancement of the relaxation dynamics.

(2): Study of "thiol-epoxy" dual-curing processing and the resulting SMPs.

- Sequential dual-curing processing using off-stoichiometric "thiol-epoxy" mixtures with an excess of epoxy has been successfully achieved by appropriately adjusting the curing conditions. The "thiol-epoxy" polycondensation takes place rapidly at low temperature leading to an intermediate, stable and processable material (1st curing stage), whereas the epoxy homopolymerization remains latent until the temperature is increased (2nd curing stage). The epoxy homopolymerization leads to a final and more rigid material.
- The physical properties of the intermediate material have been found strongly dependent on the "thiol-epoxy" ratio and both thiol an epoxy compounds. Each system has shown a gradient from liquid-like (low ratios) to solid-like intermediate materials with a critical liquid-to-solid "thiol-epoxy" ratio that mainly depends on the functionality of the system (the higher the functionality, the lower the ratio), but also is affected by other phenomenon, such as, intramolecular cyclization during the polymerization process. This ratio ensures the formation of a gelled structure after the 1st curing stage and therefore, the formation of a solid-like material with mechanical consistency. Assuming ideal step-growth behaviour, this ratio can be approached through the Flory-Stockmayer theory, however, rheological experiments have evidenced a displacement of this ratio towards higher values. This has been attributed to the presence of intramolecular cyclization, thus, a slight deviation from the ideal step-growth behaviour.
- The thermomechanical properties of both, the intermediate and final materials have been found dependent on both, the "thiol-epoxy" ratio and thiol and epoxy compounds. The intermediate materials range from uncrosslinked (liquid-like) materials with low T_g (-20 °C) up to moderately crosslinked materials (solid-like) with low rubbery modulus (< 3 MPa) and T_g ranging from 15 °C up to 40 °C. In contrast, the final materials are solid and rigid materials with T_g ranging from 50 °C up to 140 °C and rubbery modulus from 8 MPa up to 120 MPa. All

these temperatures have been efficiently approached using the Fox's law for copolymer networks.

- Complex shapes, such as, bent, plaited or spring shapes have been processed from the intermediate material and successfully fixed through the second curing stage by using the appropriate thiol-epoxy ratio, that is, a ratio equal or higher to the critical ratio to from a solid-like material.
- Shape-memory applications in both, the intermediate materials and final materials have been observed. Intermediate materials with T_g around 40 °C can be folded through shape-memory programming to reduce their volume for storage or transport steps in multi-stage applications. The original shape is further deployed by slightly increasing the temperature. The final material can be used as shape-memory mechanical actuator in a different mode than common uniaxial mode (i.e. bending or spring modes).
- Using bent samples, the capabilities as mechanical actuators under flexural mode have been extensively studied. The unconstrained recovery has shown a close relation to the network relaxation dynamics accordingly to the results obtained in category 1: the heterogeneity of the process has shown a strong impact on the recovery dynamics. Fully and partially-constrained recoveries have evidenced the higher influence of crosslinking density rather than the network relaxation, in the capability to release the energy stored as mechanical energy. The higher the crosslinking density, the higher the efficiency releasing this energy regardless the heterogeneity of the network relaxation. On the other hand, the effect of the thermal expansion has been evidenced in fully constrained experiments.

(3): Development and analysis of free-standing actuators using LCNs.

- A conceptual design for a free-standing actuator consisting of a multi-layered device containing a stretched LCN and layers of a "thiol-epoxy" glassy thermoset (GT) obtained via dual-curing has been proposed and successfully achieved.
- The free-standing actuator has been assembled using layers of the GT intermediate material and an already stretched LCN layer through a multilayer methodology. Different sandwich-like configurations (GT-LCN-GT) varying the thickness of the GT layers have been proposed to produce different flexural actuation processes. The device has been assembled through the second curing stage of the GT material, promoting the mixture of all the GT layers in a thick block and embedding the LCN with strong physical interactions. SEM analyses

demonstrated the high adhesion between layers due to the presence of crack propagation from the GT layers to the LCN layer in cryogenically fractures devices.

- The LCN has been specially-designed to fulfil the requirements of the free-standing actuator, that is, a controlled and stable SCE and a high T_{iso} (higher than both, the T_g of GT and the second T_c of the GT). For this purpose, an epoxy-based rod-like mesogen has been synthesized and the LCN has been obtained by using dicarboxylic acids with different aliphatic chain lengths as curing agents.
- The resulting LCNs have shown T_{iso} higher than 100 °C and controllable SCE with tailorable actuation strain and stress depending on the aliphatic chain length of the diacid and the load level. The degree of crystallinity and degree of order upon stretching have been found dependent on the aliphatic chain length: higher crystallinity and lower orientation were observed when the chain length was shorter. The strain actuation could be increased from 60% up to 160% by increasing the loading level and the chain length. The stress actuation showed considerably high values. Finally, the cycling stability have been found dependent on the load level and chain length, being higher with the increase of the chain length and the decrease of the load level.
- The free-standing actuators have been assembled with different programmed strain levels in the LCN layer and configurations (thickness of the different layers) resulting in free-standing flexural motion with high efficiency (no loosing of the permanent shape has been appreciated). In addition, an analytical model based on the theory for multi-layered beams subject to stress-free strains to predict the bending level in terms of angle of curvature and deflection achieved have been developed and validated through experimental results.

VI.2 Future Work

Every day, the human's scope enlarges, dealing with new horizons and therefore troubles. Technologies capable to reach such objectives demand, in many cases, **intelligent materials**, that is, materials that autonomously response to immediate necessities by changing their shape or properties. **AMPs** are responsive materials that can be designed to produce dimensional changes on-demand. In this doctoral thesis, AMPs capable to achieve complex shapes and return to the original shape in a controlled and reversible way have been developed. This has been called free-standing motion and is required in many applications where complex remote control is necessary to carry out tasks, such as, space applications

or rescue missions in remote places. Therefore, it is a must to enhance this concept of free-standing motion to develop AMPs capable to work upon different stimuli (i.e. light, pH change, magnetic fields and electrical source) to make possible patterning complex motion processes and to allow reshaping of the motion design. Overall, to develop dynamic free-standing AMPs capable of changing in response to the immediate necessities without human interaction.

We believe that the presented multilayer assembling methodology can be enhanced **to achieve dynamic and more autonomous AMPs**. For this purpose, we propose different lines of study: first, the development of different sequential curing systems and LCNs is necessary to accurately modulate the dimensional change; second, it is of utmost relevance to extend the analytical model to more complex motion designs and high actuation levels. Once the presented free-standing mechanism is completely defined and controlled, the focus is the incorporation and coordination of other materials in form of layers to the assembled device by taking advantage of the enhanced adhesion of the system. Here, we propose different materials:

- Incorporation of a **conductive net** or **oriented metallic fillers** makes possible to carry out the actuation by heating with an electrical current. This allows to focalize and control the heating in different sections of the device, thus, leading to a further control of the motion and the creation of complex patterns remotely controlled.
- Incorporation of **photo-responsive layers**, such as, azo-benzene based surfaces that can change upon irradiation with light producing patterned, high-frictional or optically-changing surfaces. The resulting device will be able to produce a large dimensional change combined with a surface change to achieve complex tasks. As an example, the increase of the surface friction combined with the movement of the material can serve to catch, hold and transport fragile objects.

In general, the possibility to mount a device with various responsive materials that are embedded in a controlled way opens the gate to the development of materials that response accordingly to the stimulus, hence, more autonomous and intelligent materials.

UNIVERSITAT ROVIRA I VIRGILI
DESIGN AND CHARACTERIZATION OF ACTIVELY-MOVING POLYMERS OBTAINED VIA DUAL-CURING PROCESSING
Alberto Francisco Belmonte Parra

Chapter VII

Appendices

VII

UNIVERSITAT ROVIRA I VIRGILI
DESIGN AND CHARACTERIZATION OF ACTIVELY-MOVING POLYMERS OBTAINED VIA DUAL-CURING PROCESSING
Alberto Francisco Belmonte Parra

VII.1 List of publications

1) Alberto Belmonte, Dailyn Guzmán, Xavier Fernández-Francos, Silvia De la Flor. "Effect of the Network Structure and Programming Temperature on the Shape-Memory Response of Thiol-Epoxy "Click" Systems". Polymers, **2015**, 7, 2146-2164.

2) Alberto Belmonte, Xavier Fernández-Francos, Silvia De la Flor, Àngels Serra. "Network structure dependence on unconstrained isothermal-recovery processes for shape-memory thiol-epoxy "click" systems". Mechanics of Time-Dependent Materials, **2016**, 21, 133-149.

3) Xavier Fernández-Francos, Ali-Osman Konuray, **Alberto Belmonte**, Silvia De la Flor, Àngels Serra, Xavier Ramis. "Sequential curing of off-stoichiometric thiol–epoxy thermosets with a custom-tailored structure". Polymer Chemistry, **2016**, 7, 2280-2290.

4) Alberto Belmonte, Xavier Fernández-Francos, Silvia De la Flor. "New understanding of the shape-memory response in thiol-epoxy click systems: towards controlling the recovery process". Journal of Materials Science, **2016**, 52 (3), 1625-1638.

5) Alberto Belmonte, Xavier Fernández-Francos, Àngels Serra, Silvia De la Flor. "Phenomenological characterization of sequential dual-curing of off-stoichiometric "thiol-epoxy" systems: Towards applicability". Materials and Design, **2017**, 113, 116-127.

6) Alberto Belmonte, Claudio Russo, Verónica Ambrogi, Xavier Fernández-Francos, Silvia De la Flor. "Epoxy-based shape-memory actuators obtained via dual-curing of off-stoichiometric "thiol-epoxy" mixtures". Polymers, **2017**, 9 (3), 113.

7) Alberto Belmonte, Giuseppe C. Lama, Gennaro Gentile, Xavier Fernández-Francos, Silvia De la Flor, Pierfrancesco Cerruti, Veronica Ambrogi. "Synthesis and Characterization of Liquid-Crystalline Networks: Toward Autonomous Shape-Memory Actuation". Journal of Physical Chemistry C, **2017**, 121 (40), 22403-22414.

8) Alberto Belmonte, Giuseppe C. Lama, Gennaro Gentile, Pierfrancesco Cerruti, Veronica Ambrogi, Xavier Fernández-Francos, Silvia De la Flor. "Thermally-triggered free-standing shape-memory actuators". European Polymer Journal, **2017**, 97, 241-252.

VII.2 Related publications

1) Alberto Belmonte, Frank Däbritz, Xavier Ramis, Àngels Serra, Brigitte Voit, Xavier Fernández-Francos. "Cure kinetics modeling and thermomechanical properties of cycloaliphatic epoxy-anhydride thermosets modified with hyperstar polymers". Journal of Polymer Science. Part B: Polymer Physics, **2014**, 52 (18), 1227-1242.

VII.3 Contributions

1) Alberto Belmonte, Dailyn Guzmán, Xavier Fernández-Francos, Silvia De la Flor. *"Thiol-epoxy thermosets with enhanced shape-memory performance"*. European Polymer Federation Congress, Dresden, Germany, **2015** (June 21th-26th). **(Oral presentation)**.

2) Alberto Belmonte, Albert Fabregat-Sanjuan, Xavier Fernández-Francos, Silvia De la Flor. "*Novel Shape Memory Thermosets with Enhanced Mechanical Properties for Actuator-like Applications*". International Conference on Materials Design and Applications. Oporto, Portugal, **2016** (June 30th-July 1st) **(Oral presentation)**.

3) Alberto Belmonte, Xavier Fernández-Francos, Silvia De la Flor, Àngels Serra. *"Thermomechanical and rheological characterization of "thiol-epoxy" dual-curing systems for smart applications".* Grupo Especializado en Polímeros, Burgos, Spain, **2016** (September 5th-8th) **(Oral presentation)**.

4) Alberto Belmonte, Xavier Fernández-Francos, Silvia De la Flor. *"Characterization of sequential dual-curing thiol-epoxy systems: processing and shape-memory applications".*

International Conference on Nanostructured Polymers and Nanocomposites, Rome, Italy, **2016** (September 19th-21th) **(Poster presentation)**.

5) Silvia De la Flor, **Alberto Belmonte**, Albert Fabregat-Sanjuan, Caue Guimares, Vicente Lorenzo, Xaiver Fernández-Francos, *Análisis de las propiedades mecánicas de polímeros con memoria de forma mediante microdureza instrumentada*. XXI Congreso Nacional de Ingeniería Mecánica, Elche, Spain, **2016** (November 9th-11th) **(Oral presentation)**.

6) Alberto Belmonte, Giuseppe C. Lama, Xavier Fernández-Francos, Gennaro Gentile, Pierfrancesco Cerruti, Veronica Ambrogi, Silvia De la Flor. *"Characterization of shape-memory liquid-crystalline elastomers towards autonomous actuation".* Jóvenes Investigadores en Polímeros, Tarragona, Spain, **2017** (Junio 5th-8th) **(Oral presentation)**.

7) Alberto Belmonte, Giuseppe C. Lama, Xavier Fernández-Francos, Gennaro Gentile, Pierfrancesco Cerruti, Veronica Ambrogi, Silvia De la Flor. *"Thermally-triggered autonomous shape-memory actuators".* European Polymer Federation Congress, Lyon, France, **2017** (Julio 2nd-7th) **(Oral presentation)**.

8) Alberto Belmonte, Xavier Fernández-Francos, Silvia De la Flor. *"Thermomechanical characterization of Thiol-epoxy Shape Memory thermosets for mechanical actuators design"*. Key Note Lecture. 7th International Conference on Structural Analysis of Advanced Materials, Bucharest, Romania, **2017** (September 19th-22nd) **(Oral presentation)**.

9) Silvia De la Flor, **Alberto Belmonte**, Xavier Fernández-Francos, Àngels Serra. "*Sistemas duales tiol-epoxy: optimizacion de sus aplicaciones funcionales y de memoria de forma"*. XIII Congresso Ibero-Americano de Engenharia Mecânica. Universidade NOVA de Lisboa, Lisboa, Portugal, **2017** (October 23rd-26th) **(Oral presentation)**.

VII.4 Internship

Period: September 2016 – December 2016.

Country/City: Italy (Napoli).

Center: Universitá degli studi di Napoli Federico II, Dipartimento di Ingegneria Chimica, dei Materiali e della Produzione Industriale.

Advisor: Veronica Ambrogi

Work developed: Synthesis and characterization of liquid-crystalline network for the designment of free-standing actuators. Preliminary evaluation of the feasibility of the free-standing actuators.

VII.5 List of Figures

VII.6 List of Tables